

**Effect of Heat Exchanger Volume and Geometry on Power Output of a Low Temperature  
Difference Stirling Engine**

by

Linda Hasanovich

A thesis submitted in partial fulfillment of the requirements for the degree of

Master of Science

Department of Mechanical Engineering  
University of Alberta

## **Abstract**

This work presents the results of an investigation into heat exchanger design for low temperature difference Stirling engines (LTDSEs). The aim of this study was to determine if there is an optimum heat exchanger geometry for producing maximum power output for a LTDSE. There are multiple factors that affect the optimum heat exchanger geometry: the gas temperature achieved by the heat exchangers, the pressure drop through the heat exchangers, and the effect of dead volume on the pressure achieved by the Stirling cycle. This study was undertaken using several models based on an experimental LTDSE.

A fundamental analysis using analytical and empirical relations for steady state heat transfer through a heat exchanger with isothermal walls showed that the output temperature of the gas is dependent on heat exchanger surface area regardless of aspect ratio. Additionally, long heat exchangers and heat exchangers with small cross-sectional area led to large pressure drops through the heat exchanger. To evaluate the effect of dead volume on output power, the Schmidt model was used. The results confirmed that the engine power output decreased with increasing dead volume ratio. The Schmidt model was used to determine a maximum optimal dead volume ratio, below which the peak power output with an optimal heat exchanger volume must be located.

To determine the optimum heat exchanger volume and geometry the 3<sup>rd</sup> order commercial Stirling engine model, Sage, was used. Sage is able to model the heat transfer in the heat exchangers and the effect on the engine gas during the cycle. A model was created in Sage based on the experimental LTDSE. This model needed to connect the liquid source and sink of the heat exchangers to the gas within the engine. This was done using a temperature drop determined by a

convective heat transfer resistance of the liquid. To determine this resistance, a multi-fluid steady state CFD study was done in the absence of experimental data in order to capture the interaction between the air and liquid in the heat exchanger. From this study, an average convective heat transfer resistance was able to be determined.

With the convective heat transfer resistance obtained the Sage model was validated against the experimental LTDSE results. Sage was found to generally agree with the experimental results, but showed overprediction and an increased dependence on speed that was not present in the experimental results. Some model tuning was done to improve the model results. The overprediction was able to be reduced by tuning the convective heat transfer to match the model gas temperatures to the experiment. The dependence of the model output power on engine speed was reduced by reducing the flow friction multiplier, which changed the phase of the pressure curve. However, this led to increased overprediction, so it was not included in the final version of the Sage model.

Using the model with tuned convective heat transfer resistance, the heat exchanger geometry was varied by changing the heat exchanger length and cross-sectional area. An optimum heat exchanger geometry was determined. This optimum geometry was at the shortest heat exchanger length with a large cross-sectional area. To maximize the power output, the surface area of the heat exchanger needs to be maximized while keeping pressure drop through the heat exchanger low and not contributing excess dead volume to the engine.

Some sensitivities were considered to better understand this result. When the engine pressure and speed were varied, it was found that the optimum heat exchanger geometry was larger for high speed and high pressure cases, as the heat transfer requirement increased. Additional dead

volume that scaled with the heat exchanger volume was added to represent a plenum volume that connects the heat exchangers to the main engine volume. The optimum heat exchanger geometry in this case had a longer heat exchanger with smaller cross-sectional area. This results from the excess dead volume associated with a large cross-sectional area having a more significant penalty than the benefit of low pressure drop through the heat exchanger. Finally, the compression ratio of the engine was held constant, and it was found that a larger heat exchanger was required, and the effect of excess dead volume on engine output power was reduced.



## Preface

This thesis is an original work by Linda Hasanovich. Aspects of this research have been published in the following conference publications:

L. Hasanovich and D. S. Nobes, “Investigations Into The Effect Of Heat Exchanger Volume And Geometry On Low-Temperature Stirling Engine Performance,” in *Progress in Canadian Mechanical Engineering*, Charlottetown, PEI, Canada, 2021, vol. 4. doi: 10.32393/csme.2021.170.

L. Hasanovich and D. S. Nobes, “Investigation of effect of heat exchanger size on power output in low-temperature difference Stirling engines,” in *19th International Stirling Engine Conference*, Rome, Italy, Sep. 2021, p. 14. doi: <https://doi.org/10.1051/e3sconf/202131303002>.

The author also contributed to conceptual design presented in the following publications. These contributions did not directly contribute to this thesis.

M. Lottmann, Z. de Rouyan, L. Hasanovich, S. M. W. Middleton, M. Nicol-Seto, C. Speer and D. S. Nobes, “Early Development of a 100 Watt Low Temperature Difference Stirling Engine,” in *Progress in Canadian Mechanical Engineering*, Charlottetown, PEI, Canada, Jun. 2021, p. 6. doi: 10.32393/csme.2021.193.

M. Lottmann, Z. de Rouyan, L. Hasanovich, S. Middleton, M. Nicol-Seto, C. Speer and D. S. Nobes, “Development of a 100-Watt-Scale Beta-Type Low Temperature Difference Stirling Engine Prototype,” in *19th International Stirling Engine Conference*, Rome, Italy, Sep. 2021, p. 15. doi: <https://doi.org/10.1051/e3sconf/202131308004>.

# Acknowledgements

The author appreciates the assistance of their supervisor,

Dr. David S. Nobes

friends and colleagues in the Dynamic Thermal Energy Conversion Laboratory,

Connor Speer

Jason Michaud

David Miller

Calynn Stumpf

Steven Middleton

Michael Nicol-Seto

Matthias Lottmann

co-op students, volunteers, friends and family that helped make this project a success.

Financial support for this research was provided by the following funding bodies:

Natural Sciences and Engineering Research Council (NSERC) of Canada

Alberta Innovates Energy and Environment Solutions

Future Energy Systems (FES)

# Table of Contents

Abstract .....	ii
Preface.....	v
Acknowledgements.....	vi
Table of Contents.....	vii
List of Tables .....	xii
List of Figures .....	xiii
List of Symbols and Abbreviations.....	xxv
1 Introduction.....	1
1.1 Motivation .....	1
1.2 Introduction to Stirling Engines .....	3
1.2.1 Ideal Stirling Cycle .....	3
1.2.2 Stirling Engine Components .....	7
1.2.3 Practical Stirling Cycle .....	9
1.2.4 Compression Ratio.....	11
1.2.5 Dead Volume .....	11
1.2.6 Appendix Gap .....	11
1.3 Effects of Dead Volume.....	12
1.4 Stirling Engine Thermodynamic Models .....	14
1.4.1 1 <sup>st</sup> Order Models .....	14
1.4.2 2 <sup>nd</sup> Order Models.....	15
1.4.3 3 <sup>rd</sup> Order Models.....	15
1.4.4 Computational Fluid Dynamics Modelling .....	16
1.4.5 Model Selection .....	17
1.5 Thesis Objectives and Structure.....	18

2	Experimental Engine Description and Results .....	19
2.1	ST05G-CNC and Modifications for Low Temperature .....	19
2.1.1	ST05G in the Literature .....	20
2.1.2	Summary of Modifications to ST05G-CNC .....	22
2.2	Experimental Engine Description .....	24
2.2.1	Description of Heat Exchanger Design.....	25
2.3	Summary of Experimental Setup .....	29
2.3.1	Engine Operation Control.....	29
2.3.2	Engine Instrumentation.....	31
2.3.3	Data Acquisition System.....	33
2.3.4	Calibration and Experimental Procedures .....	33
2.4	Summary of Key Experimental Results.....	35
3	Fundamentals Analysis of Heat Exchanger Size .....	39
3.1	Examination of Heat Transfer in Steady State Conditions .....	39
3.1.1	Analysis Assumptions.....	39
3.1.2	Definition of Geometry and Flow Conditions .....	40
3.1.3	Sensitivity Parameter Selection .....	42
3.1.4	Procedure for Determination of Output Temperature and Pressure Drop .....	43
3.1.5	Results for Fixed Engine Pressure and Speed for Heating Case .....	52
3.1.6	Results from Engine Pressure and Speed Sensitivity for Heating Case .....	59
3.1.7	Summary of Results for the Cooling Case.....	64
3.2	Schmidt Model Evaluation of Effect of Dead Volume .....	67
3.2.1	Schmidt Model as derived by Senft.....	70
3.2.2	Schmidt Model derived from Isothermal Model .....	73
3.2.3	Parameter Selection for Schmidt Model Study.....	75

3.2.4	Base Results for Schmidt Model Study .....	78
3.2.5	Sensitivity Results for Schmidt Model Study .....	81
3.3	Conclusions .....	82
4	Sage Software and Validation Model Setup .....	83
4.1	Description of Sage Software .....	83
4.1.1	Description of Model Components .....	84
4.1.2	Thermodynamic Modelling of Gas in Sage .....	85
4.1.3	Energy Transfer Modelling in Solids in Sage .....	88
4.1.4	Description of Sage Discretization and Solver .....	89
4.2	Model Setup for Validation .....	91
4.2.1	Model Component and Connections Selection and Assumptions .....	91
4.2.2	Summary of Model Inputs .....	94
4.2.3	Implementation of Convective Heat Transfer Resistance .....	96
4.2.4	Conclusions .....	97
5	Determination of Input Parameters for Stirling Engine Modelling Using CFD .....	98
5.1	Model Setup and Assumptions .....	98
5.1.1	General Simulation Parameters .....	99
5.1.2	Computational Domain and Model Geometry .....	99
5.1.3	Boundary Conditions .....	101
5.1.4	Initial Conditions .....	104
5.1.5	Convergence Parameters .....	104
5.2	Mesh Independence Study and Setup .....	105
5.2.1	Model Setup for Air Side Mesh Independence Study .....	105
5.2.2	Model Setup for Liquid Side Mesh Independence Study .....	107
5.2.3	Air Side Mesh Independence Results .....	108

5.2.4	Liquid Side Mesh Independence Results .....	110
5.2.5	Discussion on Final Mesh Setup.....	112
5.3	CFD Model Validation against Analytical Results .....	113
5.3.1	Air Side Model Validation Model Setup .....	113
5.3.2	Liquid Side Model Validation Model Setup.....	115
5.3.3	Description of Analytical Solution for Air Flow .....	116
5.3.4	Description of Analytical Solution for Liquid Flow.....	118
5.3.5	Air Side Numerical and Analytical Result Comparison .....	122
5.3.6	Liquid Side Numerical and Analytical Result Comparison.....	133
5.3.7	Conclusions.....	142
5.4	Results for Input Parameters for Stirling Model .....	143
5.4.1	Thermal Resistance Results .....	143
5.4.2	Fluid Temperature Modelling for 3 <sup>rd</sup> Order Model .....	149
5.4.3	Application of Results for 3 <sup>rd</sup> Order Model .....	150
5.5	Conclusions .....	151
6	Sage Model Validation Results.....	152
6.1	Mesh Independence Study and Setup.....	152
6.2	Validation Results of Non-tuned Model Parameters.....	157
6.3	Investigation of Tuning Parameters on Validation Results.....	167
6.3.1	Convective Heat Transfer Resistance .....	167
6.3.2	Flow Friction Multiplier .....	174
6.4	Conclusions .....	180
7	Effect of Heat Exchanger Geometry on Power Output using Sage .....	181
7.1	Sage Model Setup for Heat Exchanger Study .....	181
7.1.1	Manipulated Variables .....	181

7.1.2	Sensitivity Cases .....	182
7.2	Results of Heat Exchanger Volume Variation Study.....	185
7.3	Results of Engine Speed and Pressure Sensitivity .....	192
7.4	Results with Plenum Dead Volume .....	203
7.5	Constant Compression Ratio Results .....	209
7.6	Conclusions .....	214
8	Conclusions and Future Work .....	215
8.1	Conclusions .....	215
8.2	Future Work .....	218
	References.....	219
Appendix A	Raphael Engine Drawing Package .....	228
Appendix B	MATLAB Code for Analytical Analysis and Schmidt Model.....	247
Appendix C	Steady State Heat Transfer Base Case Results for Cooling.....	299
Appendix D	Steady State Heat Transfer Sensitivity Results for Cooling .....	302
Appendix E	Schmidt model derivation for Gamma type Stirling Engines .....	305
Appendix F	Sensitivity Results from Schmidt Model Evaluation .....	311
Appendix G	Summary of Sage Model Inputs.....	319
Appendix H	Heat Exchanger Liquids Properties.....	331
Appendix I	CFD Air Side Temperature Validation Cooling Cases.....	335

## List of Tables

Table 2.1. Engine Volumes of Raphael Engine .....	25
Table 2.2. Raphael Engine Heat Exchanger Geometry .....	27
Table 2.3. Heat Transfer Fluids and Set Points .....	29
Table 2.4. Raphael Engine Instrumentation.....	32
Table 3.1. Constant Heat Exchanger Properties for Rectangular Channel Analysis.....	40
Table 3.2. Varied Heat Exchanger Properties for Rectangular Channel Analysis.....	41
Table 3.3. Sensitivity Cases Conditions for Engine Pressure and Speed .....	43
Table 3.4. Varied Properties for Schmidt Model Evaluation.....	77
Table 4.1. Summary of geometric engine properties inputted into Sage model.....	95
Table 4.2. Summary of engine materials inputted into Sage model.....	96
Table 5.1. Summary of mesh parameters for air side mesh independence study.....	108
Table 5.2. Summary of mesh parameters for liquid side mesh independence study.....	110
Table 5.3. Sensitivity Cases Conditions for Liquid Side Heating CFD Validation.....	116
Table 5.4. Sensitivity Cases Conditions for Liquid Side Cooling CFD Validation .....	116
Table 5.5. Summary of output variables for simplified liquid model validation.....	141
Table 6.1. Number of spatial cells in Sage model components.....	155
Table 7.1. Varied Heat Exchanger Properties for Sage Analysis.....	182
Table G.1 Temperature dependent properties of aluminum 6061 alloy inputted into Sage model. .....	327
Table H.1 Measured Density of SIL180 at varying temperatures.....	332
Table H.2 Estimated Specific Heat Capacity of SIL180 at varying temperatures.....	333



# List of Figures

Figure 1.1: PV diagram of the ideal Stirling cycle processes, with cycle work shown.....	3
Figure 1.2: Indicated work of ideal Stirling cycle on a PV diagram .....	6
Figure 1.3: Simplified Gamma-type Stirling engine components .....	7
Figure 1.4: Ideal Stirling cycle steps with real engine components .....	9
Figure 1.5: Indicated work of a practical Stirling cycle within the ideal Stirling cycle on a PV diagram. ....	10
Figure 2.1: Partial section view of ST05G-CNC model.....	20
Figure 2.2: Partial section view of ST05G-CNC model following modifications for operation at lower source temperature.....	23
Figure 2.3: Partial section view of the Raphael engine with main components annotated. ....	24
Figure 2.4: (a) Cross-section of heat exchanger assembly of Raphael engine. (b) Cross-section of heat exchanger cartridge highlighting flow paths. ....	26
Figure 2.5: Piping and instrumentation diagram of charge pressure system.....	30
Figure 2.6: Location of instrumentation used on Raphael engine. ....	31
Figure 2.7: Schematic of engine instrumentation and data acquisition system.....	33
Figure 2.8: A sample PV diagram for the working space determined from experimental data. ..	36
Figure 2.9: Plot of measured indicated work against measured engine speed for various engine operating pressures.....	37
Figure 2.10: Plot of measured indicated power against measured engine speed for various engine operating pressures.....	38
Figure 3.1: Schematic of varying heat exchanger geometry showing (a) a narrow and long heat exchanger and (b) a wide and short heat exchanger. ....	42
Figure 3.2: Flowchart describing calculation steps for determination of exit temperature and pressure drop through a rectangular channel. ....	51
Figure 3.3: Plot of exit gas temperature against heat exchanger volume for various channel lengths considered at an engine speed of 2.833 Hz and engine pressure of 435 kPa for heating. 52	
Figure 3.4: Plot of exit gas temperature against Reynolds number for various channel lengths considered at an engine speed of 2.833 Hz and engine pressure of 435 kPa for heating. ....	53

Figure 3.5: Plot of exit gas temperature against heat exchanger surface area for various channel lengths considered at an engine speed of 2.833 Hz and engine pressure of 435 kPa for heating.	54
Figure 3.6: Plot of Reynolds number against heat exchanger volume for various channel lengths considered at an engine speed of 2.833 Hz and engine pressure of 435 kPa for heating. ....	56
Figure 3.7: Plot of pressure drop against heat exchanger volume for various channel lengths considered at an engine speed of 2.833 Hz and engine pressure of 435 kPa for heating. ....	57
Figure 3.8: Plot of pressure drop against Reynolds number for various channel lengths considered at an engine speed of 2.833 Hz and engine pressure of 435 kPa for heating. ....	58
Figure 3.9: Plot of exit gas temperature against heat exchanger volume for various channel lengths considered at varying engine pressure and speeds for heating. ....	59
Figure 3.10: Plot of exit gas temperature against Reynolds number for various channel lengths considered at varying engine pressures and speeds for heating. ....	60
Figure 3.11: Plot of exit gas temperature against heat exchanger surface area for various channel lengths considered at varying engine pressures and speeds for heating. ....	61
Figure 3.12: Plot of Reynolds number against heat exchanger volume for various channel lengths considered at varying engine pressures and speeds for heating. ....	61
Figure 3.13: Plot of pressure drop against heat exchanger volume for various channel lengths considered at varying engine pressures and speeds for heating. ....	62
Figure 3.14: Plot of pressure drop against Reynolds number for various channel lengths considered at varying engine pressures and speeds for heating. ....	63
Figure 3.15: Plot of transitional regime results of exit gas temperature against Reynolds number for various channel lengths considered at an engine speed of 4.000 Hz and engine pressure of 570 kPa for the cooling case. ....	64
Figure 3.16: Plot of transitional regime results of exit gas temperature against heat exchanger surface area for various channel lengths considered at an engine speed of 4.000 Hz and engine pressure of 570 kPa for cooling. ....	65
Figure 3.17: Plot of transitional regime results of pressure drop against Reynolds number for various channel lengths considered at an engine speed of 4.000 Hz and engine pressure of 570 kPa for cooling. ....	66
Figure 3.18: Isothermal model spaces and temperature profile. Figure adapted from Urieli and Berchowitz [20]. ....	67

Figure 3.19: Plot of power output calculated by Senft’s derivation for Gamma engine Schmidt model against DV ratio for various hot and cold side temperatures at an engine pressure of 435 kPa and engine speed of 2.833 Hz. ....	78
Figure 3.20: Plot of power output calculated from isothermal derivation of Schmidt model for Gamma engines against DV ratio for various hot and cold side temperatures at an engine pressure of 435 kPa and engine speed of 2.833 Hz. ....	79
Figure 4.1: Schematic showing segmentation of experimental engine into Sage model components. ....	91
Figure 4.2: Screenshot of Sage model interface showing top-level components and connections. ....	92
Figure 4.3: Schematic of Sage model components and heat and mass flow connections of sub-models. ....	92
Figure 5.1: Definition of computational domain relative to geometry. ....	100
Figure 5.2: Visualization of liquid and gas fluid subdomains. ....	101
Figure 5.3: Location of various boundary conditions in model geometry. ....	102
Figure 5.4: Figure showing air side axisymmetric model slice for mesh independence study with boundary conditions. ....	106
Figure 5.5: Figure showing liquid side symmetric model for mesh convergence with boundary conditions. ....	107
Figure 5.6: Plot of normalized air side convergence parameters against number of cells in mesh for the heating case. ....	109
Figure 5.7: Plot of normalized air side convergence parameters against number of cells in mesh for the cooling case. ....	109
Figure 5.8: Plot of normalized liquid side convergence parameters against number of cells in mesh for the heating case. ....	111
Figure 5.9: Plot of normalized liquid side convergence parameters against number of cells in mesh for the cooling case. ....	111
Figure 5.10: Figure showing mesh cut plot in the (a) horizontal and (b) vertical planes of the air side simulation with cells coloured by refinement level. ....	114
Figure 5.11: Figure showing mesh cut plot in the (a) horizontal and (b) vertical planes of the liquid side simulation with cells coloured by refinement level. ....	115

Figure 5.12: Plot of solid temperature determined from analytical solution and simulation for varying engine pressure and speed for the heating case. ....	122
Figure 5.13: Plot of absolute value solid temperature difference between analytical solution and simulation for varying engine pressure and speed for the heating case.....	123
Figure 5.14: Plot of exit air temperature determined from analytical solution and simulation for varying engine pressure and speed for the heating case. ....	124
Figure 5.15: Plot of absolute value exit temperature difference between analytical solution and simulation for varying engine pressure and speed for the heating case.....	125
Figure 5.16: Contour plot of solid temperature in the air side fins for the heating case showing (a) horizontal sections at the top, middle, and bottom of the liquid channel indicated in (b) the vertical section. ....	126
Figure 5.17: Plot of exit air temperature determined from analytical solution using simulation solid temperatures and simulation solution for varying engine pressure and speed for the heating case.....	127
Figure 5.18: Plot of absolute value exit air temperature difference between analytical solution using simulation solid temperature and simulation solution for varying engine pressure and speed for the heating case. ....	128
Figure 5.19: Plot of air pressure drop determined from analytical solution and simulation for varying engine pressure and speed for the heating case. ....	129
Figure 5.20: Plot of air pressure drop determined from analytical solution and simulation for varying engine pressure and speed for the cooling case. ....	130
Figure 5.21: Plot of absolute value air pressure drop difference between analytical solution and simulation for varying engine pressure and speed for the heating case.....	131
Figure 5.22: Plot of absolute value air pressure drop difference between analytical solution and simulation for varying engine pressure and speed for the cooling case. ....	131
Figure 5.23: Plot of liquid exit temperature determined from analytical solution and simulation for varying mass flow rate and isothermal surface temperature for the heating case.....	133
Figure 5.24: Plot of absolute value liquid exit temperature difference between analytical solution and simulation for varying mass flow rate and isothermal surface temperature for the heating case.....	134

Figure 5.25: Plot of liquid pressure drop determined from analytical solution and simulation varying mass flow rate and isothermal surface temperature for the heating case. ....	135
Figure 5.26: Plot of absolute value liquid pressure drop difference between analytical solution and simulation for varying mass flow rate and isothermal surface temperature for the heating case.....	136
Figure 5.27: Plot of liquid exit temperature determined from analytical solution and simulation varying mass flow rate and isothermal surface temperature for the cooling case. ....	137
Figure 5.28: Plot of absolute value liquid exit temperature difference between analytical solution and simulation for varying mass flow rate and isothermal surface temperature for the cooling case.....	137
Figure 5.29: Plot of liquid pressure drop determined from analytical solution and simulation for varying mass flow rate and isothermal surface temperature for the cooling case. ....	138
Figure 5.30: Plot of absolute value liquid pressure drop difference between analytical solution and simulation for varying mass flow rate and isothermal surface temperature for the cooling case.....	139
Figure 5.31: Figure showing simplified liquid side model slice for validation with boundary conditions.....	140
Figure 5.32: Plot of average thermal resistance for heating case against engine pressure for varying engine speeds. ....	144
Figure 5.33: Plot of average thermal resistance for cooling case against engine pressure for varying engine speeds. ....	145
Figure 5.34: Plot of heat flow against engine pressure for varying engine speeds for both the heating and cooling cases.....	146
Figure 5.35: Plot of average solid surface temperature against engine pressure for varying engine speeds for both the heating and cooling cases. ....	147
Figure 5.36: Plot of average liquid temperature against engine pressure for varying engine speeds for both the heating and cooling cases.....	147
Figure 5.37: Plot of normalized heat flow and temperature difference against engine pressure for varying engine speeds for both the heating and cooling cases. ....	148
Figure 5.38: Plot of normalized heat flow and temperature difference against engine speed for varying engine pressures for both the heating and cooling cases. ....	149

Figure 6.1: Plot of indicated work calculated by Sage model against number of time nodes for initial spatial node distribution.....	153
Figure 6.2: Plot of indicated work calculated by Sage model against number of spatial nodes for the cylinder space components for 13 time nodes. ....	154
Figure 6.3: Plot of indicated work calculated by Sage model against number of spatial nodes for the heat exchanger and regenerator components for 13 time nodes. ....	155
Figure 6.4: Plot of indicated work calculated by Sage model against number of time nodes for final spatial node distribution.....	156
Figure 6.5: Plot of experimental indicated work and modelled indicated work determined by Sage for various pressures against engine speed. ....	158
Figure 6.6: Plot of percent difference between experimental and modelled indicated work determined by Sage for various pressures against engine speed. ....	159
Figure 6.7: Plot of experimental indicated power and modelled indicated power determined by Sage for various pressures against engine speed. ....	160
Figure 6.8: Plot of percent difference between experimental and modelled indicated power determined by Sage for various pressures against engine speed. ....	160
Figure 6.9: Plot of experimental expansion space gas temperature and modelled expansion space gas temperature determined by Sage for various pressures against engine speed.....	161
Figure 6.10: Plot of experimental compression space gas temperature and modelled compression space gas temperature determined by Sage for various pressures against engine speed. ....	162
Figure 6.11: Plot of experimental power cylinder pressure swing and modelled power cylinder pressure swing determined by Sage for various pressures against engine speed. ....	163
Figure 6.12: Plot of experimental power cylinder pressure phase and modelled power cylinder pressure phase determined by Sage for various pressures against engine speed.....	164
Figure 6.13: PV diagram for expansion, compression, and power cylinder space determined by Sage for low pressure high speed data point.....	165
Figure 6.14: PV diagram for expansion, compression, and power cylinder space determined by Sage for low pressure high speed data point, with shifted pressure curves to match experiment pressure phase. ....	165

Figure 6.15: Plot of experimental expansion space gas temperature and modelled expansion space gas temperature determined by Sage with tuned resistances for various pressures against engine speed.....	168
Figure 6.16: Plot of experimental compression space gas temperature and modelled compression space gas temperature determined by Sage with tuned resistances for various pressures against engine speed.....	168
Figure 6.17: Plot of experimental indicated work and modelled indicated work determined by Sage with tuned resistances for various pressures against engine speed. ....	169
Figure 6.18: Plot of percent difference between experimental and modelled indicated work determined by Sage with tuned resistances for various pressures against engine speed. ....	170
Figure 6.19: Plot of experimental indicated power and modelled indicated power determined by Sage with tuned resistances for various pressures against engine speed. ....	171
Figure 6.20: Plot of percent difference between experimental and modelled indicated power determined by Sage with tuned resistances for various pressures against engine speed. ....	171
Figure 6.21: Plot of experimental power cylinder pressure swing and modelled power cylinder pressure swing determined by Sage with tuned resistances for various pressures against engine speed. ....	172
Figure 6.22: Plot of experimental power cylinder pressure phase and modelled power cylinder pressure phase determined by Sage with tuned resistances for various pressures against engine speed. ....	173
Figure 6.23: Plot of experimental indicated work and modelled indicated work determined by Sage with different tuned parameters for various pressures against engine speed. ....	175
Figure 6.24: Plot of percent difference between experimental and modelled indicated work determined by Sage with different tuned parameters for various pressures against engine speed. ....	176
Figure 6.25: Plot of experimental indicated power and modelled indicated power determined by Sage with different tuned parameters for various pressures against engine speed. ....	177
Figure 6.26: Plot of difference between experimental and modelled indicated power determined by Sage with different tuned parameters for various pressures against engine speed. ....	177

Figure 6.27: Plot of experimental expansion space gas temperature and modelled expansion space gas temperature determined by Sage with different tuned parameters for various pressures against engine speed. ....	178
Figure 6.28: Plot of experimental compression space gas temperature and modelled compression space gas temperature determined by Sage with different tuned parameters for various pressures against engine speed. ....	179
Figure 7.1: Plot of indicated power from Sage against dead volume ratio for (a) various heat exchanger lengths and (b) various numbers of heat exchanger channels. ....	186
Figure 7.2: Plot of power output from Sage against dead volume ratio for various heat exchanger lengths over an extended range of dead volume ratio.....	187
Figure 7.3: Plot of average gas temperature difference between the expansion and compression space against dead volume ratio for various heat exchanger lengths. ....	188
Figure 7.4: Plot of average gas temperature difference between the expansion and compression space against gas side heat exchanger surface area for various heat exchanger lengths. ....	188
Figure 7.5: Plot of compression space pressure swing against dead volume ratio for various heat exchanger lengths.....	189
Figure 7.6: Plot of difference in expansion and compression space pressure swings against dead volume ratio for (a) various heat exchanger lengths and (b) various numbers of heat exchanger channels.....	191
Figure 7.7: Plot of indicated power from Sage against dead volume ratio for various heat exchanger lengths at varying speeds and pressures. ....	193
Figure 7.8: Plot of indicated power from Sage against dead volume ratio for various numbers of heat exchanger channels at varying speeds and pressures. ....	194
Figure 7.9: Plot of indicated work from Sage against dead volume ratio for various heat exchanger lengths at varying speeds and pressures. ....	195
Figure 7.10: Plot of indicated work from Sage against dead volume ratio for various numbers of heat exchanger channels at varying speeds and pressures. ....	196
Figure 7.11: Plot of average gas temperature difference against dead volume ratio for various heat exchanger lengths at varying speeds and pressures. ....	198
Figure 7.12: Plot of pressure swing difference against dead volume ratio for various heat exchanger lengths at varying speeds and pressures. ....	200



Figure 7.13: Plot of pressure swing difference against dead volume ratio for various heat exchanger lengths at varying speeds and pressures. ....	201
Figure 7.14: Plot of indicated power from Sage with additional scaled dead volume against dead volume ratio for (a) various heat exchanger lengths and (b) various numbers of heat exchanger channels.....	204
Figure 7.15: Plot of indicated power from Sage with additional scaled dead volume against dead volume ratio for various short heat exchanger lengths. ....	205
Figure 7.16: Plot of average gas temperature difference between expansion and compression space from Sage with additional scaled dead volume against dead volume ratio for various heat exchanger lengths.....	206
Figure 7.17: Plot of indicated power from Sage with increased additional scaled dead volume against dead volume ratio for (a) various heat exchanger lengths and (b) various numbers of heat exchanger channels. ....	207
Figure 7.18: Zoomed in plot of indicated power from Sage with increased additional scaled dead volume against dead volume ratio for various heat exchanger lengths. ....	208
Figure 7.19: Plot of compression ratio against dead volume ratio for base case heat exchanger geometry study.....	209
Figure 7.20: Plot of indicated power from Sage with constant compression ratio against dead volume ratio for (a) various heat exchanger lengths and (b) various numbers of heat exchanger channels.....	210
Figure 7.21: Plot of average gas temperature difference between expansion and compression spaces from Sage at constant compression ratio against dead volume ratio for various heat exchanger lengths.....	211
Figure 7.22: Plot of difference in expansion and compression space pressure swings from Sage at constant compression ratio against dead volume ratio for (a) various heat exchanger lengths and (b) various numbers of heat exchanger channels.....	212
Figure C.1: Plot of exit gas temperature against heat exchanger volume for various channel lengths considered at an engine speed of 2.833 Hz and engine pressure of 435 kPa for cooling. ....	299
Figure C.2: Plot of exit gas temperature against Reynolds number for various channel lengths considered at an engine speed of 2.833 Hz and engine pressure of 435 kPa for cooling. ....	299

Figure C.3: Plot of exit gas temperature against heat exchanger surface area for various channel lengths considered at an engine speed of 2.833 Hz and engine pressure of 435 kPa for cooling. ....	300
Figure C.4: Plot of Reynolds number against heat exchanger volume for various channel lengths considered at an engine speed of 2.833 Hz and engine pressure of 435 kPa for cooling. ....	300
Figure C.5: Plot of pressure drop against heat exchanger volume for various channel lengths considered at an engine speed of 2.833 Hz and engine pressure of 435 kPa for cooling. ....	301
Figure C.6: Plot of pressure drop against Reynolds number for various channel lengths considered at an engine speed of 2.833 Hz and engine pressure of 435 kPa for cooling. ....	301
Figure D.1: Plot of exit gas temperature against heat exchanger volume for various channel lengths considered at varying engine pressure and speeds for cooling. ....	302
Figure D.2: Plot of exit gas temperature against Reynolds number for various channel lengths considered at varying engine pressures and speeds for cooling. ....	302
Figure D.3: Plot of exit gas temperature against heat exchanger surface area for various channel lengths considered at varying engine pressures and speeds for cooling. ....	303
Figure D.4: Plot of Reynolds number against heat exchanger volume for various channel lengths considered at varying engine pressures and speeds for cooling. ....	303
Figure D.5: Plot of pressure drop against heat exchanger volume for various channel lengths considered at varying engine pressures and speeds for cooling. ....	304
Figure D.6: Plot of pressure drop against Reynolds number for various channel lengths considered at varying engine pressures and speeds for cooling. ....	304
Figure F.1: Plot of power output calculated by Senft's derivation for Gamma engine Schmidt model against DV ratio for various hot and cold side temperatures at an engine pressure of 300 kPa and engine speed of 2.833 Hz. ....	311
Figure F.2: Plot of power output calculated by Senft's derivation for Gamma engine Schmidt model against DV ratio for various hot and cold side temperatures at an engine pressure of 570 kPa and engine speed of 2.833 Hz. ....	311
Figure F.3: Plot of power output calculated by Senft's derivation for Gamma engine Schmidt model against DV ratio for various hot and cold side temperatures at an engine pressure of 300 kPa and engine speed of 1.667 Hz. ....	312

Figure F.4: Plot of power output calculated by Senft's derivation for Gamma engine Schmidt model against DV ratio for various hot and cold side temperatures at an engine pressure of 435 kPa and engine speed of 1.667 Hz. ....	312
Figure F.5: Plot of power output calculated by Senft's derivation for Gamma engine Schmidt model against DV ratio for various hot and cold side temperatures at an engine pressure of 570 kPa and engine speed of 1.667 Hz. ....	313
Figure F.6: Plot of power output calculated by Senft's derivation for Gamma engine Schmidt model against DV ratio for various hot and cold side temperatures at an engine pressure of 300 kPa and engine speed of 4.000 Hz. ....	313
Figure F.7: Plot of power output calculated by Senft's derivation for Gamma engine Schmidt model against DV ratio for various hot and cold side temperatures at an engine pressure of 435 kPa and engine speed of 4.000 Hz. ....	314
Figure F.8: Plot of power output calculated by Senft's derivation for Gamma engine Schmidt model against DV ratio for various hot and cold side temperatures at an engine pressure of 570 kPa and engine speed of 4.000 Hz. ....	314
Figure F.9: Plot of power output calculated from isothermal derivation of Schmidt model for Gamma engines against DV ratio for various hot and cold side temperatures at an engine pressure of 300 kPa and engine speed of 2.833 Hz. ....	315
Figure F.10: Plot of power output calculated from isothermal derivation of Schmidt model for Gamma engines model against DV ratio for various hot and cold side temperatures at an engine pressure of 570 kPa and engine speed of 2.833 Hz. ....	315
Figure F.11: Plot of power output calculated from isothermal derivation of Schmidt model for Gamma engines against DV ratio for various hot and cold side temperatures at an engine pressure of 300 kPa and engine speed of 1.667 Hz. ....	316
Figure F.12: Plot of power output calculated from isothermal derivation of Schmidt model for Gamma engines against DV ratio for various hot and cold side temperatures at an engine pressure of 435 kPa and engine speed of 1.667 Hz. ....	316
Figure F.13: Plot of power output calculated from isothermal derivation of Schmidt model for Gamma engines model against DV ratio for various hot and cold side temperatures at an engine pressure of 570 kPa and engine speed of 1.667 Hz. ....	317

Figure F.14: Plot of power output calculated from isothermal derivation of Schmidt model for Gamma engines model against DV ratio for various hot and cold side temperatures at an engine pressure of 300 kPa and engine speed of 4.000 Hz. ....	317
Figure F.15: Plot of power output calculated from isothermal derivation of Schmidt model for Gamma engines against DV ratio for various hot and cold side temperatures at an engine pressure of 435 kPa and engine speed of 4.000 Hz. ....	318
Figure F.16: Plot of power output calculated from isothermal derivation of Schmidt model for Gamma engines against DV ratio for various hot and cold side temperatures at an engine pressure of 570 kPa and engine speed of 4.000 Hz. ....	318
Figure H.1: SIL180 datasheet from manufacturer. ....	331
Figure I.1: Plot of solid temperature determined from analytical solution and simulation for varying engine pressure and speed for the cooling case. ....	335
Figure I.2: Plot of absolute value solid temperature difference between analytical solution and simulation for varying engine pressure and speed for the cooling case. ....	335
Figure I.3: Plot of exit air temperature determined from analytical solution and simulation for varying engine pressure and speed for the cooling case. ....	336
Figure I.4: Plot of absolute value exit temperature difference between analytical solution and simulation for varying engine pressure and speed for the cooling case. ....	336
Figure I.5: Plot of exit air temperature determined from analytical solution using simulation solid temperatures and simulation solution for varying engine pressure and speed for the cooling case. ....	337
Figure I.6: Plot of absolute value exit air temperature difference between analytical solution using simulation solid temperature and simulation solution for varying engine pressure and speed for the cooling case. ....	337

# List of Symbols and Abbreviations

## Latin Alphabet Symbols

Symbol	Description	Unit
$A$	Area	$m^2$
$B$	Schmidt Model Constant	
$C$	Schmidt Model Constant	
$CR$	Compression Ratio	
$D$	Diameter	m
$D_h$	Hydraulic Diameter	m
$F$	Viscous flow resistance	$N/m/m^2$
$Gr_L$	Grashof number	
$K_L$	Minor loss coefficient	
$L$	Length	m
$Nu$	Nusselt Number	
$P$	Power	W
$Pr$	Prandtl Number	
$Q$	Heat	J
$Q_w$	Film Heat Transfer per Unit Length	W
$R$	Universal Gas Constant	J/molK
$R_t$	Heat Transfer Resistance	K/W
$Ra$	Rayleigh number	
$Re$	Reynolds number	
$T$	Temperature	K
$V$	Volume	L
$W$	Work	J
$X$	Senft Schmidt Model Constant	
$Y$	Senft Schmidt Model Constant	
$a$	Rectangular Channel Height	m
$b$	Rectangular Channel Width	m
$c_p$	Isobaric Specific Heat Capacity	J/kgK
$c_v$	Isochoric Specific Heat Capacity	J/kgK
$e$	Mass-specific total gas energy	J/kg
$f$	Frequency	Hz
$f_D$	Friction factor	
$g$	Gravitational acceleration	$m/s^2$
$h$	Convective Heat Transfer Coefficient	$W/m^2K$
$k$	Thermal Conductivity	$W/mK$

$m$	Mass	kg
$n$	Number of items	
$p$	Pressure	Pa
$p_{channel}$	Perimeter of channel	m
$q$	Axial heat flux	W
$r$	Radius	m
$t$	Time	s
$u$	Velocity	m/s
$w$	Width	m
$x$	Direction	m
$y$	Schmidt model constant	rad

---

## Greek Alphabet Symbols

<b>Symbol</b>	<b>Description</b>	<b>Unit</b>
$\alpha$	Phase Angle	rad
$\beta$	Coefficient of volume expansion	1/K
$\varepsilon$	Kinetic energy correction factor	
$\theta$	Crank Angle	rad
$\mu$	Dynamic Viscosity	kg/ms
$\nu$	Kinematic Viscosity	m <sup>2</sup> /s
$\rho$	Density	kg/m <sup>3</sup>
$\phi$	Senft Schmidt Model Constant	rad
$\omega$	Angular Velocity	rad/s
$\epsilon$	Mass-specific internal gas energy	J

## Abbreviations

<b>Abbreviation</b>	<b>Description</b>
CFD	Computational Fluid Dynamics
CNC	Computer Numerical Control
DAQ	Data Acquisition System
DTECL	Dynamic Thermal Energy Conversion Laboratory
DV	Dead Volume
GUI	Graphical User Interface
LTDSE	Low Temperature Difference Stirling Engine
ORC	Organic Rankine Cycle
PEI	Polyetherimide
PTFE	Polytetrafluoroethylene
PV	Pressure-Volume
RTD	Resistance Temperature Detector



# 1 Introduction

## 1.1 Motivation

Global electricity demand has been increasing for decades, and is projected to continue to increase into the future [1]–[3]. The majority of electricity generated globally comes from fossil fuel sources, with 37% coming from coal and 24% from natural gas in 2019 [2], [3]. In Canada in 2019, electricity generated from coal and natural gas totaled 7% and 11% respectively of the country’s total electricity generation [4], [5]. The source of electricity generation in Canada varies widely from province to province, with the populous provinces of Ontario and Quebec generating most of their electricity from hydropower and nuclear, resulting in a nationally low amount of energy generation from fossil fuels [4], [5]. In contrast, in the Canadian province of Alberta, the majority of electricity generation still comes from fossil fuels, with coal and natural gas comprising 31% and 59% of the province’s electricity generation in 2019 [4], [5]. As non-renewable sources of energy contribute to climate change through increased emission of greenhouse gases, there is a desire to increase the amount of renewable or alternative energy used for electricity production. In particular, replacing the baseload electricity generation is desirable, as intermittent renewable sources such as wind and solar are not able to supply all of the electricity energy demand due to their low capacity factor as compared to more conventional electricity generation methods of coal and natural gas [6].

One area of interest is in generating electricity from alternate thermal sources, in particular from low grade heat. These sources include waste heat and geothermal, both of which are abundantly available in Alberta [7], [8]. These heat sources are low temperature sources, typically below 150 °C. However, there are not many technologies available to convert the heat from these low temperature sources to electricity. Low temperature sources have a low thermal potential and any thermodynamic cycles that run from this heat will have a low efficiency, which can make them difficult to exploit for electricity generation. This is due to the Carnot efficiency of the cycle being lower for lower temperature sources that reject to the same sink temperature [9]. The main existing technology for exploiting these sources is the organic Rankine cycle (ORC), which uses an organic fluid in the Rankine cycle that boils at a lower temperature than water in order to

exploit these low temperature sources [10]. Another technology that is being investigated for this application is the Stirling engine.

The Stirling engine was patented by Robert Stirling in 1816 [11], [12] which is capable of converting any type of thermal energy into mechanical energy which can then be used for electricity generation. This makes it an attractive option for exploiting unconventional thermal sources, including solar [13], [14], geothermal [15], and waste heat [16]. Stirling engines that run off of low temperature sources with a low temperature difference between the source and sink are known as low temperature difference Stirling engines (LTDSEs). LTDSEs have been shown to run at temperatures as low as 0.5 °C [17] and from sources below 100 °C [18]. LTDSEs are thus an attractive option for exploiting the low grade heat available in Alberta.

## 1.2 Introduction to Stirling Engines

Stirling engines are an externally heated engine that are capable of converting any heat source to mechanical work. The principle upon which the Stirling engine operates can be simplified into the ideal cycle representation. However, a real Stirling engine does not operate on the ideal Stirling cycle, and has significant complexities in the cycle that result from the physical construction of the engine. The ideal Stirling cycle and the real Stirling engine implementation are discussed in this section, alongside some key concepts in the design and study of Stirling engines.

### 1.2.1 Ideal Stirling Cycle

The ideal Stirling cycle consists of four distinct thermodynamic processes that occur on a closed volume of gas [19]–[21]. Figure 1.1 shows the four states of the ideal Stirling cycle on a volume of gas along with the respective position and change between those states on a pressure-volume (PV) diagram. Important assumptions of the ideal Stirling cycle are that the working fluid is an ideal gas, the processes are discontinuous and reversible, and there are no leaks and no friction in the machine [19], [21].

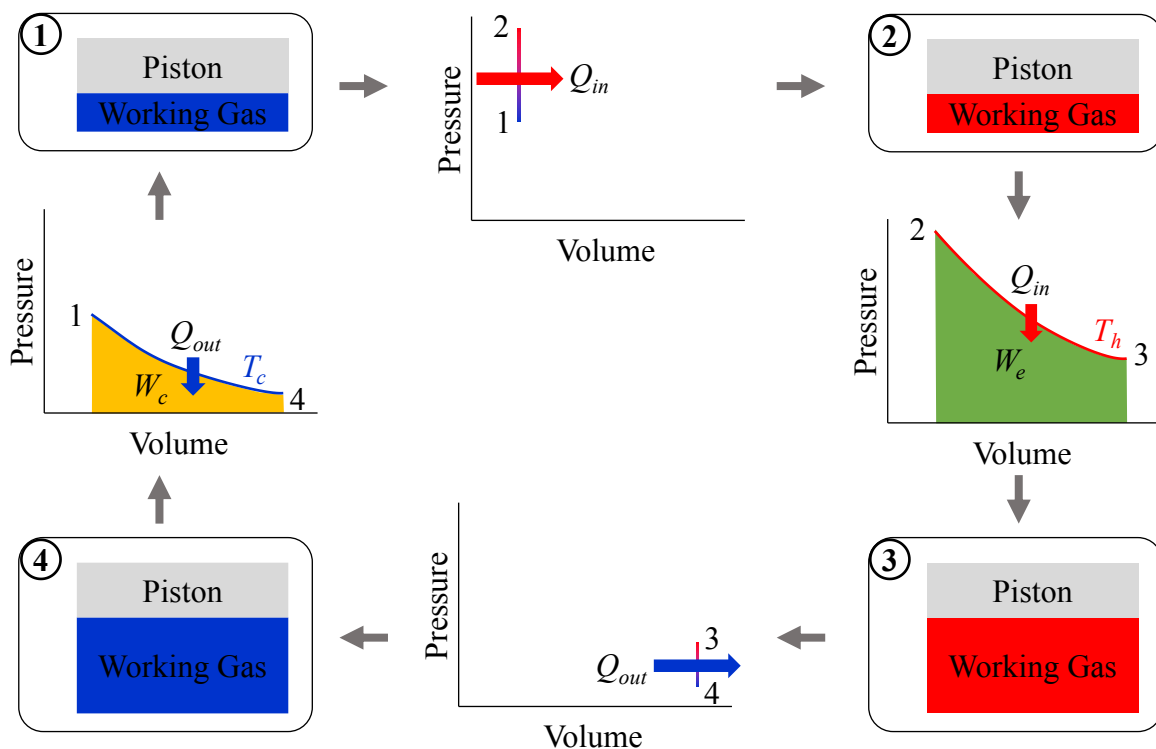


Figure 1.1: PV diagram of the ideal Stirling cycle processes, with cycle work shown.

The first process in the ideal Stirling cycle is isochoric heat addition, from state 1 to state 2. In this process heat is added to the enclosed volume of the working fluid while holding the volume constant at the minimum volume of the cycle. The working fluid temperature increases from the sink temperature to the source temperature, which causes the pressure to increase per the ideal gas law, noting that the temperature at state 2 is the source temperature and the temperature at state 1 is the sink temperature and these are related by:

$$p_2 = p_1 \frac{T_h}{T_c} \quad (1.1)$$

where:

$p_1$  – pressure at state 1 (Pa)

$p_2$  – pressure at state 2 (Pa)

$T_h$  – source temperature (K)

$T_c$  – sink temperature (K)

The second process is isothermal expansion, from state 2 to state 3. In this process the volume of the gas is expanded from the minimum volume at state 2 to the maximum volume at state 3 while holding the temperature of the gas constant at the source temperature. The pressure that was gained in the process from 1 – 2 is now used to expand the volume, causing the pressure at state 3 to be:

$$p_3 = p_2 \frac{V_{min}}{V_{max}} \quad (1.2)$$

where:

$p_3$  – pressure at state 3 (Pa)

$V_{min}$  – minimum volume (m<sup>3</sup>)

$V_{max}$  – maximum volume (m<sup>3</sup>)

The third process is isochoric heat rejection, from state 3 to state 4. In this process the volume of the gas is held constant at the maximum cycle volume, and the temperature of the working fluid is reduced from the source temperature to the sink temperature. This causes the pressure of the fluid to drop again, noting that the temperature at state 3 is the source temperature and the temperature at state 4 is the sink temperature described by:

$$p_4 = p_3 \frac{T_c}{T_h} \quad (1.3)$$

where:

$p_4$  – pressure at state 4 (Pa)

The fourth process is isothermal compression, from state 4 to state 1. In this process the volume of the gas is compressed from the maximum volume at state 4 to the minimum volume at state 1 while holding the temperature of the gas constant. This causes the pressure of the gas to increase to state 1 again as per the ideal gas law:

$$p_1 = p_4 \frac{V_{min}}{V_{max}} \quad (1.4)$$

The work done on and by the fluid through these processes is found from the PV diagram. The expansion work done by the fluid, from state 2 to state 3, is found from the area under the curve on the PV diagram, shown in Figure 1.1, as defined by:

$$W_e = \int_{V_{min}}^{V_{max}} p_e dV \quad (1.5)$$

where:

$W_e$  – expansion work (J)

$p_e$  – engine pressure during isothermal expansion (Pa)

$V$  – engine volume ( $m^3$ )

The compression work done on the fluid, from state 3 to state 4, is also found from the area under the curve on the PV diagram, as defined by:

$$W_c = \int_{V_{min}}^{V_{max}} p_c dV \quad (1.6)$$

where:

$W_c$  – compression work (J)

$p_c$  – engine pressure during isothermal compression (Pa)

The total work done by the engine, the indicated work, is the difference between the expansion work and the compression work, which is the area enclosed by the curves on the pressure-volume diagram, as shown in Figure 1.2. This can be described by the contour integral:

$$W_{ind} = W_e - W_c = \oint p dV \quad (1.7)$$

where:

$W_{ind}$  – indicated work (J)

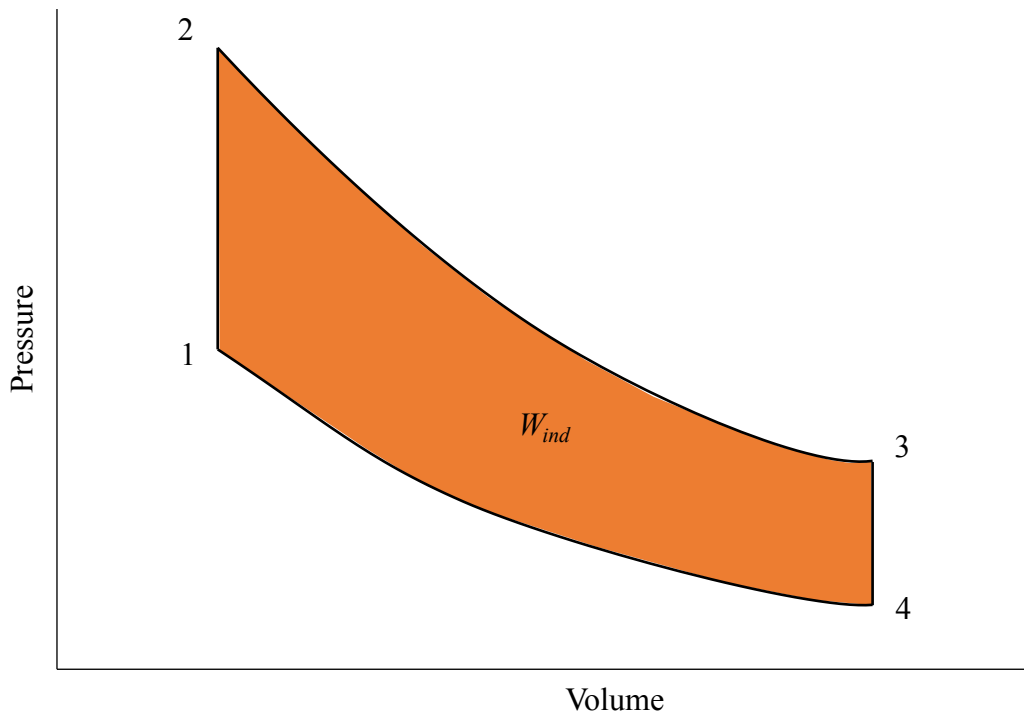


Figure 1.2: Indicated work of ideal Stirling cycle on a PV diagram

## 1.2.2 Stirling Engine Components

The actual Stirling engine is not accurately represented by the enclosed working fluid with a single piston as shown in Figure 1.1. To vary the volume of the working fluid and to add and remove heat from the fluid, additional components are required. The arrangements of these components fall into three types, which are the alpha, beta, and gamma type Stirling engines. These arrangements describe the arrangement of the pistons moving the working gas. The alpha arrangement has two pistons, one on either the hot or cold side of the engine, and both pistons combine to move the gas to be heated or cooled and to undergo expansion or compression. The beta arrangement has a displacer piston and power piston in a shared cylinder. The displacer piston moves the gas from the hot side to the cold side of the cylinder, and the power piston changes the volume of the gas to extract work. A gamma arrangement has the same pistons and principle of operation of a beta arrangement, however the two pistons do not share the same cylinder. The main components of a Stirling engine are shown in Figure 1.3 for a gamma type Stirling engine. This configuration is used most commonly for LTDSEs as the flexibility in cylinder size selection, resulting from the two separate cylinders, is beneficial in optimizing the engine for low temperature operation [22].

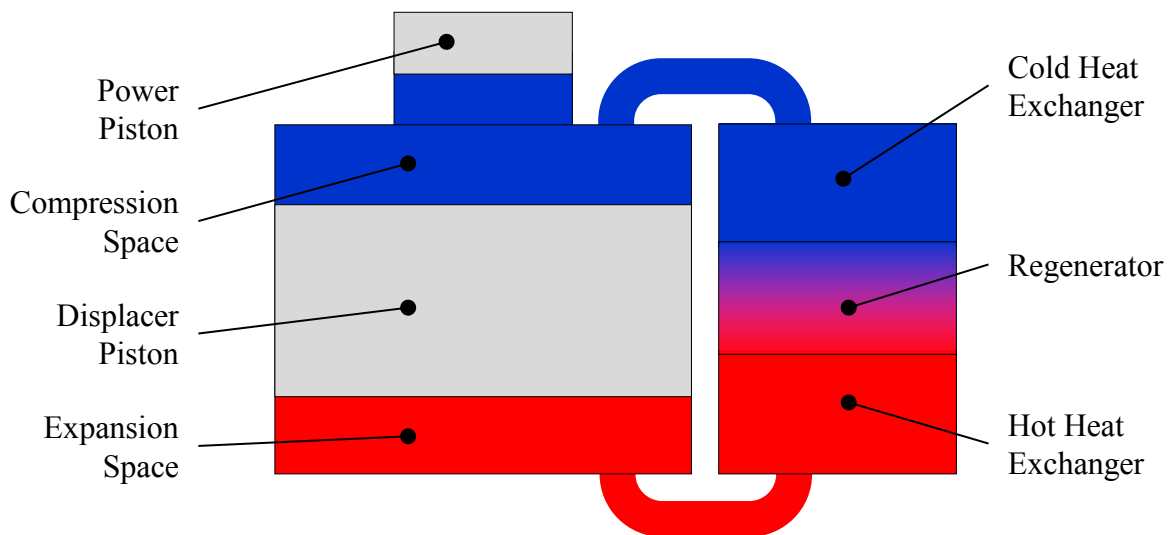


Figure 1.3: Simplified Gamma-type Stirling engine components

The power piston is used to vary the volume of the working fluid within the engine and resides within the power cylinder. The displacer piston is used to move the working fluid through the engine from the hot side to the cold side. The hot side of the engine is called the expansion space and the cold side the compression space. For a kinematic Stirling engine, the motion of these pistons is controlled by some type of mechanism, not pictured in the simplified diagram.

In order to provide heat input and output to the engine, the Stirling engine contains heat exchangers and a regenerator. The heat exchangers and regenerator are found in between the expansion and compression spaces, and the gas will flow through these components during each cycle. The heat exchangers are added to the engine to improve the heat transfer into and out of the working fluid by adding more heat transfer surface area than is available in just the cylinder walls. The hot heat exchanger adds heat to the working fluid, and the cold heat exchanger removes heat from the working fluid. The regenerator is a characteristic component of the Stirling engine [21], and is included in Stirling's original patent, termed the economiser [23]. The regenerator temporarily stores heat energy of the working fluid as it is passing through in the regenerator material, to be returned to the fluid on the next cycle. The regenerator is important to improving the engine efficiency by reusing the heat in the cycle, and reduces the load on the heat exchangers.

All the Stirling engine components described above can be moved to perform the ideal Stirling cycle. A visualization of the four states of the ideal Stirling cycle with all the Stirling engine components included is shown in Figure 1.4 and can be compared with the steps of the ideal cycle outlined in Figure 1.1.



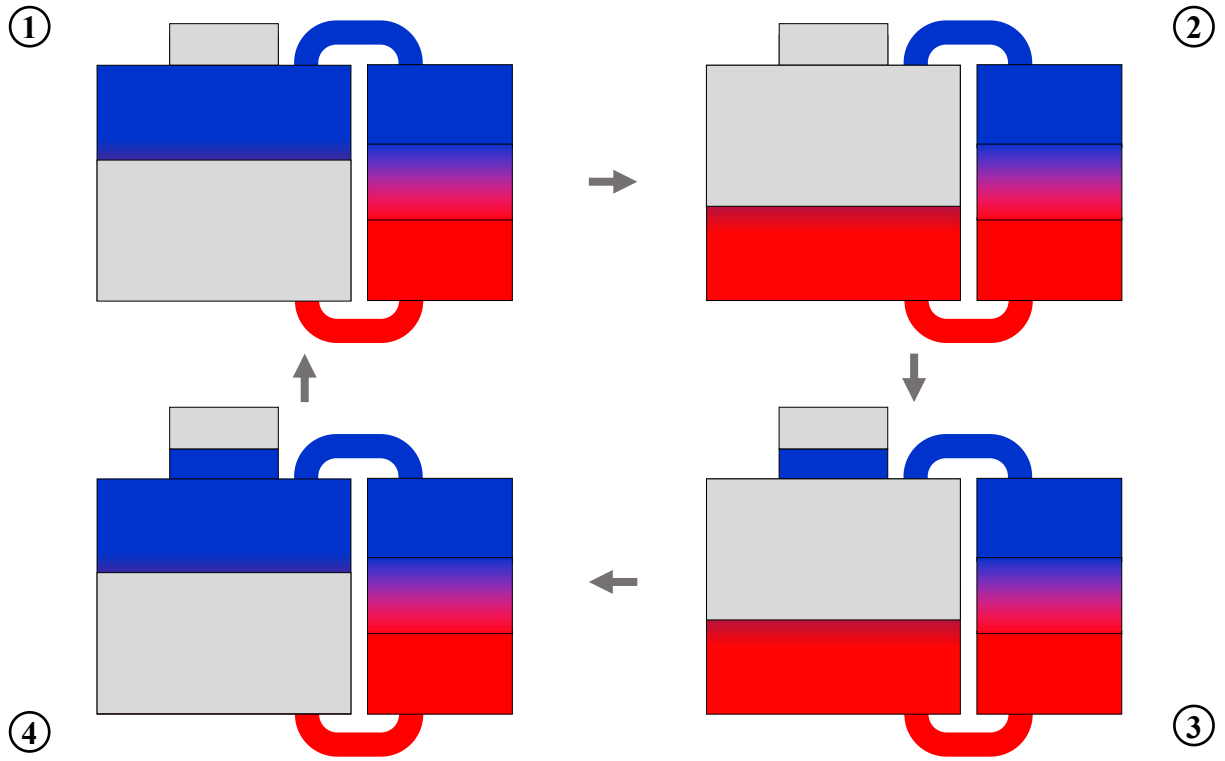


Figure 1.4: Ideal Stirling cycle steps with real engine components

### 1.2.3 Practical Stirling Cycle

Though the ideal Stirling cycle described previously is helpful in understanding the basic thermodynamic processes of the Stirling engine, it is not a good portrayal of the workings of a practical Stirling engine. This is because several of the idealizations present in the ideal Stirling cycle are not realistically achievable.

The greatest difference between the ideal cycle and the practical Stirling cycle is that isothermal expansion and compression processes are not present in reality. This is because the heat exchange in the heat exchangers and regenerator do occur over a finite temperature difference, and not a differential temperature as is the case in the isothermal assumption. Thus, the expansion and compression processes do not necessarily follow the isotherm in the PV diagram.

In addition, physically implementing the discontinuous piston motions in the ideal cycle is not possible results in high loading of the pistons and moving components in the mechanism due to the greater acceleration, which can affect the mechanism stability [24]. Commonly implemented mechanisms such as the slider-crank and Scotch yoke, cause the pistons to move in a sinusoidal continuous motion. The pistons are then phased to approximate the ideal Stirling cycle, however

the cycle processes overlap as a result of the continuous motion [19]. The expansion and compression processes occur before heating or cooling of the gas is completed, and vice versa. This causes rounding of the PV diagram and a decrease in work output, as shown in Figure 1.5.

The assumption of a frictionless machine is also not true in reality, in particular with regards to fluid friction. The pressure drop due to friction through the heat exchangers and in particular the regenerator is significant, which causes a reduction in the peak pressure achieved by the Stirling engine. All of these factors combine to cause a significant deviation from the ideal Stirling cycle in a practical Stirling engine. More advanced modelling of the engine is required to determine the overall performance of a practical Stirling engine.

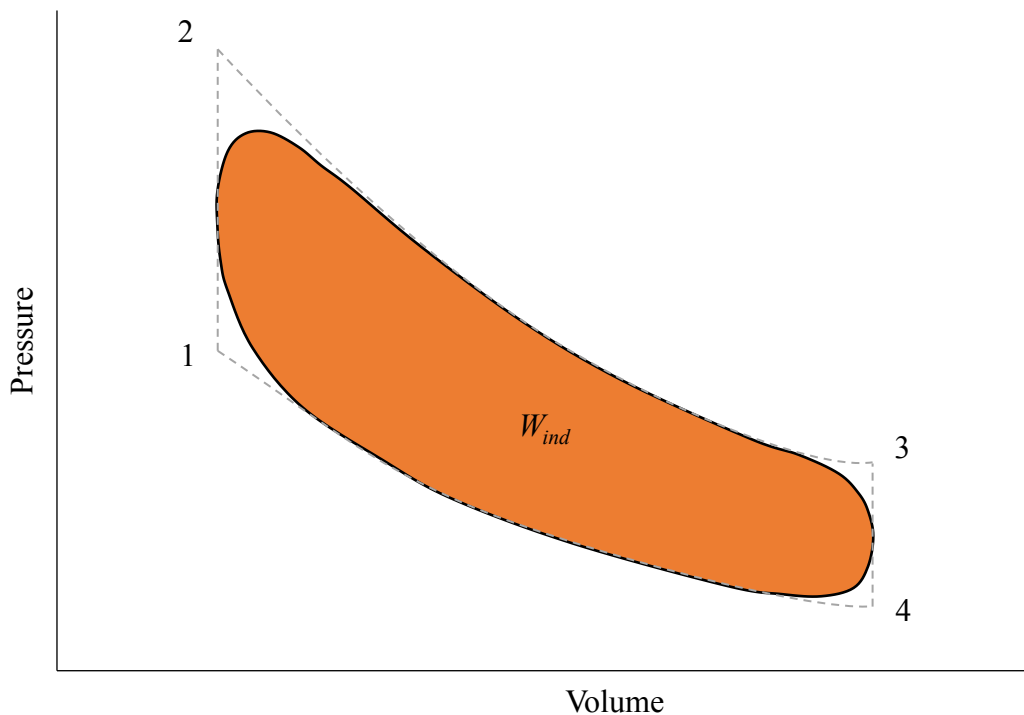


Figure 1.5: Indicated work of a practical Stirling cycle within the ideal Stirling cycle on a PV diagram.

### 1.2.4 Compression Ratio

It is common for LTDSEs to use a gamma piston configuration. The primary reason for this is that, due to the low temperature difference, a lower compression ratio is optimal [18]. The compression ratio is the ratio of maximum volume to minimum volume of the engine:

$$CR = \frac{V_{max}}{V_{min}} \quad (1.8)$$

where:

$CR$  – compression ratio

Having two individual piston cylinders allows for a low compression ratio to be achieved more easily without incurring excessive dead volume in the remainder of the engine.

### 1.2.5 Dead Volume

Dead volume in Stirling engines is defined as any volume that is not swept by a piston [19]. In the schematic of the gamma type Stirling engine presented in Figure 1.3, it can be clearly seen that the heat exchangers and regenerator are not swept by either the power piston or the displacer piston. This makes these components part of the engine dead volume. Other areas of the engine that contribute to the dead volume are connecting pipes, annular gaps between the piston and cylinder wall, and piston clearance volumes at the top and bottom of the stroke.

To characterize the amount of dead volume in the engine, the dead volume ratio (DV ratio) is used. This is defined as the ratio of total dead volume to the displacer piston swept volume [25]:

$$DV \text{ Ratio} = \frac{V_{dead}}{V_{disp}} \quad (1.9)$$

### 1.2.6 Appendix Gap

The Stirling engine displacer piston typically has a significant length, which is used to separate the hot and cold sides of the engine from each other. Often, the displacer piston seal will be located at one location along the length of the piston, typically on the cold side to avoid operating in the high temperature region of the engine [20]. The remainder of the piston is not in contact with the cylinder, forming an annular gap between the displacer piston and cylinder. This annular gap is referred to as the appendix gap, and can contribute to losses in the engine through increased heat transfer between the piston, cylinder and gas [20].

### 1.3 Effects of Dead Volume

Dead volume is known to have an impact on engine performance. This is due to the excess volume reducing the maximum pressure swing of the engine, thus narrowing the PV diagram and reducing the work output. Senft [25] investigated the optimum gamma type Stirling engine geometry using an analytical model, and notes that for an engine with all other parameters optimized an increase in dead volume ratio leads to a decrease in output work. When the dead volume ratio is increased from zero to one, the indicated work drops by as much as 43% for engine operating at a low temperature difference. Senft [25] also notes that the negative effects of excess dead volume cannot be offset by increasing the compression ratio of the engine.

Walker [19] also used an analytical model to investigate the effect of increasing dead volume ratio while holding other engine parameters constant. This investigation also found that minimizing dead volume in the engine was crucial to maximizing engine output power. However, both Senft's and Walker's analysis is limited by lacking differentiation between dead volume belonging to the heat exchange components and other dead volumes in the engine.

Hoegel [26] investigated the effect on dead volume on LTDSE performance in comparison with high temperature different Stirling engines for an alpha configuration using an analytical model. It was found that introducing dead volume that does not belong to the heat exchangers or regenerator did always result in a lower power output. The amount that the power output was lowered is dependent on the geometry of the additional dead volume, with a narrow cylindrical dead volume resulting in the poorest performance for a LTDSE, with no positive power output. Interestingly, it was noted that adding dead volume, again not belonging to the heat transfer components, was able to increase the power output over the case with optimized heat exchanger size and no dead volume in the case where the phase angle for the engine was not optimal. Hoegel states this is due to the pressure amplitude for the engine being reduced to be more optimal for a LTDSE. Namely, this is able to lower the gas temperatures in the compression phase and reduce the compression work in the cycle.

Gschwendtner and Bell [27] further investigated the phenomenon of increasing dead volume not in the heat transfer components for both low and high temperature difference alpha type Stirling engines. For a low source temperature, it was found that for a fixed phase angle, increasing the

dead volume yielded marginal gains in output power. This was observed to be due to the decrease in pressure amplitude on the compression side, and the phase shift of the pressure swing and thus the PV power of the cycle.

Hoegel [26] also investigated the effect of heat exchanger size and geometry on LTDSE power output. It was found that for the LTDSE, the optimum number of heat exchanger channels was higher than for the high temperature difference Stirling engine, and the channel length was shorter. This is due to the need for higher surface area for heat exchange with the lower temperature difference available, coupled with the need for lower flow resistance losses in the engine. The sensitivity of the engine power output to the heat exchanger size was also investigated, noting that the LTDSE is more sensitive to changing the number of heat exchanger tubes than a high temperature Stirling engine. The effect of engine speed was also considered, with lower engine speeds favoring heat exchangers with less heat exchanger tubes but with longer lengths as compared to higher engine speeds in LTDSEs. The dead volume ratio was not given in Hoegel's study.

The heat exchangers contradictory nature of being crucial to connecting the engine working fluid to the thermal source and sink, but also having negative performance effects when poorly designed, such as that due to excess volume, means that there must exist an optimum geometry. However, determining the optimum heat exchanger size and geometry for a Stirling engine that can run at varying engine conditions is a task that requires advanced modelling in order to capture the relationships between various parameters on the overall power output.

## 1.4 Stirling Engine Thermodynamic Models

Many thermodynamic models for modelling Stirling engines exist, and were categorized by Martini [28], [29] according to their complexity and assumptions. Chen and Griffin [30] also provide a review of the different orders of Stirling engine design methods. These vary in the range of information that is offered about the cycle and the complexity of the model itself. This range of models serves to provide different levels of information about the cycle depending on the design needs. The 1<sup>st</sup> order models are the simplest, offering a closed form solution that can predict power output and efficiency. The 2<sup>nd</sup> order models introduce decoupled losses to a simplified cycle analysis, and require numerical iteration to solve. A 3<sup>rd</sup> order model divides the engine into nodes over which the continuity equations for mass, momentum, and energy and the equation of state for the working fluid are solved. A description of the types of models and the key assumptions each one makes are provided below.

### 1.4.1 1<sup>st</sup> Order Models

The 1<sup>st</sup> order Stirling engine thermodynamic models share the common characteristic of being closed-form analyses of the Stirling engine. These solutions offer insight into the idealized power output and efficiency of the Stirling engine.

Some examples of 1<sup>st</sup> order models include the Beale number, which is an equation for predicting power based on empirical engine data, wherein the output power is proportional to engine pressure, speed, and displacer piston swept volume [29]. Another such model based on empirical engine data is the West number, which similarly predicts the engine output power to be proportional to all the parameters noted in the Beale number, and in addition the source and sink temperature, again based on empirical engine data [31].

The most complex closed-form solution available is that of the Schmidt model, derived by Schmidt in 1871 [32]. This model divides the engine into distinct spaces and assumes that these engine spaces are isothermal, similar to the assumption of the ideal cycle. This makes it a type of isothermal model. By assuming that the pistons follow perfectly sinusoidal motion, it is possible to obtain a closed-form solution for the engine output power. In order to determine a solution however, the expansion and compression space temperatures must be assumed.

### 1.4.2 2<sup>nd</sup> Order Models

The 2<sup>nd</sup> order Stirling engine thermodynamic models combine an idealized cycle analysis with decoupled losses. There are three ideal cycle analyses which make different assumptions about the heat transfer rate in the expansion and compression spaces [30]. These three assumptions are:

- isothermal, having infinite heat transfer rate to the fluid
- adiabatic, having zero heat transfer rate to the fluid
- semi-adiabatic, having a finite non-zero heat transfer rate to the fluid.

There are a variety of these 2<sup>nd</sup> order models for each of these simplified cycle analyses, as described by Chen and Griffin [30] as well as Martini [29]. Each of these simplified cycle analyses can have decoupled losses added, which reduce the power output calculated from the initial analyses. These decoupled losses are identified by their loss mechanism, and are assumed to not be dependent on one another. Examples of decoupled losses include friction, hysteresis losses in the cylinders, gas leakage, shuttle losses, wall conduction, and imperfect regeneration [30]. To solve these 2<sup>nd</sup> order models, the ideal cycle solution is solved using an estimate of the expansion and compression space temperatures, similar to the Schmidt model. Then, the decoupled losses are added to the model, and are used to determine new estimates of the expansion and compression space temperatures. This iterative process is repeated until the temperatures do not change.

These models provide more realistic estimations of output power and efficiency for a Stirling engine, and are able to quantify the losses present in the engine. However, these models do not capture all the interactions between the various engine components and the resulting effects on power output. Each of the 2<sup>nd</sup> order models relies on applying the appropriate decoupled losses to the ideal cycle analysis, and each of these losses has a correlation predicting its impact on the engine cycle.

### 1.4.3 3<sup>rd</sup> Order Models

3<sup>rd</sup> order models perform a nodal analysis on the engine. The engine is divided into nodes, both spatially and temporally, and the conservation of mass, energy, and momentum equations are solved along with the equation of state for the working fluid for each node. These equations are solved using numerical methods, which vary depending on the model chosen. There are a

number of simplifications that can be made to the solution of these models. The primary simplification is that steady flow correlations are used for heat transfer and pressure drop, due to a lack of unsteady correlations available. Other models may further simplify the governing equations in order to speed up the solution time.

In general, 3<sup>rd</sup> order models are discretized in one dimension spatially, though this is not necessarily the case. The first 3<sup>rd</sup> order model was developed by Finkelstein [33], and it was joined by a variety of other 3<sup>rd</sup> order models [30], including the quasi-steady flow model by Urieli [20]. Some 3<sup>rd</sup> order models being developed academically are those by Andersen [34], [35], the GGSISM model by Garcia-Granados et al. [36], [37], and the MSPM model by Middleton [38]. There is also the commercially available 3<sup>rd</sup> order model, Sage, developed by Gedeon [39], [40].

The primary benefit to 3<sup>rd</sup> order models is that the losses that are also present in the 2<sup>nd</sup> order models are not necessarily assumed to be decoupled, so the interactions between them and the effect on engine performance can be captured [28], [30]. Additionally, the models can calculate parameters within the engine, particularly those that are not able to be measured experimentally, such as temperature variation with time [28], which can be beneficial for understanding engine performance and assist in engine design.

#### **1.4.4 Computational Fluid Dynamics Modelling**

The most detailed Stirling engine model is a computational fluid dynamics (CFD) simulation of the engine. CFD simulation is being undertaken, in 2D [41], [42] and 3D simulations [43], [44]. CFD simulation can be done with a variety of commercial software. However, this approach has issues in being useful for evaluating the engine performance and doing engine design. The Stirling engine contains moving boundaries in the moving piston faces, unsteady reciprocating flow, as well as compressible flow. These conditions are computationally intensive to model, and make it unsuitable for studies involving varying many parameters of the engine geometry and operating conditions. CFD simulations have a place in engine design when more detailed information on the internal flow phenomena of the engine are of interest, but for initial engine design are too computationally intensive to yield useful results in a reasonable timeframe.



### **1.4.5 Model Selection**

In order to determine the optimal heat exchanger size and geometry for an LTDSE, at least a 3<sup>rd</sup> order model is required in order to capture the interactions between various engine losses and their effects on engine performance. The computational intensity of using CFD for Stirling engine modelling makes it prohibitive to obtain the large range of results required to determine the optimal heat exchanger size and geometry as well as to understand the trends in optimal heat exchanger size for varying engine parameters. The use of a 3<sup>rd</sup> order model to study the effect of heat exchanger size on power output balances the computational requirements while still capturing the heat transfer in the heat exchangers and the effect of various engine losses on engine performance.

## 1.5 Thesis Objectives and Structure

The primary objective of this thesis is to determine if there is an optimum heat exchanger volume and geometry that produces maximum power output for a LTDSE. A brief analytical analysis of heat exchanger performance of an experimental engine is done to contextualize the results of the Stirling engine models used. The existence of a potential optimum is identified using the 1<sup>st</sup> order Schmidt model. A CFD analysis is undertaken to examine the validity of the assumptions of the analytical analysis and the Schmidt model. With this additional information, the optimum identified by the Schmidt model is further investigated using the commercial 3<sup>rd</sup> order model, Sage, in order to capture the tradeoffs between improved heat transfer and increased dead volume in a LTDSE.

The remainder of this thesis is structured as follows:

Chapter 2 will introduce a LTDSE whose heat exchangers and performance will be studied in this thesis. A summary of the physical description of the engine and experimental setup will be provided, and the experimental results utilized for validation will be described.

Chapter 3 will examine the question of heat exchanger performance and size using steady state assumptions in an analytical analysis. The effect of heat exchanger size on engine power output is determined using the 1<sup>st</sup> order Stirling engine model derived by Schmidt.

Chapter 4 presents the setup of a 3<sup>rd</sup> order Stirling engine model based on the experimental engine presented in Chapter 2 for validation.

Chapter 5 will outline a brief CFD study of a real Stirling engine heat exchanger, where the assumptions of the analytical and 1<sup>st</sup> order Schmidt model are investigated. Information about the heat exchanger gleaned from the study will be input into a 3<sup>rd</sup> order model.

Chapter 6 presents the results of the 3<sup>rd</sup> order model validation with the parameters determined from the CFD study in Chapter 5 included.

Chapter 7 presents the setup and results of a 3<sup>rd</sup> order model study for determining the effect of heat exchanger volume on power output.

Chapter 8 summarizes conclusions and future work.

## 2 Experimental Engine Description and Results

To undertake an investigation of the effect of heat exchanger volume on power output, a Stirling engine geometry to serve as a starting point is necessary. To serve this purpose an experimental engine is used as the starting geometry for analyses of the heat exchangers and engine power output, in addition to validation of the models. This engine, named the Raphael, was designed by Speer [45] following his redesign of the ST05G-CNC engine. The Raphael engine was chosen for this purpose as it has a simple geometry, particularly of the heat exchangers, that is appropriate for modelling. This chapter presents a brief history of the design of the Raphael engine in addition to a summary of the key geometry and features. The experimental setup used by Lottmann [46] is summarized and the obtained results used for model validation are presented.

### 2.1 ST05G-CNC and Modifications for Low Temperature

The design of the Raphael engine being considered in this thesis is based on the design of the ST05G designed by Dieter Viebach [47]. The ST05G was originally designed in 1992 to promote microgeneration using biomass as fuel [47]. It is a 90 ° Gamma type Stirling engine, with the power piston being attached to the compression space of the engine. The mechanism driving the pistons is a slider-crank, which yields near-sinusoidal motion, as shown by Speer [45]. It was first demonstrated at the 1993 International Stirling Engine Conference, and drawings and castings were distributed so the engine could be manufactured by anyone [47]. It was rated to produce 500 W at a hot side temperature of 650 °C and a working pressure of 1000 kPa (gauge) [47], [48]. The lowest temperature the ST05G ran at was 200 °C [48]. The ST05G drawings were eventually updated by Stefan Viebach and Hubert Eckl to be manufacturable by way of Computer Numerical Control (CNC) machining, with the updated version being named the ST05G-CNC [47].

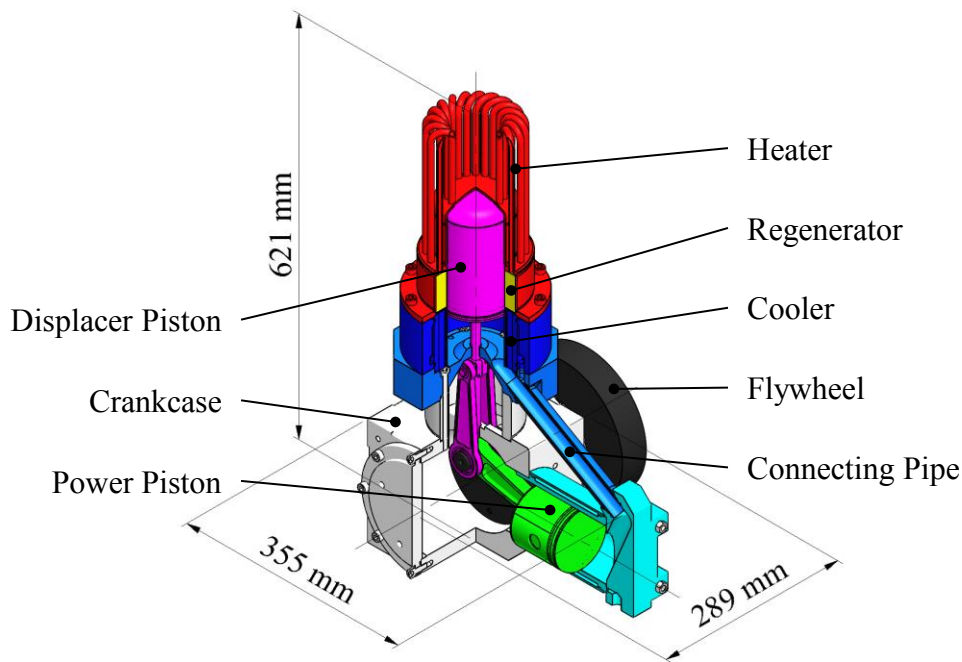


Figure 2.1: Partial section view of ST05G-CNC model.

### 2.1.1 ST05G in the Literature

The ST05G was investigated both experimentally and numerically in a wide variety of studies. Gheith et al. [49] did several experimental studies on the ST05G, beginning with a characterization of the engine performance. The influence of regenerator material on the performance of the engine and the determination of an effective regenerator for the ST05G was then considered [50], [51]. The study found that a stainless-steel regenerator was the best choice, resulting in high thermal efficiency and power output. Gheith et al. [52] theoretically and experimentally investigated the heater performance of the ST05G and performed a parametric optimization of the heater performance by modifying the operating conditions of the heater and cooler. The result of this optimization indicated that the working fluid absorbs more heat from the heater when the heating temperature is increased, when the temperature difference between the working spaces is increased, and when the cooling water flow rate is increased. The theoretical study was based on the quasi-steady model proposed by Berchowitz et al. [20]. The theoretical parametric optimization investigated the effect of heater temperature, heater efficiency, fill pressure, engine frequency, and heater volume on engine performance. It found that the engine performance improved with increases in all parameters investigated except for

increasing heater volume. They propose this is likely due to the negative effects of excess dead volume on engine performance. Gheith et al. [53] also investigated the working fluid flow within the regenerator using the quasi-steady model by Berchowitz again, comparing key theoretical parameters such as Reynolds number, Nusselt number, and Darcy friction factor to the experimentally determined values. This study found that the model results followed the same trend as the experimental results, but did not have the same magnitude.

Hachem et al. [54] performed an experimental study investigating the stability of engine operating conditions in response to load, finding that the engine speed was not able to change quickly in response to load and that the stability of the system improved when abrupt changes to the system had a smaller magnitude. Hachem et al. [55] also investigated the ST05G performance theoretically using a modified quasi-steady 2<sup>nd</sup> order model. This study considered the effect of engine speed, pressure, and hot end temperature and efficiency on brake power output, and compared the theoretical results to experimental results. Increased brake power output was seen for increases of low magnitude engine speed, increasing the engine pressure, and increasing hot end temperature and efficiency. Decreased brake power output was seen with further increase in engine speed.

The ST05G was also investigated using a 2<sup>nd</sup> order model developed by Bert et al. [56]. This model simplified the engine into three zones, and included time-dependent non-isothermal heat exchangers. The model was compared to experimental data for variation of engine parameters such as choice of working fluid, engine speed, engine pressure, and hot side temperature. The model showed good agreement with the experimental results across the varied parameters, and notably found that different working fluids were optimal at different engine speeds. Alfarawi et al. [57] also developed a non-ideal adiabatic 2<sup>nd</sup> order model validated against the ST05G wherein the engine is broken up into six spaces and various losses are subtracted from the ideal adiabatic model solution. This model was found to have good agreement with the experimental results, with a maximum deviation of 15% in the shaft power prediction.

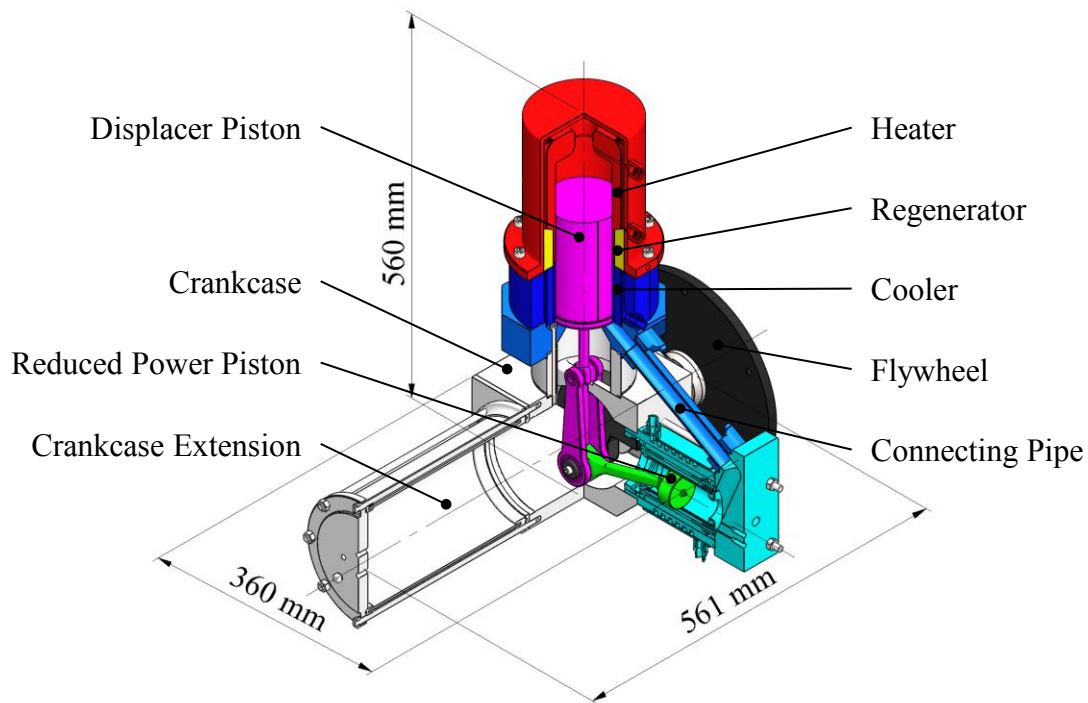
Alfarawi et al. also modelled the ST05G using a 2D CFD model in order to investigate the effect of phase angle and connecting pipe dead volume variation on engine performance [42]. The study found that there is an optimal phase angle and optimal connecting pipe size due to the negative effects that each of these parameters has on engine performance. Alfarawi et al also

performed a 3D CFD simulation of specifically the regenerator section of the ST05G engine in order to evaluate the effectiveness of a miniature-channel regenerator design [43]. The results showed that regenerators with small channels of diameter 0.5 mm can have similar power output to a random fibre regenerator, and the performance is sensitive to the channel material selection.

Across the various experimental and numerical studies described that have been done on the ST05G, there has been some investigation into the size and geometry of the heat transfer components. Numerous studies considered modifications to the regenerator to improve power output. One study by Gheith et al. [52] did consider the impact of the heater volume on the engine performance, which noted the relationship of decreasing power with increasing dead volume for the ST05G. Of course, the ST05G is a high temperature Stirling engine, so it is still an area of interest to determine the performance of a low temperature iteration of the engine design.

### **2.1.2 Summary of Modifications to ST05G-CNC**

The ST05G-CNC version of the engine with some modifications to improve low temperature operation was manufactured by the Dynamic Thermal Energy Conversion Laboratory (DTECL) from the drawings made by Viebach and Eckl and experimentally investigated by Speer [45]. The primary modification to the ST05G-CNC that was included in the version built at DTECL was the replacement of the original heater, consisting of 20 stainless steel tubes welded to the displacer cylinder, with an annular slotted hot heat exchanger made of mild steel that was located, like the cooler, between the displacer cylinder and the outside of the engine, as shown in Figure 2.2. The displacer piston and cylinder now had a flat top surface as opposed to the original hemisphere of the ST05G-CNC. This hot heat exchanger was heated electrically with the addition of a mild steel heating cap on the outside of the heat exchanger via conduction [45]. This heating cap was heated by 15 cartridge heaters with total power output of up to 5000 W [45]. Additional modifications included different piston seals, the reduction of power piston diameter, and the addition of volume to the crankcase via a crankcase extension, described in detail by Speer [45].



*Figure 2.2: Partial section view of ST05G-CNC model following modifications for operation at lower source temperature.*

The modifications implemented on the ST05G-CNC were able to lower the minimum thermal source temperature at which the engine would run to 144 °C [45]. These modifications also resulted in a reduction of power output compared to the original ST05G-CNC, producing a maximum of 3 W with a thermal source temperature of 300 °C. This left room for further modifications to the design of the ST05G-CNC to improve its performance at lower thermal source temperatures.

## 2.2 Experimental Engine Description

The Raphael engine, as shown in Figure 2.3 is a LTDSE that was designed by Speer following his modification of a ST05G-CNC to run at low temperature. A drawing package summarizing the key dimensions is provided in Appendix A. Its design is based on the modified ST05G-CNC, sharing the same engine configuration and mechanism. The Raphael engine was designed for a maximum thermal source temperature of 150 °C, approximately equal to the minimum thermal source temperature achieved by the modified ST05G-CNC. It has a maximum working pressure of 1000 kPa (gauge), the same as that of the ST05G-CNC, though it has only been run at a maximum of 500 kPa (gauge).

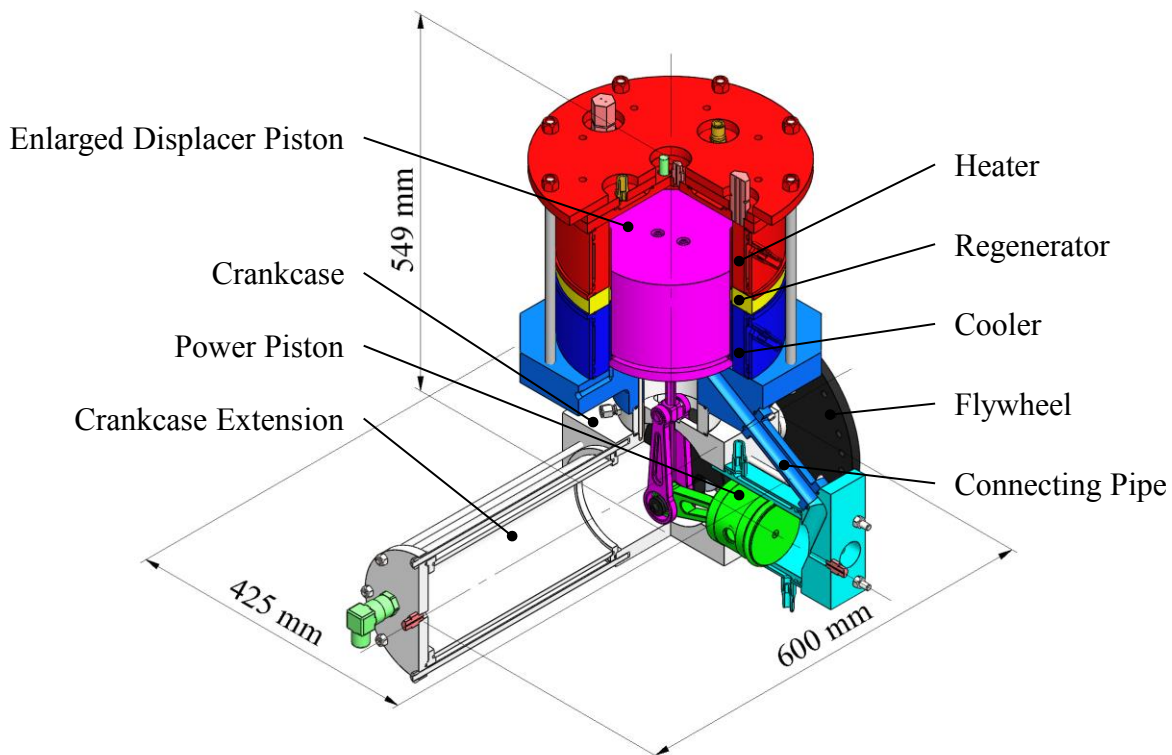


Figure 2.3: Partial section view of the Raphael engine with main components annotated.

The primary modification from the ST05G-CNC is the increased displacer diameter of 200 mm compared to the original 96 mm. This results in a lower compression ratio of 1.1 than the original ST05G-CNC, which is more optimal for low temperature performance, as shown by Kolin [18] and Egas [22]. The displacer piston is also manufactured from a high temperature foam instead of sheet metal for improved manufacturability, and reduced weight for the larger piston [58]. The power piston size of the Raphael engine is the same as that of the original



ST05G-CNC, with improved piston seals. These graphite-filled polytetrafluoroethylene (PTFE) crown seals last longer than the lubricated O-rings used previously for the original and modified ST05G-CNC. A summary of the resulting engine volumes of the Raphael engine is provided in Table 2.1.

*Table 2.1. Engine Volumes of Raphael Engine*

<b>Engine Component</b>	<b>Volume</b>
Displacer Piston Swept Volume	2.356 L
Power Piston Swept Volume	0.433 L
Hot Heat Exchanger	0.552 L
Regenerator	0.348 L
Cold Heat Exchanger	0.552 L
Connecting Pipe	0.166 L
Other Dead Volume (Appendix Gap, Clearance Volumes)	0.092 L
Total Engine	4.499 L

The original heat exchanger assembly is significantly changed with the increase in displacer cylinder diameter. Both heat exchangers are mounted annularly to the displacer cylinder, with the annular regenerator between them. A detailed description of the heat exchangers and regenerator is provided in the following section.

### **2.2.1 Description of Heat Exchanger Design**

The heat exchangers are significantly changed from the modified ST05G-CNC, shown in Figure 2.4. While the cold heat exchanger is still cooled by a liquid flow loop, the electrical heater cap used in the modified ST05G-CNC is replaced by a liquid heating loop. Both heat exchangers have the same geometry, similar to the cooler on both the original and modified ST05G-CNC, and are made of 6061 aluminum alloy.

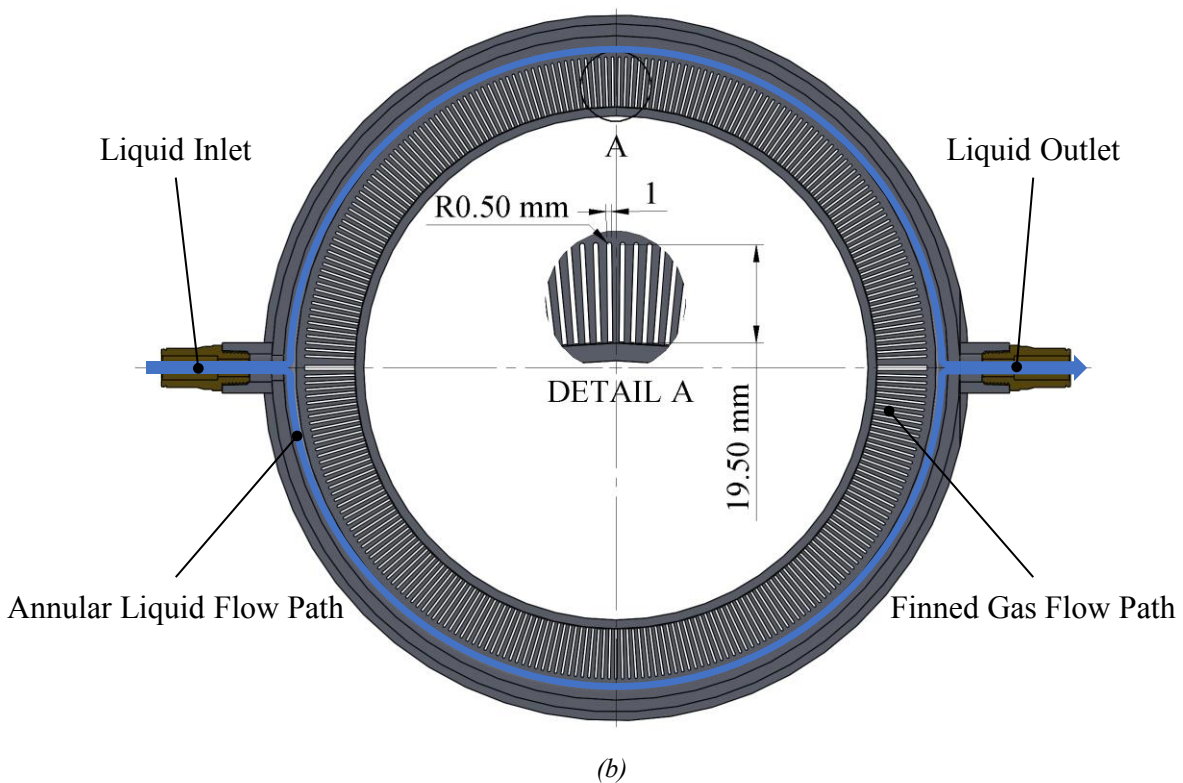
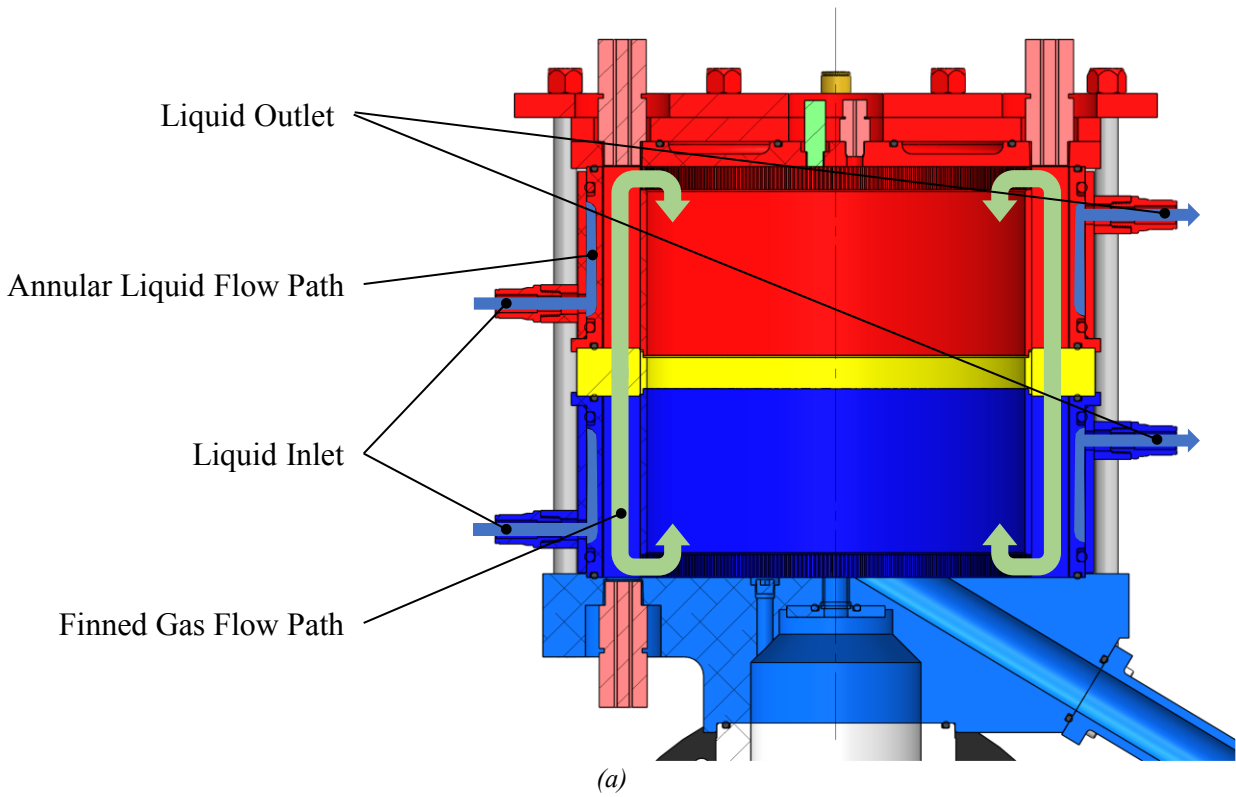


Figure 2.4: (a) Cross-section of heat exchanger assembly of Raphael engine. (b) Cross-section of heat exchanger cartridge highlighting flow paths.

The inner surface contacting the working space of both heat exchangers is made up of radial fins that were waterjet cut. The fin geometry was determined by scaling the cold heat exchanger design of the ST05G-CNC, aiming to keep the ratio of heat exchanger cross sectional area to displacer piston area and the ratio of heat exchanger volume to displacer piston swept volume the same in order to maintain the same flow conditions as in the ST05G-CNC cold heat exchanger, with similar velocity and amount of air passing through the heat exchangers [58]. This was done as the performance of the cold heat exchanger in the modified ST05G-CNC was better than the of the hot heat exchanger [45]. In order to make these ratios as similar to the ST05G-CNC as possible, the fins were made radially longer, at the risk of increasing the conduction resistance [58]. The exact fin geometry is summarized in Table 2.2. Note that the fins are tapered and the thickness varies along the length, as the fin gaps have parallel walls. Additionally, 4 of the fins are replaced with two larger fin gaps, which are included for instrumentation.

The liquid heat transfer side consists of an annular jacket around the outside of the heat exchangers. This jacket does not contain any fins. In addition to the annular jackets around the hot and cold heat exchangers, the top of the displacer cylinder contains a liquid jacket for heating the expansion space. There is not a corresponding jacket on the cold side of the displacer cylinder as that is where the mechanism connects to the displacer cylinder via the connecting rod to the crankcase.

*Table 2.2. Raphael Engine Heat Exchanger Geometry*

<b>Property</b>	<b>Value</b>
Number of Channels	287 (289 without instrumentation gaps)
Heat Exchanger Length	96 mm
Fin Length	20 mm
Finned Annulus Inner Radius	103.5 mm
Finned Annulus Outer Radius	123.5 mm
Inner Radius of Liquid Annulus	127 mm
Fin Gap Width	1 mm
Heat Exchanger Open Cross-Sectional Area	5748.98 mm <sup>2</sup>

The annular regenerator is located in between the hot and cold heat exchangers. The regenerator housing is made of polyetherimide (PEI) plastic. This plastic has a high heat resistance allowing

it to be directly in contact with the hot heat exchanger. PEI is chosen as the regenerator housing material to minimize conduction directly from the hot heat exchanger to the cold heat exchanger [19]. The regenerator material within the housing is made of polyester fibres in a random matrix. The porosity of the regenerator material was able to be varied, and a porosity of 96% was found to be optimal for the engine.

## 2.3 Summary of Experimental Setup

The engine operation was achieved by connecting the engine to liquid heating and cooling loops, and a pressure vessel for pressurization. The thermal source and sink temperature, liquid flow rates, charge pressure and engine load were controlled. Parameters of interest including gas and liquid temperature, dynamic and static pressure measurements, and engine load and speed were measured. This section provides a summary of the engine operation control systems, and the engine instrumentation. The experimental data was acquired by Lottmann [46], who provides a detailed description of the experimental setup and procedures.

### 2.3.1 Engine Operation Control

The liquid heating and cooling loops act as the source and sink for the engine. The hot heat exchanger is heated by a silicone oil (SIL 180, Thermo Fisher Scientific Inc.), chosen as it is able to provide liquid heating to the engine at temperatures above 100 °C, which is the limit for water. The cold heat exchanger is cooled by a water-glycol mixture, which is capable of reducing the cooling temperature to -10 °C, below the 0 °C limit for water. The water-glycol mixture is approximately 30% glycol and 70% water by weight, and was determined using the method described in Appendix H. Both the liquid heating and cooling systems consist of baths with a built-in controller to maintain the set point temperature. The heating bath is rated to 3140 W of heating power, and the chiller system is rated to 4832 W of cooling power. The water-glycol flow rate was controlled by a peristaltic pump. Due to limitations with appropriate tubing for the hot SIL 180 to use the peristaltic pump, the built-in pump in the bath was used. The temperature and flow rate set points of the heating and cooling system are provided in Table 2.3. Neither the hot or cold heat exchangers are insulated, with the outer surface of the jacket contacting the environment.

*Table 2.3. Heat Transfer Fluids and Set Points*

<b>Fluid</b>	<b>Temperature Set Point</b>	<b>Flow Rate Set Point</b>
SIL 180	150 °C	0.054599 kg/s
Water-Glycol Mixture	5 °C	0.023558 kg/s

The engine charge pressure was controlled by way of a pressure regulator connected to a pressure vessel, as shown in Figure 2.5. An air compressor was filled to a pressure of

approximately 690 kPa (gauge). The air then goes through a desiccant dryer to remove the moisture from the air, and then to a pressure regulator (QB3, Proportion-Air Inc.) which controls the pressure vessel and engine fill pressure to a given setpoint. The regulator is placed at the pressure vessel and not at the engine working space in order to minimize the pressure fluctuations the regulator sees from the changing engine pressure. The engine working space is pressurized by way of an orifice, which also assists in minimizing the pressure fluctuations at the regulator. In this way, the static pressure is maintained at a constant level. The crankcase can be pressurized independently for engine filling, but during operation is not connected to the pressure vessel, and instead equalizes pressure with the working space through leaks of the power piston seal and the displacer cylinder rod seal.

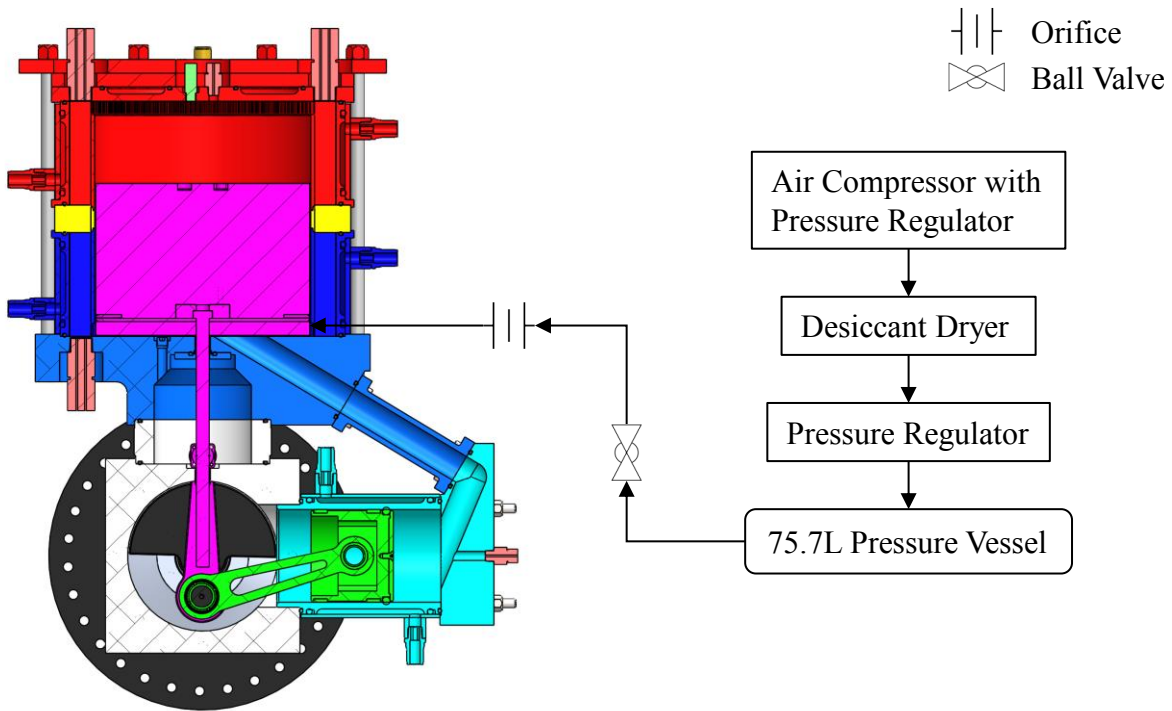


Figure 2.5: Piping and instrumentation diagram of charge pressure system.

The engine load was applied using a magnetic brake (MBZ-5.7, Magnetic Brake Systems) mounted on the output shaft next to the flywheel. The torque applied ranged from 0.1 to 1.2 Nm. The varied load application yielded varying engine operating speeds.

### 2.3.2 Engine Instrumentation

The engine was instrumented to measure the crank angle, gas and liquid temperatures, and static and dynamic pressure varying with time. These measurements enable the evaluation of the engine performance. A diagram summarizing the location of the instrumentation within the engine is shown in Figure 2.6. Note that one of the gas thermocouples is offset from the cut plane – this is because the thermocouple could not be inserted through the connecting pipe, so it is offset sufficiently in order to be inserted.

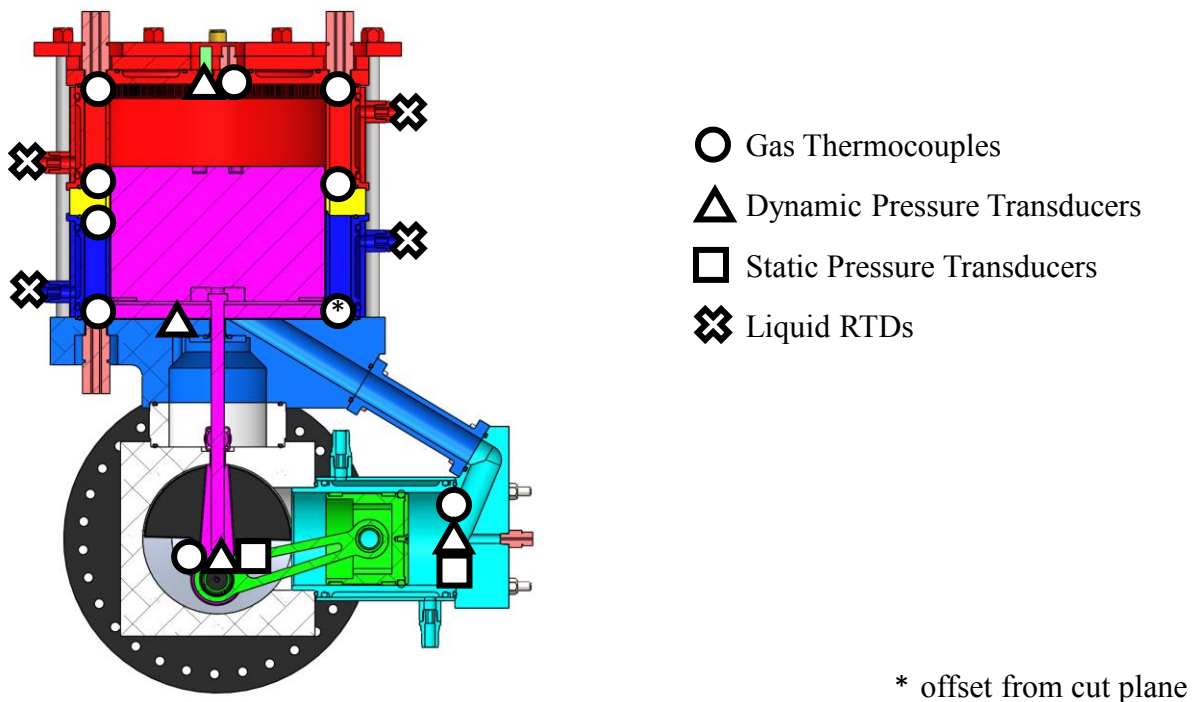


Figure 2.6: Location of instrumentation used on Raphael engine.

The instrumentation used in the engine is summarized in Table 2.4. To measure the engine speed, crank angle position with time is measured using a rotary encoder (15S, Encoder Products Company), mounted inline on the end of the engine output shaft. The mean engine speed is determined by calculating the time-varying encoder speed per cycle, and then averaging that speed over the cycle.

As shown in Figure 2.6, the heating and cooling fluid temperatures are measured at the inlet and outlet of each of the jackets using resistance temperature detectors (RTDs) (RTD-810, Omega

Engineering Inc.). RTDs were chosen to measure these temperatures due to their higher accuracy as compared to thermocouples [59].

The gas temperatures were measured using exposed-junction thermocouples due to their faster response time [59]. The grounded junction had a diameter of 0.5 mm, which has a response time of approximately 0.9 s [60]. It should be noted that the thermocouple measurement response time is still slower than the time it takes for the engine to complete one cycle, meaning that they cannot capture temperature fluctuations over a single cycle. The thermocouples used are T-type thermocouples (TJFT72, Omega Engineering Inc.), which were chosen for the best accuracy in the temperature range being investigated.

The static and dynamic pressures were measured both in the working space and the crankcase. The static pressure measurements, which provide the mean cycle pressure in the working space and the crankcase, are measured by pressure transducers (PMP300, FUTEK Advanced Sensor Technology Inc.). The dynamic pressure measurements, which measure the pressure fluctuations over the cycle, are measured by flush mount piezoelectric pressure transducers (PCB 113B28, PCB Group Inc.).

The static pressure measurements measured the average gauge pressure of the engine. To determine the absolute pressure, the atmospheric pressure was also measured using an integrated barometric sensor in a smartphone, calibrated against a reference barometer. The pressure was recorded at the beginning and end of an experiment, and the mean pressure is then used.

*Table 2.4. Raphael Engine Instrumentation*

<b>Measurement</b>	<b>Instrument</b>	<b>Model Number</b>	<b>Manufacturer</b>
Gas Temperature	Thermocouple	TJFT72	Omega Engineering Inc.
Liquid Temperature	RTD	RTD-810	Omega Engineering Inc.
Dynamic Pressure	Pressure Transducer	PCB 113B28	PCB Group Inc.
Mean Pressure	Pressure Transducer	PMP300	FUTEK Advanced Sensor Technology Inc.
Crank Position	Rotary Encoder	15S	Encoder Products Company



### 2.3.3 Data Acquisition System

The data was collected using a data acquisition system (DAQ). A summary of the DAQ system is provided in Figure 2.7. The DAQ computer used a LabVIEW program, which allowed live monitoring of the sensor readings, dataset acquisition, and set point control of the engine operating conditions. The DAQ chassis connected all the sensor readings to the computer. Each of the DAQ modules performed analog to digital conversion. The analog voltage module and the counter module sampled the data at 1000 Hz. The thermocouple module was set to the most accurate sampling mode available, which resulted in a sampling frequency of 1.8 Hz. The RTD module sampled the data at 10 Hz.

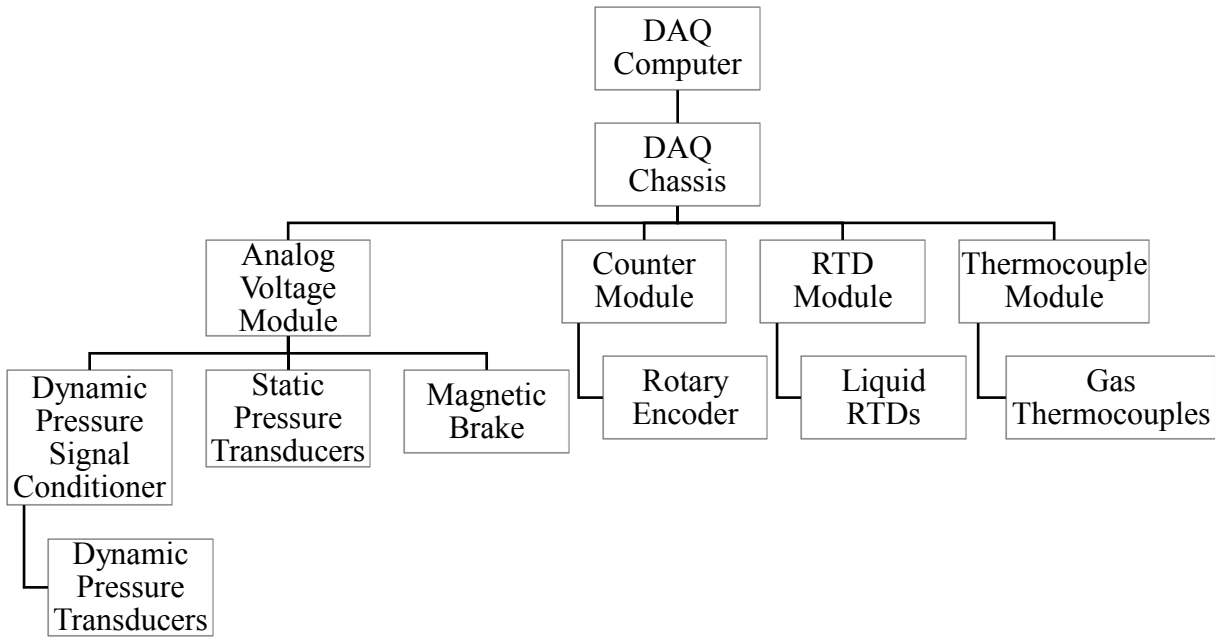


Figure 2.7: Schematic of engine instrumentation and data acquisition system.

### 2.3.4 Calibration and Experimental Procedures

A summary of the methods for calibrating the engine instrumentation is provided – the full details are provided by Lottmann [46].

The thermocouples and RTDs were calibrated against a thermometer over a range of temperatures. The thermocouples and RTDs were submerged along with the thermometer in the hot bath and the chiller and the measurement was recorded.

The pressure transducers and magnetic brake were calibrated by the manufacturers at the time of purchase. Calibration curves from the manufacturers were used to determine the pressure measurement.

The atmospheric measurement was calibrated against a mercury barometer, which was corrected for latitude and temperature. A constant offset between the barometer and the sensor was applied to the atmospheric pressure measurements.

The rotary encoder position was set using a dial gauge. The position pulse of the rotary encoder was set to the position of top dead centre of the power piston.

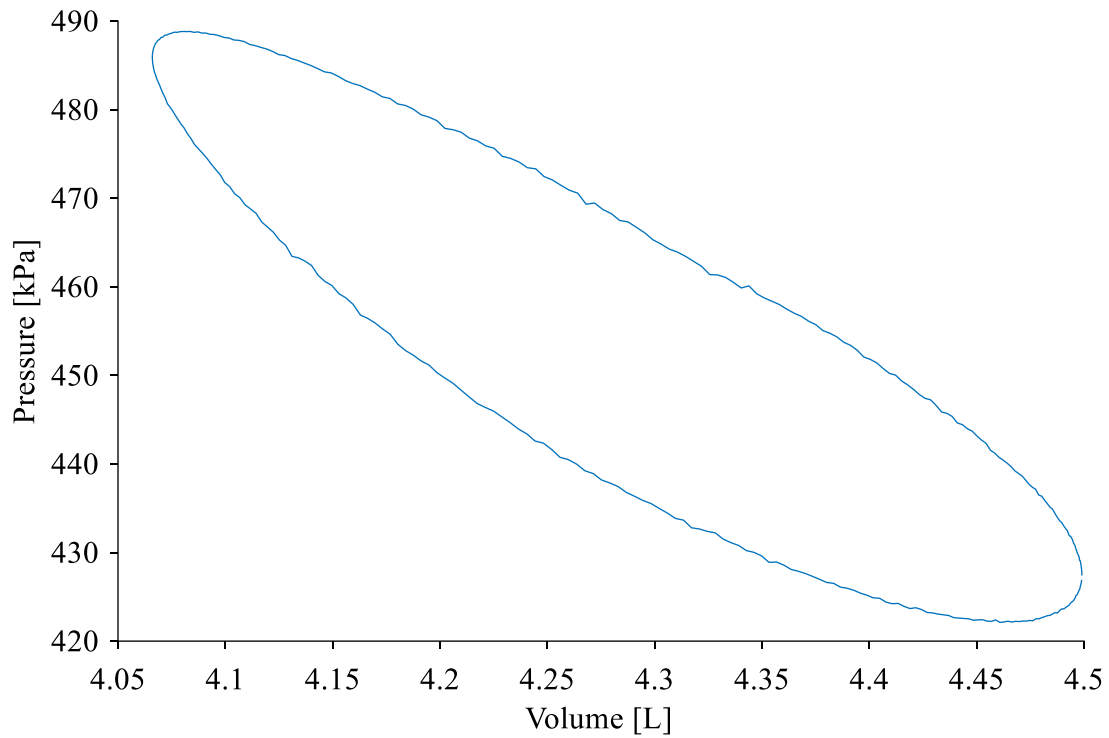
The experimental data should be collected at steady state in order to be comparable to the 3<sup>rd</sup> order model. To achieve this, the hot bath and chiller were first allowed to reach steady temperatures. The engine was then run for an hour with the baths circulating to allow the engine body to reach steady state at the setpoint engine pressure. Once this time was complete, a wait time of 10 minutes between trials was used where only the torque load was varied between trials, and the engine pressure was held constant. Lottmann [46] determined these wait times from long running experiments. The deviation from steady state should be limited to approximately 5%.

Uncertainty of the engine measurements was determined similar to Speer [45], and is detailed fully by Lottmann [46].

## 2.4 Summary of Key Experimental Results

The experimental data collected by Lottmann [46] will be used for validation of the Sage model. This data was collected at varying engine pressures and load conditions. The varying load conditions are used to vary the engine speed, enabling the generation of a plot of output power or output work against engine speed. The engine pressures investigated range from approximately 300 kPa (absolute) to 570 kPa (absolute). All pressures further referred to in this thesis will be absolute value unless otherwise noted.

To determine the output work of the engine, the pressure and volume variation of the cycle needs to be determined. The static pressure measurement and atmospheric pressure measurement is used to determine the mean pressure of the cycle. The dynamic pressure measurements of the working space and the crankcase are used to determine the pressure fluctuation over the cycle. The volume variation over the cycle in the working space is determined from the crank angle measurement, calculating the volume of the engine mathematically. The pressure fluctuation of the working space, known as the engine pressure, is plotted against the working space volume variation to generate a PV diagram, as shown in Figure 2.8. The pressure of the working space is taken to be the measurement of the pressure at the power piston. This processing of the data assumes that the instantaneous pressure in the entirety of the working space is uniform, similar to the assumptions of 1<sup>st</sup> and 2<sup>nd</sup> order models.



*Figure 2.8: A sample PV diagram for the working space determined from experimental data.*

From the PV diagrams obtained, the indicated work can be calculated. This is done by determining the area enclosed the by PV loop for the working space numerically using trapezoidal summation. This process is repeated at each operating point, and the results can then be plotted for each mean pressure against speed, as shown in Figure 2.9. Note that speed is a function of the applied load on the engine.

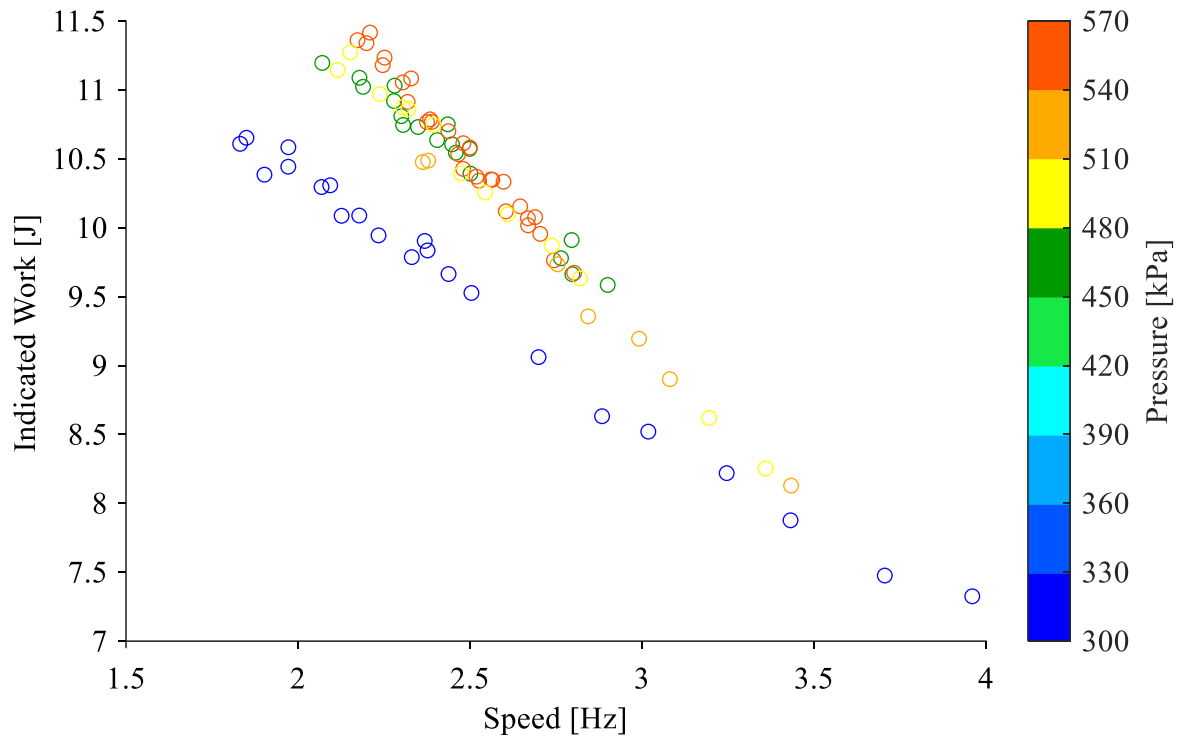


Figure 2.9: Plot of measured indicated work against measured engine speed for various engine operating pressures.

The indicated work determined experimentally can be directly compared against the indicated work determined by the Stirling engine models, namely the Schmidt model and the 3<sup>rd</sup> order modelling software, Sage.

The indicated power is determined by multiplying the indicated work by the engine frequency, and is shown in Figure 2.10. This is different from the measured shaft power due to the absence of mechanical losses. This indicated power can be compared to the power determined from the analytical models.

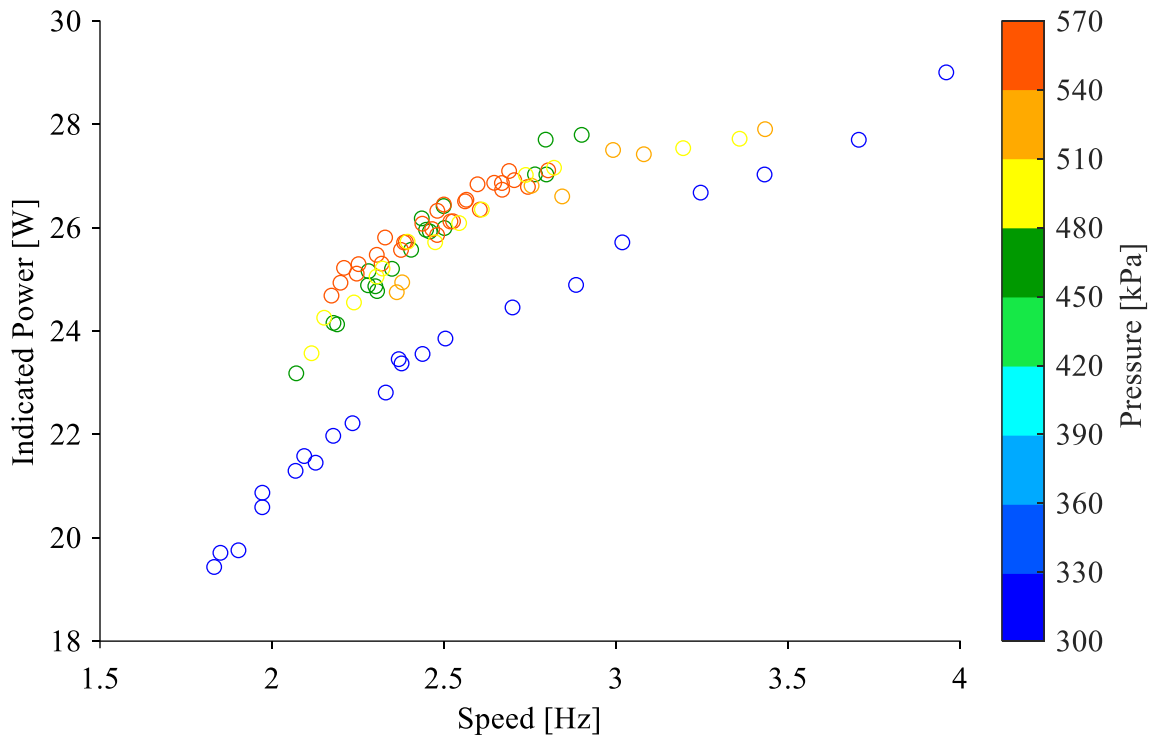


Figure 2.10: Plot of measured indicated power against measured engine speed for various engine operating pressures.

The above shown experimental results were used in validating the engine model created in Sage based on the Raphael engine geometry. Additional available engine measurements were used throughout the model validation, and are presented in context in future sections.

### **3 Fundamentals Analysis of Heat Exchanger Size**

In the design of heat exchangers for a Stirling engine, the temperature change of the gas through the heat exchangers should be maximized, as a large change in temperature will result in a large change in pressure and thus a larger work done by the cycle. However, heat exchangers also incur losses that can negatively impact the work output of the engine, namely the pressure drop through the heat exchangers as well as excess volume. Both of these losses can reduce the change in pressure of the working fluid in the engine, which would then reduce the work done by the cycle. To better understand the effects of these losses on heat exchanger design, two fundamental analyses were conducted. The first was a steady state analysis of the flow through a set of rectangular channels, in order to better understand the effects of heat exchanger size and fluid flow conditions on the heat exchanger performance. The second was an analysis using the 1<sup>st</sup> order Schmidt model to understand the impacts of excess heat exchanger volume on the power output of the Stirling cycle.

#### **3.1 Examination of Heat Transfer in Steady State Conditions**

To better understand the relationship between key parameters in heat exchanger design, an analysis of the heat transfer for a steady flow inside a set of rectangular channels was conducted. The relationship between heat exchanger geometry and impact on output temperature and pressure drop were of interest, as these parameters influence the performance of the Stirling engine.

##### **3.1.1 Analysis Assumptions**

The analysis presented in this section is based on the steady flow assumption, which is not accurate to the flow conditions in a real Stirling engine. As the engine operates on a cycle, the flow through the heat exchangers is unsteady within each cycle. Additionally, due to the location of the heat exchangers within the engine geometry, the flow also reciprocates through the heat exchangers, changing direction with each cycle. The steady flow analysis presented here is a simplified estimate of the heat exchanger performance in a Stirling engine, and is intended to only provide insight as to the relationships between heat exchange parameters. Analysis that

takes into account the reciprocating and unsteady nature of the flow is undertaken in Chapter 4 onward for the determination of engine performance using a 3<sup>rd</sup> order model.

Additionally, the air is assumed to be an ideal gas. As the engine operating conditions being considered are not near the critical point of air, the air will behave largely like an ideal gas. As a consequence, the specific heat capacity [21], [61], viscosity and thermal conductivity [62] are dependent only on temperature.

The walls of the rectangular channels are assumed to be isothermal. The walls are also assumed to be smooth.

### 3.1.2 Definition of Geometry and Flow Conditions

The analysis was done for the air side heat exchanger geometry based on the Raphael engine presented in Chapter 2. These heat exchangers consist of rectangular slots between fins in a radially symmetric arrangement, with a radius at the base due to manufacturing limitations. The channel geometry is assumed to be rectangular to simplify the analysis, neglecting the base radius. A summary of the heat exchanger constant parameters is shown in Table 3.1.

*Table 3.1. Constant Heat Exchanger Properties for Rectangular Channel Analysis.*

<b>Input Property</b>	<b>Values</b>
Channel Width	1 mm
Channel Height	20 mm
Constant Surface Temperature for Heating	150.0 °C
Constant Surface Temperature for Cooling	5.0 °C
Inlet Fluid Temperature	72.45 °C

The heat source and heat sink temperatures assumed for this analysis were 150 °C and 5 °C respectively. These temperatures were used as the constant surface temperature for the isothermal surface for the heating and cooling cases respectively. The inlet fluid temperature was assumed to be the regenerator mean effective temperature, as shown in Table 3.1. This is equivalent to the assumption of the isothermal model [20], wherein the regenerator temperature profile is linear between the temperatures of the hot and cold heat exchangers. In this case, the hot and cold heat exchanger temperatures are assumed to be that of the source and sink. Thus,



the regenerator mean effective temperature and thus the inlet fluid temperature is found using the equation described by Urieli and Berchowitz [20] as

$$T_i = \frac{T_h - T_c}{\ln\left(\frac{T_h}{T_c}\right)} \quad (3.1)$$

where:

$T_i$  – inlet fluid temperature (K)

$T_h$  – heat source temperature (K)

$T_c$  – cold sink temperature (K)

The varied heat exchanger parameters were the channel length and the open cross-sectional area. To vary the open cross-sectional area, additional channels with the same geometry were added to the heat exchanger as shown in the schematic in Figure 3.1. The channel geometry shown in the details is the same regardless of the overall size of the heat exchanger. The narrowest and longest heat exchanger and the widest and shortest heat exchanger configurations are shown. The channel length and open cross-sectional area were varied as shown in Table 3.2.

*Table 3.2. Varied Heat Exchanger Properties for Rectangular Channel Analysis.*

<b>Property</b>	<b>Minimum Value</b>	<b>Maximum Value</b>	<b>Step Size</b>
Channel Length	48 mm	192 mm	12 mm
Number of Channels	145	575	43
Heat Exchanger Open Cross-Sectional Area	2900 mm <sup>2</sup>	11500 mm <sup>2</sup>	1000 mm <sup>2</sup>

The channel length range was chosen to ensure that the channel length of the as-built heat exchangers was included. Thus, the maximum value was chosen to be twice that of the experimental length, and the minimum value was chosen to be half of the experimental length. Similarly, the cross-sectional area range investigated was chosen to encompass the cross-sectional area of the as-built heat exchangers. The maximum cross-sectional area is approximately twice that of the experimental cross-sectional area, and the minimum is approximately half of the experimental area. The cross-sectional area is rounded to the nearest whole number of channels for the calculation. Both the number of channels and the corresponding cross-sectional area is shown in Table 3.2.

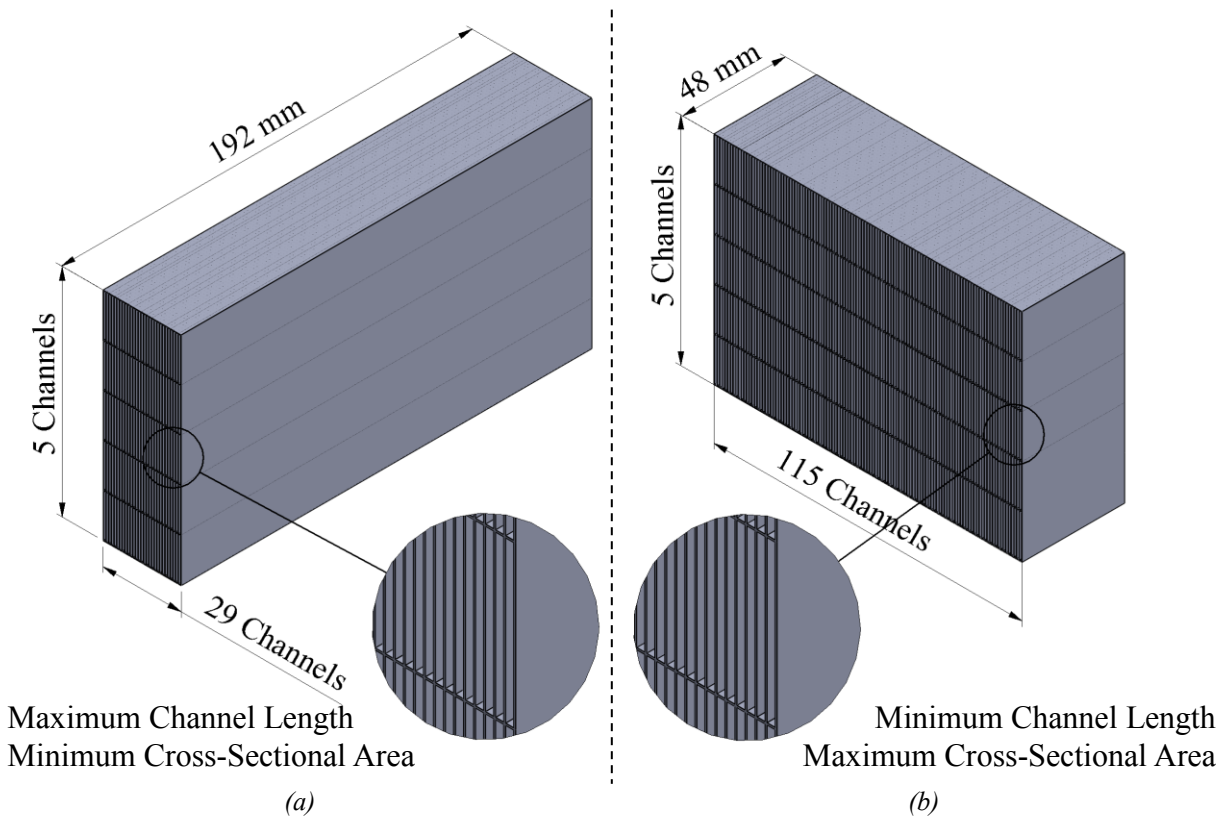


Figure 3.1: Schematic of varying heat exchanger geometry showing (a) a narrow and long heat exchanger and (b) a wide and short heat exchanger.

### 3.1.3 Sensitivity Parameter Selection

The Raphael engine operates over a range of engine pressures and frequencies, which significantly affect the flow conditions and heat transfer in the heat exchangers. Thus, the effects of engine pressure and speed should be considered.

The engine frequency was assumed to be 2.833 Hz which was the average engine speed seen in testing of the Raphael engine as shown in Chapter 2. Two sensitivities of the engine speed consider the minimum and maximum engine speeds seen in experiments. Additionally, the average engine pressure seen in the testing of the Raphael engine was 435 kPa. Two sensitivity cases of the minimum and maximum engine pressures seen in testing of the Raphael engine are considered. These cases are summarized in Table 3.3.

Table 3.3. Sensitivity Cases Conditions for Engine Pressure and Speed

Property	Base Value	Lower Value	Higher Value
Engine Pressure	435 kPa	300 kPa	570 kPa
Engine Speed	2.833 Hz	1.667 Hz	4.000 Hz

The Reynolds number will be significantly affected by the variation in pressure and engine speed due to the variation in the air density and velocity. It also depends strongly on cross-sectional area, and slightly on heat exchanger length. The dependence on heat exchanger length arises from the change in mean temperature at which the density and dynamic viscosity are evaluated. The variation of cross-sectional area changes the flow velocity, thus heat exchangers with smaller cross-sectional areas had higher Reynolds numbers.

### 3.1.4 Procedure for Determination of Output Temperature and Pressure Drop

To determine the output temperature, the flow through a single channel was analyzed. The initial air properties were determined based on an estimate of mean fluid temperature, and all air properties were found from Table A-15 in Çengel [63]. The hydraulic diameter was calculated from the channel geometry:

$$D_h = \frac{4A_{channel}}{p_{channel}} = \frac{2ab}{a + b} \quad (3.2)$$

where:

$D_h$  – hydraulic diameter of the channel (m)

$A_{channel}$  – cross-sectional flow area of rectangular channel (m<sup>2</sup>)

$p_{channel}$  – perimeter of the rectangular channel (m)

$a$  – height of rectangular channel (m)

$b$  – width of rectangular channel (m)

The Reynolds number was then determined using the hydraulic diameter of the rectangular channel:

$$Re = \frac{\rho u_{channel} D_h}{\mu} \quad (3.3)$$

where:

$Re$  – Reynolds number

$u_{channel}$  – air velocity in rectangular channel (m/s)

$\rho$  – density at mean fluid temperatures (kg/m<sup>3</sup>)

$\mu$  – dynamic viscosity at mean fluid temperatures (kg/ms)

The density of air is determined from the ideal gas law for the given pressure and temperature:

$$\rho = \frac{p}{R_{air} T_m} \quad (3.4)$$

where:

$p$  – engine fill pressure (Pa)

$R_{air}$  – individual gas constant of air (J/kgK)

$T_m$  – mean fluid temperature (K)

The air velocity in the channel is determined from the displacer speed in the engine. The angular velocity of the engine is first determined from the engine frequency using:

$$\omega = 2\pi f \quad (3.5)$$

where:

$\omega$  – angular velocity (rad/s)

$f$  – engine frequency (Hz)

The maximum displacer speed is then determined from the linear velocity of the crank arm. When the crank arm is perpendicular to the displacer piston's direction of travel, the displacer piston will be travelling with its maximum speed. As the displacer piston was physically linked to the crank arm, it can be assumed that the linear velocity of the crank arm is equal to the displacer piston velocity. The displacer piston velocity was then found using:

$$u_{disp} = \omega r \quad (3.6)$$

where:

$u_{disp}$  – displacer piston velocity (m/s)

$r$  – crank arm radius (m)

The air speed was assumed to match that of the displacer, as the displacer is pushing the mass of air. The velocity of the air in the channel is then determined using the one-dimensional continuity equation for incompressible fluids:

$$u_{channel} = \frac{A_{disp}}{nA_{channel}} u_{disp} \quad (3.7)$$

where:

$A_{disp}$  – cross-sectional area of displacer piston (m<sup>2</sup>)

$n$  – number of heat exchanger channels

The Reynolds number was then used to determine the appropriate equations for determining the heat transfer through the heat exchanger. It should be noted that approximately 85% of cases considered were laminar, with the maximum Reynolds number considered being 6211, thus including some transitional cases.

For the laminar case, the hydrodynamic entrance length for laminar flow in a pipe was determined using the equation from Kays and Crawford [64] and the hydraulic diameter

$$L_h \approx 0.05 Re D_h \quad (3.8)$$

where:

$L_h$  – hydrodynamic entrance length (m)

The thermal entrance length for laminar flow in a pipe was then determined using the equation from Kays and Crawford [64], and the Prandtl number at the overall mean fluid temperature,  $Pr$ :

$$L_t \approx 0.05 Re Pr D_h = L_h Pr \quad (3.9)$$

where:

$L_t$  – thermal entrance length (m)

$Pr$  – Prandtl number

For all cases considered, the thermal entrance length was shorter than the hydrodynamic entrance length.

To determine the Nusselt number in the entrance region, the thermal entrance length was used to bound the end of the entrance region. This is due to the equation for Nusselt number only being valid for thermally and hydrodynamically developing flow, which is only true for the thermal entrance length. The portion of the flow that is only hydrodynamically developing was treated as fully developed for this analysis. The equation used to determine the Nusselt number for the entrance region is from Edwards et al. [65] for isothermal parallel plates:

$$Nu = 7.54 + \frac{0.03 \left(\frac{D_h}{L_t}\right) Re Pr}{1 + 0.016 \left(\left(\frac{D_h}{L_t}\right) Re Pr\right)^{\frac{2}{3}}} \quad (3.10)$$

where:

$Nu$  – Nusselt number

The hydraulic diameter used is the one calculated from (3.2). Equation (3.10) is valid for Reynolds numbers up to 2800.

The heat transfer coefficient for the entrance region was found using the relation for heat transfer coefficient to Nusselt number as:

$$h = \frac{kNu}{D_h} \quad (3.11)$$

where:

$h$  – convective heat transfer coefficient (W/m<sup>2</sup>K)

$k$  – thermal conductivity of air at mean fluid temperatures (W/mK)

The exit temperature was found for isothermal surface from Çengel [63]:

$$T_e = T_s - (T_s - T_i) \exp\left(-\frac{hA_s}{\dot{m}c_p}\right) \quad (3.12)$$

where:

$T_e$  – exit temperature of the region (K)

$T_s$  – surface temperature (K)

$A_s$  – surface area of the region (m<sup>2</sup>)

$\dot{m}$  – channel mass flow rate (kg/s)

$c_p$  – specific heat capacity of air at mean fluid temperatures (J/kgK)

This relationship was used to determine the exit temperature for the entrance region by evaluating the heat transfer coefficient and surface area for the entrance region as:

$$T_{e,ent} = T_s - (T_s - T_i) \exp\left(-\frac{h_{ent}A_{s,ent}}{\dot{m}c_p}\right) \quad (3.13)$$

where:

$T_{e,ent}$  – exit temperature of the entrance region (K)

$h_{ent}$  – convective heat transfer coefficient of the entrance region (W/m<sup>2</sup>K)

$A_{s,ent}$  – surface area of the entrance region (m<sup>2</sup>)

The surface area of the entrance region was found by:

$$A_{s,ent} = L_t p_{channel} \quad (3.14)$$

The mass flow rate through a single channel was calculated using the channel velocity and the density of air:

$$\dot{m} = \rho u_{channel} A_{channel} \quad (3.15)$$

For cases where the thermally developing region exceeded the length of the pipe, the exit temperature for the entrance region was the overall exit temperature. The total length of the pipe was used as the length rather than the thermal entrance region length for equations (3.10) and (3.14).

For cases where the thermally developed region did not exceed the length of the pipe, the Nusselt number for the remaining thermally and hydrodynamically fully developed region in the pipe was found from Table 8-1 in Çengel [63] for rectangular channels. The heat transfer coefficient for the remaining region,  $h_{rem}$ , was found using equation (3.11). The exit temperature was then found similarly to the exit temperature of the entrance region:

$$T_e = T_s - (T_s - T_{e,ent}) \exp\left(-\frac{h_{rem} A_{s,rem}}{\dot{m} c_p}\right) \quad (3.16)$$

where:

$h_{rem}$  – convective heat transfer coefficient for remaining region (W/m<sup>2</sup>K)

$A_{s,rem}$  – surface area of the remaining region (m<sup>2</sup>)

The surface area of the remaining region was found by:

$$A_{s,rem} = (L - L_t)p \quad (3.17)$$

where:

$L$  – channel length (m)



For the transitional case, the assumption was made that the entrance region was small and could be neglected, thus the flow was fully developed. The Nusselt number was determined from the following equation by Gnielinski [66], valid for Prandtl number between 0.5 and 2000 and Reynolds number between 3000 and  $5 \times 10^6$ :

$$Nu = \frac{f_D}{8} \frac{(Re - 1000)Pr}{1 + 12.7 \left(\frac{f_D}{8}\right)^{0.5} (Pr^{\frac{2}{3}} - 1)} \quad (3.18)$$

where:

$f_D$  – Darcy friction factor

By determining the friction factor from the relation for smooth, parallel-plate channels from Çengel [63] below:

$$f_D = -6.38 \times 10^{-13} Re^3 + 1.17 \times 10^{-8} Re^2 - 6.69 \times 10^{-5} Re + 0.147 \quad (3.19)$$

The Gnielinski correlation is now valid for Reynolds number of 2300 to 8000, with improved accuracy. The heat transfer coefficient for the region was found using equation (3.11), and the exit temperature was found using equation (3.12).

The pressure drop through the heat exchanger was then found using the following equation for both laminar and transitional cases:

$$\Delta p = f_D \frac{L}{D_h} \frac{\rho u_{channel}^2}{2} \quad (3.20)$$

where:

$\Delta p$  – pressure drop over the length of the heat exchanger (Pa)

Equation (3.20) is only valid for fully developed flows. As the flow through the channel length is often still developing, there will be error in the pressure drop estimate calculated using this assumption. The error in the pressure drop estimate will be more significant for flows that are majority still developing. This is because the shear stress in the entrance region is higher than in the fully developed region, so the pressure drop estimates for fully developed flow will be an underestimate of the pressure drop through the entire pipe [63]. For the laminar case, the friction factor is equal to the friction factor for fully developed flow through infinite parallel plates [63], [67]:

$$f_D = \frac{96}{Re} \quad (3.21)$$

The correlation for infinite parallel plates is used as the aspect ratio of the rectangular channels is high, with the width being 20 times the height of the channel, which is greater than the maximum aspect ratio of 8 used in the table of friction factor relations for rectangular channels in Çengel [63]. For the transitional cases the friction factor was taken from equation (3.19).

The fluid parameters are evaluated at the mean temperature, which was originally estimated to be the average of the entrance temperature and the surface temperature of the heat exchanger. The overall exit temperature of the fluid determined from the above analysis is then used to estimate the bulk mean temperature of the fluid, which is used for determining the air properties. The analysis is repeated until the percent difference between the mean temperature of the fluid used for the analysis and the newly determined mean temperature is below 0.001%. This process is summarized in Figure 3.2 for clarity, and the code is included in Appendix B.

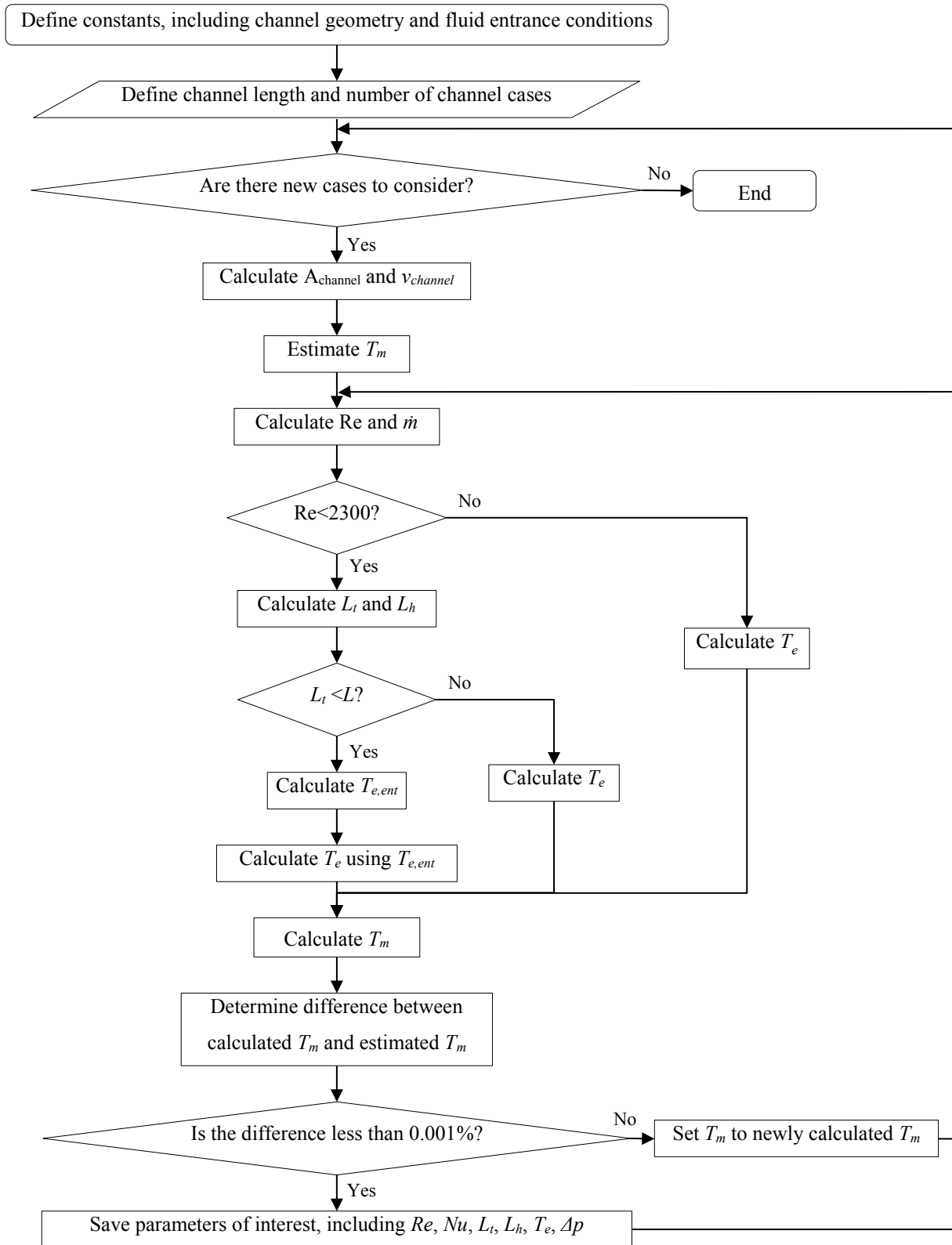


Figure 3.2: Flowchart describing calculation steps for determination of exit temperature and pressure drop through a rectangular channel.

### 3.1.5 Results for Fixed Engine Pressure and Speed for Heating Case

Shown are the results of the steady state isothermal rectangular channel analysis for the heating case, which assumed a surface temperature equal to the source temperature of 150 °C. In Figure 3.3 the exit gas temperature is plotted against heat exchanger volume for each of the channel lengths considered. The exit temperature of the gas approaches the surface temperature asymptotically for increasing heat exchanger volume. For the laminar regime, the exit gas temperatures reduce onto a single curve, with different geometries with the same heat exchanger volume resulting in the same exit gas temperature. To the right of the main curve are the exit temperatures for the transitional regime.

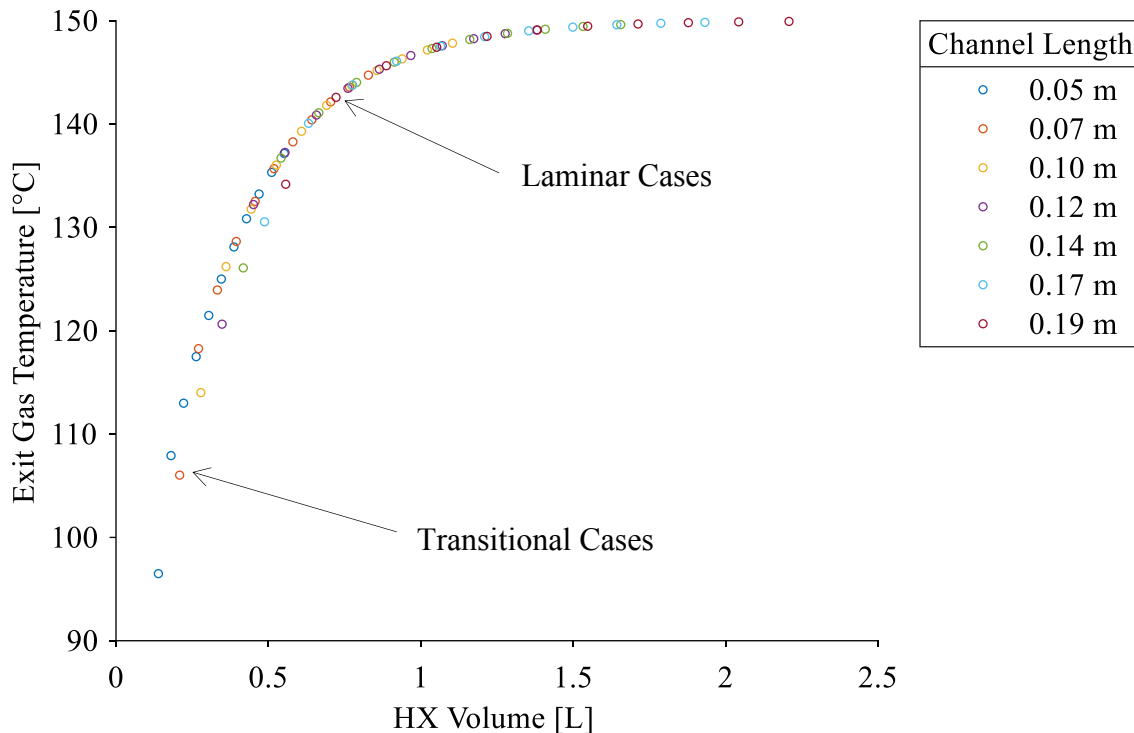


Figure 3.3: Plot of exit gas temperature against heat exchanger volume for various channel lengths considered at an engine speed of 2.833 Hz and engine pressure of 435 kPa for heating.

In Figure 3.4 the exit temperature is plotted against the Reynolds number for the various channel lengths considered. The exit gas temperature varies with Reynolds number as expected, and the longer heat exchanger lengths result in better exit gas temperatures for a given cross-sectional area. This is because the longer heat exchanger lengths have more surface area compared to the shorter ones for a given cross-sectional area.

The transitional regime results can be seen on the right of the plot. When the flow enters the transitional regime, it has a lower overall exit temperature than would be predicted for the laminar regime. This can be seen with the discontinuity between exit gas temperatures at the Reynolds number of 2300. This occurs because the two analytical equations for determining Nusselt number for each regime are not necessarily continuous. Additionally, the transitional regime is assumed to be fully developed due to the lack of available relations for heat transfer in the developing region, leading to underprediction of the heat transfer coefficient and thus exit gas temperature.

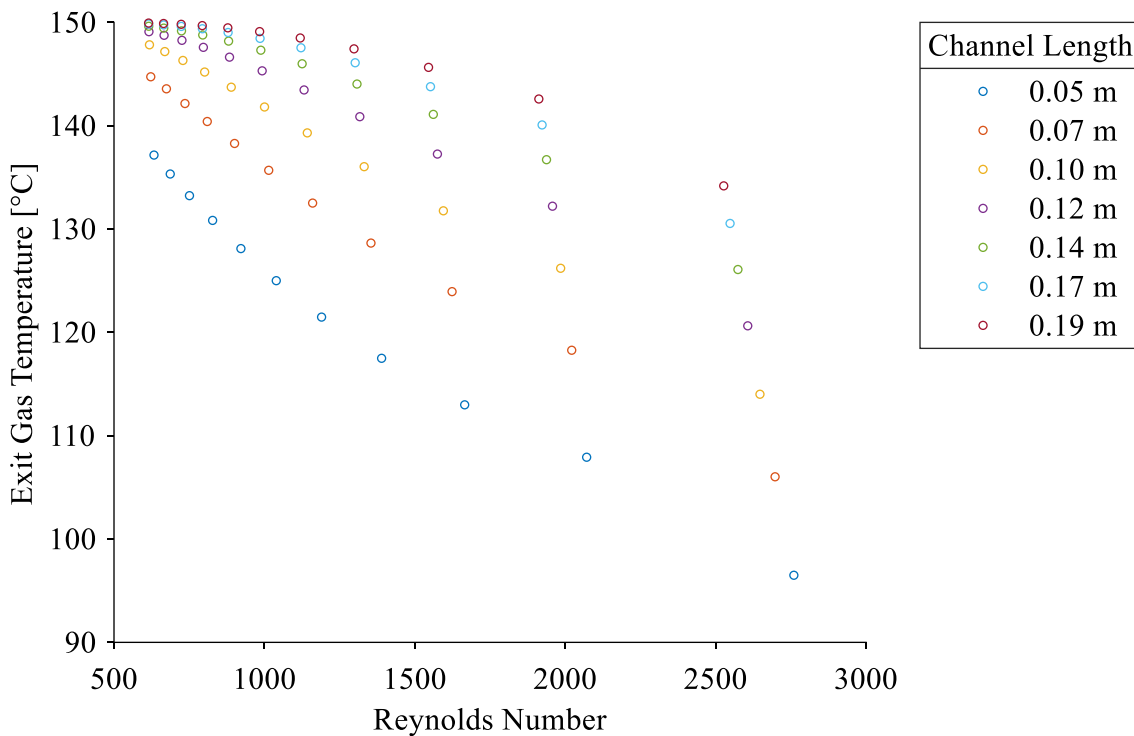


Figure 3.4: Plot of exit gas temperature against Reynolds number for various channel lengths considered at an engine speed of 2.833 Hz and engine pressure of 435 kPa for heating.

To understand why heat exchangers with the same volume have the same exit gas temperature in the laminar regime, the exit gas temperature is plotted against the heat exchanger surface area for the various channel lengths considered, as shown in Figure 3.5. In this plot it can be clearly seen that for each heat exchanger that has the same surface area, the exit gas temperature will be the same in the laminar regime. Again, the transitional regime results are to the right of the main curve.

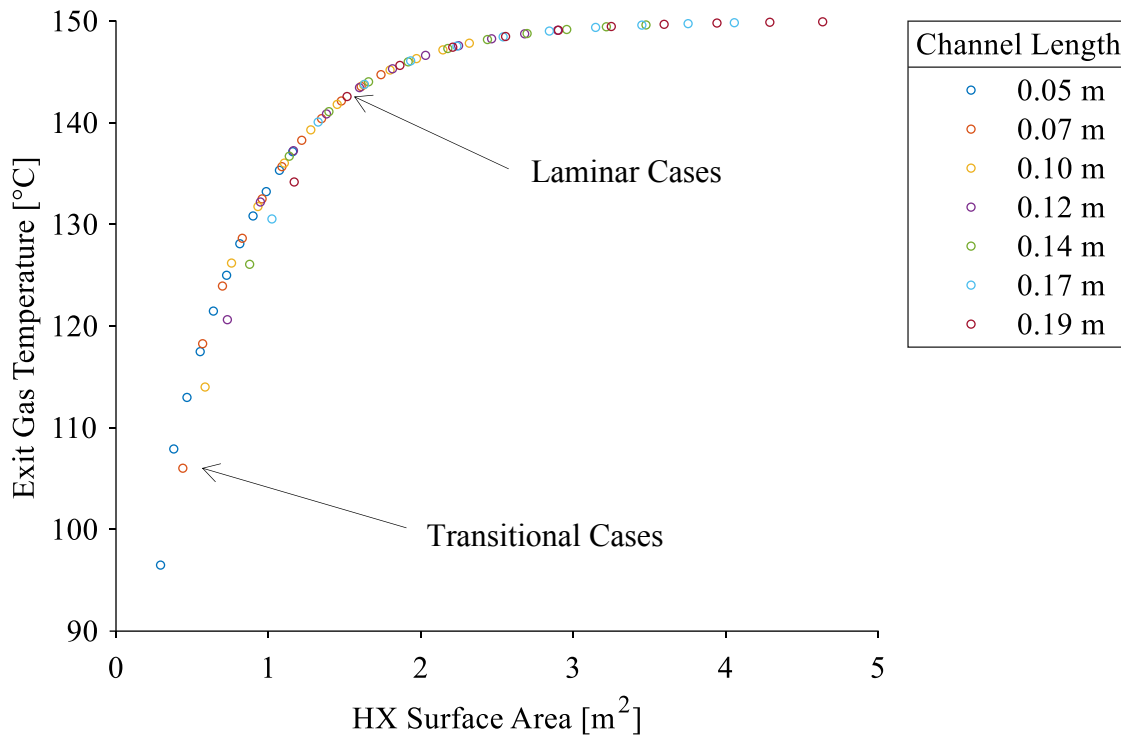


Figure 3.5: Plot of exit gas temperature against heat exchanger surface area for various channel lengths considered at an engine speed of 2.833 Hz and engine pressure of 435 kPa for heating.

As each of these heat exchangers is made up of rectangular channels of the same size, the surface area of the heat exchanger is directly proportional to its volume – they have the same surface area to volume ratio of  $2.1 \text{ m}^2/\text{m}^3$ . Additionally, the displacer velocity is held constant between cases, and the continuity equation is used to determine the air velocity in the rectangular channel. Thus, the channel air velocity is geometrically linked to the cross-sectional area of the heat exchanger. In the laminar regime, the Nusselt number is dependent on thermal entrance length, hydraulic diameter, and Reynolds number. These parameters all have dependence on the heat exchanger geometry. This yields the result that for any heat exchangers with the same surface area and with the same rectangular channel geometry, the Nusselt number is the same for the laminar regime. Thus, the heat transfer coefficient is the same, yielding the same exit gas temperature for heat exchangers with the same surface area. This is a unique result of the conditions of the Stirling engine, as the displacer velocity and displacer cross-sectional area is held constant while the heat exchanger cross-sectional area and thus channel air velocity are variable as a result.

In this case, in order to modify the exit gas temperature of the heat exchanger for a particular volume, the rectangular channel geometry itself would need to be modified. This indicates the possibility of increasing the surface area through a different channel geometry, thus modifying the surface area to volume ratio, in order to reduce the required heat exchanger volume to achieve a certain exit gas temperature.

It should be noted that in the transitional regime, heat exchangers of the same surface area will not yield the same exit gas temperature. The Nusselt number in the transitional regime is only dependent on Reynolds number, with the Nusselt number increasing with increasing Reynolds number. Thus, for heat exchangers with the same surface area, the longer heat exchangers with lower cross-sectional areas yield higher exit temperatures.

In Figure 3.6 the Reynolds number is plotted against the heat exchanger volume for the various channel lengths considered. It can be seen here that the transitional regime only occurs in low cross-sectional area heat exchangers. This limits the total surface area available for heat transfer, thus leading to overall lower exit gas temperatures. Additionally, the dependence of Reynolds number on the heat exchanger length can also be seen, with the cooler gas temperatures resulting from the shorter heat exchanger lengths increasing the Reynolds number compared to the longer heat exchanger lengths.

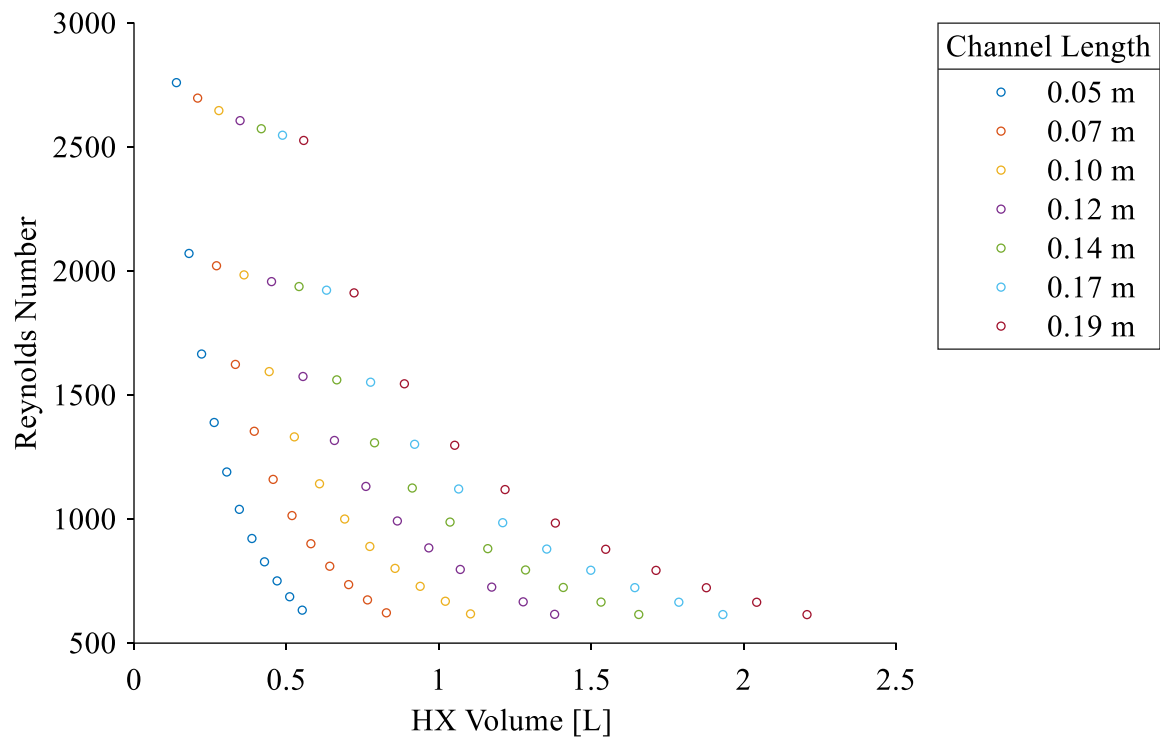


Figure 3.6: Plot of Reynolds number against heat exchanger volume for various channel lengths considered at an engine speed of 2.833 Hz and engine pressure of 435 kPa for heating.

The impact of the different heat exchanger sizes is more significant in the pressure drop through each heat exchanger. In Figure 3.7, the pressure drop across the heat exchanger is plotted against heat exchanger volume for a variety of channel lengths considered. This plot shows that with increasing heat exchanger cross-sectional area for a fixed channel length, the pressure drop through the heat exchanger decreases exponentially. Also, for a fixed heat exchanger cross-sectional area with increasing channel length, the pressure drop through the heat exchanger increases linearly. The rate at which this linear increase happens is higher for lower cross-sectional areas.



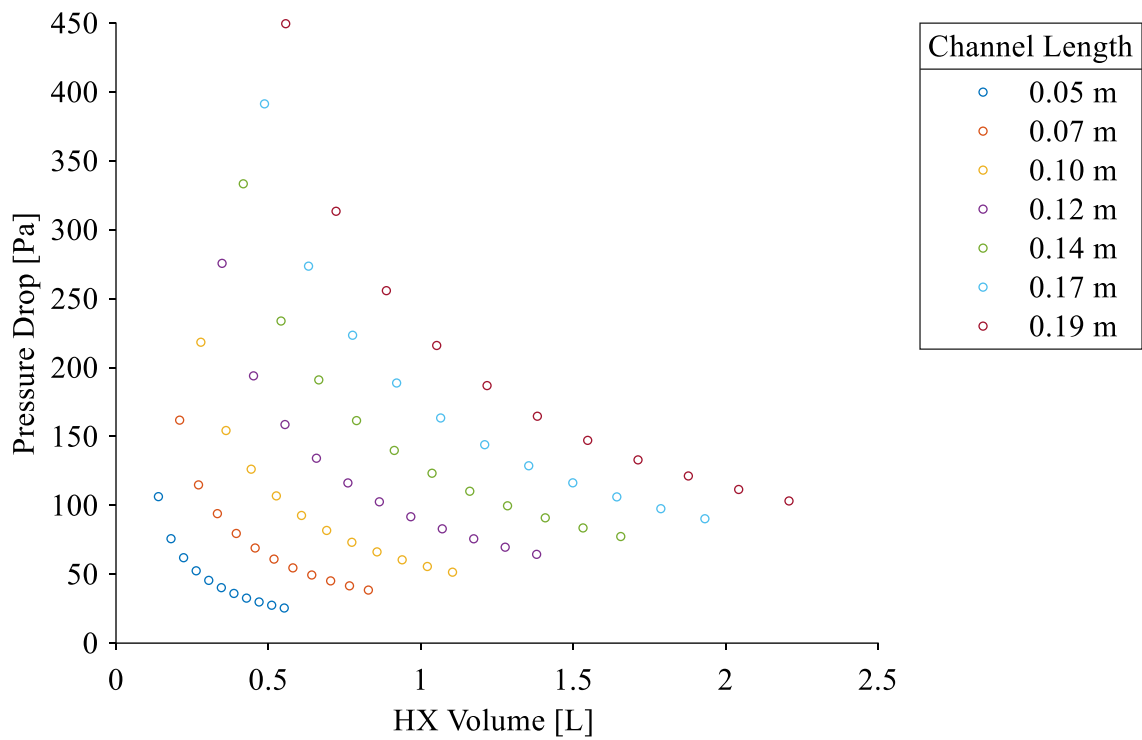


Figure 3.7: Plot of pressure drop against heat exchanger volume for various channel lengths considered at an engine speed of 2.833 Hz and engine pressure of 435 kPa for heating.

Figure 3.8 plots the pressure drop against Reynolds number for a variety of channel lengths considered. As expected, the pressure drop increases linearly with Reynolds number for a given heat exchanger length in the laminar regime. Again, the discontinuity for the change from laminar to transitional regime is visible as the slope of the pressure drop increase changes, resulting in even higher pressure drops in the transitional regime.

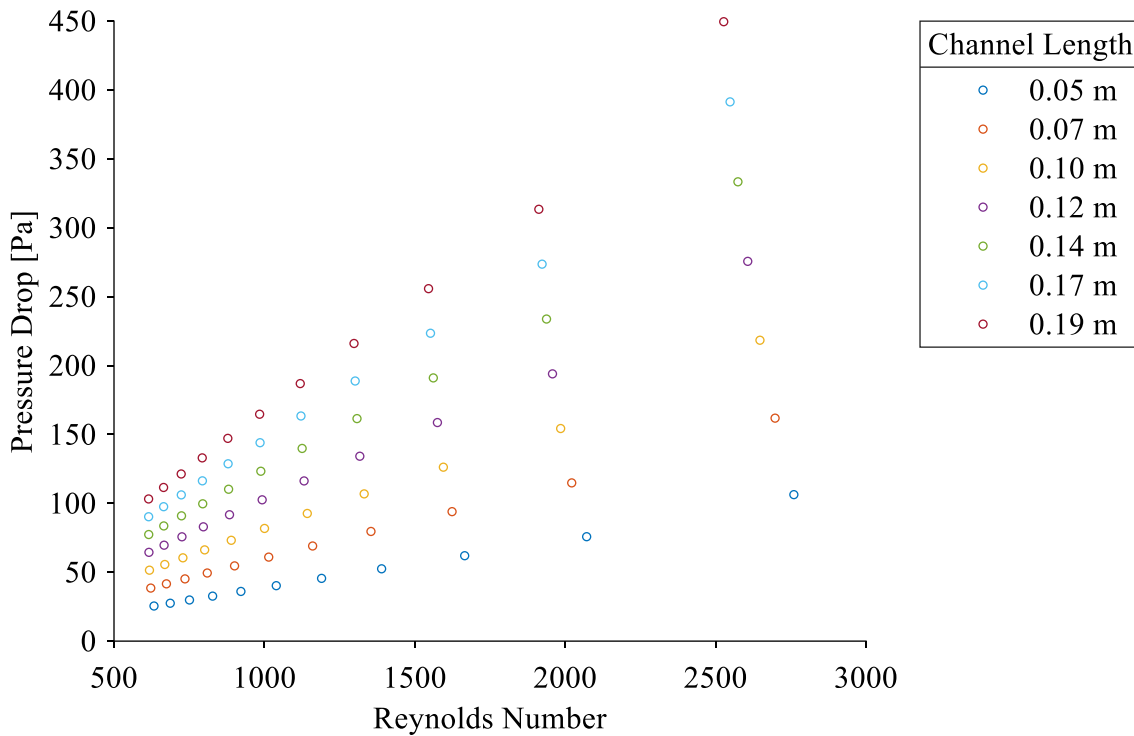


Figure 3.8: Plot of pressure drop against Reynolds number for various channel lengths considered at an engine speed of 2.833 Hz and engine pressure of 435 kPa for heating.

For the design of heat exchangers of LTDSEs, these results indicate that shorter heat exchangers with sufficient surface area are preferred over longer heat exchanger because of their lower pressure drop. The pressure drop varies more strongly with heat exchanger length than with cross-sectional area, though both have an impact.

Additionally, it should be noted that the choice of channel geometry will impact the optimal heat exchanger volume required for a LTDSE, as a heat exchanger with a higher surface area to volume ratio can achieve the same surface area with a lower overall heat exchanger volume. Thus, a potentially different optimum heat exchanger volume could be achieved.

### 3.1.6 Results from Engine Pressure and Speed Sensitivity for Heating Case

The results of the sensitivity on engine speed are presented in this section for the heating case. The variation with pressure and speed is summarized into a set of three-dimensional plots to display the changes in the overall trends. Each plot displays the same data as the two-dimensional plots shown in the previous section.

In Figure 3.9, the exit temperature is plotted against both heat exchanger volume and channel length for various pressures at a given engine speed. For all pressure and speed cases considered, the exit temperature still asymptotically approaches the surface temperature with increasing heat exchanger volume and channel length, with the same discrepancies due to the transitional regime and the thermal entry lengths visible in the surface. At a given speed, the higher pressure cases approach the exit temperature more slowly, as seen by the higher pressure surfaces being below the lower pressure surfaces. Additionally, as the engine speed increases the approach to the exit temperature is also much slower. This is due to the increased mass flow through the heat exchanger requiring more surface area to approach the surface temperature than is available, as the heat exchanger sizes remain in the same range.

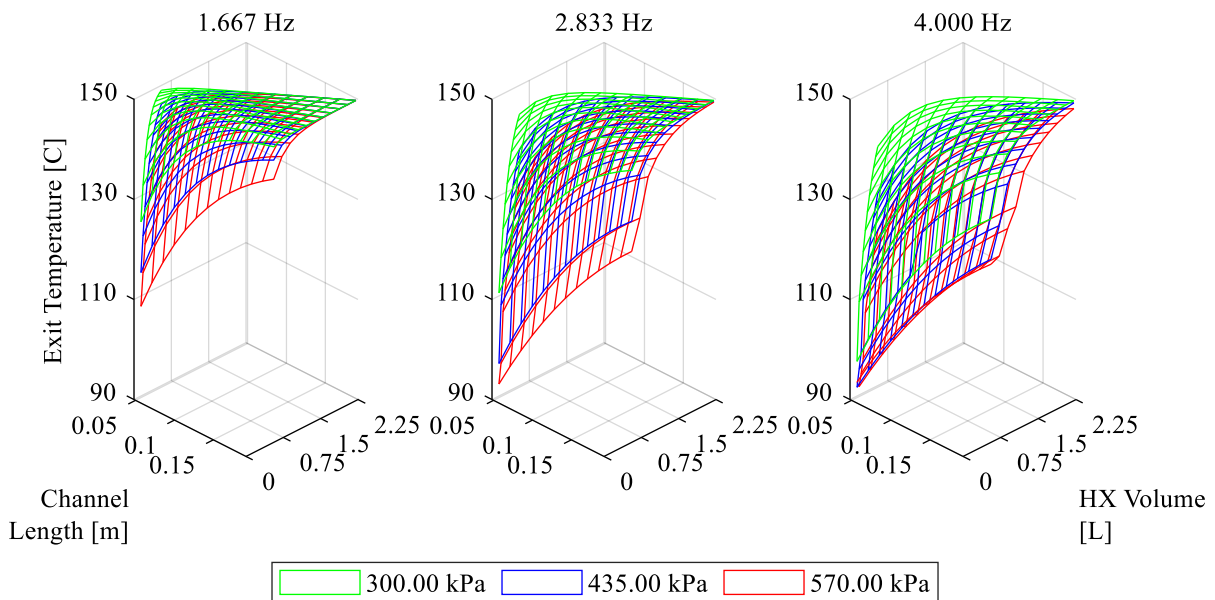


Figure 3.9: Plot of exit gas temperature against heat exchanger volume for various channel lengths considered at varying engine pressure and speeds for heating.

In Figure 3.10 the exit temperature is plotted against both Reynolds number and channel length for various pressures at given engine speeds. For all pressure and speed cases shown, the

discontinuity at a Reynolds number of 2300 is still visible. Additionally, higher pressure and higher speed cases result in overall higher Reynolds numbers, as expected. These higher Reynolds number cases do not result in improved exit gas temperatures over the lower Reynolds number cases, though a slight increase in the exit gas temperature for the high pressure and high speed case can be seen. This results from the increase in heat transfer coefficient at the high Reynolds number being sufficient to improve the exit gas temperature over a lower Reynolds number case. However, due to the lack of overall surface area, the exit gas temperature is still lower than those of lower Reynolds number cases.

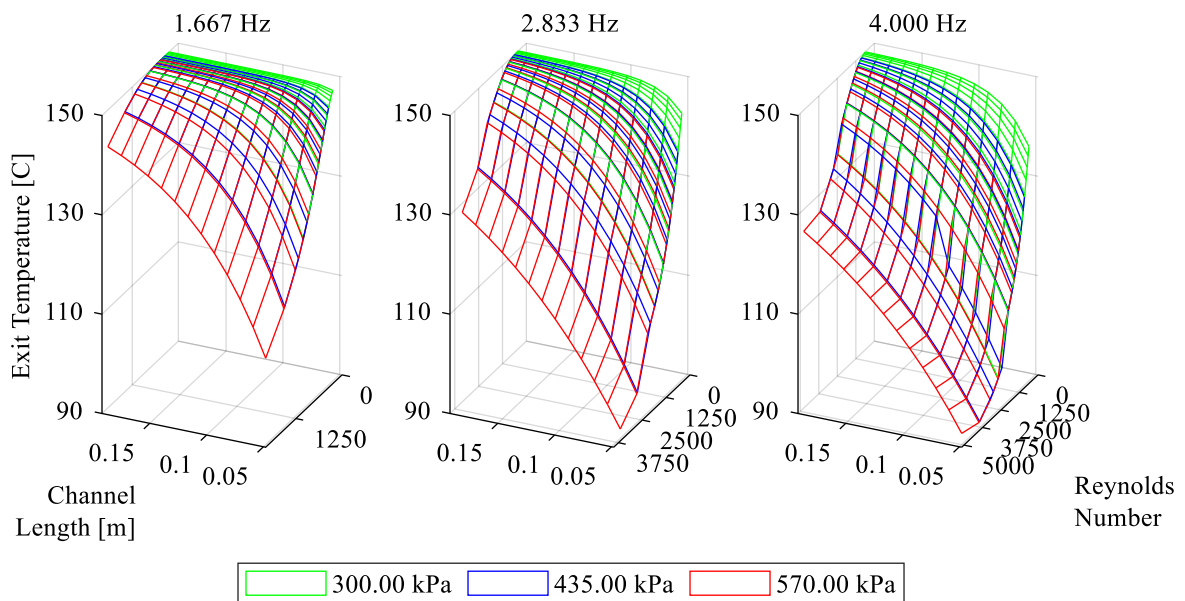


Figure 3.10: Plot of exit gas temperature against Reynolds number for various channel lengths considered at varying engine pressures and speeds for heating.

The dominant effect on exit temperature is still the heat exchanger surface area. This is shown in Figure 3.11 where the exit temperature is plotted against the heat exchanger surface area and channel length for various pressures at a given engine speed. Once again, the trends seen in the plot against heat exchanger volume in Figure 3.9 are identical to those in the plot against heat exchanger surface area.

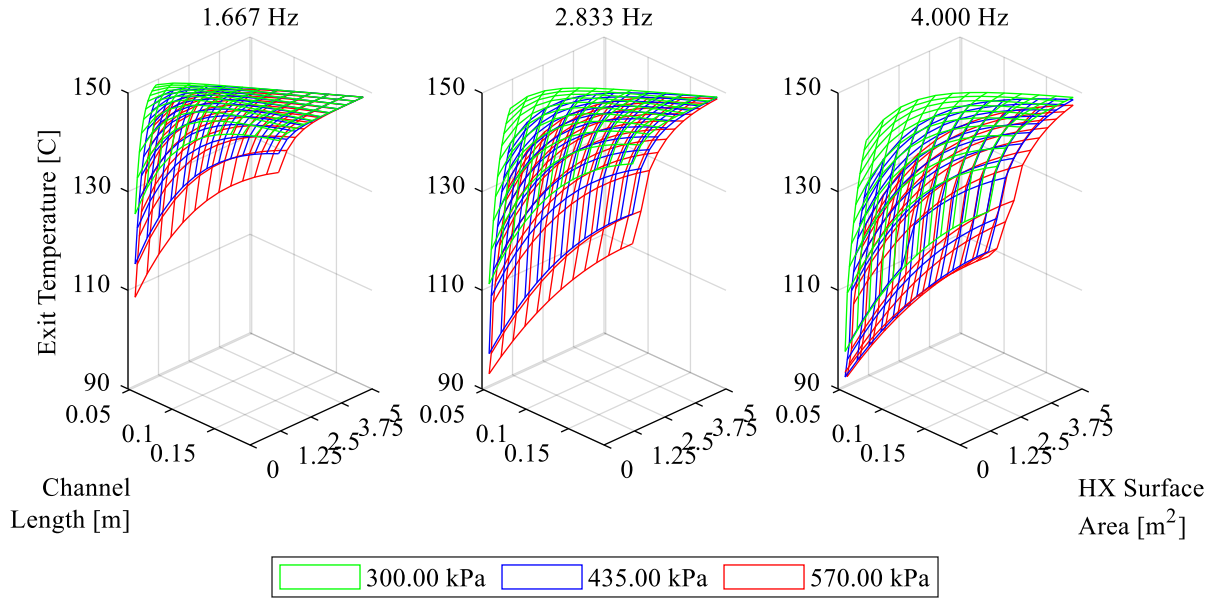


Figure 3.11: Plot of exit gas temperature against heat exchanger surface area for various channel lengths considered at varying engine pressures and speeds for heating.

In Figure 3.12 the Reynolds number is plotted against the heat exchanger volume and channel length. As was seen previously, the Reynolds number is slightly affected by the channel length, due to the difference in temperature achieved with length. The Reynolds number is also higher for smaller heat exchanger volumes, higher pressures and higher speeds, as expected.

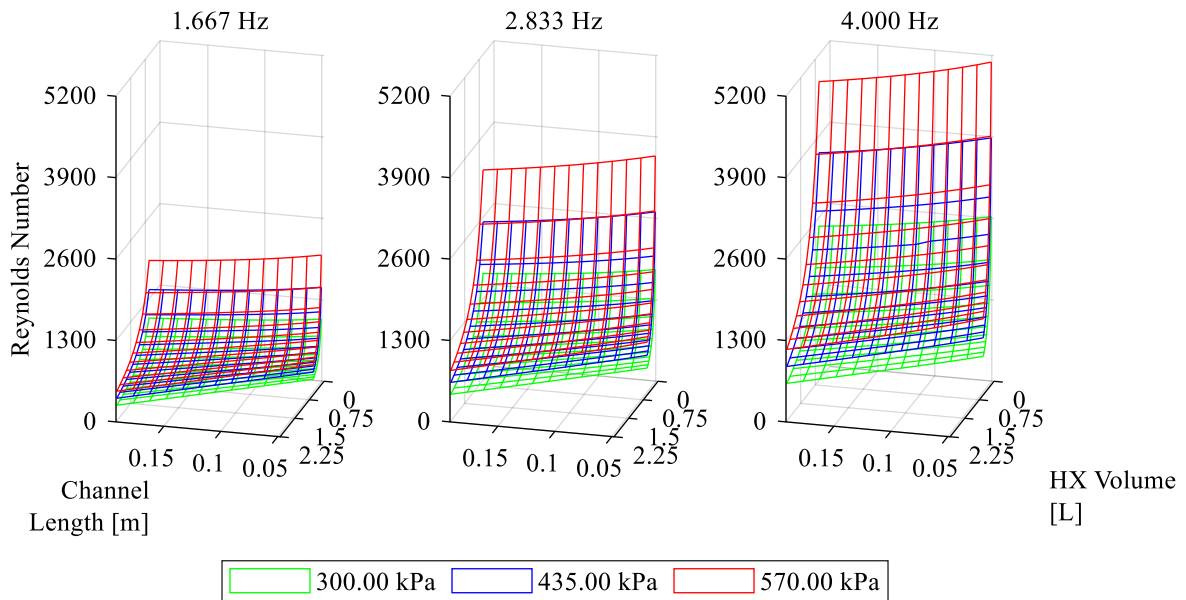


Figure 3.12: Plot of Reynolds number against heat exchanger volume for various channel lengths considered at varying engine pressures and speeds for heating.

In Figure 3.13 the pressure drop through the heat exchanger is plotted against heat exchanger volume and channel length for various pressures and engine speeds. The increase in pressure drop with increasing channel length and decreasing heat exchanger cross-sectional area is still evident. The pressure drop increases with increasing engine speed, to up to twice the value of the slower speed case. This is expected as equation (3.20) for pressure drop shows that pressure drop is proportional to the square of the channel velocity, which is proportional to engine speed. This shows that there is a significant penalty in flow friction when the engine is running at higher speeds. There is not a significant dependence on engine pressure for the pressure drop in the laminar regime. The increase in density from higher pressures results in a higher Reynolds number, which leads to a lower friction factor, so these effects largely negate each other. In the transitional regime found in smaller heat exchanger volume cases, the friction factor increases exponentially with Reynolds number. Thus, with the higher Reynolds number in high pressure cases, the pressure drop is higher than in lower pressure cases.

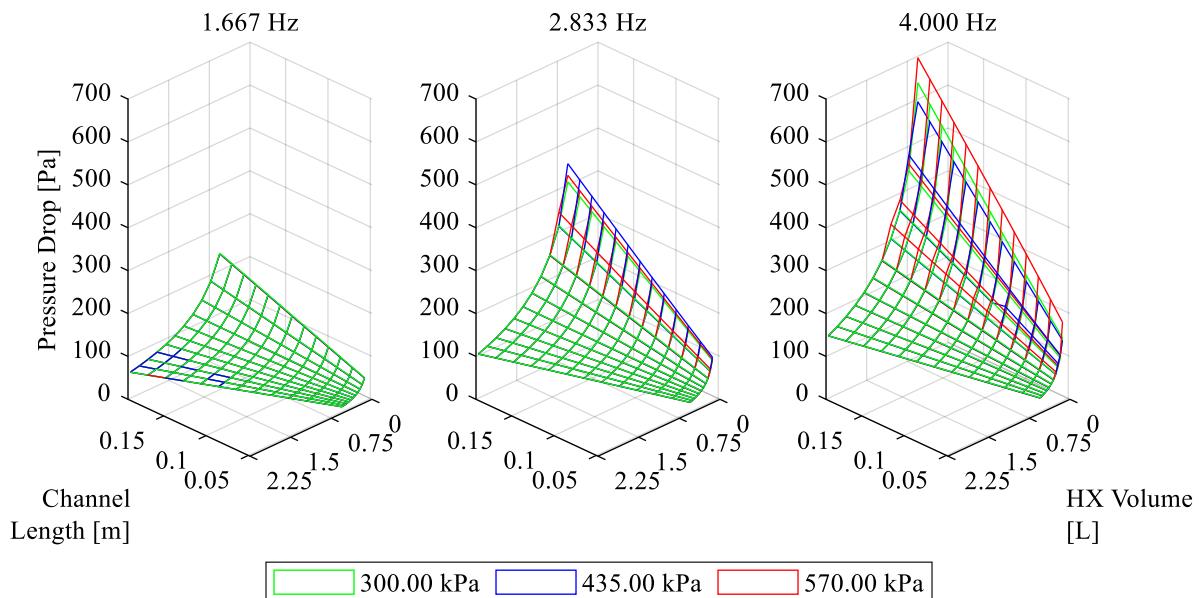


Figure 3.13: Plot of pressure drop against heat exchanger volume for various channel lengths considered at varying engine pressures and speeds for heating.

In Figure 3.14 the pressure drop is plotted against Reynolds number and channel length for various engine speeds and pressures. The discontinuity in the pressure drop is more clearly visible at Reynolds number of 2300, as well as another inflection point near a Reynolds number of 4500 where the friction factor begins to increase with Reynolds number rather than decrease

in the transitional regime. The lower pressure cases have a higher pressure drop at any given Reynolds number than the high pressure cases. This is because in order to maintain the same Reynolds number with an increase in pressure, the air velocity must decrease, leading to a lower overall pressure drop than for the equivalent lower pressure case.

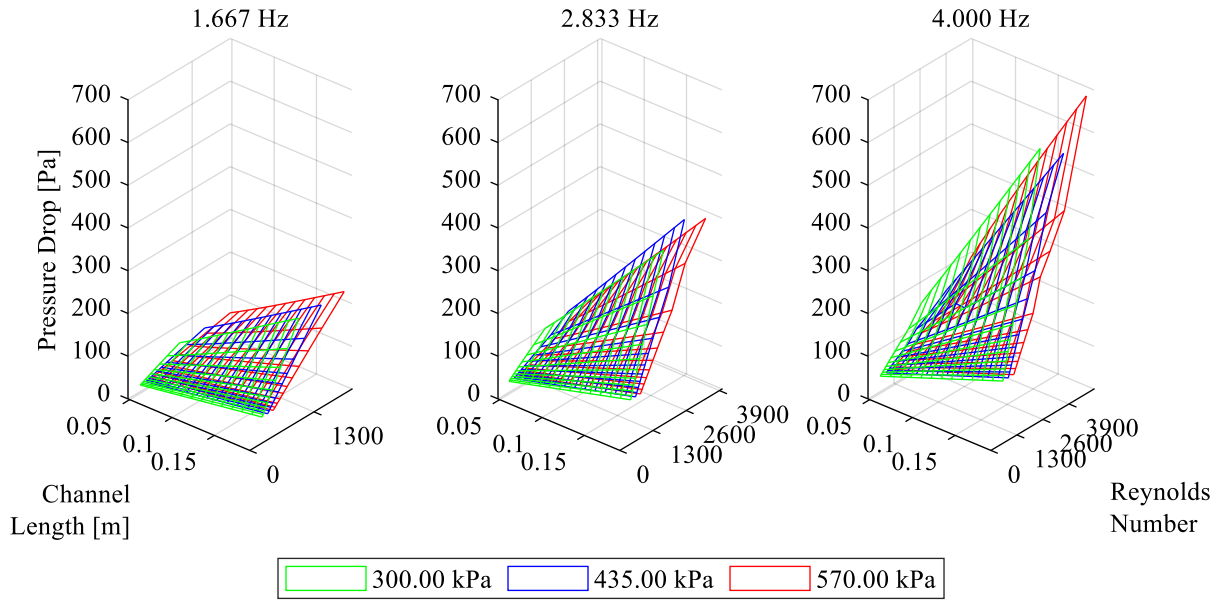


Figure 3.14: Plot of pressure drop against Reynolds number for various channel lengths considered at varying engine pressures and speeds for heating.

### 3.1.7 Summary of Results for the Cooling Case

The analysis described in section 3.1.4 was also undertaken for the cooling case. The corresponding plots to section 3.1.5 for the base cooling case are shown in Appendix C, and the corresponding plots to section 3.1.6 for the sensitivity cooling cases are shown in Appendix D.

The trends exhibited in the heating case are the same in the cooling case, for both the base case and the sensitivity cases. Due to the higher density of air for cooler temperatures the Reynolds numbers are overall higher and more cases are in the transitional regime. It is of interest to note the more obvious improvement in exit gas temperature in the cooling case with higher Reynolds numbers. To show this, the exit gas temperature is plotted against the Reynolds number for various channel lengths for the transitional regime cooling cases in Figure 3.15. The plot is from the highest pressure and speed sensitivity case as there are more transitional regime cases at those conditions. As the Reynolds number increases, the exit gas temperature decreases as the heat transfer coefficient improves sufficiently to overcome the lack of surface area available.

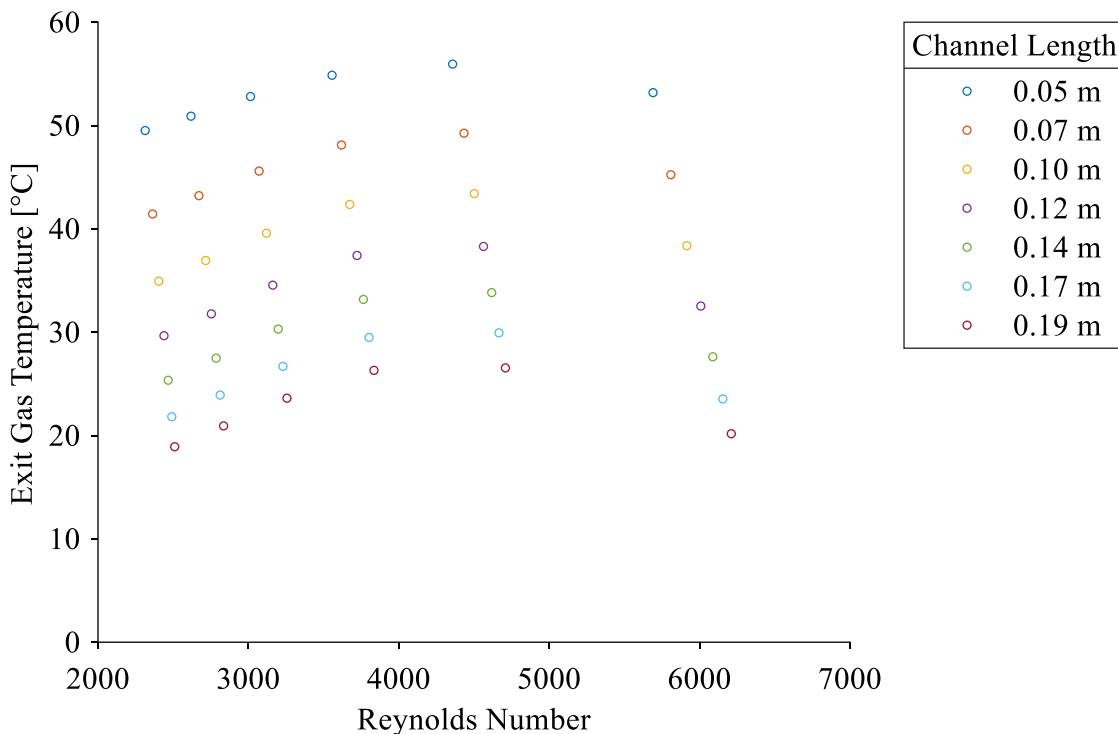


Figure 3.15: Plot of transitional regime results of exit gas temperature against Reynolds number for various channel lengths considered at an engine speed of 4.000 Hz and engine pressure of 570 kPa for the cooling case.



The variation in exit gas temperature for the same heat exchanger surface area in the transitional regime is also more visible in the cooling case. The exit gas temperature is plotted against the heat exchanger surface area for various channel lengths for the transitional cooling cases in Figure 3.16, for the highest pressure and speed sensitivity case. It can be seen that the longer heat exchangers result in lower exit gas temperatures, and the results do not all collapse onto the same curve. Instead, the aforementioned trend of decreasing exit temperature with sufficiently high Reynolds number can be seen for each of the heat exchanger lengths. The high Reynolds number case occurs for the smallest heat exchanger cross-sectional area, which corresponds to the lowest heat exchanger surface area on the plot. These points are seen on the left side of the plot.

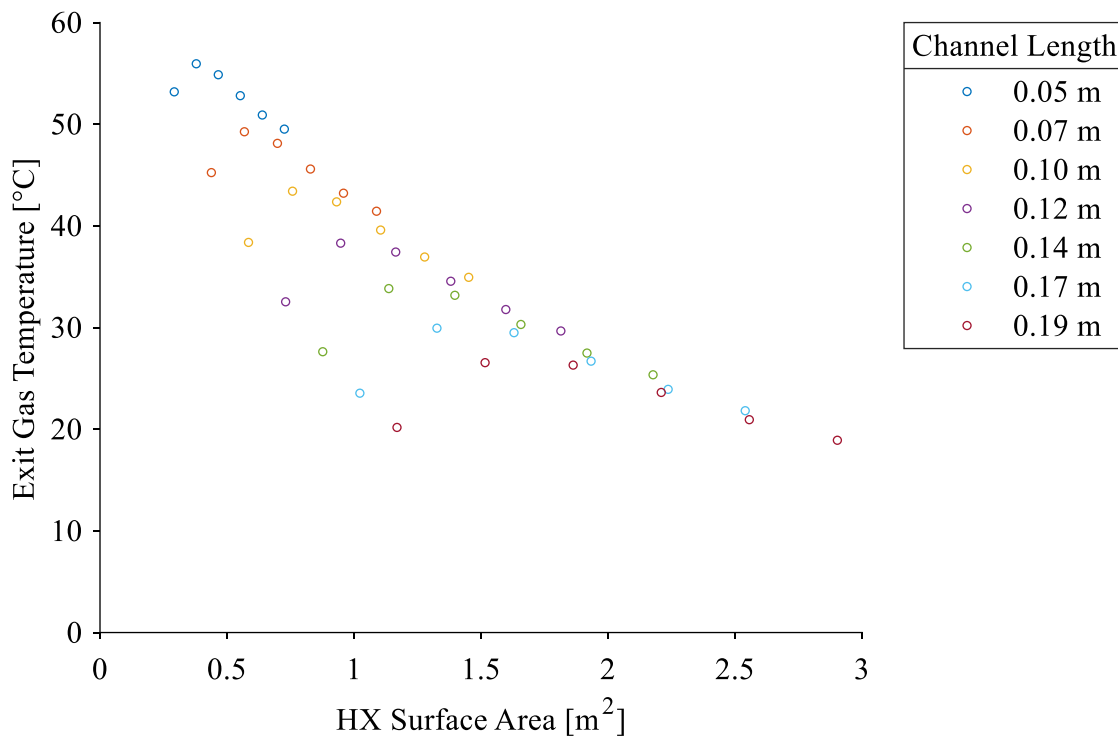


Figure 3.16: Plot of transitional regime results of exit gas temperature against heat exchanger surface area for various channel lengths considered at an engine speed of 4.000 Hz and engine pressure of 570 kPa for cooling.

Also, the pressure drop in the transitional regime varies exponentially with Reynolds number for a given heat exchanger length, as opposed to linearly as in the laminar case. This is seen in a plot of pressure drop against the Reynolds number for various channel lengths for the transitional regime cooling cases in Figure 3.17, for the highest pressure and speed sensitivity case. There are additional performance penalties on the engine output power through the increased pressure drop in the transitional regime.

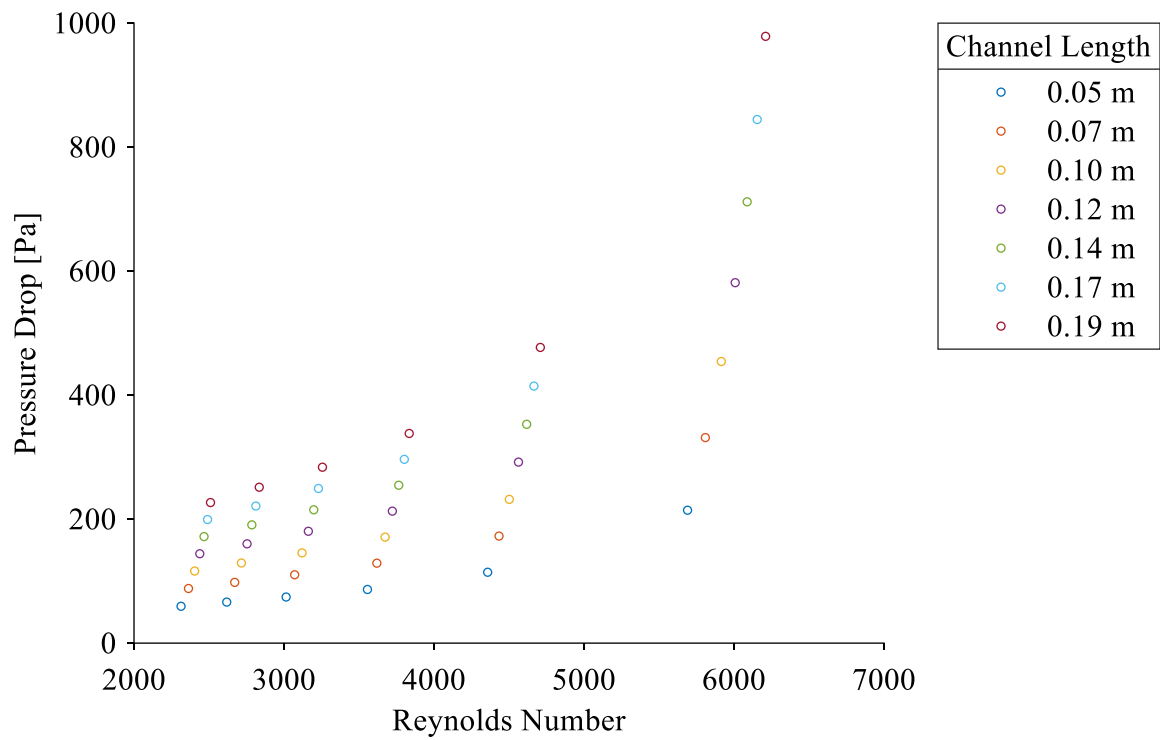


Figure 3.17: Plot of transitional regime results of pressure drop against Reynolds number for various channel lengths considered at an engine speed of 4.000 Hz and engine pressure of 570 kPa for cooling.

### 3.2 Schmidt Model Evaluation of Effect of Dead Volume

To understand the impact of dead volume on power output for a Stirling engine, the Schmidt model is used. The Schmidt model derivation, both the method used by Senft [25] and a derivation for Gamma type engines directly from the isothermal model is used. Although the Schmidt model is not able to model the performance of the heat exchangers, it is useful in determining a potential optimum power with varying dead volume and gas temperature.

The Schmidt model is a 1<sup>st</sup> order model that is a closed form solution of the isothermal model as described by Urieli and Berchowitz [20]. The isothermal model divides the engine into five connected spaces: the compression space, the cold heat exchanger, the regenerator, the hot heat exchanger, and the expansion space. These spaces assume a temperature profile as shown in Figure 3.18. Any clearance volumes in the engine, such as the connecting pipe or appendix gap, are assigned to the compression or expansion space clearance volumes.

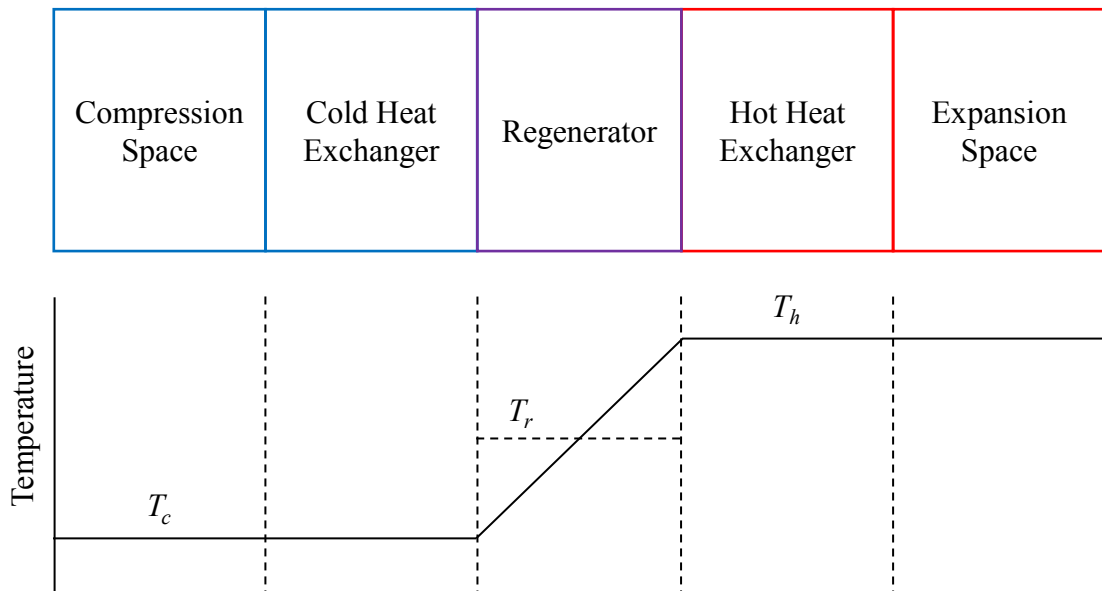


Figure 3.18: Isothermal model spaces and temperature profile. Figure adapted from Urieli and Berchowitz [20].

The isothermal model assumes that the five working spaces of the engine are isothermal, and the working fluid assumes the temperature of the space immediately upon entering. The other key assumptions of the isothermal analysis are [20]:

- The mass of the working fluid is constant; there is no leakage in the engine.
- The working fluid is an ideal gas.
- The speed of the engine is constant.
- The engine runs at a cyclic steady state.
- The kinetic and potential energies of the gas are neglected.
- The instantaneous pressure in all engine spaces is uniform.

To determine the work done by the engine, the pressure inside the spaces must be determined. This is done by using the ideal gas law to relate the pressure in the engine to the volume of each of the working spaces, in the following form:

$$p = mR \left( \frac{V_c}{T_c} + \frac{V_k}{T_c} + \frac{V_r}{T_r} + \frac{V_h}{T_h} + \frac{V_e}{T_h} \right)^{-1} \quad (3.22)$$

where:

$p$  – engine pressure (Pa)

$m$  – total mass of air in the working spaces (kg)

$R$  – universal gas constant (J/Kmol)

$V_c$  – compression space volume (m<sup>3</sup>)

$V_k$  – cold heat exchanger volume (m<sup>3</sup>)

$V_r$  – regenerator volume (m<sup>3</sup>)

$V_h$  – hot heat exchanger volume (m<sup>3</sup>)

$V_e$  – expansion space volume (m<sup>3</sup>)

$T_r$  – mean effective regenerator temperature (K)

In the above relation for the ideal gas law, the mean effective regenerator temperature is used to represent the linear temperature profile present in the regenerator. The mean effective regenerator temperature is determined from the below equation, whose derivation is shown in Urieli [20]:

$$T_r = \frac{(T_h - T_c)}{\ln\left(\frac{T_h}{T_c}\right)} \quad (3.23)$$

The volume of the compression and the expansion spaces varies with crank angle, which means that pressure will vary with crank angle. To determine the total work over a cycle, the area enclosed in the pressure-volume diagram can be calculated from:

$$W = W_c + W_e = \oint p(\theta) \left( \frac{dV_c}{d\theta} + \frac{dV_e}{d\theta} \right) d\theta \quad (3.24)$$

where:

$W$  – total work per cycle (J)

$W_c$  – compression work per cycle (J)

$W_e$  – expansion work per cycle (J)

$\theta$  – crank angle (rad)

As can be seen by the above equation, the output work of the cycle can be determined if the volume variation of the compression and expansion spaces is known. The Schmidt model assumes that the piston motion is perfectly sinusoidal, thus the volume variation of the spaces are perfectly sinusoidal, which allows for the integral to be solved in a closed form.

### 3.2.1 Schmidt Model as derived by Senft

As the engine being investigated is a gamma type Stirling engine, Senft's derivation of the closed-form Schmidt model equations for gamma type engines can be used [25]. The derivation by Senft is provided here for context.

The volume variation of the expansion ( $V_e$ ) and compression ( $V_c$ ) spaces is related to the volume variation of the displacer swept volume and the power piston swept volume by equations (3.25) and (3.26) below, which assume that the power piston is part of the compression space:

$$V_e = \frac{V_{disp}}{2} (1 + \cos(\theta + \alpha)) \quad (3.25)$$

$$V_c = \frac{V_{disp}}{2} (1 - \cos(\theta + \alpha)) + \frac{V_{power}}{2} (1 + \cos(\theta)) \quad (3.26)$$

where:

$V_{disp}$  – displacer piston swept volume ( $\text{m}^3$ )

$V_{power}$  – displacer piston swept volume ( $\text{m}^3$ )

$\alpha$  – phase angle (rad)

These relations are substituted into a simplified equation (3.22):

$$p = mR \left( \frac{V_c}{T_c} + \frac{V_{dead}}{\frac{T_h + T_c}{2}} + \frac{V_e}{T_h} \right)^{-1} \quad (3.27)$$

where:

$V_{dead}$  – total dead volume ( $\text{m}^3$ )

to determine the instantaneous pressure as related to crank angle. The  $V_{dead}$  term includes all of the dead volume of the engine, including the heat exchanger and regenerator volume, which is assumed to be at the arithmetic mean of the expansion and compression space temperatures.

The instantaneous pressure is then determined as:

$$p = \frac{2mRT_c}{V_{disp}[Y + X\cos(\theta - \phi)]} \quad (3.28)$$

where  $X$ ,  $Y$ , and  $\phi$  are defined:

$$Y = 1 + \frac{T_c}{T_h} + \frac{V_{power}}{V_{disp}} + \frac{4 \frac{V_{dead}}{V_{disp}} \frac{T_c}{T_h}}{1 + \frac{T_c}{T_h}} \quad (3.29)$$

$$X = \sqrt{\left(\frac{V_{power}}{V_{disp}}\right)^2 - 2 \frac{V_{power}}{V_{disp}} \left(1 - \frac{T_c}{T_h}\right) \cos(\alpha) + \left(1 - \frac{T_c}{T_h}\right)^2} \quad (3.30)$$

$$\phi = \arccos\left(\frac{\frac{V_{power}}{V_{disp}} - \left(1 - \frac{T_c}{T_h}\right) \cos(\alpha)}{X}\right) \quad (3.31)$$

The instantaneous pressure equation is further simplified by Senft [25] by determining the root mean pressure. This enables the engine pressure to be written as a function of the average pressure, and defines the constant mass of air in the engine by the average cycle pressure, which is a more useful design parameter. The maximum and minimum of equation (3.28) occur when the cosine function takes on a value of either -1 or 1 respectively, as shown in the equations below.

The root mean average of the pressure is then determined using:

$$p_{mean} = \frac{2mRT_c}{V_{disp}\sqrt{Y^2 - X^2}} \quad (3.32)$$

where:

$p_{mean}$  – root mean average cycle pressure (Pa)

This root mean average of the pressure is used to determine the overall mass of the air,  $m$ , used in equation (3.22) and further analyses. The average cycle pressure being analyzed is inserted into equation (3.32) and it is rearranged to determine the mass of air:

$$m = \frac{p_{mean}V_{disp}\sqrt{Y^2 - X^2}}{2RT_c} \quad (3.33)$$

Finally, the instantaneous engine pressure may be written in terms of the average pressure:

$$p = \frac{p_{mean}\sqrt{Y^2 - X^2}}{Y + X \cos(\theta - \phi)} \quad (3.34)$$

This instantaneous engine pressure is then substituted into equation (3.24) to obtain the closed-form expression for work. It should be noted that the sum of the derivatives of expansion space and compression space volume with respect to crank angle is equivalent to the derivative of the total engine volume with respect to crank angle, as the dead volume is not dependent on crank angle:

$$V_T = V_e + V_{dead} + V_c \quad (3.35)$$

$$\frac{dV_T}{d\theta} = \frac{dV_e}{d\theta} + \frac{dV_{dead}}{d\theta} + \frac{dV_c}{d\theta} = \frac{dV_e}{d\theta} + \frac{dV_c}{d\theta} \quad (3.36)$$

where:

$V_T$  – total engine volume (m<sup>3</sup>)

The closed-form expression for work is then:

$$W = -\frac{V_T p_{mean} V_{power} \sqrt{Y^2 - X^2}}{2(V_{power} + V_{disp})} \int_0^{2\pi} \frac{\sin(\theta)}{Y + X \cos(\theta - \phi)} d\theta \quad (3.37)$$

This is then integrated and the indicated work for the cycle is determined from the following expression:

$$W = \frac{\pi \left(1 - \frac{T_c}{T_h}\right) V_T p_{mean} V_{power} \sin(\alpha)}{(V_{power} + V_{disp})(\sqrt{Y^2 - X^2} + Y)} \quad (3.38)$$



### **3.2.2 Schmidt Model derived from Isothermal Model**

A key assumption in Senft's derivation of the Schmidt model for gamma type Stirling engines comes from the simplification of the temperature profile within the engine. For simplicity, Senft assumes that all dead volume in the engine is at the arithmetic mean of the expansion space and compression space temperatures. This differs from the isothermal model and the original Schmidt model temperature profile, wherein the heat exchangers are at the source and sink temperatures, the regenerator has a linear temperature profile from which the mean effective regenerator temperature shown in equation (3.23) is used for analysis, and dead space in the expansion and compression spaces is evaluated at the temperatures of each respective space. To evaluate whether this simplification has a significant impact on the power output calculated by the Schmidt model, the Schmidt model equations are derived using the volume variations presented for gamma type engines in equations (3.25) and (3.26) without simplifying the treatment of the temperatures of the dead spaces in the engine. The detailed derivation is provided in Appendix E.

The instantaneous pressure as related to crank angle is determined by directly substituting the volume variations for the expansion and compression spaces from equations (3.25) and (3.26) into the ideal gas law relation shown in equation (3.22). After simplification, the instantaneous pressure as related to crank angle, with constants  $B$ ,  $C$ , and  $y$  is:

$$p = \frac{mR}{B + C \cos(\theta + y)} \quad (3.39)$$

where  $B$ ,  $C$ , and  $y$  are defined as shown below:

$$B = \frac{V_{disp}}{2T_c} + \frac{V_{power}}{2T_c} + \frac{V_{clc}}{T_c} + \frac{V_k}{T_c} + \frac{V_r \ln\left(\frac{T_h}{T_c}\right)}{T_h - T_c} + \frac{V_h}{T_h} + \frac{V_{cle}}{T_h} + \frac{V_{disp}}{2T_h} \quad (3.40)$$

$$C = \sqrt{\left(\frac{V_{disp}(T_c - T_h)}{2T_h T_c} \cos(\alpha) + \frac{V_{power}}{2T_c}\right)^2 + \left(\frac{V_{disp}(T_c - T_h)}{2T_h T_c} \sin(\alpha)\right)^2} \quad (3.41)$$

$$y = \arctan\left(\frac{\frac{V_{disp}(T_c - T_h)}{2T_h T_c} \sin(\alpha)}{\frac{V_{disp}(T_c - T_h)}{2T_h T_c} \cos(\alpha) + \frac{V_{power}}{2T_c}}\right) \quad (3.42)$$

where:

$V_{clc}$  – compression space clearance volume ( $m^3$ )

$V_{cle}$  – expansion space clearance volume ( $m^3$ )

Note that for the isothermal model, the compression space and expansion space clearance volumes are assigned to the temperatures of the expansion and compression space, respectively.

To determine the mass of air, the cycle mean pressure is determined to be as follows:

$$p_{mean} = \frac{mR}{B \sqrt{1 - \left(\frac{C}{B}\right)^2}} \quad (3.43)$$

By rearranging the above equation and providing the cycle mean pressure, the mass of air in the engine is found as:

$$m = \frac{p_{mean} B}{R} \sqrt{1 - \left(\frac{C}{B}\right)^2} \quad (3.44)$$

This instantaneous engine pressure is then inserted into equation (3.24) to obtain the closed-form expression for work. It should be noted that the sum of the derivatives of expansion space and compression space volume with respect to crank angle is equivalent to the derivative of the total engine volume with respect to crank angle, as the heat exchanger and regenerator volumes are not dependent on crank angle:

$$V_T = V_e + V_h + V_r + V_k + V_c \quad (3.45)$$

$$\frac{dV_T}{d\theta} = \frac{dV_e}{d\theta} + \frac{dV_{cle}}{d\theta} + \frac{dV_h}{d\theta} + \frac{dV_r}{d\theta} + \frac{dV_k}{d\theta} + \frac{dV_{clc}}{d\theta} + \frac{dV_c}{d\theta} = \frac{dV_e}{d\theta} + \frac{dV_c}{d\theta} \quad (3.46)$$

The closed-form expression for work is then:

$$W = -\frac{mRV_{power}}{2B} \int_0^{2\pi} \frac{\sin(\theta)}{1 + \frac{C}{B} \cos(\theta + \gamma)} d\theta \quad (3.47)$$

This is then integrated and the indicated work for the cycle has the expression:

$$W = \frac{V_{power}\pi B}{C} p_{mean} \left( \sqrt{1 - \left(\frac{C}{B}\right)^2} - 1 \right) \sin(\gamma) \quad (3.48)$$

To determine the power output, the indicated work is multiplied by the engine frequency to determine the power output per cycle as:

$$P = Wf \quad (3.49)$$

where:

$P$  – engine power per cycle (W)

### 3.2.3 Parameter Selection for Schmidt Model Study

For this investigation of engine power output with varying heat exchanger volume, the engine considered was based on the Raphael engine introduced in Chapter 2. The total volume of both the hot and cold heat exchangers on the Raphael engine is 1.104 L. The maximum volume of both heat exchangers considered was 8 L, which is approximately eight times the actual heat exchanger volume. This yielded a maximum dead volume ratio considered of 3.66. This overestimation of the heat exchanger size was chosen to cover a range that shows the region of potential optimum dead volume for maximum power output. The heat exchanger minimum volume is zero, which represents a case where the only dead volume in the engine is the

regenerator and any additional clearance volumes in the engine. This case yielded a dead volume ratio of 0.20. This is a hypothetical “best case” dead volume scenario that is used as a theoretical minimum, wherein no additional dead volume in the heat exchangers is required for the engine to run.

For this analysis, no estimate is made of any additional clearance volumes required for the connection of the heat exchangers to the engine working spaces. A heat exchanger with large cross-sectional area may require more volume in a plenum or other connection to the engine than one with a smaller cross-sectional area. The Schmidt model analysis does not take into account the overall geometry of the heat exchangers, only the total volume. So, any potential increase in volume for varying heat exchanger geometry will not be considered here.

In order to identify a potential optimum power for varying heat exchanger volume, the hot and cold temperatures of the engine,  $T_h$  and  $T_c$ , need to be varied manually. This is because the Schmidt model cannot capture the effect of different heat exchanger size on heat transfer to the air in the engine, so a range of engine gas temperatures are examined as shown in Table 3.4. The lowest temperature difference considered is based on the experimental performance of the Raphael engine, which achieved an average cold gas temperature of 32 °C and an average hot gas temperature of 96 °C during experiments. These values are the gas temperatures of the compression and expansion spaces respectively. This results in a temperature difference of 64 °C. For the study, a temperature difference of 65 °C will be used. The highest temperature difference considered is that of the source and sink temperatures, which would represent the ideal case where the heat transfer is so effective that the engine gas temperature achieves the source and sink temperatures.

Table 3.4. Varied Properties for Schmidt Model Evaluation

<b>Varied Property</b>	<b>Minimum Value</b>	<b>Maximum Value</b>	<b>Interval</b>
Heat Exchanger Volume	0 L	8 L	0.001 L
Dead Volume Ratio	0.27	3.66	0.0008
Hot Side Gas Temperature	95 °C	150 °C	10 °C (15 °C for minimum value)
Cold Side Gas Temperature	30 °C	5 °C	5 °C
Temperature Difference	65 °C	145 °C	15 °C (20 °C for minimum value)

As the Raphael engine operates at varying engine pressures, some sensitivity cases will be run to determine the effect of pressure on the location of a potential optimum heat exchanger volume. Three pressures will be considered. Additionally, sensitivity cases will be run for varying engine speeds, as the Schmidt model cannot predict engine speed. The pressure and speed sensitivity cases are the same as those summarized in Table 3.3.

The Schmidt analysis for the Raphael engine was done using a MATLAB script. The code for the analysis, including both Senft's derivation and the isothermal model is included in Appendix B.

### 3.2.4 Base Results for Schmidt Model Study

The results from both Senft's derivation and the Schmidt model derivation from the isothermal model show the same trend, and are consistent with Senft's analysis of engine power output for varying dead volume ratios [25]. As can be seen in the plot of the power output determined from Senft's derivation against dead volume ratio shown in Figure 3.19, the power output decreases exponentially with dead volume when all other engine volumes are held constant. This trend is consistent across the different hot and cold side temperatures considered. The same trend is seen in the plot of power output calculated from the derivation of the Schmidt model against dead volume ratio shown in Figure 3.20. The plot scale is kept consistent with the sensitivity cases which appear in Appendix F.

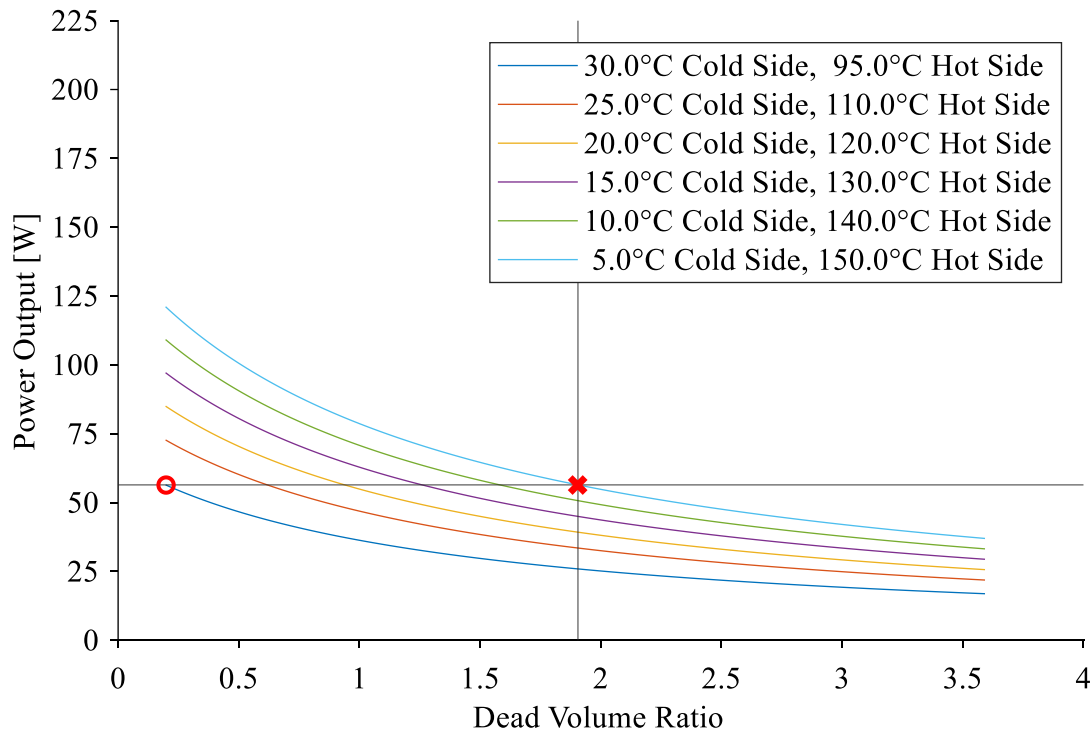


Figure 3.19: Plot of power output calculated by Senft's derivation for Gamma engine Schmidt model against DV ratio for various hot and cold side temperatures at an engine pressure of 435 kPa and engine speed of 2.833 Hz.

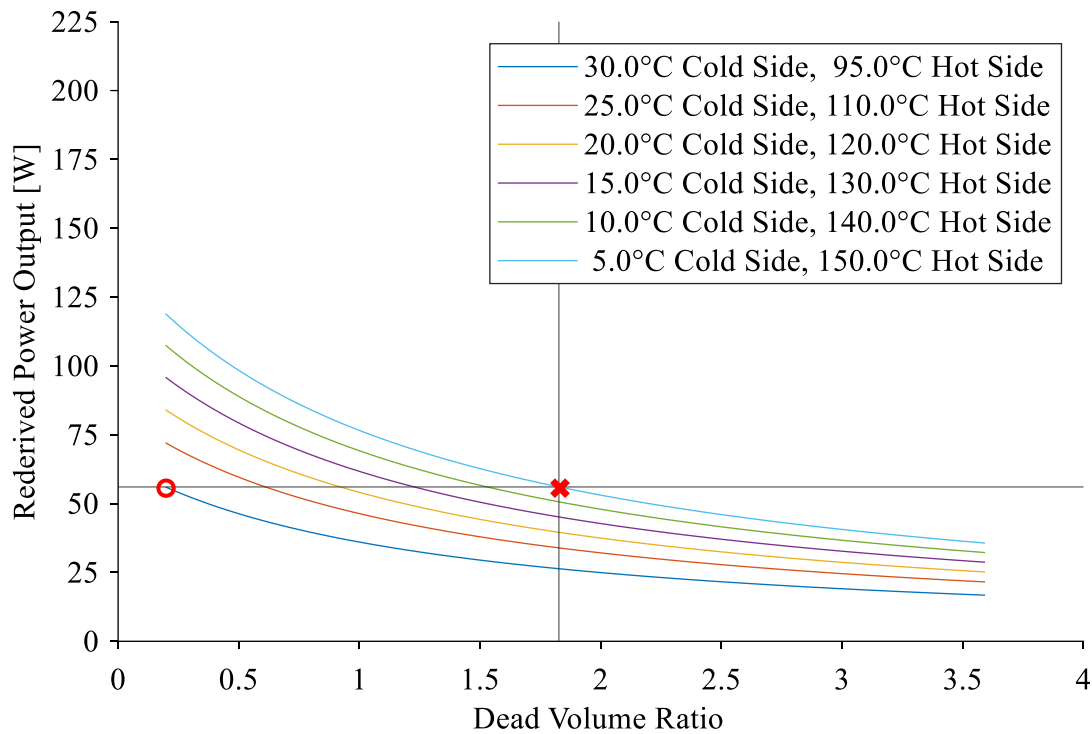


Figure 3.20: Plot of power output calculated from isothermal derivation of Schmidt model for Gamma engines against DV ratio for various hot and cold side temperatures at an engine pressure of 435 kPa and engine speed of 2.833 Hz.

For both figures, the plot is divided into quadrants. A horizontal line is placed at height of the red circle, which is the power output of the minimum dead volume of the lowest temperature difference considered. A vertical line intersects at the red cross, which is where the power output of the lowest dead volume and lowest temperature difference considered is the same as the power output of the highest temperature difference considered. This divides the plot into quadrants which aid in interpreting the results.

An improvement in heat exchanger performance would increase the temperature difference achieved by the working fluid. This can be seen on the plot as moving upward through the lines for each temperature difference. An improvement in heat exchanger performance can occur with increased heat exchanger size with the same geometry, if it increases the surface area and other heat transfer parameters, as was seen in section 3.1. Whether the change in heat exchanger size will necessarily result in an increase in power output is not known by the Schmidt model, as it is dependent on other parameters of the heat exchanger within the context of the Stirling engine. This includes the pressure drop as well as the effect of other necessary increases in dead volume

on the temperature difference, which are not considered in this study for simplicity. This would include the connection of the heat exchangers to the working spaces in the engine and any additional clearance volumes.

The top left quadrant outlines an area where an increase in dead volume by way of heat exchanger volume increase would produce higher output power, provided that a higher temperature difference is achieved. The limit of this quadrant is the point at which a low dead volume heat exchanger that achieves lower temperature difference has the same power output as a high dead volume heat exchanger that achieves the highest temperature difference, the theoretical maximum of the source and sink. The optimal heat exchanger volume for an engine should reside in the top left quadrant.

The bottom right quadrant outlines the area where any further increase in dead volume by increasing the heat exchanger volume will not result in a power increase. In this area, the effect of the dead volume is greater than that of any potential increase in temperature difference and the overall power output will drop.

The bottom left quadrant outlines the area where an increase in dead volume in the heat exchangers did not result in a sufficient increase in temperature difference for the power output to be improved. This indicates that the design of the heat exchanger should be modified to reduce dead volume or improve the temperature difference to improve the performance as opposed to simply increasing the heat exchanger size.

It is of interest that the main difference between Senft's derivation of the Schmidt model shown in Figure 3.19 and the derivation from the isothermal model shown in Figure 3.20 is that the power output is slightly higher for Senft's derivation. The Senft derivation also overpredicts the output power more for higher temperature differences. This is because of the higher difference between the source or sink temperature to the average temperature resulting in a larger change in the ratio of volume to temperature found in the model constants.

As a result of the difference in power output between the two derivations, the range of optimal dead volume ratios predicted by each is different. As Senft's derivation has a larger spread between the power predicted for the highest and lowest temperature difference cases, the maximum value that the optimal dead volume ratio should fall below is predicted to be slightly



higher than in the more compressed isothermal derivation. Senft's derivation shows that the optimal dead volume ratio should fall below a maximum of 1.91, while the derivation from the isothermal model has a maximum optimal dead volume ratio of 1.83.

### **3.2.5 Sensitivity Results for Schmidt Model Study**

Several sensitivity cases were run that varied engine speed and pressure. For increasing engine pressure, the values of engine output power calculated increased linearly. For increasing engine speed, the values of engine output power also increased linearly. These results are both expected because of the form of the equation for output power, with engine pressure and speed being directly proportional to the power output. The full plots showing the trends are shown in Appendix F. The maximum range of the optimal dead volume ratio remains the same across all the cases, with the Senft derivation predicting 1.91 and the isothermal derivation predicting 1.83, matching the base case results. This is expected as the difference between the highest power curve and the lowest power curve will be proportional even as the output power increases or decreases. The inadequacy of the Schmidt model is highlighted in the sensitivity cases as it is not possible to predict the heat transfer of the engine at varying engine pressures and speeds, thus leading to the same optimal dead volume range as for an engine operating at vastly different conditions.

### 3.3 Conclusions

In section 3.1, the effect of changing heat exchanger size on heat transfer was explored through analytical and empirical relations for steady state. This analysis showed that the output temperature of Stirling engine heat exchangers was linked to the total surface area of the heat exchangers. This was the case regardless of heat exchanger geometry in the majority of cases as the majority of conditions are in the laminar regime. Additionally, the pressure drop across the heat exchangers was investigated, and showed that longer heat exchangers incur a much more significant pressure drop than shorter ones. Generally, smaller heat exchangers also have a higher pressure drop than larger ones.

In section 3.2, the effect of changing the dead volume on power output of a Stirling engine was investigated using the 1<sup>st</sup> order Schmidt model. As expected, increasing dead volume decreases the engine output power significantly. It was possible to determine a maximum range of optimal dead volume ratio for a Stirling engine design by determining where the power output of the minimum dead volume and lowest temperature difference case is equal to that of the highest temperature difference case. The dead volume ratio in that highest temperature difference case is the point at which further improvements in engine power output will not be possible regardless of additional increases in heat exchanger size.

The Schmidt model analysis also highlighted several inadequacies in using the model for LTDSE design. Namely, the Schmidt model does not model the heat transfer within the heat exchangers, so it overpredicts the engine output power at higher engine pressures and speeds. It also cannot determine the optimum dead volume ratio for the engine at any conditions as it cannot model the relationship between the heat transfer in the heat exchangers (considered in section 3.1), the pressure drop, and increase in dead volume in the engine. This highlights the need to move to a model that is able to capture these relationships to determine an optimum heat exchanger size for maximum output power. This would be a 3<sup>rd</sup> order Stirling engine model, which will be introduced in the next chapter.

## 4 Sage Software and Validation Model Setup

To determine the optimum heat exchanger size for a LTDSE, a higher order model is required that is able to capture the interactions between heat transfer in the heat exchangers and excess dead volume to determine their effect on engine performance. For this, a 3<sup>rd</sup> order commercial Stirling engine modelling software, Sage, was used [39]. The Sage software allows any Stirling engine to be modelled. A Sage model of the Raphael engine presented in Chapter 2 was constructed. This chapter will provide a description of the Sage software and the Sage model setup of the Raphael engine.

### 4.1 Description of Sage Software

Sage is a third-order Stirling engine modelling software that was made by Gedeon that was released in 1995 [40]. It is based on previous Stirling engine modelling software GLIMPS and GLOP also made by Gedeon [39], [40]. It contains a graphical user interface that allows the user to control modular components of Stirling engines, such as the heat exchangers, pistons and cylinders, and connect to other components as desired [39], [68]. This allows almost any type of Stirling engine to be modelled in Sage.

The Sage modelling software has been used in a variety of academic studies of Stirling engines over the last two decades. Wilson utilized Sage, working directly with Gedeon, for the design and testing of Sunpower's pulse-tube cryocooler [69]. Good agreement between Sage and the experimental setup was achieved, and Sage was used to determine the sensitivity of the pulse-tube cryocooler to varying operational parameters. Demko and Penswick [70] detailed the development of a Sage model for Stirling convertors to be used in radioisotope power systems by NASA, which have since run for over 11 years [71]. Efforts to improve the Sage models used by NASA have been undertaken - for example Metscher [72] created a linear alternator model in Sage that was able to be integrated with existing Sage models of Stirling convertors. Landis and Mellot [73] used Sage to predict the performance of a Stirling power convertor for operation on Venus. Qiu et al. [74] used Sage to estimate the performance of a Stirling engine in a combined heat and power system, determining cycle efficiency for varying operating temperatures.

Hoegel [26], [75] used Sage to study the effect of varying operating parameters and engine designs on an alpha-type LTDSE as compared to an alpha-type high temperature Stirling engine. Gschwendtner and Bell [27] then further investigated the effect of dead volume on LTDSE engine performance based on Hoegel's findings in Sage.

Sage has also been used as the basis for comparison to other models, with Zhao et al. [76] comparing results of a CFD study of oscillating flow through the heat exchanger and regenerator section of the GPU3 engine to Sage results for the overall engine. Efforts to improve the Sage model have also been undertaken. For example, Xiao et al. [77] added results of a 2<sup>nd</sup> order model of the piston seal gap and cooler heat transfer to Sage to improve the model.

#### **4.1.1 Description of Model Components**

The components in Sage are the building blocks of the model. Each of these components is self-contained and contains all of the relevant equations, inputs, and outputs for the component. A component is made up of sub-models that contain the relevant model equations, inputs, and outputs for that sub-model. These components can be connected together using connections, which provide the boundary conditions for the model equations relevant to each component.

The mathematical model contained within Sage is a one-dimensional model. As such, the working fluid is discretized spatially in one dimension. The model is also discretized temporally. Each component of the Sage model thus contains model equations that are discretized one-dimensionally spatially and temporally. Each of these divisions are known as cells, and are connected by nodes. The gas model for the working fluid is separate from the solid model for the wall. These models can be connected by the appropriate connectors in the sub-models.

There are different types of boundary connectors for different boundary conditions. The main types of connectors using the Stirling model are the pressure, heat flow, gas flow, and density connections. The pressure connection represents pressure variation acting on an area face, and ensures the faces share the same volume displacement when connected together. This is used for connecting pistons to gas domains. The heat flow connections are used to connect heat flows acting on the boundary, ensuring the boundary shares the same temperature when connected. These flows can be steady, steady but spatially varying, or spatially and temporally varying. The steady and steady but spatially varying heat flows are used in most cases, while the spatially and

temporally varying heat flow is used for connecting the gas model to the solid model. The gas flow connection is used when connecting gas flows between gas model components. It conserves mass flow rate, energy, and momentum on the boundary. Finally, the density connection is used to connect the gas model to the pressure reservoir. It ensures the mean pressure between the gas model of the component and the pressure reservoir is held equal. It is generally only used once per model.

#### **4.1.2 Thermodynamic Modelling of Gas in Sage**

For each cell of a gas model, the equations of continuity for mass, momentum and energy, and an equation of state are solved for one-dimensional spatially and temporally varying flow area. Beginning with the general form of the continuity equations for multidimensional flow, several assumptions are made to derive the continuity equations for one-dimensional spatially and temporally varying flow area. The general form of the continuity equations for a variable control volume in integral form can be found in various fluid mechanics textbooks [78], [79].

First, body forces are neglected. The boundaries of the control volume are defined to have fixed inlet and outlet boundaries, but the side boundaries are allowed to move, yielding a temporally varying flow area. The side boundaries are impermeable, so flow can only enter and leave through the inlet and outlet boundaries. Next, the equations are converted to one-dimensional differential equations in conservative form. The differential of volume is replaced with the product of the area and the differential of length in the time integrals. The surface integrals are considered on a case by case basis. The full derivation of the equations is shown in the Sage User's Guide by Gedeon [68]. The continuity equations can also be derived from applying mass, momentum, and energy balances on a single cell, as shown by Hoegel [26].

For mass continuity, the resulting form of the equation is:

$$\frac{\partial \rho A}{\partial t} + \frac{\partial \rho u A}{\partial x} = 0 \quad (4.1)$$

where:

$\rho$  – gas density (kg/m<sup>3</sup>)

$u$  – mean-flow velocity in the x direction (m/s)

$A$  – flow area (m<sup>2</sup>)

$t$  – time (s)

$x$  – principle flow direction (m)

The mass continuity equation states that the net rate at which mass enters or leaves the control volume through the surface boundaries is equal to the change of mass in the control volume with time. Note that the side surface boundaries are impermeable and no mass leaves through them, so all mass that enters and leaves the control volume does so only through the defined inlet and outlet in the flow direction.

For momentum, the resulting form of the equation is:

$$\frac{\partial \rho u A}{\partial t} + \frac{\partial u \rho u A}{\partial x} + \frac{\partial p}{\partial x} A - F A = 0 \quad (4.2)$$

where:

$p$  – thermodynamic pressure (Pa)

$F$  – viscous flow resistance term (N/m/m<sup>2</sup>)

The momentum equation states that the sum of the change of momentum in the control volume with time and the net rate of momentum entering or leaving the control volume is equal to the net force acting on the control volume. For the one-dimensional reference frame, there is no momentum flux through the side boundaries, only through the inlet and outlet in the flow direction. The net force acting on all surfaces is expressed as the thermodynamic pressure and the viscous flow resistance term,  $F$ . This term replaces the stress tensor in the equation, since the stress tensor cannot be resolved in one dimension. It can be thought of as the force per unit length per unit flow area due to surface shear stress, or the frictional pressure gradient. The viscous flow resistance due to surface shear stress (or friction) is formulated in terms of the

Darcy friction factor and total local loss coefficient. Its form can also be adjusted to allow a phase shift between the viscous pressure gradient and velocity in ducts.

For gas energy, the resulting form of the equation is:

$$\frac{\partial \rho e A}{\partial t} + p \frac{\partial A}{\partial t} + \frac{\partial}{\partial x} (u \rho e A + u p A + q) - Q_w = 0 \quad (4.3)$$

where:

$e$  – mass-specific total gas energy (J/kg)

$q$  – axial heat flux (W)

$Q_w$  – empirical film heat transfer per unit length (W)

The energy equation states that the sum of the change in energy in the control volume with time and the net rate of energy entering or leaving the control volume is equal to the net heat flux through the surface boundaries plus the PV work done on its boundaries. There is no energy entering or leaving the control volume through the side boundaries, however PV work can be done on the side walls and film heat transfer occurs on the side walls. An instantaneous axial heat flux,  $q$ , is defined at the inlet and outlet boundaries. The heat flux from a solid to the gas through the side wall is denoted as the film heat transfer per unit length,  $Q_w$ . This term is determined from the Nusselt number, gas conductivity, hydraulic diameter, wetter perimeter, and temperature difference between the wall and the fluid. This formulation can allow for phase shift between the heat transfer and the film temperature difference in cylinders, and is further broken down in compression-drive and advection-driven components with different Nusselt numbers in ducts.

The mass specific total gas energy is defined as:

$$e = \epsilon + \frac{u^2}{2} \quad (4.4)$$

where:

$\epsilon$  – mass-specific internal gas energy (J)

The mass-specific internal gas energy is dependent on the gas model chosen. The relevant gas model also provides the equation of state. In this study, the ideal gas model is used, giving the mass-specific internal gas energy as:

$$\epsilon = c_v T \quad (4.5)$$

where:

$c_v$  – specific heat at constant volume (J/kgK)

and the equation of state as:

$$PV = RT \quad (4.6)$$

where:

$V$  – volume (m<sup>3</sup>)

$T$  – temperature (K)

The form of the continuity equations derived by Gedeon [68] yields the three implicit solution variables,  $\rho$ ,  $\rho uA$ , and  $\rho e$ . The equation of state is used to relate the pressure and temperature variables to the independent variables for the solution.

### 4.1.3 Energy Transfer Modelling in Solids in Sage

The solid walls of the model that interact with the gas are modelled with a one-dimensional solid energy equation, described by Gedeon [39] as:

$$\rho_s c_s A_s \frac{\partial T_s}{\partial t} + \frac{\partial q_s}{\partial x} + Q_w = 0 \quad (4.7)$$

where:

$\rho_s$  – solid density (kg/m<sup>3</sup>)

$c_s$  – solid specific heat (J/kgK)

$A_s$  – mean solid cross-section (m<sup>2</sup>)

$T_s$  – axial center-line temperature distribution (K)

$q_s$  – solid-mode axial heat flow (W)

The application of this equation is different for various types of thermal solid components available in Sage. The equation above is used in quasi-adiabatic surfaces, such as the thick surface and rigorous surface present in the cylinder and regenerator. The various heat conductors



use a further simplified version of the heat equation based on the number of heat flows in the component.

The axial heat flow in solids is independent of the axial heat flow in the gas. The surface heat transfer with the gas is calculated using the temperature difference between the wall surface temperature and the gas-solid surface interface temperature [39] and empirical correlations.

#### **4.1.4 Description of Sage Discretization and Solver**

The Sage model is solved numerically on a spatial and time grid. The spatial grid is divided into cells with nodes, with the gas and solid both being discretized on the same grid. Each cell receives a central node and two boundary nodes. The implicit variables for the gas dynamic equations are solved using a staggered grid, where  $\rho uA$  is solved at alternate nodes to  $\rho$  and  $\rho e$ . The variable  $\rho uA$  is solved at the boundary nodes using the central differencing formula, and then the value is interpolated with Lagrange polynomial interpolation for the central node, and vice versa for the variables  $\rho$  and  $\rho e$ . This staggered grid scheme is used only for the spatial grid and helps avoid solution instability.

The time grid assumes a periodic solution. Time differencing is done by way of a multipoint backward differencing scheme, which determines the number of backward sampling points from the number of nodes in the time grid. Increasing the number of backward sampling points this way allows for the annihilation of higher order harmonics, which were introducing error into the periodic solution. For integration, the time grid uses Euler's rule without modifications, giving equal weight to each time index.

Sage then uses a nonlinear solver, which iteratively solves the system of evaluation functions for each implicit variable in the model using Newton's method. Some modification is made to Newton's method to improve the solution stability, wherein discontinuities of implicit variable initial values are relaxed more slowly for certain key components. This is explained in detail the Sage User's Guide [68].

The Sage solver was not computationally intensive, and solutions could solve as quickly as a few seconds with a small number of nodes. For solutions with upwards of 15 time nodes and upwards of 9 spatial nodes for the components, the solution could take as long as 20 minutes. The time to

convergence and the number of iterations taken is highly dependent on the solution start point. If the variables had to be re-initialized or if the model parameters were changed significantly compared to the start point, the model would take much longer to solve and would take upwards of 100 iterations. For comparison, from a good solution start point the model would usually take no more than 50 iterations to reach a solution. Occasionally, the model could get stuck in a loop, but this could be solved by modifying the linear solver step size.

## 4.2 Model Setup for Validation

To create a Sage model of the Raphael engine to use for validation, model components and connections need to be selected. Each of these model components also needs to have the input defined in order to reflect the engine geometry and operating conditions.

### 4.2.1 Model Component and Connections Selection and Assumptions

To select the model components for the Sage model, the Raphael engine is broken into sections which can then be modeled in Sage with the appropriate component. This method is similar to the isothermal model where the engine is broken into five volume spaces. Figure 4.1 shows a cross-sectional view of the Raphael engine broken into sections for the Sage model. The displacer piston and power piston are also included in the engine sections, as they will introduce the piston motion to the Sage model. These sections are then converted to one-dimensional engine spaces, and are then assigned Sage model components, which are connected together, as shown on the right of the figure.

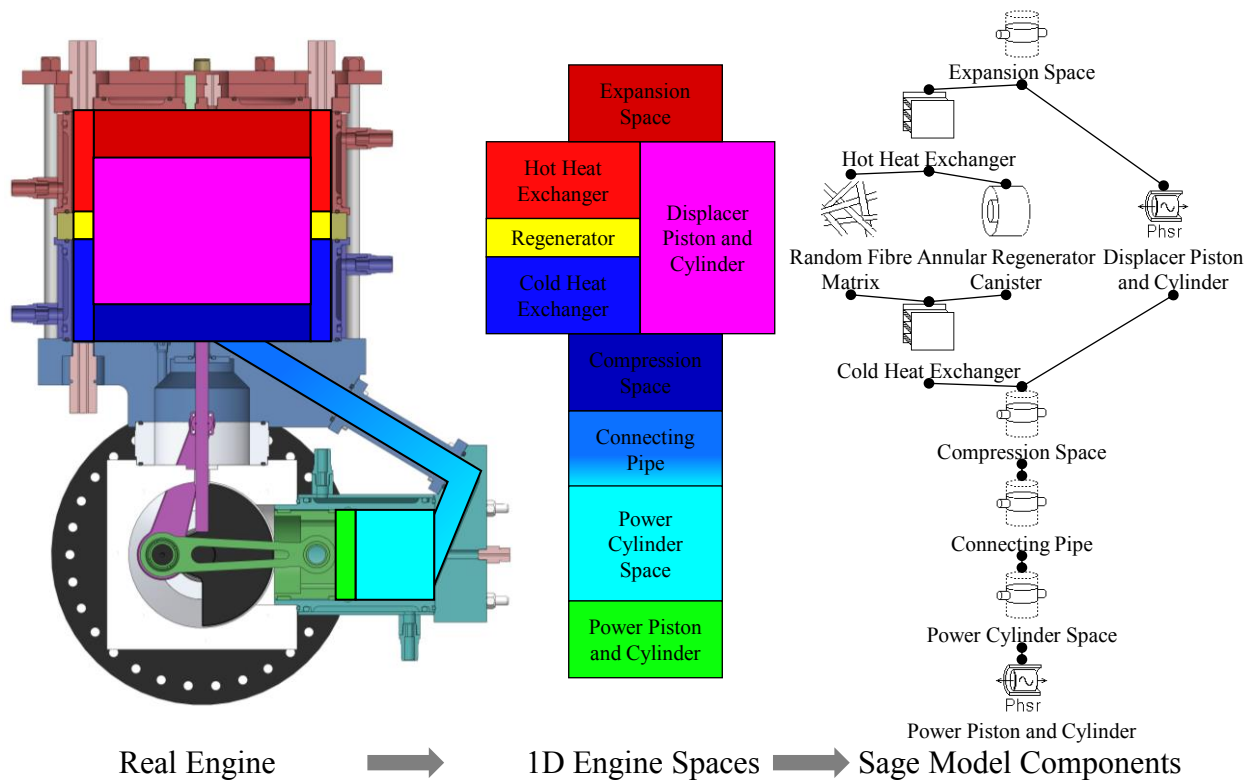


Figure 4.1: Schematic showing segmentation of experimental engine into Sage model components.

The model components selected for the various engine sections are shown in the Sage model context in Figure 4.2 which shows the Sage model graphical user interface (GUI) at the top level. The random fibre matrix component that is the regenerator fibre material is not seen at the top level, as it is a sub-model component of the annular canister component labelled the regenerator. The types of connections between model components can be seen, with connections with the same number being connected together.

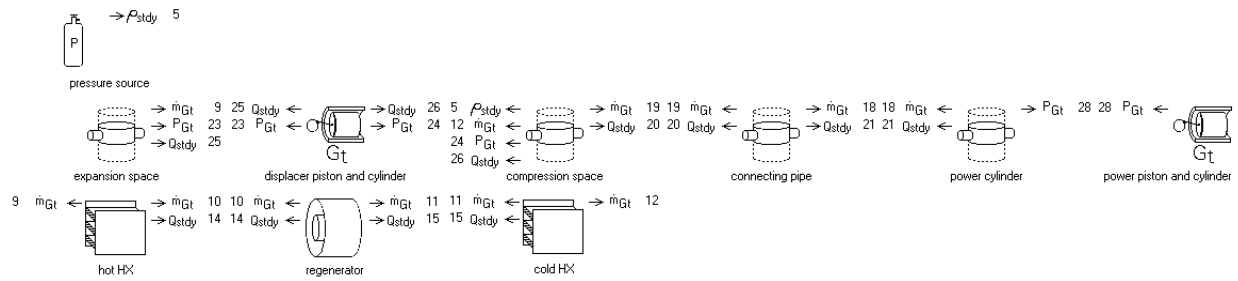


Figure 4.2: Screenshot of Sage model interface showing top-level components and connections.

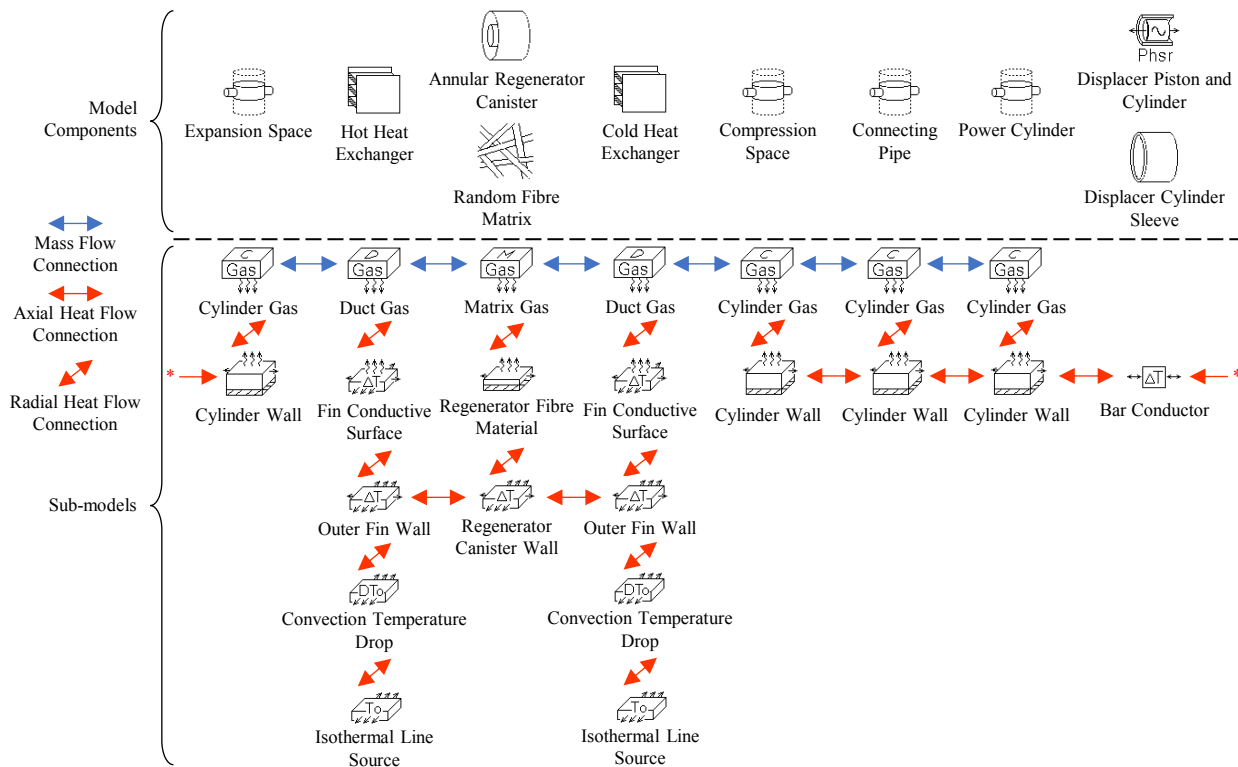


Figure 4.3: Schematic of Sage model components and heat and mass flow connections of sub-models.

The connections that can be seen in the Sage GUI connect the various sub-model components for gas and solid components. These model components and their sub-model connections are shown in Figure 4.3. The components, sub-model components, and connections chosen are inherent simplifications of the experimental engine. The compression space is separated into the compression space within the displacer cylinder, the connecting pipe, and the power cylinder volume in order to model the changing flow area and conduction losses through the spaces. In the expansion space, compression space, connecting pipe and power cylinder space, the cylinder wall is modelled as a thick surface with the assumption that those spaces are quasi-adiabatic.

The displacer and power piston are both modelled as simple slider-crank mechanisms. While this component is superseded in Sage, it is a convenient simplification of the mechanism without requiring the added complexity of modelling the flywheel. The flywheel is omitted as any fluctuation of the engine speed caused by different flywheel size has negligible effect on power output of the LTDSE [80]. Thus, a constant engine speed without a flywheel is assumed.

Both cylinders neglect the appendix gap, assuming a perfect seal between the cylinder wall and the pistons. They also neglect the shuttle heat transfer between the piston and the cylinder wall as a consequence of lacking the appendix gap model component.

The heat exchangers use rectangular finned channels to model the annular heat exchangers with the setup described in the Sage user manual. These heat exchangers also include a model of the solid conduction path through the fins. The solid of the heat exchanger fins is connected to the isothermal source via a series of conduction paths and temperature drops that are used to model the convective heat transfer resistance. This will be discussed in greater detail in section 4.2.3. An important assumption in Sage is that the heat exchangers are modelled with isothermal sources as this allows a more direct comparison between the experiment, with the heat source and sink temperatures entered directly into the model.

The regenerator is contained within an annular canister, and is modelled as a random fibre matrix to match the stuffing material used in the experimental engine. The annular canister wall is thermally connected to the heat exchanger walls to represent the physical connection of the heat exchanger stack.

## 4.2.2 Summary of Model Inputs

Each model component and sub-model component contains input variables that need to be defined to reflect the geometry and operating conditions of the engine being modelled. A full list of every input variable to the model is provided in Appendix G. There are many input parameters that are multipliers for various properties that are available for tuning the model. These parameters will be left at the default value as a starting point [68], [69].

Table 4.1 summarizes the geometric engine properties that are entered into the Sage model. Note that the heat exchangers are identical in geometry. The appendix gap between the displacer piston and cylinder is neglected and a perfect seal is assumed. The appendix gap is added to the model as excess dead volume, and the displacer piston and cylinder diameter is taken to be that of the cylinder. Additionally, the protrusion of the displacer rod into the cylinder is not modelled, as this volume is small enough to be negligible.

Each model component needs to be assigned a material in order for the thermal conductivity, density, and specific heat capacity to be known. The materials assigned to the different model components are summarized in Table 4.2. Air is assumed to be dry and an ideal gas, as the temperatures and pressures of the operating conditions are not near the critical point of air, so the ideal gas approximation is sufficient. The properties for aluminum 6061, polyurethane, and PEI were added to Sage from the references noted in Appendix G.

The engine operating conditions that the model requires are the heat source and sink temperatures, the engine frequency and charge pressure. These are taken from the experimental conditions of the various test cases presented in Chapter 2. The heat source and heat sink temperature for validation are taken from the experimental results. The experimental results included the inlet and outlet temperatures of both the SIL180 and the water-glycol mixture. The average of the inlet and outlet temperatures for each respective fluid is taken as the heat source or sink temperature. The engine frequency and charge pressure are taken directly from the experiment measurements. The inputs determined from the experimental parameters for the validation cases are summarized in Appendix G.

Table 4.1. Summary of geometric engine properties inputted into Sage model.

<b>Engine Property</b>	<b>Value</b>
Displacer Piston Diameter	0.198 m
Displacer Piston Stroke	0.075 m
Displacer Connecting Rod Length	0.130 m
Displacer Cylinder Diameter	0.20 m
Displacer Cylinder Length	0.1931 m
Power Piston Diameter	85.73 mm
Power Piston Stroke	0.075 m
Power Connecting Rod Length	0.130 m
Power Cylinder Length	0.152 m
Connecting Pipe Diameter	0.0254 m
Regenerator Porosity	0.96
Regenerator Fibre Diameter	0.1 mm
Regenerator Inner Diameter	0.207 m
Regenerator Outer Diameter	0.247 m
Regenerator Length	0.0254 m
Heat Exchanger Inner Diameter	0.207 m
Heat Exchanger Outer Diameter	0.247 m
Heat Exchanger Length	0.096 m
Heat Exchanger Channel Height	20 mm
Heat Exchanger Channel Width	1 mm
Heat Exchanger Fin Thickness	1.46 mm

Table 4.2. Summary of engine materials inputted into Sage model.

Engine Component	Material
Working Fluid	Ideal Air
All Cylinder Space Walls	Aluminum 6061
Displacer Cylinder Sleeve	Aluminum 6061
Displacer Piston	Polyurethane Foam
Power Piston Cylinder	Stainless Steel 304
Power Piston	Aluminum 6061
Heat Exchanger Walls	Aluminum 6061
Regenerator Canister	PEI
Regenerator Fibres	Polyester

### 4.2.3 Implementation of Convective Heat Transfer Resistance

As was discussed in section 4.1.1, model component sub-models are included in order to model the convective heat transfer resistance between the isothermal source and sink and the heat exchanger solid material. This is necessary as the Sage model only models the working fluid within the engine, and thus the liquid side heat transfer of the heat exchanger is not modelled.

In order to enable the modelling of various heat exchanger types, Sage includes a line temperature drop component. This component enforces a temperature drop between the components it is connected to, in this case the isothermal source or sink and the outer wall of the heat exchanger fins. This temperature drop can be implemented as an equation that is dependent on other variables in the model. This ability is used to implement the heat transfer resistance due to convection as a line temperature drop using:

$$\Delta T = R_t Q \quad (4.8)$$

where:

$\Delta T$  – temperature drop (K)

$R_t$  – convective heat transfer resistance (K/W)

$Q$  – heat transfer from source or sink (W)

The heat transfer from the source or sink is a variable determined by Sage, and is referenced in the equation used to determine the temperature drop. By using the line temperature drop



component in this way, the convective heat transfer resistance can be included in the Sage model and determined based on parameters within the Sage model.

#### **4.2.4 Conclusions**

The Sage software discretizes the Stirling engine into one dimension. To create a Sage model of the Raphael engine, the 3D engine spaces were simplified into 1D spaces. Then, appropriate Sage model components and connections to represent these 1D spaces were selected based on some simplifications of the engine geometry. The model and submodel inputs were determined from the engine geometry and operating conditions. A limitation of Sage is that it only models the working fluid within the engine. This presents an issue with modelling the heat source and sink, as the Raphael engine has a liquid heat source and sink. This liquid that flows through the heat exchangers has a convective heat transfer resistance, which limits the amount of heat flow from the liquid to the engine. This resistance can be modelled in Sage as an enforced temperature drop between an isothermal source and the engine, however in order to determine the magnitude of the temperature drop, the convective heat transfer resistance must be known. The determination of the convective heat transfer resistance must be done using another method, and then included in Sage to complete the model setup.

## **5 Determination of Input Parameters for Stirling Engine Modelling Using CFD**

While the 3<sup>rd</sup> order model is the next step in evaluating the effect of heat exchanger size on engine performance, this model lacks the ability to fully model the heat exchangers as they are in the experiment. Sage does not model other fluids that may be present in the LTDSE - in this case, this is the liquid heating and cooling loops of the heat exchangers. These liquid loops have a convection resistance between the liquid and the solid wall. To determine the appropriate resistance from the thermal source or sink to the solid wall to input into the Sage model, the surface temperature of the solid within the liquid channel would need to be measured. However, this surface is not accessible for measurement in the experiment. Thus, another model needs to be used in addition to Sage to determine the appropriate resistance value from the thermal source or sink to be used in Sage. CFD investigation of steady state air flow conditions within the heat exchanger was undertaken to provide this information. The CFD analysis models the experimental heat exchanger geometry and operating conditions to determine the convective resistance to be inputted into Sage. This is done in SOLIDWORKS using the Flow Simulation add-in. These results will serve to inform the heat exchanger conditions in the Sage model, namely the convective heat transfer resistance and the isothermal surface condition used for the liquid.

### **5.1 Model Setup and Assumptions**

For this investigation, only steady state conditions are considered for simplicity. The actual air flow conditions in the Stirling engine are both unsteady and reciprocating, but would be time consuming and complex to simulate, as discussed in section 1.4.5. Thus, the steady state conditions are used as an indication of heat exchanger performance, and the more complex reciprocating conditions are left to be considered in the 3<sup>rd</sup> order model.

Both the hot and cold heat exchangers are considered in this study, as they use different liquids that can have different convective heat transfer coefficients. Additionally, as the engine operates over a range of pressures and speeds, sensitivity cases of the engine pressure and speed are considered.

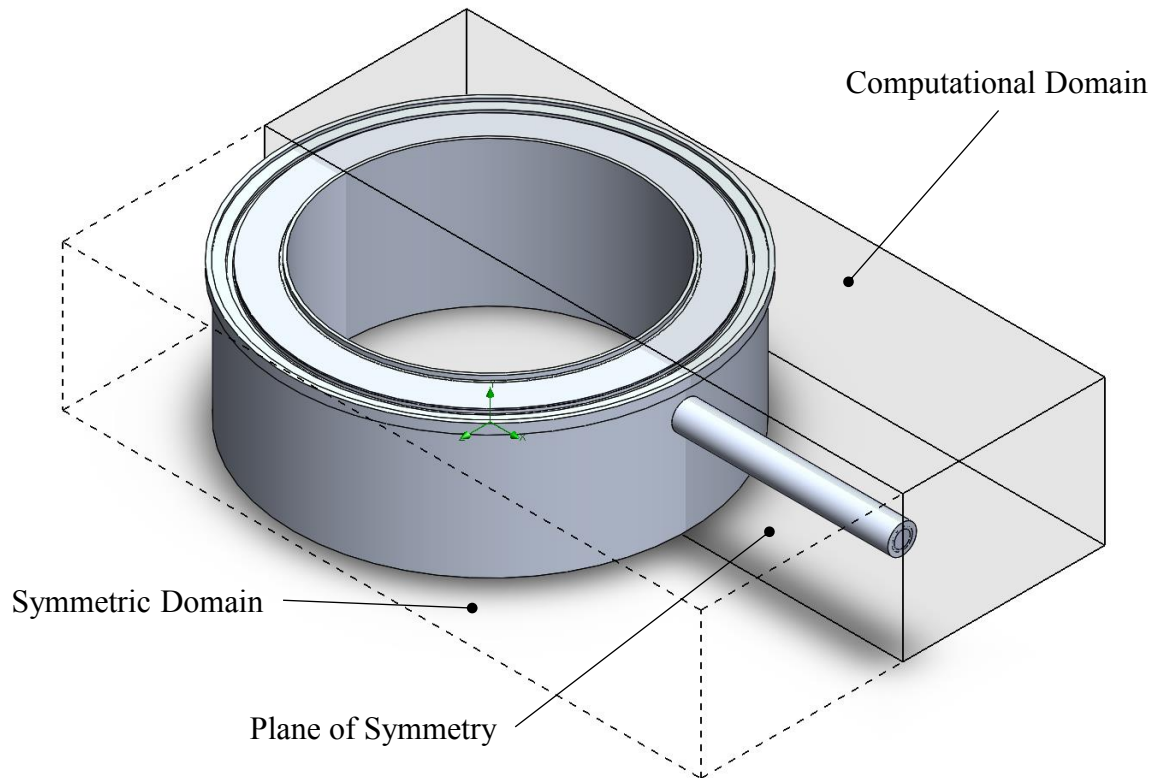
### **5.1.1 General Simulation Parameters**

The CFD simulation is an internal flow type simulation, with the fluid in a fully enclosed volume. The simulation is able to model both turbulent and laminar flow. The two fluids, the air within the finned channels of the working space and the liquid in the outer jacket, are modelled. The solid material of the heat exchanger and jacket is also included, as the simulation models the heat transfer between the three materials. The solid walls are adiabatic unless they are contacting the fluid or assigned a heat exchanger condition. The wall conduction is modelled, to connect the thermal pathway from the liquid to the air-side of the heat exchanger. Gravity was not included in this simulation, as the flow within the heat exchanger itself is forced convection. Any free convection present on the outside of the heat exchanger jacket is not of interest and is not modelled for simplicity.

The material properties for air and the aluminum 6061 alloy of the heat exchangers are those that are included in SOLIDWORKS. All solid material present in the simulation, this being the jacket and finned heat exchanger, is aluminum 6061. For the heat transfer fluids, new materials needed to be added to the database. For the heating case, the SIL180 fluid was used, and for the cooling case, the ethylene glycol water mixture was used. The material properties for SIL180 and the ethylene glycol water mixture are included in Appendix H. For SIL180 in particular, as the manufacturers datasheet did not include specific heat capacity at the operating temperature, a comparison was made between SIL180 and a similar fluid, SYLTHERM 800, in order to estimate the specific heat capacity, as shown by Lottmann [46].

### **5.1.2 Computational Domain and Model Geometry**

For this simulation the computational domain was half of the heat exchanger, with a line of symmetry through the inlet and outlet of the water jacket, as shown in Figure 5.1. This was done to reduce the simulation time, although the heat exchanger geometry is not fully symmetrical due to the uneven number of slots. However, two wider slots were added along the line of symmetry for the inclusion of instrumentation in experiment as shown in section 2.2.1. The line of symmetry along which these wider slots are located is used as the symmetry boundary of the computational domain in this study.



*Figure 5.1: Definition of computational domain relative to geometry.*

The model geometry was the same as the manufactured heat exchangers, with only slight modifications made for the CFD. The liquid outlet was extended to 150 mm from 20 mm at the entrance in order to eliminate vortices at the boundary. Additionally, some O-ring grooves and chamfers were removed from the solid in order to reduce the meshing requirements.

The liquid subdomain consists of the inlet and outlet tubes and the water jacket around the heat exchanger, as shown in Figure 5.2. The gas subdomain consists of the gaps between the heat exchanger fins.

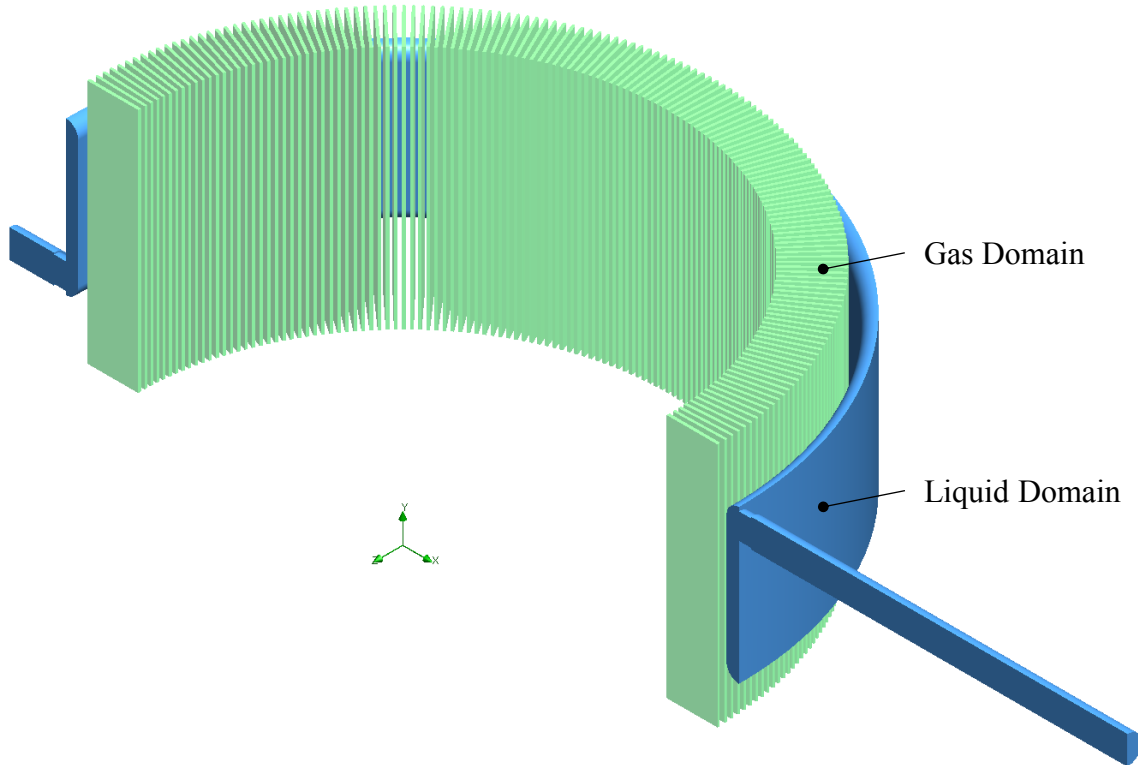


Figure 5.2: Visualization of liquid and gas fluid subdomains.

### 5.1.3 Boundary Conditions

The location of the boundary conditions for the fluid and the air was at the inlet and outlet of the flow, as shown in Figure 5.3. The liquid inlet is given a mass flow rate and inlet temperature.

The mass flow rate and inlet temperatures for each fluid is half of the experimental values listed in Table 2.3. This is done in order to account for the symmetry condition. The velocity profile at the liquid inlet is taken as uniform. The liquid outlet pressure is equal to the atmospheric pressure. This is taken from the average of the experimental results, at 92955 Pa.

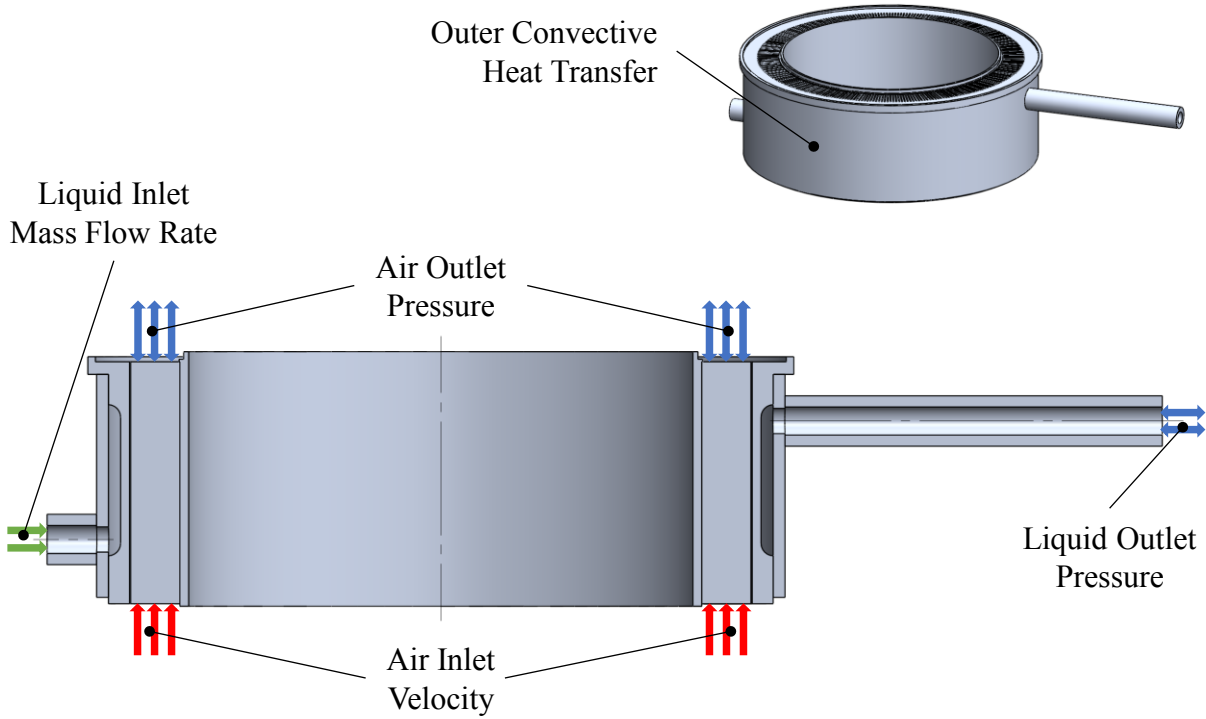


Figure 5.3: Location of various boundary conditions in model geometry.

The air inlet is given a velocity and inlet temperature. The inlet air temperature is taken as the regenerator mean effective temperature described by equation (3.1). The inlet velocity is determined from applying mass continuity to the average displacer piston speed over the cycle as:

$$u_{inlet} = \frac{A_{disp}}{A_{hx}} u_{disp} \quad (5.1)$$

where:

$u_{inlet}$  – air inlet velocity (m/s)

$A_{hx}$  – heat exchanger cross-sectional area (m<sup>2</sup>)

The heat exchanger cross-sectional area is taken as 5780 mm<sup>2</sup>. The average piston speed is determined from:

$$u_{disp} = 2(2r)f \quad (5.2)$$

The velocity profile at the air inlet is taken as uniform. The air outlet pressure is equal to the engine fill pressure. The air inlet velocity and outlet pressure will be considered at several values in the sensitivity case. These values are summarized in Table 3.3.

The boundary condition on the outer wall is convective heat transfer, defining a constant heat transfer coefficient and environment temperature. This will model the convection to the environment outside the heat exchanger. The heat transfer coefficient was estimated from the relations for natural convection. First the Grashof number needs to be determined using [63]:

$$Gr_L = \frac{g\beta(T_s - T_\infty)L_c^3}{\nu^2} \quad (5.3)$$

where:

$g$  – gravitational acceleration (m/s<sup>2</sup>)

$\beta$  – coefficient of volume expansion (1/K)

$T_s$  – temperature of the surface (K)

$T_\infty$  – temperature of the fluid far from the surface (K)

$L_c$  – characteristic length of the geometry (m)

$Gr_L$  – Grashof number (K)

The temperature of the surface is assumed to be that of the source or sink, at 150 °C or 5 °C respectively. The temperature of air far from the surface is assumed to be 25 °C. The characteristic length of the geometry is the height of the heat exchanger, in this case 96 mm. All fluid properties are taken at the film temperature for air at atmospheric pressure from Table A-15 in Çengel [63]. For ideal gases, the coefficient of volume expansion is one over the film temperature, calculated as:

$$\beta = \frac{1}{T_f} = \frac{1}{\frac{T_s + T_\infty}{2}} \quad (5.4)$$

After determining the Grashof number, the following relation can be used to determine if the cylindrical surface can be treated as a vertical flat plate in the determination of the Nusselt number [63]:

$$D \geq \frac{35L_c}{Gr_L^{\frac{1}{4}}} \quad (5.5)$$

The outside diameter of the heat exchanger jacket is 273.05 mm, which is greater than the ratio of characteristic length and Grashof number calculated for both the heating and cooling cases, at 0.070 m and 0.080 m respectively. Thus, the relation for vertical flat plates can be used in

determining the Nusselt number. The Nusselt number is found from the following relation given in Çengel [63]:

$$Nu = \left( 0.825 + \frac{0.387Ra_L^{\frac{1}{6}}}{\left(1 + \left(\frac{0.429}{Pr}\right)^{\frac{9}{16}}\right)^{\frac{8}{27}}}\right)^2 \quad (5.6)$$

This equation is valid for any Rayleigh number between  $10^4$  and  $10^{13}$ . The Rayleigh number in this case is  $2.0 \times 10^6$  or  $4.5 \times 10^6$ , determined by multiplying the Grashof number and Prandtl number:

$$Ra = Gr_L Pr \quad (5.7)$$

The heat transfer coefficient can then be determined from the Nusselt number using the characteristic length:

$$h = \frac{kNu}{L_c} \quad (5.8)$$

to be  $7.97 \text{ W/m}^2\text{K}$  for the hot heat exchanger and  $5.28 \text{ W/m}^2\text{K}$  for the cold heat exchanger.

### 5.1.4 Initial Conditions

The initial conditions for the study define the initial environmental pressure as 1 atm and the initial temperature at  $25 \text{ }^\circ\text{C}$ .

### 5.1.5 Convergence Parameters

The parameters selected for convergence are the average outlet temperature and pressure drop for both the liquid and air, and the average surface temperature of the solid contacting either the liquid or the air. The fluid average outlet temperatures and the average solid surface temperatures are parameters of interest from the simulation, and can indicate that the thermal model is converged. The fluid average outlet temperatures are used for validation against analytical solutions. The pressure drop is also used for convergence as a representation of the momentum in the fluid, and is also used for model validation against analytical solutions. Finally, the heat transfer rate from the fluid is also used as a convergence parameter, as it will be used in the determination of the convective heat transfer resistance.

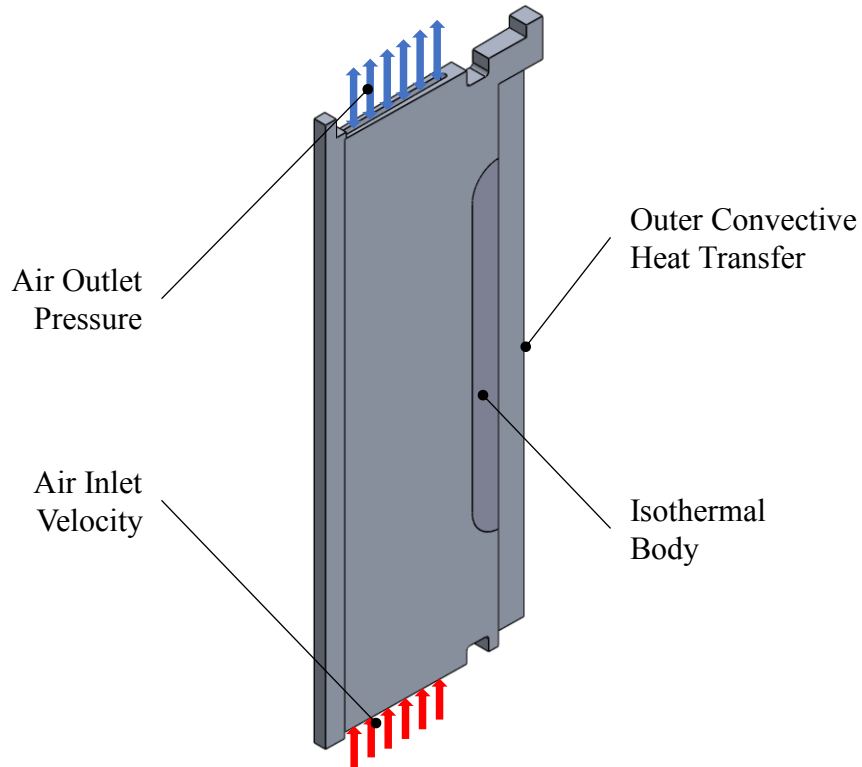


## **5.2 Mesh Independence Study and Setup**

A mesh independence study was undertaken in order to determine the required number of cells for a mesh independent solution. Due to the large size of the model of interest and the limited computational power available, the model was split into two parts for each fluid — the air and liquid — and a mesh independence study was done on each part. The model setup modifications for these two studies are described below, along with the results of the mesh independence study for each. Each of these studies are run at the base case engine pressure and speed, which is 435 kPa and 2.8333 Hz, and also run for both the heating and cooling case.

### **5.2.1 Model Setup for Air Side Mesh Independence Study**

When considering only the air side of the heat exchanger, it can be noted that the air flow is axisymmetric. This condition is used to reduce the size of the computational domain to a single channel with axisymmetric boundary conditions on both sides. The new computational domain and the boundary conditions are shown in Figure 5.4. With the liquid in the outer jacket not being modelled, it is replaced with an isothermal source at either the source or sink temperature. This is chosen as it is a simplified case that can be compared more easily to analytical solutions, and is consistent with the isothermal condition used in modelling thus far. All the other conditions, namely the air inlet velocity, temperature, and outlet pressure, and the outer wall heat transfer coefficient are the same as for the full model.



*Figure 5.4: Figure showing air side axisymmetric model slice for mesh independence study with boundary conditions.*

The basic mesh size was 0.003 m square in all directions. The mesh refinement parameters that were controlled were the curvature and the number of cells across the air channel. The curvature refinement level was allowed to be a maximum of 6. This allows the cell to be subdivided 5 times in half, as the base refinement level is considered level one. The curvature refinement criterion was set to  $20^\circ$ . Thus, the mesh will be refined anywhere where the angle between the normal of the faces is less than the value of the curvature refinement criterion. The allowed refinement level for the number of cells across the air channel was level 6 as well, to be consistent with the curvature refinement. The number of cells across the channel was changed for each mesh, starting first with a low number of cells across the channel and then increasing until mesh independence was established.

## 5.2.2 Model Setup for Liquid Side Mesh Independence Study

For the liquid side of the heat exchanger, the same symmetry boundary condition is used as for the main study. The computation domain and boundary conditions are shown in Figure 5.5. The air side fins are cut away, and where the base of the fins used to be is set to be an isothermal wall. This is done to enable comparison to the analytical solution. The wall temperature is set to be the average of the air inlet and the source or sink temperature, which is 111.225 °C or 38.725 °C respectively. The other conditions, namely the liquid inlet mass flow rate, temperature, and outlet pressure, and the outer wall heat transfer coefficient are the same as in the full model.

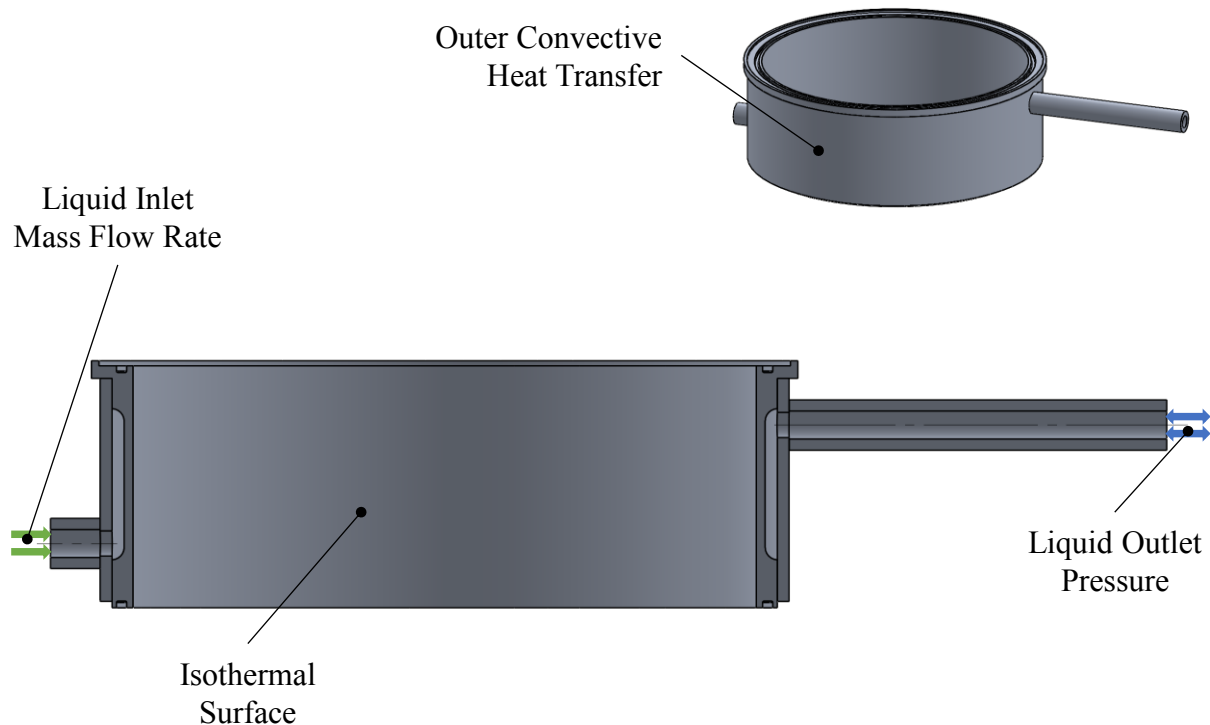


Figure 5.5: Figure showing liquid side symmetric model for mesh convergence with boundary conditions.

As was the case for the air side study, the basic mesh size was 0.003 m square in all directions. The same mesh refinement parameters were controlled in the liquid study as in the air study, except now the channel of interest is the liquid channel. The curvature refinement level was allowed to be a maximum of 4, with the curvature refinement criterion set to 20 °. The allowed refinement level for the number of cells across the air channel was level 4 as well, to be consistent with the curvature refinement. The number of cells across the channel was changed

for each mesh, starting first with a low number of cells across the channel and then increasing until mesh independence was established.

### 5.2.3 Air Side Mesh Independence Results

For each of the mesh refinement parameter settings outlined above, a mesh and solution were generated. The total number of cells for each refinement setting is summarized in Table 5.1 for the air study by number of cells across the channel. The three convergence parameters of outlet air temperature, air pressure drop, and average solid temperature contacting the air were obtained.

*Table 5.1. Summary of mesh parameters for air side mesh independence study.*

<b>Requested Number of Cells Across Channel</b>	<b>Total Number of Cells (millions)</b>
2	0.496747
5	0.999947
8	3.871429
11	10.490392

To evaluate the effect of the mesh, each of the convergence parameters was normalized against the initial value and plotted against the number of cells for both the heating and cooling case, shown in Figure 5.6 and Figure 5.7 respectively. All convergence parameters in both cases achieved a percentage change below 1%. The pressure drop parameter changed the most from the initial value, and took the longest to show convergence.

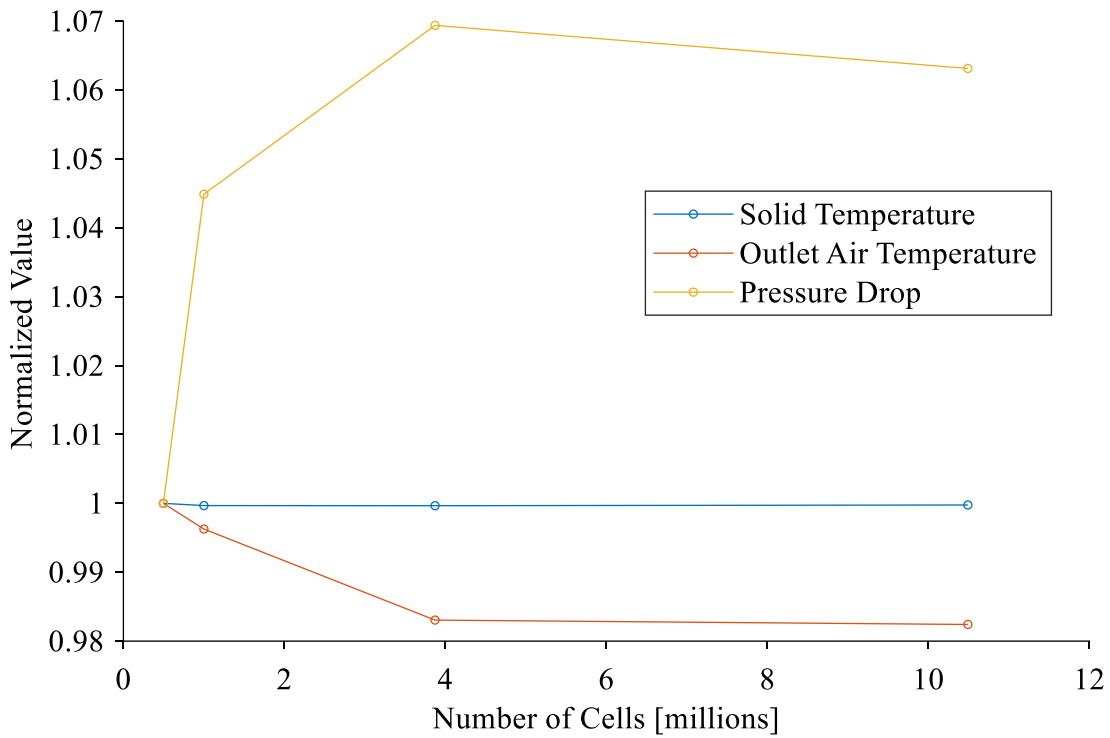


Figure 5.6: Plot of normalized air side convergence parameters against number of cells in mesh for the heating case.

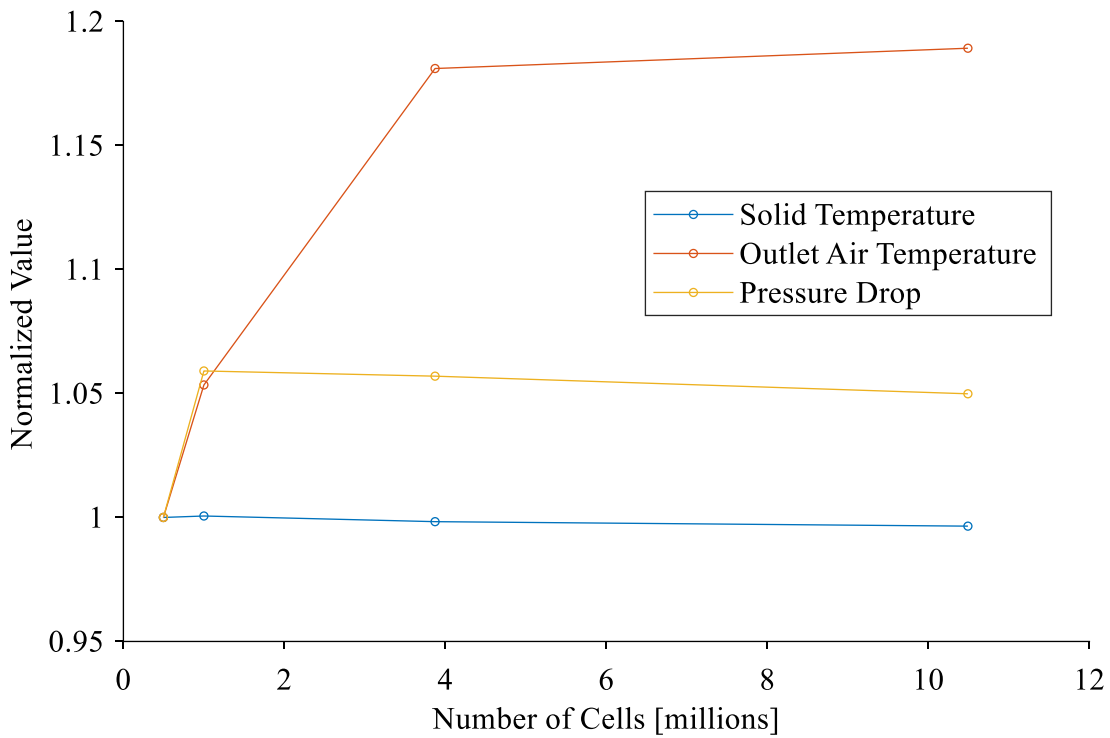


Figure 5.7: Plot of normalized air side convergence parameters against number of cells in mesh for the cooling case.

## 5.2.4 Liquid Side Mesh Independence Results

For each of the mesh refinement parameter settings outlined above, a mesh and solution were generated. The total number of cells for each refinement setting is summarized in Table 5.2 for the liquid study by number of cells across the channel. The three convergence parameters of outlet liquid temperature, liquid pressure drop, and average solid temperature contacting the liquid were obtained.

*Table 5.2. Summary of mesh parameters for liquid side mesh independence study.*

<b>Requested Number of Cells Across Channel</b>	<b>Total Number of Cells (millions)</b>
5	1.158710
8	2.936812
11	4.528318
14	10.042651

To evaluate the effect of the mesh, each of the convergence parameters was normalized against the initial value and plotted against the number of cells for both the heating and cooling case, shown in Figure 5.8 and Figure 5.9 respectively. For the heating case, all convergence parameters achieved a percentage change below 1%. The pressure drop parameter changed the most from the initial value, and took the longest to show convergence. For the cooling case, the outlet liquid temperature was the only parameter with a percentage change above 1%, at 2.2%. This difference in results is likely due to the higher density of the water glycol mixture than the SIL 180 requiring a smaller mesh size to capture the flow.

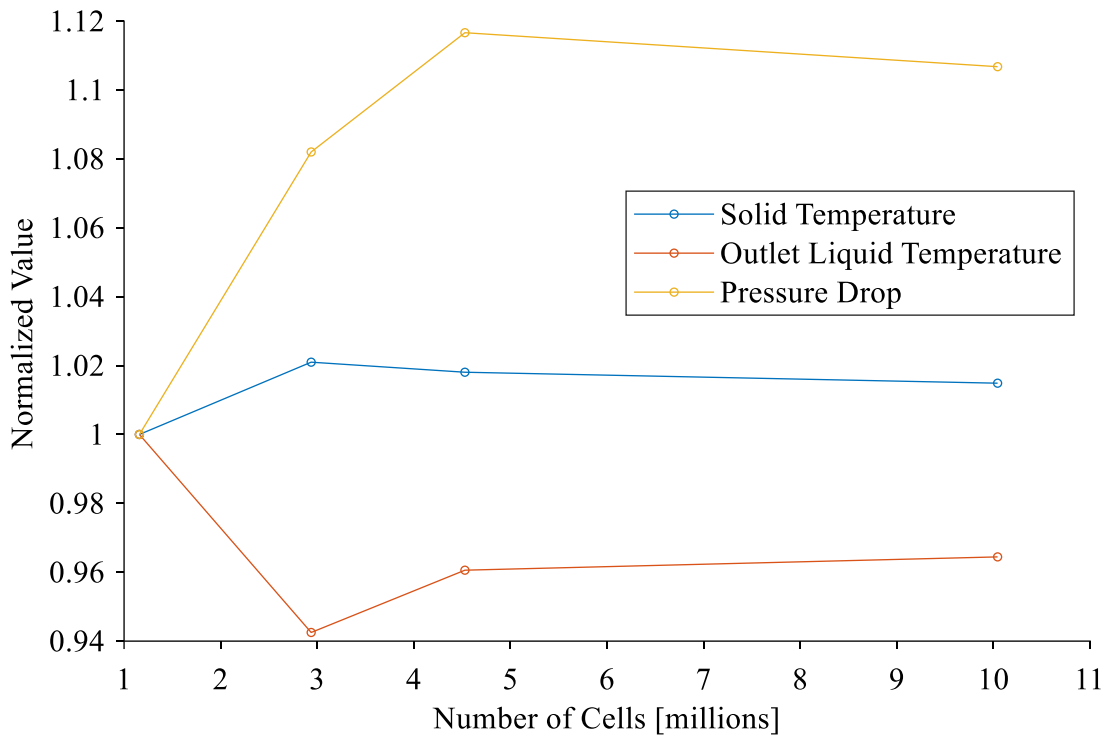


Figure 5.8: Plot of normalized liquid side convergence parameters against number of cells in mesh for the heating case.

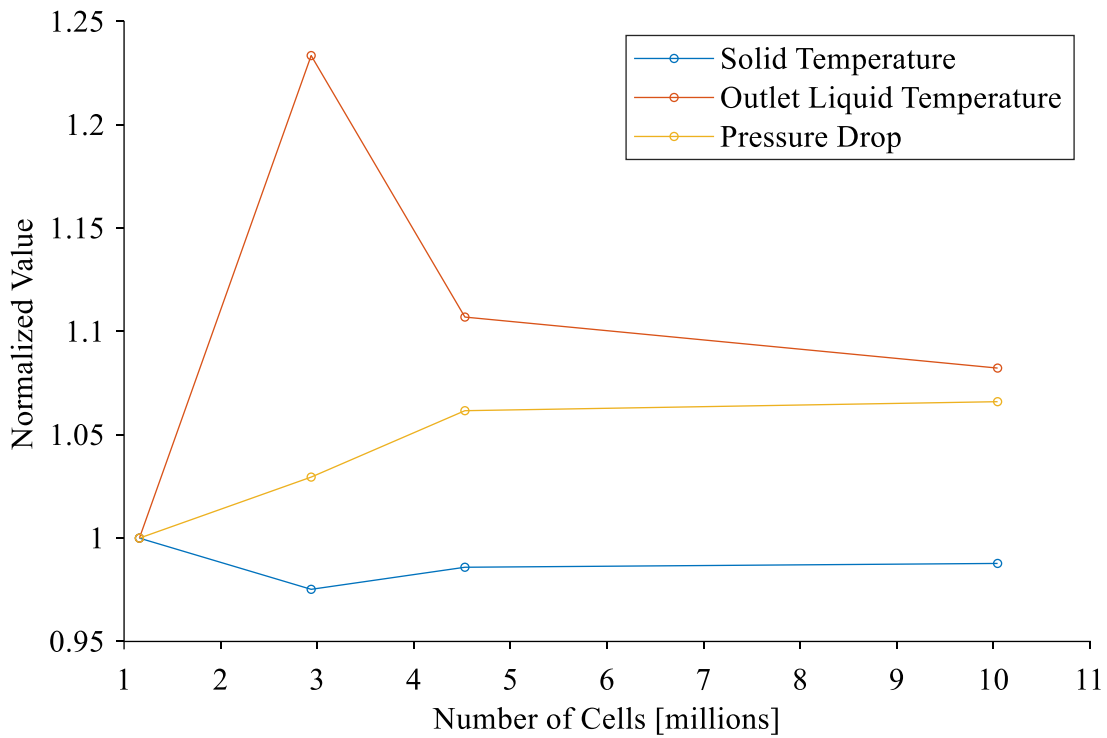


Figure 5.9: Plot of normalized liquid side convergence parameters against number of cells in mesh for the cooling case.

### **5.2.5 Discussion on Final Mesh Setup**

The final mesh setup for the full study is combined from the results of the two mesh independence studies. Due to computational limitations, the full study will not be able to use the mesh independent solution settings. As the full study contains 95 total air side fins, the full study would require approximately 380 million cells if the mesh independent solution was used. This particularly highlights the computational intensiveness of CFD studies for Stirling engines, as this study is of only half of a single heat exchanger at steady state, and would require much more computational power than is practically available.

For this study, as the liquid side is primarily of interest for the determination of the convective resistance, the air side will have a greatly reduced number of cells from the mesh independent solution, while the liquid side will retain more cells. The air side will be reduced to approximately 9 million cells, while the liquid side will have approximately 5 million cells, using the mesh independent case of 11 cells across the channel.

Using the aforementioned number of mesh cells, the air and liquid side studies will be validated against the analytical solutions for a range of parameters. This is done to understand the trends in error in the solutions, which can then be applied to the full study.



## **5.3 CFD Model Validation against Analytical Results**

In order to evaluate whether the CFD model results are realistic and can predict trends, validation studies are undertaken. Due to the lack of experimental results, analytical and empirical studies will be compared to the CFD results for the simplified air and liquid side models from the previous section. Due to computing power limitations, the air side studies will be non-mesh independent in order to prioritize the liquid side studies. The liquid side is of more interest for the final CFD study results. The convergence parameters of outlet fluid temperature, fluid pressure drop, and average solid temperature contacting the fluid will be compared.

### **5.3.1 Air Side Model Validation Model Setup**

The computational domain and boundary conditions are identical to the air side mesh independence study. Due to computational limitations, the maximum cells available for simulating the air side in the full study is approximately 9 million. Thus, the single channel simulation can have no more than 94 thousand cells. The model mesh settings were modified to yield a mesh with fewer than this number of cells.

The base cell size was increased to 0.004 m, and the allowed channel refinement and curvature refinement level was set to 3, with the curvature criterion still at 20 °. The allowed number of cells across the channel was 2. These settings resulted in a total cell count of 85, 551. Figure 5.10 shows a cut plot of the mesh generated with these settings, with cells coloured by refinement level. In this figure it shows that the mesh was refined to the maximum level around the air channel at refinement level 3 to yield 2 cells across the channel, with a cell size of 0.0005 m.

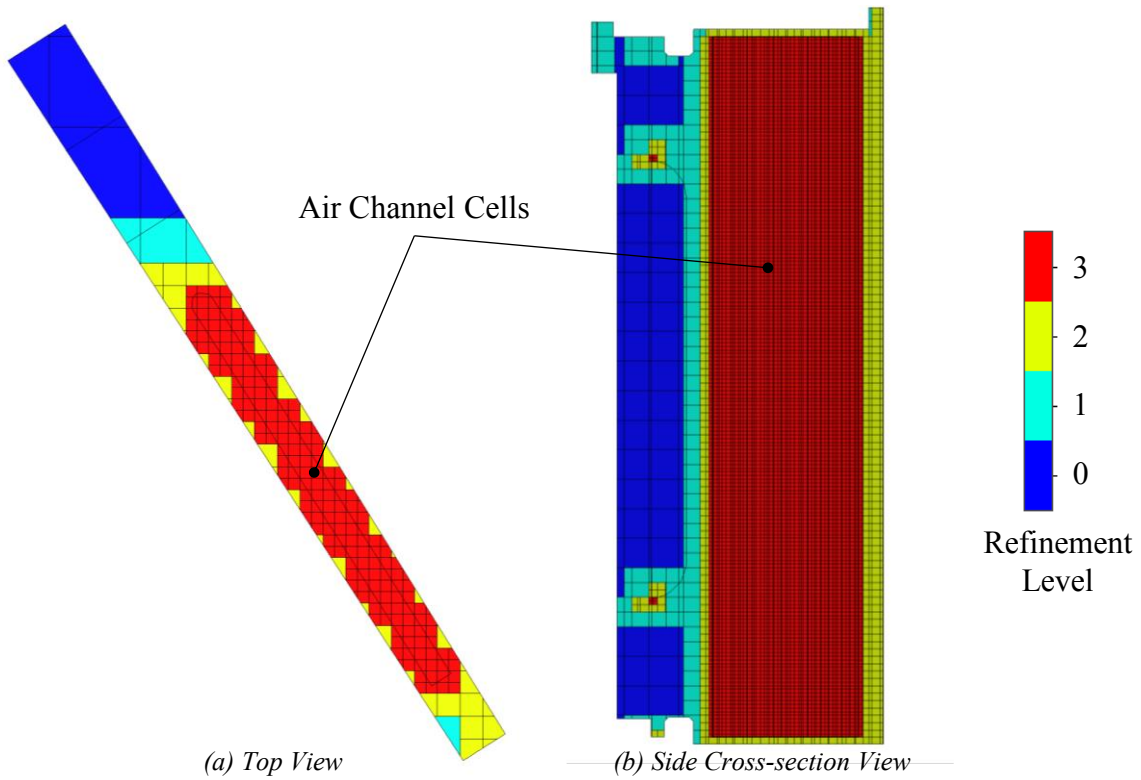


Figure 5.10: Figure showing mesh cut plot in the (a) horizontal and (b) vertical planes of the air side simulation with cells coloured by refinement level.

The air boundary conditions were varied in order to evaluate the model trends. For the air side validation, the air inlet velocity and outlet pressure were considered at several values, matching the cases outlined for the full study in section 5.1.3.

### 5.3.2 Liquid Side Model Validation Model Setup

The computational domain and boundary conditions are identical to the liquid side mesh independence study. The cells available for simulating the liquid side is approximately 5 million, using the mesh independent case of 11 cells across the channel. In order to combine the air side and liquid side model studies, for the full study, the liquid side mesh settings are slightly modified to match the required air side model mesh settings, which are more stringent.

To match the air side settings, the base cell size was increased to 0.004 m, and the allowed channel refinement and curvature refinement level was set to 4, with the curvature criterion still at 20°. The allowed number of cells across the channel was 11. These settings resulted in a total cell count of 5,548,528. Figure 5.11 shows a cut plot of the mesh generated with these settings, with cells coloured by refinement level. The refinement level in the channel ranged from level 2 in the inlet and outlet pipes to level 3 in the main jacket with level 4 near the walls.

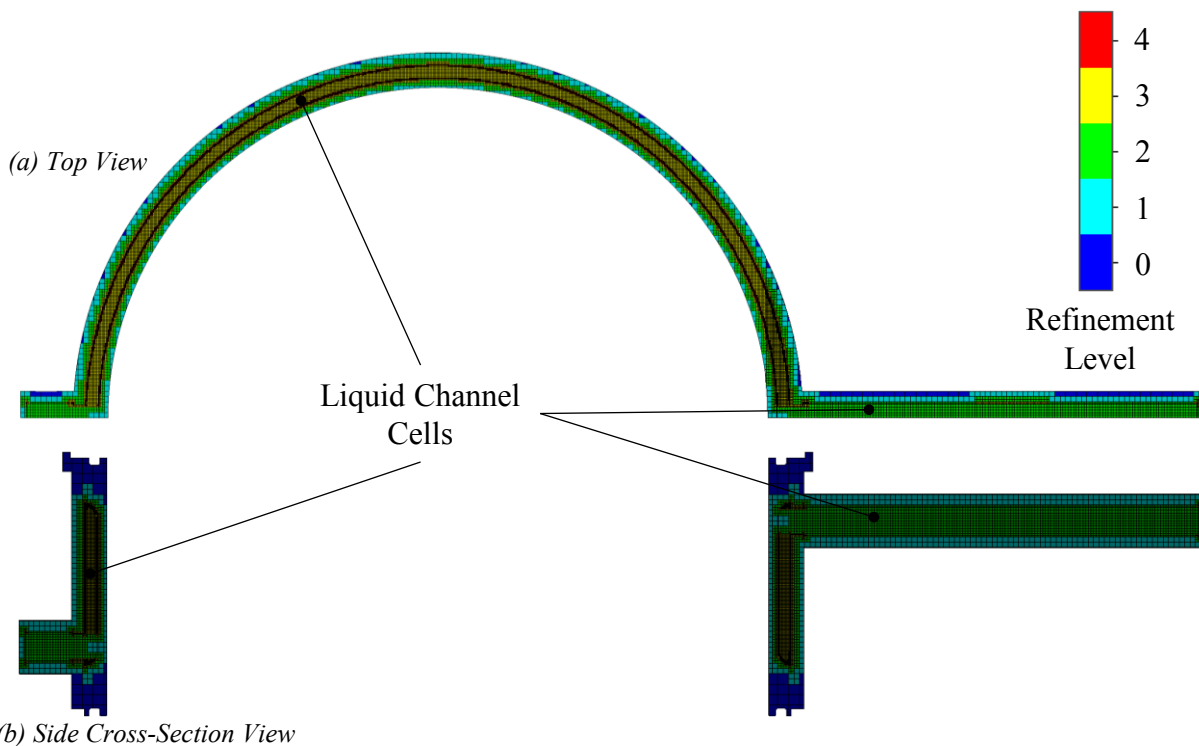


Figure 5.11: Figure showing mesh cut plot in the (a) horizontal and (b) vertical planes of the liquid side simulation with cells coloured by refinement level.

For the liquid side validation, the isothermal surface temperature and the inlet mass flow rate was varied, with a base case and two sensitivity cases on either side. The values considered for the

heating case are summarized in Table 5.3, and the values for the cooling case are summarized in Table 5.4.

*Table 5.3. Sensitivity Cases Conditions for Liquid Side Heating CFD Validation*

<b>Property</b>	<b>Base Value</b>	<b>Lower Value</b>	<b>Higher Value</b>
Isothermal Surface Temperature	111.225 °C	100 °C	120 °C
SIL 180 Mass Flow Rate	0.027300 kg/s	0.024570 kg/s	0.030029 kg/s

*Table 5.4. Sensitivity Cases Conditions for Liquid Side Cooling CFD Validation*

<b>Property</b>	<b>Base Value</b>	<b>Lower Value</b>	<b>Higher Value</b>
Isothermal Surface Temperature	38.75 °C	30 °C	50 °C
Water Glycol Mass Flow Rate	0.0117790 kg/s	0.0106011 kg/s	0.0129569 kg/s

The isothermal surface temperature in the base case is determined from the average of the air inlet temperature and the source or sink temperature. The lower and higher cases select the next closest round number divisible by 10. The mass flow rate for the base case is the same as for the full study, as described in section 5.1.3. The lower and higher cases are 10% away from the base case in either direction. These cases are used in order to have a range of input conditions so that the trend between the CFD and analytical solution can be compared.

### **5.3.3 Description of Analytical Solution for Air Flow**

The analytical solution for the air side starts with the analytical solution method described in section 3.1.4. This procedure is taken as described for the determination of the outlet air temperature and pressure drop. The key assumption in this solution is that the solid surface temperature is uniform across the entire channel, which will not exactly be the case for the CFD. To determine the solid surface temperature, an iterative process is used. First, the solid surface temperature is estimated and the outlet air temperature and pressure drop are found using the previous procedure for the air speed and pressure used in the CFD simulation. Then, the total heat flow into or out of the fluid over one entire channel is found using:

$$\dot{Q} = \dot{m}c_p(T_e - T_i) \quad (5.9)$$

where:

$\dot{Q}$  – heat flow into the fluid (W)

As the only heat added to the fluid comes from the isothermal source or sink, that heat must travel through the aluminum of the heat exchanger. Thus, the heat flow through the aluminum is equal to the total heat flow into or out of the fluid:

$$\dot{Q} = \frac{T_{iso} - T_s}{R_{t,alum}} \quad (5.10)$$

where:

$R_{t,alum}$  – thermal resistance of aluminum (K/W)

$T_{iso}$  – temperature of isothermal source or sink (K)

To be consistent with the heat flow being calculated for a single channel, the resistance through the aluminum is determined for a single channel slice of the cylinder, where there are 289 channels around the cylinder:

$$R_{t,alum} = \frac{\ln\left(\frac{r_{out}}{r_{in}}\right)}{\frac{2\pi}{289} kL} \quad (5.11)$$

where:

$r_{out}$  – outer radius of aluminum heat exchanger (m)

$r_{in}$  – inner radius of aluminum heat exchanger (m)

$k$  – thermal conductivity of aluminum (W/mK)

$L$  – heat exchanger length (m)

The outer radius of the aluminum heat exchanger is the radius that contacts the isothermal source or sink, and is 127 mm. The inner radius is the radius at the base of the fins at 123.5 mm. This simplification only considers the conduction up to the base of the fin, and not through the length of the fin which would cause additional temperature drop. The impact of this simplification will be discussed when considering the results. The thermal conductivity of aluminum is variable with temperature, matching the properties used by SOLIDWORKS.

Finally, the surface temperature is calculated by rearranging equation (5.10) to solve for the surface temperature. This new surface temperature is then used to determine the outlet air temperature and pressure drop. This process is repeated until the change in the surface temperature is below 0.001%. The code for this analysis is included in Appendix B for reference.

### 5.3.4 Description of Analytical Solution for Liquid Flow

The analytical solution for the liquid side is largely based on the methodology of section 3.1.4. The liquid path length is divided into three sections: the entrance tube, the curved rectangular channel, and the exit tube. For each section, the solid surface temperature is estimated. Then, the liquid exit temperature and pressure drop is determined from the iterative process described in chapter 3. The surface temperature is then calculated from an energy balance of the heat flow between the fluid and the wall and convection or the isothermal surface. This is used to estimate a new surface temperature, and the exit fluid temperature and pressure drop is calculated again. This process is repeated until the change in surface temperature is below 0.001%. For each section, the exit temperature of the previous section is used as the entrance temperature of the next section. Due to liquid flow path geometry including multiple turns and constrictions and expansions, each section is not assumed to be developed, regardless of if it is a consecutive section.

For the curved rectangular channel that makes up the water jacket, the curvature of the channel is neglected and it is treated as a straight rectangular channel. The method for determining exit temperature and pressure drop and the relations used are the same as previously described in section 3.1.4.

To determine the solid surface temperature, first the total heat flow into or out of the fluid is determined as shown in equation (5.9). This is set equal to the total flow through the wall of the heat exchanger to the isothermal surface, calculated from equation (5.10). The resistance through the aluminum wall is determined from:

$$R_{t,alum} = \frac{\ln\left(\frac{r_{out}}{r_{in}}\right)}{2\pi kL} \quad (5.12)$$

The outer radius is the radius contacting the liquid channel, at 127 mm. The inner radius is the radius of the isothermal surface, at 123.5 mm. The newly calculated surface temperature from a rearranged equation (5.10) is then used as the new estimate of surface temperature for the section, and the calculation is repeated until the change in surface temperature meets the criteria.

The convection applied to the outer surface of the curved rectangular channel section is neglected, as it is not possible to determine the proportion of heat flow that goes through each

section, which makes it impossible to determine an estimate for surface temperature. The convection resistance is several orders of magnitude higher than the conduction resistance, so the amount of heat flow to the convective surface will be much lower than that to the isothermal surface, and can be neglected.

For the entrance tube and exit tube sections, slightly different relations are used for determining the Nusselt number and friction factor than in the rectangular section. To determine the Nusselt number for the entrance region in the laminar regime, the following relation for circular tubes from Edwards et al. [65] is used:

$$Nu = 3.66 + \frac{0.065 \left(\frac{D}{L}\right) RePr}{1 + 0.04 \left(\left(\frac{D}{L}\right) RePr\right)^{\frac{2}{3}}} \quad (5.13)$$

This equation is valid for hydrodynamically and thermally developing flows for Prandtl numbers above 5 [63], which is the case for the heat transfer liquids considered. The diameter,  $D$ , is the diameter of the entrance and exit tube, at 11.125 mm.

To determine the pressure drop for the laminar regime, equation (3.20) is used, where the friction factor in the equation is the fully developed friction factor for laminar flow in a circular pipe:

$$f_D = \frac{64}{Re} \quad (5.14)$$

For the transitional regime, the Nusselt number was determined from the relation by Gnielski [66] shown in equation (3.18), with the friction factor determined from the relation for round tubes from Çengel [63]

$$f_D = 3.03 \times 10^{-12} Re^3 - 3.67 \times 10^{-8} Re^2 + 1.46 \times 10^{-4} Re - 0.151 \quad (5.15)$$

When the Gnielski correlation is used with the above relation for friction factor, it is valid for Reynold's number between 2300 and 4500. This friction factor is also used in the determination of the pressure drop for the transitional regime, using equation (3.20).

To determine the surface temperature in the entrance tube and exit tube sections, the total heat flow into the fluid determined from equation (5.9), is set equal to the flow of heat to the outer surface with the convection boundary condition:

$$\dot{Q} = \frac{T_{\infty} - T_s}{R_{t,alum} + R_{t,conv}} \quad (5.16)$$

where:

$R_{t,conv}$  – thermal resistance due to convection (K/W)

$T_{\infty}$  – temperature of fluid far from surface (K)

The temperature of the fluid far from the surface is 25 °C. The convective heat transfer resistance is determined using the values of convective heat transfer resistance calculated in section 5.1.3 using:

$$R_{t,conv} = \frac{1}{hA_s} \quad (5.17)$$

The surface area is determined from the following equation:

The surface temperature calculated from the rearranged equation (5.16) is then used to indicate the direction in which the estimate of surface temperature should be modified. If the newly calculated value was lower, the estimate was decreased, and vice versa. This was done in small increments until the surface temperature changed by less than 0.001%.

As was mentioned earlier, the liquid flow path includes multiple turns and constrictions and expansions. These were included in the pressure drop calculation via minor loss coefficients. For the entrance to the rectangular section the minor loss coefficient for sudden contraction from the rectangular channel was determined from the chart given in Çengel [67]. This chart plots the loss coefficient against the ratio of the smaller diameter over the larger diameter. For the smaller diameter, the hydraulic diameter of the rectangular channel was used, which was lower than the diameter of the entrance tube.



For the exit from the rectangular region the minor loss coefficient for sudden expansion from the rectangular tube was determined from the following relation in Çengel [67]:

$$K_L = \varepsilon \left( 1 - \frac{D_h^2}{D^2} \right)^2 \quad (5.18)$$

where:

$K_L$  – minor loss coefficient

$\varepsilon$  – kinetic energy correction factor

The kinetic energy correction factor value is 2 for fully developed laminar flow, and 1.05 for fully developed turbulent flow. Though flow in each case is not necessarily fully developed, these values are used for the laminar and turbulent regimes respectively in order to estimate the value of this minor loss.

Finally, both regions include a minor loss for the 90 ° turn into and out of the rectangular section. This value is 1.1 for a miter bend without vanes, from Çengel [67], and is used as an estimate despite the geometry not being a mitered bend.

For each minor loss, the pressure drop is calculated from:

$$\Delta p = K_L \frac{\rho u^2}{2} \quad (5.19)$$

To determine the total pressure drop through the system, the pressure drop calculated for each section and the pressure drop for each minor loss are added together.

The code for the analysis of the liquid flow is included in Appendix B for reference.

### 5.3.5 Air Side Numerical and Analytical Result Comparison

The results of the air side model validation study and the air side analytical results described are compared against each other for the convergence parameters of solid temperature, exit air temperature, and air pressure drop. Figure 5.12 plots the solid temperatures determined by the SOLIDWORKS simulation and the solid surface temperature determined by the analytical solution for varying engine speeds against engine pressure for the heating case. It also plots the mesh independent solution determined in the previous section for the base engine speed and pressure case, which had 11 cells across the channel. It can be seen that the simulation tends to underpredict the analytical solid surface temperature, but generally follows the trends with engine pressure and speed. The mesh independent solution from the simulation predicts an even lower solid temperature than the non-mesh independent solution.

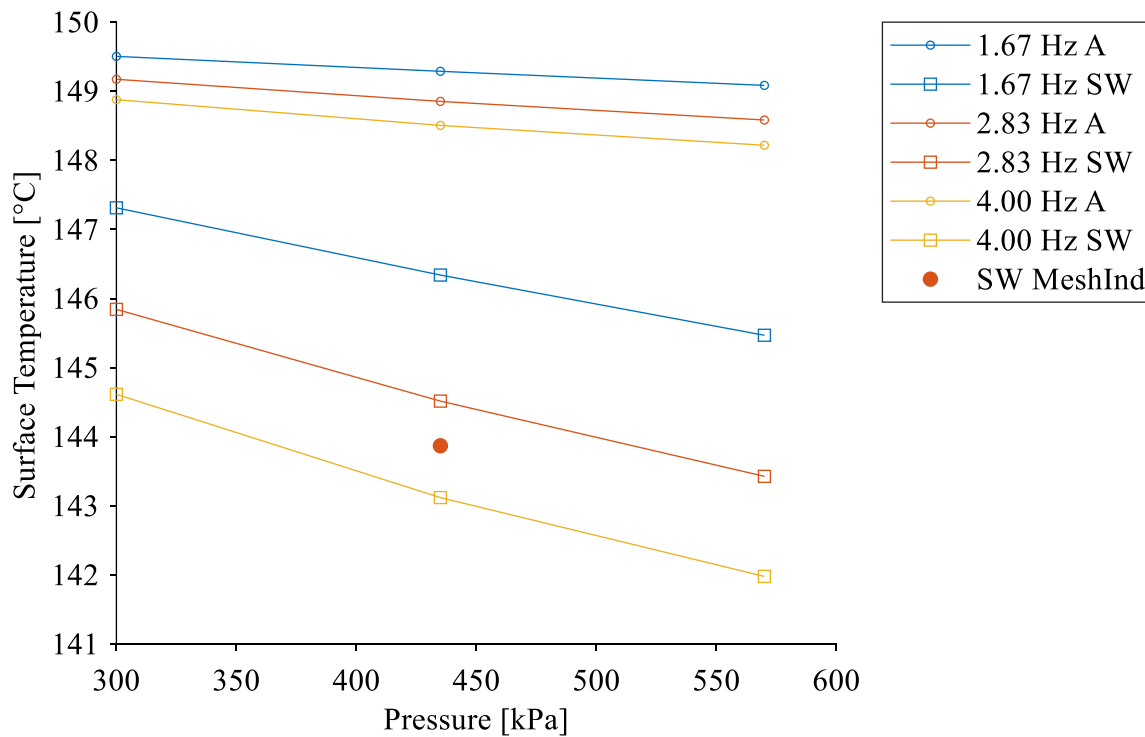


Figure 5.12: Plot of solid temperature determined from analytical solution and simulation for varying engine pressure and speed for the heating case.

The absolute value of the difference between the simulation and analytical solution for solid temperature is plotted against engine pressure for varying engine speeds in Figure 5.13. It can be seen that the difference between the analytical solution and the simulation is between 2 to 6.5 degrees. The mesh independent solution has a higher deviation than the mesh dependent

solution. The higher speed and pressure cases have higher differences than the lower speed and pressure cases. This can be due to the mesh dependence of the simulation, which would require smaller cells at higher pressures and speeds in order to capture the phenomenon more accurately.

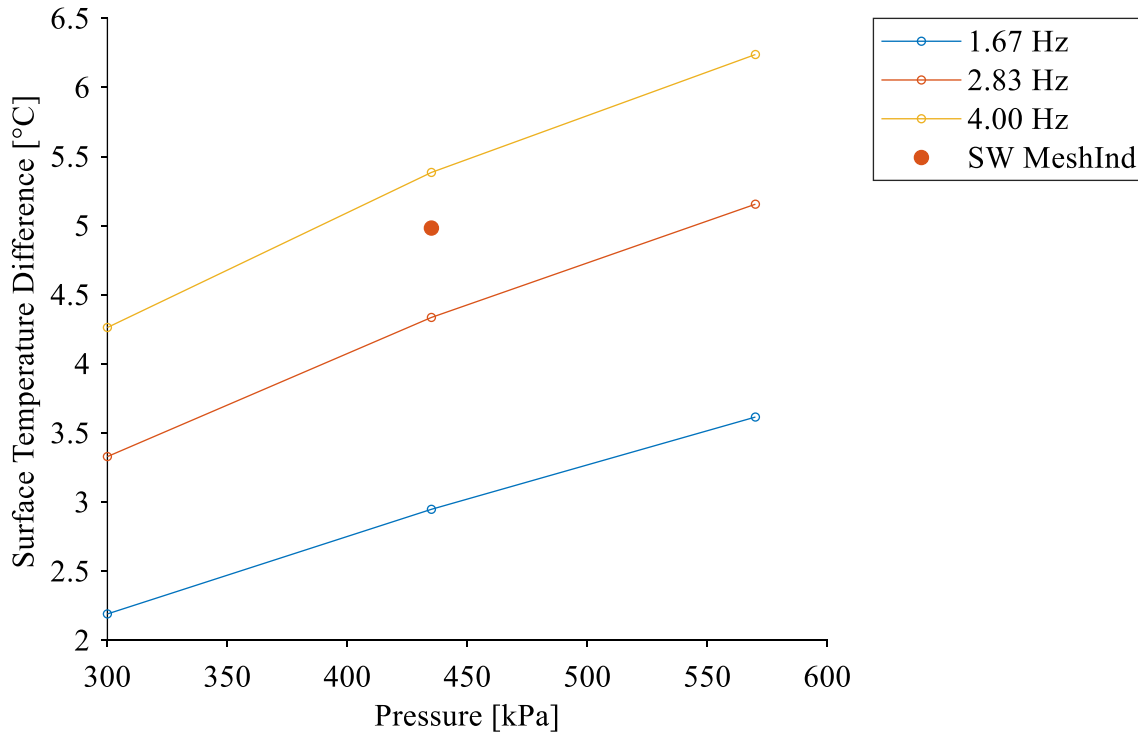


Figure 5.13: Plot of absolute value solid temperature difference between analytical solution and simulation for varying engine pressure and speed for the heating case.

Figure 5.14 plots the air exit temperatures determined by the simulation and the analytical solution for varying engine speeds against engine pressure. It also plots the mesh independent solution determined in the previous section for the base engine speed and pressure case. Again, the exit temperatures are underpredicted in the simulation compared to the analytical solution, however they generally follow the trends with varying engine pressure and speed.

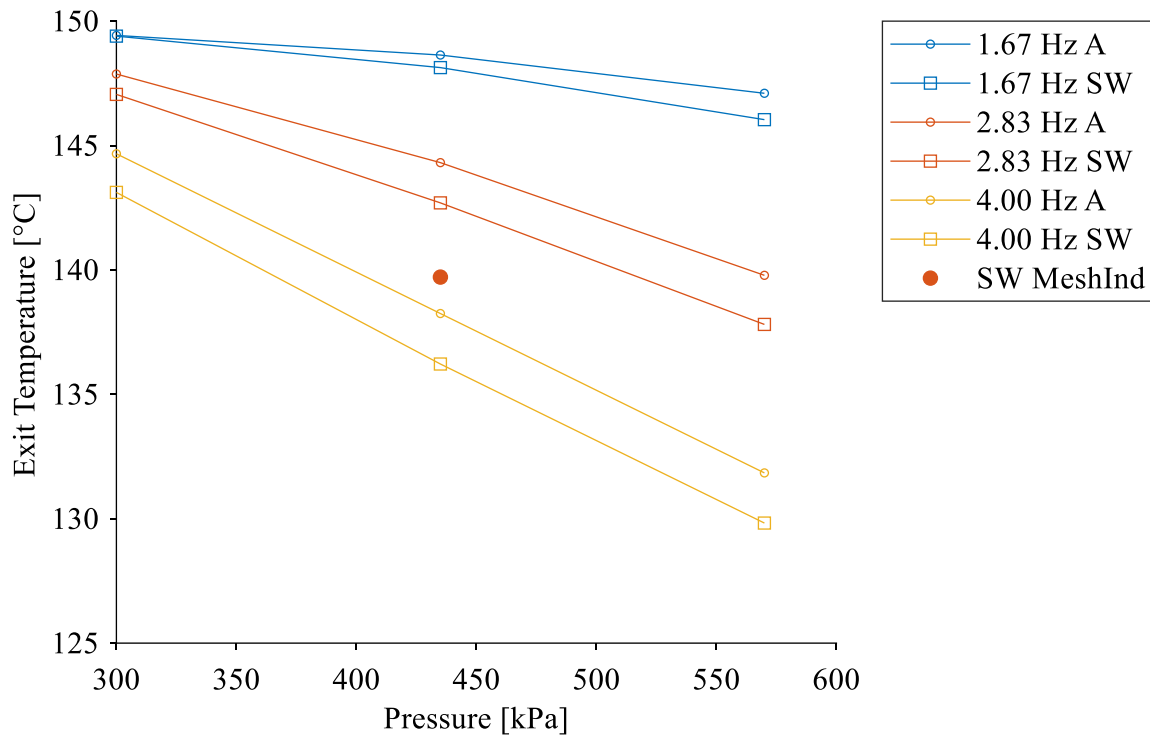


Figure 5.14: Plot of exit air temperature determined from analytical solution and simulation for varying engine pressure and speed for the heating case.

The difference between the simulation and analytical solution for air exit temperature is plotted against engine pressure for varying engine speeds in Figure 5.15. It can be seen that the difference in exit temperature is below approximately 2 °C for all cases, again with higher pressure and speed cases deviating more than lower pressure and speed cases. The mesh independent solution for the base engine pressure and speed case differs by 4.6 °C, with more underprediction than the mesh dependent cases.

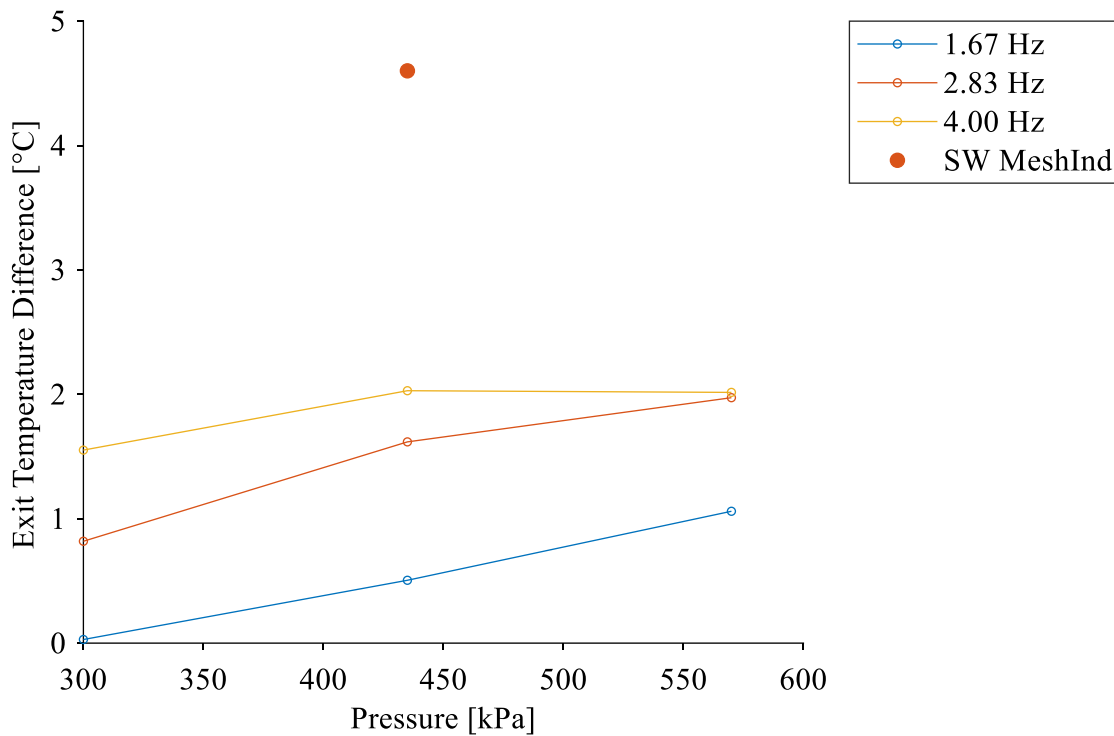


Figure 5.15: Plot of absolute value exit temperature difference between analytical solution and simulation for varying engine pressure and speed for the heating case.

The analytical solution only considers the conduction through the aluminum from the source or sink to the base of the fin contacting the air side. There is additional temperature drop due to conduction through the fin which would yield a reduced average solid temperature and air exit temperature than is currently included in the analytical solution. This is visible in the simulation solution, as shown in the temperature plot of the solid for the heating base case conditions in Figure 5.16. The solid temperature varies along both the length of the fin and the length of the heat exchanger, and drops from a temperature of 150 °C to as low as 134 °C at the entrance to the air channel where the air temperature is coldest.

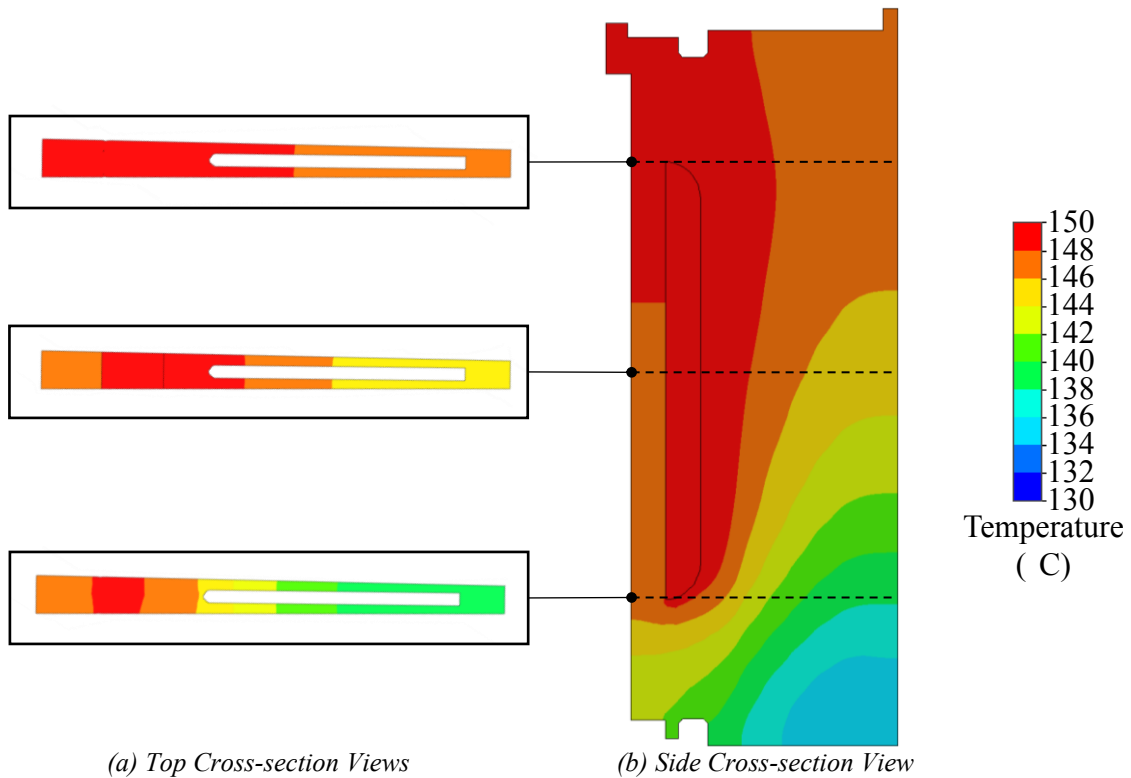


Figure 5.16: Contour plot of solid temperature in the air side fins for the heating case showing (a) horizontal sections at the top, middle, and bottom of the liquid channel indicated in (b) the vertical section.

It is complex to solve this multidimensional heat transfer problem analytically, where the gas temperature and solid surface temperature are changing along both the length of the fin and the length of the air channel. To evaluate how well the CFD solution matches the empirical relations for air, the solid temperatures from the CFD can be used for the analytical solution and the air exit temperatures can be determined. A plot of the exit air temperature from the analytical solution using the simulation solid temperature and the simulation exit air temperature for the heating case is shown in Figure 5.17, plotted against engine pressure for various speeds. It can be seen that the trend is followed almost exactly, with a constant offset where the CFD overpredicts the analytical solution. The mesh independent solution is almost the same as the analytical solution however, with only a slight underprediction.

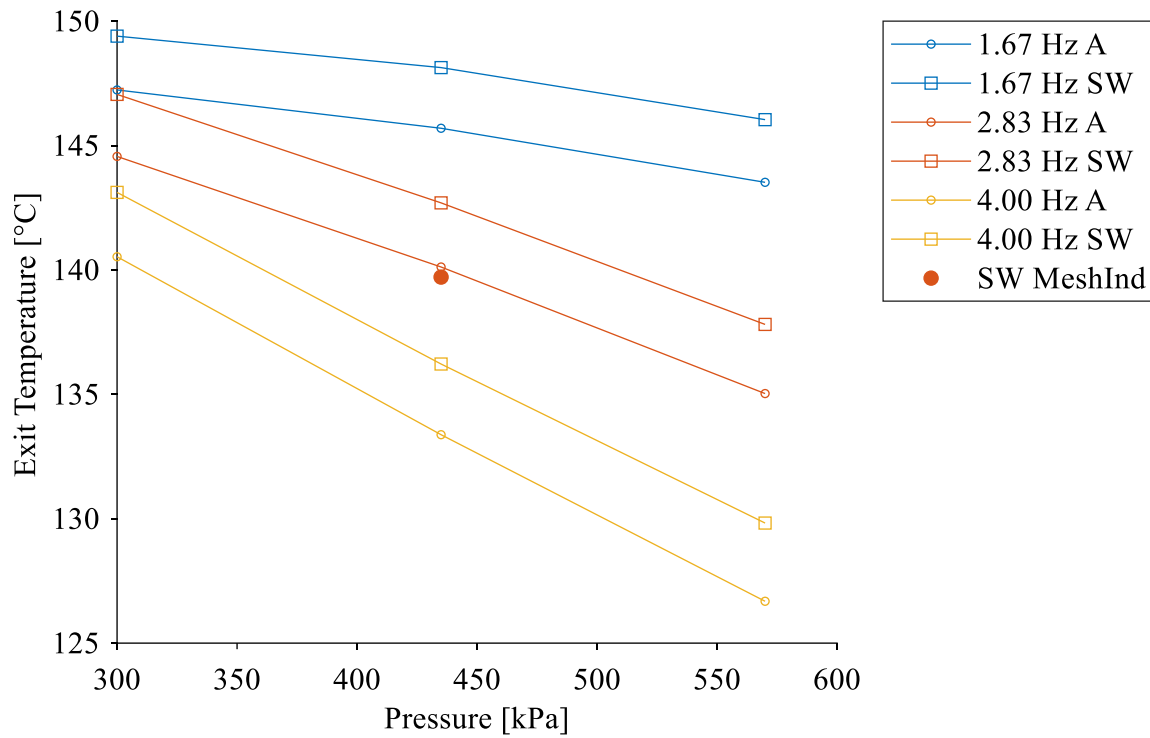


Figure 5.17: Plot of exit air temperature determined from analytical solution using simulation solid temperatures and simulation solution for varying engine pressure and speed for the heating case.

Figure 5.18 plots the absolute value difference between this analytical solution and the simulation solution for exit air temperature against engine pressure for varying speeds. The difference between the simulation solution and analytical solution is offset approximately 2.5 °C for all cases, and the mesh independent solution is offset 0.5 °C.

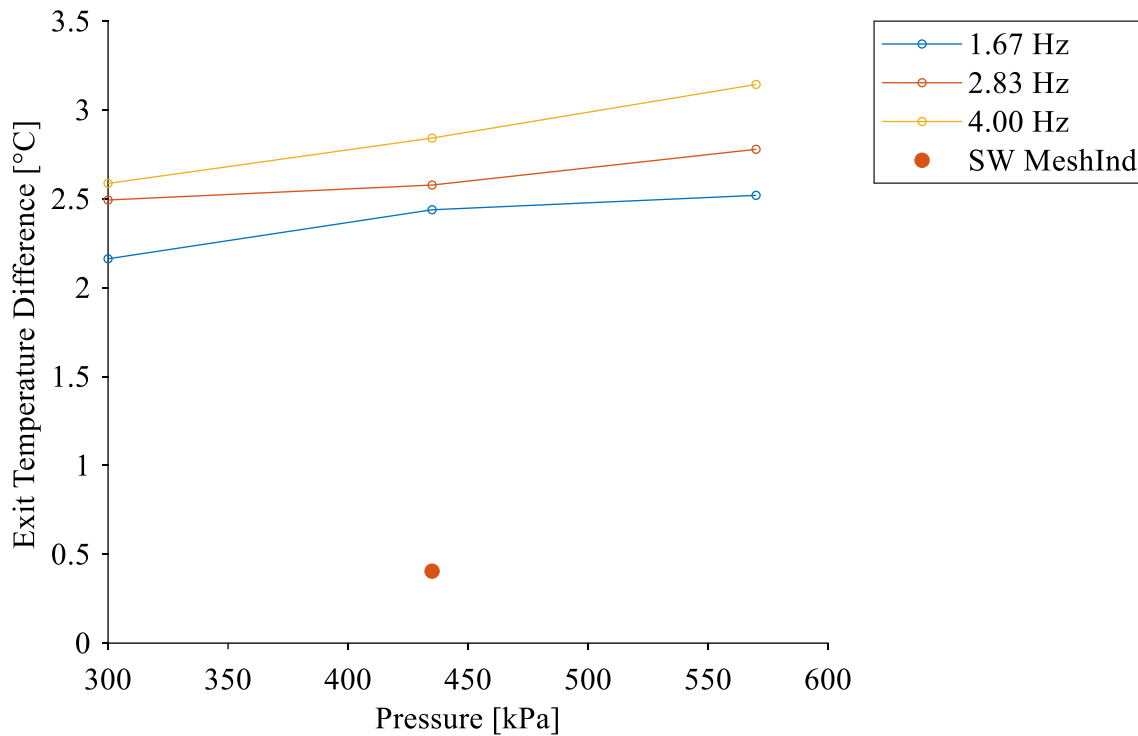


Figure 5.18: Plot of absolute value exit air temperature difference between analytical solution using simulation solid temperature and simulation solution for varying engine pressure and speed for the heating case.

The results for the cooling case follow similarly to the heating case for solid temperature and exit air temperature. The corresponding plots to the plots presented thus far in this section are included in Appendix I. There is more deviation from the analytical solution for cases with higher engine speed and pressure than the heating case, likely due to the lower density of air leading to the simulation solution having more mesh dependency effects.

Figure 5.19 plots the air pressure drop through the finned channel determined by the simulation and the analytical solution for varying engine speeds against engine pressure for the heating case. It also plots the mesh independent solution determined in the previous section for the base engine speed and pressure case. The trend of increasing pressure drop with increasing engine speed is clearly seen. Once again, the simulation follows the trend of the analytical solution well, though the simulation overpredicts the analytical solution.



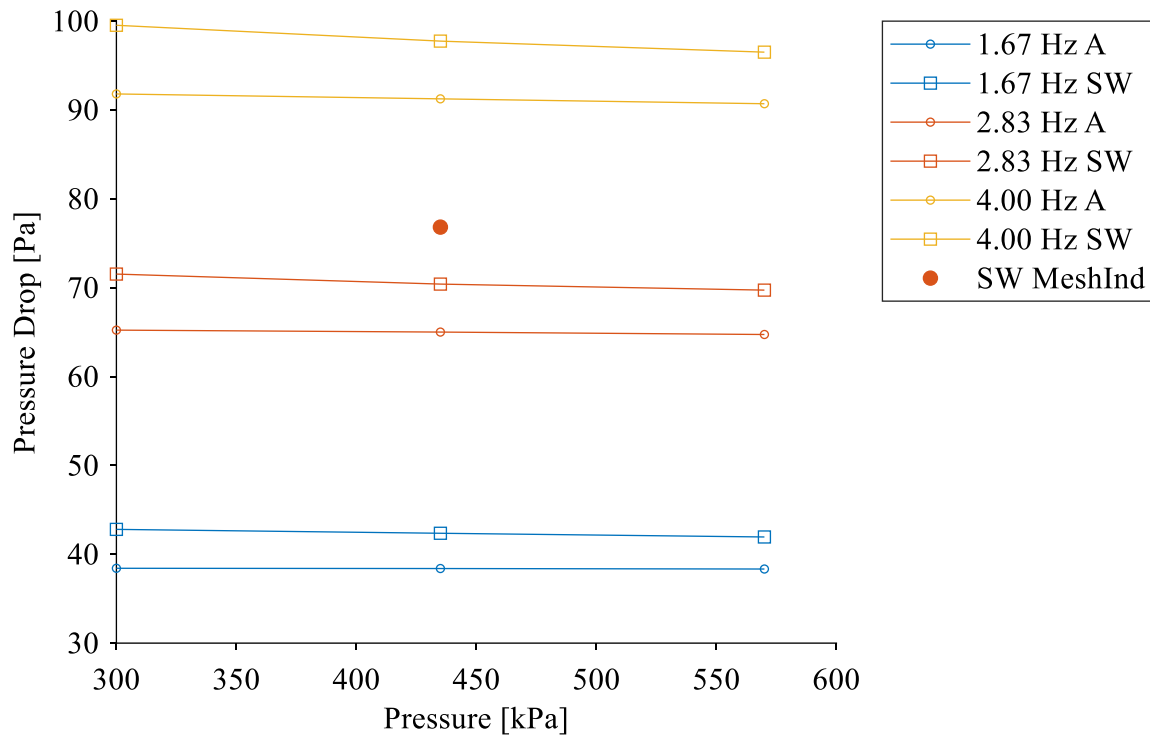


Figure 5.19: Plot of air pressure drop determined from analytical solution and simulation for varying engine pressure and speed for the heating case.

In Figure 5.20 the air pressure drop through the finned channel determined by the simulation and the analytical solution is plotted for varying engine speeds against engine pressure for the cooling case, along with the mesh independent solution. The same trend of increasing pressure drop with increasing engine speed is present, however the pressure drop from the simulation is significantly underpredicted compared to the analytical results.

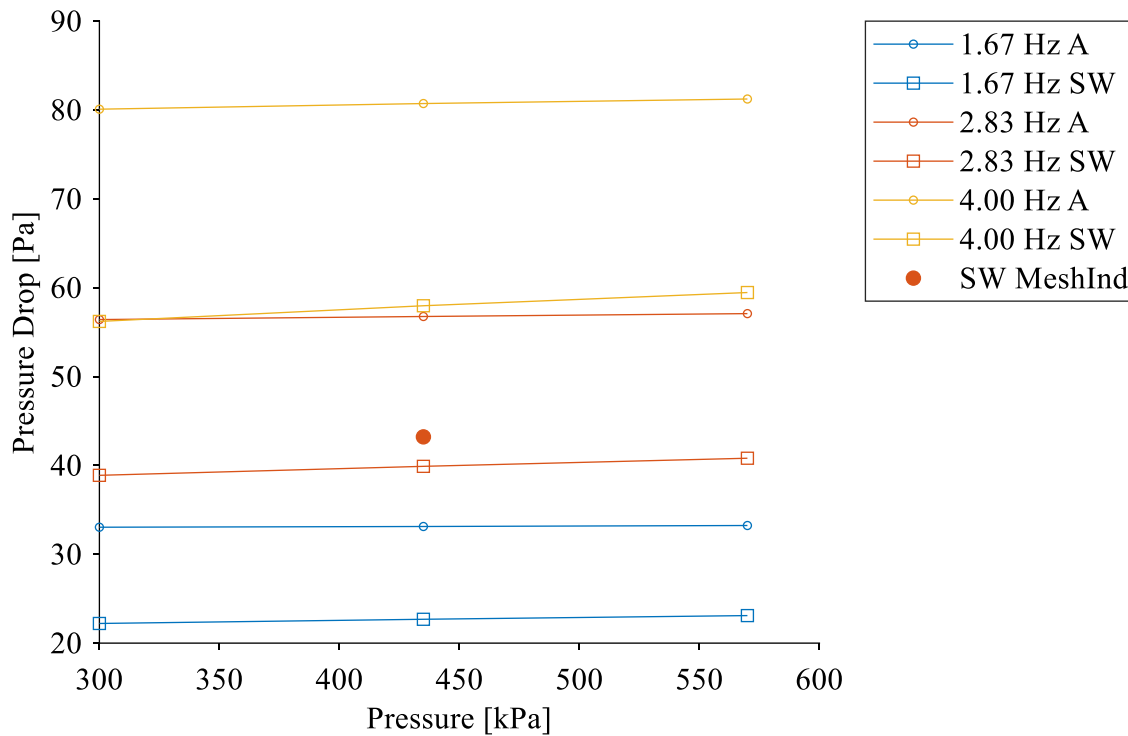


Figure 5.20: Plot of air pressure drop determined from analytical solution and simulation for varying engine pressure and speed for the cooling case.

The absolute value of the difference between the simulation and analytical solution for air pressure drop through the channel is plotted against engine pressure for varying engine speeds in Figure 5.21 for the heating case, and in Figure 5.22 for the cooling case. It can be seen that the difference in air pressure drop increases with increasing engine speeds in both cases, as expected. There is a slight decrease in the air pressure drop difference with increasing engine pressure, but the trend is relatively flat. Of interest to note is the mesh independent solution overpredicting the analytical solution by approximately 12 Pa in the heating case, and the mesh independent solution underpredicting the analytical solution by approximately 13.5 Pa. This is likely due to the effect of the heat transfer from the wall to the fluid changing the boundary layer development and resulting in an increased pressure drop [81] that is not captured in the analytical solution. The opposite offset of the same order of magnitude occurs in the cooling case.

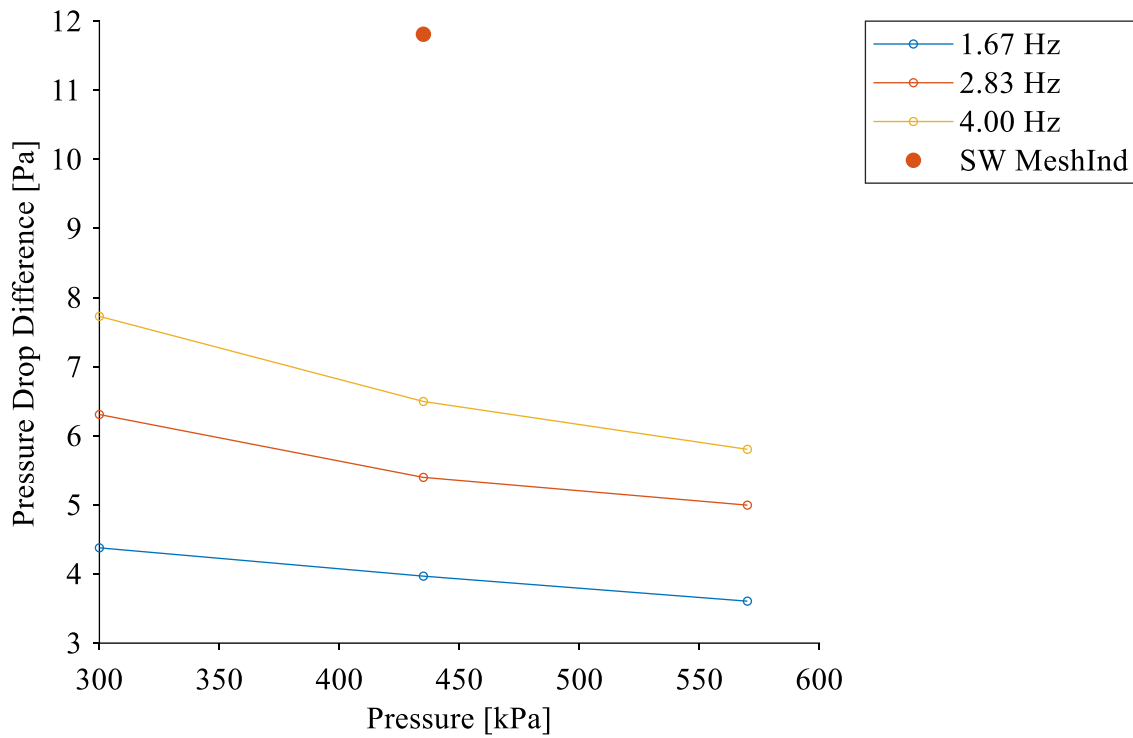


Figure 5.21: Plot of absolute value air pressure drop difference between analytical solution and simulation for varying engine pressure and speed for the heating case.

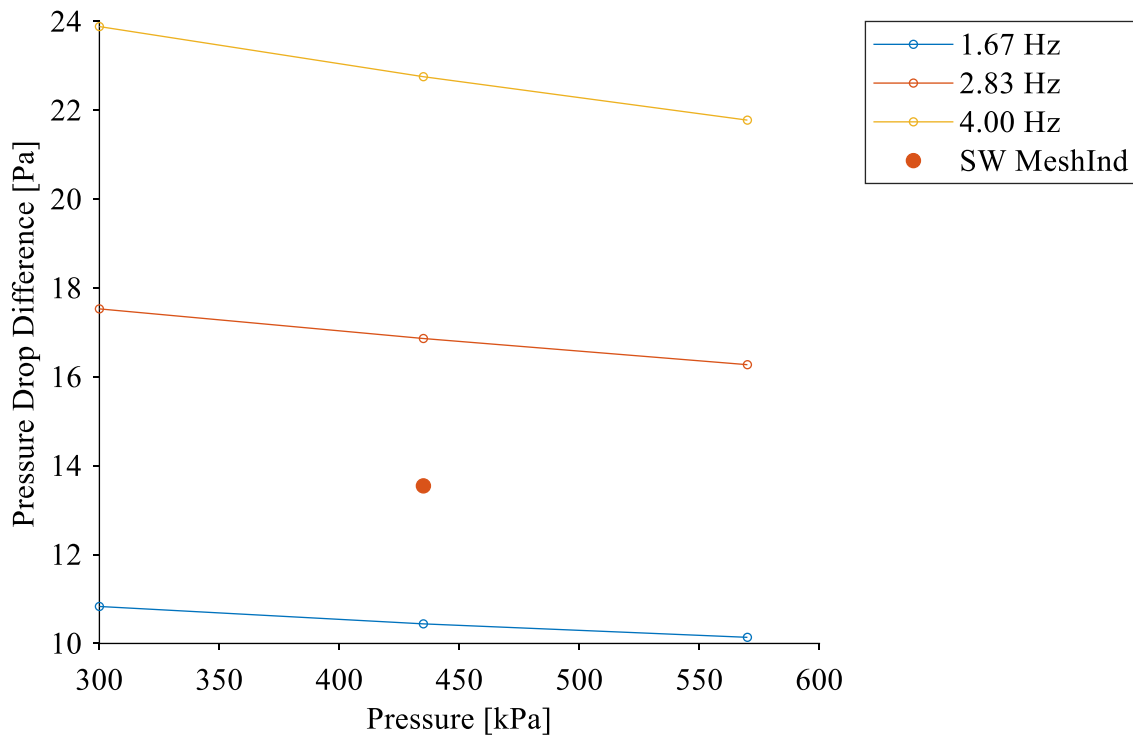


Figure 5.22: Plot of absolute value air pressure drop difference between analytical solution and simulation for varying engine pressure and speed for the cooling case.

This discrepancy in the results points to the need for an experiment for validation of the CFD simulation result. There is a lack of analytical solutions for the pressure drop with heating and cooling, and using a steady state experiment to measure the pressure drop through the air channels during heating and cooling would provide a better point of comparison.

Overall, the simulation is able to adequately follow the trends as expected in the analytical solution. The mesh dependence of the solution yields larger deviation in the results as the engine speed and pressure increases, except in the case of pressure drop where the deviation decreases with increased engine pressure.

### 5.3.6 Liquid Side Numerical and Analytical Result Comparison

The results of the liquid side model validation study and the liquid side analytical results described are compared against each other for the convergence parameters of exit liquid temperature and liquid pressure drop. Figure 5.23 plots the liquid exit temperature against the mass flow rate for various isothermal surface temperatures for both the analytical solution and the CFD solution for the heating case. The mesh independent CFD solution determined in the previous section is also included, which had 14 cells across the channel. In this plot it can be seen that the simulation underpredicts the exit temperature, but generally follows the trends of increasing exit temperature with mass flow rate and isothermal surface temperature.

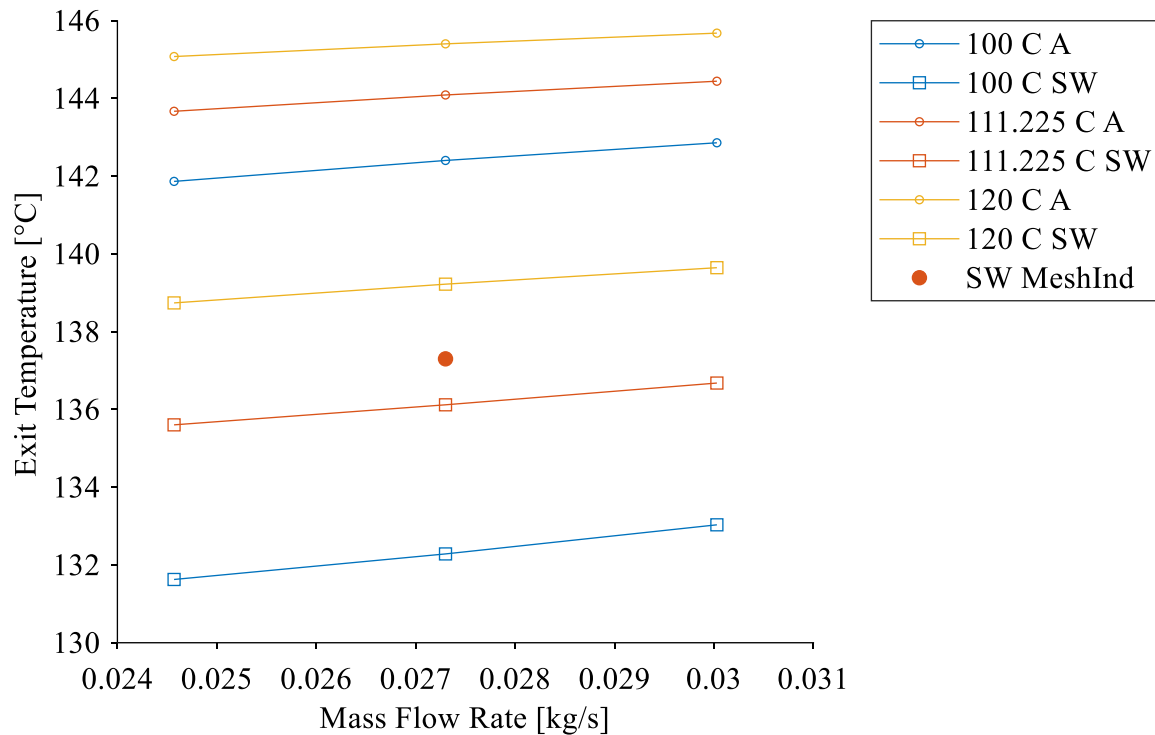


Figure 5.23: Plot of liquid exit temperature determined from analytical solution and simulation for varying mass flow rate and isothermal surface temperature for the heating case.

Figure 5.24 plots the absolute value of the difference between the simulation and analytical solution for liquid exit temperature against mass flow rate for varying isothermal surface temperatures for the heating case. Here it is clear that due to the spread between the different isothermal surface temperatures in the CFD solution, the lower temperature with the greater difference between the inlet temperature has a larger offset than the higher temperature with the smaller difference between the inlet temperature. Also, the mesh independent solution for the

base case has a lower offset, indicating that there may still be some effects from the mesh dependency.

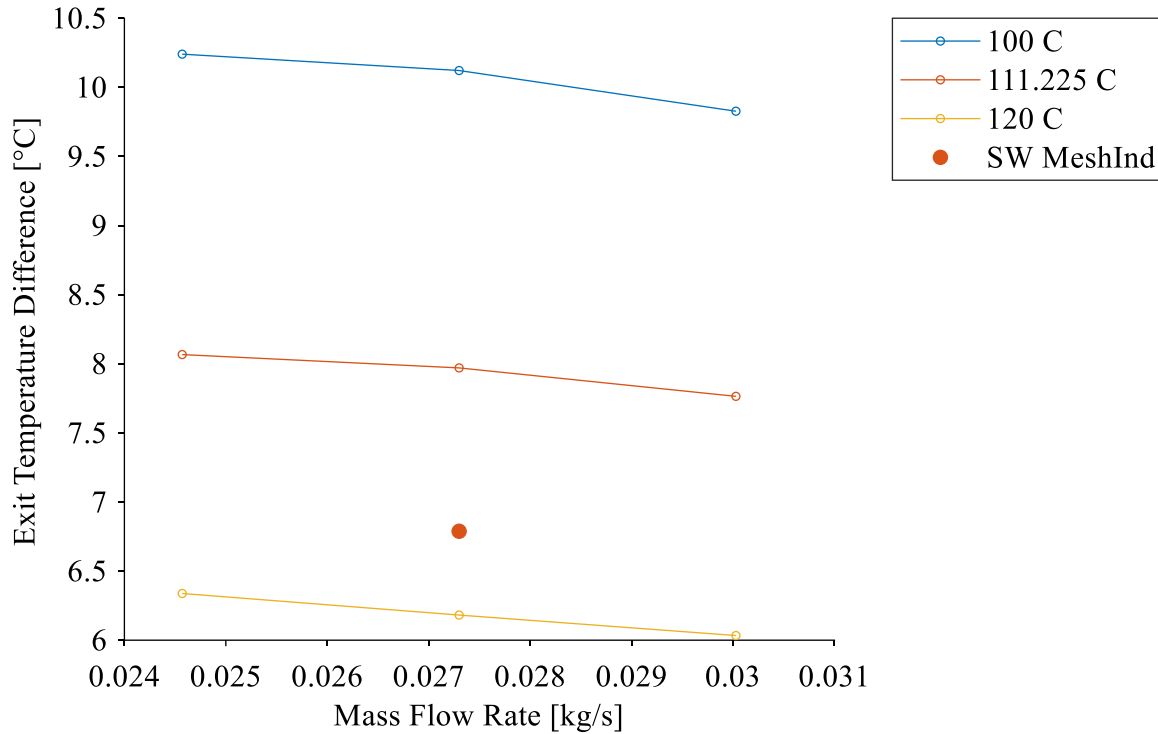


Figure 5.24: Plot of absolute value liquid exit temperature difference between analytical solution and simulation for varying mass flow rate and isothermal surface temperature for the heating case.

The liquid pressure drop is plotted against the mass flow rate for varying isothermal surface temperatures for both the analytical solution and the CFD solution for the heating case in Figure 5.25. In this plot it can be seen that the CFD overpredicts the analytical solution significantly, however the trend of increasing pressure drop with increasing mass flow rate is followed quite well.

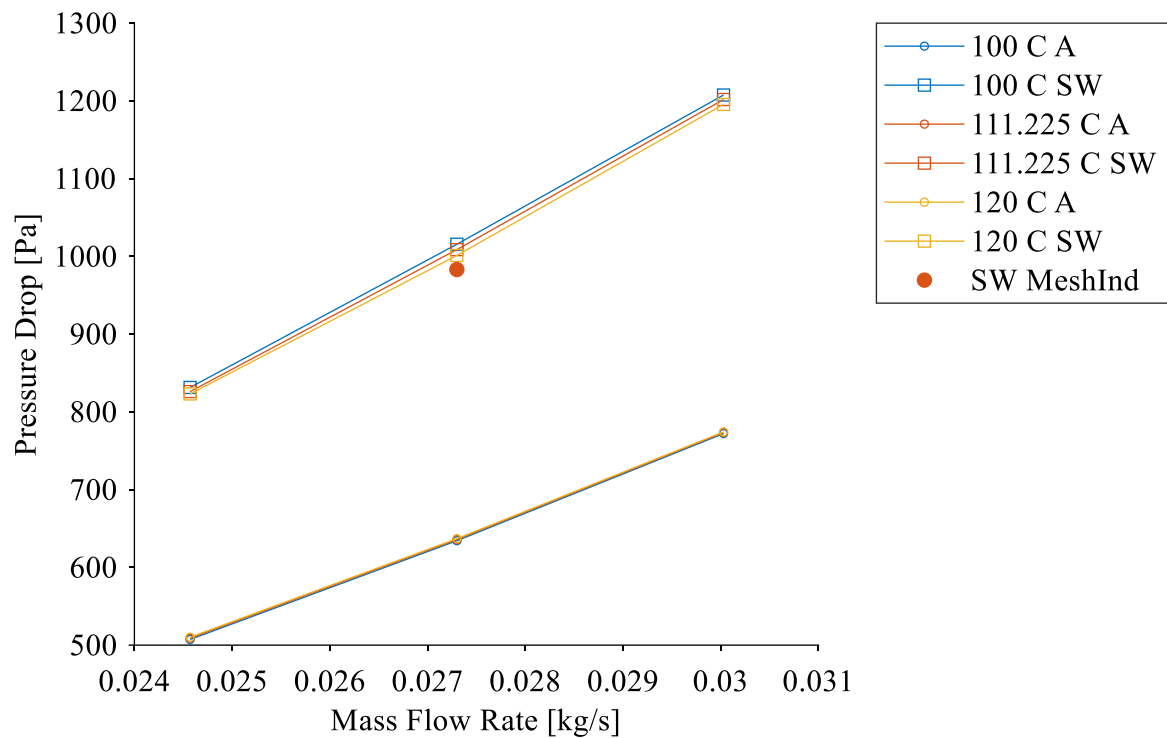


Figure 5.25: Plot of liquid pressure drop determined from analytical solution and simulation varying mass flow rate and isothermal surface temperature for the heating case.

Figure 5.26 plots the absolute value of the difference between the simulation and analytical solution for liquid pressure drop against mass flow rate for varying isothermal surface temperatures for the heating case. Here it can be seen that the rate of increase in pressure drop with mass flow rate varies somewhat, as the difference plot has a slope.

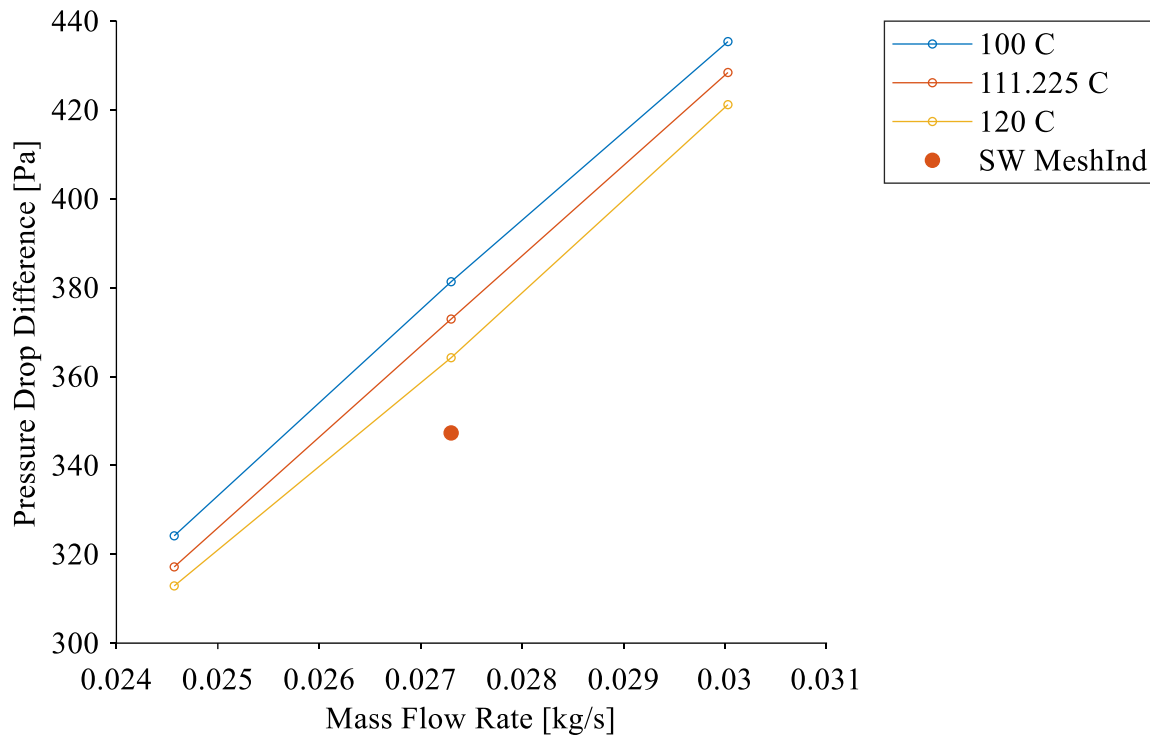


Figure 5.26: Plot of absolute value liquid pressure drop difference between analytical solution and simulation for varying mass flow rate and isothermal surface temperature for the heating case.

The results of the cooling case follow similarly to the heating case. The plot of liquid exit temperature in Figure 5.27 shows that the simulation solution overpredicts the analytical solution, but the trend of increasing exit temperature with increasing isothermal surface temperature and decreasing mass flow rate is followed well. The plot of absolute difference of liquid exit temperature in Figure 5.28 shows that the larger spread of liquid exit temperature determined from the simulation yields larger offsets from the analytical solution for higher isothermal surface temperatures, which has a greater difference from the inlet temperature, just as in the heating case.



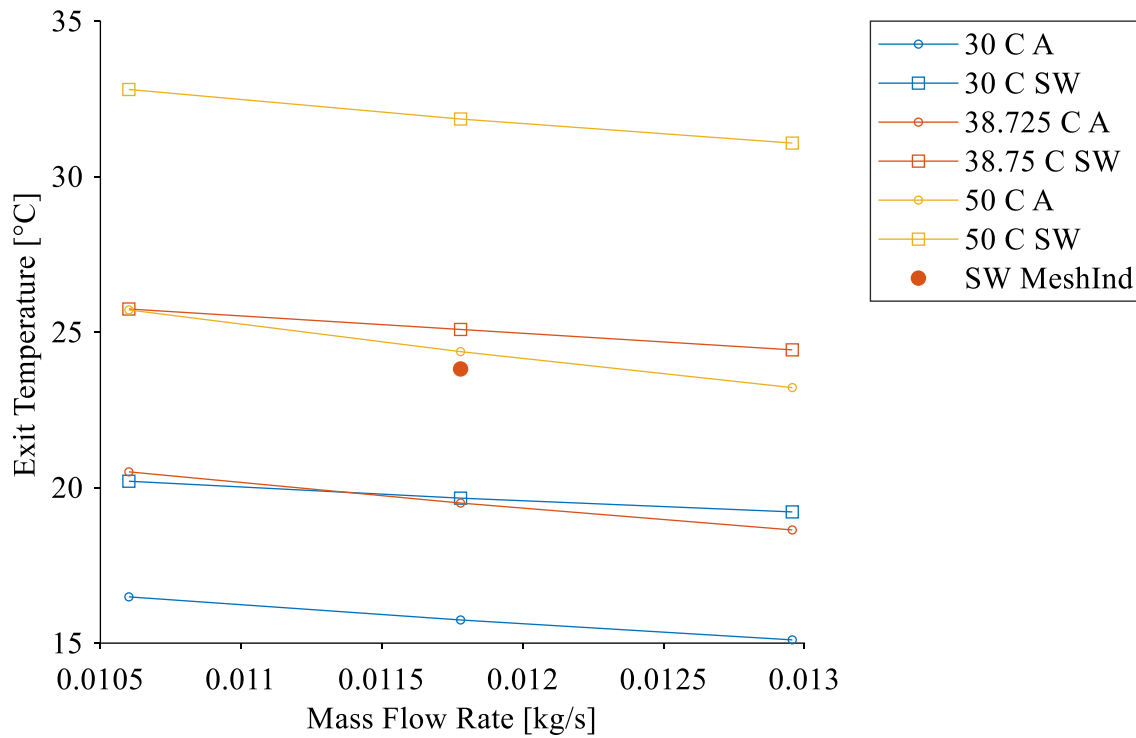


Figure 5.27: Plot of liquid exit temperature determined from analytical solution and simulation varying mass flow rate and isothermal surface temperature for the cooling case.

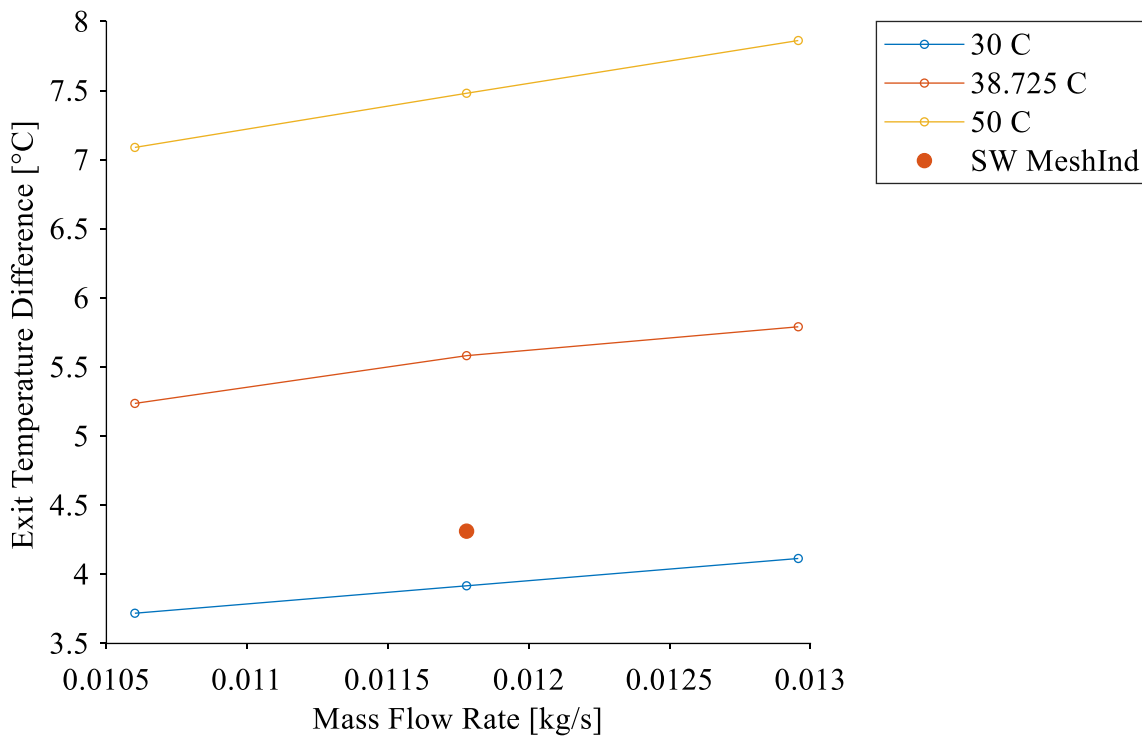


Figure 5.28: Plot of absolute value liquid exit temperature difference between analytical solution and simulation for varying mass flow rate and isothermal surface temperature for the cooling case.

For the liquid pressure drop in the cooling case, the simulation once again overpredicts the pressure drop compared to the analytical solution, as seen in Figure 5.29 with the plot of liquid pressure drop for the cooling case. Of note is a slight inversion of the analytical pressure drop trend, where for the lowest mass flow rate the pressure drop is higher for the 30 °C isothermal surface than for the other two temperatures. This is due to the exit tube section in that case being in the laminar regime as opposed to the transitional regime, thus resulting in slightly different values of friction factor determined from the two correlations. This results in a discontinuity in the pressure drop trend for the exit region, as the two correlations are independent.

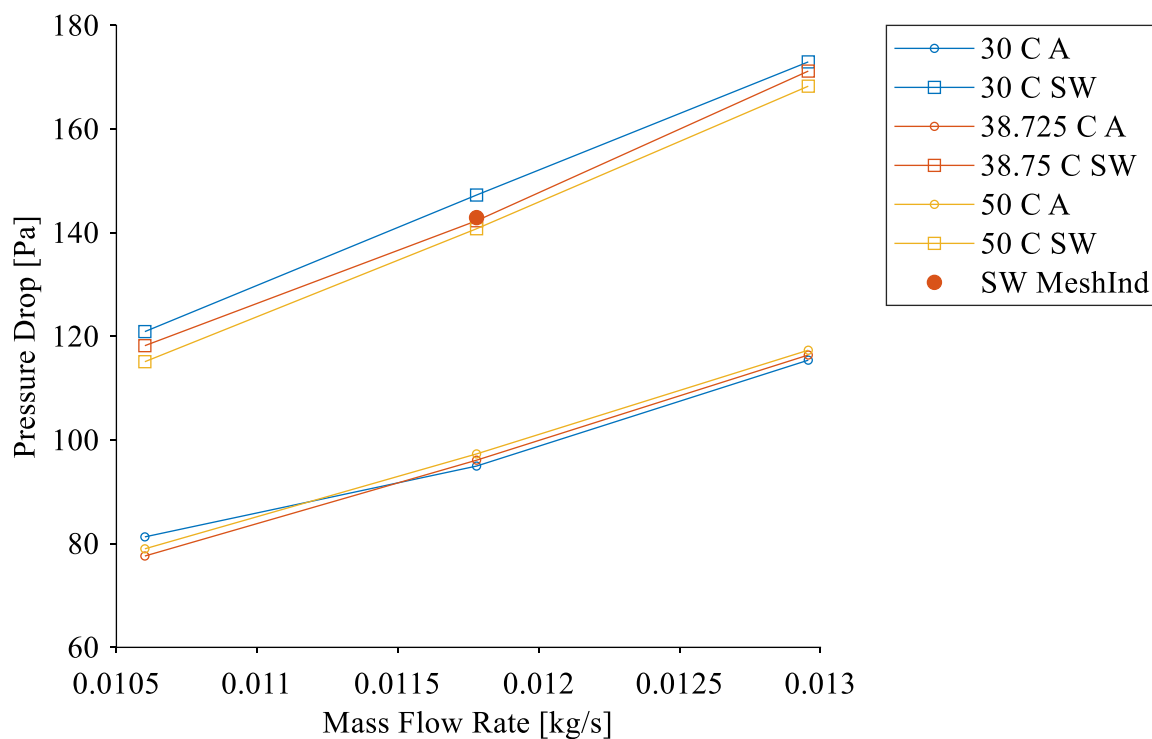


Figure 5.29: Plot of liquid pressure drop determined from analytical solution and simulation for varying mass flow rate and isothermal surface temperature for the cooling case.

In the plots of the absolute value of the difference in liquid pressure drop between the two solutions shown in Figure 5.30, it can again be seen that the rate of increase in pressure drop with mass flow rate varies somewhat. The difference in magnitude of the pressure drop between the heating and cooling case is due to the viscosity of the SIL180 fluid being an order of magnitude larger than that of water glycol at the respective liquid temperatures. Additionally, the pressure drop difference is approximately the same proportion of the total pressure drop for the heating and cooling case.

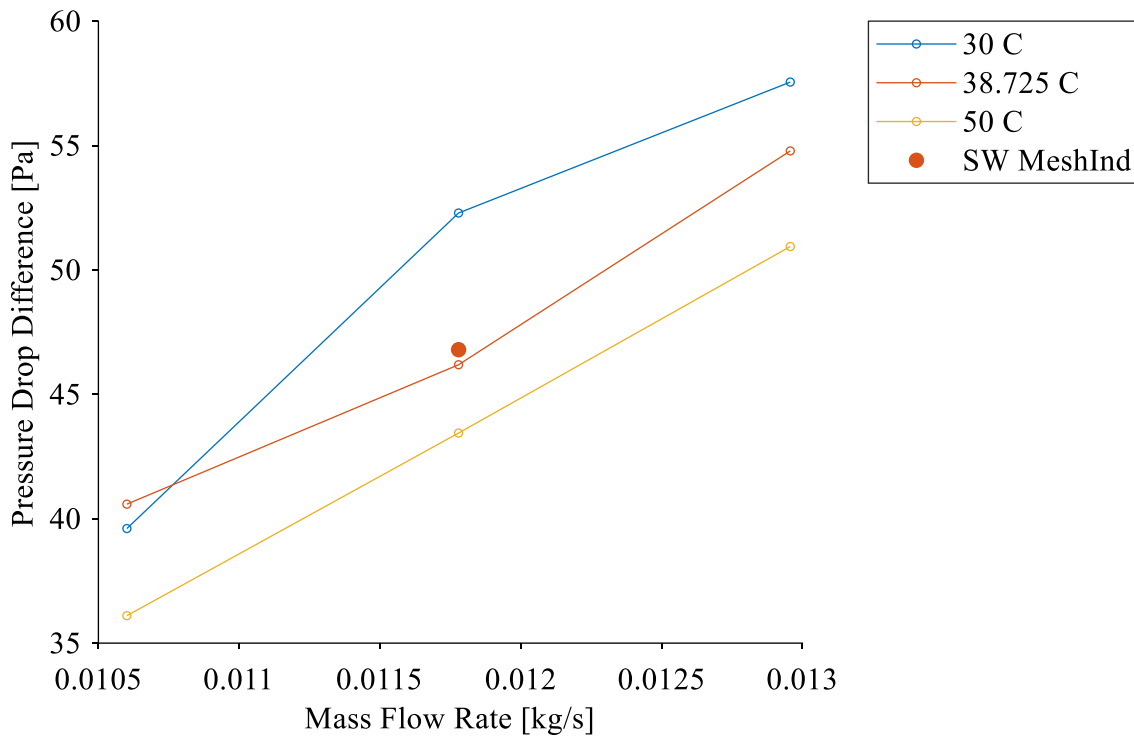


Figure 5.30: Plot of absolute value liquid pressure drop difference between analytical solution and simulation for varying mass flow rate and isothermal surface temperature for the cooling case.

While the offset in liquid exit temperature is relatively small for each case, the difference in liquid pressure drop is significantly overpredicted by the CFD in both the heating and cooling case. More accurately, the analytical solution is underpredicting the total pressure drop. This is due to the fact that the minor loss coefficients used for capturing the effect of the contractions, expansions, and turns of the fluid are not consistent with the actual flow geometry. These minor loss coefficients are determined for fully developed flows in round pipes, and the liquid flow geometry present in the CFD contains a rectangular channel with a high aspect ratio of approximately 12. By removing the entrance and exit tubes and simplifying the liquid flow path geometry to just the rectangular section, the prediction of liquid pressure drop by the simulation can be better evaluated. The simplified CFD study with boundary conditions is shown in Figure 5.31. The computational domain is no longer symmetric at the centerline as this would be physically illogical, so only the semicircle is considered. The code for analysis of this simplified CFD is included in Appendix B.

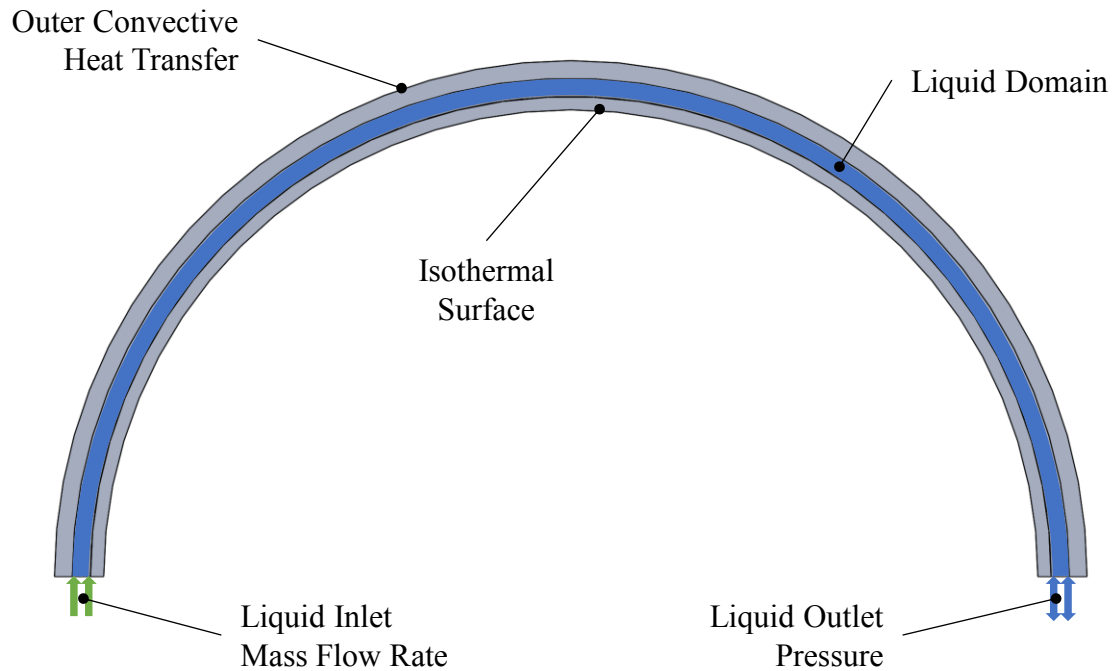


Figure 5.31: Figure showing simplified liquid side model slice for validation with boundary conditions.

For both the heating and cooling case, the difference between this simplified CFD solution and the analytical solution for just the rectangular section at the base case mass flow rate and isothermal surface temperature are summarized in Table 5.5. The solid surface temperature is almost identical between the two results, and the pressure drop predicted by the simulation is much closer. It also has similar behavior to the air pressure drop, wherein the effect of heat transfer on the boundary layer, which is not captured by the analytical model causes the simulation to underpredict the pressure drop on the cooling side and overpredict the pressure drop on the heating side. The exit temperature is still underpredicted for the heating case and overpredicted for the cooling case at approximately the same order of magnitude as in the non-simplified liquid study, indicating that the CFD is predicting more heat transfer between the fluid and the wall than the empirical correlations used for determining the heat transfer coefficient.

Table 5.5. Summary of output variables for simplified liquid model validation.

<b>Case</b>	<b>Output Variable</b>	<b>Simulation</b>	<b>Analytical</b>	<b>Difference</b>
Heating	Solid Surface Temperature	111.66 C	111.39 C	0.27 C
	Liquid Exit Temperature	137.19 C	144.19 C	7.00 C
	Liquid Pressure Drop	75.04 Pa	63.54 Pa	11.50 Pa
Cooling	Solid Surface Temperature	38.08 C	38.34 C	0.26 C
	Liquid Exit Temperature	23.82 C	19.50 C	4.32 C
	Liquid Pressure Drop	9.86 Pa	11.72 Pa	1.86 Pa

To properly evaluate the non-simplified liquid study pressure drop for validity, it would be ideal to run an experimental study where the pressure drop in the liquid is measured, and a loss coefficient for the system as a whole could be determined. This is a fairly simple experiment to run, and is in the process of being run in the laboratory, however, results are not yet available at this time.

### **5.3.7 Conclusions**

This section presented the model validation of the CFD model. The model was split into two parts, the air side and the liquid side in order to compare it to the analytical model. This lowered the computational time, and also provided clear boundary conditions to compare to the analytical and empirical equations available. There was generally good agreement in the trends of the CFD prediction, though there was some significant over and underprediction. The deviation in the CFD results from the analytical was the result of two issues. The first was the insufficient computational resources to run a fully mesh independent model, thus resulting in some mesh dependency effects. The second was the lack of appropriate analytical solutions and empirical correlations for the flow conditions. For example, the pressure drop of a fluid undergoing heating or cooling is significantly different from that of a fluid at a constant temperature.

The analytical solution was able to provide a verification of the validity of the simplified CFD cases in the absence of experimental results. Even so, as it lacked the ability to model certain phenomena, it could still be supplemented with experimental verification. The analytical solution is limited by the assumptions used to enable the use of established empirical correlations. Additionally, the analytical solution cannot model the interaction of the air and liquid side together, as there are several parameters which are unknown that must be determined from the interaction of the liquid and air side. This points to the need for a multifluid CFD study to capture those interactions.

## 5.4 Results for Input Parameters for Stirling Model

The results from the full CFD study described in section 5.1 for all the cases of engine pressure and speed considered are discussed in this section, with emphasis on determining the input parameter of interest for the Sage model: the convective heat transfer resistance. As the Sage model is only discretized in one-dimension, and that dimension is not in the direction of the liquid flow, the average parameters from the CFD simulation will be used for determining the convective heat transfer resistance. As was mentioned in section 4.2.3, the convective heat transfer resistance can be determined from the temperature drop and heat flow rate, as shown for the heating case where the fluid temperature is higher than the surface temperature:

$$R_t = \frac{T_{fluid} - T_{surface}}{Q_{surface}} \quad (5.20)$$

where:

$T_{fluid}$  – average fluid temperature (K)

$T_{surface}$  – average solid surface temperature contacting fluid (K)

$Q_{surface}$  – total heat flow through surface contacting fluid (W)

These parameters are taken from the CFD results, where the fluid temperature is the spatially averaged liquid temperature over the entire heat exchanger, the surface temperature is the average solid surface temperature of the inner channel surface, and the total heat flow is through the inner channel surface. Note that the total heat flow modelled is only for half of the heat exchanger due to the symmetry boundary condition, while the Sage model includes the entire heat exchanger. The total heat flow from the CFD will be doubled to eliminate the effect of the symmetric solution. The surface temperature of the solid walls of the channel to the outside of the heat exchanger and the heat flow passing through that wall are not considered, as that heat does not contribute to the heating or cooling of the air inside the engine.

### 5.4.1 Thermal Resistance Results

The convective heat transfer resistance calculated from the CFD is plotted against the engine air pressure for varying engine speeds. The plot for the heating case is shown in Figure 5.32 and the cooling case is shown in Figure 5.33. In each of these plots there is a trend with speed and pressure of the convective heat transfer resistance value. However, the total range that the

convective heat transfer resistance varies over is very small. The percent difference between the highest value and lowest value of convective heat transfer resistance is 3.4% for the heating case and 2.6% for the cooling case. This small range of variance is expected, as the heat transfer resistance for convection is related to the heat transfer coefficient by:

$$R_t = \frac{1}{hA_s} \quad (5.21)$$

where:

$A_s$  – surface area (m<sup>2</sup>)

The surface area is constant, so the convective heat transfer resistance is dependent only on the convective heat transfer coefficient. This coefficient is dependent on the fluid properties, fluid velocity, and geometry of the fluid flow path. For the liquid flow, these three properties are almost constant. The temperature from inlet to outlet does not change significantly so the fluid properties are almost constant. The fluid velocity is almost constant, as the mass flow rate of the fluid is constant. Finally, the geometry of the flow path does not change. This results in an almost constant convective heat transfer coefficient, and thus an almost constant convective heat transfer resistance.

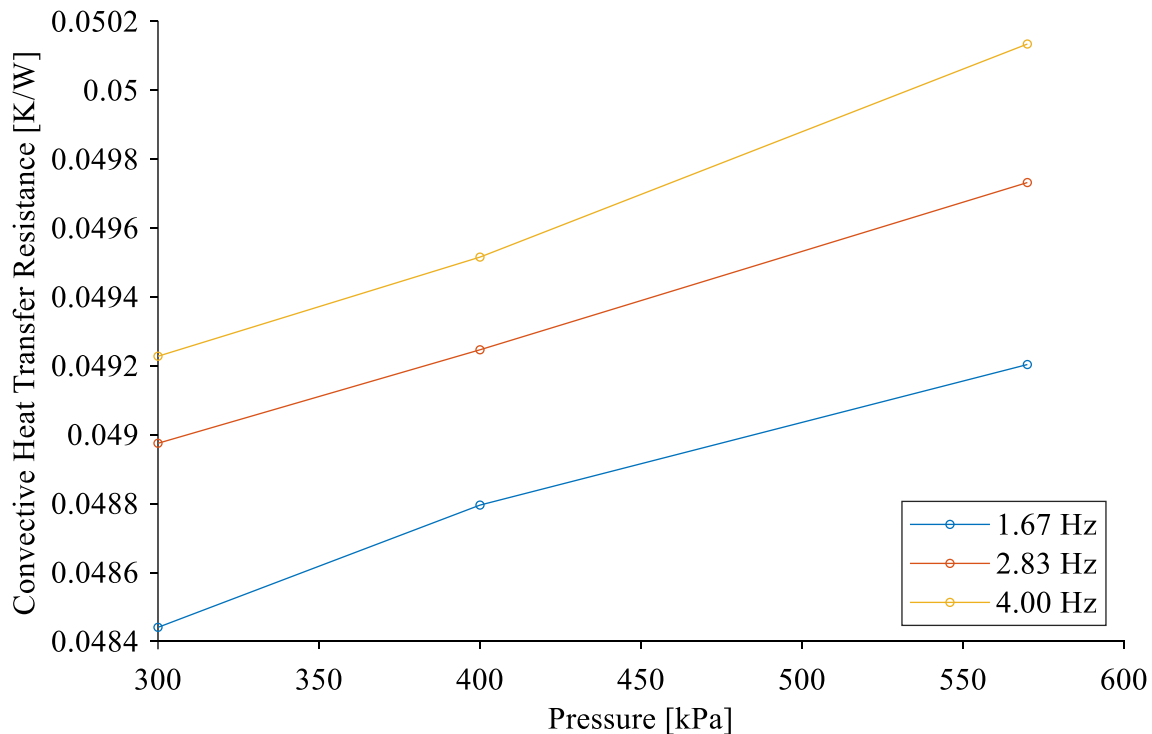


Figure 5.32: Plot of average thermal resistance for heating case against engine pressure for varying engine speeds.



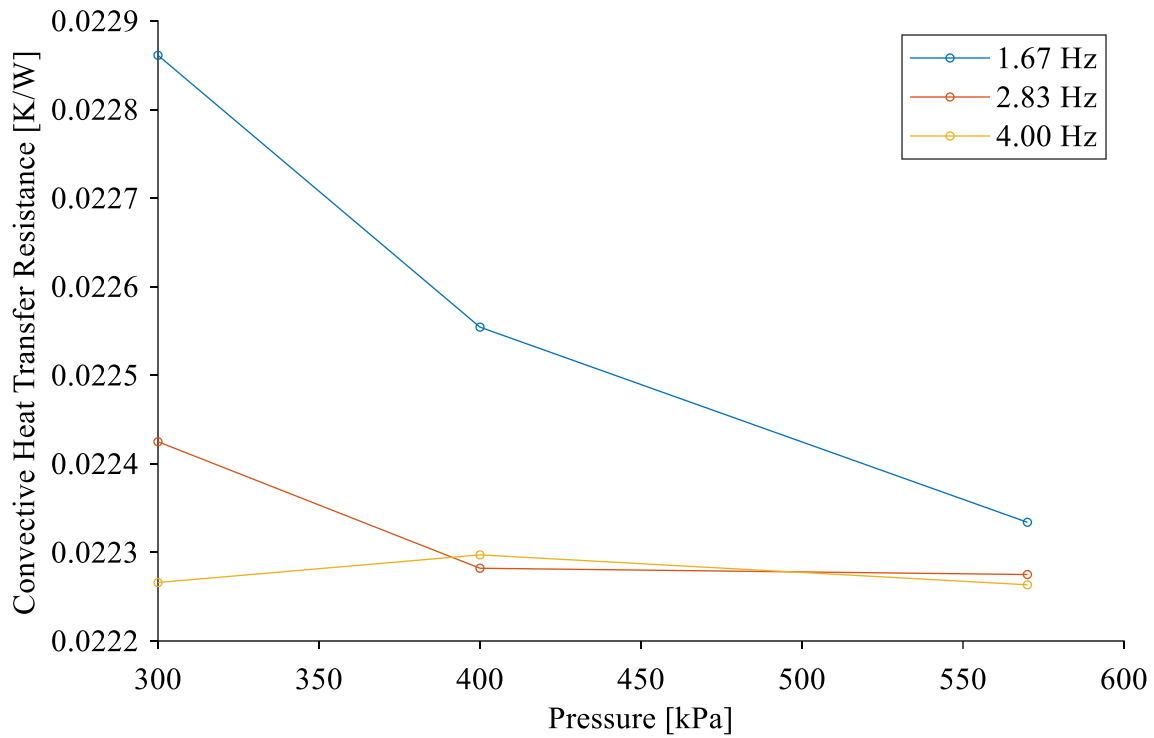


Figure 5.33: Plot of average thermal resistance for cooling case against engine pressure for varying engine speeds.

The slight trends with engine pressure and speed occur as a result of the changing heating load on the air side. With increased pressure and speed, there is an increase in the amount of air that needs to undergo a temperature change. This leads to an increased heat flow between the air and liquid for the higher pressure and speed cases, as can be seen in Figure 5.34.

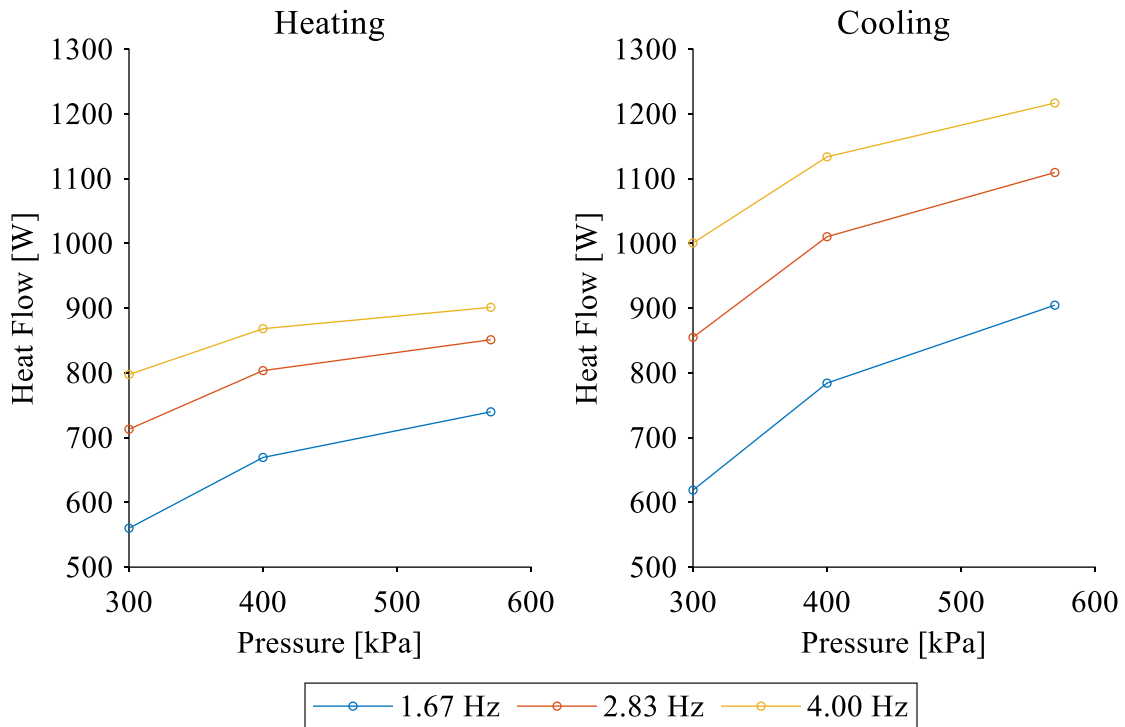


Figure 5.34: Plot of heat flow against engine pressure for varying engine speeds for both the heating and cooling cases.

This also results in the solid surface temperature becoming closer to the inlet air temperature with increasing pressure and speed, as seen in Figure 5.35. This is due to the amount of heat flow being delivered from the liquid to the air becoming insufficient to change the temperature of the air to the liquid temperature. As this heating load increases with engine pressure and speed, the average liquid temperature also moves farther from its inlet temperature, as seen in Figure 5.36.

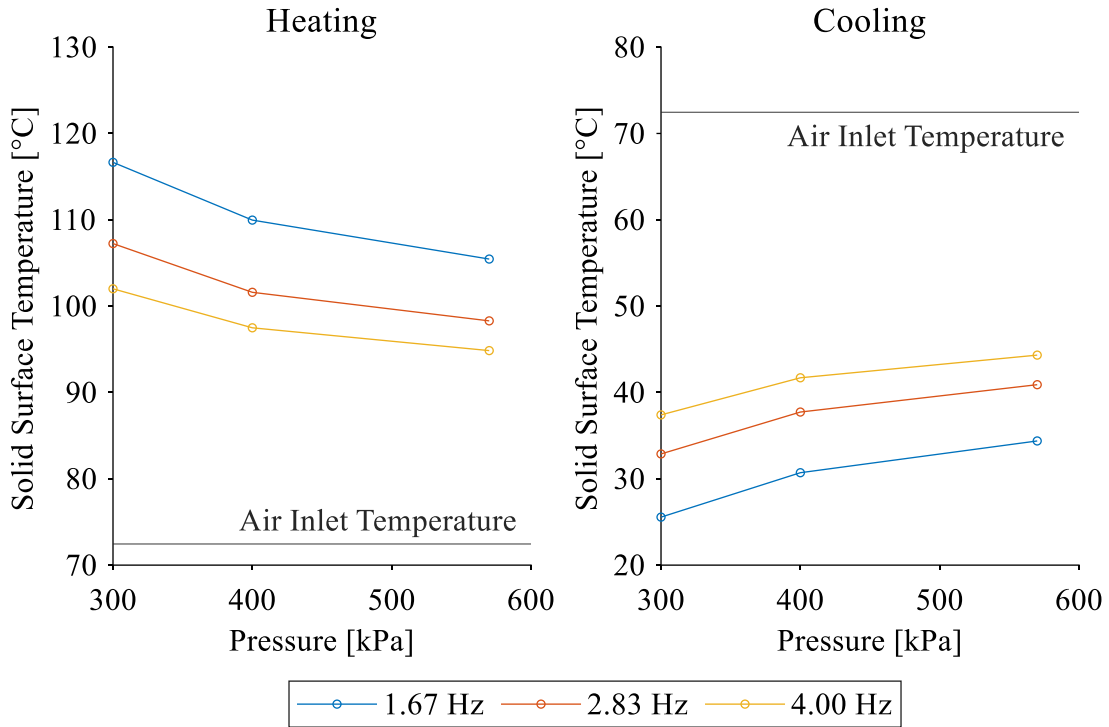


Figure 5.35: Plot of average solid surface temperature against engine pressure for varying engine speeds for both the heating and cooling cases.

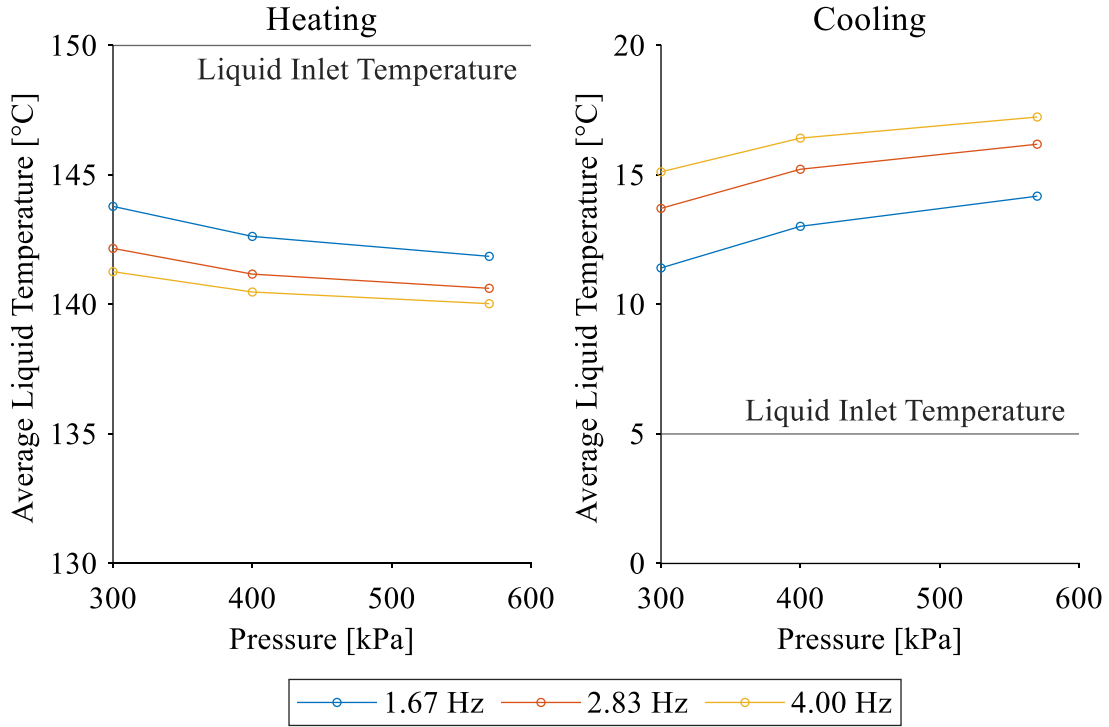


Figure 5.36: Plot of average liquid temperature against engine pressure for varying engine speeds for both the heating and cooling cases.

Due to the difference in fluid properties between the SIL180 and water glycol however, the amount of change of these parameters as the engine pressure and speed changes yield slightly different convective heat transfer resistance values. In the heating case, as the pressure and speed increases, the temperature difference increases slightly faster than the heat flow, leading to the increase in convective heat transfer resistance. This trend is reversed for the cooling case. This can be seen clearly for increasing pressure in Figure 5.37 where the heat flow and temperature difference parameters are normalized against the respective first value for a given speed and plotted against the engine pressure. Figure 5.38 similarly shows this trend for increasing pressure by normalizing the heat flow and temperature difference against the first value for a given pressure, and plotting against speed. The SIL180 average temperature changes less significantly than the water glycol mixture with changing pressure and speed, which is likely due to the difference in the temperature dependence on specific heat capacity between the two fluids, where SIL180 has slightly less of a temperature dependence and water glycol has slightly more.

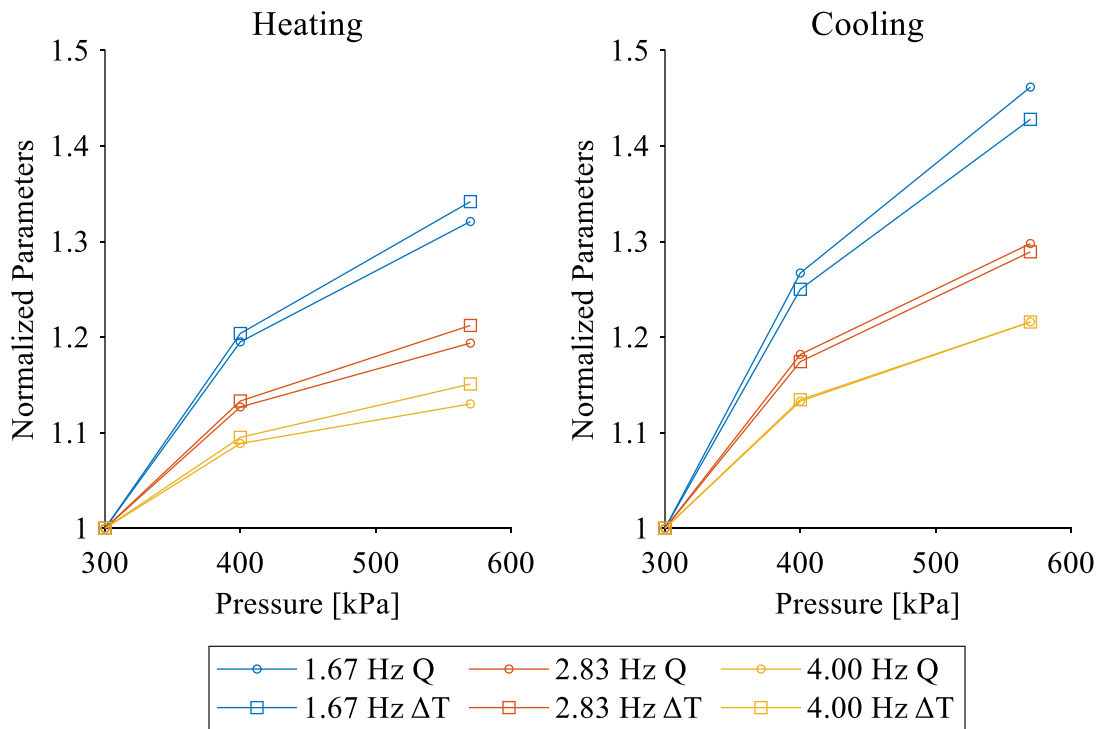


Figure 5.37: Plot of normalized heat flow and temperature difference against engine pressure for varying engine speeds for both the heating and cooling cases.

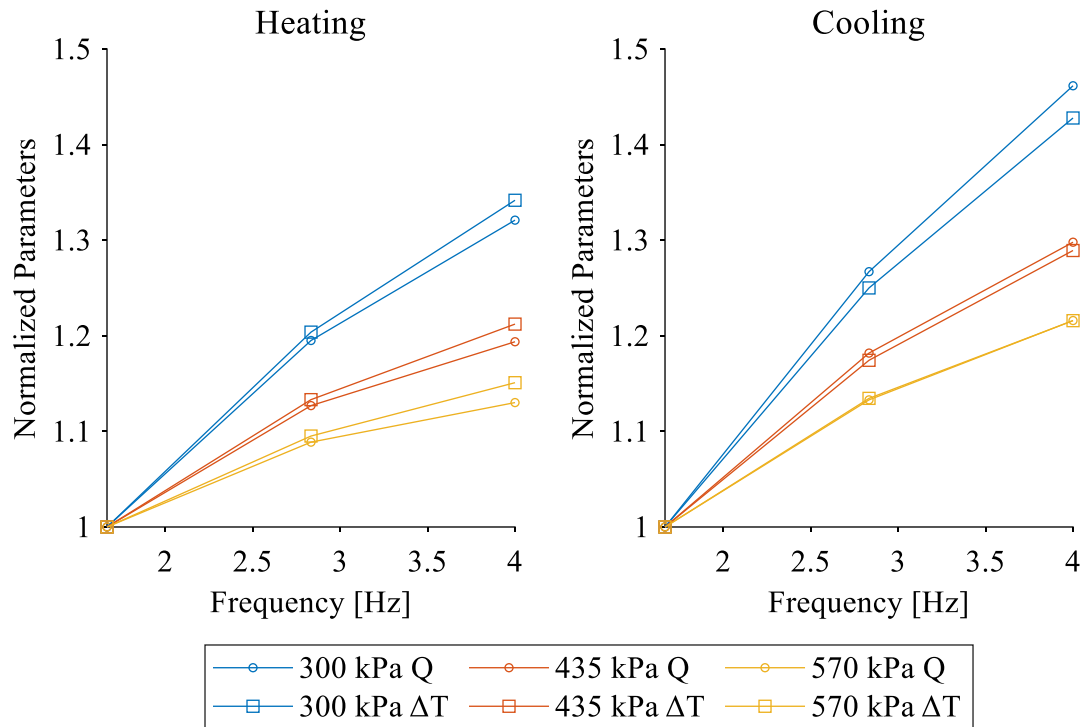


Figure 5.38: Plot of normalized heat flow and temperature difference against engine speed for varying engine pressures for both the heating and cooling cases.

### 5.4.2 Fluid Temperature Modelling for 3<sup>rd</sup> Order Model

The CFD results also offer the opportunity to evaluate whether the isothermal surface model component in Sage is the appropriate choice for modelling the heat input to the engine. The Sage model begins at the fluid temperature, as that is the known parameter and is able to be controlled in the experiment.

The CFD results show that there is some variation in the average fluid temperature with varying engine speed and pressure, thus it is not truly an isothermal surface, as the temperature changes depending on the heat flow. However, as the variation in average fluid temperature is small, particularly compared to the heat flow variation, the isothermal surface is the most appropriate idealization and model component choice for representing the heat input and output to the engine. The other ideal condition, constant heat flux, is not appropriate as the heat flow changes significantly with changing engine pressure and speed. Thus, the use of the isothermal surface idealization is reasonable given the liquid and heat flow conditions seen in the CFD results.

### 5.4.3 Application of Results for 3<sup>rd</sup> Order Model

There are some limitations to the Sage model that limit that parameters that can be included in the model from the CFD solution. Namely, the Sage model is only discretized in one dimension, which is the direction of air flow through the heat exchangers. As the heat exchangers have a cross-flow configuration in reality, it is not possible to capture any gradients in the temperature or convective heat transfer resistance along the liquid path length in the model as there is no discretization in that dimension. This limits the type of data that can be included in the Sage model from the CFD. The results are averaged over the fluid path length in order to be useful for the Sage model. If the heat exchanger configuration was such that the liquid flow path was discretized in the same direction as the air flow, it would be possible to determine the convective heat transfer resistance along the path length, and include the effect of liquid temperature drop in the Sage model.

From the above results discussed, two main results are used in the Sage model: the average convective heat transfer resistances for the heating and cooling sides, and the modelling of the liquid as an isothermal surface. The base case convective heat transfer resistances are used for the line temperature difference model item in Sage, at 0.04925 K/W for the heating case and 0.02228 K/W for the cooling case. This is done as the dependence of the resistances on engine pressure and speed is small, as is expected, thus it is appropriate to simplify to a single value. The CFD results also indicated that modelling the liquid as an isothermal surface is appropriate, as the averaged liquid temperature was not found to significantly depend on pressure and speed as compared to the solid surface temperature and the heat flow.

## 5.5 Conclusions

This CFD analysis was able to provide input parameters for the Sage model in the absence of the experimental setup required for determining the convective heat transfer resistance. The CFD was validated against analytical and empirical relations for the air and liquid side independently, and was found to have generally good trend agreement with the analytical result, though there was often an offset in the results. These validation studies provide insight into potential error in the Sage model input parameter values, which is useful for future model tuning. To better evaluate the validity of the CFD results, a simpler experimental setup measuring the fluid pressure drop and exit temperature could be used. Work is underway in the laboratory to complete this experiment; however, the results are not yet available at the time of writing.

The convective heat transfer resistance determined by the CFD was found to be approximately constant with varying engine pressure and speed, as expected given the liquid flow conditions. The convective heat transfer resistance determined from the base case simulations for the heating and cooling side is used as the input to the Sage model. The CFD also provides spatially varying information, which could be of use in a scenario where the liquid flow path is in the same dimension as the air flow path, or in a multidimensional Stirling model.

The completion of this CFD study also highlights the intensive computational requirements for doing CFD simulations of a Stirling engine. The model was not able to be mesh independent due to the memory requirements for mesh independence. The half model of the Stirling engine heat exchanger at steady state considered required over 400 hours to complete the 18 cases for this study.

## 6 Sage Model Validation Results

The Sage model was validated against the experimental data for the Raphael engine shown in Chapter 2. The heat exchanger input parameter of convective heat transfer resistance was determined from the CFD study undertaken in Chapter 5, and completed the Sage model setup. To evaluate the Sage model, first a mesh independence study was done to ensure the model had sufficient discretization. Then, the results of the model validation setup presented in Chapter 4 are discussed and the model validity for LTDSEs is evaluated.

### 6.1 Mesh Independence Study and Setup

The Sage model is discretized spatially and temporally using a grid. The spatial grid is defined in each of the top-level components as the number of cells used in that component. The temporal grid is defined globally as the number of time nodes for the model. If the model is not sufficiently discretized spatially then the spatial gradients across a particular component may not be captured. This is particularly noticeable across components with a significant temperature gradient, such as the regenerator. Additionally, if the temporal resolution is insufficient, then higher order harmonics in the response of time-varying parameters may not be captured. As such, it is necessary to validate that the results of the Sage model are grid independent.

The mesh dependence study was conducted at the base case engine pressure and speed, with the source temperature equal to 150 °C and the sink temperature equal to 5 °C. First, the number of time nodes was increased while the number of spatial cells was held constant. The number of spatial cells used for each component was 3, except for the heat exchangers and regenerator which had 5. The normalized indicated work was then plotted against the total number of time nodes, as shown in Figure 6.1. It can be seen that as the number of time nodes increases, the indicated work calculated by Sage stabilizes to a constant value. The percent change drops below 1% very quickly, and changes less than 0.1% with increasing number of time nodes. From this plot, the number of time nodes chosen for determining the spatial node distribution was chosen to 13 as the change in the indicated work stabilizes at this point.



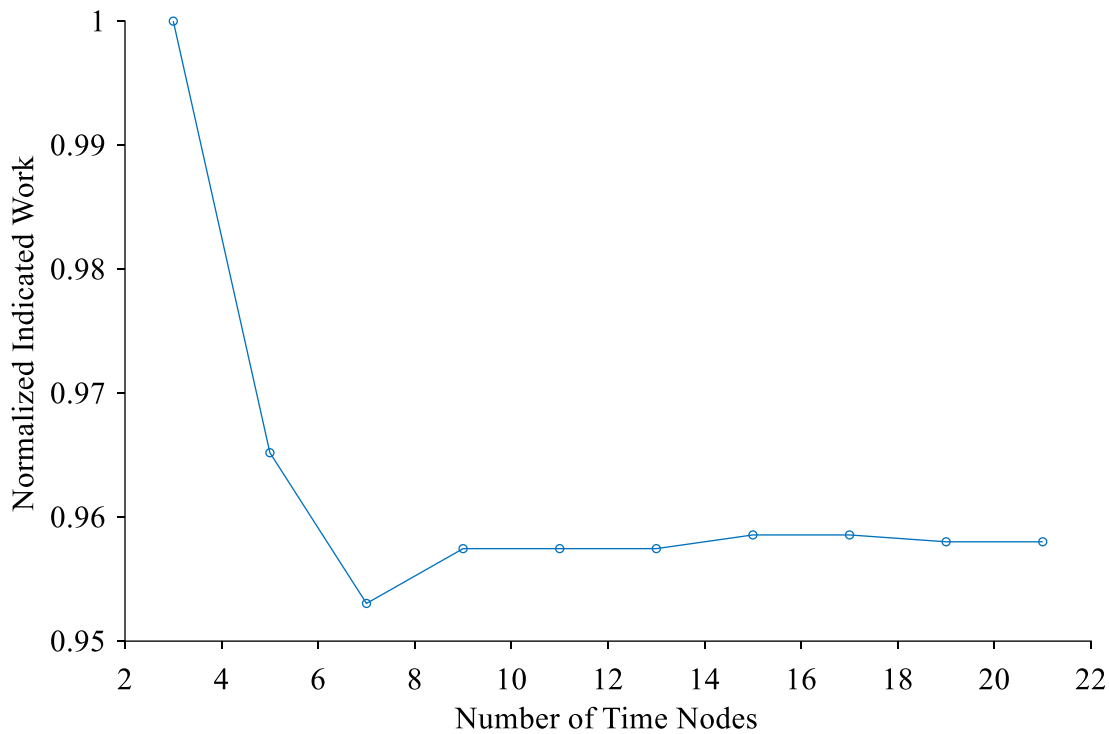


Figure 6.1: Plot of indicated work calculated by Sage model against number of time nodes for initial spatial node distribution.

A study was then run where the number of spatial cells was increased in all components except for the heat exchangers and regenerator, which remained at 5 spatial nodes. Since the heat exchangers and regenerator tend to have higher thermal gradients, they will likely require more spatial cells than the cylinder spaces. Thus, the appropriate number of spatial cells for the cylinder spaces is first determined from this study. The normalized indicated work is plotted against the number of spatial cells used for the remaining model components in Figure 6.2. Again, with increasing number of spatial cells the indicated work calculated by the model approaches a constant value. It is clearly visible that the percent change drops below 1% quickly, and is close to zero with increasing spatial nodes. The number of spatial cells for the cylinder space components was chosen to be 5 as the change is already below 1% at that point, and this reduces the computational time requirements.

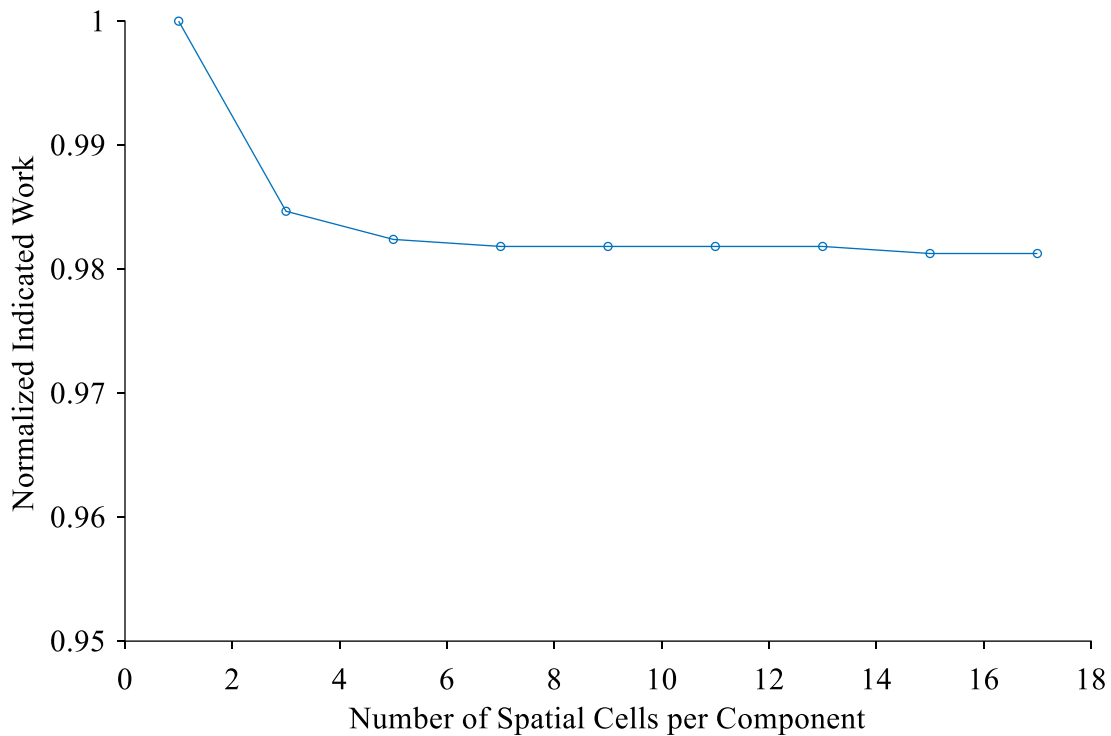


Figure 6.2: Plot of indicated work calculated by Sage model against number of spatial nodes for the cylinder space components for 13 time nodes.

The number of spatial cells for the heat exchangers and regenerator is then increased with a constant number of 5 spatial cells for the cylinder components and 13 time nodes. The normalized indicated work is plotted against the number of spatial cells per component in Figure 6.3. The indicated work for only one spatial cell across the heat exchangers and regenerator is half the value that the work stabilizes to. With any number of spatial nodes above 3 in the heat exchangers and regenerator, the indicated work approaches a constant value and the percent change never exceeds 1%. The number of spatial cells chosen for the heat exchangers and the regenerator was 7. The final spatial cell distribution chosen for the model is summarized in Table 6.1.

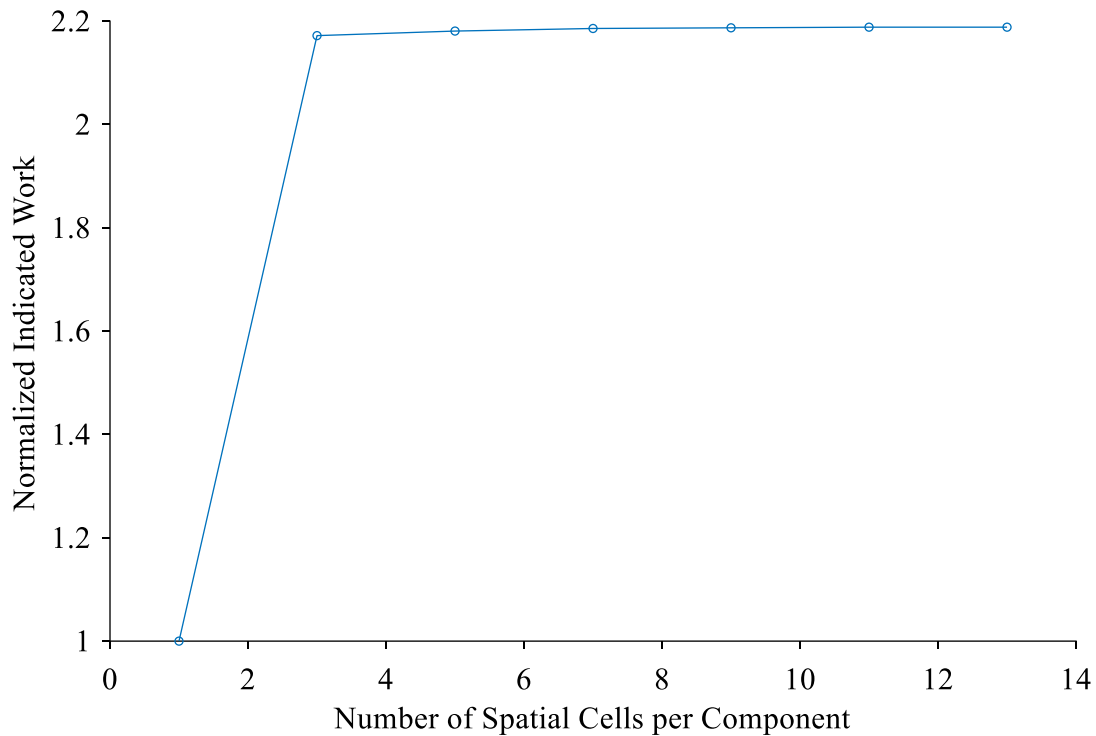


Figure 6.3: Plot of indicated work calculated by Sage model against number of spatial nodes for the heat exchanger and regenerator components for 13 time nodes.

Table 6.1. Number of spatial cells in Sage model components.

Model Component	Number of Cells
Expansion Space	5
Displacer Piston and Cylinder	5
Compression Space	5
Connecting Pipe	5
Power Cylinder	5
Power Piston and Cylinder	5
Hot Heat Exchanger	7
Regenerator	7
Cold Heat Exchanger	7

Finally, another study was run with increasing time nodes to verify that 13 time nodes is still an appropriate number with the changed spatial grid. Figure 6.4 shows the normalized indicated work plotted against the number of time nodes. Once again, the indicated work approaches a constant value with increasing number of time nodes, with the percent change falling below 1%

quickly as the number of time nodes increases. Thus, the number of time nodes chosen for the study is 13 time nodes.

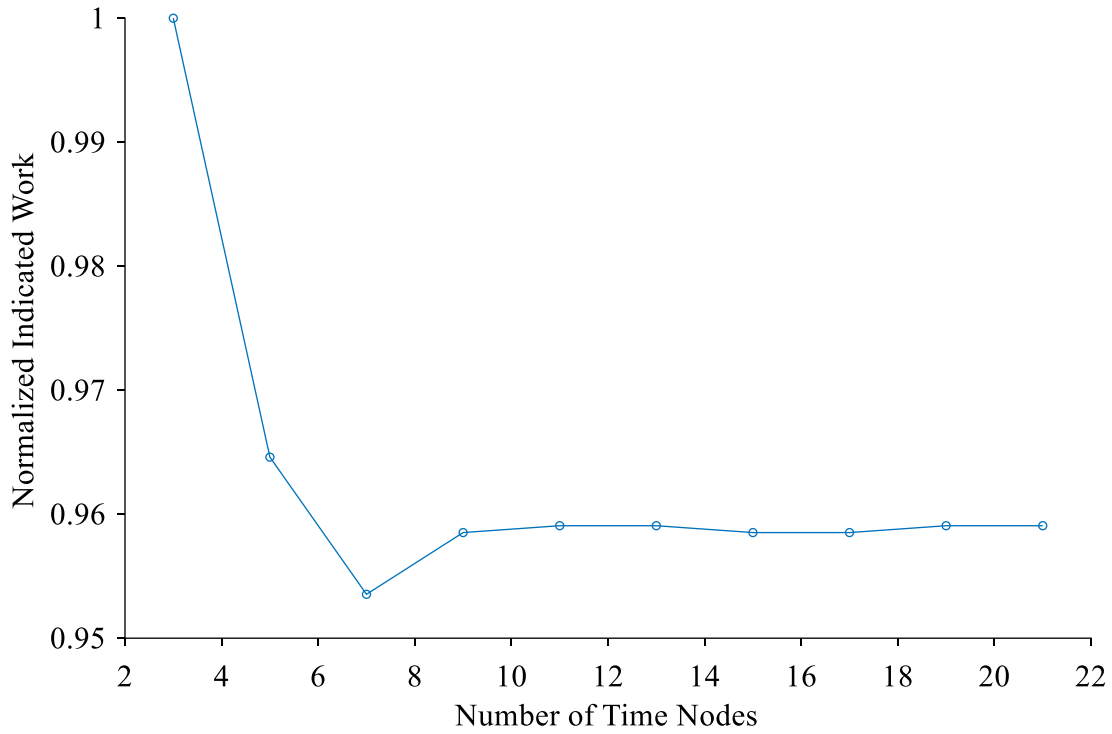


Figure 6.4: Plot of indicated work calculated by Sage model against number of time nodes for final spatial node distribution.

## 6.2 Validation Results of Non-tuned Model Parameters

To validate the Sage model, various parameters are compared to the experimental data in order to assess the level of agreement between the model and experiment. The indicated work and indicated power are used to evaluate the agreement of the model with experiment.

Note that the experimental data presented lacks a complete understanding of uncertainty, as the determination of uncertainty was not yet completed at the time of writing. Previous work with the modified ST05G-CNC in the DTECL group, with similar instrumentation [80], showed the measured indicated work uncertainty was approximately  $\pm 0.25$  J and the indicated power uncertainty was approximately  $\pm 0.70$  W. This gives an indication of the scale of the uncertainty in the presented experimental results.

The indicated work from both the experiment and Sage are plotted against engine speed for varying engine pressures in Figure 6.5. The indicated work determined from Sage is approximately on the same order of magnitude as the experimental results, though the Sage results are overpredicting the experiment. This overprediction is increased for the higher pressure cases compared to the low pressure cases, with the high pressure cases overpredicting the experimental results by almost double at worst. The results are grouped by pressure similarly to the experiment, with the lower pressure case on its own and the higher pressure cases grouping together. However, there is a difference in the speed dependence of the indicated work determined from the Sage model compared to the experimental results.

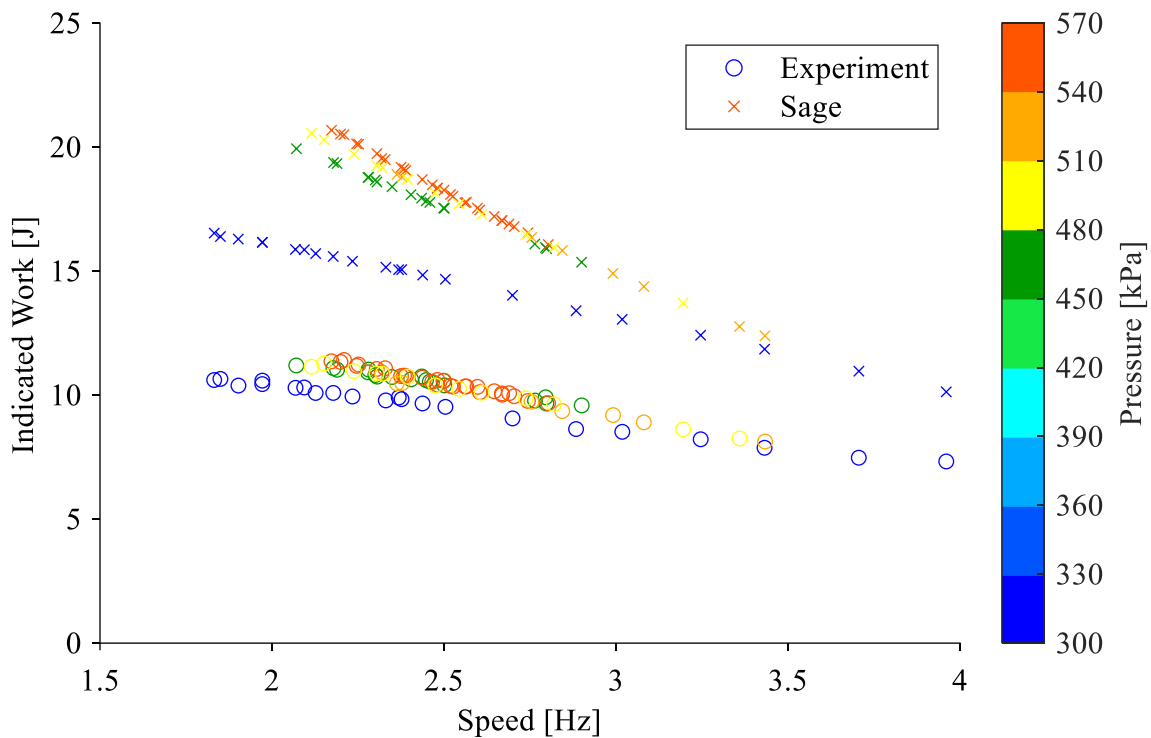


Figure 6.5: Plot of experimental indicated work and modelled indicated work determined by Sage for various pressures against engine speed.

This is more clearly visible in the plot of the percent difference between the model results and the experimental results plotted against engine speed for varying engine pressures shown in Figure 6.6. Here, the percent difference has a clear slope, particularly for the high pressure cases, where there is a distinct linear trend with speed. This indicates that one of the model parameters affecting work output has a strong dependence on speed that is not present in the experimental results.

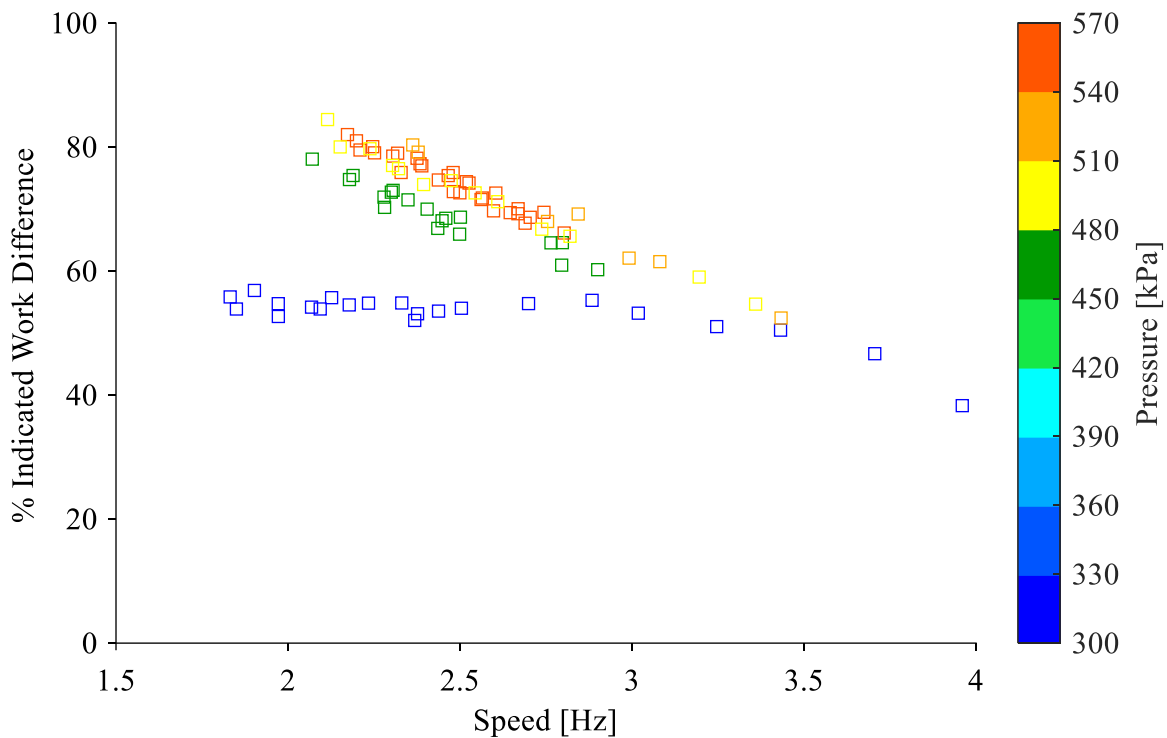


Figure 6.6: Plot of percent difference between experimental and modelled indicated work determined by Sage for various pressures against engine speed.

The indicated power from both the experiment and Sage are plotted against engine speed for varying engine pressures in Figure 6.7. This follows the same trend as the results for indicated work, where there is an overprediction in the output power determined by Sage compared to the experimental work. The slope of the curve with engine speed for the power determined by Sage compared to the experimental power is different. This results in a linear trend in the percent difference between the model results and experimental results, as seen in the plot of percent difference in indicated power against engine speed in Figure 6.8. The high pressure cases have a stronger linear trend with speed than the lower pressure cases, similarly to the work output.

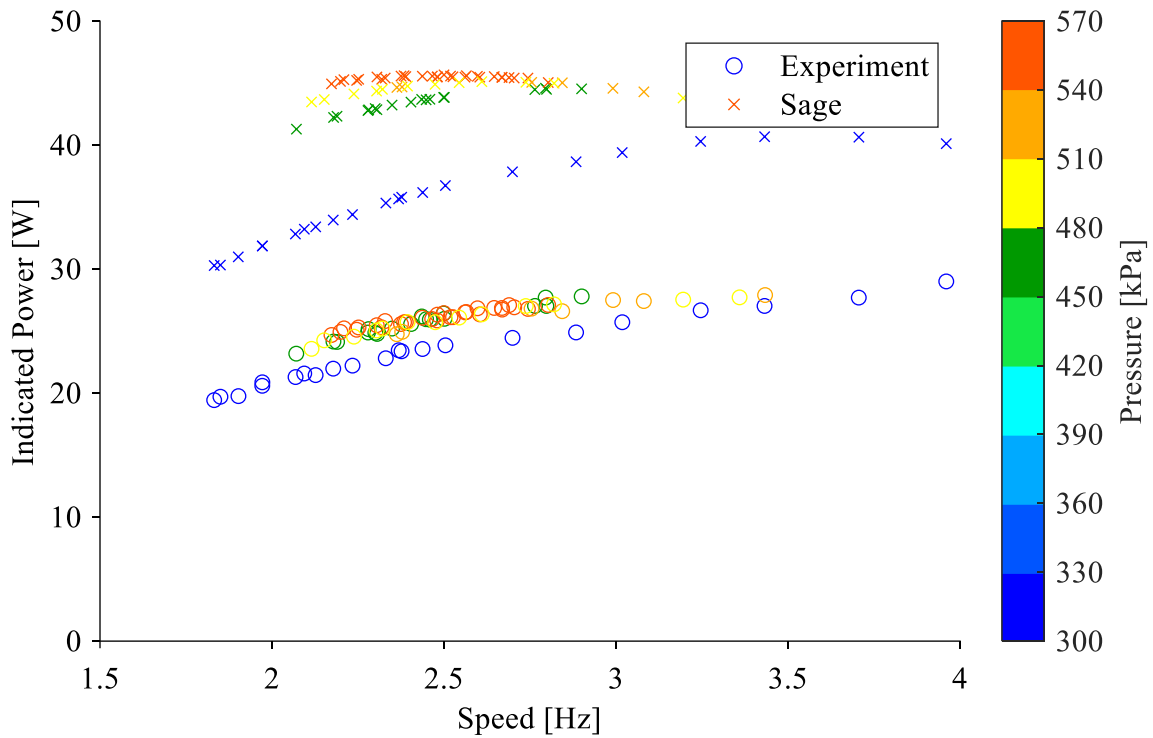


Figure 6.7: Plot of experimental indicated power and modelled indicated power determined by Sage for various pressures against engine speed.

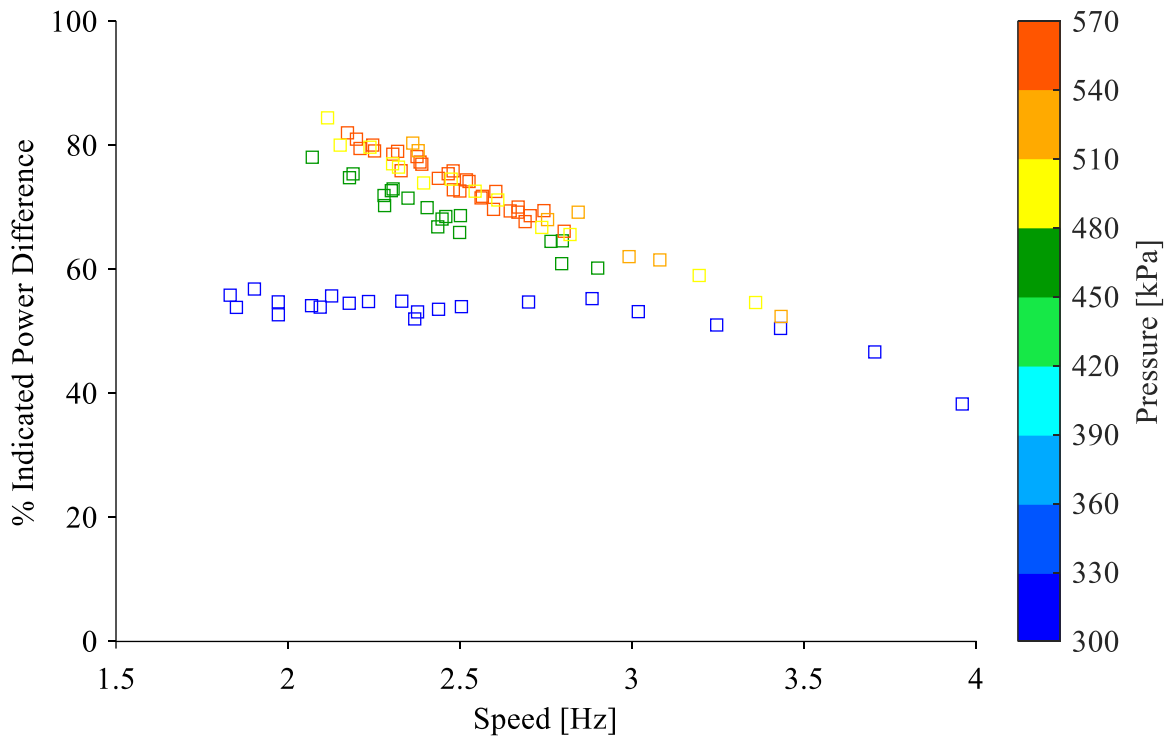


Figure 6.8: Plot of percent difference between experimental and modelled indicated power determined by Sage for various pressures against engine speed.



To evaluate whether the enforced line temperature drop is resulting in appropriate temperature values in the working space, the expansion space and compression space average temperatures from both the model and experiment are plotted against engine speed for varying pressures in Figure 6.9 and Figure 6.10 respectively. For the expansion space temperature, the trend determined by Sage agrees with the experimental trend well. However, the model overpredicts the expansion space temperature, indicating that the heat transfer to the gas is too high. The convective heat transfer resistance determined from the CFD may be too low. Considering that the heat flows for the heating case of the CFD were lower than the cooling case, but the opposite must be true for an engine to produce positive power, it is reasonable that the CFD determined convective heat transfer resistance would result in excess heat transfer to the gas.

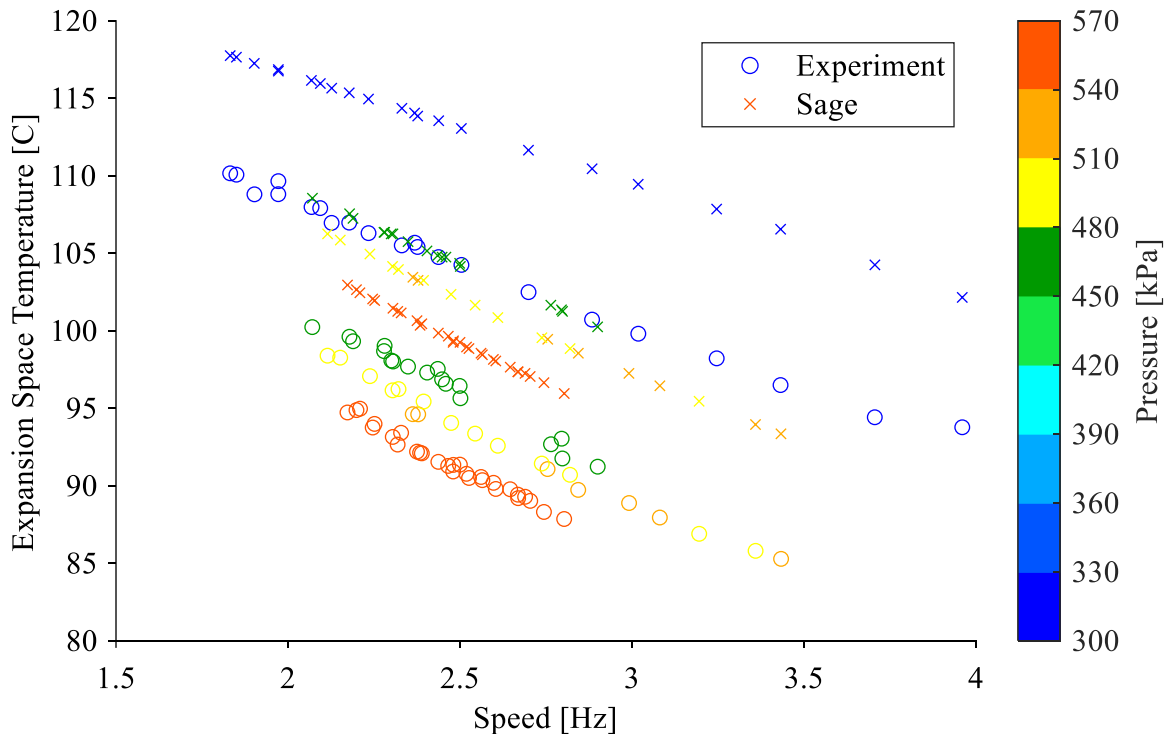


Figure 6.9: Plot of experimental expansion space gas temperature and modelled expansion space gas temperature determined by Sage for various pressures against engine speed.

For the compression space temperature shown in Figure 6.10, again the trend determined by Sage agrees with the experimental trend well. The model compression space temperature is similar to the experiment, indicating that the convective heat transfer resistance for the cooling case was appropriate.

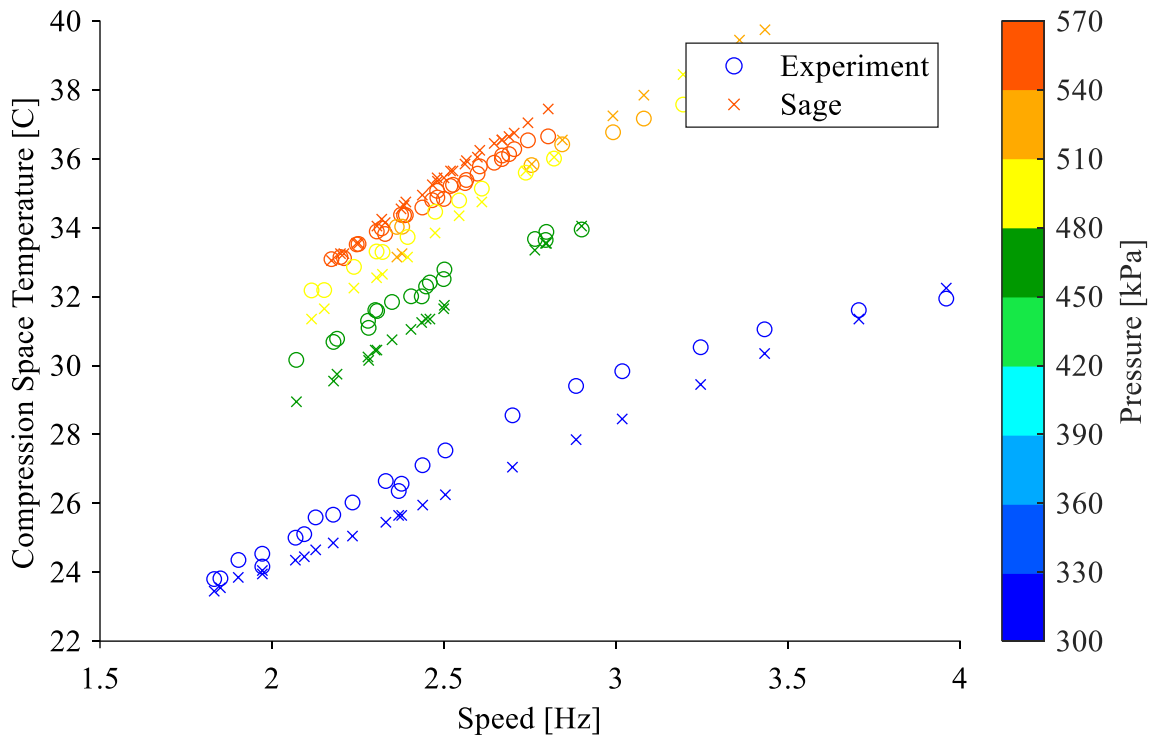


Figure 6.10: Plot of experimental compression space gas temperature and modelled compression space gas temperature determined by Sage for various pressures against engine speed.

To further investigate why the Sage model output is overpredicting the experimental results, the pressure swing is considered. The experimental results are calculated using the pressure measured at the power cylinder. To compare this to the Sage model, the pressure swing magnitude measured from the experiment is compared to the pressure swing of the power cylinder in the Sage model. The magnitude of the power cylinder pressure swing is plotted against the engine speed for varying engine pressures in Figure 6.11. It is evident that the Sage model is overpredicting the pressure swing as compared to the experiment. There is also a difference in the slope of the pressure swing variation with speed determined by the model compared to the experiment for the high pressure cases. The model pressure swing decreases with increasing engine speed more quickly than the experiment. This is likely contributing to the difference in slope of the work output determined by Sage compared to the experiment.

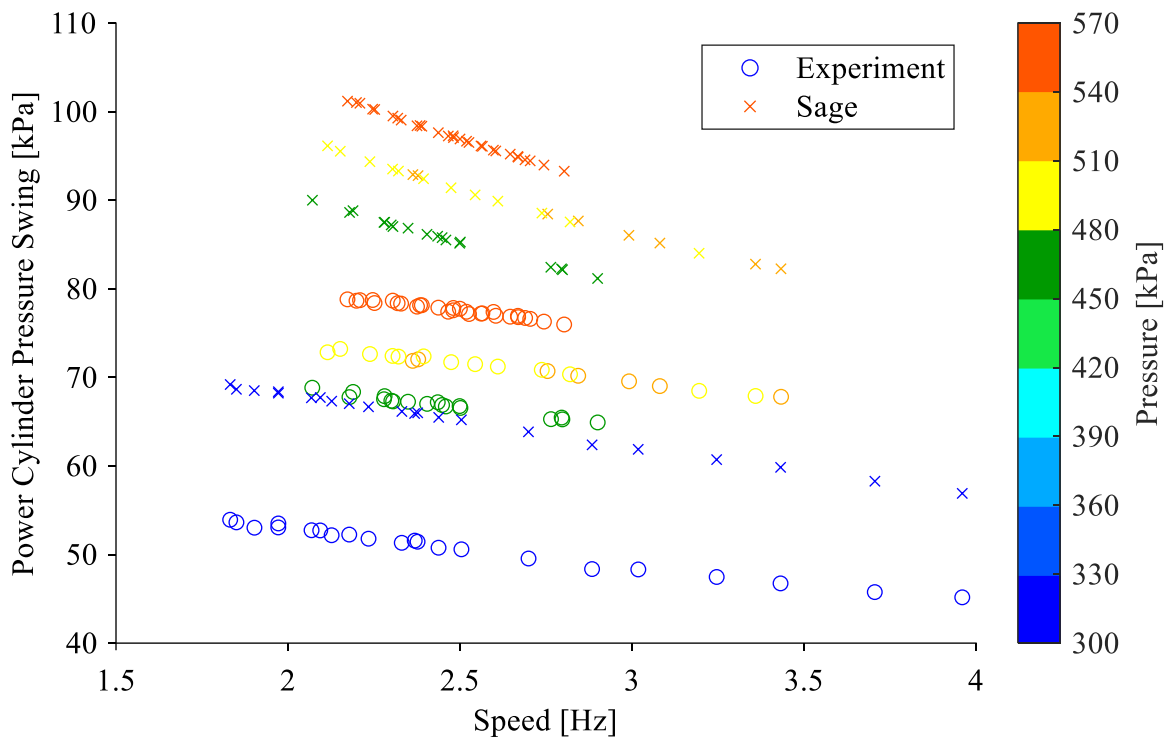


Figure 6.11: Plot of experimental power cylinder pressure swing and modelled power cylinder pressure swing determined by Sage for various pressures against engine speed.

In addition to the magnitude of the pressure swing in the power cylinder, there is also the matter of pressure phase. The sinusoidal variation in pressure is not necessarily aligned with the volume variation, and the amount of phase shift between the volume variation and pressure variation is dependent on many factors. To examine the difference between the pressure phase of the model compared to the experiment, the crank angle of the maximum pressure in the power cylinder is determined. The crank angle of the minimum volume of the engine is also determined, as a point of reference. The phase shift is then calculated as the difference between the crank angle of the maximum power cylinder pressure and the crank angle of the minimum engine volume. This phase shift is plotted for the model and experimental results against engine speed for varying engine pressures in Figure 6.12. The Sage model results indicate that the pressure variation in the power cylinder is lagging the volume variation compared to the experiment.

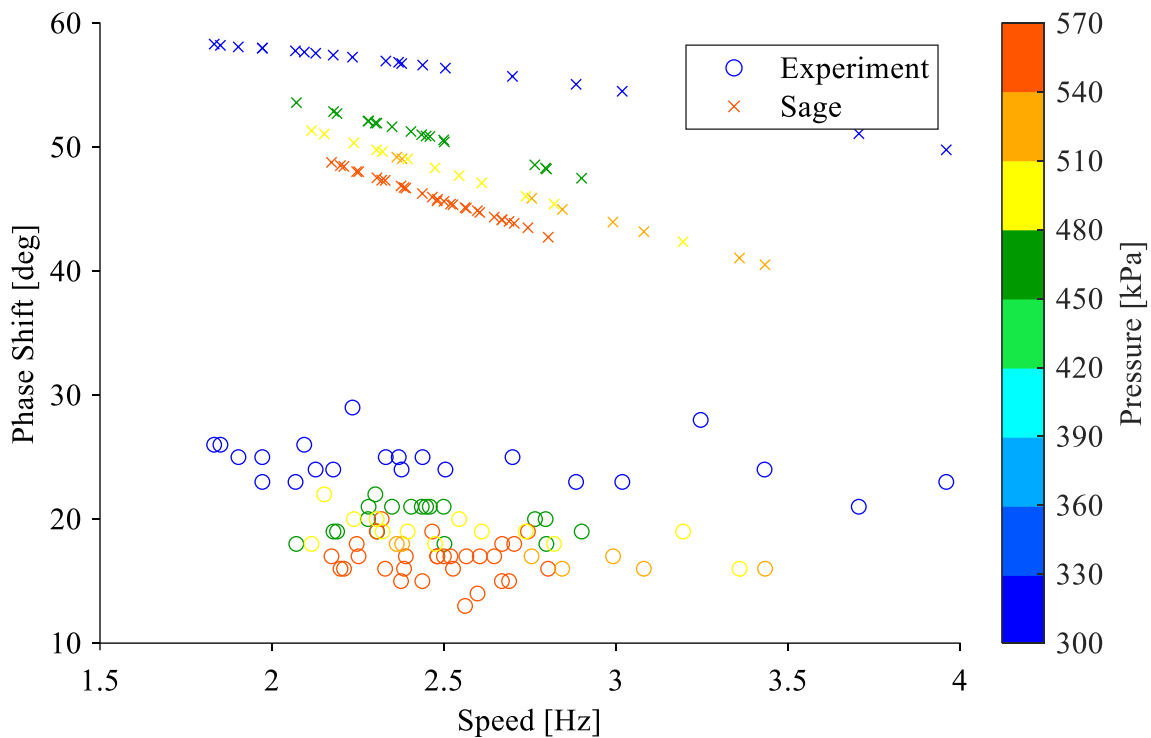


Figure 6.12: Plot of experimental power cylinder pressure phase and modelled power cylinder pressure phase determined by Sage for various pressures against engine speed.

The phase of the pressure variation has a significant impact on engine work and power output. To demonstrate this, the PV diagram of the highest speed low pressure case for the Sage model is plotted for the expansion, compression, and power cylinder space in Figure 6.13. The indicated work is the sum of the PV work for the expansion, compression, and power space. The work for the compression space is negative, as the phasing of the volume is opposite to that of the expansion space. The sum of the expansion and compression space PV diagrams represent the work done by the displacer piston on the gas to shuttle the gas back and forth. In the Sage solution, the indicated work is 10.15 J. Next, the pressure curves moved to have the phase shift of the experimental data for the same data point, with no other modifications to the Sage solution. Note that the power cylinder pressure variation is moved to match the experiment, with the other space's phases remaining the same relative to the power cylinder. The PV diagrams for this model solution with modified pressure phase are plotted in Figure 6.14. The expansion and compression work are significantly increased, as the work done by the displacer piston increases. In addition, the indicated work is significantly reduced, as the maximum pressure is significantly farther from the maximum volume. The indicated work for this case is much lower, at 2.75 J.

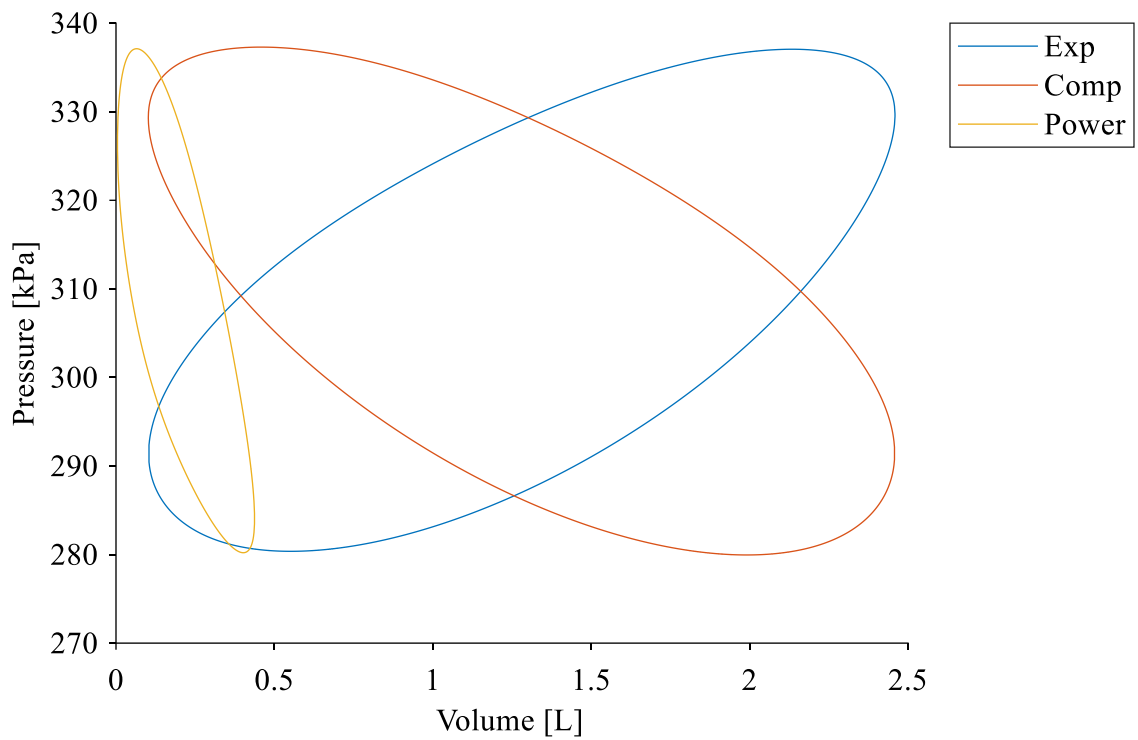


Figure 6.13: PV diagram for expansion, compression, and power cylinder space determined by Sage for low pressure high speed data point.

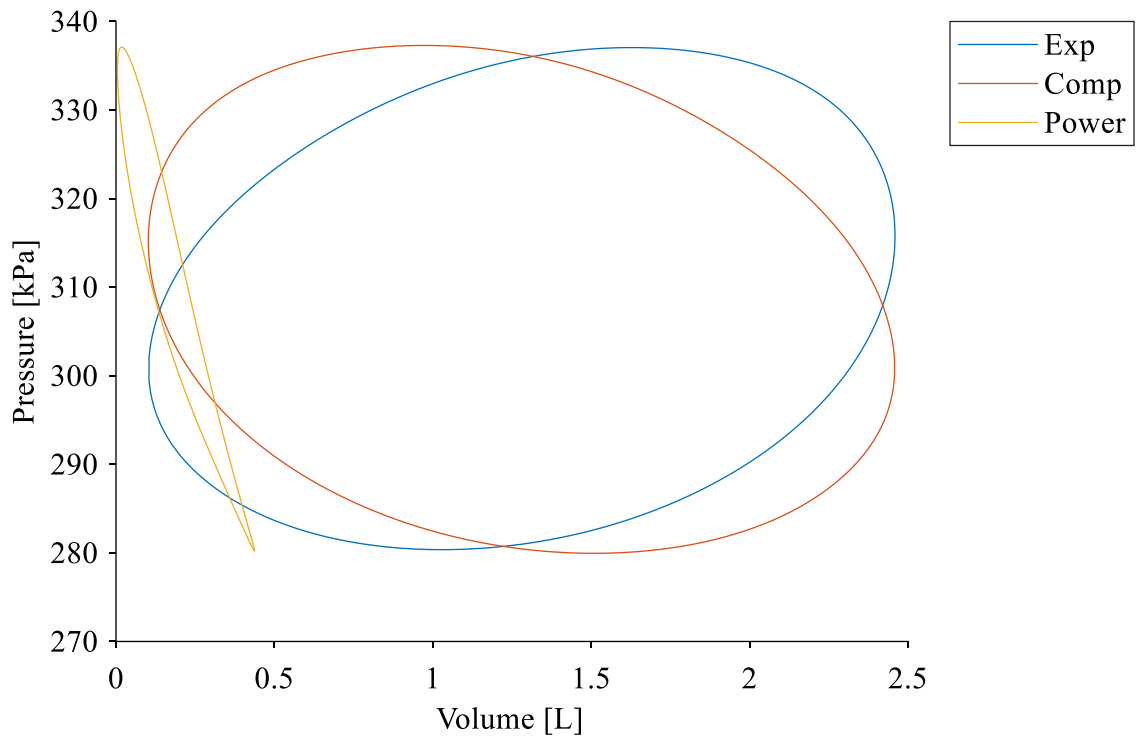


Figure 6.14: PV diagram for expansion, compression, and power cylinder space determined by Sage for low pressure high speed data point, with shifted pressure curves to match experiment pressure phase.

The Sage model, with input parameters untuned, tends to overpredict the indicated work and power as compared to the experiment. This is likely due to the incorrect pressure swing and pressure curve phase, which also contribute to the difference in the model trend with speed as compared to the experiment. There may be parameters that can be tuned to improve the model prediction which would need to be identified.

## **6.3 Investigation of Tuning Parameters on Validation Results**

As the Sage model results deviate from the experimental results, the model needs to be adjusted to better match the experimental results. A brief investigation was done to determine which parameters affect the model results. Presented in this section are two parameters which were able to influence the model output to yield better agreement with the experiment.

### **6.3.1 Convective Heat Transfer Resistance**

In the non-tuned model results, the convective heat transfer resistance as determined from the CFD led to an overprediction in the expansion space temperature. The convective heat transfer resistances for Sage were tuned to yield a better agreement between the model and experiment for the average expansion space and compression space temperatures. The original values of convective heat transfer resistance determined from the CFD were 0.04925 K/W for the heating case and 0.02228 K/W for the cooling case. In comparison, the tuned values of convective heat transfer resistance were 0.067 W/mK for the heating side and 0.024 W/mK for the cooling side. The heating case resistance was increased significantly, while the cooling case remained almost the same. In the plot of the expansion space temperature against engine speed in Figure 6.15, the agreement between the experiment and Sage is improved, with only a slight overpredict at the low pressure case and underprediction at the high speed case. In the plot of compression space temperature against engine speed in Figure 6.16, there is only a slight change in the convective heat transfer resistance which yielded slightly better agreement for the high pressure case.

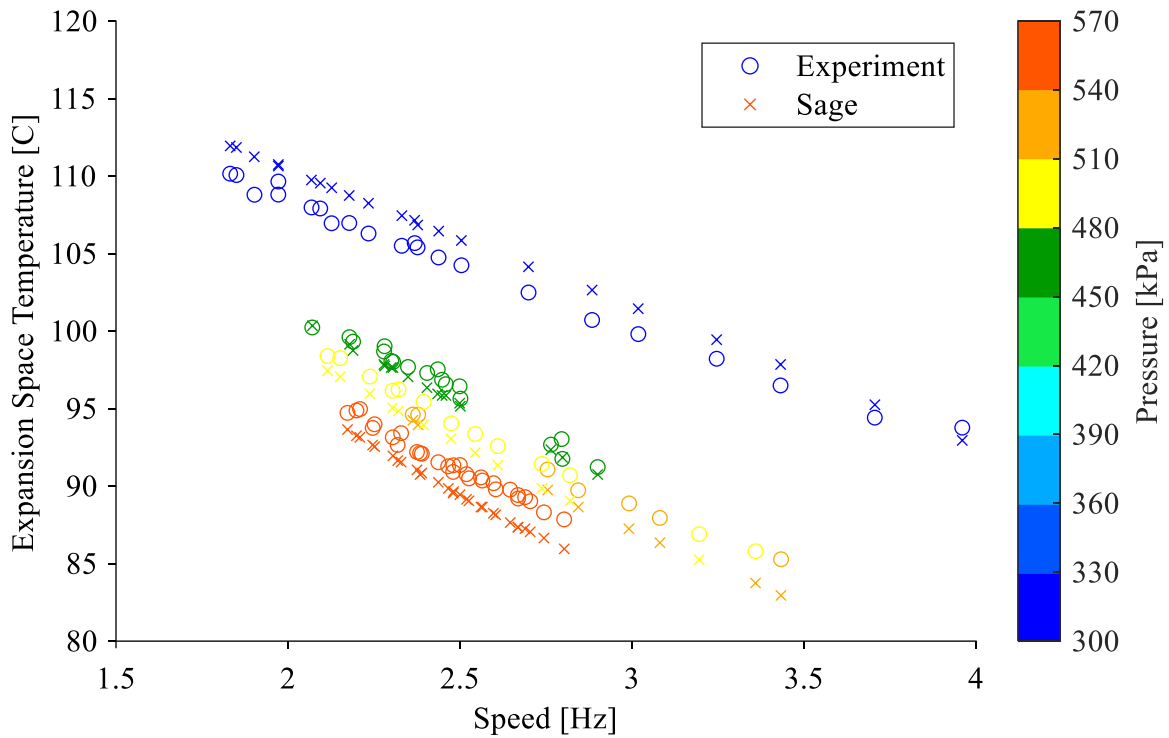


Figure 6.15: Plot of experimental expansion space gas temperature and modelled expansion space gas temperature determined by Sage with tuned resistances for various pressures against engine speed.

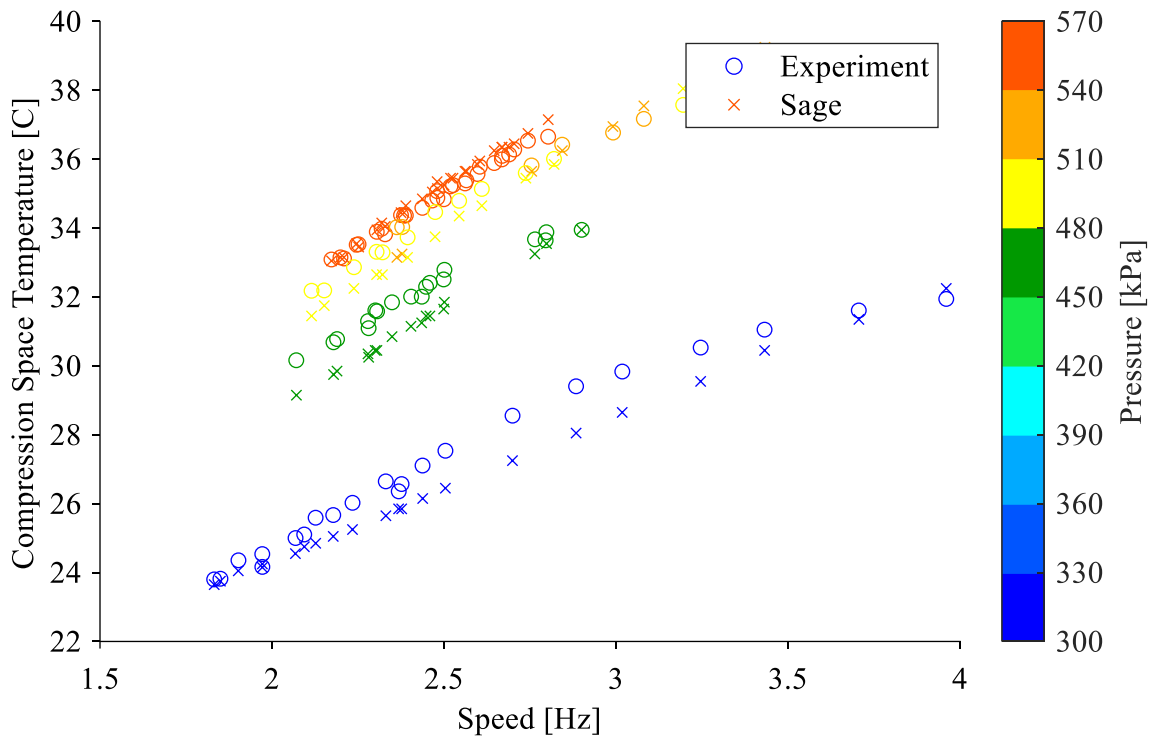


Figure 6.16: Plot of experimental compression space gas temperature and modelled compression space gas temperature determined by Sage with tuned resistances for various pressures against engine speed.



The plot of indicated work against engine speed shown in Figure 6.17 shows that with the reduction in the expansion space temperatures the model overprediction of indicated work decreased, though it did not fully align with the experimental results. The spread between the pressure results also decreased, which is more similar to the experimental results. The trend of the indicated work with speed is still different between the model and the experiment, so changing the convective heat transfer resistance did not affect the slope.

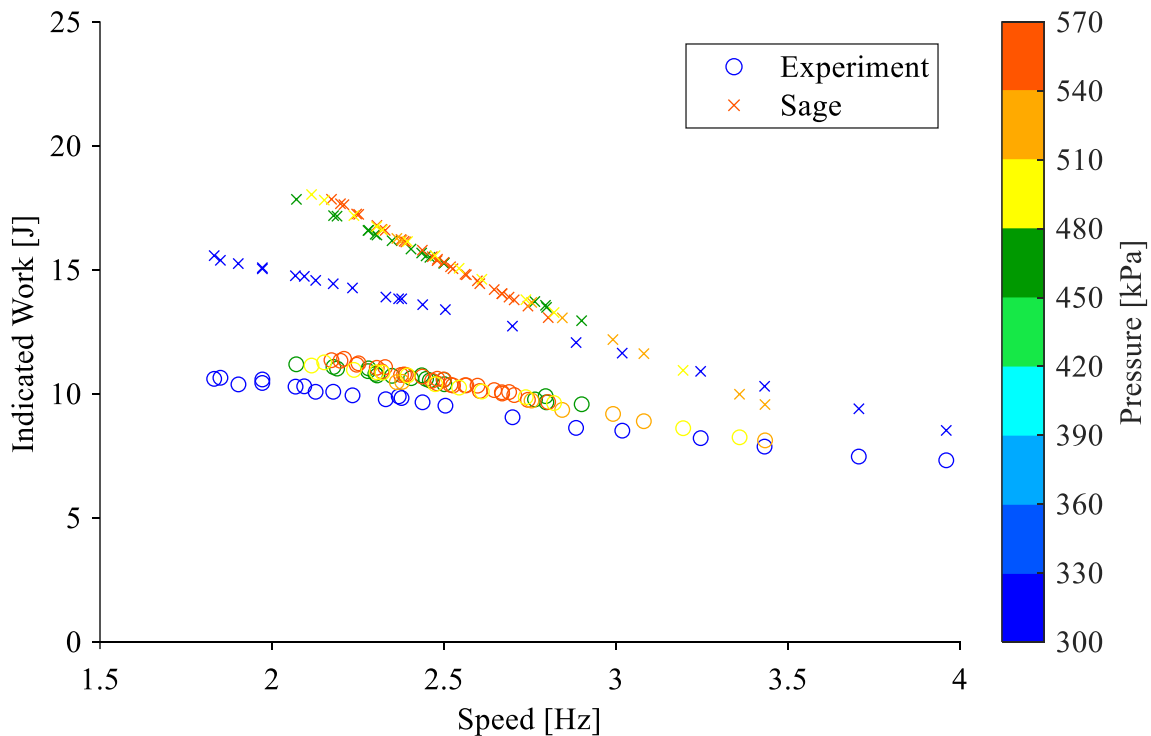


Figure 6.17: Plot of experimental indicated work and modelled indicated work determined by Sage with tuned resistances for various pressures against engine speed.

Figure 6.18 plots the percent difference in indicated work between the model and experiment against the engine speed, and it is visible here in the change of the slope that the model now has an increased dependence on engine speed compared to the un-tuned results. However, the magnitude of the work output is improved, with a percent difference maximum of 60%. The reduction in overprediction is also more significant for the higher pressure cases, as the percent difference now overlaps the low pressure case.

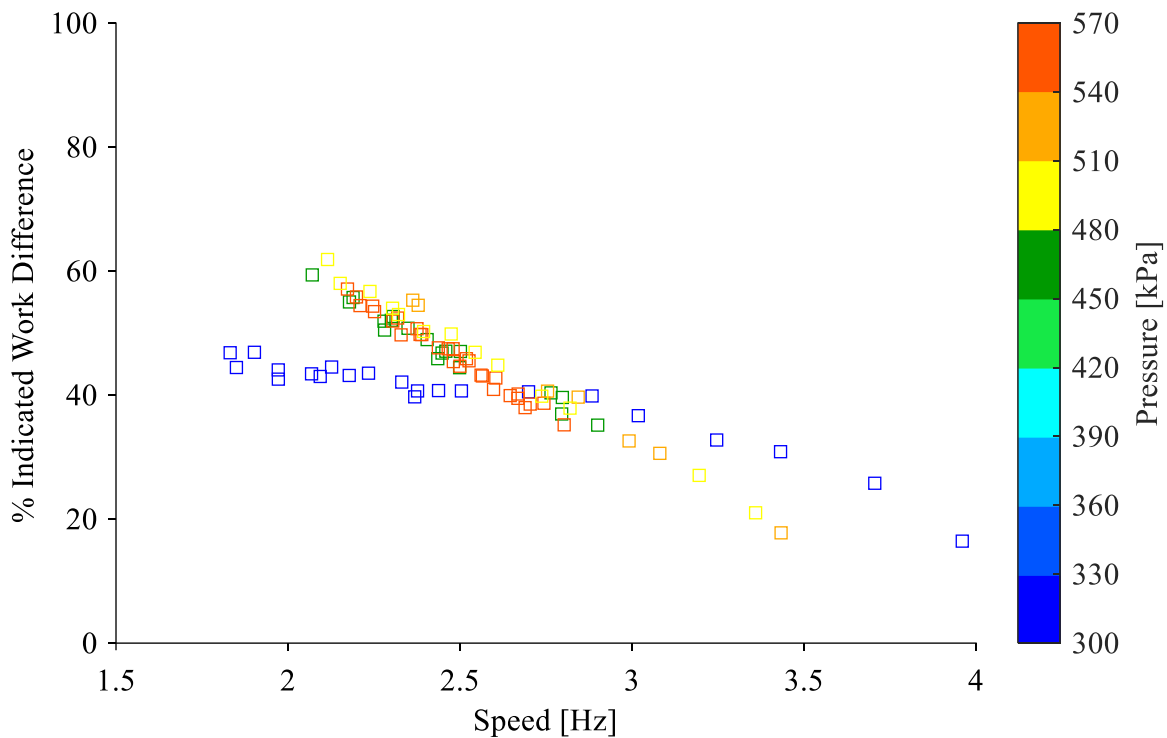


Figure 6.18: Plot of percent difference between experimental and modelled indicated work determined by Sage with tuned resistances for various pressures against engine speed.

The indicated power also shows the same reduction in model overprediction, as seen in the plot of indicated power against engine speed in Figure 6.19. The model results show an increased dependence on engine speed as compared to the experimental results. This is a combined result of the indicated work having an increased dependence on engine speed, and the reduced magnitude of the indicated work. When the magnitude of the indicated work trend decreases without a change in the slope, and is then multiplied by engine speed, it leads to a more negative slope of the indicated power trend with speed. Hence, the indicated power decreases much more quickly with increased engine speed at a lower overall magnitude of indicated work. Figure 6.20 plots the percent difference in indicated power between the model and experiment against engine speed, and it shows the reduction in overprediction by the model, again to a maximum of approximately 60%, with the higher pressure cases having more of a reduction than the lower pressure cases. The change in dependence of indicated power with speed is also visible, with a greater slope than in the original model results.

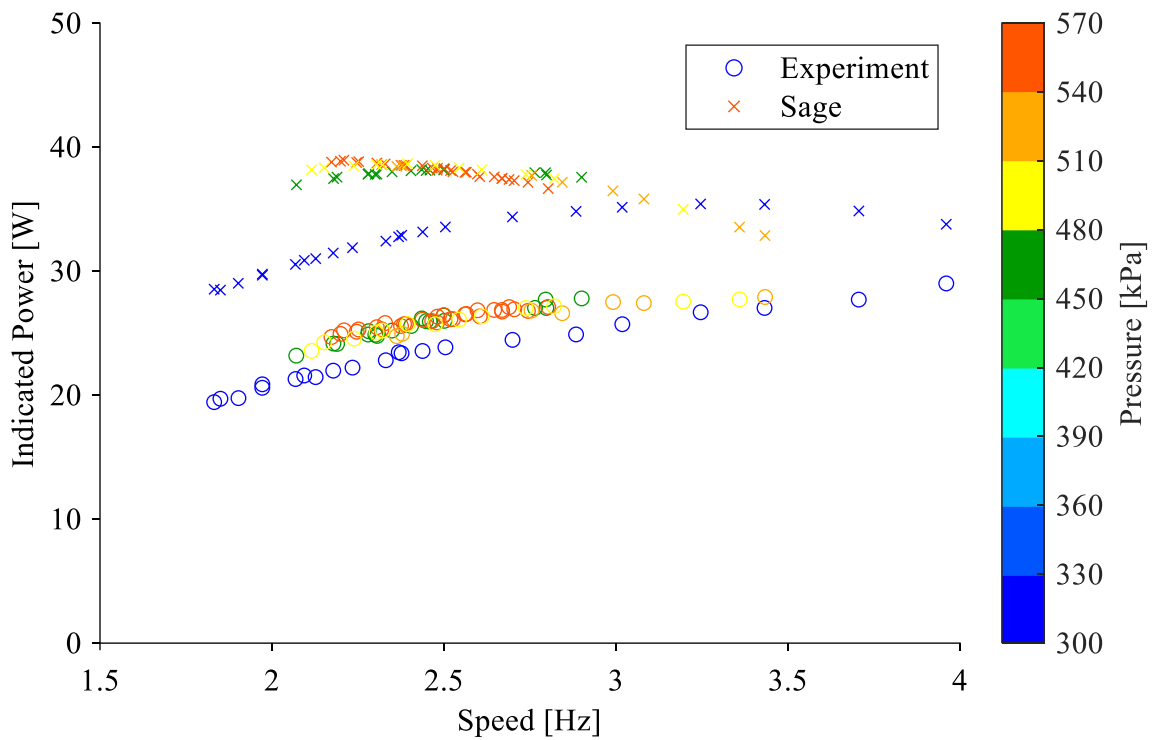


Figure 6.19: Plot of experimental indicated power and modelled indicated power determined by Sage with tuned resistances for various pressures against engine speed.

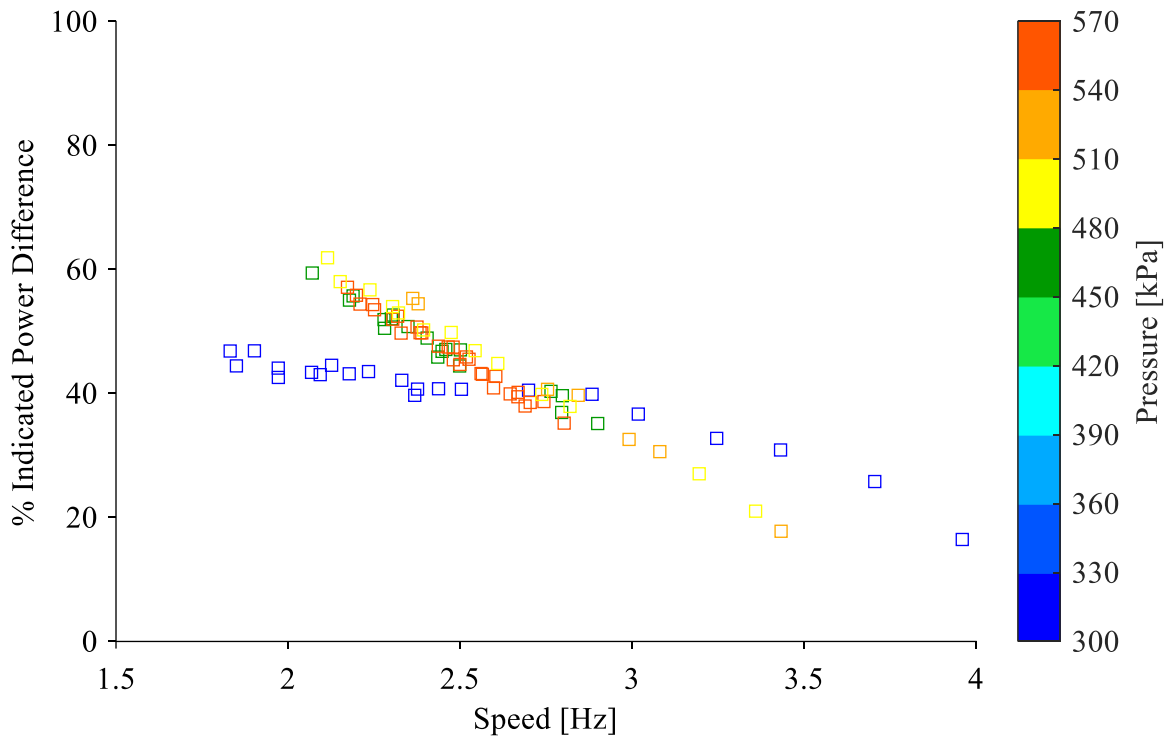


Figure 6.20: Plot of percent difference between experimental and modelled indicated power determined by Sage with tuned resistances for various pressures against engine speed.

Figure 6.21 plots the power cylinder pressure swing against engine speed, showing the reduction in the pressure swing as the expansion space temperature is reduced. However, the pressure swing is still overpredicted, and the dependence of the pressure swing on engine speed is still greater for the model than the experimental results for the high pressure cases.

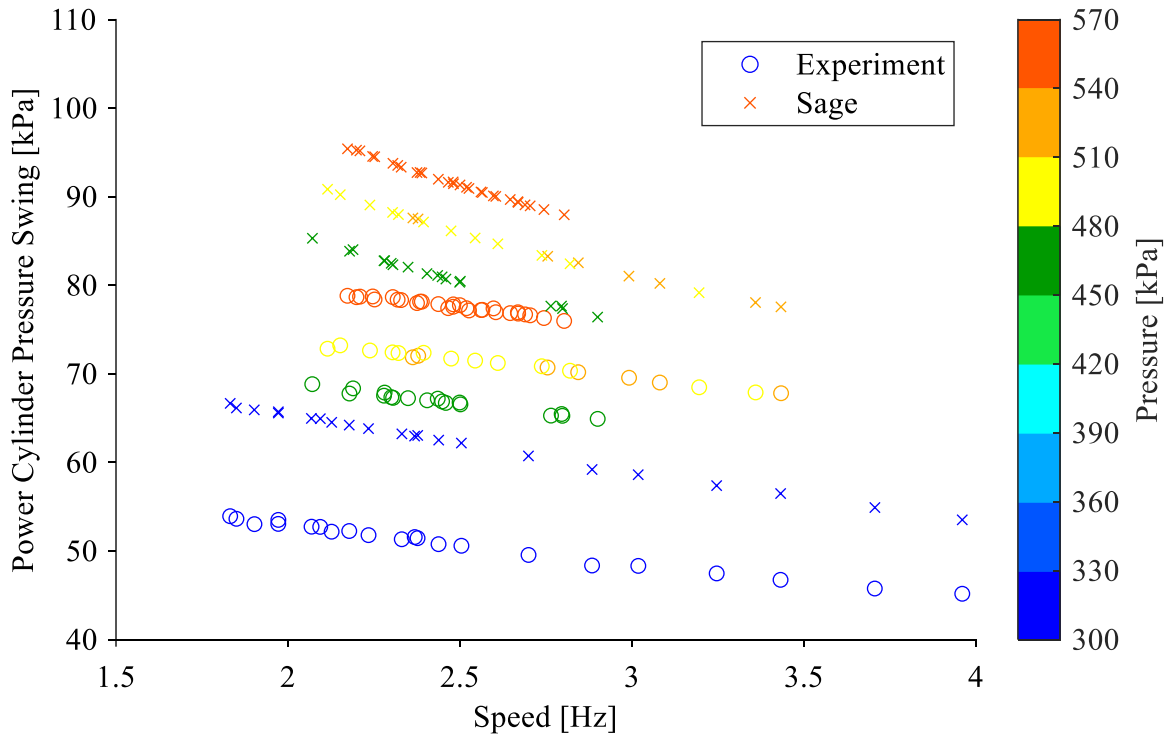


Figure 6.21: Plot of experimental power cylinder pressure swing and modelled power cylinder pressure swing determined by Sage with tuned resistances for various pressures against engine speed.

Figure 6.22 plots the phase shift of the power cylinder pressure variation compared to the volume variation against engine speed. There is a slight reduction in the magnitude of overprediction of the phase shift by the model, however the phase shift still has a strong dependence on speed as compared to the experiment.

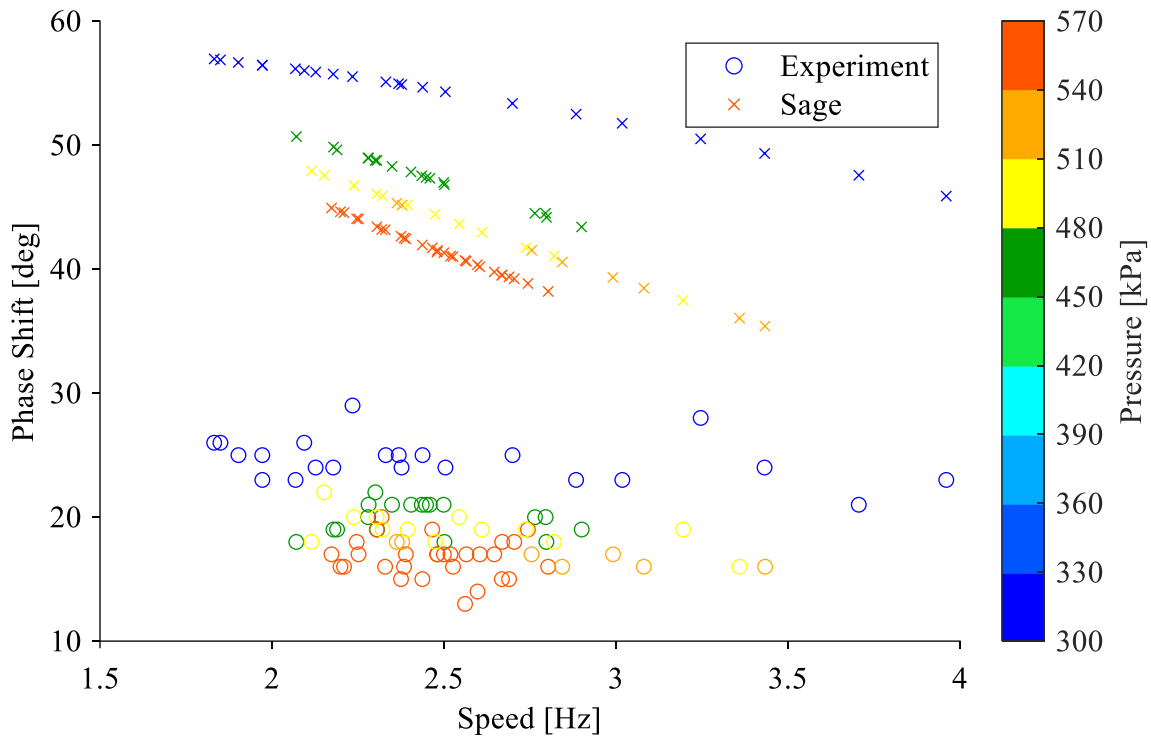


Figure 6.22: Plot of experimental power cylinder pressure phase and modelled power cylinder pressure phase determined by Sage with tuned resistances for various pressures against engine speed.

By tuning the convective heat transfer resistances, the overall magnitude of the work and power output was able to be improved, as the temperature difference between the expansion space and compression space was reduced. This led to a reduction in the overall pressure swing which resulted in a decrease in the work output. However, the model results still show a significant dependence with engine speed that is not the case with the experimental results.

### 6.3.2 Flow Friction Multiplier

To address the issue of the model dependence on engine speed as compared to the experiment, finding a variable that would impact the pressure swing and phase shift was of interest. Both the pressure swing and phase shift show a dependence on engine speed that is not present in the experimental results. Demko and Penswick [70] did a brief sensitivity analysis of the tuning parameters in Sage for their Stirling convertor Sage model. One of the parameters considered was the flow friction multiplier, denoted as “Fmult” in Sage. This parameter normally has a value of 1. The flow friction multiplier was noted to shift the phase of the pressure swing, which would impact the indicated work and power output. The model was run with both an increased and decreased value of flow friction multiplier, however only decreasing the flow friction multiplier improved the trend in the model results. The flow friction multiplier was set to 0.5 for all gas spaces (cylinders, heat exchangers, and regenerator). This will reduce the flow friction in all engine spaces.

Figure 6.23 plots the indicated work determined by four different model parameters: the original non-tuned case presented in section 6.2, the tune convective heat transfer resistance case presented in section 6.3.1, and each of those cases with the flow friction multiplier set to 0.5. It also plots the experimental work, against engine speed for varying pressures. From this plot it can be seen that for both the original and tuned resistance cases, by decreasing the flow friction multiplier the indicated work is increased. In particular, the indicated work is increased more for higher speed cases than for low speed cases. Since the flow friction is decreased, there is less loss to flow friction, leading to a higher indicated work, and this effect is speed dependent as the pressure drop is dependent on the flow speed.

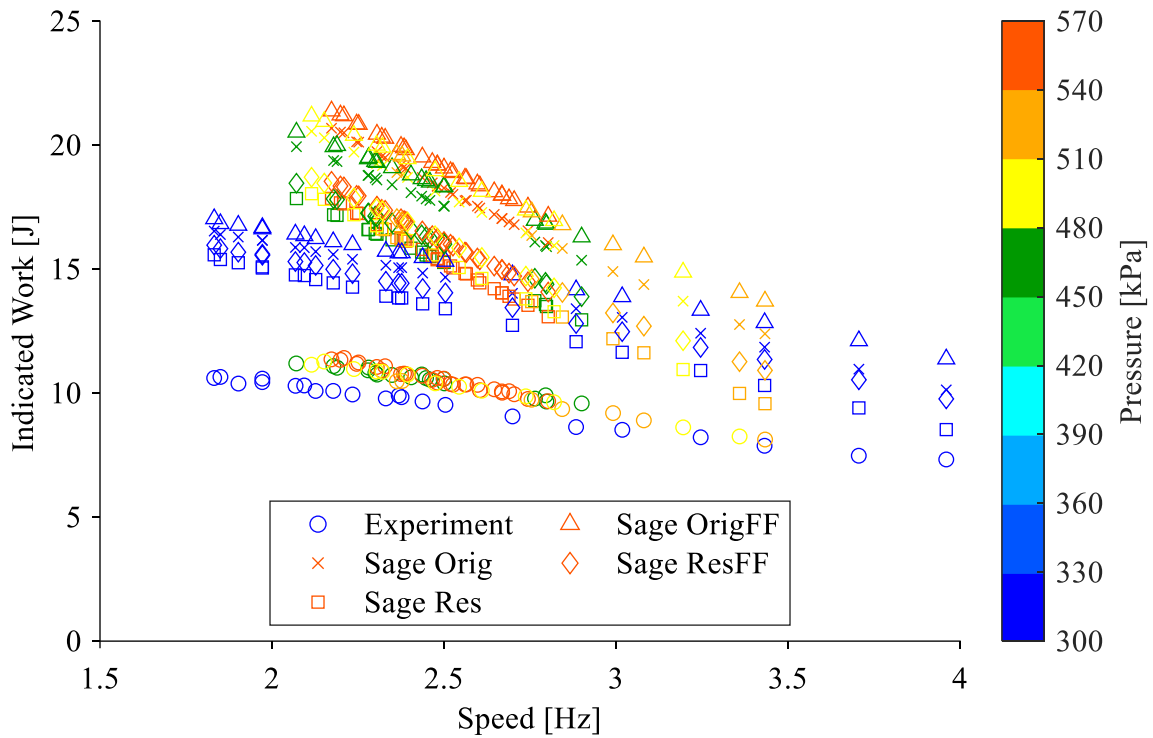


Figure 6.23: Plot of experimental indicated work and modelled indicated work determined by Sage with different tuned parameters for various pressures against engine speed.

Figure 6.24 plots the percent difference between the indicated work determined by the four different Sage parameter cases and the experimental results against the engine speed. Here the change in slope with respect to engine speed is more visible, as the cases with reduced flow friction multiplier have a flatter trend than the cases without.

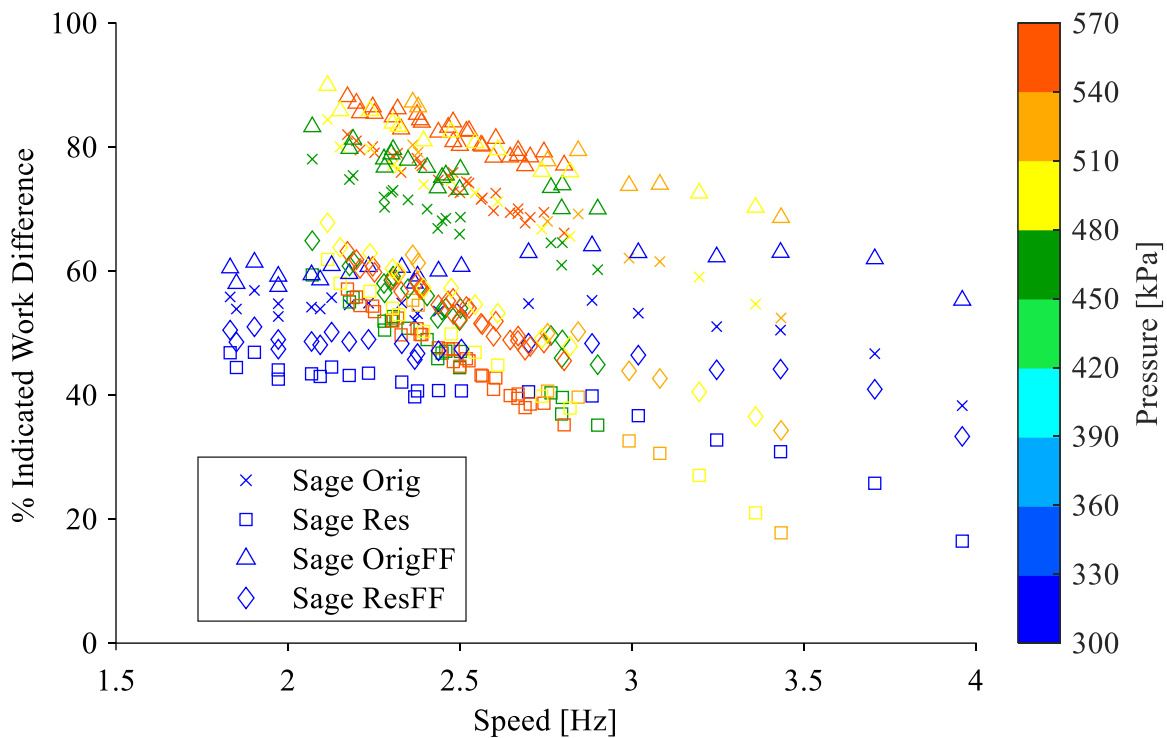


Figure 6.24: Plot of percent difference between experimental and modelled indicated work determined by Sage with different tuned parameters for various pressures against engine speed.

Figure 6.25 plots the indicated power for all the cases discussed above and the experiment against engine speed. Again, the reduced flow friction multiplier results in a flatter trend with respect to engine speed, and better agreement with the experimental result trend. This is made more obvious in the plot of percent difference in indicated work for the four cases against engine speed shown in Figure 6.26. Once again, the trend in percent difference flattens out with the decrease in flow friction, and the overall magnitude of the trend increases.



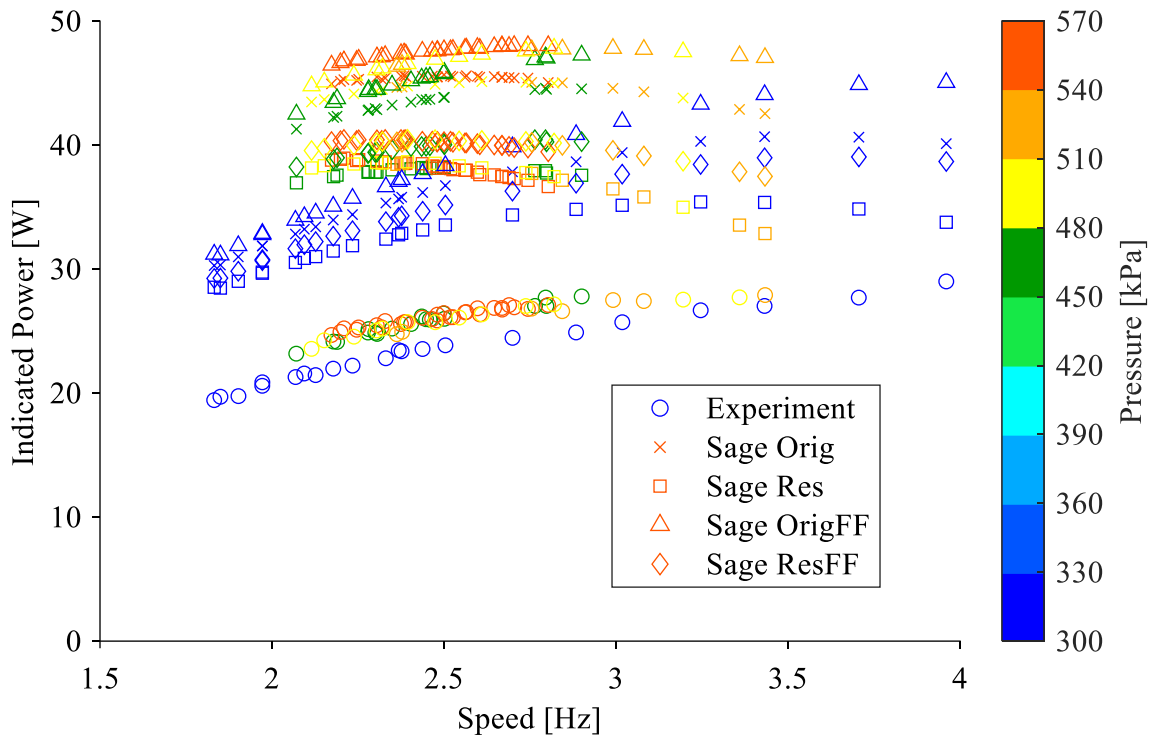


Figure 6.25: Plot of experimental indicated power and modelled indicated power determined by Sage with different tuned parameters for various pressures against engine speed.

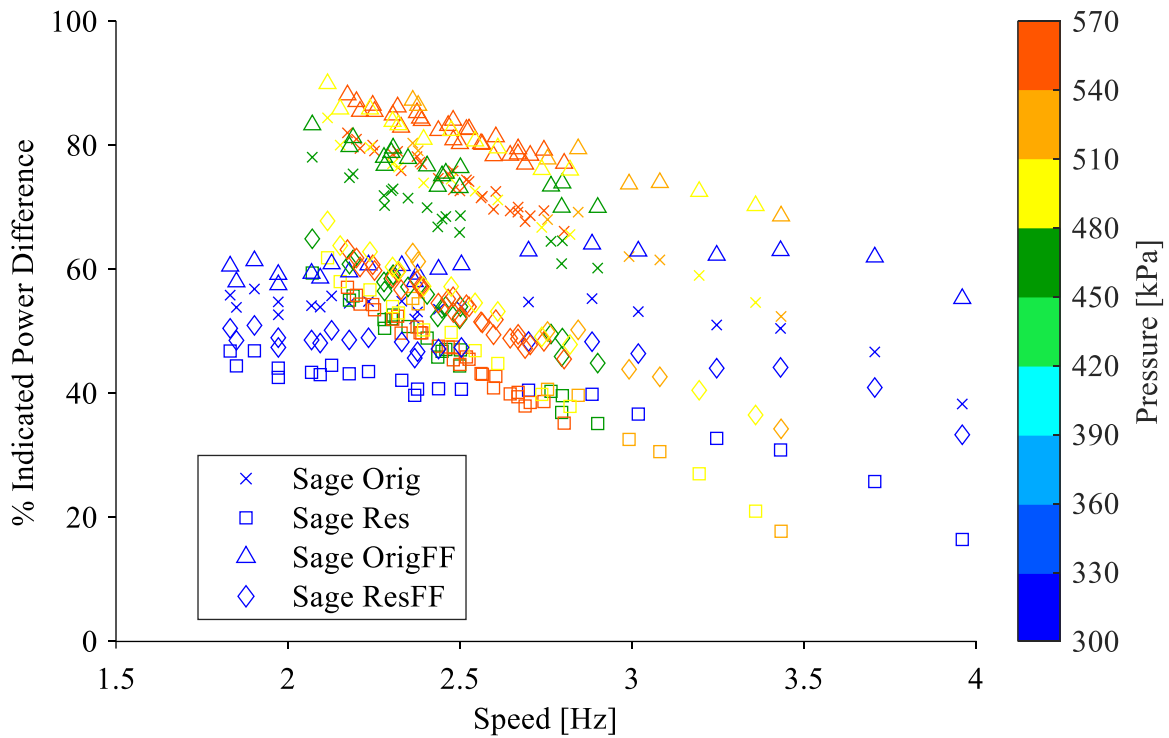


Figure 6.26: Plot of difference between experimental and modelled indicated power determined by Sage with different tuned parameters for various pressures against engine speed.

To see the effect of the flow friction multiplier on pressure, the power cylinder pressure swing for the four cases considered and the experimental results is plotted against engine speed in Figure 6.27. The pressure swing in the power cylinder changes very little with reduced flow friction multiplier, with only a slight decrease in the pressure swing at higher speeds. This however, doesn't lead to decreased indicated work.

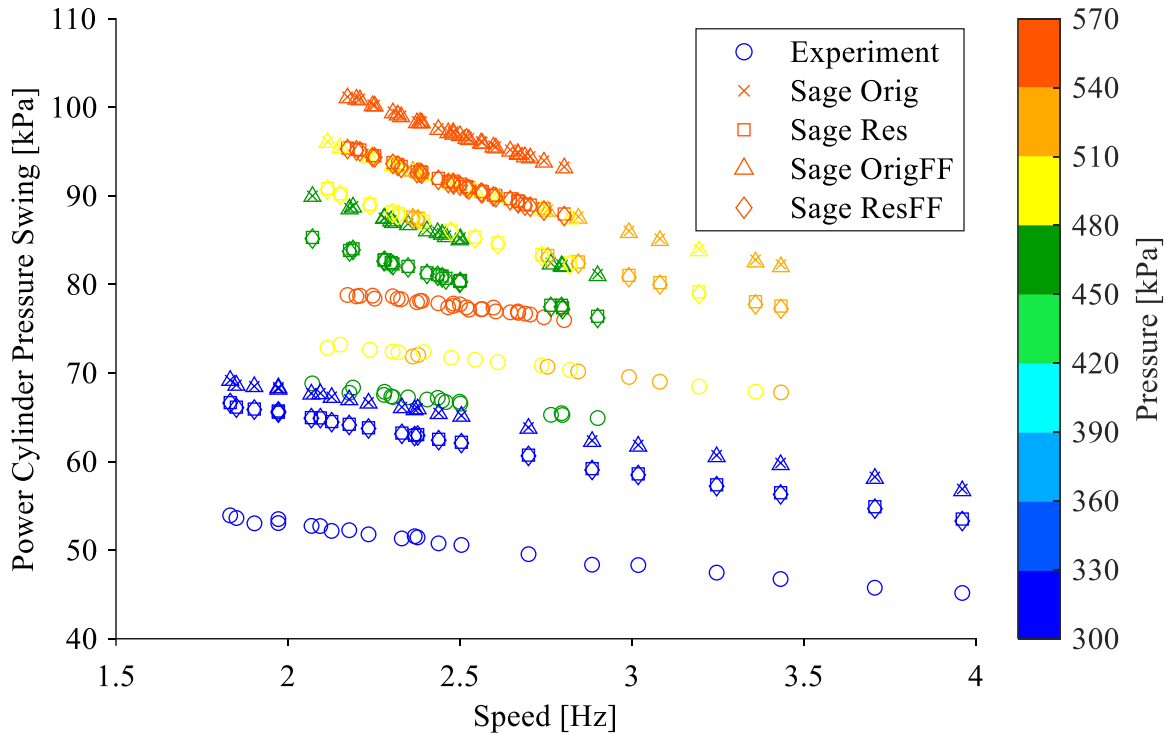


Figure 6.27: Plot of experimental expansion space gas temperature and modelled expansion space gas temperature determined by Sage with different tuned parameters for various pressures against engine speed.

In the plot of the pressure variation phase shift against engine speed for the four cases considered and the experiment, shown in Figure 6.28, it can be seen that there is a slight increase in the phase shift with increasing engine speed. This means that the peak of the pressure curve is further from the minimum engine volume and closer to the maximum engine volume, leading to an increase in the indicated work.

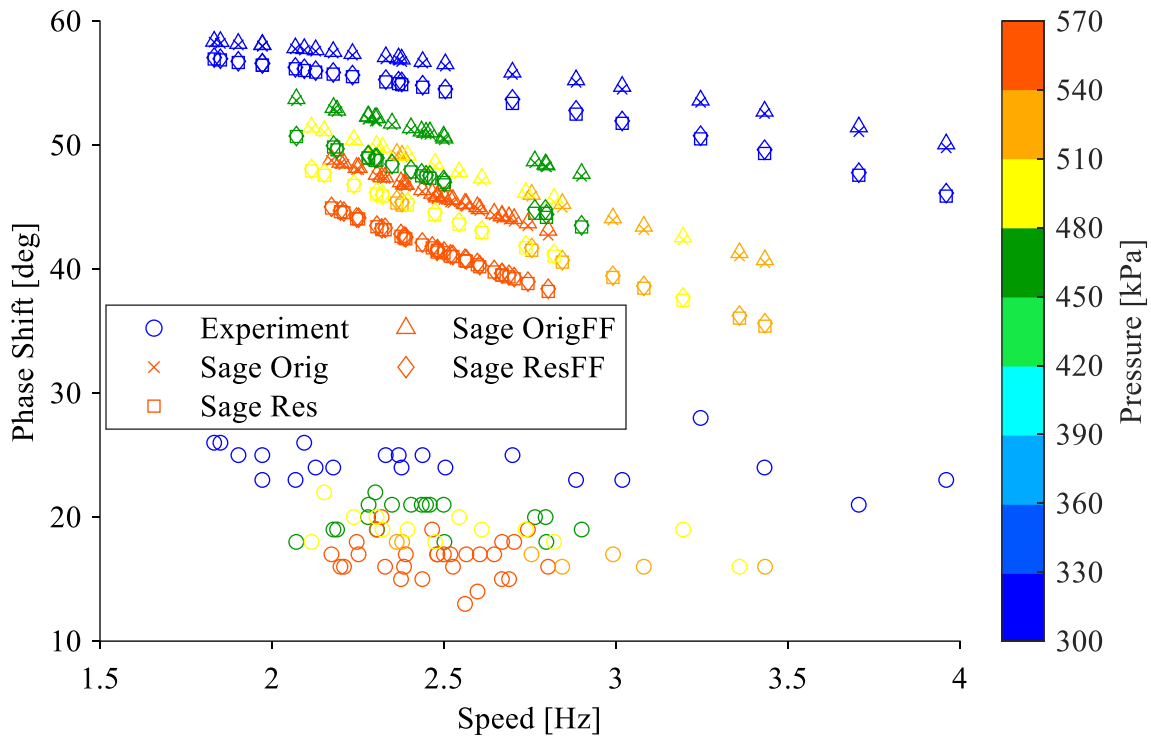


Figure 6.28: Plot of experimental compression space gas temperature and modelled compression space gas temperature determined by Sage with different tuned parameters for various pressures against engine speed.

By decreasing the flow friction multiplier, it is possible to improve the trend of the model to better agree with the experiment, due to the phase shift of the pressure curve changing with decreased flow friction. However, decreasing the flow friction also increases the magnitude of the indicated work, which is already overpredicted by the model. This provides some helpful information as to the cause of the difference between the model and the experiment, but does not provide a solution to bring the model and experiment into full agreement.

## 6.4 Conclusions

The Sage model results are on the same order of magnitude as the experimental results, but are overpredicted. Also, the model results have a greater dependence on engine speed than the experiment, but the trend with pressure is similar. The convective heat transfer coefficients determined from the CFD were found to be suitable for the cold side, but were underpredicted for the heating side. By tuning these parameters it was possible to bring the expansion and compression space temperatures into good agreement. However, the power cylinder pressure swing and pressure phase shift were still overpredicted and had a greater dependence on speed. Decreasing the flow friction multiplier was able to improve the trend of the indicated work output as it led to an increase in the pressure phase shift with increased engine speed, leading to a greater increase in indicated work for higher engine speeds than lower engine speeds.

There were several setbacks that prevented the attainment of a close agreement between the model and the experiment. First was the numerous parameters in the Sage model that would need to be evaluated, which would require a large amount of time to run the study which was not able to be done programmatically. There is a limited amount of literature available on adjusting a Stirling engine model in Sage beyond the examples provided with the software. The experiment setup would also benefit from additional measurements, particularly of solid temperatures, to aid in evaluating the suitability of the model connections. Finally, the method of calculating the experimental indicated work is fundamentally different from Sage. The experimental processing only considers a single PV diagram, which is the pressure measured at the power cylinder against the total engine volume. Sage considers the pressure in the expansion, compression, and power cylinder spaces separately. This better captures the work required to move the displacer piston. The experimental results as processed assume that the engine pressure is uniform across the engine, which is likely not the case.

As a result of all these factors, the model was not able to be tuned to agree fully with the experimental results. However, the model does show a general agreement in the trends with the experimental results, albeit with deviation, and shows good agreement with the temperature predictions in the expansion and compression spaces, indicating that the heat transfer of the Sage model is modelled appropriately. The Sage model with the tuned convective heat transfer resistances will be used to study the effect of heat exchanger geometry on the power output.

## **7 Effect of Heat Exchanger Geometry on Power Output using Sage**

Using the Sage model of the Raphael engine that has the tuned convective heat transfer resistances, a study investigating the effect of varying heat exchanger geometry on power output was conducted. This study using the 3<sup>rd</sup> order model, Sage, will be able to determine the optimal heat exchanger geometry for a LTDSE. This result will be able to be compared to the fundamental analyses from Chapter 3, for both the heat transfer in the heat exchanger channels and the range within the optimal dead volume ratio lies as compared to the estimate from the Schmidt model. Additional sensitivity cases were run to consider the effect of engine operating conditions and modified engine geometry.

### **7.1 Sage Model Setup for Heat Exchanger Study**

The Sage model has the exact same components, connections, and input values as the model originally described in Chapter 4. The convective heat transfer resistances were updated in the validation chapter to be 0.067 W/mK and 0.024 W/mK for the heating and cooling side respectively. The heat source temperature is set to 150 °C and the sink temperature is 5 °C.

#### **7.1.1 Manipulated Variables**

The heat exchanger inputs in the Sage model are manipulated in this study. The heat exchanger geometry is varied in the same way as section 3.1, where the geometry of the heat exchanger channels remains constant, but the length and number of heat exchanger channels is modified. This means that the channel height and width remained constant. This is equivalent to selecting a different size of the same type of heat exchanger, from which an optimum size can be determined for that type. While the Raphael heat exchangers are annular, this restriction is neglected in order to consider a range of heat exchanger sizes beyond those that will fit the annulus of the engine. This is more similar to a Stirling engine design with externally mounted heat exchangers, such as the one designed by DTECL [82], [83], wherein the heat exchangers size does not have the same restriction as annular heat exchangers.

The range of heat exchanger channel lengths and number of channels considered is shown in Table 7.1, where the model is solved for every possible combination of these parameters. For each heat exchanger length, all number of channels are considered, and vice versa. This results in a range of dead volume ratios between 0.4 and 2.2. The Schmidt model predicted that the optimal dead volume ratio would lie somewhere below 1.91, so this covers most of the range predicted by Schmidt. An extended study was run to confirm that the optimum is not beyond the range considered, with a maximum dead volume ratio of approximately 4.

Note that for simplicity in the base case, there is no additional dead volume for any connections to the heat exchangers considered. All the other dead volume in the engine remains constant.

*Table 7.1. Varied Heat Exchanger Properties for Sage Analysis.*

<b>Property</b>	<b>Minimum Value</b>	<b>Maximum Value</b>	<b>Step Size</b>
Channel Length	48 mm	192 mm	12 mm
Number of Channels	145	575	43

### **7.1.2 Sensitivity Cases**

Some of the engine properties can have a range of values which may affect the optimal heat exchanger geometry for maximum power. These properties are explored using sensitivity cases. The engine operating conditions of engine pressure and speed are considered, with sensitivity cases run at the same conditions outlined in Table 3.3, covering the same range of operating conditions.

Two sensitivities are considered that modify the engine geometry. The first study addresses the ongoing simplification that no additional dead volume is added to the engine to represent the connections to the heat exchangers. As the cross-sectional area of the heat exchanger increases with the increased number of channels, there must be some engine volume reserved for a plenum to allow the air to flow through all the available channels. This is added to the model by including the volume of a rectangular prism to the engine volume that scales with the frontal area of the heat exchangers. For each heat exchanger in the engine, the volume of a rectangular prism is added to the expansion or compression space models using the following relation:

$$V_{plenum} = (w_{fin} + b)aL_{plenum}n \quad (7.1)$$

where:

$V_{plenum}$  – volume of heat exchanger plenum (m<sup>3</sup>)

$w_{fin}$  – average fin width (m)

$b$  – channel width (m)

$a$  – channel height (m)

$L_{plenum}$  – length of plenum entrance (m)

$n$  – number of heat exchanger channels

This multiplies the frontal area of the heat exchanger, including the solid fin thickness, by the length of the plenum entrance. In the Raphael engine as built, there is a 12.15 mm gap between the heat exchanger and the top of the displacer cylinder. This is initially used as the length scale for defining the size of the additional plenum volume for varying heat exchanger sizes. An additional study with an even larger plenum length of 25.4 mm is also considered.

The second sensitivity that modifies the engine geometry considers the effect of compression ratio on the optimal heat exchanger geometry. In the base case, all the engine geometry remains fixed except for the heat exchanger size. This will lead to an increase in the compression ratio for small heat exchanger volumes and a decrease in compression ratio for large heat exchanger volumes. However, the compression ratio affects the power output [25], and would be optimized for maximum output power [84]. In order to evaluate the influence of different heat exchanger geometry without the influence of changing compression ratio, the compression ratio will be held

constant by changing the power piston stroke. The power piston stroke is calculated from the compression ratio as follows:

$$L_{power} = \frac{(CR - 1)V_{dead}}{\pi r_{power}^2} \quad (7.2)$$

where:

$L_{power}$  – power piston stroke (m)

$r_{power}$  – radius of power piston (m)

The compression ratio is held constant at the compression ratio of 1.1 of the as-built Raphael engine.



## 7.2 Results of Heat Exchanger Volume Variation Study

Results from the Sage model indicate that there is an optimum heat exchanger volume and geometry for producing maximum power. In Figure 7.1 the indicated power is plotted against the dead volume ratio for various heat exchanger lengths and for various numbers of heat exchanger slots. The same data is plotted in two different ways. First, the curves of constant heat exchanger length are plotted against dead volume ratio, where the increase in dead volume ratio corresponds to an increase in the number of heat exchanger slots. Then, the curves of constant number of heat exchanger slots is plotted against dead volume ratio, where the increase in dead volume ratio now corresponds to an increase in the heat exchanger length. As expected, the effect of excess dead volume is apparent as the indicated power peaks and then decreases with increasing dead volume. The peak power output occurs along the shortest heat exchanger length, and for the largest number of slots considered.

To ensure the maximum can be determined, the study was extended to include longer channel lengths and more slots, with a maximum dead volume ratio considered of 4. The results of the indicated power output of this study are plotted against dead volume ratio in Figure 7.2. The maximum engine power of 45.13 W occurs for a heat exchanger length of 48 mm with 575 channels. This occurs at a dead volume ratio of 0.76 which is also within the maximum bound predicted by the Schmidt model. In this figure it is also evident that the power output decreases exponentially with increasing dead volume ratio, which matches the trend seen in the Schmidt model in Chapter 3.

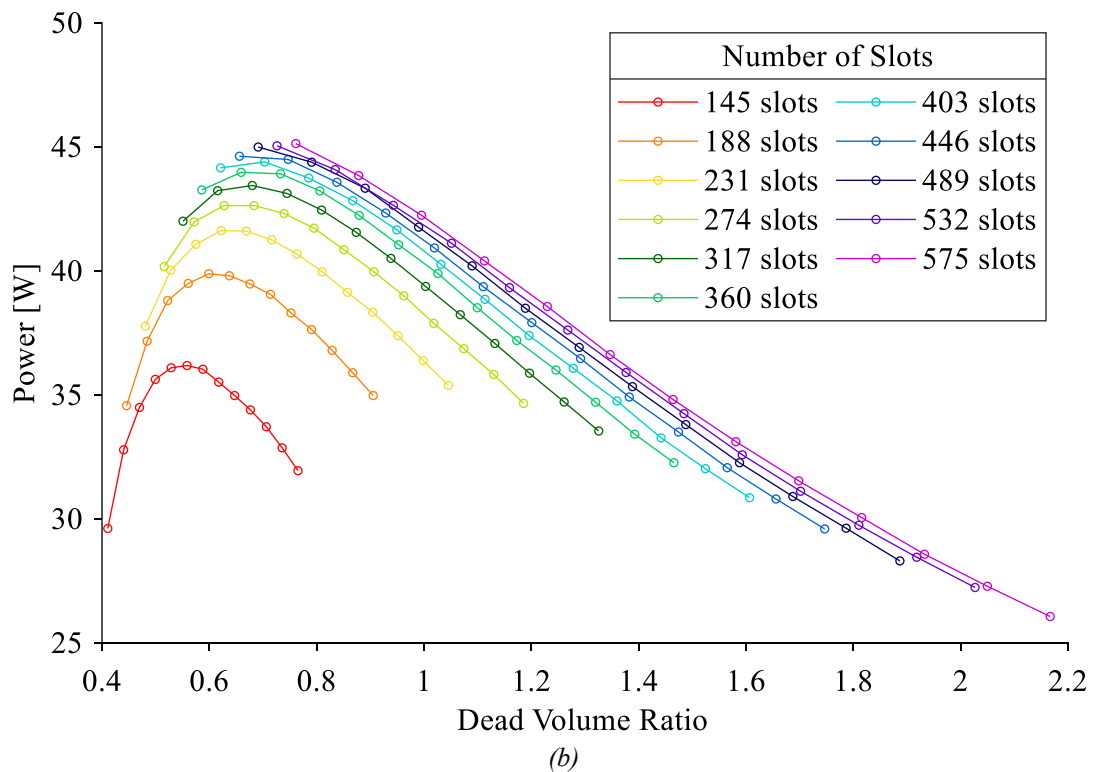
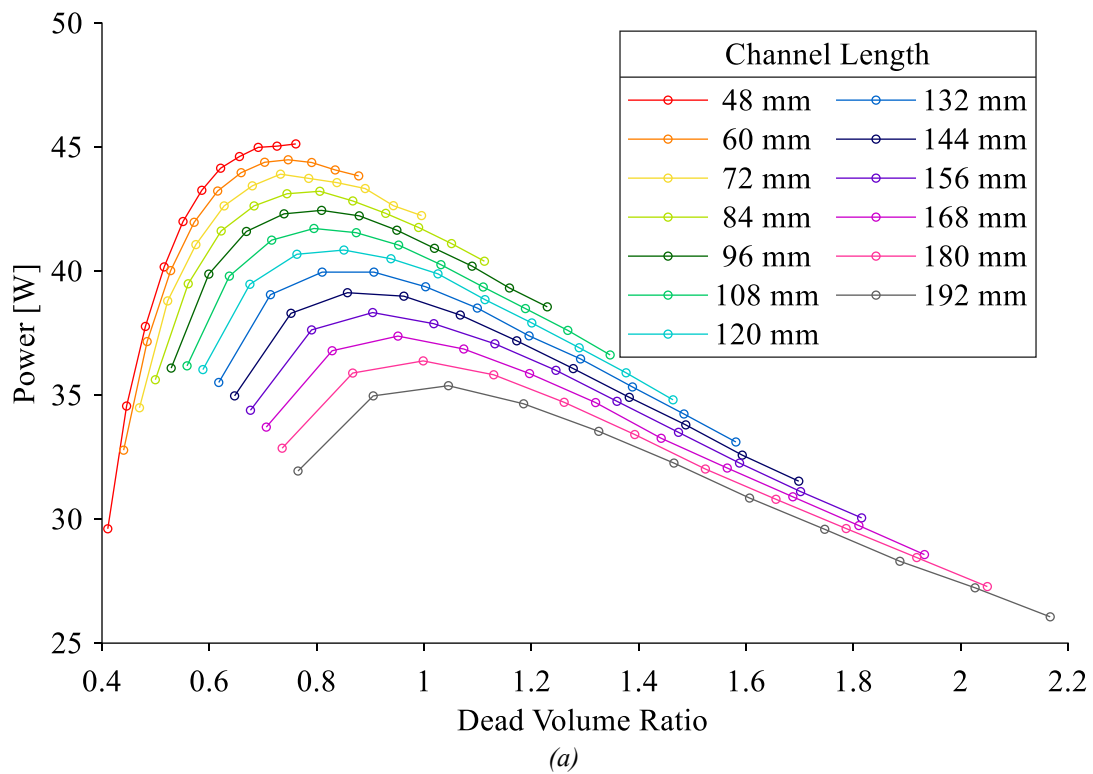


Figure 7.1: Plot of indicated power from Sage against dead volume ratio for (a) various heat exchanger lengths and (b) various numbers of heat exchanger channels.

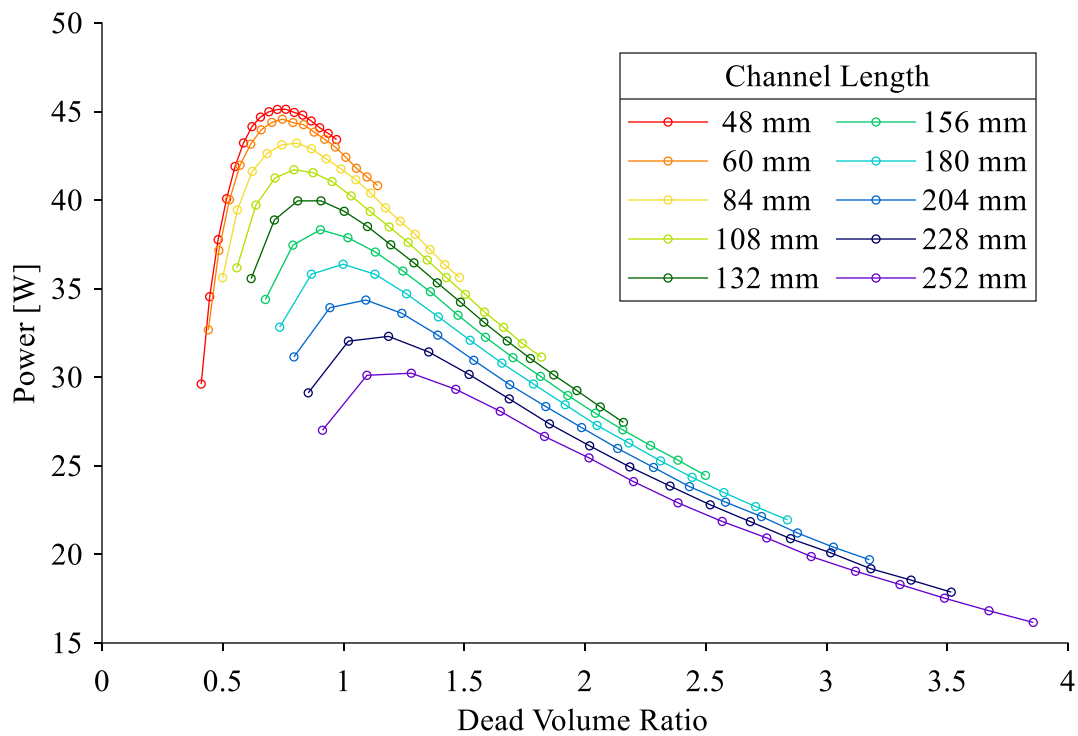


Figure 7.2: Plot of power output from Sage against dead volume ratio for various heat exchanger lengths over an extended range of dead volume ratio.

To better understand why the maximum power occurs at the lowest heat exchanger length, the gas temperature is considered. To evaluate the heat exchanger's ability to change the gas temperature in the engine, the difference between the time-average expansion space and compression space temperature is used. This is the average gas temperature difference, which is the difference between the hot and cold side of the engine. This is plotted against the dead volume ratio in Figure 7.3. The average gas temperature difference increases with increasing dead volume ratio asymptotically toward the maximum possible temperature difference, which is expected and aligns with the results of Chapter 3. Once again, all the different heat exchanger configurations considered collapse onto the same curve with some slight variation, due to the increase in surface area associated with the increase in heat exchanger volume. As was identified previously, heat exchangers that have similar surface areas will yield approximately the same average gas temperature change. To confirm this, the average gas temperature difference is plotted against surface area in Figure 7.4. The trend of the average gas temperature difference with increasing surface area is exactly the same as with increasing dead volume ratio, since the surface area and heat exchanger volume are directly proportional.

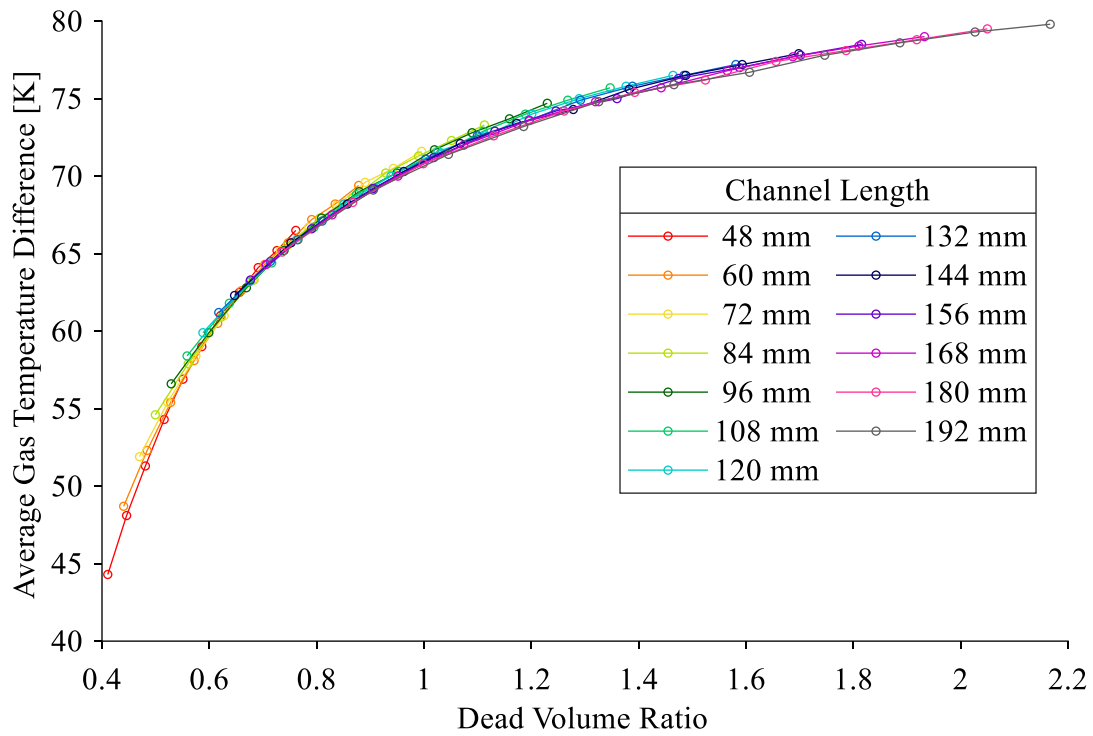


Figure 7.3: Plot of average gas temperature difference between the expansion and compression space against dead volume ratio for various heat exchanger lengths.

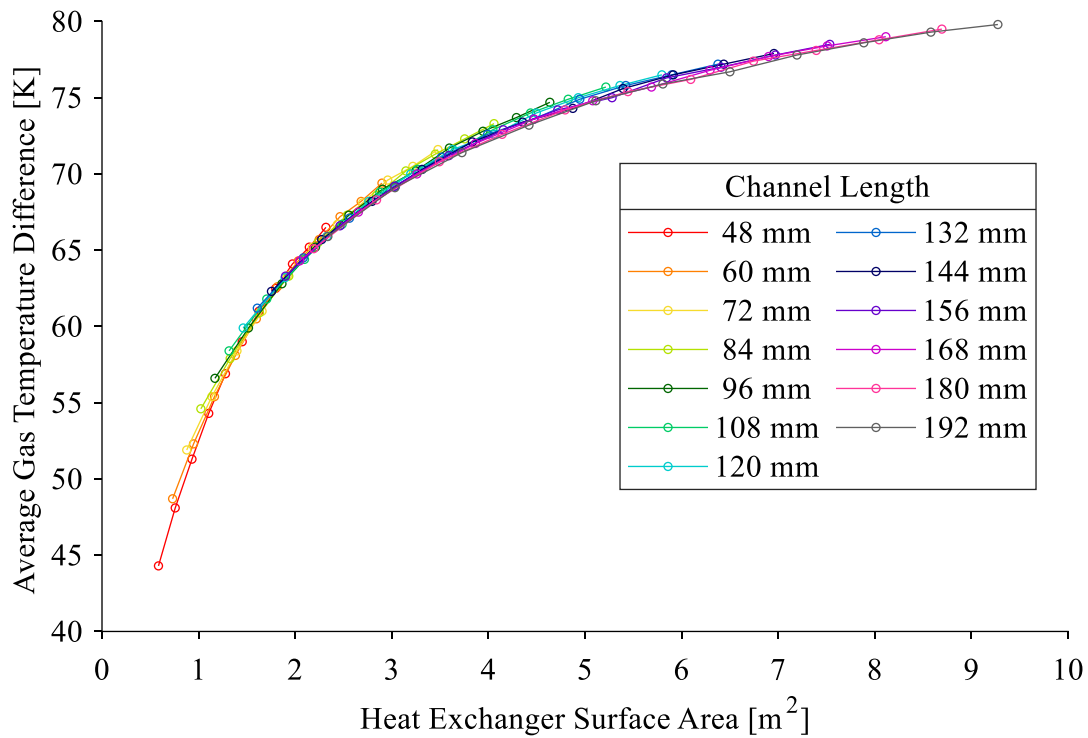


Figure 7.4: Plot of average gas temperature difference between the expansion and compression space against gas side heat exchanger surface area for various heat exchanger lengths.

The other contributing factor to the engine performance is the pressure swing of the engine spaces, which will change the size of the PV diagram and thus the indicated work and power. In Figure 7.5 the compression space pressure swing is plotted against the dead volume ratio for varying heat exchanger lengths. The detrimental effect of excess dead volume can be seen through the decrease in pressure swing with increased dead volume ratio, which is also exponential, matching the trend of the power curve. This decrease in the pressure swing of both spaces decreases the engine power despite the increase average gas temperature difference at the same dead volume ratio.

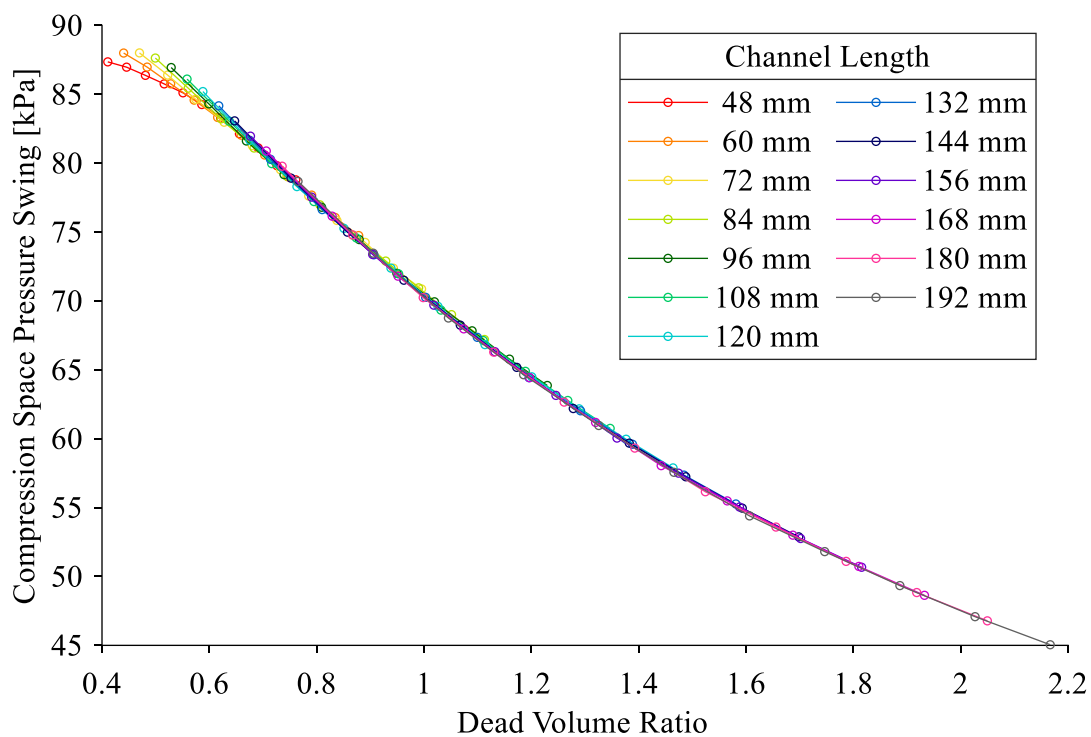


Figure 7.5: Plot of compression space pressure swing against dead volume ratio for various heat exchanger lengths.

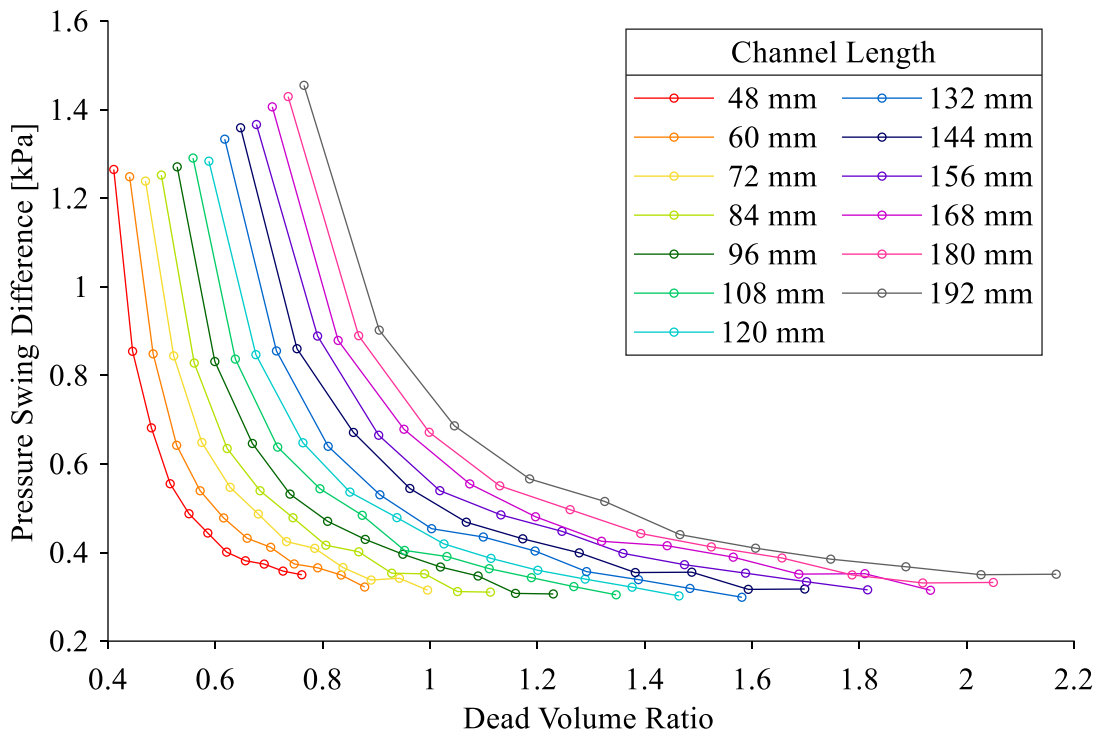
The same decrease in compression space pressure swing is seen in the expansion space pressure swing. The magnitude of the pressure swing is different between the two spaces, and this difference in magnitude results from the pressure drop through the heat exchangers and regenerator. In Figure 7.6 the difference in the pressure swing between the compression space and the expansion space is plotted against dead volume ratio for varying heat exchanger lengths and numbers of channels. There are slight deviations present in the results, which are likely due to residuals effects of the mesh which are more present at the pressure drop values, as they are of relatively low magnitude compared to the overall pressure swing. The heat exchanger length

does impact the pressure drop through the heat exchangers, with increasing heat exchanger length resulting in increased pressure drop. However, this effect is almost negligible for heat exchangers with a high number of channels. The pressure drop depends much more strongly on the number of heat exchanger channels, or cross-sectional area. This is due to the smaller cross-sectional area resulting in much higher velocities through the heat exchanger channels, which increases the pressure drop. The effect is much stronger since pressure drop is dependent on the square of velocity, but only linearly varies with heat exchanger length. This aligns with the results seen in Chapter 3, though the dependence of pressure drop on length is lower when modelled with Sage.

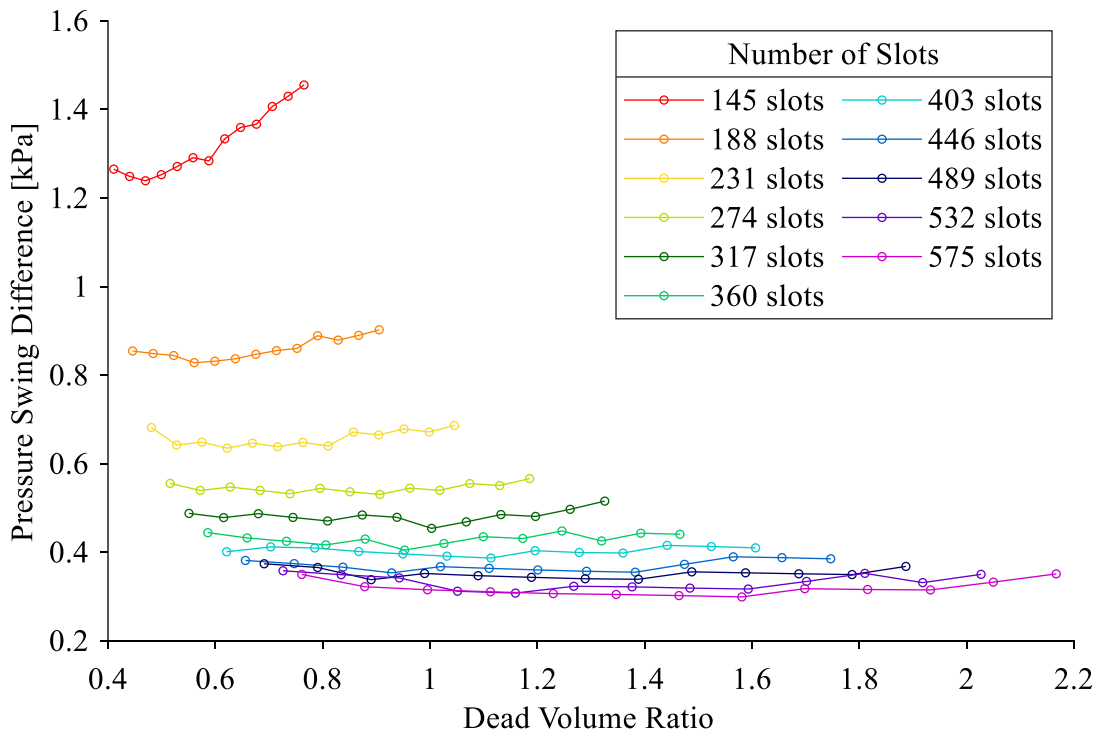
The Sage results confirm what was expected from the analysis of Chapter 3:

- The output temperature of the gas for heat exchangers of varying size is directly correlated with the surface area of the heat exchangers
- Heat exchangers with higher surface area will result in better output temperatures
- The pressure drop across the heat exchangers is dependent on the heat exchanger length and strongly dependent on the heat exchanger cross-sectional area
- Heat exchangers with a high cross-sectional area result in the lowest pressure drop
- The location of maximum power is below the maximum dead volume ratio predicted by the Schmidt model.

The Sage model is also able to finally determine the optimum heat exchanger geometry by modelling the interaction of heat transfer in the heat exchangers with the Stirling cycle. The optimum heat exchanger geometry for a LTDSE has a low heat exchanger length with high cross-sectional area. The maximum cross-sectional area is limited in order to minimize the negative effects of dead volume while benefiting from the low pressure drop through the heat exchangers. The total surface area of the heat exchanger needs to be sufficient, but excess surface area resulting from an increase in dead volume is not beneficial, regardless of the additional gains in gas temperature, due to the excess dead volume lowering the pressure swing in the engine.



(a)



(b)

Figure 7.6: Plot of difference in expansion and compression space pressure swings against dead volume ratio for (a) various heat exchanger lengths and (b) various numbers of heat exchanger channels.

### **7.3 Results of Engine Speed and Pressure Sensitivity**

A set of sensitivity cases varying the engine operating conditions of engine pressure and engine speeds were run. The Sage results for varying heat exchanger volume over the range of parameters considered provide insight into selecting a heat exchanger for an engine that operates over a range of conditions.

The indicated power is plotted against the dead volume ratio for all the engine pressure and speed cases considered for varying heat exchanger lengths in Figure 7.7 and for varying numbers of heat exchanger channels in Figure 7.8. From these figures it can be seen that the power increases with increasing engine pressure at low speeds. However, at higher speeds, the additional pressure results in more flow friction, which leads to a decrease in engine output power overall. Also, at low pressure increasing the engine speed leads to an increase in power with more engine revolutions, while at high pressure the excess flow friction leads to a decrease in output power. The indicated work output does not show this trend of magnitude, as can be seen in the plots of indicated work against dead volume ratio for all the engine pressure and speed cases for varying heat exchanger lengths in Figure 7.9 and for various numbers of heat exchanger channels in Figure 7.10. Here, the magnitude of the work decreases with decreases engine pressure and increasing engine speed. The magnitudes of the indicated work and indicated power across the sensitivity cases considered, matching the results from the validation done in Chapter 6, which had a known overdependence on engine speed, which was particularly noticeable for the output power.



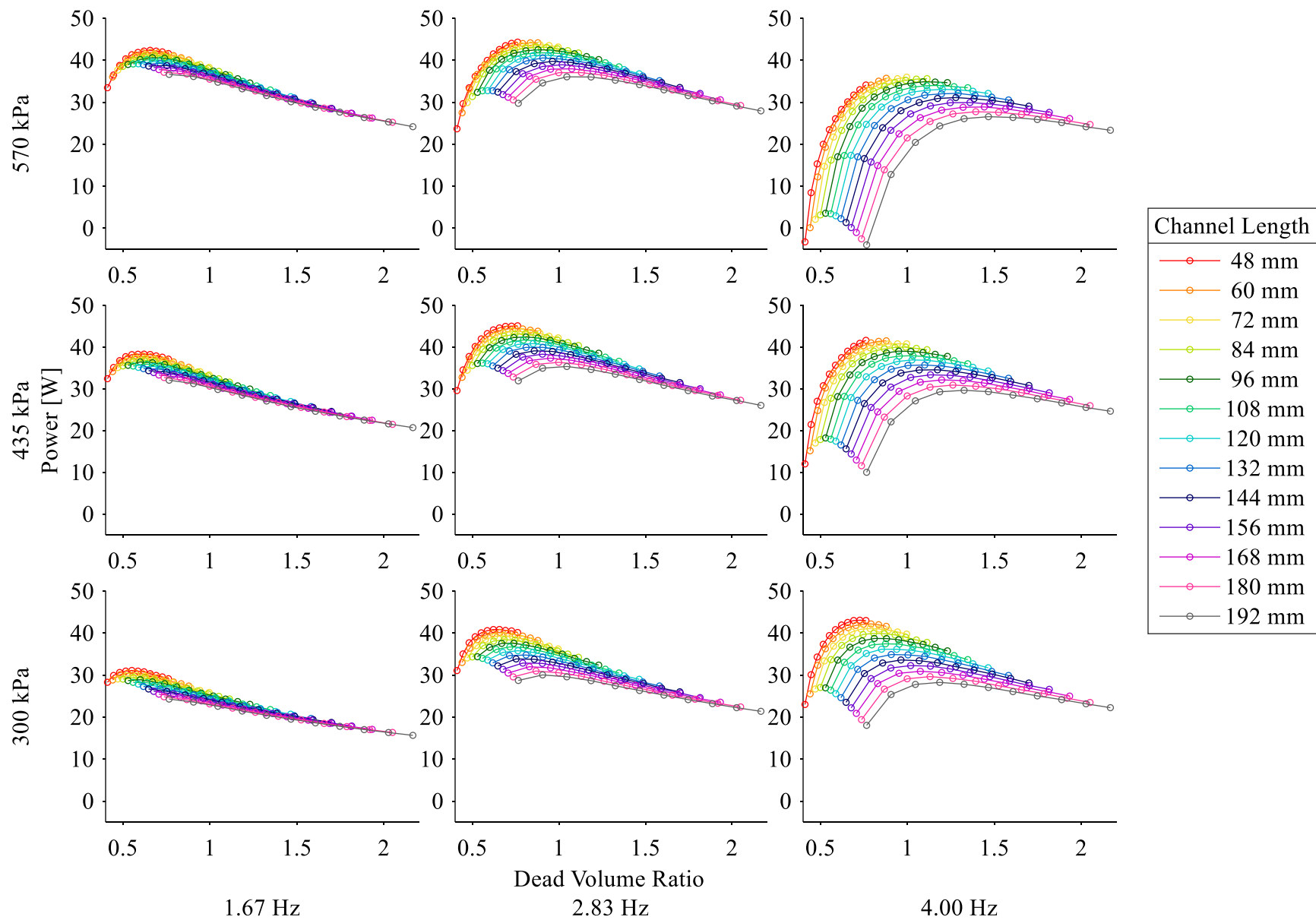


Figure 7.7: Plot of indicated power from Sage against dead volume ratio for various heat exchanger lengths at varying speeds and pressures.

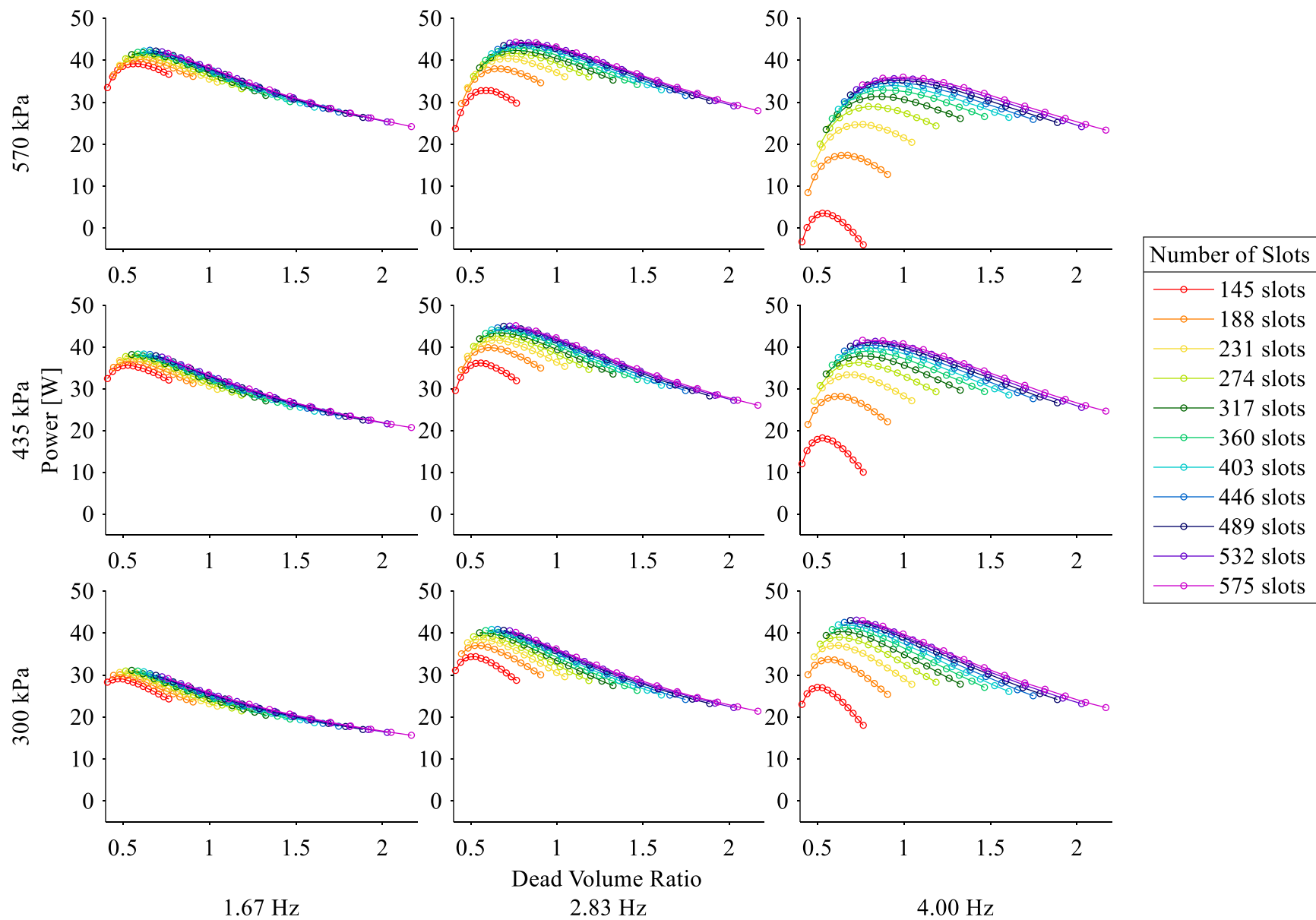


Figure 7.8: Plot of indicated power from Sage against dead volume ratio for various numbers of heat exchanger channels at varying speeds and pressures.

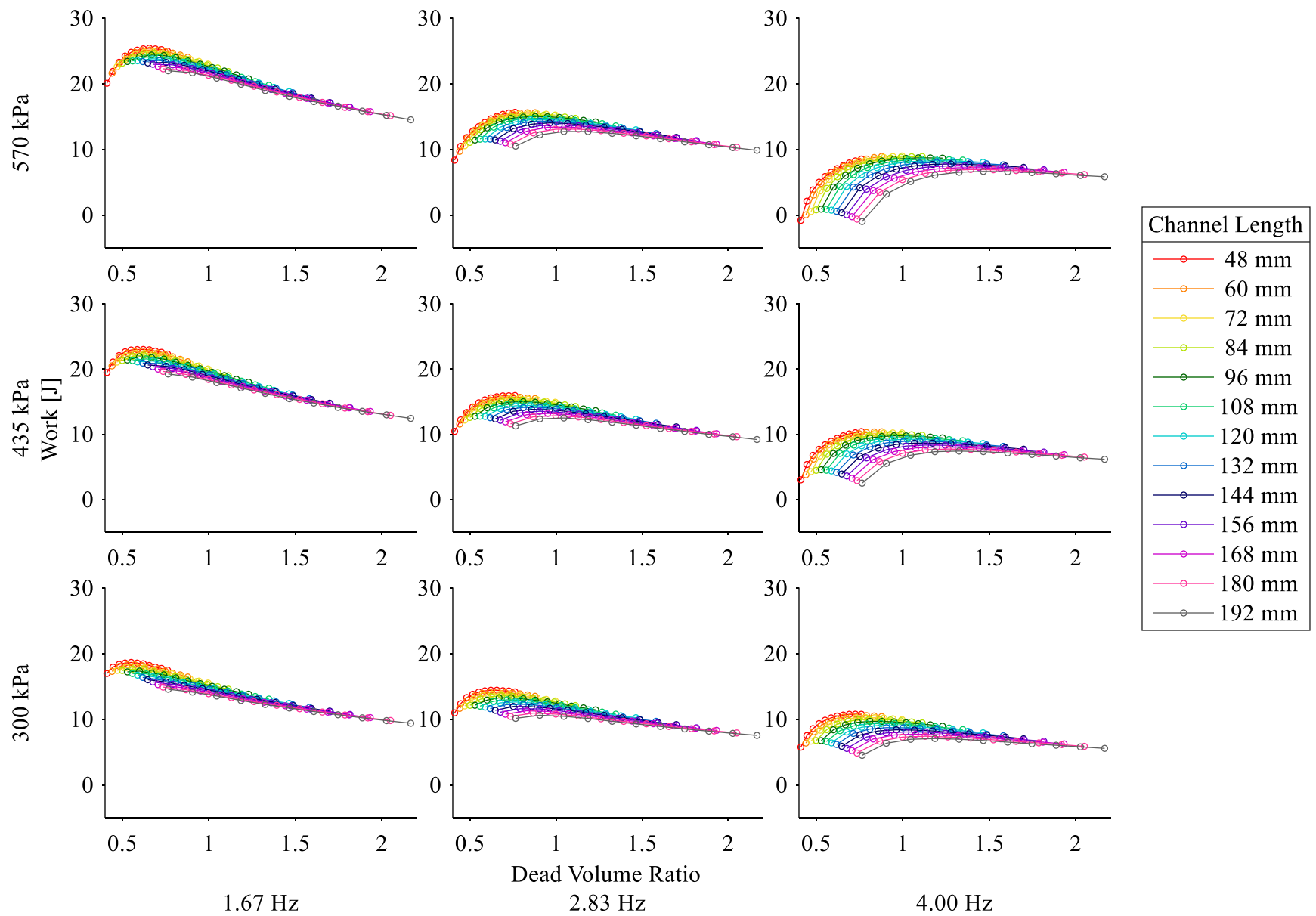


Figure 7.9: Plot of indicated work from Sage against dead volume ratio for various heat exchanger lengths at varying speeds and pressures.

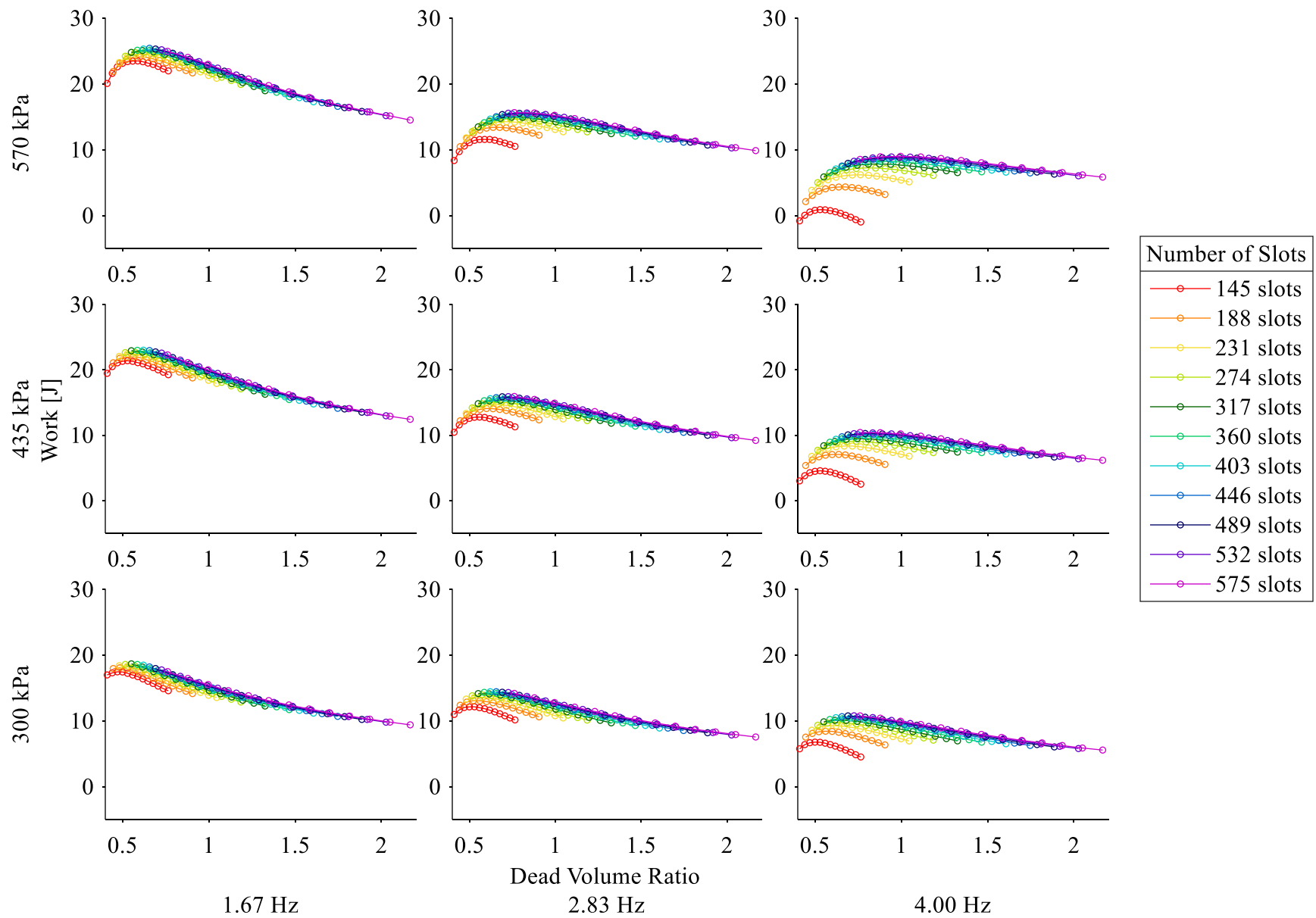


Figure 7.10: Plot of indicated work from Sage against dead volume ratio for various numbers of heat exchanger channels at varying speeds and pressures.

The results of the heat exchanger volume variation show that the optimal heat exchanger volume increases with increasing engine speed and increasing engine pressure. For example, the dead volume ratio at which maximum power is achieved for the low speed case increases from 0.55 to 0.66 with increasing engine pressure. The optimal dead volume ratio for the low pressure case increases from 0.55 to 0.73 with increasing engine speed. This is caused by the increased mass flow rate through the heat exchangers requiring additional surface area, which is directly correlated with dead volume, in order to heat the gas in the engine sufficiently. The additional heat transfer requirement can be so high that the heat exchangers cannot provide the required heat transfer, and the engine will not run, which is seen as negative power output. The effect of the additional heat transfer load on engine temperatures can be seen clearly in Figure 7.11, which plots the average temperature difference against dead volume ratio for varying engine pressure and speeds. It can be seen that the attained temperature difference decreases with both increasing engine speed and pressure, with the worst performance at high speed and pressure. This agrees with the results from Chapter 3, where increased engine pressure and speed led to heat exchanger output temperatures that were farther from the wall temperature. The difference in the Sage results is that even with significant increase in heat exchanger volume, it is not possible to attain the maximum temperature difference at high engine pressures and speeds, as they asymptote to a lower value. Also, at the lower pressure and speed cases, the different heat exchanger geometries do not all collapse onto the same curve. The shorter length heat exchangers perform better than the longer length heat exchangers at the same surface area. This likely results from the increased heat transfer coefficient of the entrance region yielding better output temperatures over the same surface area as the longer heat exchangers.

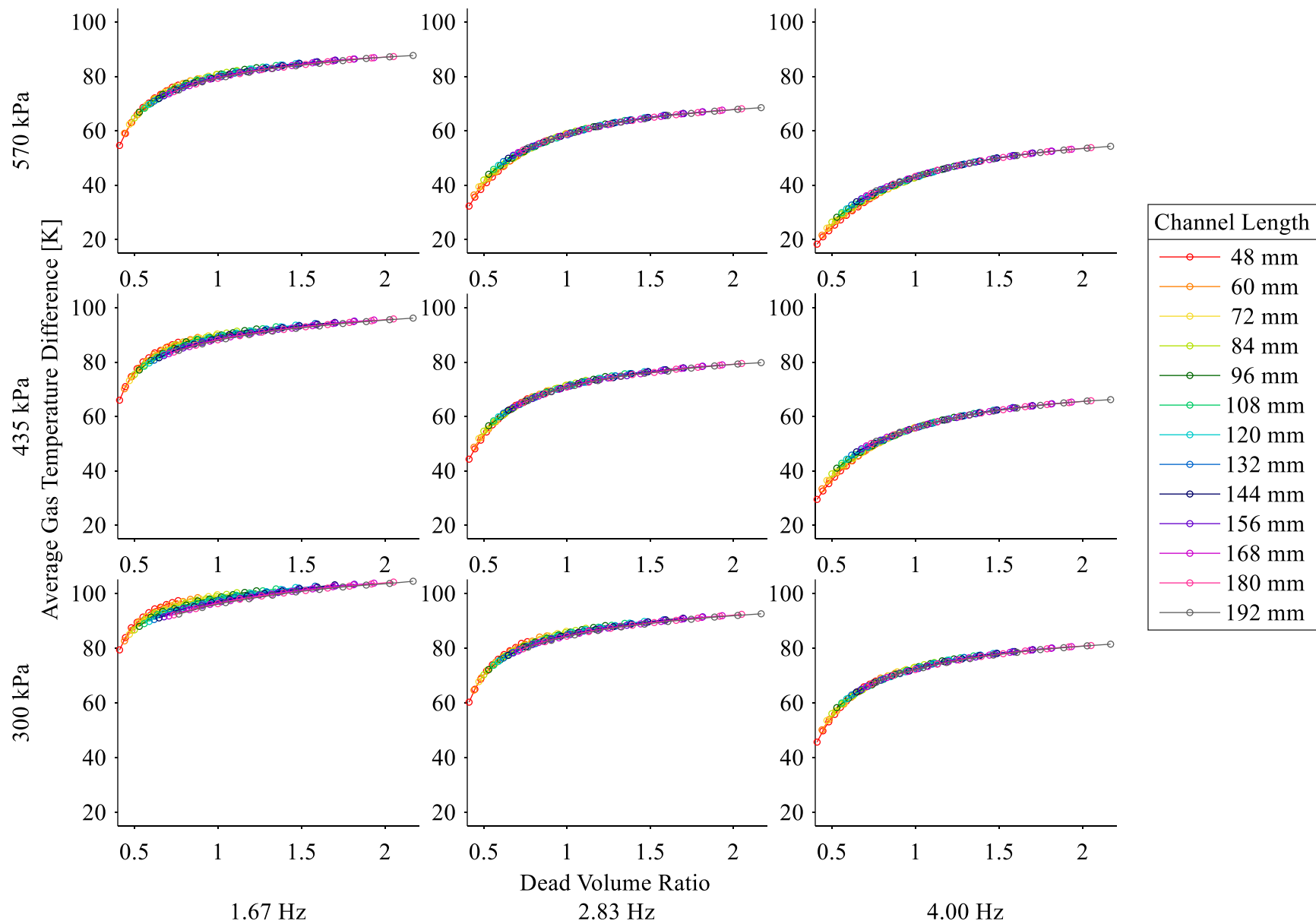


Figure 7.11: Plot of average gas temperature difference against dead volume ratio for various heat exchanger lengths at varying speeds and pressures.

The work and power output are also far more sensitive to the number of heat exchanger channels at high speed cases, which is due to the pressure drop. The difference in pressure swing between the compression and expansion space is plotted against dead volume ratio for all the engine pressure and speed cases for varying heat exchanger lengths in Figure 7.12 and various numbers of heat exchanger channels in Figure 7.13. Increasing engine pressure and speed both increase the pressure drop through the engine, which agrees with the results seen in Chapter 3. It can be seen that at low engine speed, the effect of increasing engine pressure is not very significant, with a small increase in the pressure drop through the heat exchangers resulting from the increased density. However, at high speeds, the pressure drop is greatly increased due to the increased velocity, and the same changes in density result in greater changes in the pressure drop. Likewise, the effect of velocity is more significant at high pressure, with the pressure drop magnitude being up to 5 times greater in the high speed high pressure case than the low speed high pressure case. Also, the high speed and high pressure cases asymptote to larger values of minimum pressure drop in the engine, which limits the maximum work and power output at those engine operating conditions

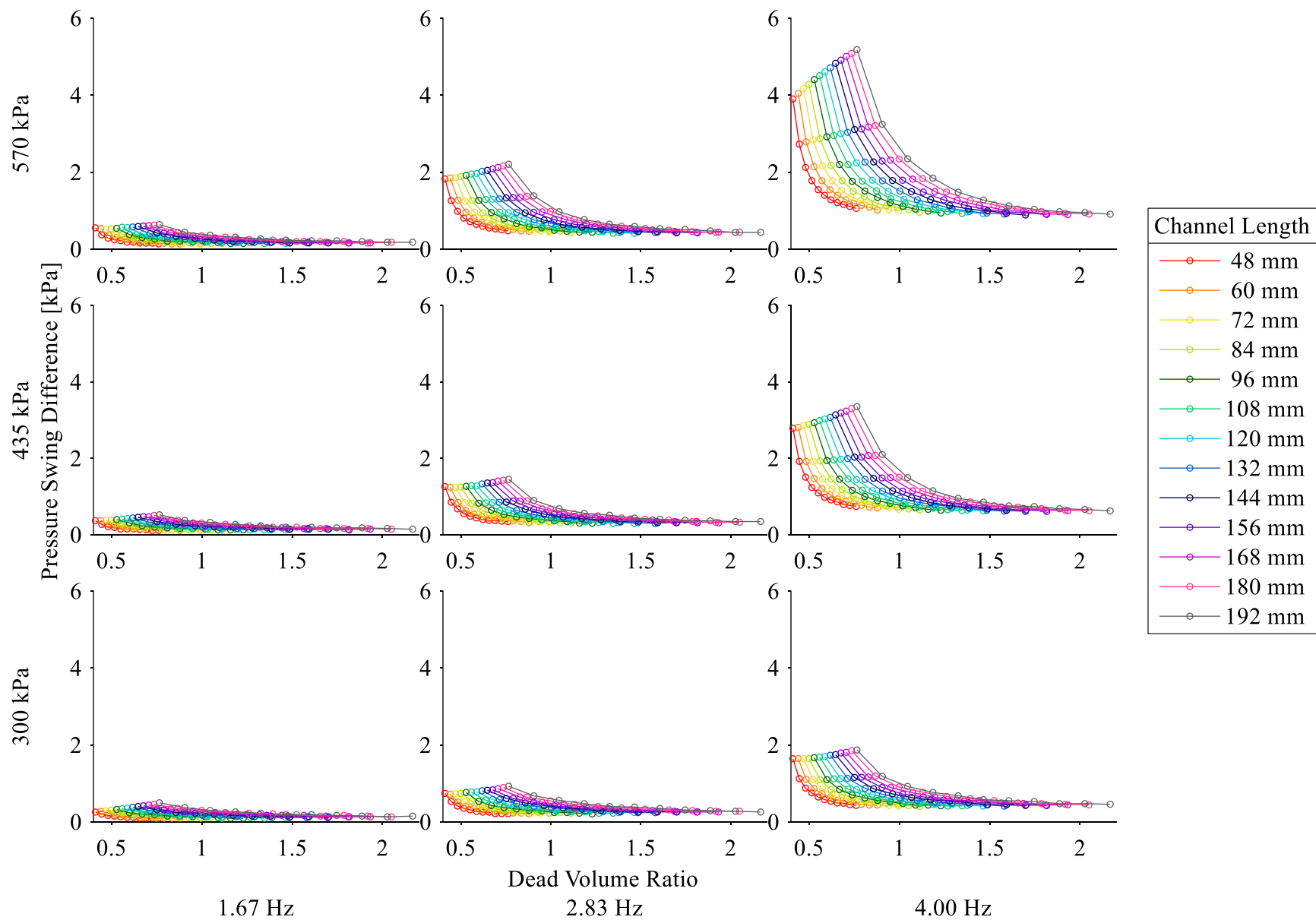


Figure 7.12: Plot of pressure swing difference against dead volume ratio for various heat exchanger lengths at varying speeds and pressures.



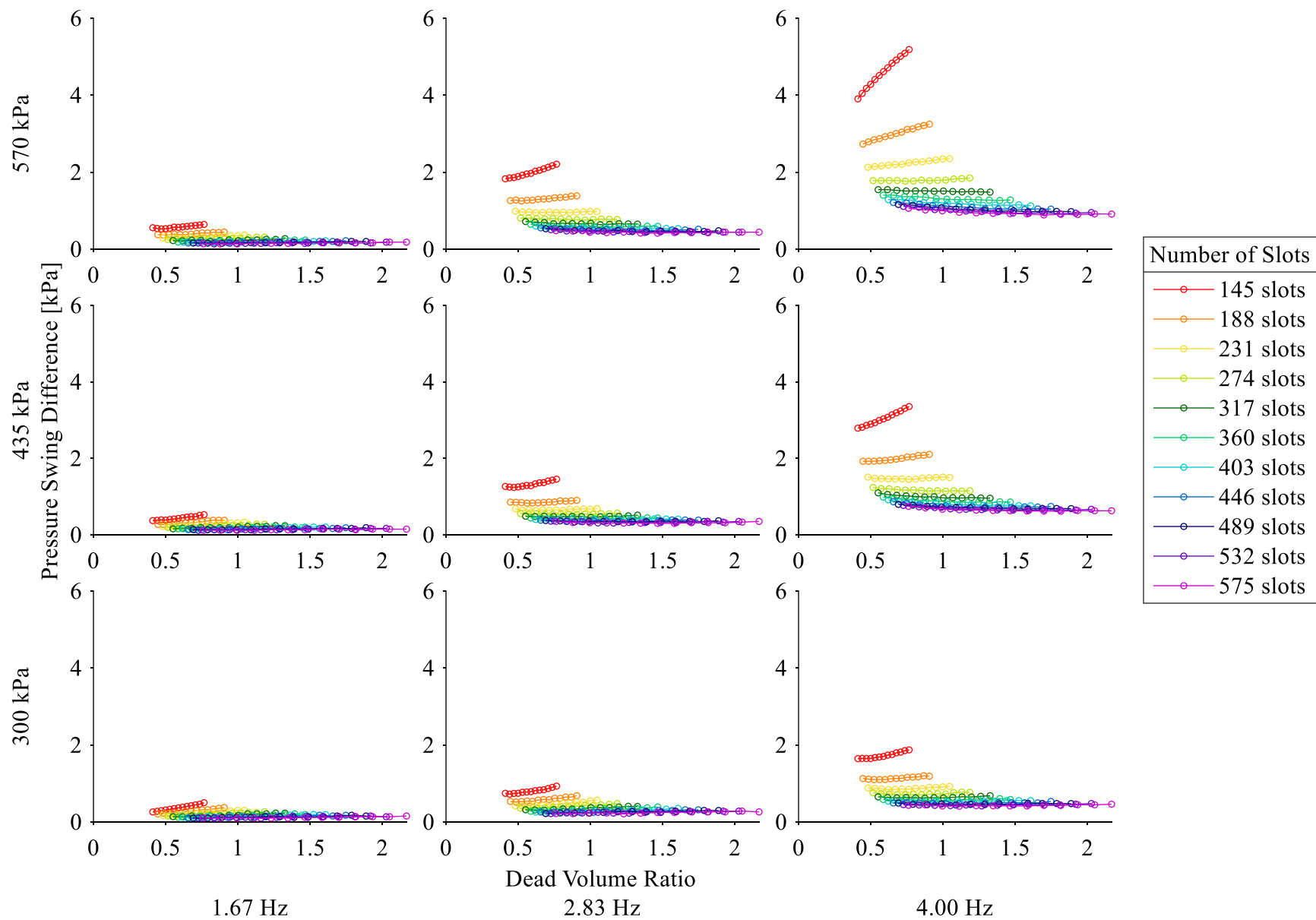


Figure 7.13: Plot of pressure swing difference against dead volume ratio for various heat exchanger lengths at varying speeds and pressures.

A limitation of the study as shown is that the same range of heat exchanger geometries is considered for all cases, and this range fails to cover the optimal size for the high pressure and high speed cases. This does highlight clearly the importance of considering the desired operating condition of the engine when selecting the heat exchangers, as an engine that may run close to the optimum at a low speed will have a significant decrease in power with increasing speed, even to the point of preventing the engine from running at all. Thus, the selection of the heat exchanger size requires a compromise on which operating condition will yield the optimal power output.

Another interesting result of the Sage model is that it is able to predict a decrease in output power with increasing engine speed and pressure, contradicting the results of the Schmidt model from Chapter 3 where the power output increases with increasing engine pressure and speed forever. The Sage model includes the effect of flow friction, which removes energy from the cycle by reducing the pressure swing and results in a lower power.

## 7.4 Results with Plenum Dead Volume

Up to this point, all the studies done in Sage have assumed that there is no additional dead volume associated with attaching various heat exchanger sizes to the engine. This has resulted in the optimum heat exchanger geometry always being the shortest length, with a large number of heat exchanger channels in order to minimize the pressure drop through the heat exchangers while maintaining sufficient surface area for adequate heat transfer. This is not possible in reality, as there must be a way for the air to reach all the heat exchanger channels in order to take advantage of their volume. This effect is included in the model in a sensitivity analysis where additional dead volume that scales with the heat exchanger frontal area is added. This results in the curve of power plotted against dead volume for varying heat exchanger lengths and numbers of heat exchanger channels seen in Figure 7.14. These results include an additional plenum with a length of 12.15 mm above both of the heat exchangers. In this plot it can be seen that overall peak power is lower than in the case without excess dead volume, which is an expected result from the addition of dead volume. Also, the curves near the peak power start to overlap, with the shortest heat exchanger length curve overlapping the next curve of heat exchanger length.

The peak power for this case occurs at a heat exchanger length 48 mm and 489 heat exchanger channels. This is a lower number of channels than the case without additional dead volume, which had peak power at the same length but at 575 channels. To confirm that the heat exchanger length is the optimum, a study considering only the shorter heat exchanger lengths was run, and the power results for that study are plotted against the dead volume ratio for varying heat exchanger lengths in Figure 7.15. It is made clear that the shorter heat exchanger lengths do not achieve a higher output power, and have overall lower output power than the longer heat exchanger lengths. There is a clear peak in the power curve where both shorter and longer heat exchangers do not result in higher output power than the optimum.

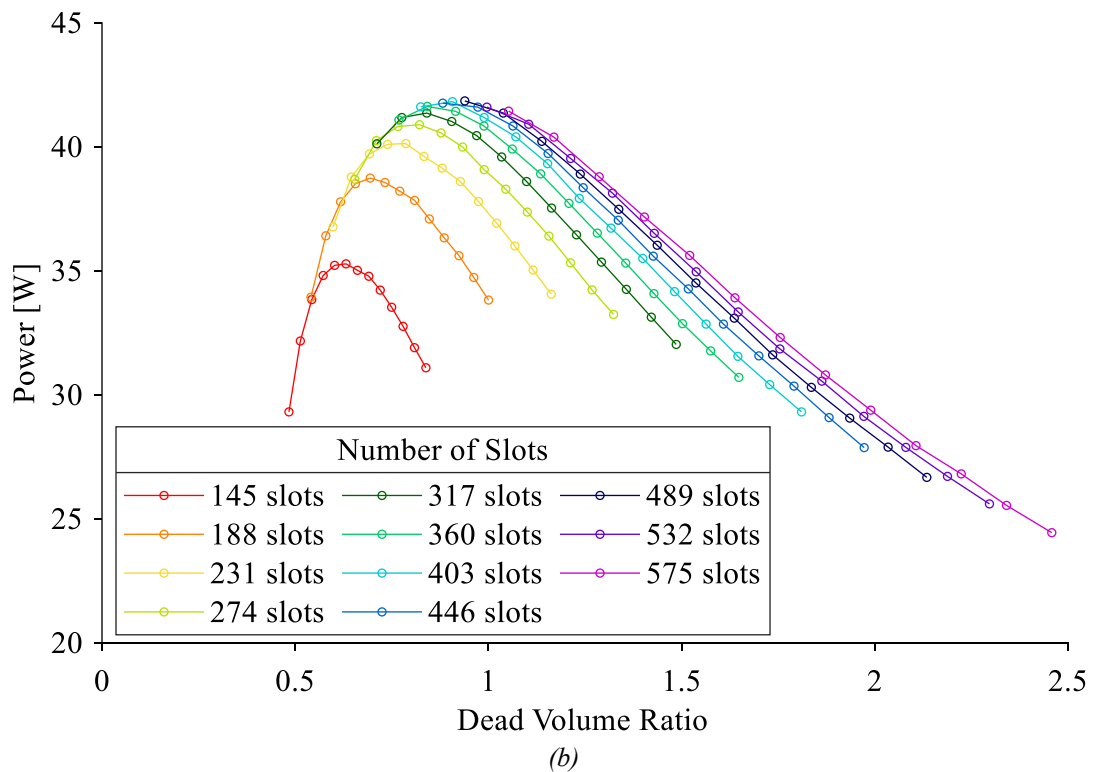
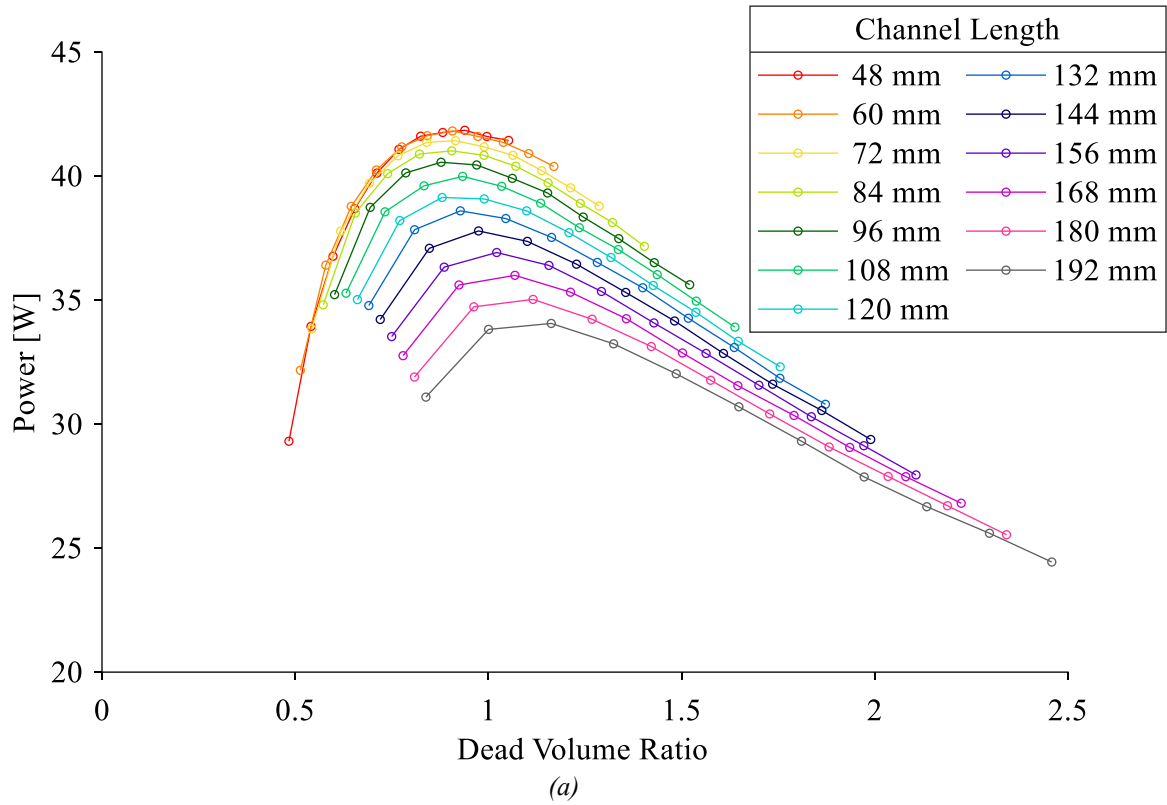


Figure 7.14: Plot of indicated power from Sage with additional scaled dead volume against dead volume ratio for (a) various heat exchanger lengths and (b) various numbers of heat exchanger channels.

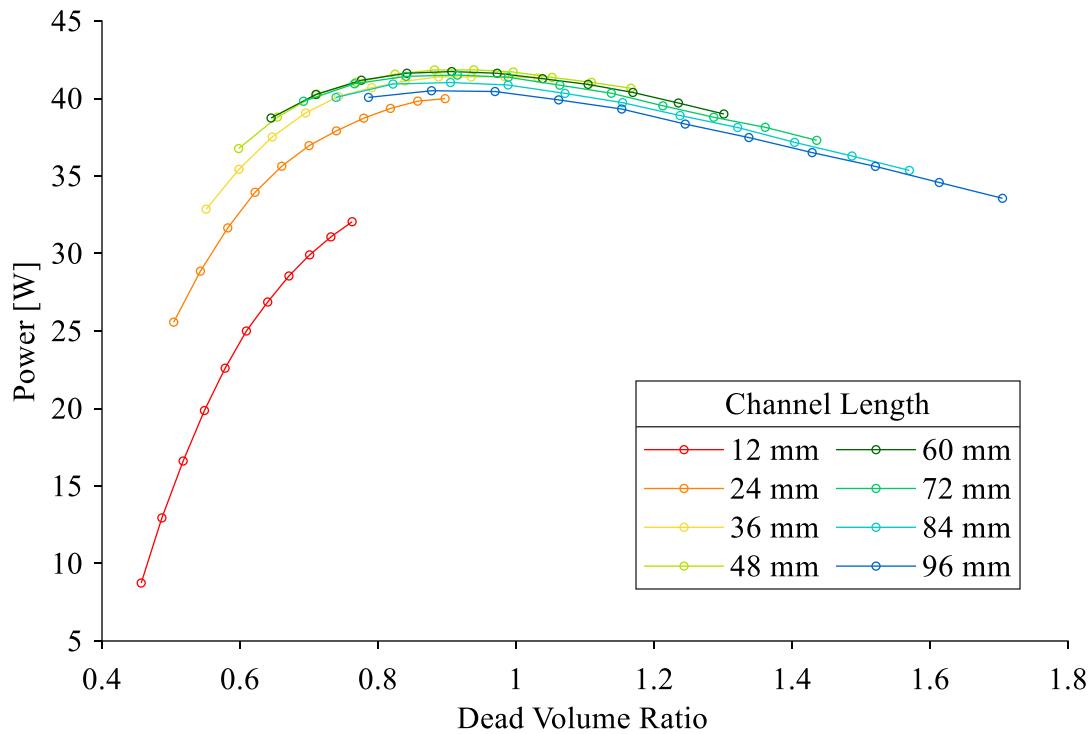


Figure 7.15: Plot of indicated power from Sage with additional scaled dead volume against dead volume ratio for various short heat exchanger lengths.

The shortest heat exchanger is no longer the optimal heat exchanger geometry, as it is not able to provide sufficient surface area for heat transfer, as adding additional channels adds excess dead volume to the engine. This can be seen in the plot of average gas temperature difference against dead volume ratio for varying heat exchanger lengths shown in Figure 7.16, where the curves for the shorter heat exchangers are below those of the longer heat exchangers. The additional dead volume is reducing the average gas temperature in the expansion and compression spaces, and the heat exchanger is undersized.

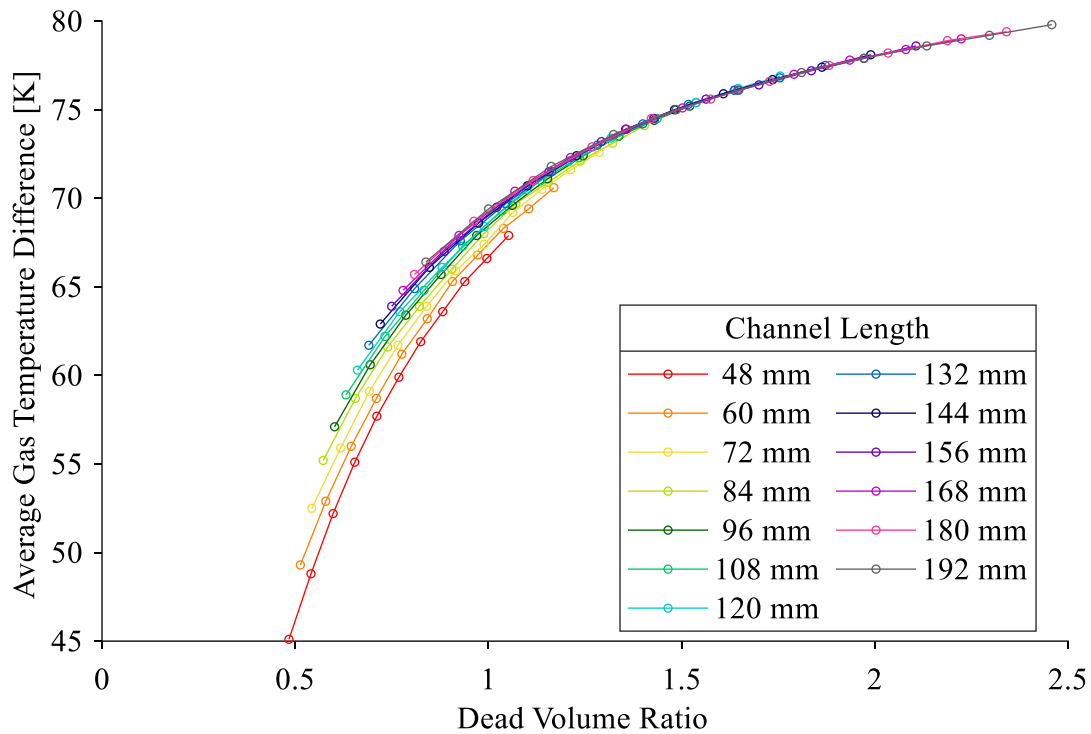


Figure 7.16: Plot of average gas temperature difference between expansion and compression space from Sage with additional scaled dead volume against dead volume ratio for various heat exchanger lengths.

To see the effect of different sized plenums, a case was run where the plenum length was increased to 25.4 mm. This approximately doubles the amount of excess dead volume added to each heat exchanger variant. The power output of this case is plotted against dead volume ratio for varying heat exchanger lengths and numbers of heat exchanger channels in Figure 7.17. In this plot it can be seen that the shortest heat exchanger case is no longer the optimal geometry, as the effect of additional dead volume is too high to be overcome. For this case, the optimum heat exchanger geometry is a 60 mm length and 360 slots, which is seen clearly in the zoomed in plot of power output against dead volume ratio in Figure 7.18. This is expected as there is additional dead volume penalty with increased heat exchanger frontal area, so the maximum number of channels is reduced.

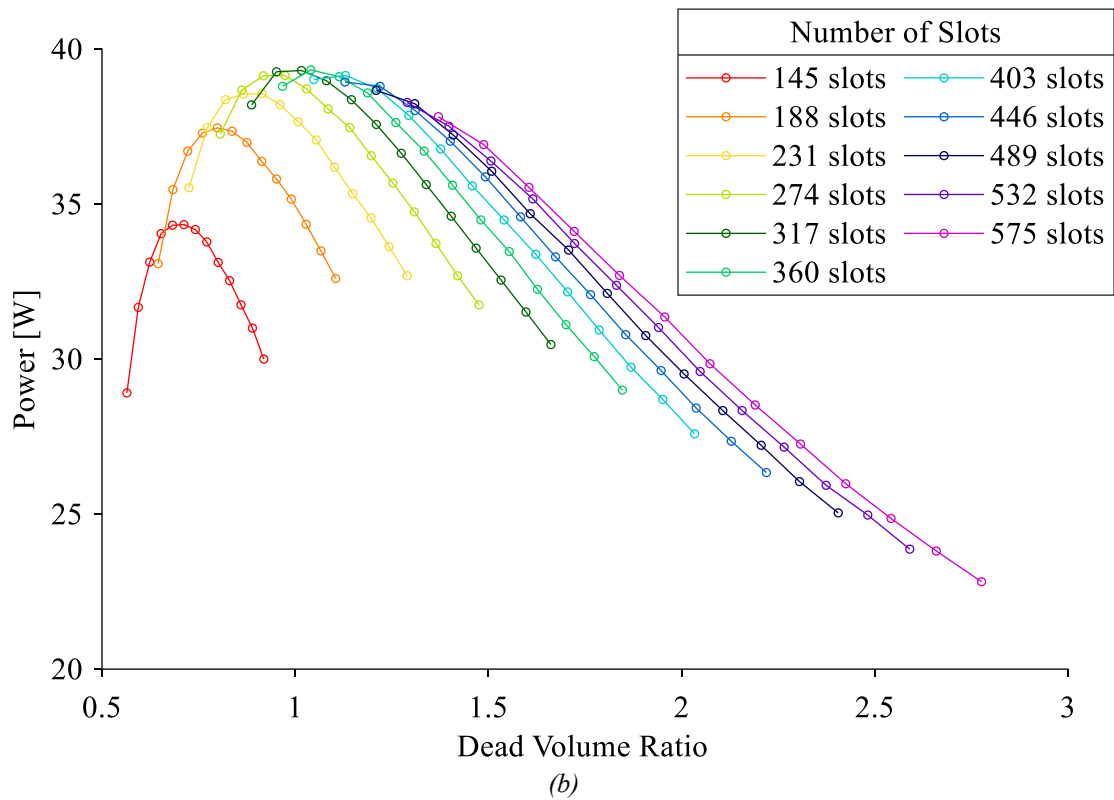
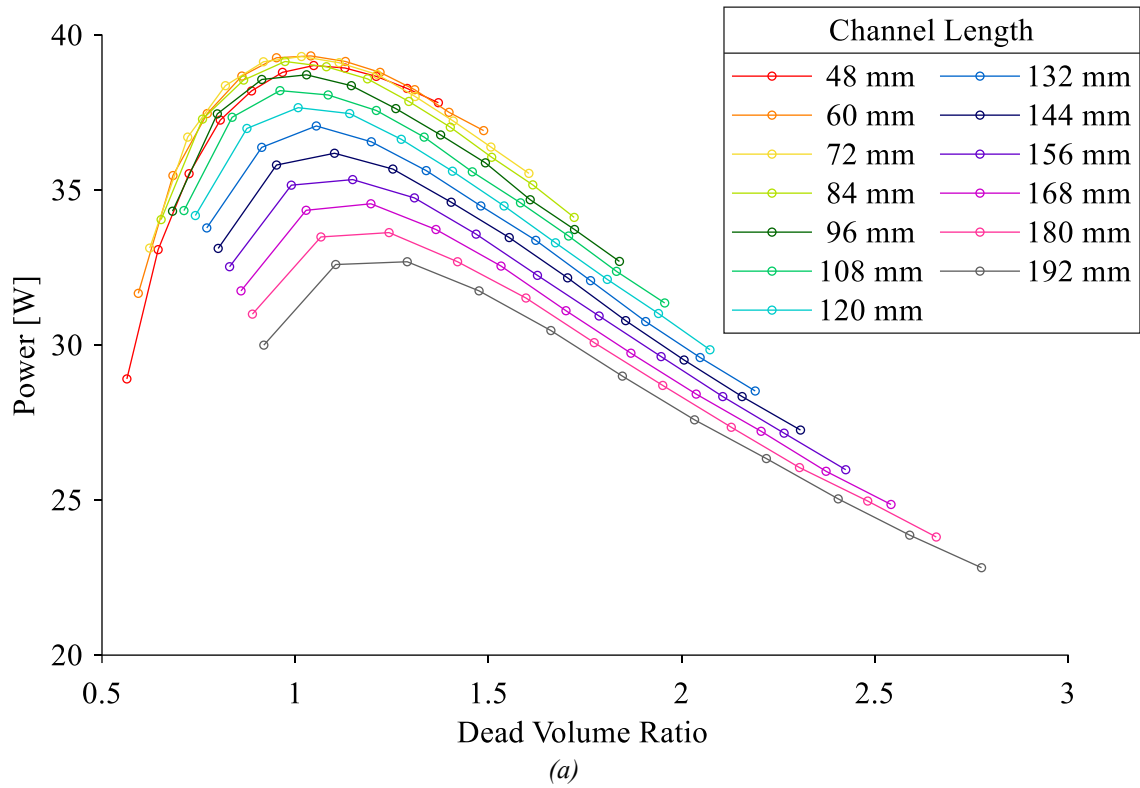


Figure 7.17: Plot of indicated power from Sage with increased additional scaled dead volume against dead volume ratio for (a) various heat exchanger lengths and (b) various numbers of heat exchanger channels.

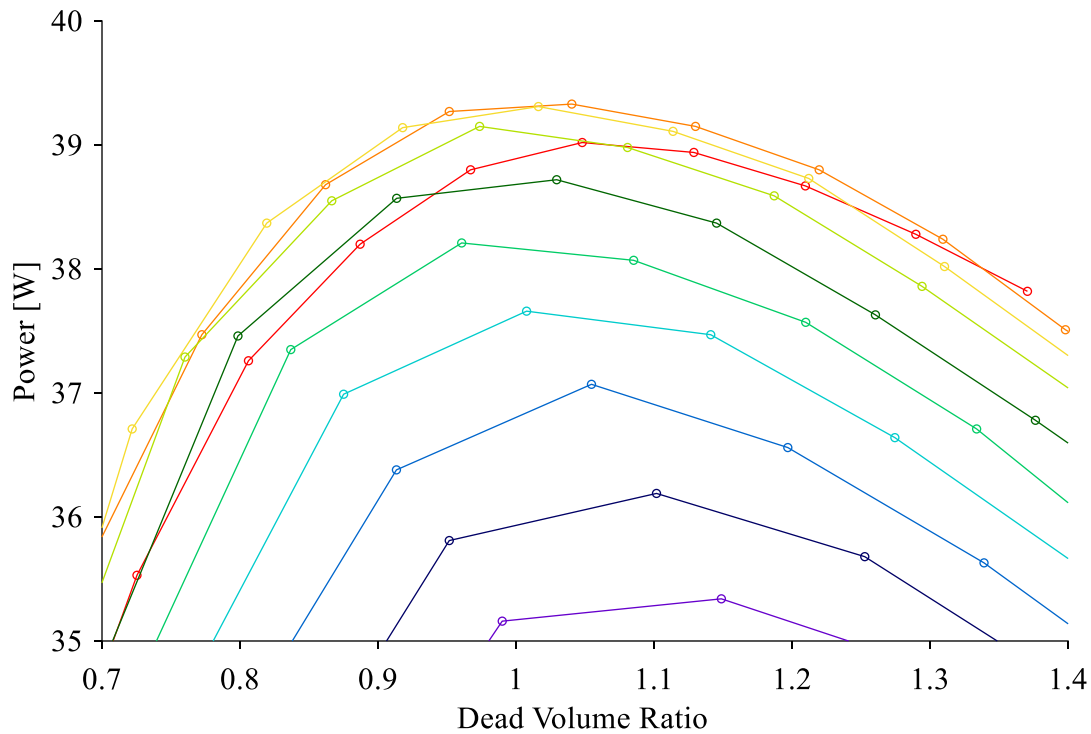


Figure 7.18: Zoomed in plot of indicated power from Sage with increased additional scaled dead volume against dead volume ratio for various heat exchanger lengths.

The importance of considering the physical geometry of the engine and how the heat exchangers are connected is highlighted in this sensitivity. The dead volume ratio of the optimal heat exchanger geometry is higher in this case, as expected with the increased overall dead volume in the engine. The impossible solution of a short and massively wide heat exchanger is not possible in reality due to the detrimental effects of dead volume, which are necessarily present in the physical engine geometry. When selecting a heat exchanger for a LTDSE, the connecting volume for the heat exchangers must be taken into consideration.



## 7.5 Constant Compression Ratio Results

In all the studies considered, all engine volumes other than the heat exchanger volume are held fixed. This results in a change in compression ratio with heat exchanger volume, as the total engine volume is changing. This can be seen in Figure 7.19 which plots the compression ratios of the various heat exchanger geometries considered against dead volume ratio. The compression ratio increases for low dead volume cases and decreases for high dead volume cases. The compression ratio is known to affect the output power of the engine. So, a sensitivity study was undertaken where the compression ratio was held constant at 1.1 by increasing the power piston stroke.

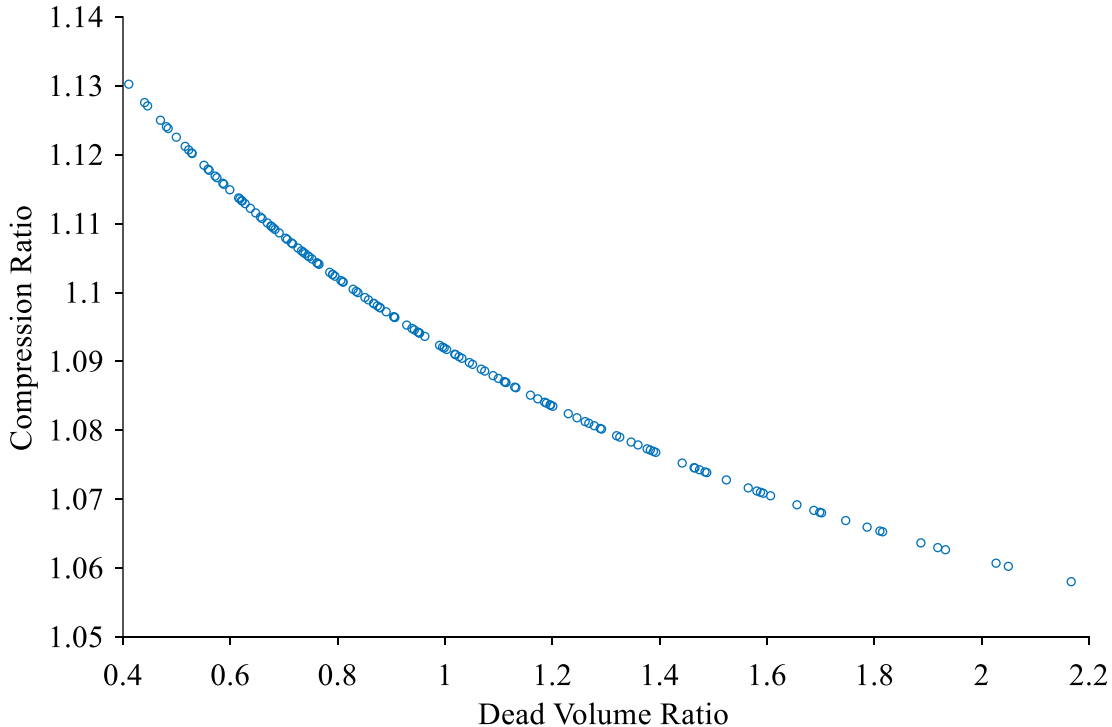


Figure 7.19: Plot of compression ratio against dead volume ratio for base case heat exchanger geometry study.

Figure 7.20 plots the power output against dead volume ratio for varying heat exchanger length and number of channels. Unlike in the case with varying compression ratio, the range of heat exchanger geometries considered is insufficient to determine the maximum power output. This is similar to the behaviour of the high pressure case considered in section 7.3.

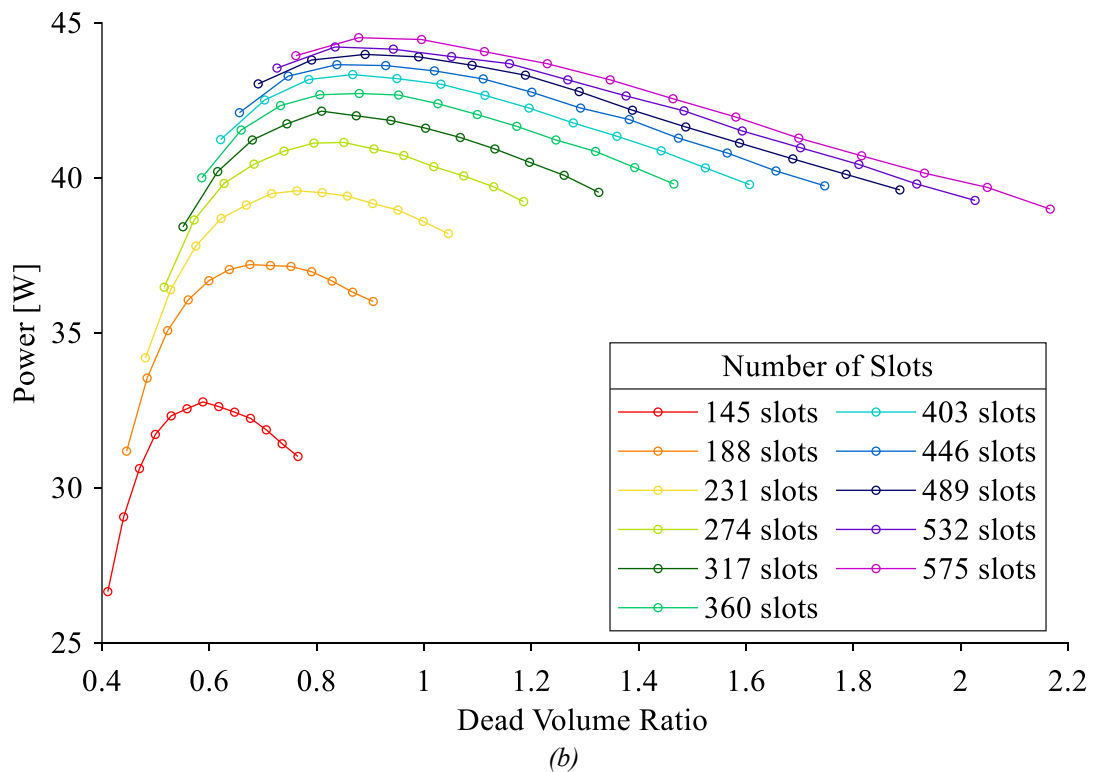
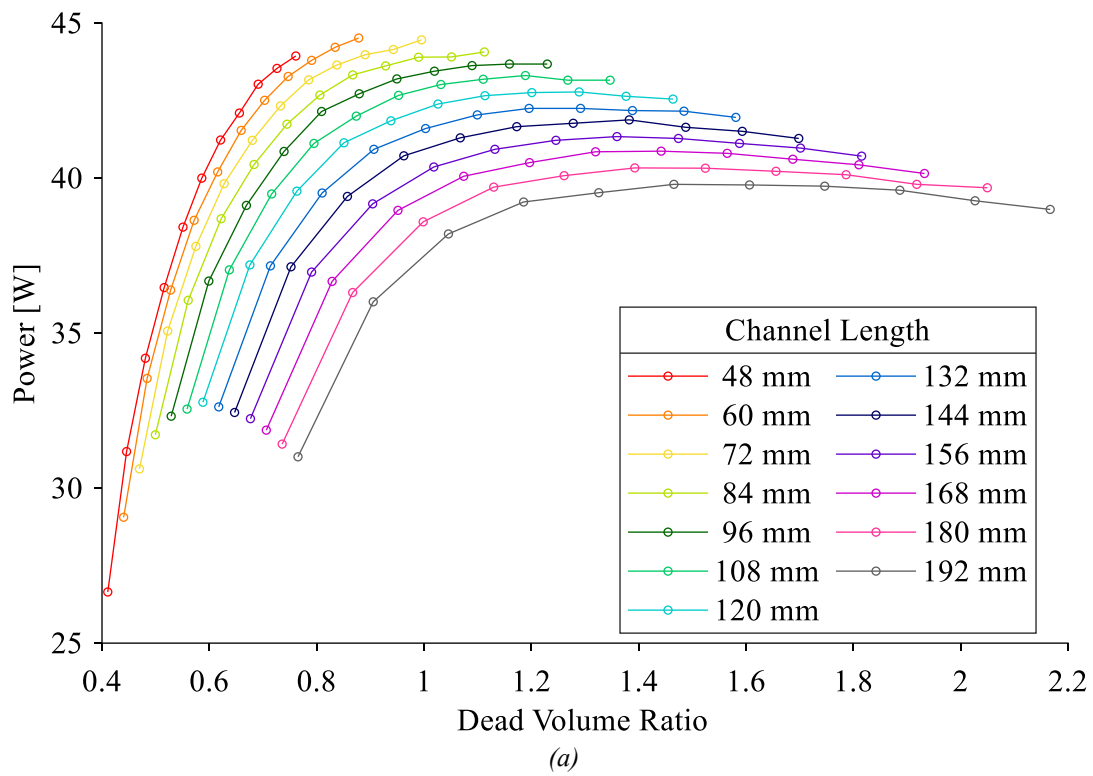


Figure 7.20: Plot of indicated power from Sage with constant compression ratio against dead volume ratio for (a) various heat exchanger lengths and (b) various numbers of heat exchanger channels.

Noting from Figure 7.19 that the compression ratio of 1.1 corresponds to a dead volume ratio of approximately 0.8 in the original study, it can be seen that for cases with a dead volume ratio below 0.8, there is no longer a benefit from the increased compression ratio. So, the same heat exchanger size results in a lower overall power output. On the other side, cases with a dead volume ratio above 0.8 have an increased compression ratio, and have higher output power for the same heat exchanger size. This results in each of the curves of constant heat exchanger length leveling off as opposed to quickly decreasing, and the curve of constant cross-sectional area reduce more linearly as opposed to exponentially. This suggests that the exponential decrease in power output in the original study is due to the exponential decrease in compression ratio, and that additional dead volume leads to a linear decrease in power.

In the plot of average gas temperature difference against dead volume ratio for varying heat exchanger lengths in Figure 7.21, the average gas temperature difference asymptotes to a lower value than in the base case. This is likely a result of the inability of the heat exchangers to keep up with the increased heat transfer requirements caused by higher maximum cycle pressures for the higher dead volume cases with higher compression ratio.

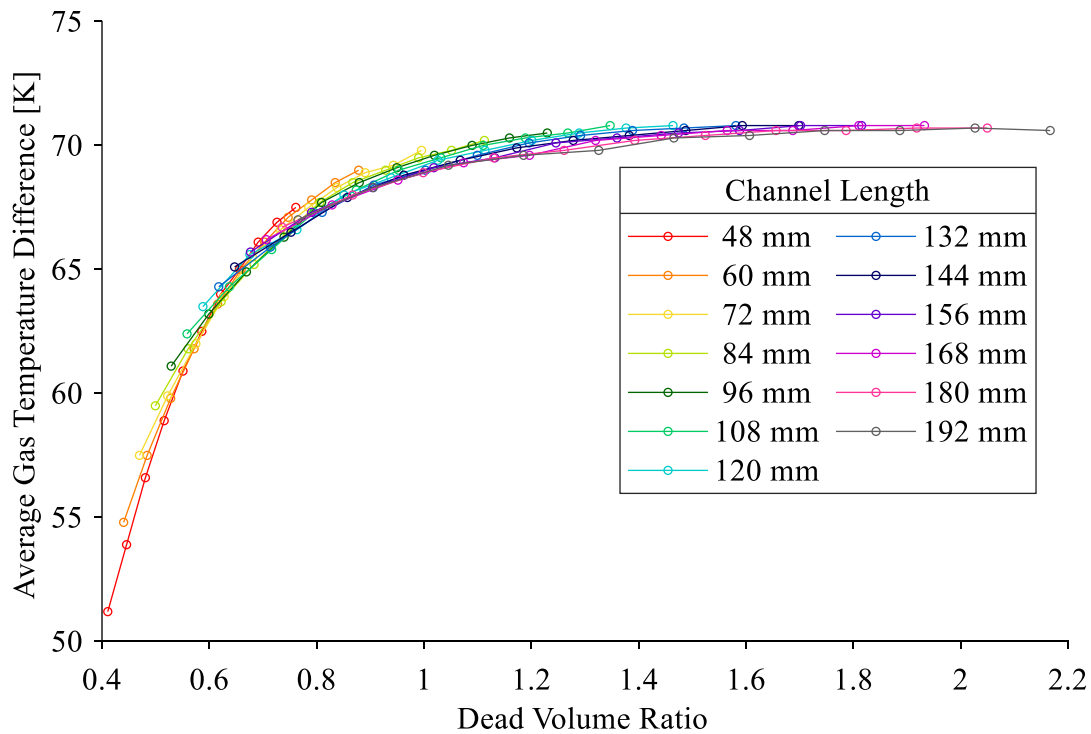


Figure 7.21: Plot of average gas temperature difference between expansion and compression spaces from Sage at constant compression ratio against dead volume ratio for various heat exchanger lengths.

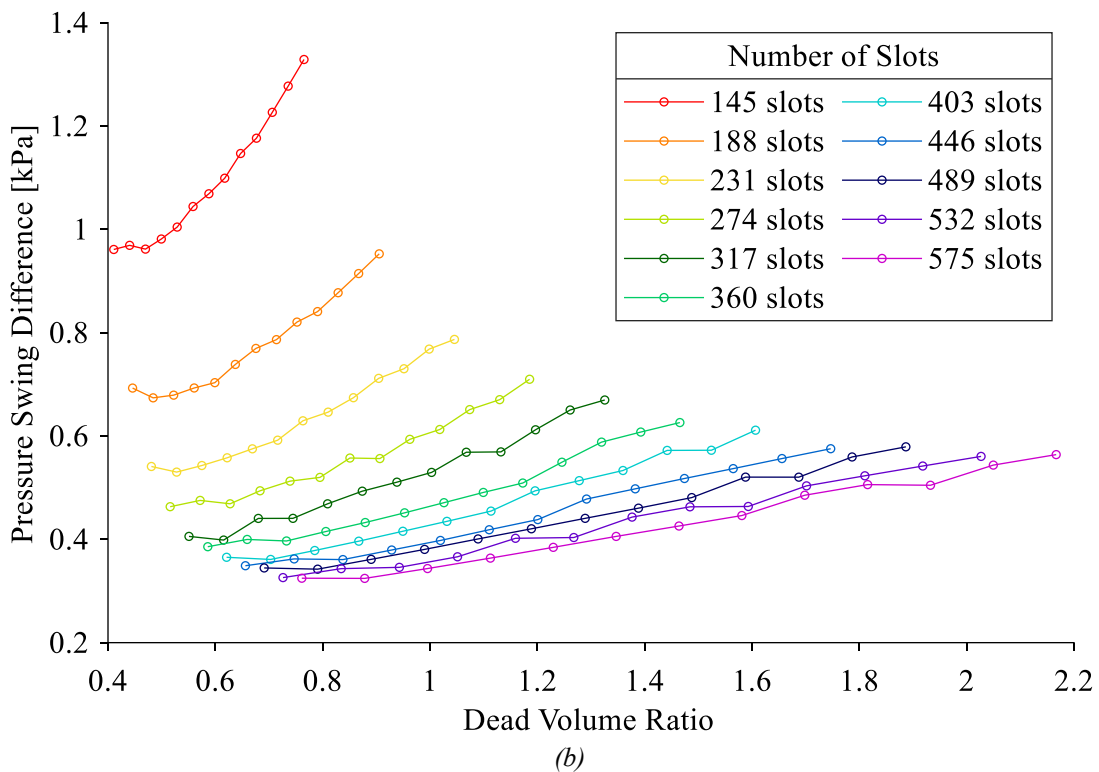
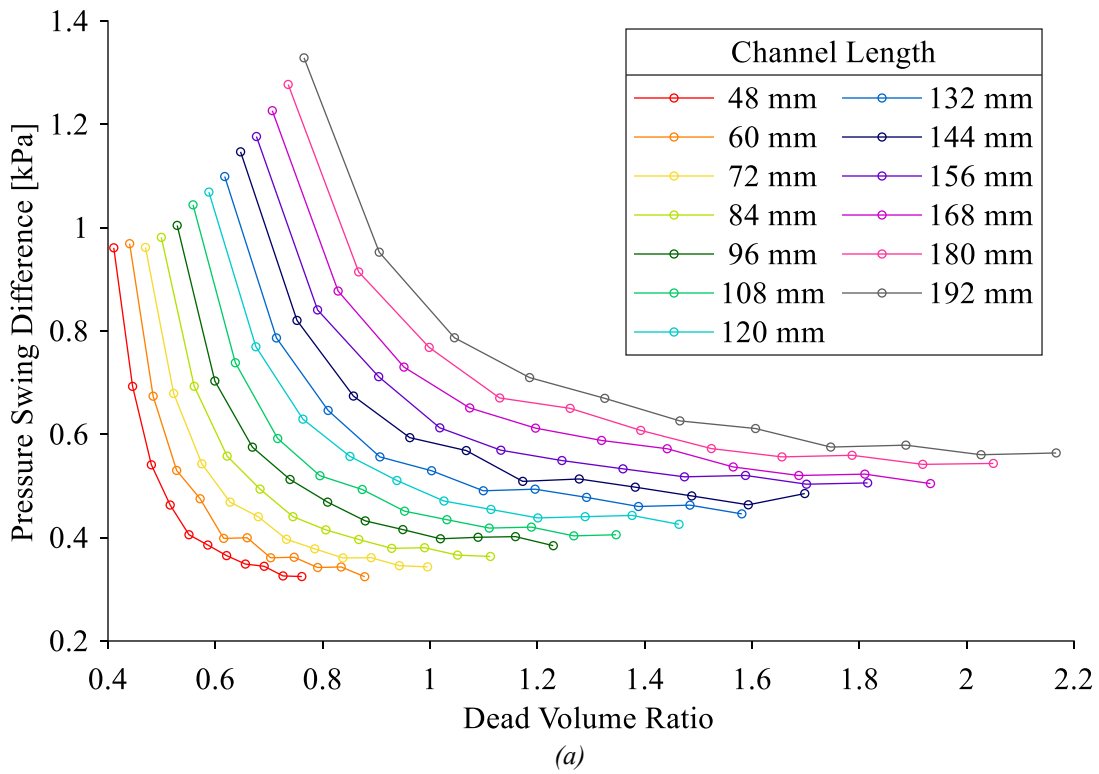


Figure 7.22: Plot of difference in expansion and compression space pressure swings from Sage at constant compression ratio against dead volume ratio for (a) various heat exchanger lengths and (b) various numbers of heat exchanger channels.

Figure 7.22 plots the pressure drop through the heat exchangers for the constant compression ratio case against dead volume ratio for varying heat exchanger length and number of channels. The pressure drop has a stronger dependence on heat exchanger length, again likely resulting from the reduced maximum cycle pressure for low dead volume ratios and increased maximum cycle pressure for high dead volume ratios leading to a reduced pressure drop in the smaller dead volume cases and increased pressure drop in the higher dead volume cases. This is more similar to the results seen in Chapter 3, as the pressure drop still has a dependence on length even at the highest number of heat exchanger channels.

By holding the compression ratio constant the detrimental effects of excess heat exchanger volume can be minimized, which is an important consideration when designing a LTDSE. The piston size and stroke should be determined alongside the heat exchanger size when designing as it will influence the optimum heat exchanger size. A larger sized heat exchanger may be required for a given compression ratio to achieve the optimum power output.

## 7.6 Conclusions

A Sage model of the Raphael engine was used to study the effects of various heat exchanger geometries on engine power output. It was found that the optimal power output occurred at a dead volume ratio below the maximum predicted by the Schmidt model in Chapter 3 for all cases considered, indicating that the Schmidt model is suitable for predicting a maximum bound for heat exchanger size when designing. The optimum heat exchanger geometry was a short heat exchanger with large frontal area, due to the decreased pressure drop through the heat exchangers, which also aligned with the results of Chapter 3.

When varying the engine operating conditions of speed and pressure, it was found that the optimum heat exchanger geometry can vary significantly for different operating conditions. In particular, high pressure and high speed operating conditions require additional heat exchanger volume in order to adequately heat the increased volume of gas passing through the heat exchanger. This indicated the need for considering the desired operating condition for the engine when selecting an optimum heat exchanger.

The issue of the physical connection between the heat exchanger and the engine was also considered with a study that included a plenum dead volume which scaled with the heat exchanger frontal area. In this more realistic study, it was found that there is an optimum heat exchanger length which varies depending on the amount of excess dead volume added with a plenum. The optimum heat exchanger geometry had a lower cross-sectional area, since excess cross-sectional area was penalized with excess dead volume, reducing overall output power.

Finally, the issue of the variable compression ratio present in the previous studies was considered. It was found that when the compression ratio is held constant while selecting the heat exchanger size, a larger heat exchanger size was required than was predicting in the case with variable compression ratio. By eliminating the effect of compression ratio from the results, the decrease in power output was found to vary linearly with excess dead volume as opposed to exponentially. This highlighted the need to select the engine piston size and stroke in conjunction with the heat exchanger volume.

## 8 Conclusions and Future Work

### 8.1 Conclusions

The objective of this thesis was to determine if there is an optimum heat exchanger volume and geometry for maximum power output of a LTDSE. This was investigated for an experimental LTDSE using a variety of models, including steady state analytical and empirical heat transfer analysis, the 1<sup>st</sup> order Stirling engine Schmidt model, a steady state multi-fluid CFD simulation, and the 3<sup>rd</sup> order Stirling engine model Sage.

The steady state analytical and empirical heat transfer analysis investigated the heat exchanger performance of an isothermal surface steady state flow regime for a variety of heat exchanger sizes at different flow conditions. There were two key takeaways from this analysis: that output temperature is directly proportional to heat exchanger surface area, the pressure drop across the heat exchanger increases with increasing heat exchanger length and decreasing cross-sectional area. Additionally, increased engine pressure and speed led to poorer heat exchanger performance, with lower output temperatures and higher pressure drops through the heat exchanger.

The Schmidt model analysis investigated the effect of changing dead volume on the output power of a LTDSE. This analysis confirmed the expectation that as the dead volume increases the output power of the engine will decrease. The Schmidt model was also able to determine the maximum optimal dead volume ratio, below which the optimal dead volume ratio should be located and above which it is impossible to make an additional gain in power. This maximum optimal dead volume ratio of 1.83 to 1.91 was the same across all engine pressures and speeds considered.

The Schmidt model was unable to determine the actual location of the optimum, as it does not model the heat transfer in the heat exchangers. To fill this gap, the 3<sup>rd</sup> order commercial Stirling engine model Sage was used, which discretizes the engine in one dimension and is able to model the heat transfer in the engine at varying operating conditions. A model of the experimental engine was created in Sage. To complete the model, the liquid side of the heat exchangers

needed to be modelled. This was done using a temperature drop in the model, which was determined from a convective heat transfer resistance for the liquid.

To determine the convective heat transfer resistance a multi-fluid CFD study was done at steady state conditions at various engine pressures and speeds for both the heating and cooling case. A mesh independence study was completed to determine the mesh size for the study. Then, the CFD was validated for both the air side and liquid side against an analytical and empirical study. The average convective heat transfer resistance for the entire liquid flow path of the heat exchanger was determined from the multi-fluid study, and was found to not vary significantly with engine pressure or speed as expected. The CFD results had to be reduced to a single parameter due to the one-dimensional nature of the Sage model.

With these CFD results, the Sage model was validated against the experimental results of the experimental LTDSE. The indicated power and work from the model were found to be overpredicted by almost 80% at worst, and the model results had a greater dependence on engine speed than the experimental results. Adjustment of two model parameters was able to improve the model agreement – the convective heat transfer resistance and the friction factor multiplier. The convective heat transfer resistance determined from the CFD was underpredicted for the heating case, so the parameter was tuned to align the expansion and compression space gas temperatures between the model and experiment. This model validation was able to reduce the overprediction of the model to a maximum of approximately 60%, however there was still a significant dependence on engine speed. By reducing the friction factor multiplier by 50% in all the gas spaces in the model, the model dependence on engine speed was reduced. This was a result of the phase of the pressure curve of the engine being changed and reducing the speed dependence on the phase shift. The model with the tuned convective heat transfer resistances was selected for investigating the effect of heat exchanger geometry on output power in Sage.

The heat exchanger length and cross-sectional area were varied over a range of values, and the model results showed that there is an optimum heat exchanger geometry that produces maximum power. The location of the maximum is dependent on the interaction of three factors: the surface area of the heat exchangers, the pressure drop through the heat exchangers, and the dead volume of the heat exchangers. The peak power output occurred for a heat exchanger with a dead volume ratio of 0.76 and a length of 48 mm and 575 channels. The dead volume ratio of the peak power



output was below the maximum optimal dead volume ratio predicted by the Schmidt model. Also, the Sage model agreed with the results of the analytical and empirical steady state study, as the temperature drop across the heat exchangers was directly proportional to the surface area, and the pressure drop across the heat exchangers increased with increased heat exchanger length and decreased heat exchanger cross-sectional area.

Some sensitivity cases were considered in order to evaluate the effect of varying engine operating conditions and varying engine geometry on the optimal heat exchanger geometry. When considering multiple engine pressures and speeds, it was found that the optimum heat exchanger geometry for varying conditions can vary significantly. High pressure and high speed operating conditions have higher heat transfer requirements that required larger heat exchanger geometries. A study was run where additional dead volume that scales with the heat exchangers was added, to represent a plenum that connects the heat exchangers to the engine. With this included in the model, the optimal heat exchanger geometry was slightly longer with smaller heat exchanger cross-sectional area, as the impact of excess dead volume incurred a penalty that was more significant than the pressure drop. Finally, the compression ratio of the engine was held constant by changing the power piston stroke. By eliminating the impact of compression ratio on the results, the power output varied linearly with dead volume ratio for heat exchanger with excess dead volume, as opposed to exponentially. The constant compression ratio case required a larger heat exchanger size. These studies highlighted the need to consider the desired engine operating conditions and the engine geometry – the connection to the heat exchangers and the piston swept volumes – when designing LTDSEs.

## 8.2 Future Work

The 3<sup>rd</sup> order model Sage showed that there is an optimum heat exchanger geometry which produces peak power output, and it generally tends to have a short length with high cross-sectional area. This result was expected based on the fundamental analysis at steady state. To better validate the model result, additional tuning of the Sage model with the experimental LTDSE results can be done. This may require improved instrumentation of the engine to ensure that all the engine losses are captured in the results. The steady state CFD study of the engine heat exchangers would benefit from experimental verification on a steady state flow rig, which is in progress at the time of writing. Finally, determination of the optimal heat exchanger geometry experimentally would verify the correctness of the model results and provide confidence in using a 3<sup>rd</sup> order model for sizing LTDSE heat exchangers. This could be done by way of an externally mounted heat exchanger setup on a LTDSE, which allows for varying heat exchanger sizes.

Further investigation using different channel geometry or heat exchanger types would also be of interest. These may yield improved performance at a lower dead volume due to the different surface area and flow conditions through the heat exchanger. Further investigation of the optimal heat exchanger geometry for different engine geometries and operating conditions would be beneficial. Different engine geometries include different engine scale, piston geometry, and flow connections, and different engine operating conditions include different heater and cooler temperatures or resistances, and a different working fluid, for example helium. These different conditions would have different relationships between the parameters affecting the heat exchanger selection, including flow friction, gas temperature, and pressure swing. By investigating these cases, more generalized heat exchanger design advice for LTDSEs could be determined.

## References

- [1] International Energy Agency, “Electricity Market Report - July 2022,” Jul. 2022. Accessed: Sep. 03, 2022. [Online]. Available: <https://iea.blob.core.windows.net/assets/660c2410-218c-4145-9348-c782e185dcdf/ElectricityMarketReport-July2022.pdf>
- [2] International Energy Agency, “Key World Energy Statistics 2021,” Statistics Report, Sep. 2021. [Online]. Available: <https://iea.blob.core.windows.net/assets/52f66a88-0b63-4ad2-94a5-29d36e864b82/KeyWorldEnergyStatistics2021.pdf>
- [3] International Energy Agency, “Energy Statistics Data Browser,” *Data Tools*, Aug. 19, 2022. <https://www.iea.org/data-and-statistics/data-tools/energy-statistics-data-browser> (accessed Sep. 03, 2022).
- [4] Canada Energy Regulator, “Canada’s Energy Future 2021 - Energy Supply and Demand Projections to 2050,” Government of Canada, May 2022. [Online]. Available: <https://www.cer-rec.gc.ca/en/data-analysis/canada-energy-future/2021/canada-energy-futures-2021.pdf>
- [5] Canada Energy Regulator, “Canada’s Energy Future Data Appendices.” Government of Canada, 2019. doi: 10.35002/ZJR8-8X75.
- [6] J. D. Hughes, *Canada’s Energy Outlook: Current realities and implications for a carbon-constrained future*. Parkland Institute, 2018. [Online]. Available: [https://energyoutlook.ca/wp-content/uploads/2018/05/cmp\\_canadas-energy-outlook-2018\\_full.pdf](https://energyoutlook.ca/wp-content/uploads/2018/05/cmp_canadas-energy-outlook-2018_full.pdf)
- [7] Natural Resources Canada, “Community Integrated Energy Mapping Feasibility Study in Alberta’s Industrial Heartland and Strathcona Industrial Area,” Government of Canada, May 2014. Accessed: Aug. 19, 2021. [Online]. Available: <https://www.nrcan.gc.ca/science-and-data/funding-partnerships/funding-opportunities/current-investments/community-integrated-energy-mapping-feasibility-study-gateway-albertas-energy-demand/16067>
- [8] J. Banks, “Deep-Dive Analysis of the Best Geothermal Reservoirs for Commercial Development in Alberta: Final Report,” University of Alberta, 2018. [Online]. Available: [https://www.cangea.ca/uploads/3/0/9/7/30973335/2288\\_deep\\_dive\\_analysis\\_of\\_best\\_geothermal\\_reservoirs\\_for\\_commercial\\_development\\_in\\_alberta\\_-\\_final\\_report\\_20170404.pdf](https://www.cangea.ca/uploads/3/0/9/7/30973335/2288_deep_dive_analysis_of_best_geothermal_reservoirs_for_commercial_development_in_alberta_-_final_report_20170404.pdf)
- [9] S. Carnot, *Reflections on the Motive Power of Heat*, 2nd ed. John Wiley & Sons, 1897.

- [10] S. Quoilin, “Sustainable Energy Conversion Through the Use of Organic Rankine Cycles for Waste Heat Recovery and Solar Applications,” University of Liège, Belgium, 2011. [Online]. Available: <https://hdl.handle.net/2268/96436>
- [11] A. J. Organ, *Thermodynamics and Gas Dynamic of the Stirling Cycle Machine*. Cambridge University Press, 1992.
- [12] R. Stirling, “Improvements for Diminishing the Consumption of Fuel, and in Particular an Engine Capable of Being Applied to the Moving of Machinery on a Principle Entirely New,” 4081, Jan. 20, 1817
- [13] U. R. Singh and A. Kumar, “Review on solar Stirling engine: Development and performance,” *Therm. Sci. Eng. Prog.*, vol. 8, pp. 244–256, Dec. 2018, doi: 10.1016/j.tsep.2018.08.016.
- [14] K. Wang, S. R. Sanders, S. Dubey, F. H. Choo, and F. Duan, “Stirling cycle engines for recovering low and moderate temperature heat: A review,” *Renew. Sustain. Energy Rev.*, vol. 62, pp. 89–108, Sep. 2016, doi: 10.1016/j.rser.2016.04.031.
- [15] I. Kolin, S. Koscak-Kolin, and M. Golub, “Geothermal Electricity Production by Means of the Low Temperature Difference Stirling Engine,” in *Proceedings World Geothermal Congress 2000*, Kyushu - Tohoku, Japan, May 2000, p. 6. [Online]. Available: <https://www.geothermal-energy.org/pdf/IGAstandard/WGC/2000/R0856.PDF>
- [16] L.-L. Lemaire, “Miniaturized Stirling Engines for Waste Heat Recovery,” McGill University, Montréal, Canada, 2012. [Online]. Available: <https://escholarship.mcgill.ca/downloads/zc77sv05x>
- [17] J. R. Senft, “Mechanical Efficiency Considerations in the Design of an Ultra Low Temperature Differential Stirling Engine,” in *27th Intersociety Energy Conversion Engineering Conference*, San Diego, California, Aug. 1992, vol. 5, p. 259.
- [18] I. Kolin, *Stirling Motor: History, Theory, Practice*. Dubrovnik: Zagreb University Publications, 1991.
- [19] G. Walker, *Stirling-cycle Machines*. University of Calgary, Canada: Clarendon Press, Oxford, 1973.
- [20] I. Urieli and D. M. Berchowitz, *Stirling Cycle Engine Analysis*. Adam Hilger Ltd, 1984.
- [21] Y. A. Çengel and M. A. Boles, *Thermodynamics: An Engineering Approach*, 8th ed. McGraw-Hill Education, 2015.

- [22] J. Egas and D. M. Clucas, “Stirling Engine Configuration Selection,” *Energies*, vol. 11, no. 3, p. 584, Mar. 2018, doi: 10.3390/en11030584.
- [23] I. Woerlen, “The Stirling Engine of 1816,” *Hot Air Engines*.  
<http://hotairengines.org/closed-cycle-engine/stirling-1816> (accessed Jul. 25, 2022).
- [24] N. Boutammachte and J. Knorr, “Field-test of a solar low delta-T Stirling engine,” *Sol. Energy*, vol. 86, no. 6, pp. 1849–1856, Jun. 2012, doi: 10.1016/j.solener.2012.03.001.
- [25] J. R. Senft, *Mechanical Efficiency of Heat Engines*. University of Wisconsin–River Falls: Cambridge University Press, 2007. doi: 10.1017/CBO9780511546105.
- [26] B. Hoegel, “Thermodynamics-Based Design of Stirling Engines for Low-Temperature Heat Sources,” University of Canterbury, 2014. Accessed: Aug. 17, 2021. [Online]. Available: <https://ir.canterbury.ac.nz/handle/10092/9344>
- [27] M. Gschwendtner and G. Bell, “The Myth About Dead Volume in Stirling Engines,” *Proc. Inst. Mech. Eng. Part C J. Mech. Eng. Sci.*, vol. 231, no. 19, pp. 3665–3675, Oct. 2017, doi: 10.1177/0954406216651303.
- [28] W. R. Martini, *Stirling Engine Design Manual*. University of Washington: U.S. Department of Energy, Office of Conservation and Solar Applications, Division of Transportation Energy Conservation, 1978.
- [29] W. R. Martini, *Stirling Engine Design Manual*, 2nd ed. Washington: U.S. Department of Energy, Conservation and Renewable Energy, Office of Vehicle and Engine R&D, 1983.
- [30] N. C. J. Chen and F. P. Griffin, “A Review of Stirling Engine Mathematical Models,” Oak Ridge National Laboratory, Springfield, Virginia, ORNL/CON-135, Aug. 1983.
- [31] C. D. West, *Principles and Applications of Stirling Engines*. Oliver Springs, Tennessee: Van Nostrand Reinhold Company, 1986.
- [32] G. Schmidt, “Theory of Lehmann’s Heat Machine,” *J. Ger. Eng. Union*, vol. 15, no. 1,2, pp. 1–12, 1871.
- [33] T. Finkelstein, “Cyclic Processes in Closed Regenerative Gas Machines Analyzed by a Digital Computer Simulating a Differential Analyzer,” *J. Eng. Ind.*, vol. 84, no. 1, pp. 165–178, Feb. 1962, doi: 10.1115/1.3667408.
- [34] S. K. Andersen, H. Carlsen, and P. G. Thomsen, “Preliminary results from simulations of temperature oscillations in Stirling engine regenerator matrices,” *Energy*, vol. 31, no. 10–11, pp. 1371–1383, Aug. 2006, doi: 10.1016/j.energy.2005.05.008.

- [35] S. Kildegård Andersen, “Numerical simulation of cyclic thermodynamic processes,” Technical University of Denmark, Department of Mechanical Engineering, Lyngby, 2006.
- [36] F. J. Garcia-Granados, M. A. Silva-Perez, J.-I. Prieto, and D. Garcia, “Validation of a Stirling engine thermodynamic simulation program,” presented at the 14th International Stirling Engine Conference, Netherlands, 2009.
- [37] Mesonero I., López S., García-Granados F. J., Jiménez-Espadafor F. J., García D., and Prieto J.I., “Characterization and Simulation of a restored V160 Stirling Engine,” presented at the 16th International Stirling Engine Conference and Exhibition, Spain, 2014.
- [38] S. M. W. Middleton, “Stirling Engines and Single-Phase Thermodynamic Machines,” University of Alberta, Edmonton, Alberta, Canada, 2021.
- [39] D. Gedeon, “Sage: Object Oriented Software for Stirling Machine Design,” presented at the Intersociety Energy Conversion Engineering Conference, Monterey, CA, USA, Aug. 1994. doi: 10.2514/6.1994-4106.
- [40] D. Gedeon, “History,” *Sage*. <http://www.sageofathens.com/history.php> (accessed Jan. 14, 2022).
- [41] M. Ibrahim, “2-D CFD simulation of the heat transfer and fluid dynamics in an experimental model of the hot end of a stirling engine,” in *2012 IEEE Energytech*, Cleveland, OH, USA, May 2012, pp. 1–11. doi: 10.1109/EnergyTech.2012.6304662.
- [42] S. Alfarawi, R. AL-Dadah, and S. Mahmoud, “Influence of Phase Angle and Dead Volume on Gamma-Type Stirling Engine Power Using CFD Simulation,” *Energy Convers. Manag.*, vol. 124, pp. 130–140, Sep. 2019, doi: 10.1016/j.enconman.2016.07.016.
- [43] S. Alfarawi, R. AL-Dadah, and S. Mahmoud, “Potentiality of New Miniature-Channels Stirling Regenerator,” *Energy Convers. Manag.*, vol. 133, pp. 264–274, Feb. 2017, doi: 10.1016/j.enconman.2016.12.017.
- [44] K. Mahkamov, “An Axisymmetric Computational Fluid Dynamics Approach to the Analysis of the Working Process of a Solar Stirling Engine,” *J. Sol. Energy Eng.*, vol. 128, no. 1, pp. 45–53, Feb. 2006, doi: 10.1115/1.2148979.
- [45] C. P. Speer, “Modifications to Reduce the Minimum Thermal Source Temperature of the ST05G-CNC Stirling Engine,” University of Alberta, Edmonton, Alberta, Canada, 2018.

- [46] M. Lottmann, “Scaling Up Low Temperature Difference Stirling Engines: Validation and Testing of a Numerical Model and Design of an Experimental Setup,” University of Alberta, 2022.
- [47] S. Viebach and H. Eckl, “The ST05G Stirling Engine Project,” *ve-ingenieure*, Dec. 30, 2017. [https://web.archive.org/web/20171230195025/http://www.ve-ingenieure.de:80/projekt\\_st05g\\_cnc\\_engl.html](https://web.archive.org/web/20171230195025/http://www.ve-ingenieure.de:80/projekt_st05g_cnc_engl.html) (accessed Jan. 11, 2022).
- [48] S. Viebach and H. Eckl, “ST05G Technical Specifications,” Mar. 05, 2012. <https://web.archive.org/web/20120305023128/http://www.ve-ingenieure.de/viebachstirling/index.htm> (accessed Jan. 11, 2022).
- [49] R. Gheith, F. Aloui, M. Tazerout, and S. B. Nasrallah, “Experimental Investigations of a Gamma Stirling Engine,” *Int. J. Energy Res.*, vol. 36, no. 12, pp. 1175–1182, 2012, doi: 10.1002/er.1872.
- [50] R. Gheith, F. Aloui, and S. Ben Nasrallah, “Study of the regenerator constituting material influence on a gamma type Stirling engine,” *J. Mech. Sci. Technol.*, vol. 26, no. 4, pp. 1251–1255, Apr. 2012, doi: 10.1007/s12206-012-0218-9.
- [51] R. Gheith, F. Aloui, and S. Ben Nasrallah, “Determination of Adequate Regenerator for a Gamma-Type Stirling Engine,” *Appl. Energy*, vol. 139, pp. 272–280, Feb. 2015, doi: 10.1016/j.apenergy.2014.11.011.
- [52] R. Gheith, H. Hachem, F. Aloui, and S. Ben Nasrallah, “Experimental and Theoretical Investigation of Stirling Engine Heater: Parametrical Optimization,” *Energy Convers. Manag.*, vol. 105, pp. 285–293, Nov. 2015, doi: 10.1016/j.enconman.2015.07.063.
- [53] R. Gheith, H. Hachem, F. Aloui, and S. Ben Nasrallah, “Experimental and Theoretical Investigation of Flows Inside a Gamma Stirling Engine Regenerator,” in *Exergy for A Better Environment and Improved Sustainability 1: Fundamentals*, F. Aloui and I. Dincer, Eds. Springer International Publishing, 2018, pp. 383–395. doi: 10.1007/978-3-319-62572-0\_27.
- [54] H. Hachem, R. Gheith, F. Aloui, and S. Ben Nasrallah, “Experimental Study of the Operation Conditions of Stability on a Gamma Stirling Engine,” presented at the ASME 2016 Fluids Engineering Division Summer Meeting, Washington, DC, USA, Jul. 2016. doi: 10.1115/FEDSM2016-7912.
- [55] H. Hachem, R. Gheith, F. Aloui, and S. Ben Nasrallah, “Numerical Characterization of a  $\gamma$ -Stirling Engine Considering Losses and Interaction Between Functioning Parameters,”

- Energy Convers. Manag.*, vol. 96, pp. 532–543, May 2015, doi: 10.1016/j.enconman.2015.02.065.
- [56] J. Bert, D. Chrenko, T. Sophy, L. Le Moyne, and F. Sirot, “Simulation, Experimental Validation and Kinematic Optimization of a Stirling Engine Using Air and Helium,” *Energy*, vol. 78, pp. 701–712, Dec. 2014, doi: 10.1016/j.energy.2014.10.061.
- [57] S. Alfarawi, R. AL-Dadah, and S. Mahmoud, “Enhanced Thermodynamic Modelling of a Gamma-type Stirling Engine,” *Appl. Therm. Eng.*, vol. 106, pp. 1380–1390, Aug. 2016, doi: 10.1016/j.applthermaleng.2016.06.145.
- [58] C. Speer, “Personal Communication.”
- [59] Omega Engineering, “RTD vs Thermocouples.” <https://www.omega.com/en-us/resources/rtd-vs-thermocouple> (accessed Mar. 23, 2022).
- [60] Omega Engineering, “Thermocouple Response Time.” <https://www.omega.ca/en/resources/thermocouples-response-time> (accessed May 27, 2022).
- [61] F. M. White, *Fluid Mechanics*, 4th ed. WCB/McGraw-Hill, 1999.
- [62] R. B. Bird, W. E. Stewart, and E. N. Lightfoot, *Transport Phenomena*, 2nd ed. J. Wiley, 2002.
- [63] Y. A. Çengel and A. J. Ghajar, *Heat and Mass Transfer: Fundamentals & Applications*, 5th ed. McGraw Hill Education, 2015.
- [64] W. M. Kays and M. E. Crawford, *Convective Heat and Mass Transfer*, 2nd ed. McGraw-Hill, 1980.
- [65] D. K. Edwards, V. E. Denny, and A. F. Mills, *Transfer Processes: An Introduction to Diffusion, Convection, and Radiation*, 2nd ed. Hemisphere Publishing Corp., 1979.
- [66] V. Gnielinski, “New Equations For Heat And Mass Transfer In Turbulent Flow Through Pipes And Ducts,” *Forsch. Im Ingenieurwesen*, vol. 41, no. 1, pp. 8–16, 1975.
- [67] Y. A. Çengel and J. M. Cimbala, *Fluid Mechanics: Fundamentals and Applications*, Third edition. New York: McGraw Hill, 2014.
- [68] D. Gedeon, “Sage User’s Guide: Stirling, Pulse-Tube and Low-T Cooler Model Classes.” Jan. 04, 2016.
- [69] K. B. Wilson, “The Use of Sage Simulation Software in the Design and Testing of Sunpower’s Pulse Tube Cryocooler,” Ohio University, 2005.



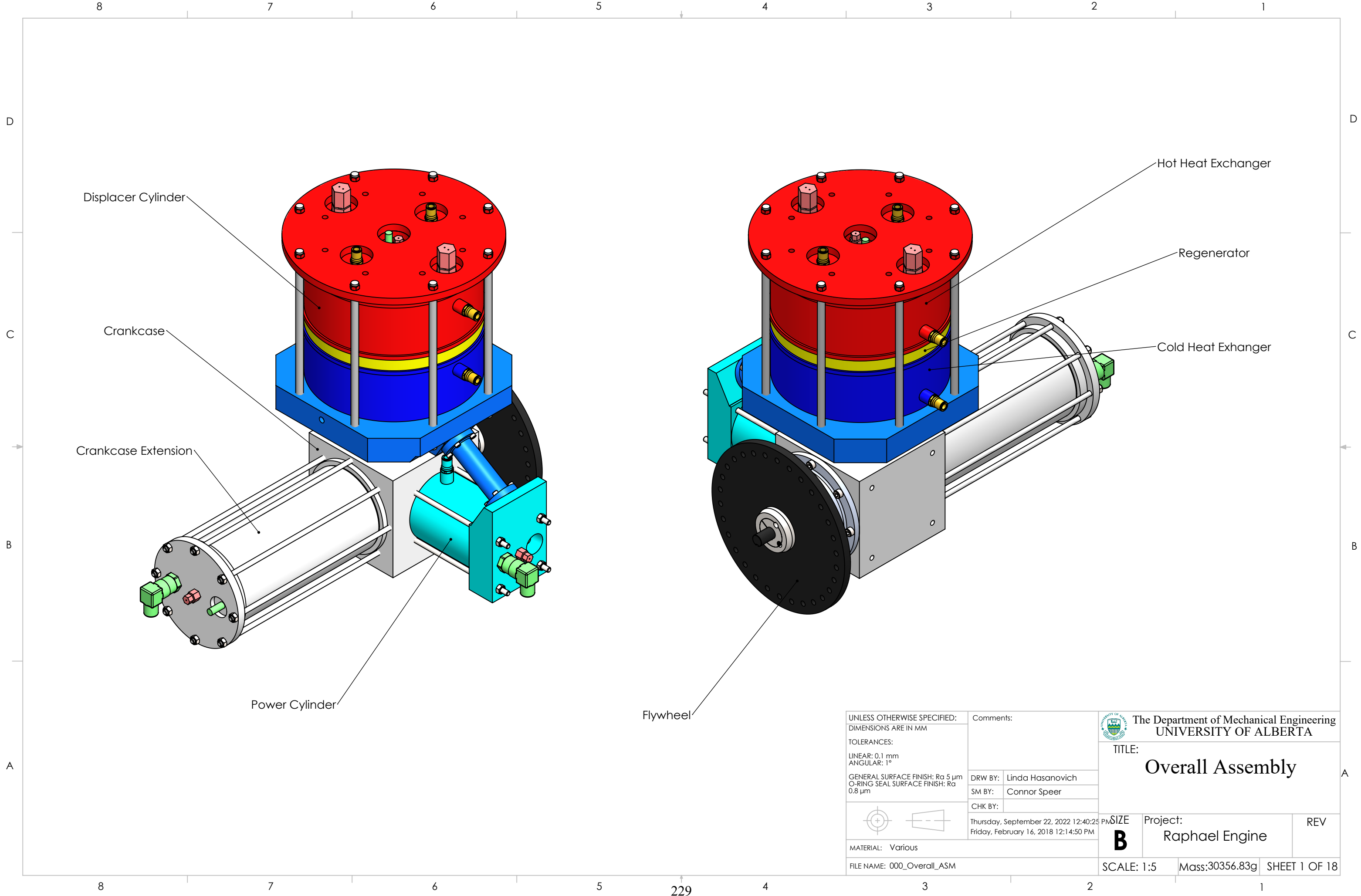
- [70] R. Demko and L. B. Penswick, "Sage Simulation Model for Technology Demonstration Convertor by a Step-by-Step Approach," presented at the 3rd International Energy Conversion Engineering Conference, Middleburg Heights, Ohio, Aug. 2005. doi: 10.2514/6.2005-5538.
- [71] "Science Missions Directorate Technology Highlights," National Aeronautics and Space Administration, 2016. Accessed: Jul. 11, 2022. [Online]. Available: [https://smd-prod.s3.amazonaws.com/science-red/s3fs-public/atoms/files/NASA\\_2016SMD\\_Report\\_final\\_highres.pdf](https://smd-prod.s3.amazonaws.com/science-red/s3fs-public/atoms/files/NASA_2016SMD_Report_final_highres.pdf)
- [72] J. F. Metscher, "Free-Piston Stirling Convertor Model Development, Validation, and Analysis for Space Power Systems," Embry-Riddle Aeronautical University, Daytona Beach, 2014.
- [73] G. A. Landis and K. C. Mellott, "Venus surface power and cooling systems," *Acta Astronaut.*, vol. 61, no. 11–12, pp. 995–1001, Dec. 2007, doi: 10.1016/j.actaastro.2006.12.031.
- [74] S. Qiu, Y. Gao, G. Rinker, and K. Yanaga, "Development of an Advanced Free-Piston Stirling Engine for Micro Combined Heating and Power Application," *Appl. Energy*, vol. 235, pp. 987–1000, Feb. 2019, doi: 10.1016/j.apenergy.2018.11.036.
- [75] B. Hoegel, D. Pons, M. Gschwendtner, A. Tucker, and M. Sellier, "Thermodynamic Peculiarities of Alpha-Type Stirling Engines for Low-Temperature Difference Power Generation: Optimisation of Operating Parameters and Heat Exchangers Using a Third-Order Model," *Inst. Mech. Eng. Part C J. Mech. Eng. Sci.*, vol. 228, no. 11, pp. 1936–1947, Aug. 2014, doi: 10.1177/0954406213512120.
- [76] W. Zhao, R. Li, H. Li, Y. Zhang, and S. Qiu, "Numerical Analysis of Fluid Dynamics and Thermodynamics in a Stirling Engine," *Appl. Therm. Eng.*, vol. 189, May 2021, doi: 10.1016/j.applthermaleng.2021.116727.
- [77] G. Xiao *et al.*, "An Approach to Combine the Second-Order and Third-Order Analysis Methods for Optimization of a Stirling Engine," *Energy Convers. Manag.*, vol. 165, pp. 447–458, Jun. 2018, doi: 10.1016/j.enconman.2018.03.082.
- [78] R. Peyret and T. D. Taylor, *Computational Methods for Fluid Flow*. Springer-Verlag, 1983. doi: 10.1007/978-3-642-85952-6.

- [79] P. K. Kundu, I. M. Cohen, and H. H. Hu, *Fluid Mechanics*, 2nd ed. San Diego: Elsevier Science Publishers, 2002.
- [80] D. A. Miller, “Experimental Investigation of Stirling Engine Modelling Techniques at Reduced Source Temperatures,” University of Alberta, Edmonton, Alberta, Canada, 2019.
- [81] M. Everts and J. P. Meyer, “Relationship Between Pressure Drop and Heat Transfer of Developing and Fully Developed Flow in Smooth Horizontal Circular Tubes in the Laminar, Transitional, Quasi-Turbulent and Turbulent Flow Regimes,” *Int. J. Heat Mass Transf.*, vol. 117, pp. 1231–1250, Feb. 2018, doi: 10.1016/j.ijheatmasstransfer.2017.10.072.
- [82] M. Lottmann *et al.*, “Early Development of a 100 Watt Low Temperature Difference Stirling Engine,” in *Progress in Canadian Mechanical Engineering*, Charlottetown, PEI, Canada, Jun. 2021, p. 6. doi: 10.32393/csme.2021.193.
- [83] M. Lottmann *et al.*, “Development of a 100-Watt-Scale Beta-Type Low Temperature Difference Stirling Engine Prototype,” in *19th International Stirling Engine Conference*, Rome, Italy, Sep. 2021, p. 15. doi: <https://doi.org/10.1051/e3sconf/202131308004>.
- [84] C. J. A. Stumpf, “Parameter Optimization of a Low Temperature Difference Gamma-Type Stirling Engine to Maximize Shaft Power,” University of Alberta, Edmonton, Alberta, Canada, 2019. doi: 10.7939/r3-jb09-7t31.
- [85] G. B. Arfken, H.-J. Weber, and F. E. Harris, *Mathematical Methods for Physicists*, 7th ed. Elsevier Science Publishers, 2012.
- [86] H. B. Dwight, *Tables of Integrals and Other Mathematical Data*, 4th ed. The Macmillan Company, 1961.
- [87] M. Hossfeld and E. Roos, “A New Approach to Modelling Friction Stir Welding Using the CEL Method,” in *Proceedings of the International Conference on Advanced Manufacturing Engineering and Technologies NEWTECH 2013*, Stockholm, Sweden, Oct. 2013, vol. 2, p. 12. doi: 10.18419/OPUS-8825.
- [88] M. Sedighi, D. Afshari, and F. Nazari, “Investigation of the Effect of Sheet Thickness on Residual Stresses in Resistance Spot Welding of Aluminum Sheets,” *Proc. Inst. Mech. Eng. Part C J. Mech. Eng. Sci.*, vol. 232, no. 4, pp. 621–638, Feb. 2018, doi: 10.1177/0954406216685124.

- [89] “Aluminum 6061-T6; 6061-T651,” *Material Property Data*.  
<https://www.matweb.com/search/DataSheet.aspx?MatGUID=b8d536e0b9b54bd7b69e4124d8f1d20a&ckck=1> (accessed Jul. 18, 2022).
- [90] “Material Properties of Thermoplastic Ultem – Polyetherimide, PEI,” *Dielectric Manufacturing*, Feb. 27, 2019. <https://dielectricmfg.com/knowledge-base/ultem/> (accessed Jul. 18, 2022).
- [91] “Thermal Properties of Plastic Materials.” Professional Plastics. Accessed: Jul. 18, 2022. [Online]. Available:  
<https://www.professionalplastics.com/professionalplastics/ThermalPropertiesofPlasticMaterials.pdf>
- [92] “LAST-A-FOAM® FR-4700 Rigid Polyurethane Foam.” General Plastics Manufacturing Company, Aug. 30, 2019.
- [93] “Thermal insulation materials made of rigid polyurethane foam (PUR/PIR): Properties - Manufacture.” Federation of European Rigid Polyurethane Foam Associations, Oct. 2006. Accessed: Jul. 18, 2022. [Online]. Available: [http://highperformanceinsulation.eu/wp-content/uploads/2016/08/Thermal\\_insulation\\_materials\\_made\\_of\\_rigid\\_polyurethane\\_foam.pdf](http://highperformanceinsulation.eu/wp-content/uploads/2016/08/Thermal_insulation_materials_made_of_rigid_polyurethane_foam.pdf)
- [94] “Syltherm 800 Heat Transfer Fluid: Product Data.” The DOW Chemical Company. Accessed: Jul. 18, 2022. [Online]. Available:  
<https://www.npl.washington.edu/TRIMS/sites/sand.npl.washington.edu/TRIMS/files/manuals-documentation/syltherm-800-product-brochure.pdf>
- [95] “Ethylene Glycol Product Guide.” ME Global, Sep. 12, 2013. Accessed: Jul. 18, 2022. [Online]. Available: <https://www.meglobal.biz/wp-content/uploads/2019/01/Monoethylene-Glycol-MEG-Technical-Product-Brochure-PDF.pdf>

## **Appendix A Raphael Engine Drawing Package**

The drawing package presented contains high-level assembly drawings of the Raphael engine to provide dimensions and a detailed orthogonal view of the assembly. Orthogonal section views of the heat exchanger assembly and a detailed part drawing of the heat exchanger cartridge containing the finned channels is also included as the focus is on the heat exchangers.



Displacer Cylinder

Crankcase

Crankcase Extension

Power Cylinder


Flywheel

Hot Heat Exchanger

Regenerator

Cold Heat Exchanger

UNLESS OTHERWISE SPECIFIED: DIMENSIONS ARE IN MM	Comments:
TOLERANCES: LINEAR: 0.1 mm ANGULAR: 1°	
GENERAL SURFACE FINISH: Ra 5 µm O-RING SEAL SURFACE FINISH: Ra 0.8 µm	DRW BY: Linda Hasanovich
	SM BY: Connor Speer
	CHK BY:
	Thursday, September 22, 2022 12:40:25 PM
	Friday, February 16, 2018 12:14:50 PM
MATERIAL: Various	
FILE NAME: 000_Overall_ASM	

 The Department of Mechanical Engineering UNIVERSITY OF ALBERTA	
TITLE: <h1>Overall Assembly</h1>	
Project: <h2>Raphael Engine</h2>	REV
SCALE: 1:5	Mass:30356.83g
SHEET 1 OF 18	

8

7

6

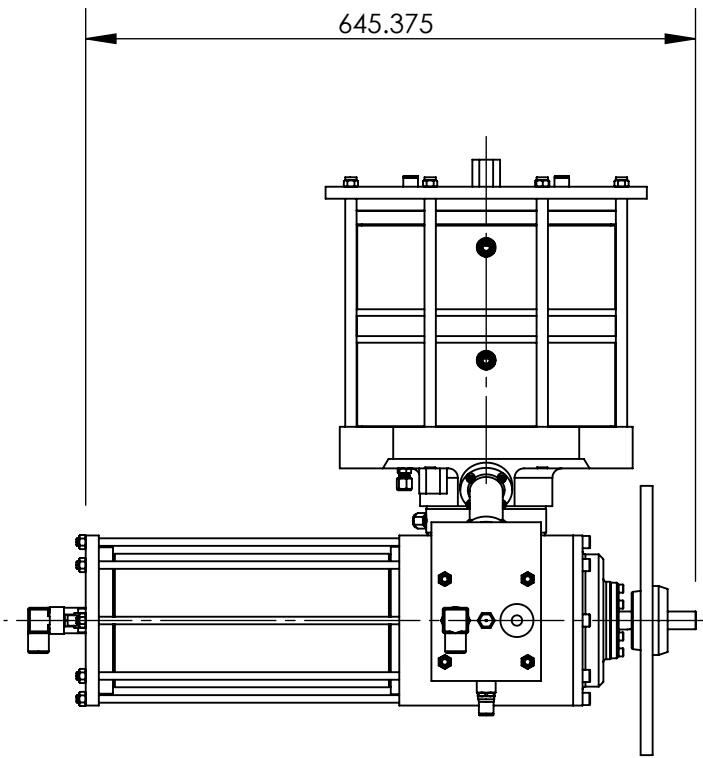
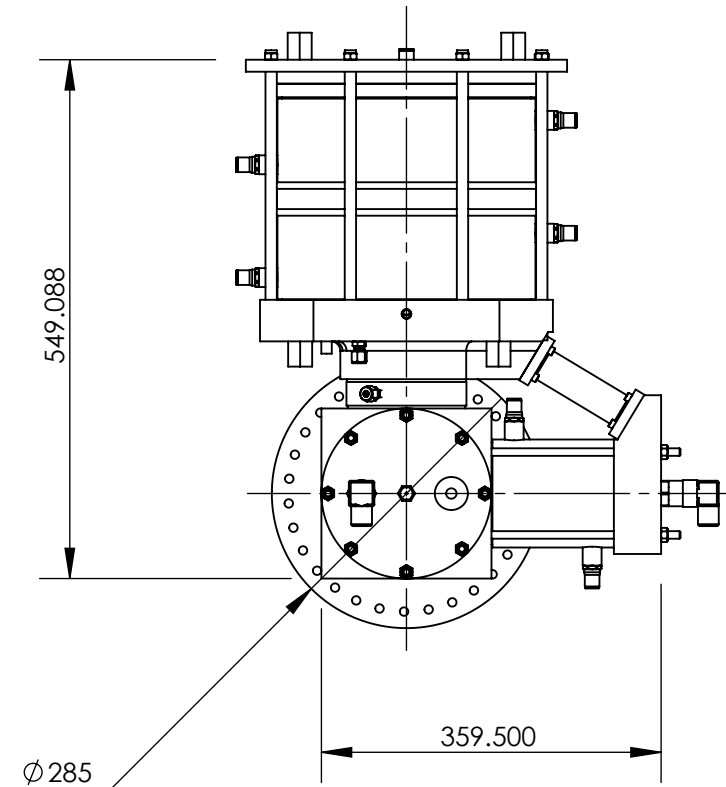
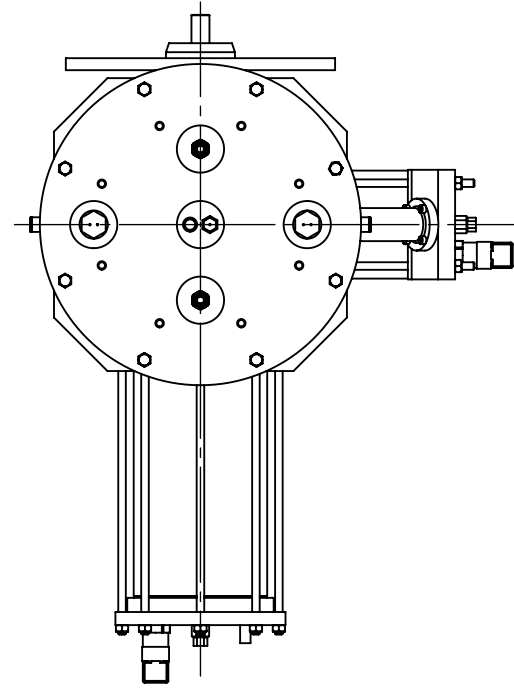
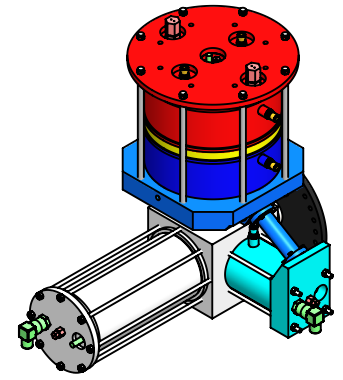
5


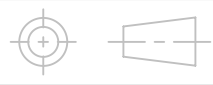
4

3

2

1



UNLESS OTHERWISE SPECIFIED: DIMENSIONS ARE IN MM TOLERANCES: LINEAR: 0.1 mm ANGULAR: 1° GENERAL SURFACE FINISH: Ra 5 µm O-RING SEAL SURFACE FINISH: Ra 0.8 µm	Comments:		 The Department of Mechanical Engineering UNIVERSITY OF ALBERTA
	TITLE: <h3>Overall Dimensions Orthogonal View</h3>		
 MATERIAL: Various FILE NAME: 000_Overall_ASM	DRW BY: Linda Hasanovich SM BY: Connor Speer CHK BY:	Thursday, September 22, 2022 12:40:25 PM Friday, February 16, 2018 12:14:50 PM	Project: <b>Raphael Engine</b>
	SCALE: 1:8	Mass: 30356.83g	SHEET 2 OF 18

8

7

6

5

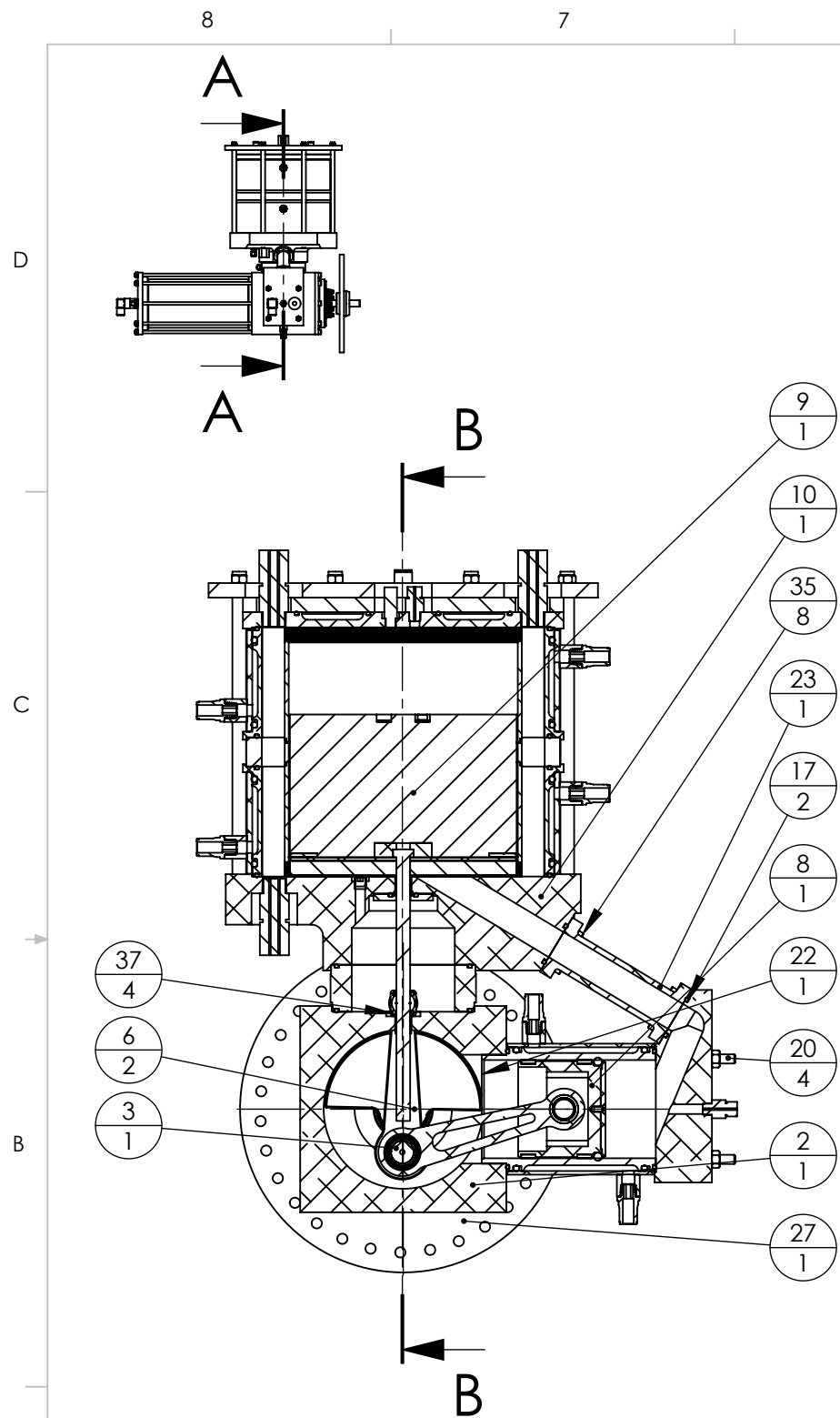
230

4

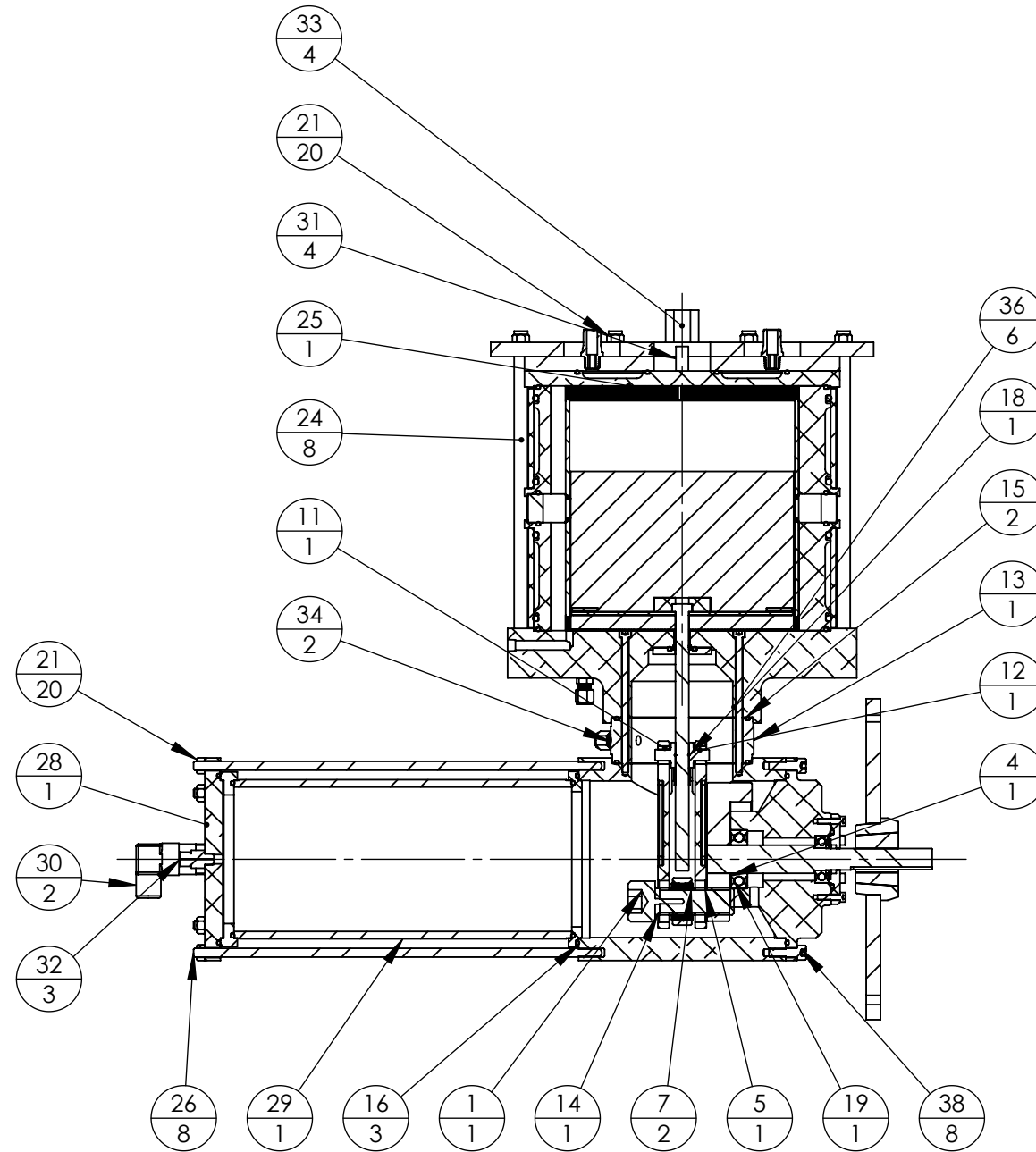
3

2

1



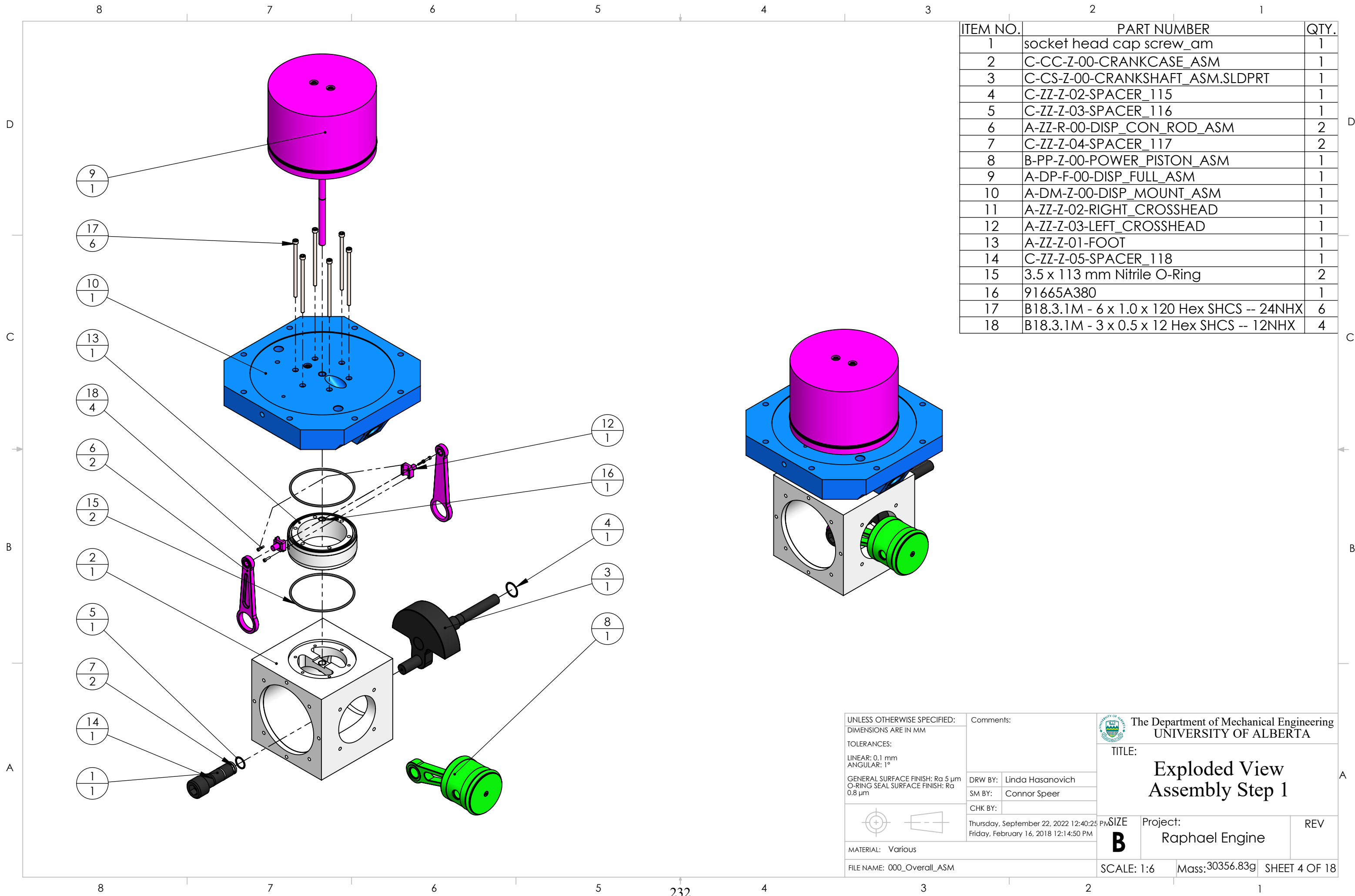
SECTION A-A



SECTION B-B

ITEM NO.	PART NUMBER	QTY.
1	socket head cap screw_am	1
2	C-CC-Z-00-CRANKCASE_ASM	1
3	C-CS-Z-00-CRANKSHAFT_ASM.SLDPRT	1
4	C-ZZ-Z-02-SPACER_115	1
5	C-ZZ-Z-03-SPACER_116	1
6	A-ZZ-R-00-DISP_CON_ROD_ASM	2
7	C-ZZ-Z-04-SPACER_117	2
8	B-PP-Z-00-POWER_PISTON_ASM	1
9	A-DP-F-00-DISP_FULL_ASM	1
10	A-DM-Z-00-DISP_MOUNT_ASM	1
11	A-ZZ-Z-02-RIGHT_CROSSHEAD	1
12	A-ZZ-Z-03-LEFT_CROSSHEAD	1
13	A-ZZ-Z-01-FOOT	1
14	C-ZZ-Z-05-SPACER_118	1
15	3.5 x 113 mm Nitrile O-Ring	2
16	3.5 x 145 mm Nitrile O-Ring	3
17	3.5 x 33 mm Nitrile O-Ring	2
18	91665A380	1
19	C-BC-Z-00-BEARING_CARTRIDGE_ASM	1
20	C-ZZ-Z-06-PC_THREADED_ROD	4
21	prevailing torque hex nut_am	20
22	B-PC-Z-00-POWER_CYL_ASM	1
23	B-CP-Z-01-CON_PIPE	1
24	A-DC-Z-04-DISPLACER_CYL_THREADED_ROD	8
25	A-DC-Z-00-DISP_CYL_ASM	1
26	C-ZZ-Z-07-CC_EXT_THREADED_ROD	8
27	C-ZZ-F-00-FLYWHEEL_ASM.SLDPRT	1
28	C-ZZ-Z-01-COVER	1
29	C-ZZ-CE-00-CRANKCASE_EXTENSION_ASM	1
30	I-ZZ-Z-01-STATIC_PRESSURE_TRANSDUCER	2
31	I-ZZ-Z-02-DYNAMIC_PRESSURE_TRANSDUCER	4
32	I-ZZ-Z-03-GAS_TC_FITTING	3
33	I-ZZ-Z-03-TWO_ELEMENT_GAS_TC_FITTING	4
34	5182K807	2
35	B18.3.1M - 5 x 0.8 x 20 Hex SHCS -- 20NHX	8
36	B18.3.1M - 6 x 1.0 x 120 Hex SHCS -- 24NHX	6
37	B18.3.1M - 3 x 0.5 x 12 Hex SHCS -- 12NHX	4
38	B18.3.1M - 8 x 1.25 x 25 Hex SHCS -- 25NHX	8

UNLESS OTHERWISE SPECIFIED: DIMENSIONS ARE IN MM TOLERANCES: LINEAR: 0.1 mm ANGULAR: 1° GENERAL SURFACE FINISH: Ra 5 µm O-RING SEAL SURFACE FINISH: Ra 0.8 µm	Comments:	The Department of Mechanical Engineering UNIVERSITY OF ALBERTA TITLE: <h2 style="text-align: center;">Overall Assembly Section Views</h2>
	DRW BY: Linda Hasanovich SM BY: Connor Speer CHK BY:	
MATERIAL: Various FILE NAME: 000_Overall_ASM	Thursday, September 22, 2022 12:40:25 PM Friday, February 16, 2018 12:14:50 PM	Project Size: <h1 style="font-size: 2em; font-weight: bold;">B</h1>
SCALE: 1:6    Mass: 30356.83g    SHEET 3 OF 18		REV

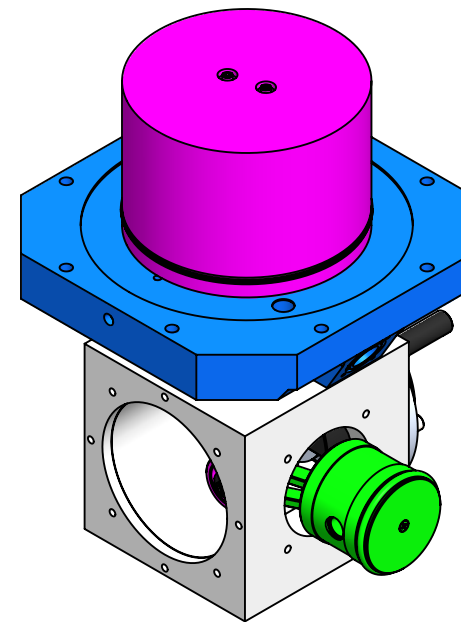
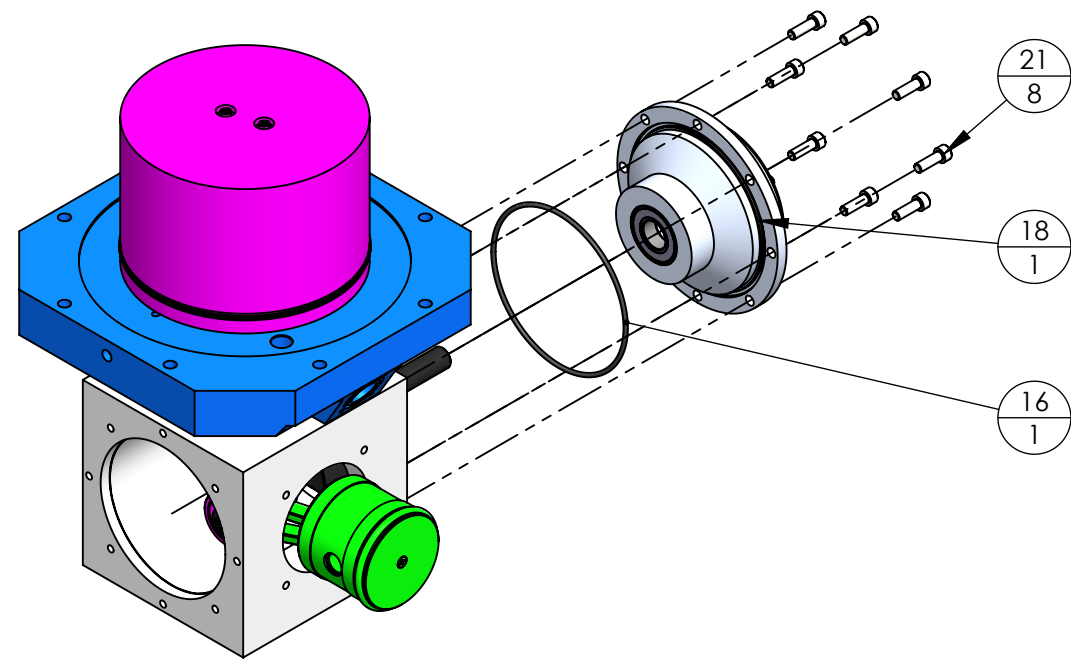



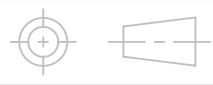
ITEM NO.	PART NUMBER	QTY.
1	socket head cap screw_am	1
2	C-CC-Z-00-CRANKCASE_ASM	1
3	C-CS-Z-00-CRANKSHAFT_ASM.SLDPRT	1
4	C-ZZ-Z-02-SPACER_115	1
5	C-ZZ-Z-03-SPACER_116	1
6	A-ZZ-R-00-DISP_CON_ROD_ASM	2
7	C-ZZ-Z-04-SPACER_117	2
8	B-PP-Z-00-POWER_PISTON_ASM	1
9	A-DP-F-00-DISP_FULL_ASM	1
10	A-DM-Z-00-DISP_MOUNT_ASM	1
11	A-ZZ-Z-02-RIGHT_CROSSHEAD	1
12	A-ZZ-Z-03-LEFT_CROSSHEAD	1
13	A-ZZ-Z-01-FOOT	1
14	C-ZZ-Z-05-SPACER_118	1
15	3.5 x 113 mm Nitrile O-Ring	2
16	91665A380	1
17	B18.3.1M - 6 x 1.0 x 120 Hex SHCS -- 24NHX	6
18	B18.3.1M - 3 x 0.5 x 12 Hex SHCS -- 12NHX	4

UNLESS OTHERWISE SPECIFIED: DIMENSIONS ARE IN MM TOLERANCES: LINEAR: 0.1 mm ANGULAR: 1° GENERAL SURFACE FINISH: Ra 5 µm O-RING SEAL SURFACE FINISH: Ra 0.8 µm	Comments:	The Department of Mechanical Engineering <b>UNIVERSITY OF ALBERTA</b>
	DRW BY: Linda Hasanovich SM BY: Connor Speer CHK BY:	
MATERIAL: Various FILE NAME: 000_Overall_ASM	Thursday, September 22, 2022 12:40:25 PM Friday, February 16, 2018 12:14:50 PM	Project: <b>Raphael Engine</b>
SCALE: 1:6 Mass: 30356.83g	SHEET 4 OF 18	REV

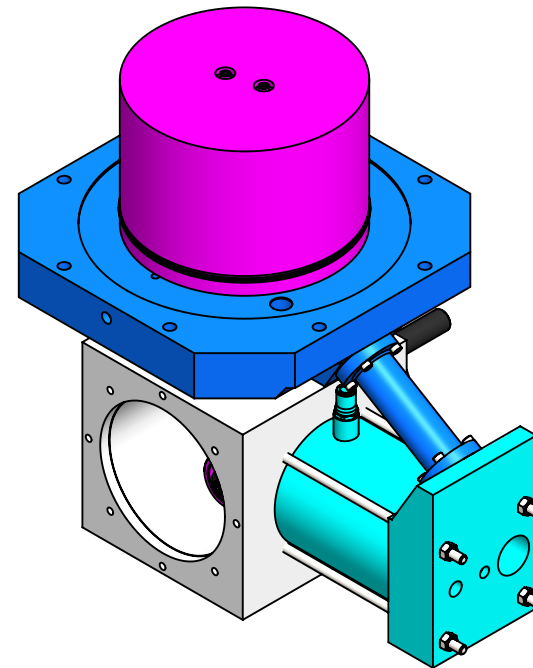
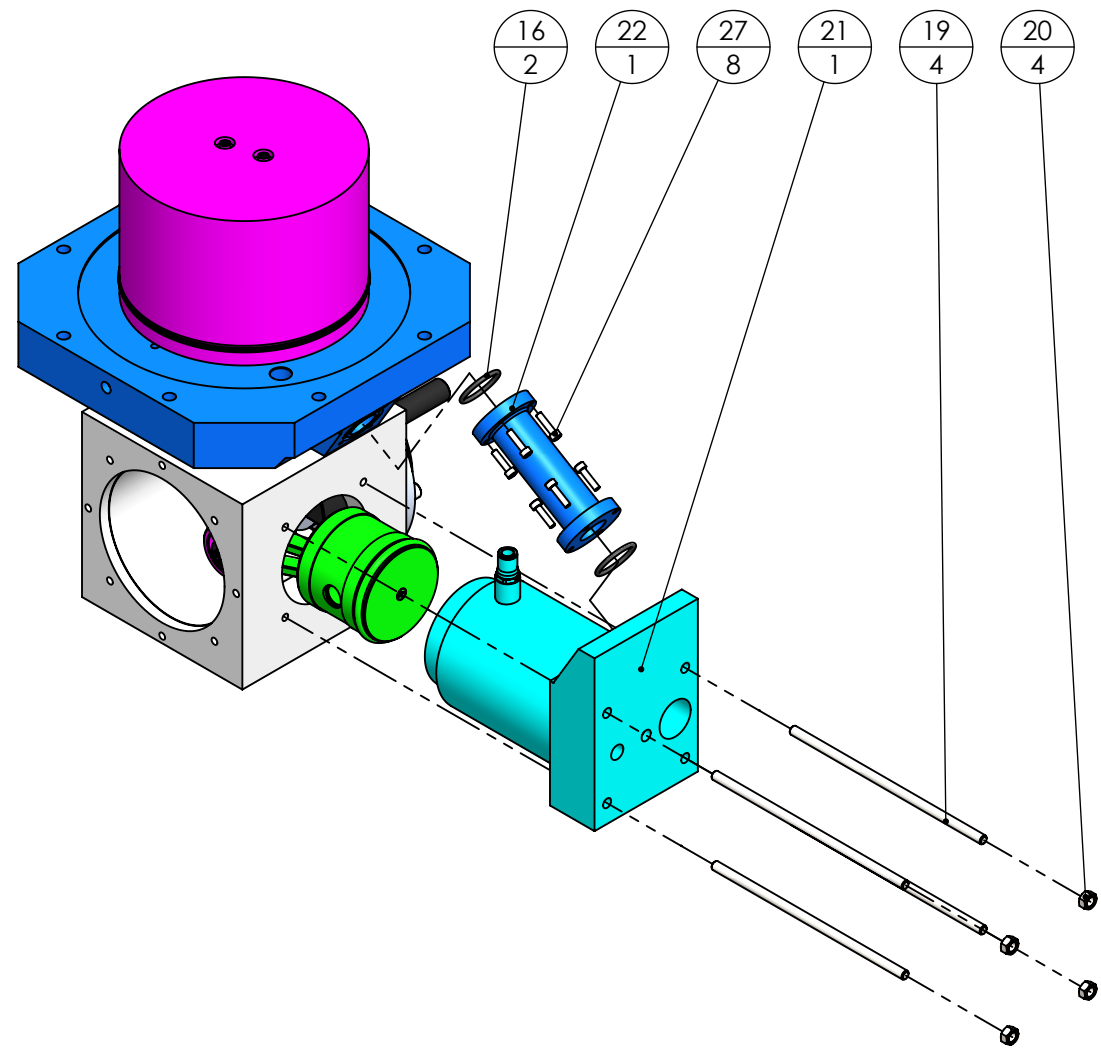




ITEM NO.	PART NUMBER	QTY.
16	145 x 3.5 Nitrile O-Ring	1
18	C-BC-Z-00-BEARING_CARTRIDGE_ASM	1
19	B18.3.1M - 3 x 0.5 x 12 Hex SHCS -- 12NHX	4
20	B18.3.1M - 6 x 1.0 x 20 Hex SHCS -- 20NHX	1
21	B18.3.1M - 8 x 1.25 x 25 Hex SHCS -- 25NHX	8

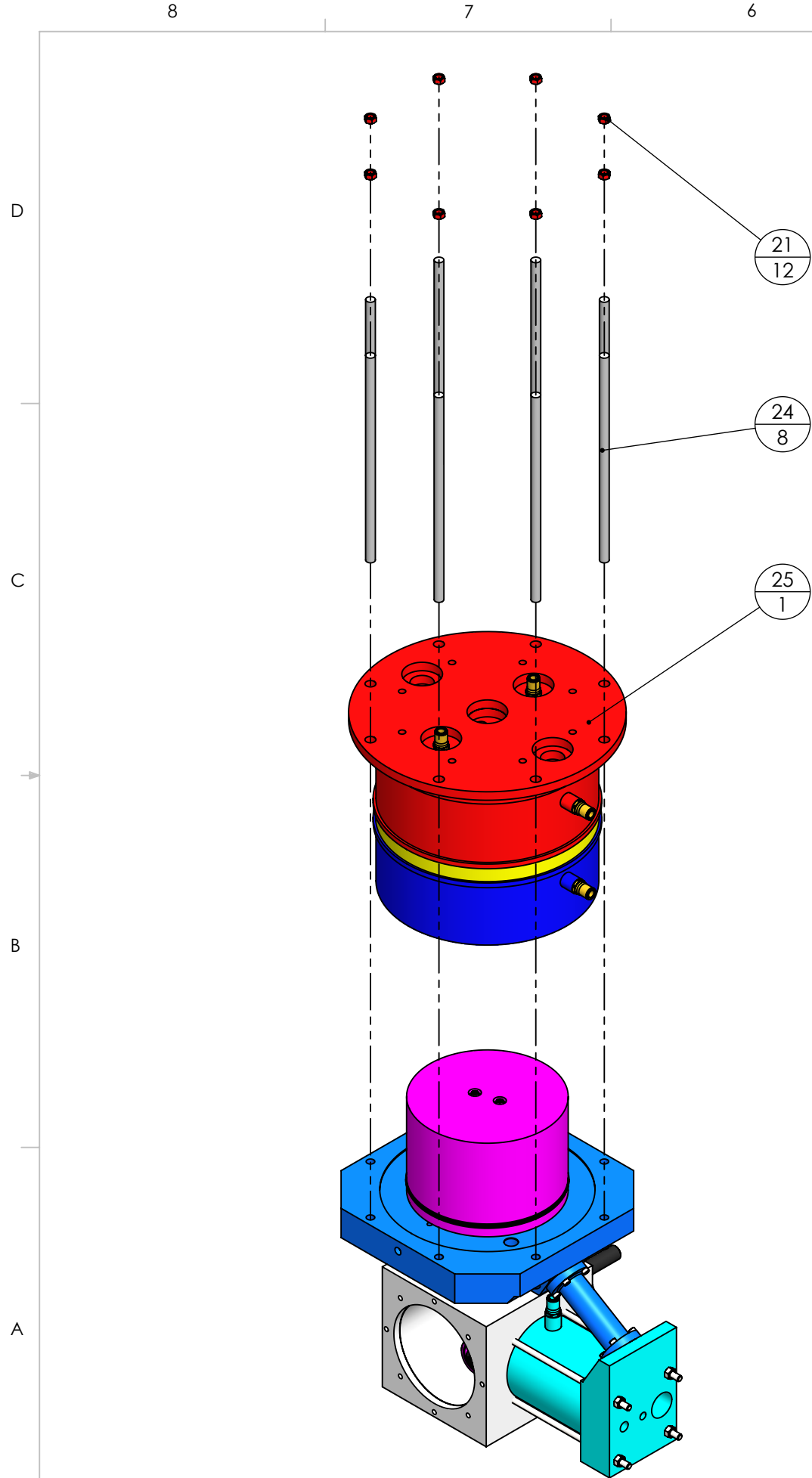


UNLESS OTHERWISE SPECIFIED: DIMENSIONS ARE IN MM TOLERANCES: LINEAR: 0.1 mm ANGULAR: 1° GENERAL SURFACE FINISH: Ra 5 µm O-RING SEAL SURFACE FINISH: Ra 0.8 µm	Comments:		 The Department of Mechanical Engineering <b>UNIVERSITY OF ALBERTA</b>	
	DRW BY: Linda Hasanovich SM BY: Connor Speer CHK BY:			<b>TITLE:</b> <h2 style="text-align: center;">Exploded View Assembly Step 2</h2>
	Thursday, September 22, 2022 12:40:25 PM Friday, February 16, 2018 12:14:50 PM	<b>SIZE</b> <b>B</b>	Project: <b>Raphael Engine</b>	REV
MATERIAL: Various FILE NAME: 000_Overall_ASM	SCALE: 1:6	Mass: 30356.83g	SHEET 5 OF 18	

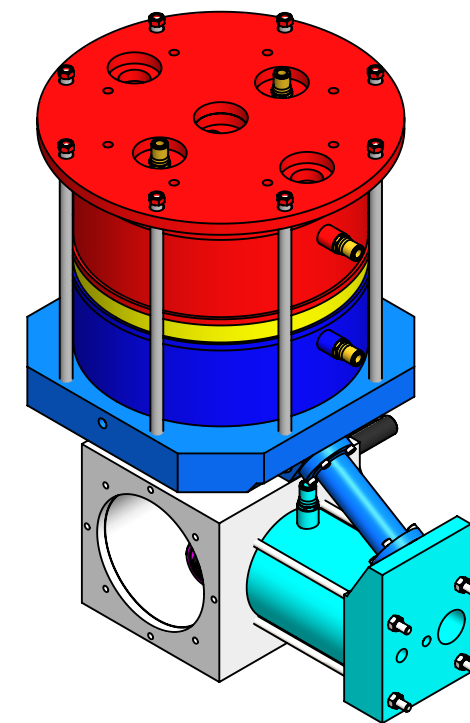
ITEM NO.	PART NUMBER	QTY.
16	33 x 3.5 mm Nitrile O-Ring	2
19	C-ZZ-Z-06-PC_THREADED_ROD	4
20	prevailing torque hex nut_am	4
21	B-PC-Z-00-POWER_CYL_ASM	1
22	B-CP-Z-01-CON_PIPE	1
23	B18.3.1M - 6 x 1.0 x 120 Hex SHCS -- 24NHX	6
24	B18.3.1M - 3 x 0.5 x 12 Hex SHCS -- 12NHX	4
25	B18.3.1M - 6 x 1.0 x 20 Hex SHCS -- 20NHX	1
26	B18.3.1M - 8 x 1.25 x 25 Hex SHCS -- 25NHX	8
27	B18.3.1M - 5 x 0.8 x 20 Hex SHCS -- 20NHX	8




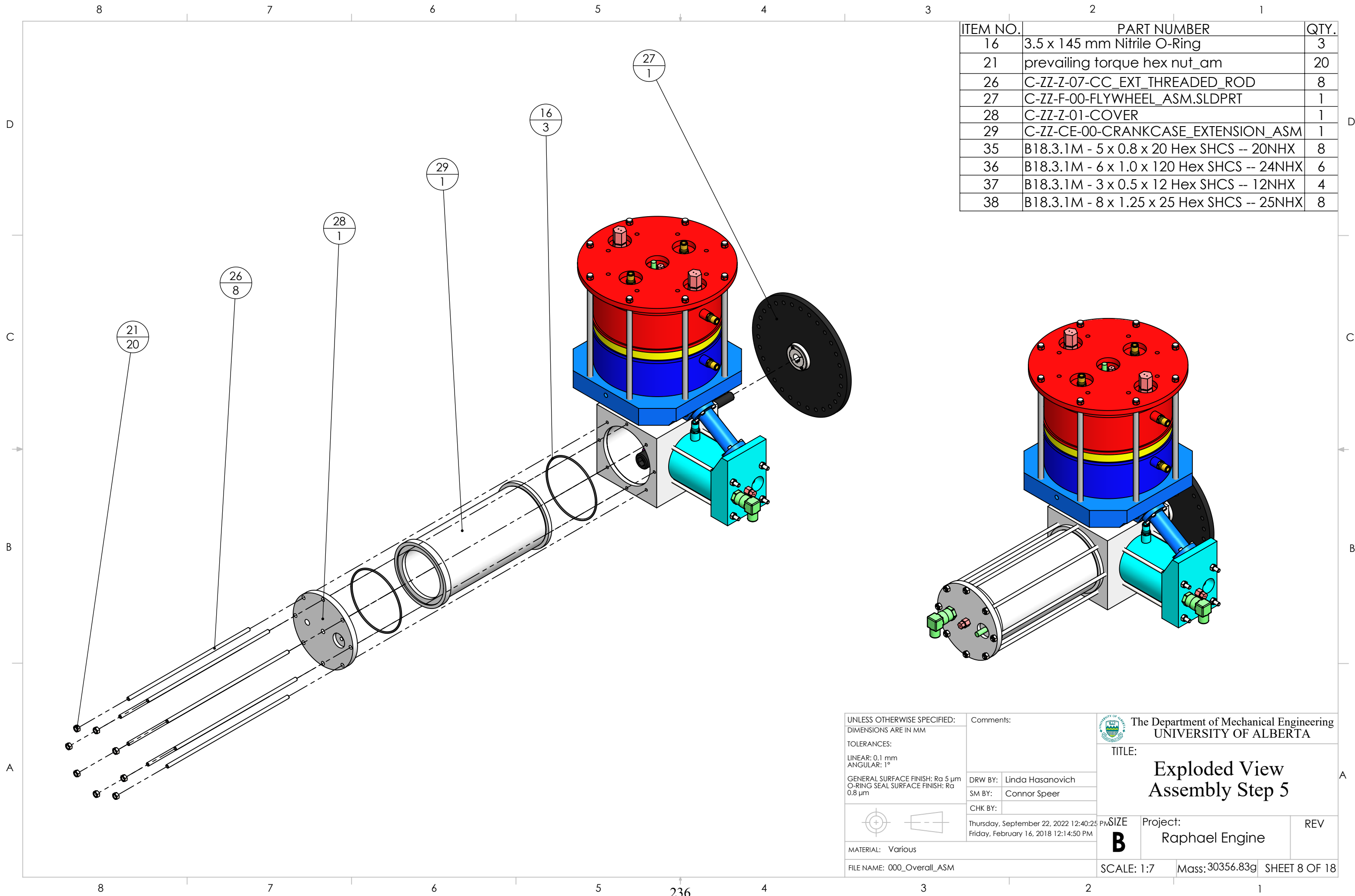
UNLESS OTHERWISE SPECIFIED: DIMENSIONS ARE IN MM TOLERANCES: LINEAR: 0.1 mm ANGULAR: 1° GENERAL SURFACE FINISH: Ra 5 µm O-RING SEAL SURFACE FINISH: Ra 0.8 µm	Comments:	 <b>The Department of Mechanical Engineering UNIVERSITY OF ALBERTA</b>
	DRW BY: Linda Hasanovich SM BY: Connor Speer CHK BY:	
 MATERIAL: Various FILE NAME: 000_Overall_ASM	Thursday, September 22, 2022 12:40:25 PM Friday, February 16, 2018 12:14:50 PM	<b>Project:</b> <b>Raphael Engine</b>
<b>SIZE</b> <b>B</b>	<b>REV</b> 	<b>SCALE:</b> 1:6 <b>Mass:</b> 30356.83g <b>SHEET 6 OF 18</b>



ITEM NO.	PART NUMBER	QTY.
24	A-DC-Z-04-DISPLACER_CYL_THREADED_ROD	8
25	A-DC-Z-00-DISP_CYL_ASM	1
26	B18.3.1M - 3 x 0.5 x 12 Hex SHCS -- 12NHX	4
27	B18.3.1M - 6 x 1.0 x 20 Hex SHCS -- 20NHX	1
28	B18.3.1M - 8 x 1.25 x 25 Hex SHCS -- 25NHX	8
29	B18.3.1M - 5 x 0.8 x 20 Hex SHCS -- 20NHX	8

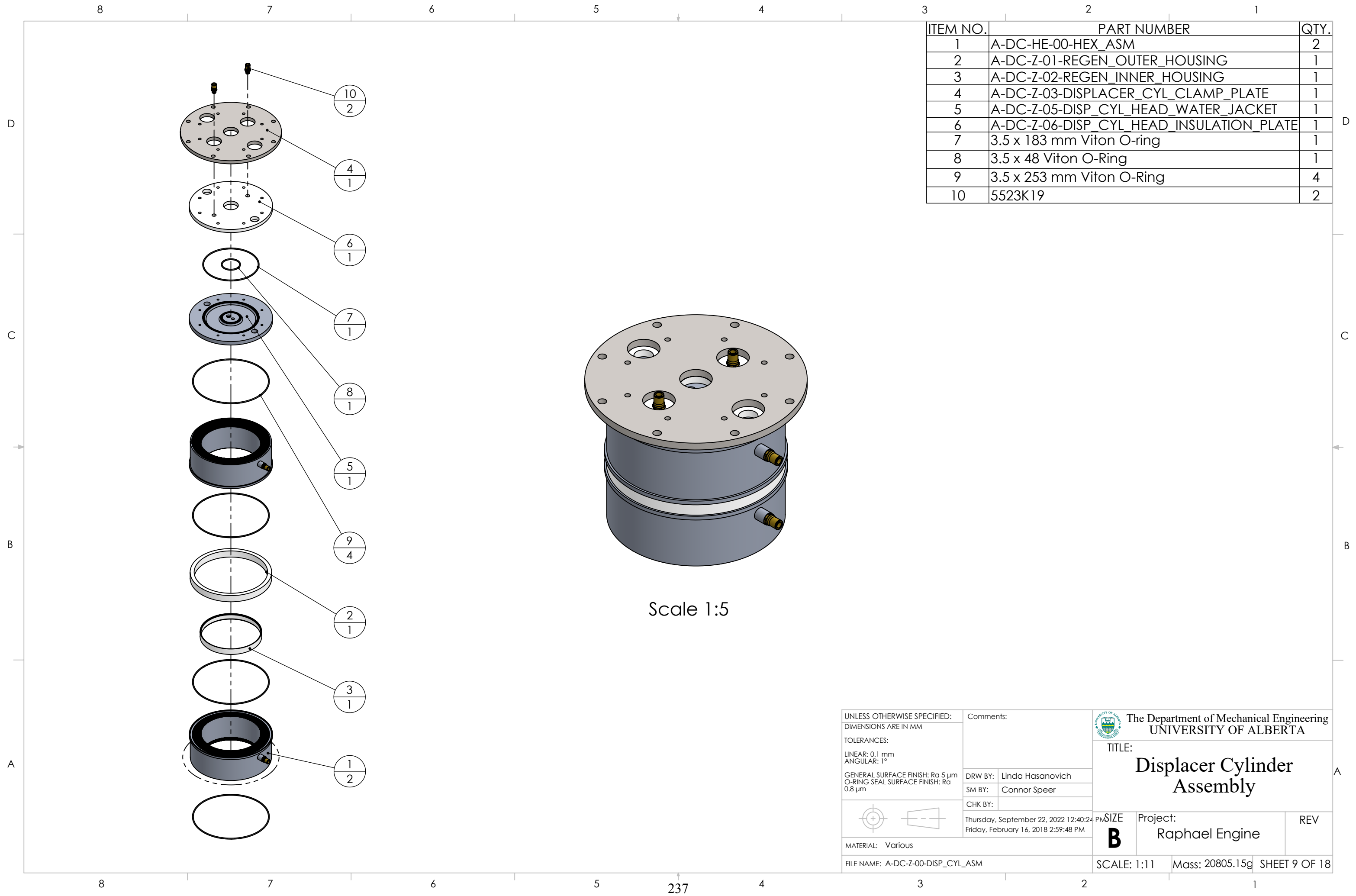


UNLESS OTHERWISE SPECIFIED: DIMENSIONS ARE IN MM TOLERANCES: LINEAR: 0.1 mm ANGULAR: 1° GENERAL SURFACE FINISH: Ra 5 µm O-RING SEAL SURFACE FINISH: Ra 0.8 µm	Comments:	 The Department of Mechanical Engineering UNIVERSITY OF ALBERTA
	DRW BY: Linda Hasanovich SM BY: Connor Speer CHK BY:	
MATERIAL: Various FILE NAME: 000_Overall_ASM	Thursday, September 22, 2022 12:40:25 PM Friday, February 16, 2018 12:14:50 PM	Project: <h3 style="text-align: center;">Raphael Engine</h3>
SCALE: 1:7 Mass: 30356.83g	SHEET 7 OF 18	REV





ITEM NO.	PART NUMBER	QTY.
16	3.5 x 145 mm Nitrile O-Ring	3
21	prevailing torque hex nut_am	20
26	C-ZZ-Z-07-CC_EXT_THREADED_ROD	8
27	C-ZZ-F-00-FLYWHEEL_ASM.SLDPRT	1
28	C-ZZ-Z-01-COVER	1
29	C-ZZ-CE-00-CRANKCASE_EXTENSION_ASM	1
35	B18.3.1M - 5 x 0.8 x 20 Hex SHCS -- 20NHX	8
36	B18.3.1M - 6 x 1.0 x 120 Hex SHCS -- 24NHX	6
37	B18.3.1M - 3 x 0.5 x 12 Hex SHCS -- 12NHX	4
38	B18.3.1M - 8 x 1.25 x 25 Hex SHCS -- 25NHX	8

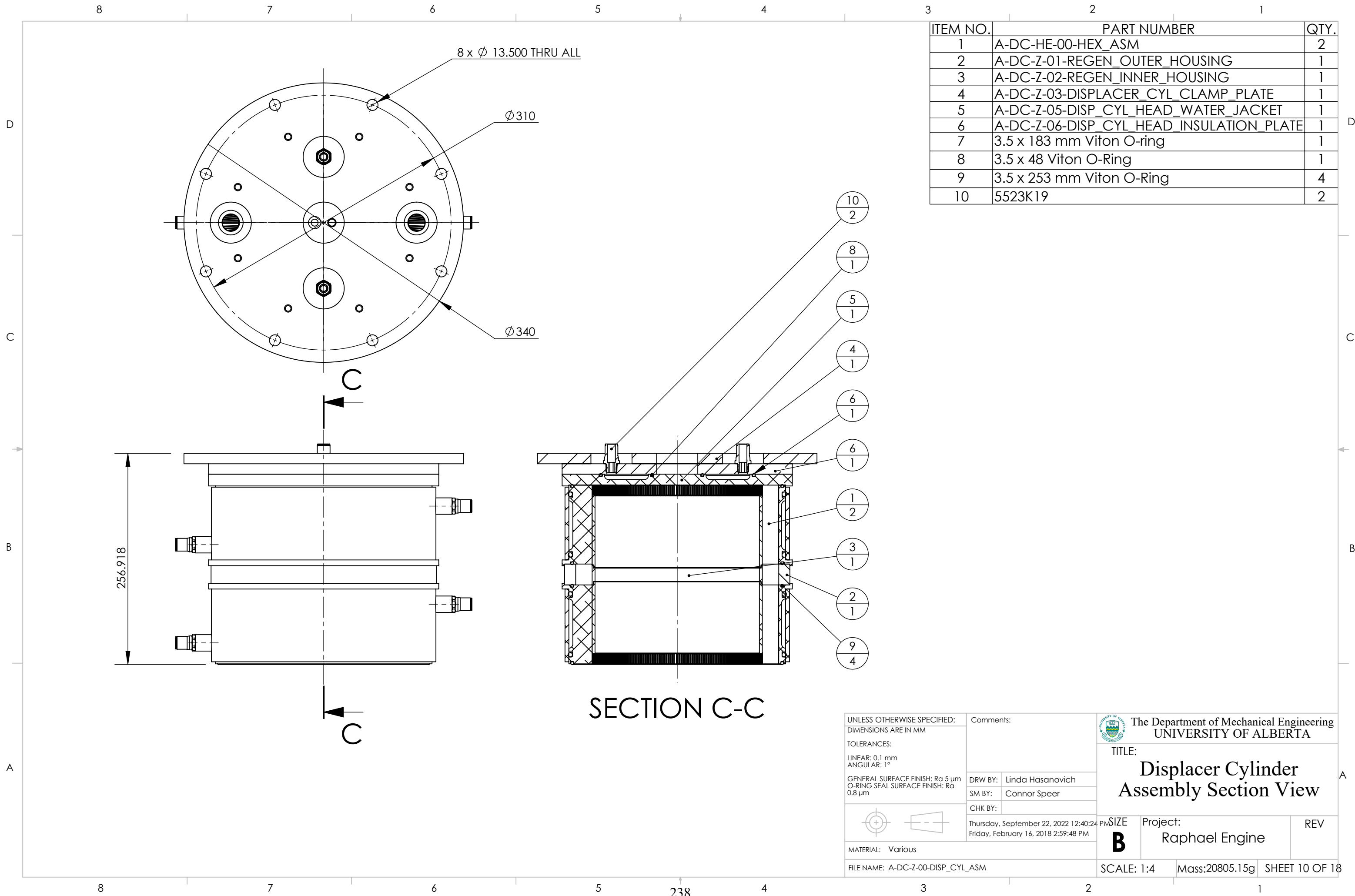
UNLESS OTHERWISE SPECIFIED: DIMENSIONS ARE IN MM TOLERANCES: LINEAR: 0.1 mm ANGULAR: 1° GENERAL SURFACE FINISH: Ra 5 µm O-RING SEAL SURFACE FINISH: Ra 0.8 µm	Comments:	The Department of Mechanical Engineering <b>UNIVERSITY OF ALBERTA</b>
	DRW BY: Linda Hasanovich SM BY: Connor Speer CHK BY:	
MATERIAL: Various FILE NAME: 000_Overall_ASM	Thursday, September 22, 2022 12:40:25 PM Friday, February 16, 2018 12:14:50 PM	Project: <b>Raphael Engine</b>
SCALE: 1:7 Mass: 30356.83g	SHEET 8 OF 18	REV



ITEM NO.	PART NUMBER	QTY.
1	A-DC-HE-00-HEX_ASM	2
2	A-DC-Z-01-REGEN_OUTER_HOUSING	1
3	A-DC-Z-02-REGEN_INNER_HOUSING	1
4	A-DC-Z-03-DISPLACER_CYL_CLAMP_PLATE	1
5	A-DC-Z-05-DISP_CYL_HEAD_WATER_JACKET	1
6	A-DC-Z-06-DISP_CYL_HEAD_INSULATION_PLATE	1
7	3.5 x 183 mm Viton O-ring	1
8	3.5 x 48 Viton O-Ring	1
9	3.5 x 253 mm Viton O-Ring	4
10	5523K19	2

Scale 1:5

UNLESS OTHERWISE SPECIFIED: DIMENSIONS ARE IN MM TOLERANCES: LINEAR: 0.1 mm ANGULAR: 1° GENERAL SURFACE FINISH: Ra 5 µm O-RING SEAL SURFACE FINISH: Ra 0.8 µm	Comments:		 The Department of Mechanical Engineering UNIVERSITY OF ALBERTA
	DRW BY: Linda Hasanovich	SM BY: Connor Speer	
	CHK BY: Thursday, September 22, 2022 12:40:24 PM Friday, February 16, 2018 2:59:48 PM	Project: <b>Raphael Engine</b>	REV
MATERIAL: Various	FILE NAME: A-DC-Z-00-DISP_CYL_ASM	SCALE: 1:11 Mass: 20805.15g	SHEET 9 OF 18



ITEM NO.	PART NUMBER	QTY.
1	A-DC-HE-00-HEX_ASM	2
2	A-DC-Z-01-REGEN_OUTER_HOUSING	1
3	A-DC-Z-02-REGEN_INNER_HOUSING	1
4	A-DC-Z-03-DISPLACER_CYL_CLAMP_PLATE	1
5	A-DC-Z-05-DISP_CYL_HEAD_WATER_JACKET	1
6	A-DC-Z-06-DISP_CYL_HEAD_INSULATION_PLATE	1
7	3.5 x 183 mm Viton O-ring	1
8	3.5 x 48 Viton O-Ring	1
9	3.5 x 253 mm Viton O-Ring	4
10	5523K19	2

SECTION C-C

UNLESS OTHERWISE SPECIFIED:  
 DIMENSIONS ARE IN MM  
 TOLERANCES:  
 LINEAR: 0.1 mm  
 ANGULAR: 1°  
 GENERAL SURFACE FINISH: Ra 5 µm  
 O-RING SEAL SURFACE FINISH: Ra 0.8 µm

Comments:  
 DRW BY: Linda Hasanovich  
 SM BY: Connor Speer  
 CHK BY:  
 Thursday, September 22, 2022 12:40:24 PM  
 Friday, February 16, 2018 2:59:48 PM

The Department of Mechanical Engineering  
 UNIVERSITY OF ALBERTA

TITLE:  
**Displacer Cylinder  
 Assembly Section View**

Project: Raphael Engine

SCALE: 1:4 Mass:20805.15g SHEET 10 OF 18

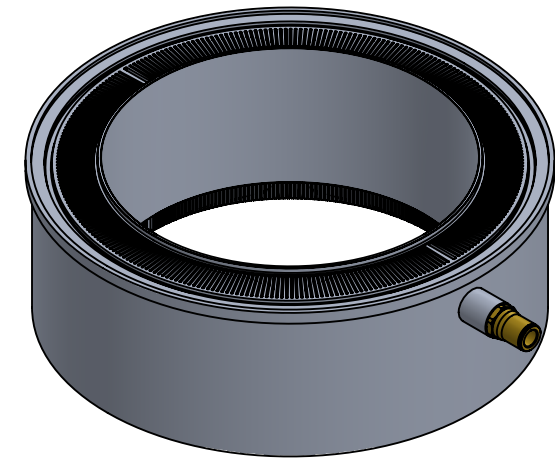
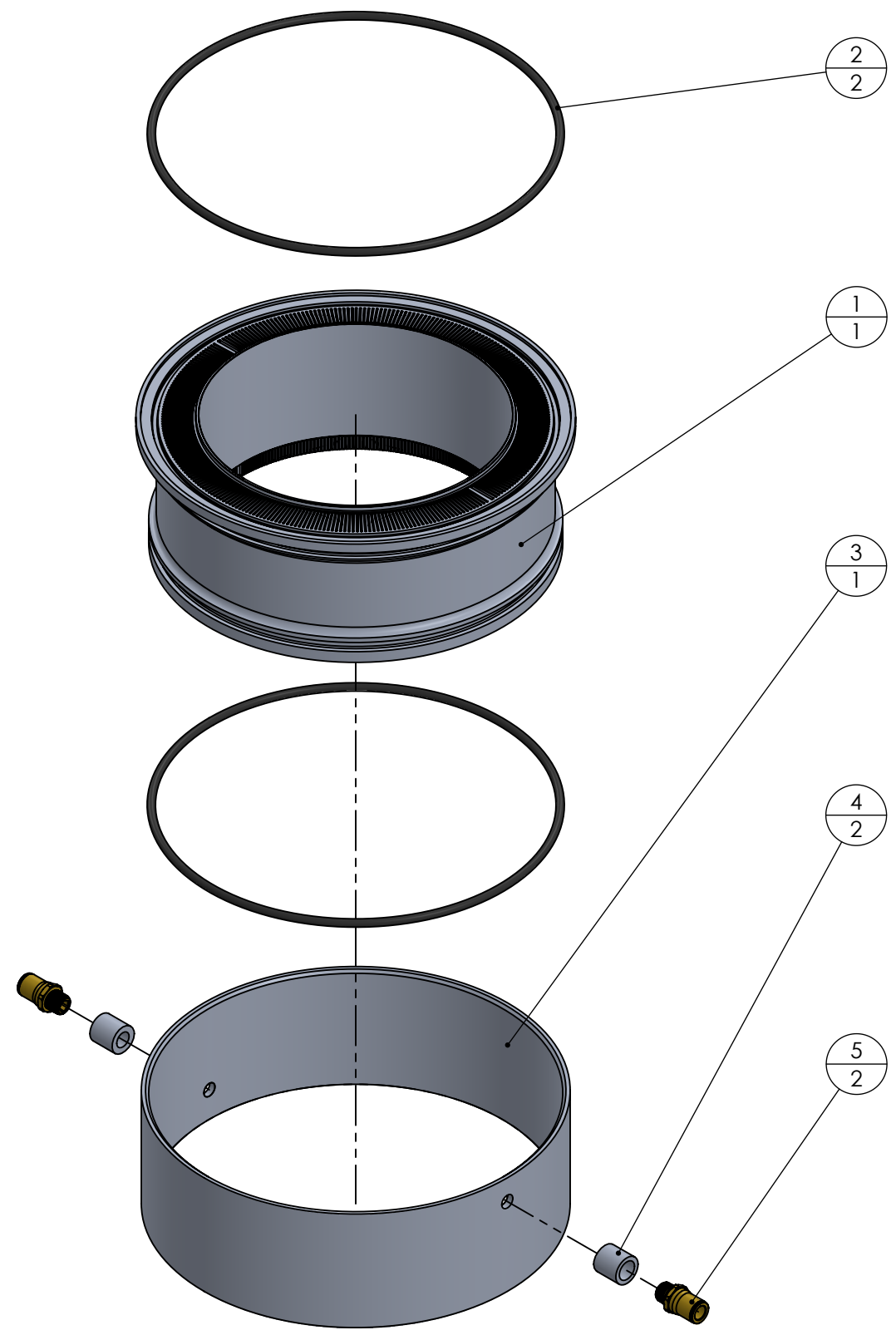




MATERIAL: Various

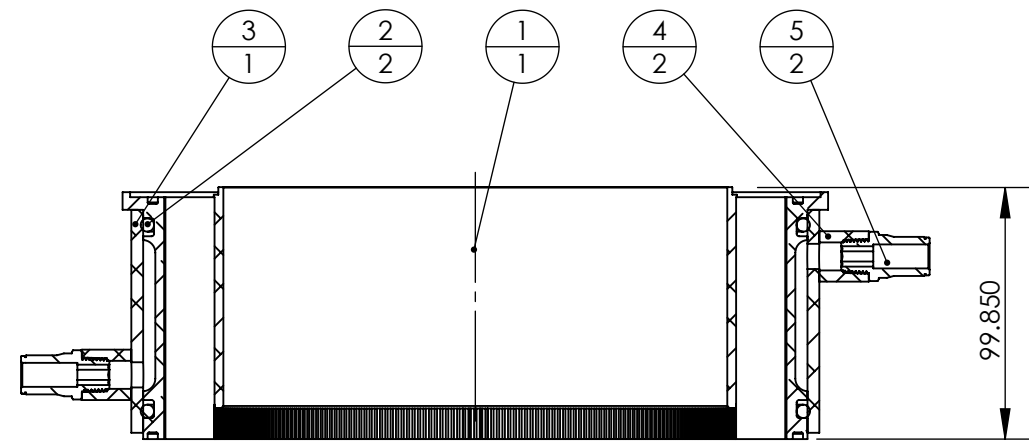
FILE NAME: A-DC-Z-00-DISP\_CYL\_ASM



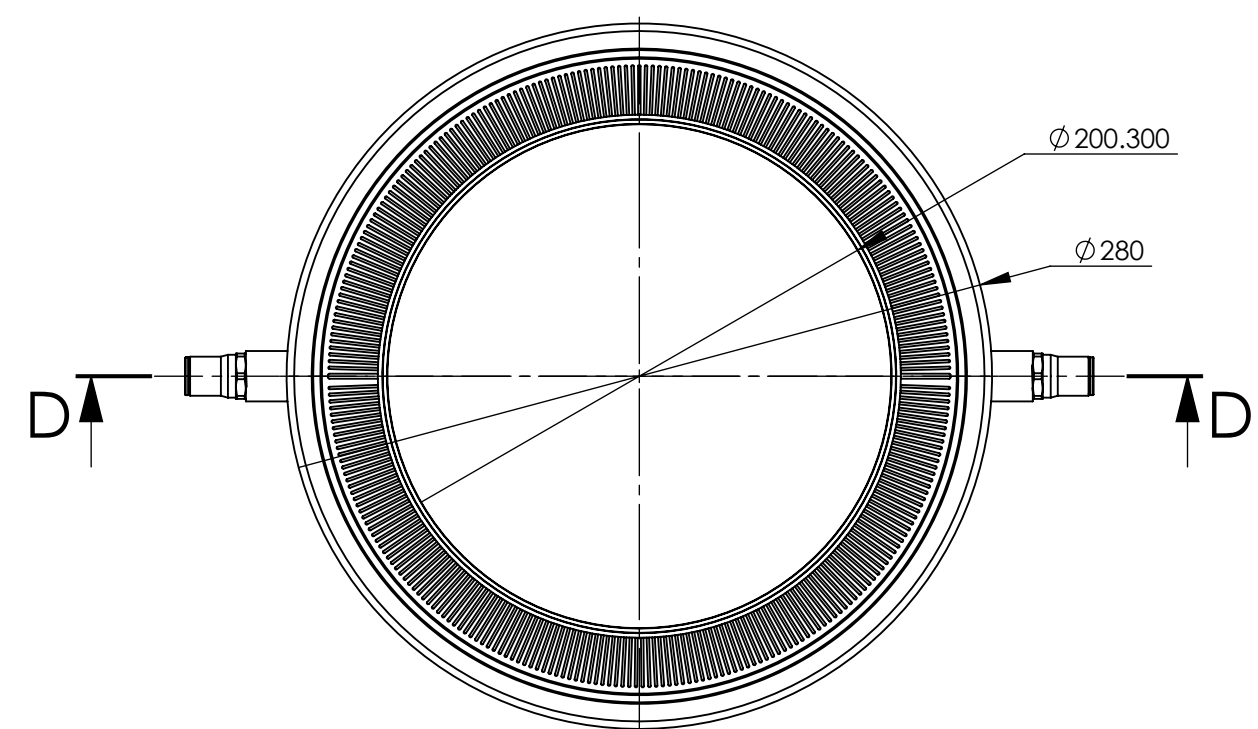
ITEM NO.	PART NUMBER	QTY.
1	A-DC-HC-00-HEX_CARTRIDGE_ASM	1
2	5.33 x 266.07 mm Viton O-Ring	2
3	A-DC-HE-01-HEX_JACKET	1
4	A-DC-HE-02-HEX_JACKET_INLET	2
5	5523K19	2






UNLESS OTHERWISE SPECIFIED: DIMENSIONS ARE IN MM TOLERANCES: LINEAR: 0.1 mm ANGULAR: 1° GENERAL SURFACE FINISH: Ra 5 µm O-RING SEAL SURFACE FINISH: Ra 0.8 µm	Comments:		 The Department of Mechanical Engineering UNIVERSITY OF ALBERTA	
	DRW BY: Linda Hasanovich	SM BY: Connor Speer		TITLE: <b>Heat Exchanger Assembly Exploded View</b>
	CHK BY: Tuesday, September 6, 2022 12:54:57 PM Friday, February 16, 2018 11:55:32 AM	SIZE <b>B</b>	Project: Raphael Engine	REV
MATERIAL: Various FILE NAME: A-DC-HE-00-HEX_ASM	SCALE: 1:4	Mass: 4845.42g	SHEET 11 OF 18	



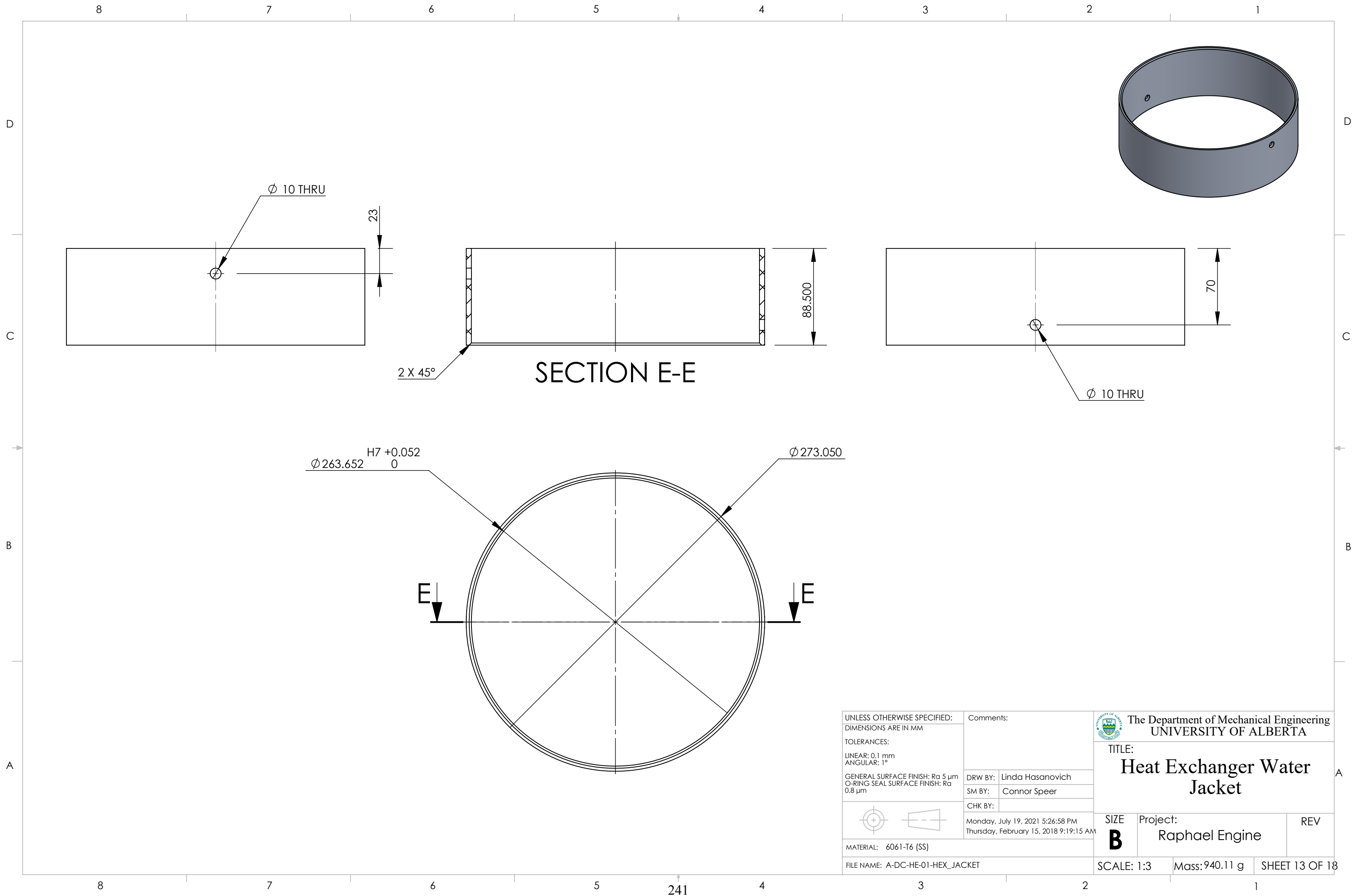
SECTION D-D



ITEM NO.	PART NUMBER	QTY.
1	A-DC-HC-00-HEX_CARTRIDGE_ASM	1
2	5.33 x 266.07 mm Viton O-Ring	2
3	A-DC-HE-01-HEX_JACKET	1
4	A-DC-HE-02-HEX_JACKET_INLET	2
5	5523K19	2

UNLESS OTHERWISE SPECIFIED: DIMENSIONS ARE IN MM TOLERANCES: LINEAR: 0.1 mm ANGULAR: 1° GENERAL SURFACE FINISH: Ra 5 µm O-RING SEAL SURFACE FINISH: Ra 0.8 µm	Comments:		 The Department of Mechanical Engineering UNIVERSITY OF ALBERTA	
	DRW BY: Linda Hasanovich	SM BY: Connor Speer		TITLE: <b>Heat Exchanger Assembly Section View</b>
 	CHK BY: Tuesday, September 6, 2022 12:54:57 PM Friday, February 16, 2018 11:55:32 AM	SIZE <b>B</b>	Project: Raphael Engine	REV
FILE NAME: A-DC-HE-00-HEX_ASM	SCALE: 1:3	Mass: 4845.42g	SHEET 12 OF 18	






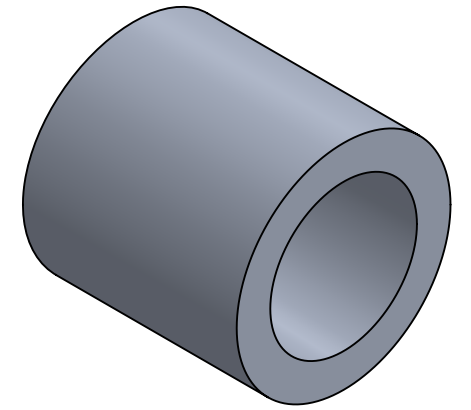


SECTION E-E

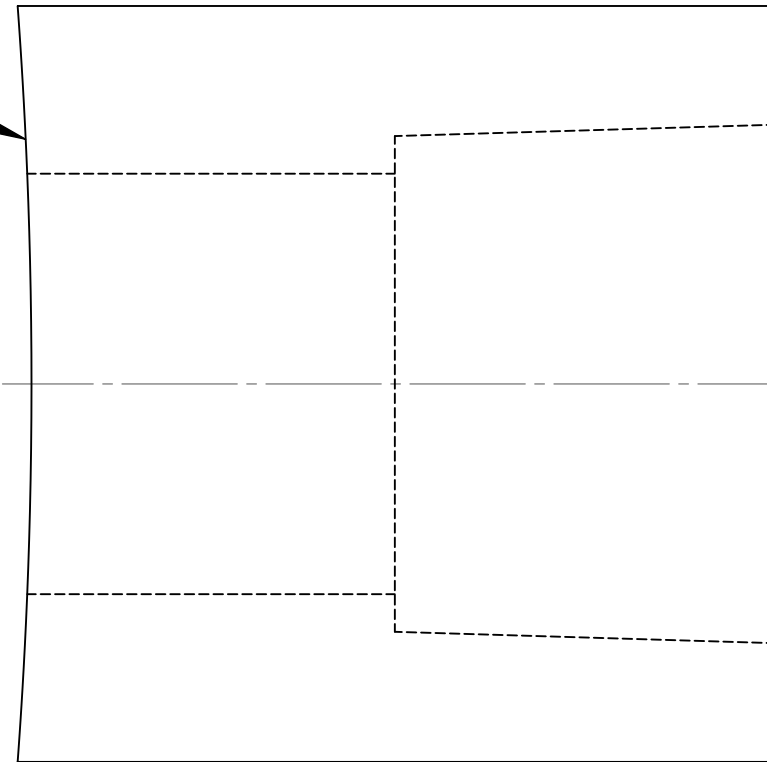
$\phi 263.652$  H7 +0.052 / 0

$\phi 273.050$

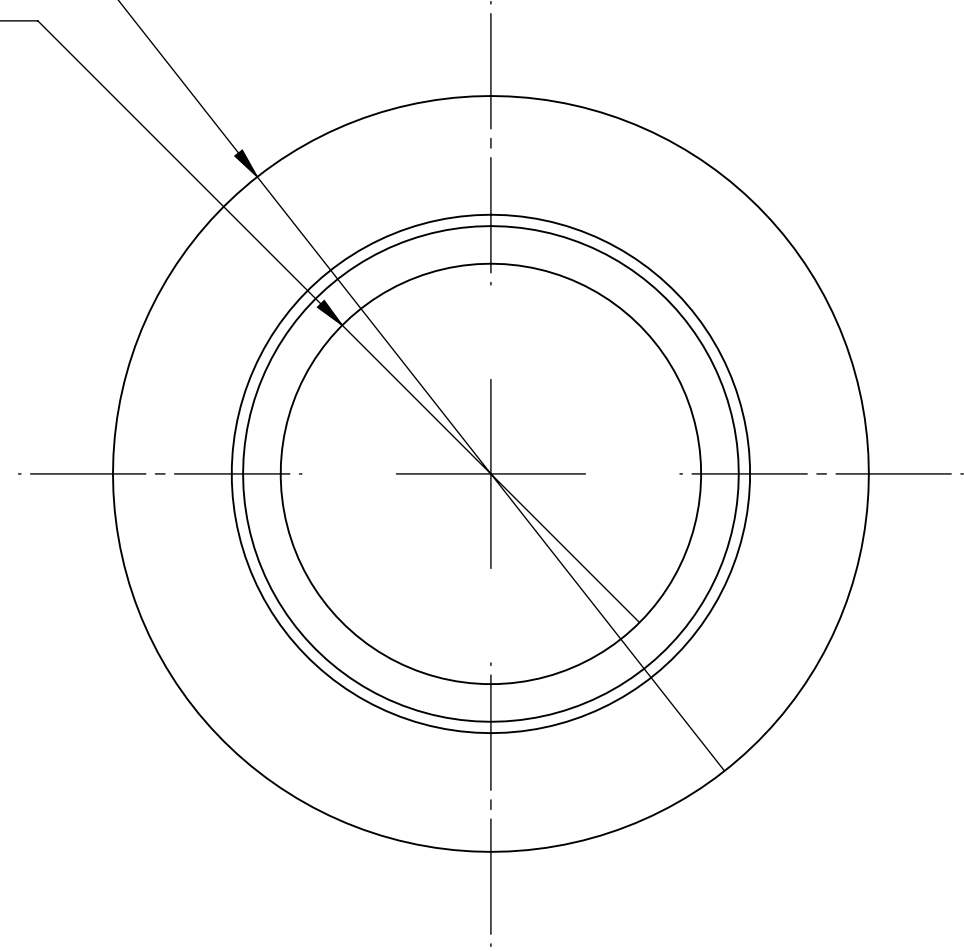
UNLESS OTHERWISE SPECIFIED: DIMENSIONS ARE IN MM TOLERANCES: LINEAR: 0.1 mm ANGULAR: 1° GENERAL SURFACE FINISH: Ra 5 µm O-RING SEAL SURFACE FINISH: Ra 0.8 µm	Comments:		 The Department of Mechanical Engineering UNIVERSITY OF ALBERTA
	DRW BY:	Linda Hasanovich	
SM BY:	Connor Speer	SIZE <b>B</b> Project: Raphael Engine	
 	CHK BY:	Monday, July 19, 2021 5:26:58 PM Thursday, February 15, 2018 9:19:15 AM	REV
MATERIAL: 6061-T6 (SS)	FILE NAME: A-DC-HE-01-HEX_JACKET	SCALE: 1:3	Mass: 940.11 g SHEET 13 OF 18



R57.15 FOR POWER CYLINDER INLETS (QTY 2)  
 R136.53 FOR DISPLACER CYLINDER INLETS (QTY 4)



$\varnothing 20$   
 $\varnothing 11.125$  THRU ALL  
 1/4 NPT

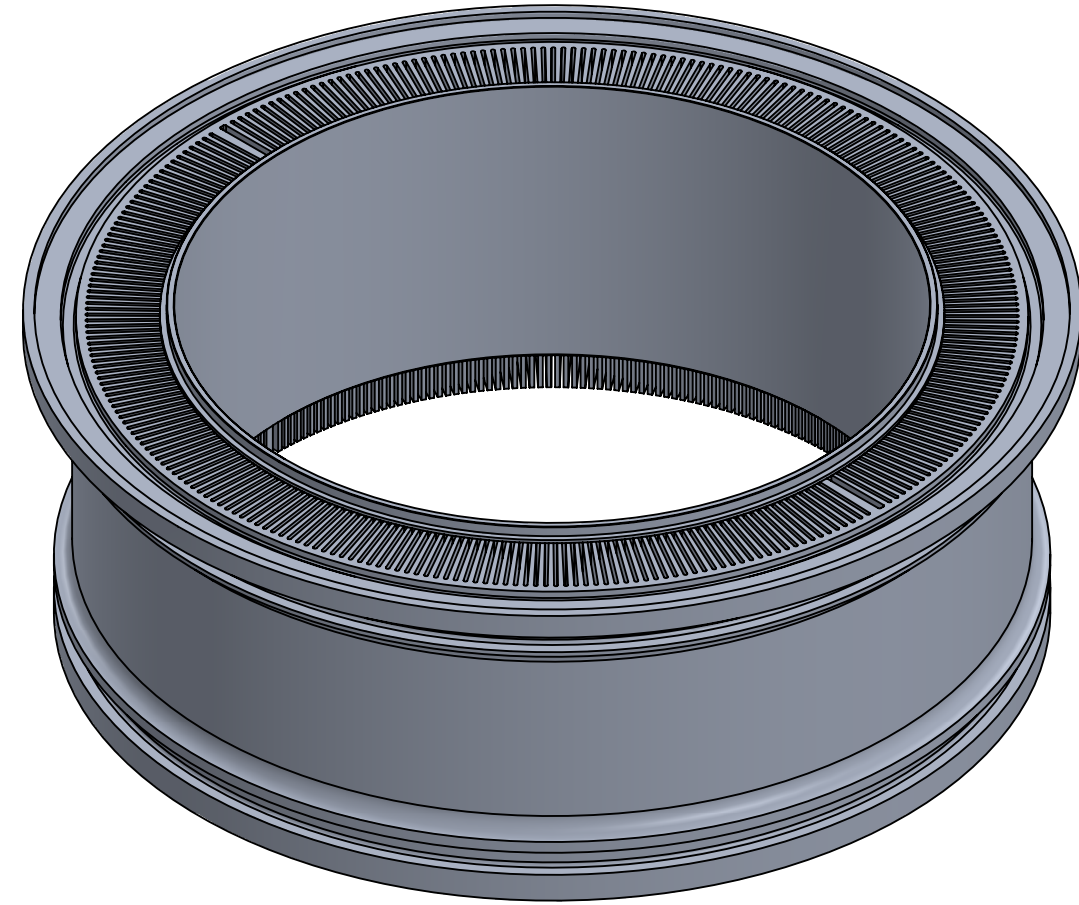
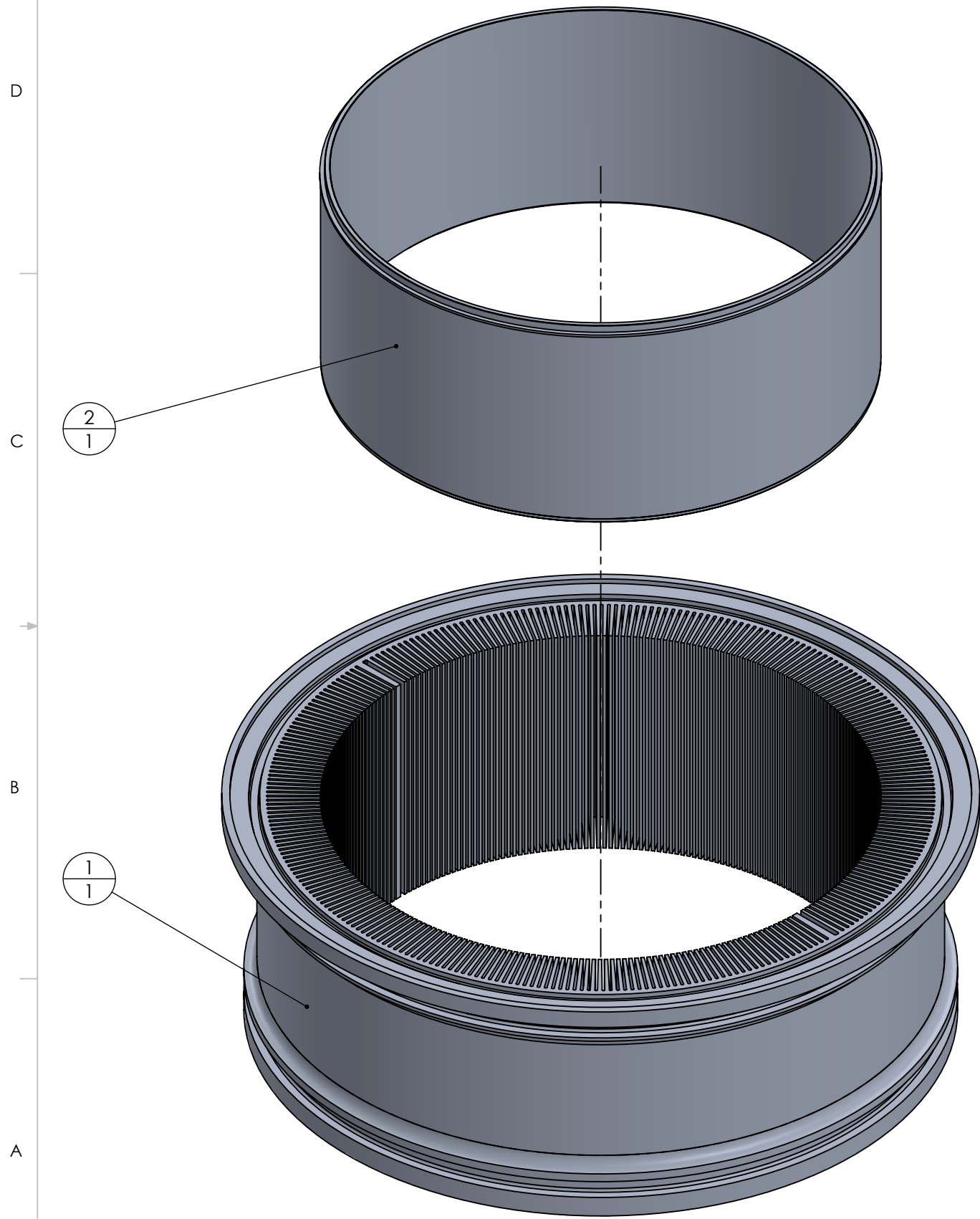



UNLESS OTHERWISE SPECIFIED: DIMENSIONS ARE IN MM TOLERANCES: LINEAR: 0.1 mm ANGULAR: 1° GENERAL SURFACE FINISH: Ra 5 µm O-RING SEAL SURFACE FINISH: Ra 0.8 µm	Comments:		The Department of Mechanical Engineering UNIVERSITY OF ALBERTA TITLE: <b>Weld-On Water Inlet</b>
	DRW BY:	Linda Hasanovich	
	SM BY:	Connor Speer	SIZE <b>B</b>
	CHK BY:		
MATERIAL: 6061-T6 (SS)	Monday, July 19, 2021 5:26:58 PM Wednesday, April 11, 2018 8:41:13 AM		Project: Raphael Engine
FILE NAME: A-DC-HE-02-HEX_JACKET_INLET	SCALE: 5:1	Mass: 10.38 g	REV

8 7 6 5 4 3 2 1

8 7 6 5 4 3 2 1

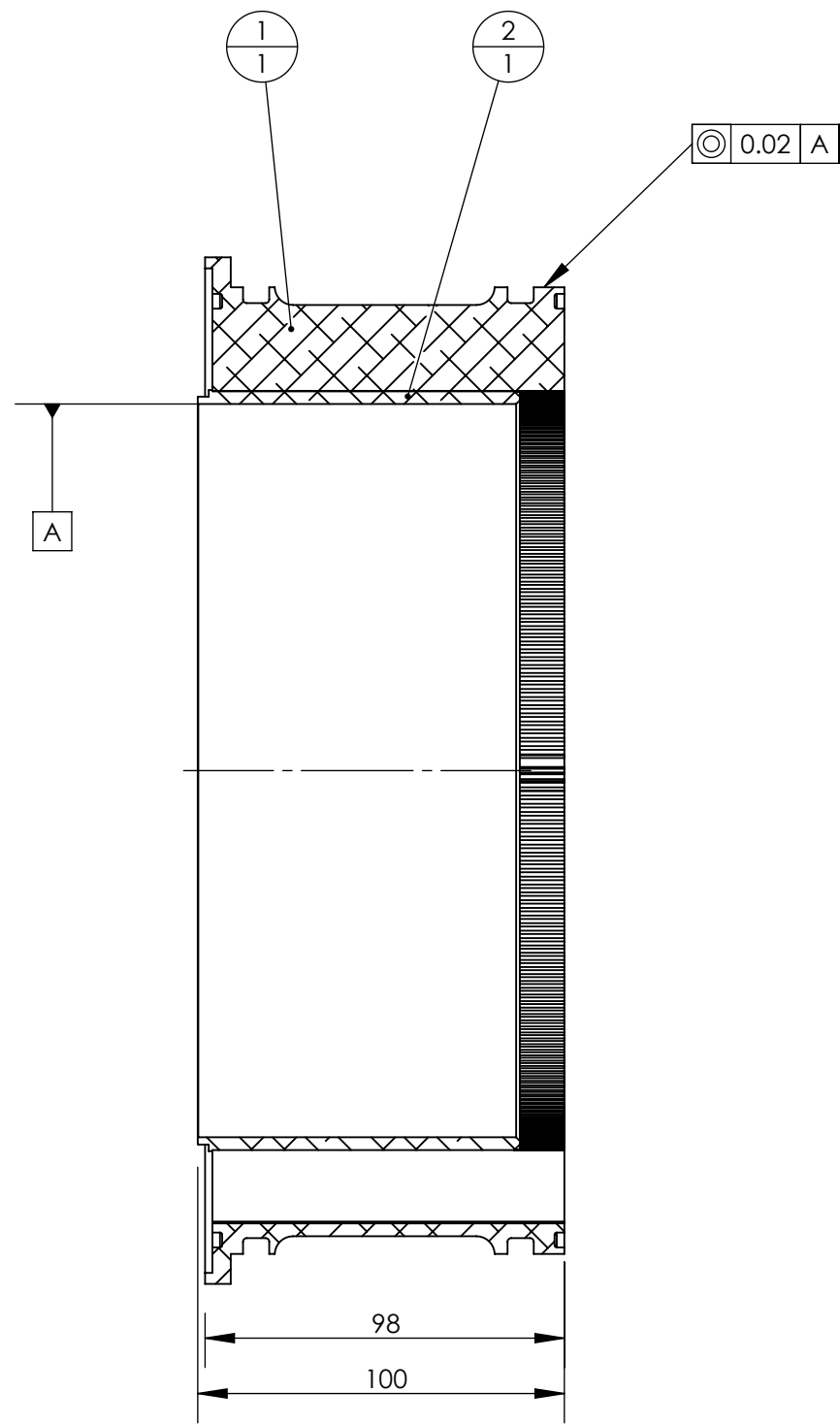
ITEM NO.	PART NUMBER	QTY.
1	A-DC-HC-01-HEX_CARTRIDGE	1
2	A-DC-HC-02-HEX_CARTRIDGE_PIPE	1



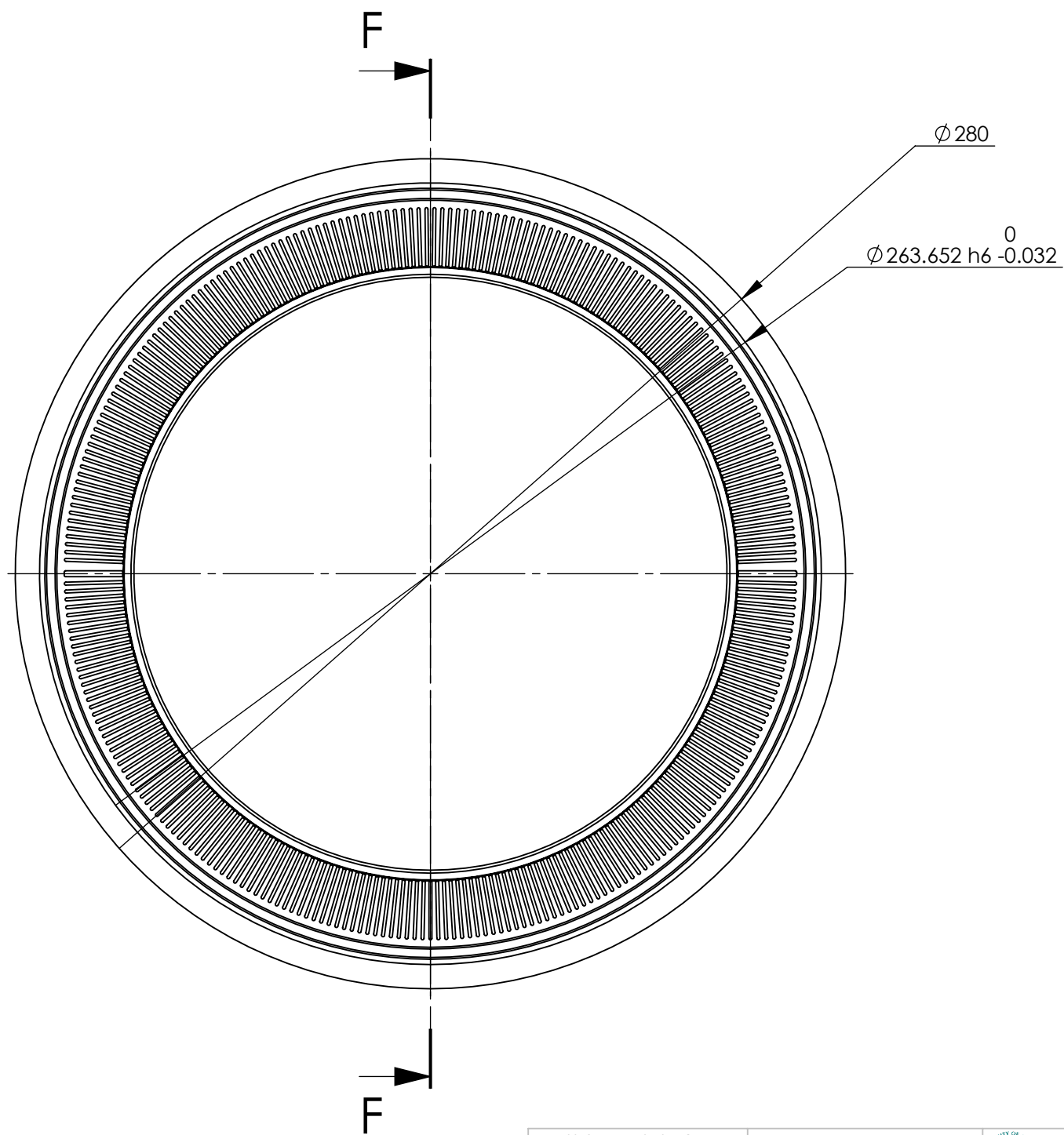
UNLESS OTHERWISE SPECIFIED: DIMENSIONS ARE IN MM TOLERANCES: LINEAR: 0.1 mm ANGULAR: 1° GENERAL SURFACE FINISH: Ra 5 µm O-RING SEAL SURFACE FINISH: Ra 0.8 µm	Comments: Shrink fit using liquid nitrogen.	 The Department of Mechanical Engineering UNIVERSITY OF ALBERTA
	DRW BY: Linda Hasanovich SM BY: Connor Speer CHK BY:	
MATERIAL: Various	Tuesday, September 6, 2022 12:54:55 PM Friday, February 16, 2018 11:53:24 AM	Project: <b>Raphael Engine</b>
FILE NAME: A-DC-HC-00-HEX_CARTRIDGE_ASM	SCALE: 1:2	Mass: 3776.11g

SIZE <b>B</b>	REV
SHEET 15 OF 18	SHEET 15 OF 18

ITEM NO.	PART NUMBER	QTY.
1	A-DC-HC-01-HEX_CARTRIDGE	1
2	A-DC-HC-02-HEX_CARTRIDGE_PIPE	1



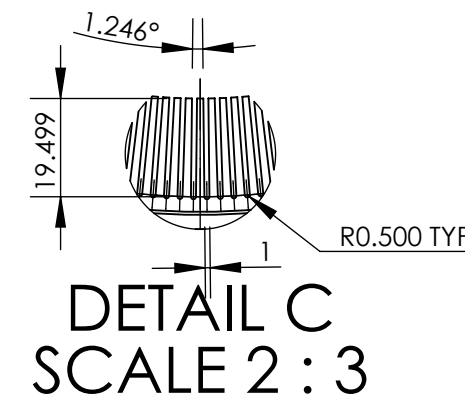
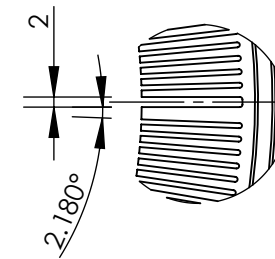
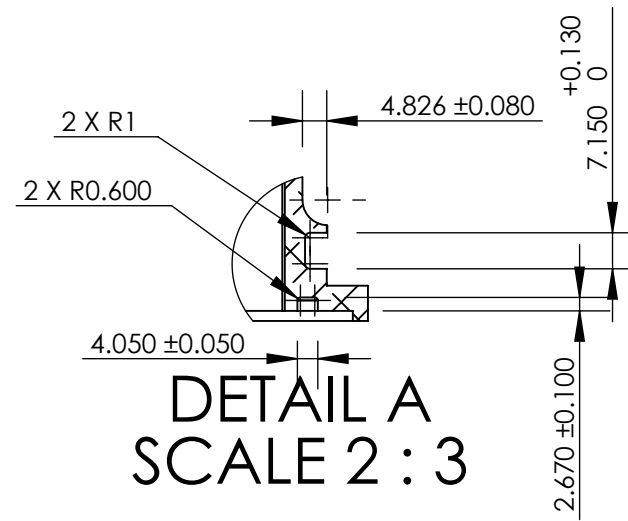
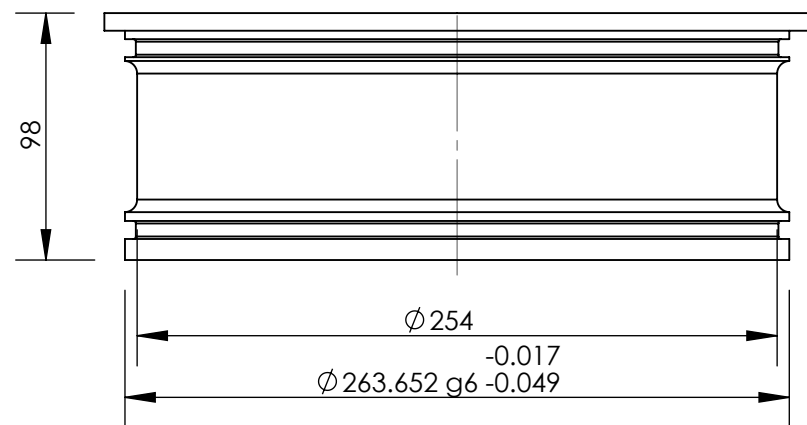
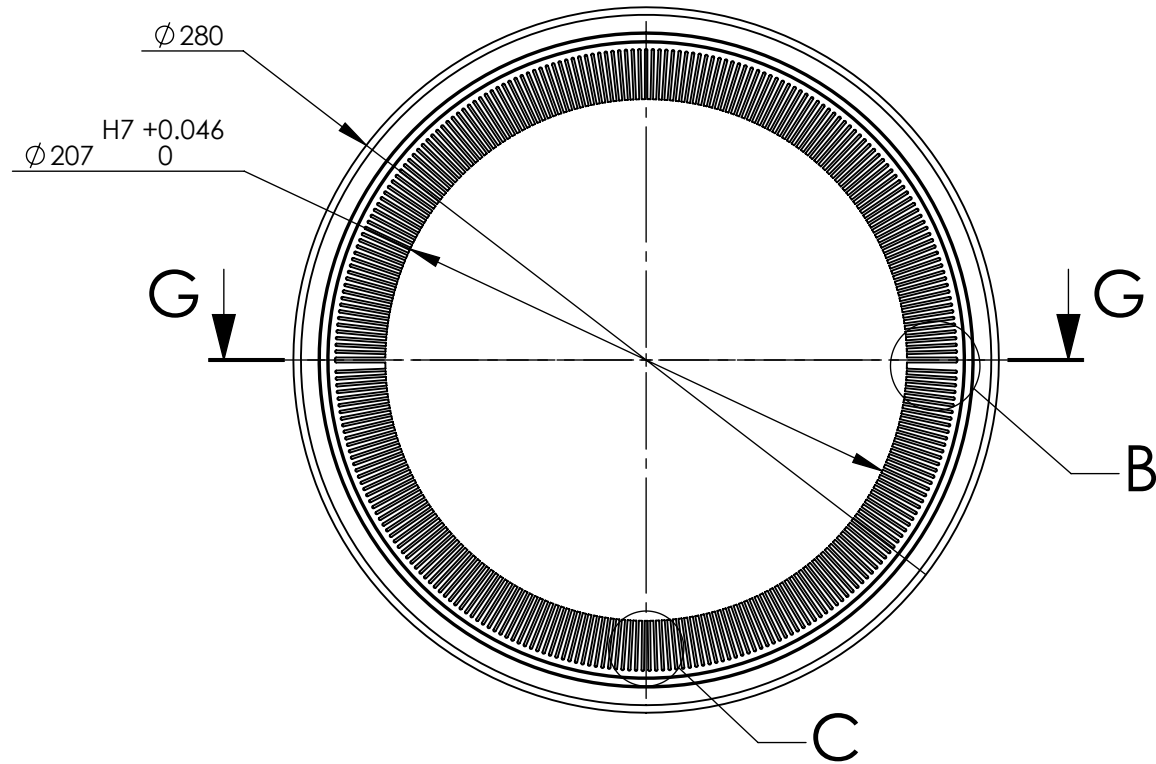
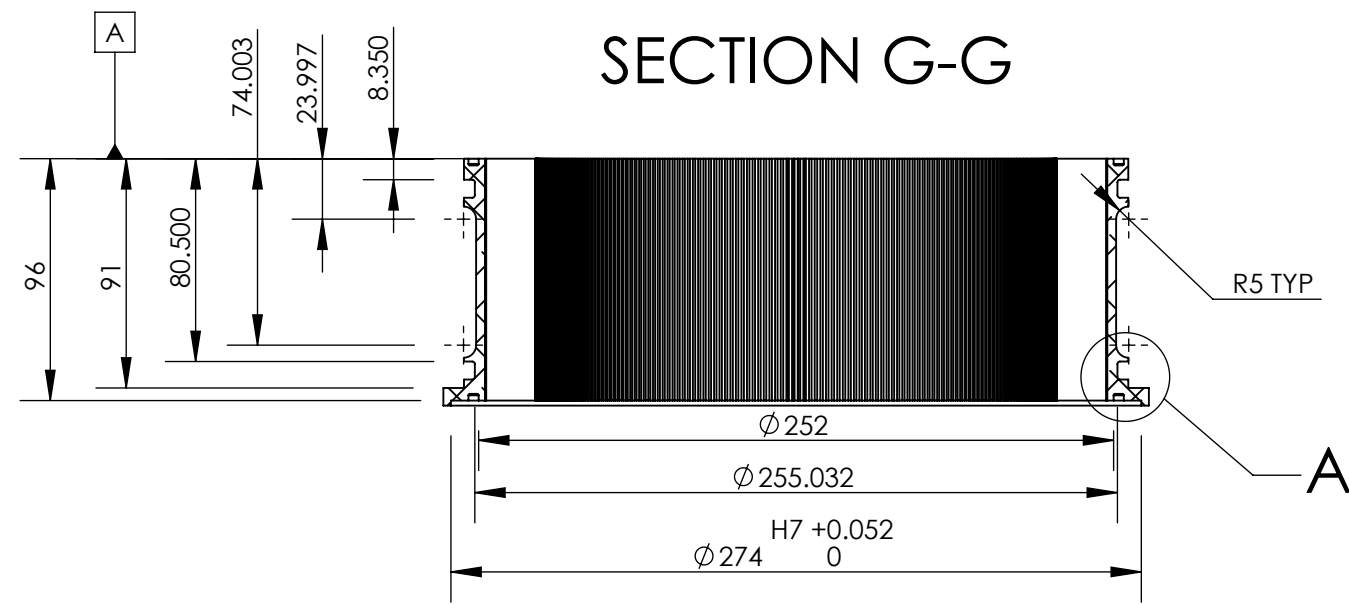
SECTION F-F





<p>UNLESS OTHERWISE SPECIFIED: DIMENSIONS ARE IN MM</p> <p>TOLERANCES: LINEAR: 0.1 mm ANGULAR: 1°</p> <p>GENERAL SURFACE FINISH: Ra 5 <math>\mu</math>m O-RING SEAL SURFACE FINISH: Ra 0.8 <math>\mu</math>m</p>	Comments:	<p>The Department of Mechanical Engineering UNIVERSITY OF ALBERTA</p>
	DRW BY: Linda Hasanovich	
	SM BY: Connor Speer	<p>Project: Raphael Engine</p>
	<p>MATERIAL: Various</p> <p>FILE NAME: A-DC-HC-00-HEX_CARTRIDGE_ASM</p>	<p>CHK BY:</p> <p>Tuesday, September 6, 2022 12:54:55 PM Friday, February 16, 2018 11:53:24 AM</p>

8 7 6 5 4 3 2 1

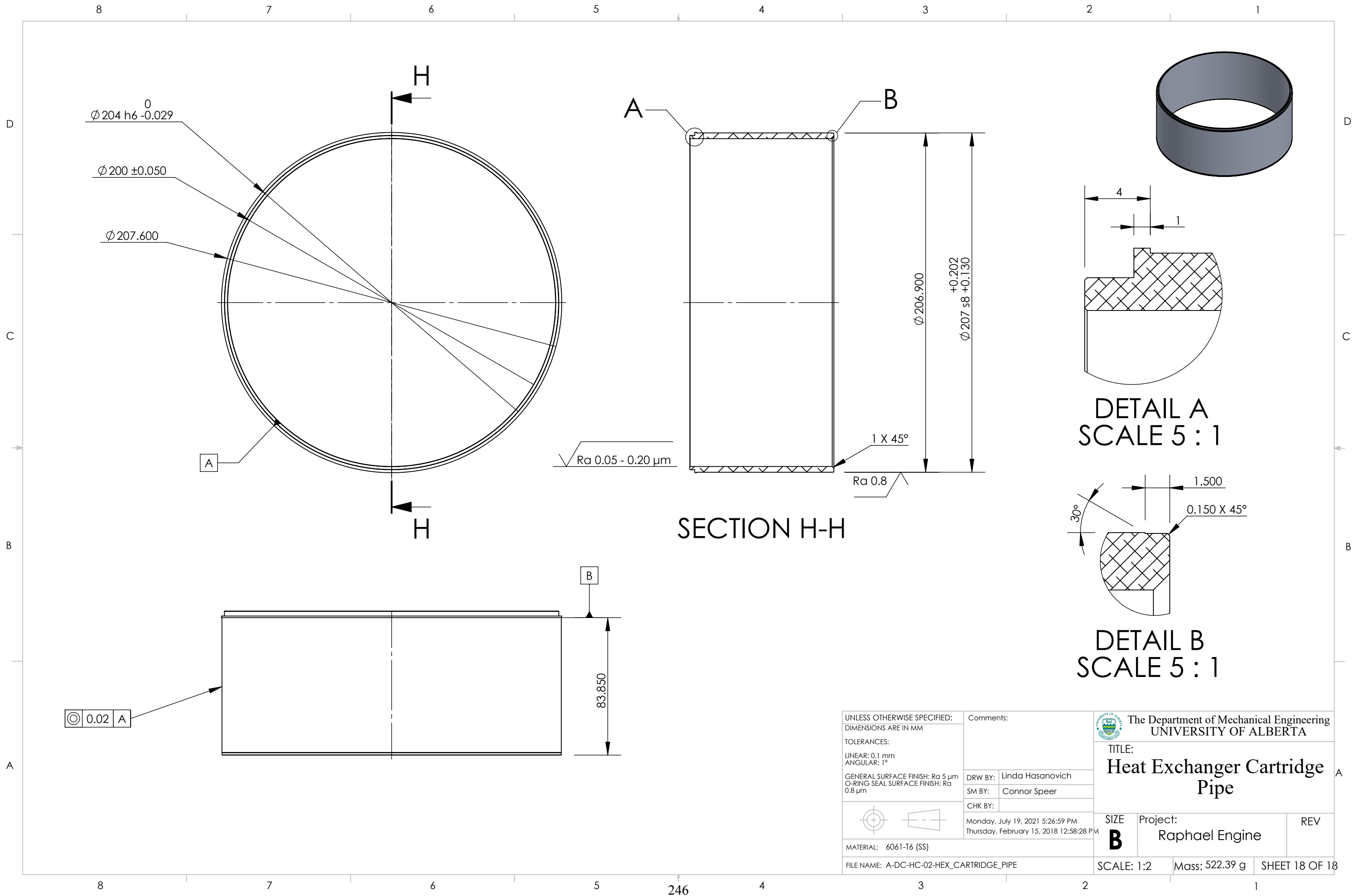
8 7 6 5 4 3 2 1



Note: There are 289 slots in total.  
Slots are evenly spaced.

UNLESS OTHERWISE SPECIFIED: DIMENSIONS ARE IN MM TOLERANCES: LINEAR: 0.1 mm ANGULAR: 1° GENERAL SURFACE FINISH: Ra 5 µm O-RING SEAL SURFACE FINISH: Ra 0.8 µm	Comments:		 <b>The Department of Mechanical Engineering UNIVERSITY OF ALBERTA</b>
	DRW BY:	Linda Hasanovich	
 MATERIAL: 6061-T6 (SS)	SM BY:	Connor Speer	<b>SIZE</b> Project: REV <b>B</b> Raphael Engine
	CHK BY:		
FILE NAME: A-DC-HC-01-HEX_CARTRIDGE	Monday, July 19, 2021 5:26:59 PM Thursday, February 15, 2018 12:46:18 PM		





UNLESS OTHERWISE SPECIFIED:  
 DIMENSIONS ARE IN MM  
 TOLERANCES:  
 LINEAR: 0.1 mm  
 ANGULAR: 1°  
 GENERAL SURFACE FINISH: Ra 5  $\mu\text{m}$   
 O-RING SEAL SURFACE FINISH: Ra 0.8  $\mu\text{m}$   
 MATERIAL: 6061-T6 (SS)  
 FILE NAME: A-DC-HC-02-HEX\_CARTRIDGE\_PIPE

Comments:  
 DRW BY: Linda Hasanovich  
 SM BY: Connor Speer  
 CHK BY:  
 Monday, July 19, 2021 5:26:59 PM  
 Thursday, February 15, 2018 12:58:28 PM

The Department of Mechanical Engineering  
 UNIVERSITY OF ALBERTA  
 TITLE:  
**Heat Exchanger Cartridge Pipe**  
 SIZE **B** Project: Raphael Engine REV  
 SCALE: 1:2 Mass: 522.39 g SHEET 18 OF 18

# Appendix B MATLAB Code for Analytical Analysis and Schmidt Model

## B.1 Analytical Analysis of Section 3.1 for Heating Case

```
%%%%%%%%%%%%%%%%%%%%%%%%%%%%%%%%%%%%%%%%%%%%%%%%%%%%%%%%%%%%%%%%%%%%%%%%%
% INTERNAL FLOW CALCULATOR
%
% Linda Hasanovich
% Updated July 2022
% V1.0
%
% Description: Determines the output temperature of air flowing through a
rectangular channel with isothermal walls using iteration of the bulk mean
temperature.
%
%
% Important Assumptions:
% 1. Assuming steady flow
% 2. Neglecting compressibility effects
%%%%%%%%%%%%%%%%%%%%%%%%%%%%%%%%%%%%%%%%%%%%%%%%%%%%%%%%%%%%%%%%%%%%%%%%%

clear;
clc;
close all;

% Load property tables
load('PropertyTables','AirProp');

% Transcription of table 8-1 Cengel for Nu and f values for rectangular
channel flow in tubes (neglecting the infinite data points for
interpolation).
% Only valid for hydrodynamically and thermally developed flow.
rectNuf = [1 2 3 4 6 8 inf; 2.98 3.39 3.96 4.44 5.14 5.60 7.54; 3.61 4.12
4.79 5.33 6.05 6.49 8.24; 56.92 62.20 68.36 72.92 78.80 82.32 96.00];

% Define hx channel geometry
a = 20/1000; % Channel width [m]
b = 1/1000; % Channel height [m]
Dh = 2*a*b/(a+b); % Hydraulic diameter [m]
Ac = a*b; % Individual channel cross sectional area [m^2]

% Define heat transfer conditions
Ts = 150+273.15; % Constant surface temperature of walls [K]
Tk = 5+273.15; % Cold temperature [K]
P = [300 435 570].*1000; % Engine fill pressure [Pa]
Rair = 287; % Specific gas constant for air [J/kgK]

% Estimate of average fluid velocity based on maximum displacer speed
freq = [100 170 240]./60; % Engine frequency [Hz]
r = 75/1000/2; % Crank length (half of stroke) [m]
```

```

Accdisp = pi/4*(200/1000)^2; % Displacer cross section area [m^2]

% Define inlet fluid parameters
Tin = (Ts-Tk)/log(Ts/Tk); % Inlet fluid average temperature [K]

% Define variable properties
L = [48:12:192]./1000; % Hx channel length [m]
numchan = [145:43:575];

% Define output variable storage
Te_out = zeros(length(L),length(numchan));
Te_ent_out = zeros(length(L),length(numchan));
NTU_ent_out = zeros(length(L),length(numchan));
NTU_out = zeros(length(L),length(numchan));
h_ent_out = zeros(length(L),length(numchan));
h_out = zeros(length(L),length(numchan));
Re_out = zeros(length(L),length(numchan));
deltaP_out = zeros(length(L),length(numchan));
Pr_out = zeros(length(L),length(numchan));
Lh_out = zeros(length(L),length(numchan));
Lt_out = zeros(length(L),length(numchan));
Vhx_out = zeros(length(L),length(numchan));
Vavg_out = zeros(length(L),length(numchan));
Ashx_out = zeros(length(L),length(numchan));
Achx_out = zeros(length(L),length(numchan));
Nu_out = zeros(length(L),length(numchan));
Nu_ent_out = zeros(length(L),length(numchan));

Te_ALL.pressure = struct('freq',{});
Te_ent_ALL.pressure = struct('freq',{});
NTU_ALL.pressure = struct('freq',{});
NTU_ent_ALL.pressure = struct('freq',{});
h_ALL.pressure = struct('freq',{});
h_ent_ALL.pressure = struct('freq',{});
Re_ALL.pressure = struct('freq',{});
deltaP_ALL.pressure = struct('freq',{});
Pr_ALL.pressure = struct('freq',{});
Lh_ALL.pressure = struct('freq',{});
Lt_ALL.pressure = struct('freq',{});
Ldiff_ALL.pressure = struct('freq',{});
Vhx_ALL.pressure = struct('freq',{});
Vavg_ALL.pressure = struct('freq',{});
Ashx_ALL.pressure = struct('freq',{});
Achx_ALL.pressure = struct('freq',{});
Nu_ALL.pressure = struct('freq',{});
Nu_ent_ALL.pressure = struct('freq',{});

counter=0;
nonlamcounter=0;
count=0;
for n=1:length(freq)
    for m=1:length(P)
        for i = 1:length(L)
            for j = 1:length(numchan)
                counter=counter+1;
                % Calculate dependent variable hx geometry properties

```



```

As = 2*(a+b)*L(i); % Heat transfer surface area [m^2]
Ashx = As*numchan(j);
Achx = numchan(j)*Ac; % Cross sectional area of overall heat
exchanger [m^2]
Vhx = L(i)*Achx; % Hx volume [m^3]

% Estimate fluid parameters
Tmi = (Tin+Ts)/2; % Estimate of bulk mean temperature in the
remaining pipe [K]

% Use the continuity equation to get the estimate of air
speed for the hx
omega = 2*pi*freq(n); % Angular velocity [rad/s]
vdisp = omega*r; % Displacer maximum speed [m/s]
vchannel = Acdisp/Achx*vdisp; % Velocity of air in the
channel [m/s]
Vavg = vchannel; % Average fluid velocity [m/s]

deltaTm = 1; % Percent difference between the mean temp guess
and calculated [K]

reps = 0;
while deltaTm > 0.001
    reps=reps+1;

    % Determine properties of air at the mean temperature
    (estimate)
    % AirProp table is in celsius (requires correction
    factor)
    k = interp1(AirProp(:,1),AirProp(:,4),Tmi-273.15); %
Thermal conductivity of fluid at mean temperature [W/mK]
    Pr = interp1(AirProp(:,1),AirProp(:,6),Tmi-273.15); %
Fluid prandtl number at mean temperature
    mu = interp1(AirProp(:,1),AirProp(:,5),Tmi-273.15); %
Fluid dynamic viscosity at mean temperature [kg/ms]
    cp = interp1(AirProp(:,1),AirProp(:,3),Tmi-273.15); %
Fluid specific heat capacity at mean temperature [J/kgK]

    rho = P(m)/(Rair*Tmi); % Fluid density at mean
temperature [kg/m^3]

    nu = mu/rho; % Fluid kinematic viscosity at mean
temperature [m^2/s]

    % Calculate fluid flow characteristics
    Re = Vavg*Dh/nu; % Reynold's number
    mdot = rho*Vavg*Ac; % Mass flow rate [kg/s] thru one
channel

    % Check if laminar or turbulent
    if Re < 2300 % Laminar
        Lh = 0.05*Re*Dh; % Hydrodynamic entrance length [m]
        Lt = Lh*Pr; % Thermal entrance length [m]
        if Lt<L(i)

```

```

        if Lt<Lh % Calculate the entrance region nusselt
numbers for both hydro and thermally developing flow using (8-64)
        % Equation below is valid for Re<=2800
        % Equation 8-64 in Cengel (pg 492)
        Nu_ent =
7.54+(0.03*(Dh/Lt)*Re*Pr)/(1+0.016*((Dh/Lt)*Re*Pr)^(2/3));
        h_ent = Nu_ent*k/Dh; % Entrance region heat
transfer coefficient [W/m^2K]
        As_ent = As*Lt/L(i);
        Te_ent = Ts-(Ts-Tin)*exp(-
h_ent*As_ent/(mdot*cp)); % Exit temperature of entrance region [K]
        NTU_ent = h_ent*As_ent/(mdot*cp);

        % Calculate for fully developed flow
        if a/b <= 8
            Nu = interp1(rectNuf(1,1:end-
1),rectNuf(2,1:end-1),a/b); % Nusselt number for fully developed laminar flow
        else
            Nu = rectNuf(2,end);
        end
        h = Nu*k/Dh; % Heat transfer coefficient
[W/m^2K]
        As_rem = As-As_ent;
        Te = Ts-(Ts-Te_ent)*exp(-h*As_rem/(mdot*cp));
% Estimate of exit temperature [K]
        NTU = h*As_rem/(mdot*cp);
    end
    else % Calculate the entrance region nusselt numbers
for both hydro and thermally developing flow using (8-63)
        % Equation below is valid for Re<=2800
        % Equation 8-64 in Cengel (pg 492)
        count=count+1;
        Nu_ent =
7.54+(0.03*(Dh/L(i))*Re*Pr)/(1+0.016*((Dh/L(i))*Re*Pr)^(2/3));
        h_ent = Nu_ent*k/Dh; % Entrance region heat
transfer coefficient [W/m^2K]
        As_ent = As;
        Te_ent = Ts-(Ts-Tin)*exp(-
h_ent*As_ent/(mdot*cp)); % Exit temperature of entrance region [K]
        NTU_ent = h_ent*As_ent/(mdot*cp);

        Nu = NaN;
        h = NaN;
        Te = Te_ent;
        NTU = NaN;
    end
    % Determine pressure loss from eqn for fully
developed flow
    % The equation is the friction factor for a single
tube
    if a/b <= 8
        f = interp1(rectNuf(1,1:end-1),rectNuf(4,1:end-
1),a/b)/Re; % Friction factor for fully developed laminar flow
    else
        f = rectNuf(4,end)/Re;
    end
end

```

```

else
    % Assumption: The entrance length is small.
    % Equation 8-71 in cengel, valid for Re of 3000 to
5x10^6 and Pr of 0.5 up to 2000, with the f factor calculated from 8-74 its
validity is now 2300 to 4500.
    % Both relations are for smooth tubes.
    % Equation 8-75 FOR f, valid for 2300<8000 Re.
    f = -6.38*10^(-13)*Re^3+1.17*10^(-8)*Re^2-6.69*10^(-
5)*Re+0.147;
    Nu = ((f/8)*(Re-
1000)*Pr)/(1+12.7*(f/8)^0.5*(Pr^(2/3)-1));
    h = Nu*k/Dh; % Entrance region heat transfer
coefficient [W/m^2K]
    Te = Ts-(Ts-Tin)*exp(-h*As/(mdot*cp)); % Exit
temperature of entrance region [K]
    NTU = h*As/(mdot*cp);

    Nu_ent = NaN;
    h_ent = NaN;
    Te_ent = NaN;
    NTU_ent = NaN;
    nonlamcounter=nonlamcounter+1;
end

    deltaP = f*L(i)/Dh*rho*Vavg^2/2; % Pressure loss for all
types of fully developed internal flows (8-45 Cengel) [Pa]

    Tm = mean([Tin Te]); % Calculated mean fluid temperature
[K]

    deltaTm = abs(Tm-Tmi)/mean([Tm,Tmi])*100; % Percent
difference between entrance mean temp guess and calculated [K]
    if reps<100
        Tmi = Tm;
    else
        if Tm>Tmi
            break
        elseif Tm<Tmi
            Tmi=Tmi-0.0001;
        end
    end
end

Te_out(i,j) = Te;
Te_ent_out(i,j) = Te_ent;
NTU_ent_out(i,j) = NTU_ent;
NTU_out(i,j) = NTU;
Nu_out(i,j) = Nu;
Nu_ent_out(i,j) = Nu_ent;
h_ent_out(i,j) = h_ent;
h_out(i,j) = h;
Re_out(i,j) = Re;
deltaP_out(i,j) = deltaP;
Pr_out(i,j) = Pr;
Lh_out(i,j) = Lh;
Lt_out(i,j) = Lt;

```

```

        Vhx_out(i,j) = Vhx;
        Vavg_out(i,j) = Vavg;
        Ashx_out(i,j) = Ashx;
        Achx_out(i,j) = Achx;
    end
end
Te_ALL(m).pressure(n).freq=Te_out;
Te_ent_ALL(m).pressure(n).freq=Te_ent_out;
NTU_ALL(m).pressure(n).freq=NTU_out;
NTU_ent_ALL(m).pressure(n).freq=NTU_ent_out;
h_ent_ALL(m).pressure(n).freq=h_ent_out;
h_ALL(m).pressure(n).freq=h_out;
Re_ALL(m).pressure(n).freq=Re_out;
deltaP_ALL(m).pressure(n).freq=deltaP_out;
Pr_ALL(m).pressure(n).freq=Pr_out;
Lh_ALL(m).pressure(n).freq=Lh_out;
Lt_ALL(m).pressure(n).freq=Lt_out;
Ldiff_ALL(m).pressure(n).freq=Lh_out-Lt_out;
Vhx_ALL(m).pressure(n).freq=Vhx_out;
Vavg_ALL(m).pressure(n).freq=Vavg_out;
Ashx_ALL(m).pressure(n).freq=Ashx_out;
Achx_ALL(m).pressure(n).freq=Achx_out;
Nu_ALL(m).pressure(n).freq=Nu_out;
Nu_ent_ALL(m).pressure(n).freq=Nu_ent_out;
end
end

```

## B.2 Analytical Analysis of Section 3.1 for Cooling Case

```
%%%%%%%%%%%%%%%%%%%%%%%%%%%%%%%%%%%%%%%%%%%%%%%%%%%%%%%%%%%%%%%%%%%%%%%%
% INTERNAL FLOW CALCULATOR, COLD SIDE
%
% Linda Hasanovich
% Updated July 2022
% V1.0
%
% Description: Determines the output temperature of air flowing through a
rectangular channel with isothermal walls using iteration of the bulk mean
temperature.
%
%
% Important Assumptions:
% 1. Assuming steady flow
% 2. Neglecting compressibility effects
%%%%%%%%%%%%%%%%%%%%%%%%%%%%%%%%%%%%%%%%%%%%%%%%%%%%%%%%%%%%%%%%%%%%%%%%

clear;
clc;
close all;

% Load property tables
load('PropertyTables','AirProp');

% Transcription of table 8-1 Cengel for Nu and f values for rectangular
channel flow in tubes (neglecting the infinite data points for
interpolation).
% Only valid for hydrodynamically and thermally developed flow.
rectNuf = [1 2 3 4 6 8 inf; 2.98 3.39 3.96 4.44 5.14 5.60 7.54; 3.61 4.12
4.79 5.33 6.05 6.49 8.24; 56.92 62.20 68.36 72.92 78.80 82.32 96.00];

% Define hx channel geometry
a = 20/1000; % Channel width [m]
b = 1/1000; % Channel height [m]
Dh = 2*a*b/(a+b); % Hydraulic diameter [m]
Ac = a*b; % Individual channel cross sectional area [m^2]

% Define heat transfer conditions
Ts = 5+273.15; % Constant surface temperature of walls [K]
Tk = 150+273.15; % Cold temperature
P = [300 435 570].*1000; % Engine fill pressure [Pa]
Rair = 287; % Specific gas constant for air [J/kgK]

% Estimate of average fluid velocity based on maximum displacer speed
freq = [100 170 240]./60; % Engine frequency [Hz]
r = 75/1000/2; % Crank length (half of stroke) [m]
Acdisp = pi/4*(200/1000)^2; % Displacer cross section area [m^2]

% Define inlet fluid parameters
Tin = (Tk-Ts)/log(Tk/Ts); % Inlet fluid average temperature [K]

% Define variable properties
```

```

L = [48:12:192]./1000; % Hx channel length [m]
numchan = [145:43:575];

% Define output variable storage
Te_out = zeros(length(L),length(numchan));
Te_ent_out = zeros(length(L),length(numchan));
NTU_ent_out = zeros(length(L),length(numchan));
NTU_out = zeros(length(L),length(numchan));
h_ent_out = zeros(length(L),length(numchan));
h_out = zeros(length(L),length(numchan));
Re_out = zeros(length(L),length(numchan));
deltaP_out = zeros(length(L),length(numchan));
Pr_out = zeros(length(L),length(numchan));
Lh_out = zeros(length(L),length(numchan));
Lt_out = zeros(length(L),length(numchan));
Vhx_out = zeros(length(L),length(numchan));
Vavg_out = zeros(length(L),length(numchan));
Ashx_out = zeros(length(L),length(numchan));
Achx_out = zeros(length(L),length(numchan));
Nu_out = zeros(length(L),length(numchan));
f_out = zeros(length(L),length(numchan));

Te_ALL.pressure = struct('freq',{});
Te_ent_ALL.pressure = struct('freq',{});
NTU_ALL.pressure = struct('freq',{});
NTU_ent_ALL.pressure = struct('freq',{});
h_ALL.pressure = struct('freq',{});
h_ent_ALL.pressure = struct('freq',{});
Re_ALL.pressure = struct('freq',{});
deltaP_ALL.pressure = struct('freq',{});
Pr_ALL.pressure = struct('freq',{});
Lh_ALL.pressure = struct('freq',{});
Lt_ALL.pressure = struct('freq',{});
Ldiff_ALL.pressure = struct('freq',{});
Vhx_ALL.pressure = struct('freq',{});
Vavg_ALL.pressure = struct('freq',{});
Ashx_ALL.pressure = struct('freq',{});
Achx_ALL.pressure = struct('freq',{});
Nu_ALL.pressure = struct('freq',{});
f_ALL.pressure = struct('freq',{});

counter=0;
nonlamcounter=0;
for n=1:length(freq)
    for m=1:length(P)
        for i = 1:length(L)
            for j = 1:length(numchan)
                counter=counter+1;
                % Calculate dependent variable hx geometry properties
                As = 2*(a+b)*L(i); % Heat transfer surface area [m^2]
                Ashx = As*numchan(j);
                Achx = numchan(j)*Ac; % Cross sectional area of overall heat
exchanger [m^2]
                Vhx = L(i)*Achx; % Hx volume [m^3]

                % Estimate fluid parameters

```

```

Tmi = (Tin+Ts)/2; % Estimate of bulk mean temperature in the
remaining pipe [K]

% Use the continuity equation to the get estimate of air
speed for the hx
omega = 2*pi*freq(n); % Angular velocity [rad/s]
vdisp = omega*r; % Displacer maximum speed [m/s]
vchannel = Acdisp/Achx*vdisp; % Velocity of air in the
channel [m/s]
Vavg = vchannel; % Average fluid velocity [m/s]

deltaTm = 1; % Percent difference between the mean temp guess
and calculated [K]

reps = 0;
while deltaTm > 0.001
    reps=reps+1;

    % Determine properties of air at the mean temperature
    (estimate)
    % AirProp table is in celsius (requires correction
    factor)
    k = interp1(AirProp(:,1),AirProp(:,4),Tmi-273.15); %
Thermal conductivity of fluid at mean temperature [W/mK]
    Pr = interp1(AirProp(:,1),AirProp(:,6),Tmi-273.15); %
Fluid prandtl number at mean temperature
    mu = interp1(AirProp(:,1),AirProp(:,5),Tmi-273.15); %
Fluid dynamic viscosity at mean temperature [kg/ms]
    cp = interp1(AirProp(:,1),AirProp(:,3),Tmi-273.15); %
Fluid specific heat capacity at mean temperature [J/kgK]

    rho = P(m)/(Rair*Tmi); % Fluid density at mean
temperature [kg/m^3]

    nu = mu/rho; % Fluid kinematic viscosity at mean
temperature [m^2/s]

    % Calculate fluid flow characteristics
    Re = Vavg*Dh/nu; % Reynold's number
    mdot = rho*Vavg*Ac; % Mass flow rate [kg/s] thru one
channel

    % Check if laminar or turbulent
    if Re < 2300 % Laminar
        Lh = 0.05*Re*Dh; % Hydrodynamic entrance length [m]
        Lt = Lh*Pr; % Thermal entrance length [m]
        if Lt<L(i)
            if Lt<Lh % Calculate the entrance region nusselt
numbers for both hydro and thermally developing flow using (8-63)
                % Equation below is valid for Re<=2800
                % Equation 8-64 in Cengel (pg 492)
                Nu_ent =
7.54+(0.03*(Dh/Lt)*Re*Pr)/(1+0.016*((Dh/Lt)*Re*Pr)^(2/3));
                h_ent = Nu_ent*k/Dh; % Entrance region heat
transfer coefficient [W/m^2K]

```

```

        As_ent = As*Lt/L(i);
        Te_ent = Ts-(Ts-Tin)*exp(-
h_ent*As_ent/(mdot*cp)); % Exit temperature of entrance region [K]
        NTU_ent = h_ent*As_ent/(mdot*cp);

        % Calculate for fully developed flow
        if a/b <= 8
            Nu = interp1(rectNuf(1,1:end-
1),rectNuf(2,1:end-1),a/b); % Nusselt number for fully developed laminar flow
        else
            Nu = rectNuf(2,end);
        end
        h = Nu*k/Dh; % Heat transfer coefficient
[W/m^2K]

        As_rem = As-As_ent;
        Te = Ts-(Ts-Te_ent)*exp(-h*As_rem/(mdot*cp));
% Estimate of exit temperature [K]
        NTU = h*As_rem/(mdot*cp);
    end
    else % Calculate the entrance region nusselt numbers
for both hydro and thermally developing flow using (8-63)
        % Equation below is valid for Re<=2800
        % Equation 8-64 in Cengel (pg 492)
        Nu_ent =
7.54+(0.03*(Dh/L(i))*Re*Pr)/(1+0.016*((Dh/L(i))*Re*Pr)^(2/3));
        h_ent = Nu_ent*k/Dh; % Entrance region heat
transfer coefficient [W/m^2K]
        As_ent = As;
        Te_ent = Ts-(Ts-Tin)*exp(-
h_ent*As_ent/(mdot*cp)); % Exit temperature of entrance region [K]
        NTU_ent = h_ent*As_ent/(mdot*cp);

        Nu = NaN;
        h = NaN;
        Te = Te_ent;
        NTU = NaN;
    end
    % Determine pressure loss from eqn for fully
developed flow
    % The equation is the friction factor for a single
tube
    if a/b <= 8
        f = interp1(rectNuf(1,1:end-1),rectNuf(4,1:end-
1),a/b)/Re; %Friction factor for fully developed laminar flow
    else
        f = rectNuf(4,end)/Re;
    end
    else
        % Assumption: The entrance length is small.
        % Equation 8-71 in cengel, valid for Re of 3000 to
5x10^6 and Pr of 0.5 up to 2000, with the f factor calculated from 8-74 its
validity is now 2300 to 4500.
        % Both relations are for smooth tubes.
        % Equation 8-75 for f, valid for 2300<8000 Re.
        f = -6.38*10^(-13)*Re^3+1.17*10^(-8)*Re^2-6.69*10^(-
5)*Re+0.147;

```



```

        Nu = ((f/8)*(Re-
1000)*Pr)/(1+12.7*(f/8)^0.5*(Pr^(2/3)-1));
        h = Nu*k/Dh; % Entrance region heat transfer
coefficient [W/m^2K]
        Te = Ts-(Ts-Tin)*exp(-h*As/(mdot*cp)); % Exit
temperature of entrance region [K]
        NTU = h*As/(mdot*cp);

        Nu_ent = NaN;
        h_ent = NaN;
        Te_ent = NaN;
        NTU_ent = NaN;
        Lh = NaN;
        Lt = NaN;
        nonlamcounter=nonlamcounter+1;
    end

        deltaP = f*L(i)/Dh*rho*Vavg^2/2; % Pressure loss for all
types of fully developed internal flows (8-45 Cengel) [Pa]

        Tm = mean([Tin Te]); % Calculated mean fluid temperature
[K]

        deltaTm = abs(Tm-Tmi)/mean([Tm,Tmi])*100; % Percent
difference between the entrance mean temp guess and calculated [K]
        if reps<100
            Tmi = Tm;
        else
            if Tm>Tmi
                break
            elseif Tm<Tmi
                Tmi=Tmi-0.0001;
            end
        end
    end
end

Te_out(i,j) = Te;
Te_ent_out(i,j) = Te_ent;
NTU_ent_out(i,j) = NTU_ent;
NTU_out(i,j) = NTU;
Nu_out(i,j) = Nu;
h_ent_out(i,j) = h_ent;
h_out(i,j) = h;
Re_out(i,j) = Re;
deltaP_out(i,j) = deltaP;
Pr_out(i,j) = Pr;
Lh_out(i,j) = Lh;
Lt_out(i,j) = Lt;
Vhx_out(i,j) = Vhx;
Vavg_out(i,j) = Vavg;
Ashx_out(i,j) = Ashx;
Achx_out(i,j) = Achx;
f_out(i,j) = f;
end
end
Te_ALL(m).pressure(n).freq=Te_out;

```

```
Te_ent_ALL(m).pressure(n).freq=Te_ent_out;
NTU_ALL(m).pressure(n).freq=NTU_out;
NTU_ent_ALL(m).pressure(n).freq=NTU_ent_out;
h_ent_ALL(m).pressure(n).freq=h_ent_out;
h_ALL(m).pressure(n).freq=h_out;
Re_ALL(m).pressure(n).freq=Re_out;
deltaP_ALL(m).pressure(n).freq=deltaP_out;
Pr_ALL(m).pressure(n).freq=Pr_out;
Lh_ALL(m).pressure(n).freq=Lh_out;
Lt_ALL(m).pressure(n).freq=Lt_out;
Ldiff_ALL(m).pressure(n).freq=Lh_out-Lt_out;
Vhx_ALL(m).pressure(n).freq=Vhx_out;
Vavg_ALL(m).pressure(n).freq=Vavg_out;
Ashx_ALL(m).pressure(n).freq=Ashx_out;
Achx_ALL(m).pressure(n).freq=Achx_out;
Nu_ALL(m).pressure(n).freq=Nu_out;
f_ALL(m).pressure(n).freq=f_out;
end
end
```

## B.3 Schmidt Model Analysis of Section 3.2

```
%%%%%%%%%%%%%%%%%%%%%%%%%%%%%%%%%%%%%%%%%%%%%%%%%%%%%%%%%%%%%%%%%%%%%%%%
% GAMMA SCHMIDT ANALYSIS
%
% Jason Michaud
% June 2016
%
% Modified by:
% Linda Hasanovich
% Updated July 2022
% V1.0
%
% Description: This script calculates the pressure, heat transfer rates, work
done, and efficiency of a Gamma Stirling engine using the Schmidt analysis
equations which may be found in Appendix C of "Mechanical Efficiency of Heat
Engines" by James R. Senft. It also adds the Schmidt model derived directly
from the isothermal assumptions.
%
% Important Assumptions: The Schmidt analysis uses the Isothermal model and
assumes sinusoidal volume variations to obtain closed form solutions.
%%%%%%%%%%%%%%%%%%%%%%%%%%%%%%%%%%%%%%%%%%%%%%%%%%%%%%%%%%%%%%%%%%%%%%%%
% Nomenclature for input variables:
%
% R: Specific ideal gas constant of working gas [J/kgK]
%   287 for Air, 297 for Nitrogen, 2077 for Helium, 4124 for Hydrogen
% Vswd: Displacer swept volume [m^3]
% Vcle: Expansion space clearance volume [m^3]
% Vswp: Powerpiston swept volume [m^3]
% Vclc: Compression space clearance volume [m^3]
% Vh: Heater volume [m^3]
% Vr: Regenerator volume [m^3]
% Vk: Cooler volume [m^3]
% Th: Hot Side side gas temperature [K] (heater and expansion space)
% Tk: Cold Side side gas temperature [K] (cooler and compression space)
% f: Operating frequency [cycles/s]
% Pwork: The average working pressure in the engine [Pa]
% alpha: Phase angle of the expansion space volume variations relative to the
compression space volume variations
%%%%%%%%%%%%%%%%%%%%%%%%%%%%%%%%%%%%%%%%%%%%%%%%%%%%%%%%%%%%%%%%%%%%%%%%

clc,clear,close all

VhxSET = (0:1:4000).*0.000001.*2; % Heat exchanger volume [m^3]
Temps = [30 25 20 15 10 5; 95 110 120 130 140 150]; % Temperature [deg C]
Power = zeros(length(VhxSET),size(Temps,2));
Power_L = zeros(length(VhxSET),size(Temps,2));
Work = zeros(length(VhxSET),size(Temps,2));
Work_L = zeros(length(VhxSET),size(Temps,2));
Work_ALL.pressure = struct('freq',{});
Work_L_ALL.pressure = struct('freq',{});
Power_ALL.pressure = struct('freq',{});
Power_L_ALL.pressure = struct('freq',{});
freq = [100 170 240]./60; % Engine frequency [Hz]
Pmeans = [300 435 570].*1000; % Engine fill pressure [Pa]
```

```

% Loop to see the effect of increasing dead volume (via hx)

for n=1:length(freq)
    for m=1:length(Pmeans)
        j = 1;
        while j < size(Temps,2)+1
            i = 1;
            for Vhx = VhxSET

                % Variable definitons
                R = 287; % [J/kgK]
                Vswd = 2356.193*0.000001; % [m^3]
                Vcle = (204.980/2+87.775/2)*0.000001; % [m^3]
                Vswp = 432.929*0.000001; % [m^3]
                Vclc = (204.980/2+4.62+165.98+87.775/2)*0.000001; % [m^3]
                Vh = Vhx/2; % [m^3]
                Vr = 347.789*0.000001; % [m^3]
                Vk = Vhx/2; % [m^3]
                Th = Temps(2,j)+273.15; % [K]
                Tk = Temps(1,j)+273.15; % [K]
                Pmean = Pmeans(m); % [Pa]
                alpha = (90/180)*pi; % [rad] phase angle
                f = freq(n); % [cycles/s]

                % Constant calculations
                Vd = Vcle + Vclc + Vh + Vr + Vk; % Dead volume [m^3]
                tao = Tk/Th; % Temperature ratio
                kappa = Vswp/Vswd; % Ratio of piston swept volume to
displacer swept volume
                chi = Vd/Vswd; % Dead volume ratio

                % Senft pressure calculations
                Y = 1 + tao + kappa + ((4*chi*tao)/(1+tao));
                A = kappa - ((1-tao)*cos(alpha));
                B = (1-tao)*sin(alpha);
                phi = acos(A/(sqrt((A^2) + (B^2))));
                X = sqrt((A^2) + (B^2));

                % Calculation of heat and work (Senft calculation)
                W = (pi*(1-
tao)*(Vswd+Vswp)*Pmean*kappa*sin(alpha))/((kappa+1)*(sqrt((Y^2)-(X^2))+Y));
                Power(i,j) = (W*f); % Power output [W]
                Work(i,j) = W; % Work output [J]

                % Rederivation for gammas
                A = Vswd/(2*Tk)+Vswp/(2*Tk)+Vclc/Tk+Vk/Tk+Vr*log(Th/Tk)/(Th-
Tk)+Vh/Th+Vcle/Th+Vswd/(2*Th);
                B = Vswd*(Tk-Th)/(2*Th*Tk);
                C = sqrt((B*cos(alpha)+Vswp/(2*Tk))^2+(B*sin(alpha))^2);
                y = atan((B*sin(alpha))/(B*cos(alpha)+Vswp/(2*Tk)));
                W_L = Vswp*pi*A/C*Pmean*sin(y)*(sqrt(1-(C/A)^2)-1);

                Power_L(i,j) = (W_L*f);
            end
            j = j + 1;
        end
    end
end

```

```
        Work_L(i,j) = W_L;

        i = i+1;
    end
    j = j + 1;
end
Work_ALL(m).pressure(n).freq=Work;
Work_L_ALL(m).pressure(n).freq=Work_L;
Power_ALL(m).pressure(n).freq=Power;
Power_L_ALL(m).pressure(n).freq=Power_L;
end
end
```

## B.4 Analytical Comparison for Air Side CFD of Section 5.3 for Heating Case

```

%%%%%%%%%%%%%%%%%%%%%%%%%%%%%%%%%%%%%%%%%%%%%%%%%%%%%%%%%%%%%%%%%%%%%%%%
% INTERNAL FLOW CALCULATOR, CFD GAS COMPARISON
%
% Linda Hasanovich
% Updated July 2022
% V1.0
%
% Description: Determines the output temperature of air flowing through a
rectangular channel with isothermal walls using iteration of the bulk mean
temperature.
%
%
% Important Assumptions:
% 1. Assuming steady flow
% 2. Neglecting compressibility effects
%%%%%%%%%%%%%%%%%%%%%%%%%%%%%%%%%%%%%%%%%%%%%%%%%%%%%%%%%%%%%%%%%%%%%%%%

clear;
clc;
close all;

% Load property tables
load('D:\Linda Hasanovich\04_HX Calculators\PropertyTables','AirProp');

% Thermal conductivity of aluminum
propalum = [4 5.4; 10 14.2; 20 28.5; 40 52.3; 80 85.7; 100 97.8; 150 120.5;
200 136.2; 250 147.5; 300 155.5];

% Transcription of table 8-1 Cengel for Nu and f values for rectangular
channel flow in tubes (neglecting the infinite data points for
interpolation).
% Only valid for hydrodynamically and thermally developed flow.
rectNuf = [1 2 3 4 6 8 inf; 2.98 3.39 3.96 4.44 5.14 5.60 7.54; 3.61 4.12
4.79 5.33 6.05 6.49 8.24; 56.92 62.20 68.36 72.92 78.80 82.32 96.00];

% Define hx channel geometry
a = 20/1000; % Channel width [m]
b = 1/1000; % Channel height [m]
Dh = 2*a*b/(a+b); % Hydraulic diameter [m]
Ac = a*b; % Individual channel cross sectional area [m^2]

% Define heat transfer conditions
Ts = 150+273.15; % Constant surface temperature of walls [K]
Tk = 5+273.15; % Cold temperature [k]
P = [300 435 570].*1000; % Engine fill pressure [Pa]
Rair = 287; % Specific gas constant for air [J/kgK]

% Estimate of average fluid velocity based on maximum displacer speed
freq = [100 170 240]/60; % Engine frequency [Hz]
r = 75/1000/2; % Crank length (half of stroke) [m]

```

```

Acdisp = pi/4*(200/1000)^2; % Displacer cross section area [m^2]

% Define inlet fluid parameters
Tin = (Ts-Tk)/log(Ts/Tk); % Inlet fluid average temperature [K]

% Define variable properties
L = 96/1000; % Hx channel length [m]
numchan = 289;

% Calculate dependent variable hx geometry properties
As = 2*(a+b)*L; % Heat transfer surface area [m^2]
Ashx = As*numchan;
Achx = numchan*Ac; % Cross sectional area of overall heat exchanger [m^2]
Vhx = L*Achx; % Hx volume [m^3]

Tsurall = zeros(length(P),length(freq));
Teall = zeros(length(P),length(freq));
deltaPall = zeros(length(P),length(freq));

for j = 1:length(P)
    for i=1:length(freq)

        % Estimate fluid parameters
        deltaTs = 1;

        Tsuri=Ts-10;

        reps = 0;
        repb = 0;
        while deltaTs > 0.001

            repb=repb+1;
            Tmi = (Tin+Ts)/2; % Estimate of bulk mean temperature in the
remaining pipe [K]

            deltaTm = 1; % Percent difference between the mean temp guess and
calculated [K]

            while deltaTm > 0.001

                % Use the continuity equation to get the estimate of air
speed for the hx
                vdisp = 2*2*r*freq(i); % Displacer average speed [m/s]
                vchannel = Acdisp/Achx*vdisp; % Velocity of air in the
channel [m/s]
                Vavg = vchannel; % Average fluid velocity [m/s]

                reps=reps+1;

                % Determine properties of air at the mean temperature
(estimate)
                % AirProp table is in celsius (requires correction factor)
                k = interp1(AirProp(:,1),AirProp(:,4),Tmi-273.15); % Thermal
conductivity of fluid at mean temperature [W/mK]

```

```

        Pr = interp1(AirProp(:,1),AirProp(:,6),Tmi-273.15); % Fluid
prandtl number at mean temperature
        mu = interp1(AirProp(:,1),AirProp(:,5),Tmi-273.15); % Fluid
dynamic viscosity at mean temperature [kg/ms]
        cp = interp1(AirProp(:,1),AirProp(:,3),Tmi-273.15); % Fluid
specific heat capacity at mean temperature [J/kgK]
        mus = interp1(AirProp(:,1),AirProp(:,5),Tsurf-273.15); %
Fluid dynamic viscosity at surface temperature [kg/ms]

        rho = P(j)/(Rair*Tmi); % Fluid density at mean temperature
[kg/m^3]

        nu = mu/rho; % Fluid kinematic viscosity at mean temperature
[m^2/s]

% Calculate fluid flow characteristics
Re = Vavg*Dh/nu; % Reynold's number
mdot = rho*Vavg*Ac; % Mass flow rate [kg/s] thru one channel

% Check if laminar or turbulent
if Re < 2300 % Laminar
    Lh = 0.05*Re*Dh; % Hydrodynamic entrance length [m]
    Lt = Lh*Pr; % Thermal entrance length [m]
    if Lt<L
        if Lt<Lh % Calculate the entrance region nusselt
numbers for both hydro and thermally developing flow using (8-63)
            % Equation below is valid for Re<=2800
            % Equation 8-64 in Cengel (pg 492)
            Nu_ent =
7.54+(0.03*(Dh/Lt)*Re*Pr)/(1+0.016*((Dh/Lt)*Re*Pr)^(2/3));
            h_ent = Nu_ent*k/Dh; % Entrance region heat
transfer coefficient [W/m^2K]
            As_ent = As*Lt/L;
            Te_ent = Tsurf-(Tsurf-Tin)*exp(-
h_ent*As_ent/(mdot*cp)); % Exit temperature of entrance region [K]
            NTU_ent = h_ent*As_ent/(mdot*cp);

            % Calculate for fully developed flow
            if a/b <= 8
                Nu = interp1(rectNuf(1,1:end-
1),rectNuf(2,1:end-1),a/b); % Nusselt number for fully developed laminar flow
            else
                Nu = rectNuf(2,end);
            end
            h = Nu*k/Dh; % Heat transfer coefficient [W/m^2K]
            As_rem = As-As_ent;
            Te = Tsurf-(Tsurf-Te_ent)*exp(-
h*As_rem/(mdot*cp)); % Estimate of exit temperature [K]
            NTU = h*As_rem/(mdot*cp);
        end
    else % Calculate the entrance region nusselt numbers for
both hydro and thermally developing flow using (8-63)
        % Equation below is valid for Re<=2800
        % Equation 8-64 in Cengel (pg 492)

```



```

        Nu_ent =
7.54+(0.03*(Dh/L)*Re*Pr)/(1+0.016*((Dh/L)*Re*Pr)^(2/3));
        h_ent = Nu_ent*k/Dh; % Entrance region heat transfer
coefficient [W/m^2K]
        As_ent = As;
        Te_ent = Tsuri-(Tsuri-Tin)*exp(-
h_ent*As_ent/(mdot*cp)); % Exit temperature of entrance region [K]
        NTU_ent = h_ent*As_ent/(mdot*cp);

        % Variable reassignment
        Nu = Nu_ent;
        h = h_ent;
        Te = Te_ent;
        NTU = NTU_ent;
    end
    % Determine pressure loss from eqn for fully developed
flow
    % The equation is the friction factor for a single tube
    if a/b <= 8
        f = interp1(rectNuf(1,1:end-1),rectNuf(4,1:end-
1),a/b)/Re; % Friction factor for fully developed laminar flow
    else
        f = rectNuf(4,end)/Re;
    end
end

    Tm = mean([Tin Te]); % Calculated mean fluid temperature [K]

    deltaTm = abs(Tm-Tmi)/mean([Tm,Tmi])*100; % Percent
difference between the entrance mean temp guess and calculated [K]
    if reps<100
        Tmi = Tm;
    else
        if Tm>Tmi
            break
        elseif Tm<Tmi
            Tmi=Tmi-0.0001;
        end
    end
end

    % Evaluate aluminum thermal conductivity
    kalum=interp1(propalum(:,1),propalum(:,2),Tsuri); % [W/mK] for
aluminum 6061
    if isnan(kalum)
        kalum = propalum(end,2);
    end
    % Equation for thermal resistance of a cylinder
    Rcond1=log(127/(127-3.5))/(2*pi*L*kalum)*289;
    Rcond2=log((127-3.5)/(127-3.5-10))/(2*pi*L*kalum*3/5);
    Rcond=Rcond1;

    Tsur = Ts-(Te-Tin)*mdot*cp*Rcond;
    deltaTs=abs(Tsur-Tsuri)/mean([Tsur,Tsuri])*100;
    Tsuri=Tsur;
end
end

```

```

h=b/2;

if L>Lh
    Kaxis=(Lh/h)/(Vavg*h/nu);
else
    Kaxis=(L/h)/(Vavg*h/nu);
end

if Kaxis > 0.4
    K = 0.686;
else
    disp("axial position less")
end
deltaP=0.5*rho*Vavg^2*(f*L/Dh);

Tsurall(i,j)=Tsur-273.15;
Teall(i,j)=Te-273.15;
deltaPall(i,j)=deltaP;
end
end

```

## B.5 Analytical Comparison for Air Side CFD of Section 5.3 for Cooling Case

```

%%%%%%%%%%%%%%%%%%%%%%%%%%%%%%%%%%%%%%%%%%%%%%%%%%%%%%%%%%%%%%%%%%%%%%%%
% INTERNAL FLOW CALCULATOR, CFD GAS COMPARISON COLD SIDE
%
% Linda Hasanovich
% Updated July 2022
% V1.0
%
% Description: Determines the output temperature of air flowing through a
rectangular channel with isothermal walls using iteration of the bulk mean
temperature.
%
%
% Important Assumptions:
% 1. Assuming steady flow
% 2. Neglecting compressibility effects
%%%%%%%%%%%%%%%%%%%%%%%%%%%%%%%%%%%%%%%%%%%%%%%%%%%%%%%%%%%%%%%%%%%%%%%%

clear;
clc;
close all;

% Load property tables
load('X:\01_Current_Students\Linda Hasanovich\04_HX
Calculators\PropertyTables','AirProp');

% Thermal conductivity of aluminum
propalum = [4 5.4; 10 14.2; 20 28.5; 40 52.3; 80 85.7; 100 97.8; 150 120.5;
200 136.2; 250 147.5; 300 155.5];

% Transcription of table 8-1 Cengel for Nu and f values for rectangular
channel flow in tubes (neglecting the infinite data points for
interpolation).
% Only valid for hydrodynamically and thermally developed flow.
rectNuf = [1 2 3 4 6 8 inf; 2.98 3.39 3.96 4.44 5.14 5.60 7.54; 3.61 4.12
4.79 5.33 6.05 6.49 8.24; 56.92 62.20 68.36 72.92 78.80 82.32 96.00];

% Define hx channel geometry
a = 20/1000; % Channel width [m]
b = 1/1000; % Channel height [m]
Dh = 2*a*b/(a+b); % Hydraulic diameter [m]
Ac = a*b; % Individual channel cross sectional area [m^2]

% Define heat transfer conditions
Ts = 150+273.15; % Constant surface temperature of walls [K]
Tk = 5+273.15; % Cold temperature
P = [300 435 570].*1000; % Engine fill pressure [Pa]
Rair = 287; % Specific gas constant for air [J/kgK]

% Estimate of average fluid velocity based on maximum displacer speed
freq = [100 170 240]/60; % Engine frequency [Hz]

```

```

r = 75/1000/2; % Crank length (half of stroke) [m]
Acdisp = pi/4*(200/1000)^2; % Displacer cross section area [m^2]

% Define inlet fluid parameters
Tin = (Ts-Tk)/log(Ts/Tk); % Inlet fluid average temperature [K]

% Define variable properties
L = 96/1000; % Hx channel length [m]
numchan = 289;

% Calculate dependent variable hx geometry properties
As = 2*(a+b)*L; % Heat transfer surface area [m^2]
Ashx = As*numchan;
Achx = numchan*Ac; % Cross sectional area of overall heat exchanger [m^2]
Vhx = L*Achx; % Hx volume [m^3]

Tsurall = zeros(length(P),length(freq));
Teall = zeros(length(P),length(freq));
deltaPall = zeros(length(P),length(freq));

for j = 1:length(P)
    for i=1:length(freq)

        % Estimate fluid parameters
        deltaTs = 1;

        Tsuri=Ts-10;

        reps = 0;
        repb = 0;
        while deltaTs > 0.001
            repb=repb+1;
            Tmi = (Tin+Tk)/2; % Estimate of the bulk mean temperature in the
remaining pipe [K]

            deltaTm = 1; % Percent difference between the mean temp guess and
calculated [K]

            while deltaTm > 0.001

                % Use the continuity equation to get estimate of air speed
for the hx
                vdisp = 2*2*r*freq(i); % Displacer average speed [m/s]
                vchannel = Acdisp/Achx*vdisp; % Velocity of air in the
channel [m/s]
                Vavg = vchannel; % Average fluid velocity [m/s]

                reps=reps+1;

                % Determine properties of air at the mean temperature
                (estimate)
                % AirProp table is in celsius (requires correction factor)
                k = interp1(AirProp(:,1),AirProp(:,4),Tmi-273.15); % Thermal
conductivity of fluid at mean temperature [W/mK]

```

```

        Pr = interp1(AirProp(:,1),AirProp(:,6),Tmi-273.15); % Fluid
prandtl number at mean temperature
        mu = interp1(AirProp(:,1),AirProp(:,5),Tmi-273.15); % Fluid
dynamic viscosity at mean temperature [kg/ms]
        cp = interp1(AirProp(:,1),AirProp(:,3),Tmi-273.15); % Fluid
specific heat capacity at mean temperature [J/kgK]
        mus = interp1(AirProp(:,1),AirProp(:,5),Tsurf-273.15); %
Fluid dynamic viscosity at surface temperature [kg/ms]

        rho = P(j)/(Rair*Tmi); % Fluid density at mean temperature
[kg/m^3]

        nu = mu/rho; % Fluid kinematic viscosity at mean temperature
[m^2/s]

        % Calculate fluid flow characteristics
Re = Vavg*Dh/nu; % Reynold's number
mdot = rho*Vavg*Ac; % Mass flow rate [kg/s] thru one channel

        % Check if laminar or turbulent
if Re < 2300 % Laminar
    Lh = 0.05*Re*Dh; % Hydrodynamic entrance length [m]
    Lt = Lh*Pr; % Thermal entrance length [m]
    if Lt<L
        if Lt<Lh % Calculate the entrance region nusselt
numbers for both hydro and thermally developing flow using (8-63)
            % Equation below is valid for Re<=2800
            % Equation 8-64 in Cengel (pg 492)
            Nu_ent =
7.54+(0.03*(Dh/Lt)*Re*Pr)/(1+0.016*((Dh/Lt)*Re*Pr)^(2/3));
            h_ent = Nu_ent*k/Dh; % Entrance region heat
transfer coefficient [W/m^2K]
            As_ent = As*Lt/L;
            Te_ent = Tsurf-(Tsurf-Tin)*exp(-
h_ent*As_ent/(mdot*cp)); % Exit temperature of entrance region [K]
            NTU_ent = h_ent*As_ent/(mdot*cp);

            % Calculate for fully developed flow
            if a/b <= 8
                Nu = interp1(rectNuf(1,1:end-
1),rectNuf(2,1:end-1),a/b); %Nusselt number for fully developed laminar flow
            else
                Nu = rectNuf(2,end);
            end
            h = Nu*k/Dh; % Heat transfer coefficient [W/m^2K]
            As_rem = As-As_ent;
            Te = Tsurf-(Tsurf-Te_ent)*exp(-
h*As_rem/(mdot*cp)); % Estimate of exit temperature [K]
            NTU = h*As_rem/(mdot*cp);
        end
    else % Calculate the entrance region nusselt numbers for
both hydro and thermally developing flow using (8-63)
        % Equation below is valid for Re<=2800
        % Equation 8-64 in Cengel (pg 492)
        Nu_ent =
7.54+(0.03*(Dh/L)*Re*Pr)/(1+0.016*((Dh/L)*Re*Pr)^(2/3));

```

```

        h_ent = Nu_ent*k/Dh; % Entrance region heat transfer
coefficient [W/m^2K]
        As_ent = As;
        Te_ent = Tsuri-(Tsuri-Tin)*exp(-
h_ent*As_ent/(mdot*cp)); % Exit temperature of entrance region [K]
        NTU_ent = h_ent*As_ent/(mdot*cp);

        % Variable reassignment
        Nu = Nu_ent;
        h = h_ent;
        Te = Te_ent;
        NTU = NTU_ent;
    end
    % Determine pressure loss from eqn for fully developed
flow
    % The equation is the friction factor for a single tube
    if a/b <= 8
        f = interp1(rectNuf(1,1:end-1),rectNuf(4,1:end-
1),a/b)/Re; % Friction factor for fully developed laminar flow
    else
        f = rectNuf(4,end)/Re;
    end
    end

    Tm = mean([Tin Te]); % Calculated mean fluid temperature [K]

    deltaTm = abs(Tm-Tmi)/mean([Tm,Tmi])*100; % Percent
difference between the entrance mean temp guess and calculated [K]
    if reps<100
        Tmi = Tm;
    else
        if Tm>Tmi
            break
        elseif Tm<Tmi
            Tmi=Tmi-0.0001;
        end
    end

    % Evaluate aluminum thermal conductivity
    kalum=interp1(propalum(:,1),propalum(:,2),Tsuri); % [W/mK]
for aluminum 6061
    if isnan(kalum)
        kalum = propalum(end,2);
    end
    % Using equation for thermal resistance of a cylinder
    Rcond1=log(127/(127-3.5))/(2*pi*L*kalum);
    Rcond2=log((127-3.5)/(127-3.5-20))/(2*pi*L*kalum*3/5);
    Rcond=Rcond1;

    Tsur = Tk-289*(Te-Tin)*mdot*cp*Rcond;
    deltaTs=abs(Tsur-Tsuri)/mean([Tsur,Tsuri])*100;
    Tsuri=Tsur;
end
end

h=b/2;

```

```

if L>Lh
    Kaxis=(Lh/h) / (Vavg*h/nu);
else
    Kaxis=(L/h) / (Vavg*h/nu);
end

if Kaxis > 0.4
    K = 0.686;
else
    disp("axial position less")
end
deltaP=0.5*rho*Vavg^2*(f*L/Dh);

Tsurall(i,j)=Tsur-273.15;
Teall(i,j)=Te-273.15;
deltaPall(i,j)=deltaP;
end
end

```

## B.6 Analytical Comparison for Liquid Side CFD of Section 5.3 for Heating Case

```

%%%%%%%%%%%%%%%%%%%%%%%%%%%%%%%%%%%%%%%%%%%%%%%%%%%%%%%%%%%%%%%%%%%%%%%%
% INTERNAL FLOW CALCULATOR, CFD LIQUID COMPARISON
%
% Linda Hasanovich
% Updated July 2022
% V1.0
%
% Description: Determines the output temperature of liquid flowing around the
Raphael heat exchanger channel by dividing the channel into entrance,
rectangular channel, and exit sections. The different sections have
isothermal walls with different heat transfer conditions applied using
iteration. The overall output temperature is determined iteratively.
%
%
% Important Assumptions:
% 1. Assuming steady flow
% 2. Neglecting compressibility effects
%%%%%%%%%%%%%%%%%%%%%%%%%%%%%%%%%%%%%%%%%%%%%%%%%%%%%%%%%%%%%%%%%%%%%%%%

clear;
clc;
close all;

% Thermal conductivity of aluminum
propalum = [4 5.4; 10 14.2; 20 28.5; 40 52.3; 80 85.7; 100 97.8; 150 120.5;
200 136.2; 250 147.5; 300 155.5];

% Liquid properties SIL180
silvisc = [20 70 80 90 100 110 120 130 140 150 160; ...
0.010255556 0.004893878 0.00416701 0.003673939 0.003364706 0.003183542
0.002821837 0.002620619 0.002426531 0.002237143 0.002040816];
silvisc(1,:)=silvisc(1,)+273.15; % [K], [m^2/s]

silrho = [21.5 30.1 49.5 61.5 72.3 80.1 89.8 100.1 112 120 130 141 152 160
170;...
932.3232323 904 902 894.1176471 889.7959184 886.5979381 874.7474747
862.745098 860.4166667 855.1020408 845.3608247 836.7346939 828.5714286
816.3265306 813.8613861];
silrho(1,:)=silrho(1,)+273.15; % [K], [kg/m^3]

silcp = [293.15 303.15 313.15 323.15 333.15 343.15 353.15 363.15 373.15
383.15 393.15 403.15 413.15 423.15 433.15 443.15;...
1511 1528 1545 1562 1579 1596 1613 1630 1647 1664 1681 1698 1715 1732
1749 1766]; % [K], [J/kgK]

k = 0.1; % Thermal conductivity of fluid at mean temperature [W/mK]

% Transcription of table 8-1 Cengel for Nu and f values for rectangular
channel flow in tubes (neglecting the infinite data points for
interpolation).

```



```

% Only valid for hydrodynamically and thermally developed flow.
rectNuf = [1 2 3 4 6 8 inf; 2.98 3.39 3.96 4.44 5.14 5.60 7.54; 3.61 4.12
4.79 5.33 6.05 6.49 8.24; 56.92 62.20 68.36 72.92 78.80 82.32 96.00];

% Sudden contraction minor loss coefficient
doverD = [0 0.1 0.2 0.3 0.4 0.5 0.6 0.7 0.8 0.9 1];
Kexitvalues = [0.5 0.475 0.425 0.375 0.3 0.225 0.18 0.12 0.08 0.05 0];

mdoto = [0.02457 0.0273 0.030029]; % [kg/s] (the half flow)
Tsur = [100 111.225 120]+273.15; % [K]

Teall = zeros(length(mdoto),length(Tsur));
deltaPall = zeros(length(mdoto),length(Tsur));

for j = 1:length(mdoto)
    for i=1:length(Tsur)
        %% Entrance tube section - convection outside

        % Define inlet fluid parameters
        Ti = 150+273.15; % Inlet fluid average temperature [K]

        % Define hx channel geometry
        D = 11.125/1000; % Diameter [m]
        Ac = pi/4*D^2; % Individual channel cross sectional area [m^2]
        L = 20/1000; % Hx channel length [m]
        As = pi*D*L; % Heat transfer surface area [m^2]

        % Setting up convection
        hnat = 7.97; % Natural convection heat transfer coefficient [W/m^2K]
        Tinf = 25+273.15; % Temperature far from tube [K]
        Dout = 20/1000; % Outer diameter [m]
        Asout = pi*(Dout)*L; % Outer surface area of pipe [m^2]

        deltaTs = 1;

        Tsi=Ti-5;

        reps = 0;
        repb = 0;

        while deltaTs > 0.001

            repb=repb+1;
            Tmi = (Ti+Tsi)/2; % Estimate of the bulk mean temperature in the
remaining pipe [K]

            deltaTm = 1; % Percent difference between the mean temp guess and
calculated [K]

            while deltaTm > 0.001
                reps=reps+1;

                mu = interp1(silvisc(1,:),silvisc(2,:),Tmi); % Fluid
kinematic viscosity at mean temperature [m^2/s]

```

```

        rho = interp1(silrho(1,:),silrho(2,:),Tmi); % Fluid density
at mean temperature [kg/m^3]
        cp = interp1(silcp(1,:),silcp(2,:),Tmi); % Fluid specific
heat capacity at mean temperature [J/kgK]

        nu=mu/rho;
        Pr = cp*mu/k; % Prandtl number

        % Estimate fluid parameters
        mdot=mdoto(j)*2;
        Vavg = mdot/(rho*Ac); % Average fluid velocity [m/s]

        % Calculate fluid flow characteristics
        Re = Vavg*D/nu; % Reynold's number

        % Check if laminar or turbulent
        if Re < 2300 % Laminar
            error("laminar"); % Alert if laminar

        else % Calculate the entrance region nusselt numbers for both
hydro and thermally developing flow using (8-63)
            % Equation below is valid for Re<=2800
            % Equation 8-64 in Cengel (pg 492)
            f=3.03*10^(-12)*Re^3-3.67*10^(-8)*Re^2+1.46*10^(-4)*Re-
0.151;
            Nu = ((f/8)*(Re-1000)*Pr)/(1+12.7*(f/8)^0.5*(Pr^(2/3)-
1));
            h = Nu*k/D; % Entrance region heat transfer coefficient
[W/m^2K]
            Te = Tsi-(Tsi-Ti)*exp(-h*As/(mdot*cp)); % Exit
temperature of entrance region [K]
            NTU = h*As/(mdot*cp);

            Nu_ent = NaN;
            h_ent = NaN;
            Te_ent = NaN;
            NTU_ent = NaN;
        end

        Tm = mean([Ti Te]); % Calculated mean fluid temperature [K]

        deltaTm = abs(Tm-Tmi)/mean([Tm,Tmi])*100; % Percent
difference between the entrance mean temp guess and calculated [K]
        Tmi = Tm;
    end

    % Evaluate aluminum thermal conductivity
    kalum=interp1(propalum(:,1),propalum(:,2),Tsi); % [W/mK] for
aluminum 6061
    if isnan(kalum)
        kalum = propalum(end,2);
    end
    % Using the equation for thermal resistance of a cylinder
    Rcond=log(Dout/D)/(2*pi*L*kalum);
    Rconv = 1/(hnat*Asout);

```

```

    Ts = Tinf+mdot*cp*(Ti-Te)*(Rcond+Rconv);
    deltaTs=abs(abs(Ts-Tsi)/mean([Ts,Tsi]))*100;
    if Ts < Tsi
        Tsi=Tsi-0.00001;
    else
        Tsi=Tsi+0.00001;
    end
end

deltaP1=0.5*rho*Vavg^2*(f*L/D);

a = 60/1000; % Channel width [m]
b = (263.65-254)/2/1000; % Channel height [m]
Dh = 2*a*b/(a+b); % Hydraulic diameter [m]
Kent=interp1(doverD,Kexitvalues,(Dh^2/D^2));
Kbend = 1.1;

deltaPent = rho*Vavg^2/2*(Kent+Kbend);

Tel=Te;

%% Rectangular jacket section - specified temperature
% Define hx channel geometry
a = 60/1000; % Channel width [m]
b = (263.65-254)/2/1000; % Channel height [m]
Dh = 2*a*b/(a+b); % Hydraulic diameter [m]
Ac = a*b; % Individual channel cross sectional area [m^2]
L = pi*mean([263.65,254])/1000/2; % Length [m]
As = 2*(a+b)*L;

% Define inlet fluid parameters
Ti = Te; % Inlet fluid average temperature [K]

% Setting up convection
hnat = 7.97; % Natural convection heat transfer coefficient [W/m^2K]
Tinf = 25+273.15; % Temperature far from tube [K]
Dout = 273.05/1000; % Outer diameter [m]
Asout = pi*(Dout)*96/1000/2; % Outer surface area of pipe [m^2]

deltaTs = 1;

Tsi=Tsur(i);

reps = 0;
repb = 0;

while deltaTs > 0.001
    repb=repb+1;
    Tmi = (Ti+Tsi)/2; % Estimate of bulk mean temperature in
remaining pipe [K]

```

```

    deltaTm = 1; % Percent difference between the mean temp guess and
calculated [K]

    while deltaTm > 0.001
        reps=reps+1;
        mu = interp1(silvisc(1,:),silvisc(2,:),Tmi); % Fluid
kinematic viscosity at mean temperature [m^2/s]
        rho = interp1(silrho(1,:),silrho(2,:),Tmi); % Fluid density
at mean temperature [kg/m^3]
        cp = interp1(silcp(1,:),silcp(2,:),Tmi); % Fluid specific
heat capacity at mean temperature [J/kgK]

        nu=mu/rho;
        Pr = cp*mu/k; % Prandtl number

        % Estimate fluid parameters
        mdot=mdoto(j);
        Vavg = mdot/(rho*Ac); % Average fluid velocity [m/s]

        % Calculate fluid flow characteristics
        Re = Vavg*Dh/nu; % Reynold's number

        % Check if laminar or turbulent
        if Re < 2300 % Laminar
            Lh = 0.05*Re*Dh; % Hydrodynamic entrance length [m]
            Lt = Lh*Pr; % Thermal entrance length [m]
            if Lt<L
                if Lt<Lh % Calculate the entrance region nusselt
numbers for both hydro and thermally developing flow using (8-63)
                    % Equation below is valid for Re<=2800
                    % Equation 8-64 in Cengel (pg 492)
                    Nu_ent =
7.54+(0.03*(Dh/Lt)*Re*Pr)/(1+0.016*((Dh/Lt)*Re*Pr)^(2/3));
                    h_ent = Nu_ent*k/Dh; % Entrance region heat
transfer coefficient [W/m^2K]
                    As_ent = As*Lt/L;
                    Te_ent = Tsi-(Tsi-Ti)*exp(-
h_ent*As_ent/(mdot*cp)); % Exit temperature of entrance region [K]
                    NTU_ent = h_ent*As_ent/(mdot*cp);

                    %Calculate for fully developed flow
                    if a/b <= 8
                        Nu = interp1(rectNuf(1,1:end-
1),rectNuf(2,1:end-1),a/b); % Nusselt number for fully developed laminar flow
                    else
                        Nu = rectNuf(2,end);
                    end
                    h = Nu*k/Dh; % Heat transfer coefficient [W/m^2K]
                    As_rem = As-As_ent;
                    Te = Tsi-(Tsi-Te_ent)*exp(-h*As_rem/(mdot*cp)); %
Estimate of exit temperature [K]
                    NTU = h*As_rem/(mdot*cp);
                end
            else % Calculate the entrance region nusselt numbers for
both hydro and thermally developing flow using (8-63)
                % Equation below is valid for Re<=2800

```

```

        % Equation 8-64 in Cengel (pg 492)
        Nu_ent =
7.54+(0.03*(Dh/L)*Re*Pr)/(1+0.016*((Dh/L)*Re*Pr)^(2/3));
        h_ent = Nu_ent*k/Dh; % Entrance region heat transfer
coefficient [W/m^2K]
        As_ent = As;
        Te_ent = Tsi-(Tsi-Ti)*exp(-h_ent*As_ent/(mdot*cp)); %
Exit temperature of entrance region [K]
        NTU_ent = h_ent*As_ent/(mdot*cp);

        % Variable reassignment
        Nu = Nu_ent;
        h = h_ent;
        Te = Te_ent;
        NTU = NTU_ent;
    end
    % Determine pressure loss from eqn for fully developed
flow
    % The equation is the friction factor for a single tube
    if a/b <= 8
        f = interp1(rectNuf(1,1:end-1),rectNuf(4,1:end-
1),a/b)/Re; % Friction factor for fully developed laminar flow
    else
        f = rectNuf(4,end)/Re;
    end

    end

    Tm = mean([Ti Te]); % Calculated mean fluid temperature [K]

    deltaTm = abs(Tm-Tmi)/mean([Tm,Tmi])*100; % Percent
difference between the entrance mean temp guess and calculated [K]
    Tmi = Tm;

    % Evaluate aluminum thermal conductivity
    kalum=interp1(propalum(:,1),propalum(:,2),Tsi); %[W/mK] for
aluminum 6061
    if isnan(kalum)
        kalum = propalum(end,2);
    end
    % Using the equation for thermal resistance of a cylinder
    Rcond=log(254/247)/(2*pi*96/1000*kalum)*2;

    Ts = Tsur(i)-mdot*cp*Rcond*(Te-Ti);
    deltaTs=abs(Ts-Tsi)/mean([Ts,Tsi])*100;
    Tsi=Ts;
    end
end

deltaP2=0.5*rho*Vavg^2*(f*L/Dh);
Te2=Te;

%% Exit tube section

% Constant fluid properties are assumed for liquids

```

```

% Define hx channel geometry
D = 11.125/1000; % Diameter [m]
Ac = pi/4*D^2; % Individual channel cross sectional area [m^2]
L = 150/1000; % Hx channel length [m]
As = pi*D*L; % Heat transfer surface area [m^2]

% Setting up convection
hnat = 7.97; % Natural convection heat transfer coefficient [W/m^2K]
Tinf = 25+273.15; % Temperature far from tube [K]
Dout = 20/1000; % Outer diameter [m]
Asout = pi*(Dout)*L; % Outer surface area of pipe [m^2]

% Define inlet fluid parameters
Ti = Te; % Inlet fluid average temperature [K]

deltaTs = 1;

Tsi=Ti-5;

reps = 0;
repb = 0;

while deltaTs > 0.001

    repb=repb+1;
    Tmi = (Ti+Tsi)/2; % Estimate of the bulk mean temperature in
remaining pipe [K]

    deltaTm = 1; % Percent difference between the mean temp guess and
calculated [K]

    while deltaTm > 0.001
        reps=reps+1;

        mu = interp1(silvisc(1,:),silvisc(2,:),Tmi); % Fluid
kinematic viscosity at mean temperature [m^2/s]
        rho = interp1(silrho(1,:),silrho(2,:),Tmi); % Fluid density
at mean temperature [kg/m^3]
        cp = interp1(silcp(1,:),silcp(2,:),Tmi); % Fluid specific
heat capacity at mean temperature [J/kgK]

        nu=mu/rho;
        Pr = cp*mu/k; % Prandtl number

        % Estimate fluid parameters
mdot=mdoto(j)^2;
        Vavg = mdot/(rho*Ac); % Average fluid velocity [m/s]

        % Calculate fluid flow characteristics
Re = Vavg*D/nu; % Reynold's number

        % Check if laminar or turbulent
if Re < 2300 % Laminar

```

```

        Lh = 0.05*Re*D; % Hydrodynamic entrance length [m]
        Lt = Lh*Pr; % Thermal entrance length [m]
        if Lt<L
            else % Calculate the entrance region nusselt numbers for
both hydro and thermally developing flow using (8-63)
                % Equation below is valid for Re<=2800
                % Equation 8-64 in Cengel (pg 492)
                Nu_ent = 3.66 +
(0.065*(D/L)*Re*Pr)/(1+0.04*((D/L)*Re*Pr)^(2/3));
                h_ent = Nu_ent*k/D; % Entrance region heat transfer
coefficient [W/m^2K]
                As_ent = As;
                Te_ent = Tsi-(Tsi-Ti)*exp(-h_ent*As_ent/(mdot*cp)); %
Exit temperature of entrance region [K]
                NTU_ent = h_ent*As_ent/(mdot*cp);

                % Variable reassignment
                Nu = Nu_ent;
                h = h_ent;
                Te = Te_ent;
                NTU = NTU_ent;
            end
            % Determine pressure loss from eqn for fully developed
flow

            % The equation is the friction factor for a single tube
            f = 64/Re; % Friction factor for fully developed laminar
flow

        else
            % Assumption: The entrance length is small.
            % Equation 8-71 in cengel, valid for Re of 3000 to 5x10^6
and Pr of 0.5 up to 2000, with the f factor calculated from 8-74 its validity
is now 2300 to 4500.
            % Both relations are for smooth tubes.
            % Equation 8-75 for f, valid for 2300<8000 Re.
            f=3.03*10^(-12)*Re^3-3.67*10^(-8)*Re^2+1.46*10^(-4)*Re-
0.151;
            Nu = ((f/8)*(Re-1000)*Pr)/(1+12.7*(f/8)^0.5*(Pr^(2/3)-
1));
            h = Nu*k/D; % Entrance region heat transfer coefficient
[W/m^2K]
            Te = Tsi-(Tsi-Ti)*exp(-h*As/(mdot*cp)); % Exit
temperature of entrance region [K]
            NTU = h*As/(mdot*cp);

            Nu_ent = NaN;
            h_ent = NaN;
            Te_ent = NaN;
            NTU_ent = NaN;
        end

        Tm = mean([Ti Te]); % Calculated mean fluid temperature [K]

        deltaTm = abs(Tm-Tmi)/mean([Tm,Tmi])*100; % Percent
difference between the entrance mean temp guess and calculated [K]
        Tmi = Tm;

```

```

end

% Evaluate aluminum thermal conductivity
kalum=interp1(propalum(:,1),propalum(:,2),Tsi); % [W/mK] for
aluminum 6061
if isnan(kalum)
    kalum = propalum(end,2);
end
% Using the equation for thermal resistance of a cylinder
Rcond=log(Dout/D)/(2*pi*L*kalum);
Rconv = 1/(hnat*Asout);

Ts = Tinf+mdot*cp*(Ti-Te)*(Rcond+Rconv);
deltaTs=abs(abs(Ts-Tsi)/mean([Ts,Tsi]))*100;
if Ts < Tsi
    Tsi=Tsi-0.00001;
else
    Tsi=Tsi+0.00001;
end
end

if Re < 2300
    a = 60/1000; % Channel width [m]
    b = (263.65-254)/2/1000; % Channel height [m]
    Dh = 2*a*b/(a+b); % Hydraulic diameter [m]
    Kexit=2*(1-Dh^2/D^2)^2;
else
    a = 60/1000; % Channel width [m]
    b = (263.65-254)/2/1000; % Channel height [m]
    Dh = 2*a*b/(a+b); % Hydraulic diameter [m]
    Kexit=1.05*(1-Dh^2/D^2)^2;
end
Te3=Te;
deltaP3=0.5*rho*Vavg^2*(f*L/D);

deltaPexit= rho*Vavg^2/2*(Kexit+Kbend);

deltaP = deltaP1+deltaP2+deltaP3+deltaPent+deltaPexit;

Teall(i,j)=Te-273.15;
deltaPall(i,j)=deltaP;
end
end

```



## B.7 Analytical Comparison for Liquid Side CFD of Section 5.3 for Cooling Case

```

%%%%%%%%%%%%%%%%%%%%%%%%%%%%%%%%%%%%%%%%%%%%%%%%%%%%%%%%%%%%%%%%%%%%%%%%
% INTERNAL FLOW CALCULATOR, CFD LIQUID COMPARISON COLD SIDE
%
% Linda Hasanovich
% Updated July 2022
% V1.0
%
% Description: Determines the output temperature of liquid flowing around the
Raphael heat exchanger channel by dividing the channel into entrance,
rectangular channel, and exit sections. The different sections have
isothermal walls with different heat transfer conditions applied using
iteration. The overall output temperature is determined iteratively.
%
%
% Important Assumptions:
% 1. Assuming steady flow
% 2. Neglecting compressibility effects
%%%%%%%%%%%%%%%%%%%%%%%%%%%%%%%%%%%%%%%%%%%%%%%%%%%%%%%%%%%%%%%%%%%%%%%%

clear;
clc;
close all;

% Thermal conductivity of aluminum
propalum = [4 5.4; 10 14.2; 20 28.5; 40 52.3; 80 85.7; 100 97.8; 150 120.5;
200 136.2; 250 147.5; 300 155.5];

% Liquid properties SIL180
glyvisc = [272.0388889 283.15 310.9277778; ...
0.001931193 0.001274363 0.000679177]; % [K], [m^2/s]

glyrho = [255.3722222 283.15 310.9277778; ...
1048.929 1041.93614 1028.9494]; % [K], [kg/m^3]

glycp = [273.15 283.15 293.15 303.15; ...
3763.47 3785.06 3806.64 3828.23]; % [K], [J/kgK]

glyk = [273.15 283.15 293.15 303.15; ...
0.4678 0.4752 0.4818 0.4876]; % [K], [W/mK]

% Transcription of table 8-1 Cengel for Nu and f values for rectangular
channel flow in tubes (neglecting the infinite data points for
interpolation).
% Only valid for hydrodynamically and thermally developed flow.
rectNuf = [1 2 3 4 6 8 inf; 2.98 3.39 3.96 4.44 5.14 5.60 7.54; 3.61 4.12
4.79 5.33 6.05 6.49 8.24; 56.92 62.20 68.36 72.92 78.80 82.32 96.00];

% Sudden contraction minor loss coefficient
doverD = [0 0.1 0.2 0.3 0.4 0.5 0.6 0.7 0.8 0.9 1];
Kexitvalues = [0.5 0.475 0.425 0.375 0.3 0.225 0.18 0.12 0.08 0.05 0];

```

```

mdoto = [0.0106011 0.011779 0.0129569]; % [kg/s] (The half flow)
Tsur = [30 38.725 50]+273.15; % [K]

Teall = zeros(length(mdoto),length(Tsur));
deltaPall = zeros(length(mdoto),length(Tsur));

for j = 1:length(mdoto)
    for i=1:length(Tsur)
        %% Entrance tube section - convection outside

        % Define inlet fluid parameters
        Ti = 5+273.15; % Inlet fluid average temperature [K]

        % Define hx channel geometry
        D = 11.125/1000; % Diameter [m]
        Ac = pi/4*D^2; % Individual channel cross sectional area [m^2]
        L = 20/1000; % Hx channel length [m]
        As = pi*D*L; % Heat transfer surface area [m^2]

        % Setting up convection
        hnat = 5.28; % Natural convection heat transfer coefficient [W/m^2K]
        Tinf = 25+273.15; % Temperature far from tube [K]
        Dout = 20/1000; % Outer diameter [m]
        Asout = pi*(Dout)*L; % Outer surface area of pipe [m^2]

        deltaTs = 1;

        Tsi=Ti+2;

        reps = 0;
        repb = 0;

        while deltaTs > 0.001

            repb=repb+1;
            Tmi = (Ti+Tsi)/2; % Estimate of the bulk mean temperature in
remaining pipe [K]

            deltaTm = 1; % Percent difference between the mean temp guess and
calculated [K]

            while deltaTm > 0.001
                reps=reps+1;

                mu = interp1(glyvisc(1,:),glyvisc(2,:),Tmi); % Fluid
kinematic viscosity at mean temperature [m^2/s]
                k = interp1(glyk(1,:),glyk(2,:),Tmi); % Fluid kinematic
viscosity at mean temperature [m^2/s]
                rho = interp1(glyrho(1,:),glyrho(2,:),Tmi); % Fluid density
at mean temperature [kg/m^3]
                cp = interp1(glycp(1,:),glycp(2,:),Tmi); % Fluid specific
heat capacity at mean temperature [J/kgK]

```

```

nu=mu/rho;
Pr = cp*mu/k; % Prandtl number

% Estimate fluid parameters
mdot=mdoto(j)*2;
Vavg = mdot/(rho*Ac); % Average fluid velocity [m/s]

% Calculate fluid flow characteristics
Re = Vavg*D/nu; % Reynold's number

% Check if laminar or turbulent
if Re < 2300 % Laminar
    Lh = 0.05*Re*D; % Hydrodynamic entrance length [m]
    Lt = Lh*Pr; % Thermal entrance length [m]
    if Lt<L
        else % Calculate the entrance region nusselt numbers for
both hydro and thermally developing flow using (8-63)
            % Equation below is valid for Re<=2800
            % Equation 8-64 in Cengel (pg 492)
            Nu_ent = 3.66 +
(0.065*(D/L)*Re*Pr)/(1+0.04*((D/L)*Re*Pr)^(2/3));
            h_ent = Nu_ent*k/D; % Entrance region heat transfer
coefficient [W/m^2K]
            As_ent = As;
            Te_ent = Tsi-(Tsi-Ti)*exp(-h_ent*As_ent/(mdot*cp)); %
Exit temperature of entrance region [K]
            NTU_ent = h_ent*As_ent/(mdot*cp);

            % Variable reassignment
            Nu = Nu_ent;
            h = h_ent;
            Te = Te_ent;
            NTU = NTU_ent;
        end
        % Determine pressure loss from eqn for fully developed
flow
        % The equation is the friction factor for a single tube
f = 64/Re; % Friction factor for fully developed laminar
flow

    else
        % Assumption: The entrance length is small.
        % Equation 8-71 in cengel, valid for Re of 3000 to 5x10^6
and Pr of 0.5 up to 2000, with the f factor calculated from 8-74 its validity
is now 2300 to 4500.
        % Both relations are for smooth tubes.
        % Equation 8-75 for f, valid for 2300<8000 Re.
f=3.03*10^(-12)*Re^3-3.67*10^(-8)*Re^2+1.46*10^(-4)*Re-
0.151;
        Nu = ((f/8)*(Re-1000)*Pr)/(1+12.7*(f/8)^0.5*(Pr^(2/3)-
1));
        h = Nu*k/D; % Entrance region heat transfer coefficient
[W/m^2K]
        Te = Tsi-(Tsi-Ti)*exp(-h*As/(mdot*cp)); % Exit
temperature of entrance region [K]
        NTU = h*As/(mdot*cp);
    end
end

```

```

        Nu_ent = NaN;
        h_ent = NaN;
        Te_ent = NaN;
        NTU_ent = NaN;
    end

    Tm = mean([Ti Te]); % Calculated mean fluid temperature [K]

    deltaTm = abs(Tm-Tmi)/mean([Tm,Tmi])*100; % Percent
difference between the entrance mean temp guess and calculated [K]
    Tmi = Tm;
    end

    % Evaluate aluminum thermal conductivity
    kalum=interp1(propalum(:,1),propalum(:,2),Tsi); % [W/mK] for
aluminum 6061
    if isnan(kalum)
        kalum = propalum(end,2);
    end
    % Using the equation for thermal resistance of a cylinder
    Rcond=log(Dout/D)/(2*pi*L*kalum);
    Rconv = 1/(hnat*Asout);

    Ts = Tinf+mdot*cp*(Ti-Te)*(Rcond+Rconv);
    deltaTs=abs(abs(Ts-Tsi)/mean([Ts,Tsi]))*100;
    if Ts < Tsi
        Tsi=Tsi-0.00001;
    else
        Tsi=Tsi+0.00001;
    end
end

deltaP1=0.5*rho*Vavg^2*(f*L/D);

a = 60/1000; % Channel width [m]
b = (263.65-254)/2/1000; % Channel height [m]
Dh = 2*a*b/(a+b); % Hydraulic diameter [m]
Kent=interp1(doverD,Kexitvalues,(Dh^2/D^2));
Kbend = 1.1;

deltaPent = rho*Vavg^2/2*(Kent+Kbend);
Tel=Te;

%% Rectangular jacket section - specified temperature
% Define hx channel geometry
a = 60/1000; % Channel width [m]
b = (263.65-254)/2/1000; % Channel height [m]
Dh = 2*a*b/(a+b); % Hydraulic diameter [m]
Ac = a*b; % Individual channel cross sectional area [m^2]
L = pi*mean([263.65,254])/1000/2; % Length [m]
As = 2*(a+b)*L;

% Define inlet fluid parameters
Ti = Te; % Inlet fluid average temperature [K]

```

```

% Setting up convection
hnat = 5.28; % Natural convection heat transfer coefficient [W/m^2K]
Tinf = 25+273.15; % Temperature far from tube [K]
Dout = 273.05/1000; % Outer diameter [m]
Asout = pi*(Dout)*96/1000/2; % Outer surface area of pipe [m^2]

deltaTs = 1;

Tsi=Tsur(i);

reps = 0;
repb = 0;

while deltaTs > 0.001

    repb=repb+1;
    Tmi = (Ti+Tsi)/2; % Estimate of the bulk mean temperature in the
remaining pipe [K]

    deltaTm = 1; % Percent difference between the mean temp guess and
calculated [K]

    while deltaTm > 0.001
        reps=reps+1;

        mu = interp1(glyvisc(1,:),glyvisc(2,:),Tmi); % Fluid
kinematic viscosity at mean temperature [m^2/s]
        k = interp1(glyk(1,:),glyk(2,:),Tmi); % Fluid kinematic
viscosity at mean temperature [m^2/s]
        rho = interp1(glyrho(1,:),glyrho(2,:),Tmi); % Fluid density
at mean temperature [kg/m^3]
        cp = interp1(glycp(1,:),glycp(2,:),Tmi); % Fluid specific
heat capacity at mean temperature [J/kgK]

        nu=mu/rho;
        Pr = cp*mu/k; % Prandtl number

        % Estimate fluid parameters
        mdot=mdoto(j);
        Vavg = mdot/(rho*Ac); % Average fluid velocity [m/s]

        % Calculate fluid flow characteristics
        Re = Vavg*Dh/nu; % Reynold's number

        % Check if laminar or turbulent
        if Re < 2300 % Laminar
            Lh = 0.05*Re*Dh; % Hydrodynamic entrance length [m]
            Lt = Lh*Pr; % Thermal entrance length [m]
            if Lt<L
                if Lt<Lh % Calculate the entrance region nusselt
numbers for both hydro and thermally developing flow using (8-63)
                    % Equation below is valid for Re<=2800
                    % Equation 8-64 in Cengel (pg 492)

```

```

        Nu_ent =
7.54+(0.03*(Dh/Lt)*Re*Pr)/(1+0.016*((Dh/Lt)*Re*Pr)^(2/3));
        h_ent = Nu_ent*k/Dh; % Entrance region heat
transfer coefficient [W/m^2K]
        As_ent = As*Lt/L;
        Te_ent = Tsi-(Tsi-Ti)*exp(-
h_ent*As_ent/(mdot*cp)); % Exit temperature of entrance region [K]
        NTU_ent = h_ent*As_ent/(mdot*cp);

        % Calculate for fully developed flow
        if a/b <= 8
            Nu = interp1(rectNuf(1,1:end-
1),rectNuf(2,1:end-1),a/b); % Nusselt number for fully developed laminar flow
        else
            Nu = rectNuf(2,end);
        end
        h = Nu*k/Dh; % Heat transfer coefficient [W/m^2K]
        As_rem = As-As_ent;
        Te = Tsi-(Tsi-Te_ent)*exp(-h*As_rem/(mdot*cp)); %
Estimate of exit temperature [K]
        NTU = h*As_rem/(mdot*cp);
    end
    else % Calculate the entrance region nusselt numbers for
both hydro and thermally developing flow using (8-63)
        % Equation below is valid for Re<=2800
        % Equation 8-64 in Cengel (pg 492)
        Nu_ent =
7.54+(0.03*(Dh/L)*Re*Pr)/(1+0.016*((Dh/L)*Re*Pr)^(2/3));
        h_ent = Nu_ent*k/Dh; % Entrance region heat transfer
coefficient [W/m^2K]
        As_ent = As;
        Te_ent = Tsi-(Tsi-Ti)*exp(-h_ent*As_ent/(mdot*cp)); %
Exit temperature of entrance region [K]
        NTU_ent = h_ent*As_ent/(mdot*cp);

        % Variable reassignment
        Nu = Nu_ent;
        h = h_ent;
        Te = Te_ent;
        NTU = NTU_ent;
    end
    % Determine pressure loss from eqn for fully developed
flow
        % The equation is the friction factor for a single tube
        if a/b <= 8
            f = interp1(rectNuf(1,1:end-1),rectNuf(4,1:end-
1),a/b)/Re; % Friction factor for fully developed laminar flow
        else
            f = rectNuf(4,end)/Re;
        end
    end

    Tm = mean([Ti Te]); % Calculated mean fluid temperature [K]

    deltaTm = abs(Tm-Tmi)/mean([Tm,Tmi])*100; % Percent
difference between the entrance mean temp guess and calculated [K]

```

```

Tmi = Tm;

% Evaluate aluminum thermal conductivity
kalum=interp1(propalum(:,1),propalum(:,2),Tsi); % [W/mK] for
aluminum 6061
if isnan(kalum)
    kalum = propalum(end,2);
end
% Using the equation for thermal resistance of a cylinder
Rcond=log(254/247)/(2*pi*96/1000*kalum)*2;

Ts = Tsur(i)-mdot*cp*Rcond*(Te-Ti);
deltaTs=abs(Ts-Tsi)/mean([Ts,Tsi])*100;
Tsi=Ts;
end
end

deltaP2=0.5*rho*Vavg^2*(f*L/Dh);
Te2=Te;

%% Exit tube section

% Assuming constant fluid properties

% Define hx channel geometry
D = 11.125/1000; % Diameter [m]
Ac = pi/4*D^2; % Individual channel cross sectional area [m^2]
L = 150/1000; % Hx channel length [m]
As = pi*D*L; % Heat transfer surface area [m^2]

% Setting up convection
hnat = 5.28; % Natural convection heat transfer coefficient [W/m^2K]
Tinf = 25+273.15; % Temperature far from tube [K]
Dout = 20/1000; % Outer diameter [m]
Asout = pi*(Dout)*L; % Outer surface area of pipe [m^2]

% Define inlet fluid parameters
Ti = Te; % Inlet fluid average temperature [K]

deltaTs = 1;

Tsi=Ti+2;

reps = 0;
repb = 0;

while deltaTs > 0.001
    repb=repb+1;
    Tmi = (Ti+Tsi)/2; % Estimate of the bulk mean temperature in the
remaining pipe [K]

    deltaTm = 1; % Percent difference between the mean temp guess and
calculated [K]

```

```

while deltaTm > 0.001
    reps=reps+1;

    mu = interp1(glyvisc(1,:),glyvisc(2,:),Tmi); % Fluid
kinematic viscosity at mean temperature [m^2/s]
    k = interp1(glyk(1,:),glyk(2,:),Tmi); % Fluid kinematic
viscosity at mean temperature [m^2/s]
    rho = interp1(glyrho(1,:),glyrho(2,:),Tmi); % Fluid density
at mean temperature [kg/m^3]
    cp = interp1(glycp(1,:),glycp(2,:),Tmi); % Fluid specific
heat capacity at mean temperature [J/kgK]

    nu=mu/rho;
Pr = cp*mu/k; % Prandtl number

    % Estimate fluid parameters
mdot=mdoto(j)*2;
Vavg = mdot/(rho*Ac); % Average fluid velocity [m/s]

    % Calculate fluid flow characteristics
Re = Vavg*D/nu; % Reynold's number

    % Check if laminar or turbulent
if Re < 2300 % Laminar
    Lh = 0.05*Re*D; % Hydrodynamic entrance length [m]
    Lt = Lh*Pr; % Thermal entrance length [m]
    if Lt<L
        else % Calculate the entrance region nusselt numbers for
both hydro and thermally developing flow using (8-63)
            % Equation below is valid for Re<=2800
            % Equation 8-64 in Cengel (pg 492)
            Nu_ent = 3.66 +
(0.065*(D/L)*Re*Pr)/(1+0.04*((D/L)*Re*Pr)^(2/3));
            h_ent = Nu_ent*k/D; % Entrance region heat transfer
coefficient [W/m^2K]
            As_ent = As;
            Te_ent = Tsi-(Tsi-Ti)*exp(-h_ent*As_ent/(mdot*cp)); %
Exit temperature of entrance region [K]
            NTU_ent = h_ent*As_ent/(mdot*cp);

            % Variable reassignment
            Nu = Nu_ent;
            h = h_ent;
            Te = Te_ent;
            NTU = NTU_ent;
        end
        % Determine pressure loss from eqn for fully developed
flow
        % The equation is the friction factor for a single tube
f = 64/Re; % Friction factor for fully developed laminar
flow
    else
        % Assumption: The entrance length is small.

```



```

                                % Equation 8-71 in cengel, valid for Re of 3000 to 5x10^6
and Pr of 0.5 up to 2000, with the f factor calculated from 8-74 its validity
is now 2300 to 4500.
                                % Both relations are for smooth tubes.
                                % Equation 8-75 for f, valid for 2300<8000 Re.
                                f=3.03*10^(-12)*Re^3-3.67*10^(-8)*Re^2+1.46*10^(-4)*Re-
0.151;
                                Nu = ((f/8)*(Re-1000)*Pr)/(1+12.7*(f/8)^0.5*(Pr^(2/3)-
1));
                                h = Nu*k/D; % Entrance region heat transfer coefficient
[W/m^2K]
                                Te = Tsi-(Tsi-Ti)*exp(-h*As/(mdot*cp)); % Exit
temperature of entrance region [K]
                                NTU = h*As/(mdot*cp);

                                Nu_ent = NaN;
                                h_ent = NaN;
                                Te_ent = NaN;
                                NTU_ent = NaN;
                                end

                                Tm = mean([Ti Te]); % Calculated mean fluid temperature [K]

                                deltaTm = abs(abs(Tm-Tmi)/mean([Tm,Tmi]))*100; % Percent
difference between the entrance mean temp guess and calculated [K]
                                Tmi = Tm;
                                end

                                % Evaluate aluminum thermal conductivity
                                kalum=interp1(propalum(:,1),propalum(:,2),Tsi); % [W/mK] for
aluminum 6061
                                if isnan(kalum)
                                    kalum = propalum(end,2);
                                end
                                % Using the equation for thermal resistance of a cylinder
                                Rcond=log(Dout/D)/(2*pi*L*kalum);
                                Rconv = 1/(hnat*Asout);

                                Ts = Tinf+mdot*cp*(Ti-Te)*(Rcond+Rconv);
                                deltaTs=abs(abs(Ts-Tsi)/mean([Ts,Tsi]))*100;
                                if Ts < Tsi
                                    Tsi=Tsi-0.00001;
                                else
                                    Tsi=Tsi+0.00001;
                                end
                                if rem(reps,10000) == 0
                                    disp([deltaTs deltaTm])
                                end
                                end

                                if Re < 2300

                                    a = 60/1000; % Channel width [m]
                                    b = (263.65-254)/2/1000; % Channel height [m]
                                    Dh = 2*a*b/(a+b); % Hydraulic diameter [m]

```

```

        Kexit=2*(1-Dh^2/D^2)^2;
    else
        a = 60/1000; % Channel width [m]
        b = (263.65-254)/2/1000; % Channel height [m]
        Dh = 2*a*b/(a+b); % Hydraulic diameter [m]
        Kexit=1.05*(1-Dh^2/D^2)^2;
    end
    deltaP3=0.5*rho*Vavg^2*(f*L/D);
    Te3=Te;

    Kbend = 1.1;

    deltaPexit= rho*Vavg^2/2*(Kexit+Kbend);

    deltaP = deltaP1+deltaP2+deltaP3+deltaPent+deltaPexit;

    Teall(i,j)=Te-273.15;
    deltaPall(i,j)=deltaP;
end
end

```

## B.8 Analytical Comparison for Simplified Liquid Side CFD of Section 5.3 for Heating Case

```

%%%%%%%%%%%%%%%%%%%%%%%%%%%%%%%%%%%%%%%%%%%%%%%%%%%%%%%%%%%%%%%%%%%%%%%%
% INTERNAL FLOW CALCULATOR, CFD LIQUID COMPARISON SIMPLIFIED
%
% Linda Hasanovich
% Updated July 2022
% V1.0
%
% Description: Determines the output temperature of liquid flowing through a
rectangular channel with different heat transfer conditions applied using
iteration. The overall output temperature is determined iteratively.
%
%
% Important Assumptions:
% 1. Assuming steady flow
% 2. Neglecting compressibility effects
%%%%%%%%%%%%%%%%%%%%%%%%%%%%%%%%%%%%%%%%%%%%%%%%%%%%%%%%%%%%%%%%%%%%%%%%

clear;
clc;
close all;

% Thermal conductivity of aluminum
propalum = [4 5.4; 10 14.2; 20 28.5; 40 52.3; 80 85.7; 100 97.8; 150 120.5;
200 136.2; 250 147.5; 300 155.5];

% Liquid properties SIL180
silvisc = [20 70 80 90 100 110 120 130 140 150 160; ...
0.010255556 0.004893878 0.00416701 0.003673939 0.003364706 0.003183542
0.002821837 0.002620619 0.002426531 0.002237143 0.002040816];
silvisc(1,:)=silvisc(1,)+273.15; % [K], [m^2/s]

silrho = [21.5 30.1 49.5 61.5 72.3 80.1 89.8 100.1 112 120 130 141 152 160
170;...
932.3232323 904 902 894.1176471 889.7959184 886.5979381 874.7474747
862.745098 860.4166667 855.1020408 845.3608247 836.7346939 828.5714286
816.3265306 813.8613861];
silrho(1,:)=silrho(1,)+273.15; % [K], [kg/m^3]

silcp = [293.15 303.15 313.15 323.15 333.15 343.15 353.15 363.15 373.15
383.15 393.15 403.15 413.15 423.15 433.15 443.15;...
1511 1528 1545 1562 1579 1596 1613 1630 1647 1664 1681 1698 1715 1732
1749 1766]; % K, J/kgK

k = 0.1; % Thermal conductivity of fluid at mean temperature [W/mK]

% Transcription of table 8-1 Cengel for Nu and f values for rectangular
channel flow in tubes (neglecting the infinite data points for
interpolation).
% Only valid for hydrodynamically and thermally developed flow.

```

```

rectNuf = [1 2 3 4 6 8 inf; 2.98 3.39 3.96 4.44 5.14 5.60 7.54; 3.61 4.12
4.79 5.33 6.05 6.49 8.24; 56.92 62.20 68.36 72.92 78.80 82.32 96.00];

% Sudden contraction minor loss coefficient
doverD = [0 0.1 0.2 0.3 0.4 0.5 0.6 0.7 0.8 0.9 1];
Kexitvalues = [0.5 0.475 0.425 0.375 0.3 0.225 0.18 0.12 0.08 0.05 0];

mdoto = [0.02457 0.0273 0.030029]; % [kg/s] (the half flow)
Tsur = [100 111.225 120]+273.15; % [K]

Teall = zeros(length(mdoto),length(Tsur));
deltaPall = zeros(length(mdoto),length(Tsur));

%% Rectangular jacket section - specified temperature
% Define hx channel geometry
a = 60/1000; % Channel width [m]
b = (263.65-254)/2/1000; % Channel height [m]
Dh = 2*a*b/(a+b); % Hydraulic diameter [m]
Ac = a*b; % Individual channel cross sectional area [m^2]
L = pi*mean([263.65,254])/1000/2; % Length [m]
As = 2*(a+b)*L;

% Define inlet Fluid Parameters
Ti = 150+273.15; % Inlet fluid average temperature [K]

% Setting up convection
hnat = 7.97; % Natural convection heat transfer coefficient [W/m^2K]
Tinf = 25+273.15; % Temperature far from tube [K]
Dout = 273.05/1000; % Outer diameter [m]
Asout = pi*(Dout)*96/1000/2; % Outer surface area of pipe [m^2]

deltaTs = 1;

Tsi=Tsur(2);

reps = 0;
repb = 0;

while deltaTs > 0.001

    repb=repb+1;
    Tmi = (Ti+Tsi)/2; % Estimate of the bulk mean temperature in the remaining
    pipe [K]

    deltaTm = 1; % Percent difference between the mean temp guess and
    calculated [K]

    while deltaTm > 0.001
        reps=reps+1;
        mu = interp1(silvisc(1,:),silvisc(2,:),Tmi); % Fluid kinematic
        viscosity at mean temperature [m^2/s]
        rho = interp1(silrho(1,:),silrho(2,:),Tmi); % Fluid density at mean
        temperature [kg/m^3]
    end
end

```

```

    cp = interp1(silcp(1,:),silcp(2,:),Tmi); % Fluid specific heat
    capacity at mean temperature [J/kgK]

    nu=mu/rho;
    Pr = cp*mu/k; % Prandtl number

    % Estimate fluid parameters
    mdot=mdoto(2);
    Vavg = mdot/(rho*Ac); % Average fluid velocity [m/s]

    % Calculate fluid flow characteristics
    Re = Vavg*Dh/nu; % Reynold's number

    % Check if laminar or turbulent
    if Re < 2300 % Laminar
        Lh = 0.05*Re*Dh; % Hydrodynamic entrance length [m]
        Lt = Lh*Pr; % Thermal entrance length [m]
        if Lt<L
            if Lt<Lh % Calculate the entrance region nusselt numbers for
both hydro and thermally developing flow using (8-63)
                % Equation below is valid for Re<=2800
                % Equation 8-64 in Cengel (pg 492)
                Nu_ent =
7.54+(0.03*(Dh/Lt)*Re*Pr)/(1+0.016*((Dh/Lt)*Re*Pr)^(2/3));
                h_ent = Nu_ent*k/Dh; % Entrance region heat transfer
coefficient [W/m^2K]
                As_ent = As*Lt/L;
                Te_ent = Tsi-(Tsi-Ti)*exp(-h_ent*As_ent/(mdot*cp)); %
Exit temperature of entrance region [K]
                NTU_ent = h_ent*As_ent/(mdot*cp);

                % Calculate for fully developed flow
                if a/b <= 8
                    Nu = interp1(rectNuf(1,1:end-1),rectNuf(2,1:end-
1),a/b); % Nusselt number for fully developed laminar flow
                else
                    Nu = rectNuf(2,end);
                end
                h = Nu*k/Dh; % Heat transfer coefficient [W/m^2K]
                As_rem = As-As_ent;
                Te = Tsi-(Tsi-Te_ent)*exp(-h*As_rem/(mdot*cp)); %
Estimate of exit temperature [K]
                NTU = h*As_rem/(mdot*cp);
            end
        else % Calculate the entrance region nusselt numbers for both
hydro and thermally developing flow using (8-63)
            % Equation below is valid for Re<=2800
            % Equation 8-64 in Cengel (pg 492)
            Nu_ent =
7.54+(0.03*(Dh/L)*Re*Pr)/(1+0.016*((Dh/L)*Re*Pr)^(2/3));
            h_ent = Nu_ent*k/Dh; % Entrance region heat transfer
coefficient [W/m^2K]
            As_ent = As;
            Te_ent = Tsi-(Tsi-Ti)*exp(-h_ent*As_ent/(mdot*cp)); % Exit
temperature of entrance region [K]
            NTU_ent = h_ent*As_ent/(mdot*cp);
        end
    end

```

```

        % Variable reassignment
        Nu = Nu_ent;
        h = h_ent;
        Te = Te_ent;
        NTU = NTU_ent;
    end
    % Determine pressure loss from eqn for fully developed flow
    % The equation is the friction factor for a single tube
    if a/b <= 8
        f = interp1(rectNuf(1,1:end-1),rectNuf(4,1:end-1),a/b)/Re; %
Friction factor for fully developed laminar flow
    else
        f = rectNuf(4,end)/Re;
    end
end

Tm = mean([Ti Te]); % Calculated mean fluid temperature [K]

deltaTm = abs(Tm-Tmi)/mean([Tm,Tmi])*100; % Percent difference
between the entrance mean temp guess and calculated [K]
Tmi = Tm;

% Evaluate aluminum thermal conductivity
kalum=interp1(propalum(:,1),propalum(:,2),Tsi); % [W/mK] for aluminum
6061
if isnan(kalum)
    kalum = propalum(end,2);
end
% Using the equation for thermal resistance of a cylinder
Rcond=log(254/247)/(2*pi*96/1000*kalum)*2;

Ts = Tsur(2)-mdot*cp*Rcond*(Te-Ti);
deltaTs=abs(Ts-Tsi)/mean([Ts,Tsi])*100;
Tsi=Ts;
end
end

deltaP2=0.5*rho*Vavg^2*(f*L/Dh);
Te2=Te;

```

## B.9 Analytical Comparison for Simplified Liquid Side CFD of Section 5.3 for Cooling Case

```

%%%%%%%%%%%%%%%%%%%%%%%%%%%%%%%%%%%%%%%%%%%%%%%%%%%%%%%%%%%%%%%%%%%%%%%%
% INTERNAL FLOW CALCULATOR, CFD LIQUID COMPARISON COLD SIDE SIMPLIFIED
%
% Linda Hasanovich
% Updated July 2022
% V1.0
%
% Description: Determines the output temperature of liquid flowing through a
rectangular channel with different heat transfer conditions applied using
iteration. The overall output temperature is determined iteratively.
%
%
% Important Assumptions:
% 1. Assuming steady flow
% 2. Neglecting compressibility effects
%%%%%%%%%%%%%%%%%%%%%%%%%%%%%%%%%%%%%%%%%%%%%%%%%%%%%%%%%%%%%%%%%%%%%%%%

clear;
clc;
close all;

% Thermal conductivity of aluminum
propalum = [4 5.4; 10 14.2; 20 28.5; 40 52.3; 80 85.7; 100 97.8; 150 120.5;
200 136.2; 250 147.5; 300 155.5];

% Liquid properties SIL180
glyvisc = [272.0388889 283.15 310.9277778; ...
0.001931193 0.001274363 0.000679177]; % [K], [m^2/s]

glyrho = [255.3722222 283.15 310.9277778;...
1048.929 1041.93614 1028.9494]; % [K], [kg/m^3]

glycp = [273.15 283.15 293.15 303.15;...
3763.47 3785.06 3806.64 3828.23]; % [K], [J/kgK]

glyk = [273.15 283.15 293.15 303.15;...
0.4678 0.4752 0.4818 0.4876]; % [K], [W/mK]

% Transcription of table 8-1 Cengel for Nu and f values for rectangular
channel flow in tubes (neglecting the infinite data points for
interpolation).
% Only valid for hydrodynamically and thermally developed flow.
rectNuf = [1 2 3 4 6 8 inf; 2.98 3.39 3.96 4.44 5.14 5.60 7.54; 3.61 4.12
4.79 5.33 6.05 6.49 8.24; 56.92 62.20 68.36 72.92 78.80 82.32 96.00];

% Sudden contraction minor loss coefficient
doverD = [0 0.1 0.2 0.3 0.4 0.5 0.6 0.7 0.8 0.9 1];
Kexitvalues = [0.5 0.475 0.425 0.375 0.3 0.225 0.18 0.12 0.08 0.05 0];

mdoto = [0.0106011 0.011779 0.0129569]; % [kg/s] (The half flow)

```

```

Tsur = [30 38.725 50]+273.15; % [K]

Teall = zeros(length(mdoto),length(Tsur));
deltaPall = zeros(length(mdoto),length(Tsur));

%% Rectangular jacket section - specified temperature
% Define hx channel geometry
a = 60/1000; % Channel width [m]
b = (263.65-254)/2/1000; % Channel height [m]
Dh = 2*a*b/(a+b); % Hydraulic diameter [m]
Ac = a*b; % Individual channel cross sectional area [m^2]
L = pi*mean([263.65,254])/1000/2; % Length [m]
As = 2*(a+b)*L;

% Define inlet fluid parameters
Ti = 5+273.15; % Inlet fluid average temperature [K]

% Setting up convection
hnat = 5.28; % Natural convection heat transfer coefficient [W/m^2K]
Tinf = 25+273.15; % Temperature far from tube [K]
Dout = 273.05/1000; % Outer diameter [m]
Asout = pi*(Dout)*96/1000/2; % Outer surface area of pipe [m^2]

deltaTs = 1;

Tsi=Tsur(2);

reps = 0;
repb = 0;

while deltaTs > 0.001

    repb=repb+1;
    Tmi = (Ti+Tsi)/2; % Estimate of the bulk mean temperature in the
remaining pipe [K]

    deltaTm = 1; % Percent difference between the mean temp guess and
calculated [K]

    while deltaTm > 0.001
        reps=reps+1;

        mu = interp1(glyvisc(1,:),glyvisc(2,:),Tmi); % Fluid
kinematic viscosity at mean temperature [m^2/s]
        k = interp1(glyk(1,:),glyk(2,:),Tmi); % Fluid kinematic
viscosity at mean temperature [m^2/s]
        rho = interp1(glyrho(1,:),glyrho(2,:),Tmi); % Fluid density
at mean temperature [kg/m^3]
        cp = interp1(glycp(1,:),glycp(2,:),Tmi); % Fluid specific
heat capacity at mean temperature [J/kgK]

        nu=mu/rho;
        Pr = cp*mu/k; % Prandtl number
    end
end

```



```

% Estimate fluid parameters
mdot=mdoto(2);
Vavg = mdot/(rho*Ac); % Average fluid velocity [m/s]

% Calculate fluid flow characteristics
Re = Vavg*Dh/nu; % Reynold's number

% Check if laminar or turbulent
if Re < 2300 % Laminar
    Lh = 0.05*Re*Dh; % Hydrodynamic entrance length [m]
    Lt = Lh*Pr; % Thermal entrance length [m]
    if Lt<L
        if Lt<Lh % Calculate the entrance region nusselt
numbers for both hydro and thermally developing flow using (8-63)
            % Equation below is valid for Re<=2800
            % Equation 8-64 in Cengel (pg 492)
            Nu_ent =
7.54+(0.03*(Dh/Lt)*Re*Pr)/(1+0.016*((Dh/Lt)*Re*Pr)^(2/3));
            h_ent = Nu_ent*k/Dh; % Entrance region heat
transfer coefficient [W/m^2K]
            As_ent = As*Lt/L;
            Te_ent = Tsi-(Tsi-Ti)*exp(-
h_ent*As_ent/(mdot*cp)); % Exit temperature of entrance region [K]
            NTU_ent = h_ent*As_ent/(mdot*cp);

            % Calculate for fully developed flow
            if a/b <= 8
                Nu = interp1(rectNuf(1,1:end-
1),rectNuf(2,1:end-1),a/b); % Nusselt number for fully developed laminar flow
            else
                Nu = rectNuf(2,end);
            end
            h = Nu*k/Dh; % Heat transfer coefficient [W/m^2K]
            As_rem = As-As_ent;
            Te = Tsi-(Tsi-Te_ent)*exp(-h*As_rem/(mdot*cp)); %
Estimate of exit temperature [K]
            NTU = h*As_rem/(mdot*cp);
        end
    else % Calculate the entrance region nusselt numbers for
both hydro and thermally developing flow using (8-63)
        % Equation below is valid for Re<=2800
        % Equation 8-64 in Cengel (pg 492)
        Nu_ent =
7.54+(0.03*(Dh/L)*Re*Pr)/(1+0.016*((Dh/L)*Re*Pr)^(2/3));
        h_ent = Nu_ent*k/Dh; % Entrance region heat transfer
coefficient [W/m^2K]
        As_ent = As;
        Te_ent = Tsi-(Tsi-Ti)*exp(-h_ent*As_ent/(mdot*cp)); %
Exit temperature of entrance region [K]
        NTU_ent = h_ent*As_ent/(mdot*cp);

        % Variable reassignment
        Nu = Nu_ent;
        h = h_ent;
        Te = Te_ent;
        NTU = NTU_ent;

```

```

        end
        % Determine pressure loss from eqn for fully developed
flow
        % The equation is the friction factor for a single tube
        if a/b <= 8
            f = interp1(rectNuf(1,1:end-1),rectNuf(4,1:end-
1),a/b)/Re; % Friction factor for fully developed laminar flow
        else
            f = rectNuf(4,end)/Re;
        end
    end

    Tm = mean([Ti Te]); % Calculated mean fluid temperature [K]

    deltaTm = abs(Tm-Tmi)/mean([Tm,Tmi])*100; % Percent
difference between the entrance mean temp guess and calculated [K]
    Tmi = Tm;

    % Evaluate aluminum thermal conductivity
    kalum=interp1(propalum(:,1),propalum(:,2),Tsi); % [W/mK] for
aluminum 6061
    if isnan(kalum)
        kalum = propalum(end,2);
    end
    % Using the equation for thermal resistance of a cylinder
    Rcond=log(254/247)/(2*pi*96/1000*kalum)*2;

    Ts = Tsur(2)-mdot*cp*Rcond*(Te-Ti);
    deltaTs=abs(Ts-Tsi)/mean([Ts,Tsi])*100;
    Tsi=Ts;
end
end

deltaP2=0.5*rho*Vavg^2*(f*L/Dh);
Te2=Te;

```

# Appendix C Steady State Heat Transfer Base Case Results for Cooling

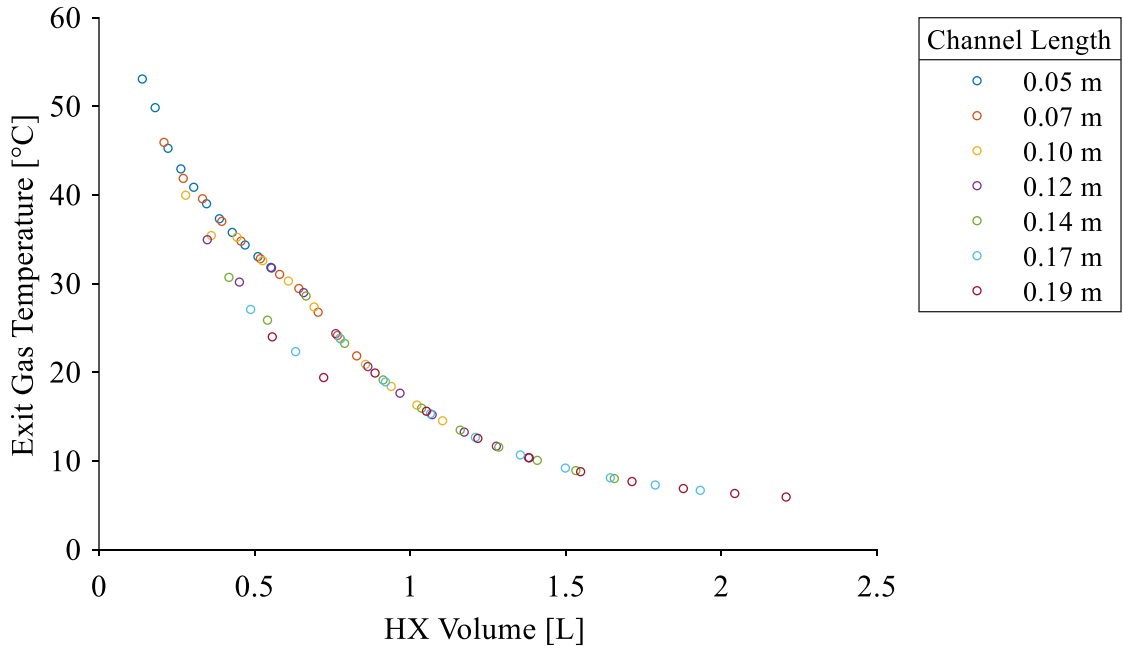


Figure C.1: Plot of exit gas temperature against heat exchanger volume for various channel lengths considered at an engine speed of 2.833 Hz and engine pressure of 435 kPa for cooling.

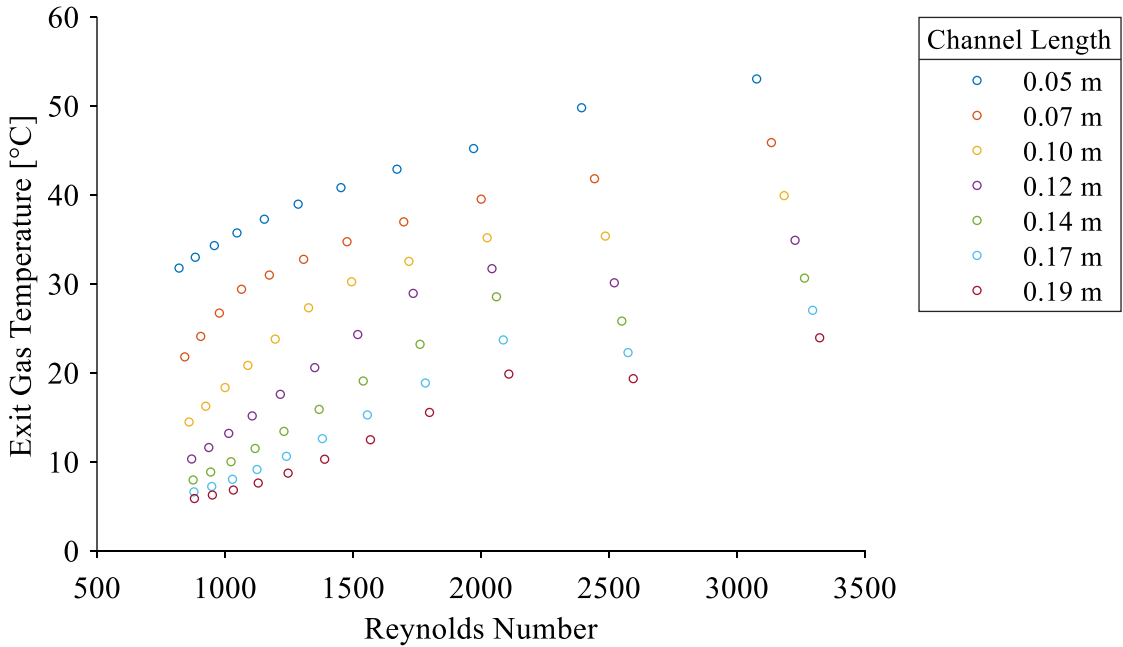


Figure C.2: Plot of exit gas temperature against Reynolds number for various channel lengths considered at an engine speed of 2.833 Hz and engine pressure of 435 kPa for cooling.

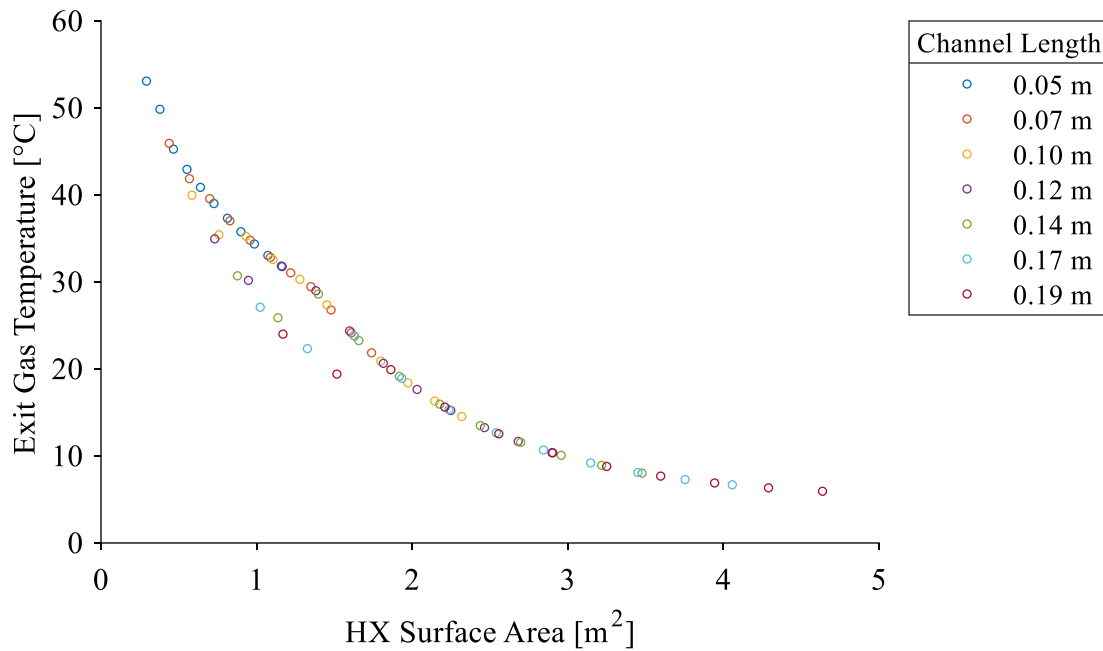


Figure C.3: Plot of exit gas temperature against heat exchanger surface area for various channel lengths considered at an engine speed of 2.833 Hz and engine pressure of 435 kPa for cooling.

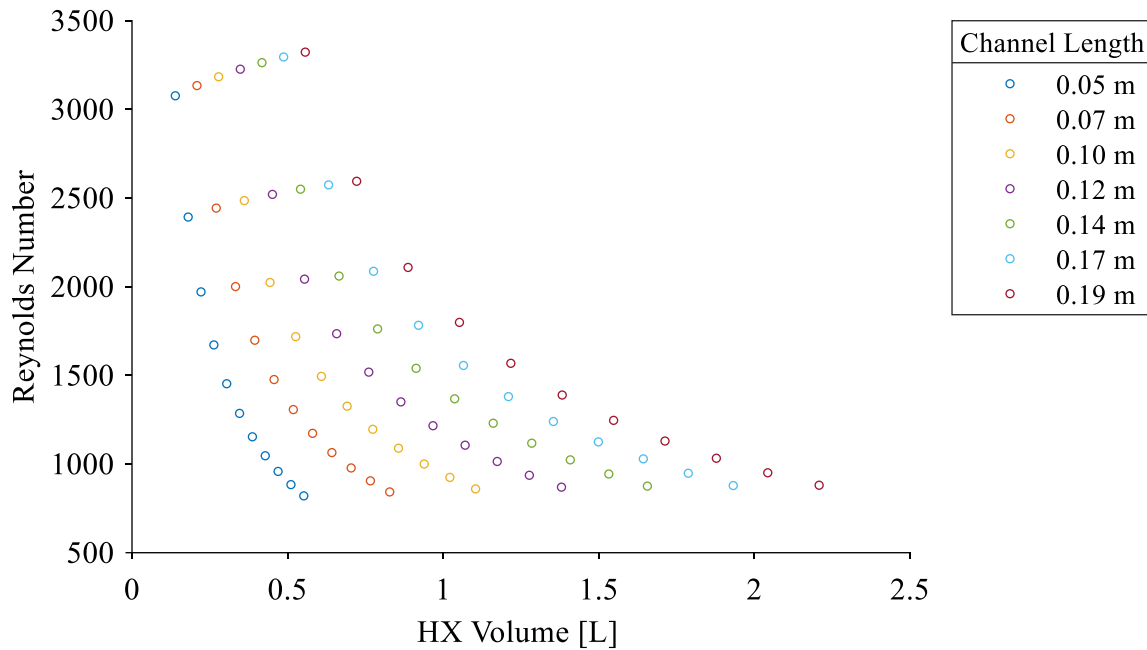


Figure C.4: Plot of Reynolds number against heat exchanger volume for various channel lengths considered at an engine speed of 2.833 Hz and engine pressure of 435 kPa for cooling.

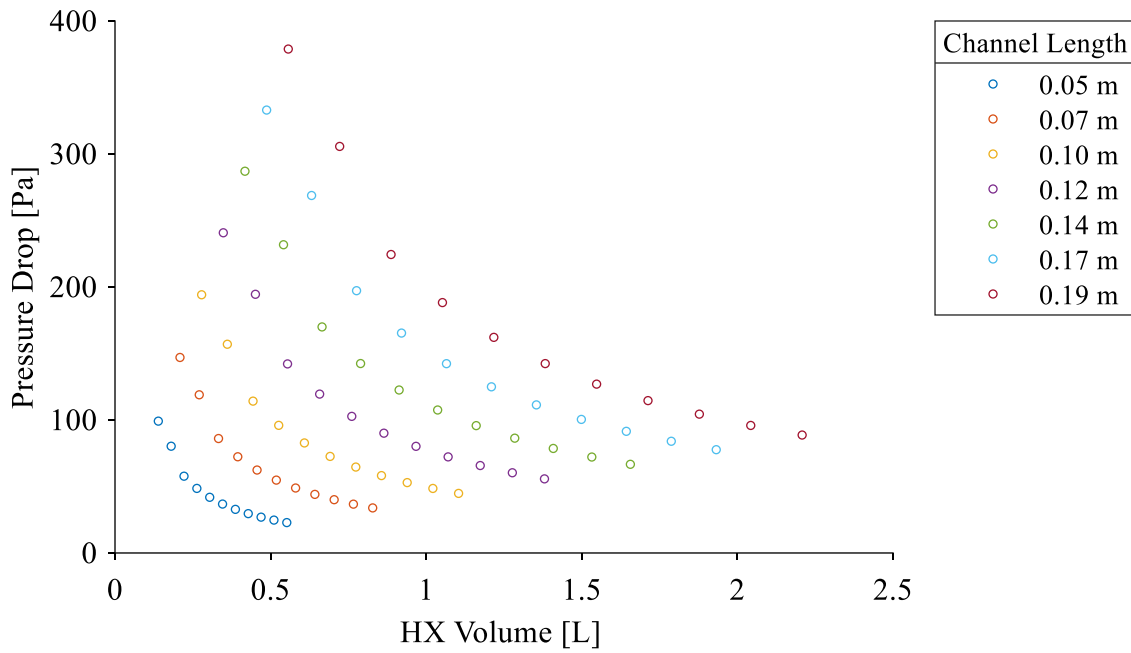


Figure C.5: Plot of pressure drop against heat exchanger volume for various channel lengths considered at an engine speed of 2.833 Hz and engine pressure of 435 kPa for cooling.

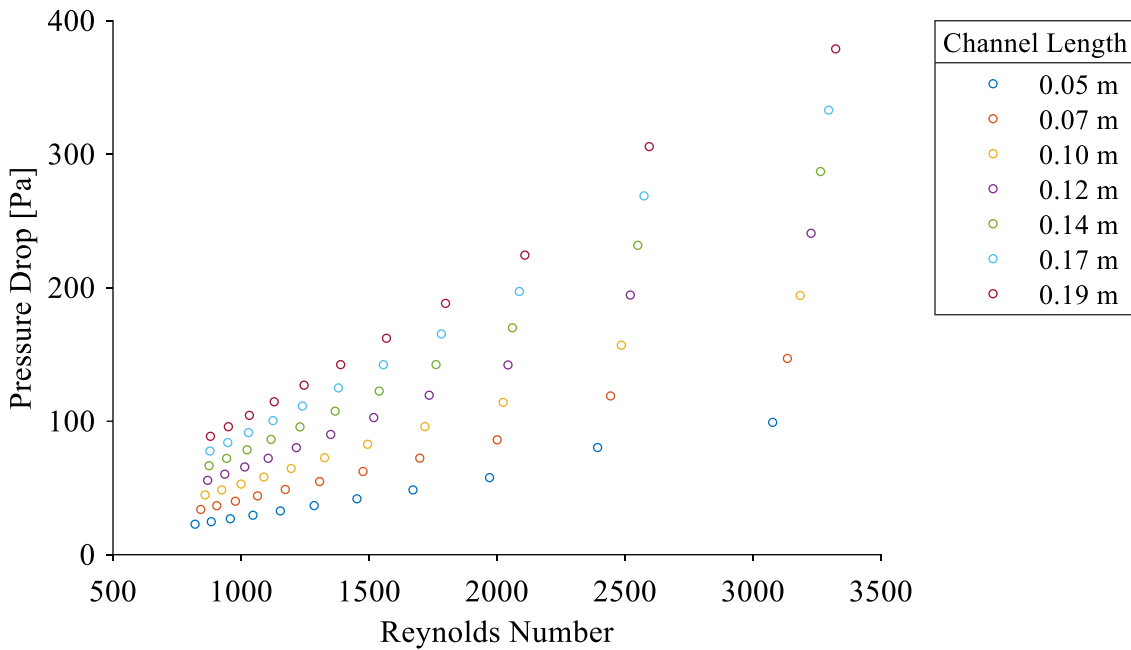


Figure C.6: Plot of pressure drop against Reynolds number for various channel lengths considered at an engine speed of 2.833 Hz and engine pressure of 435 kPa for cooling.

# Appendix D Steady State Heat Transfer Sensitivity Results for Cooling

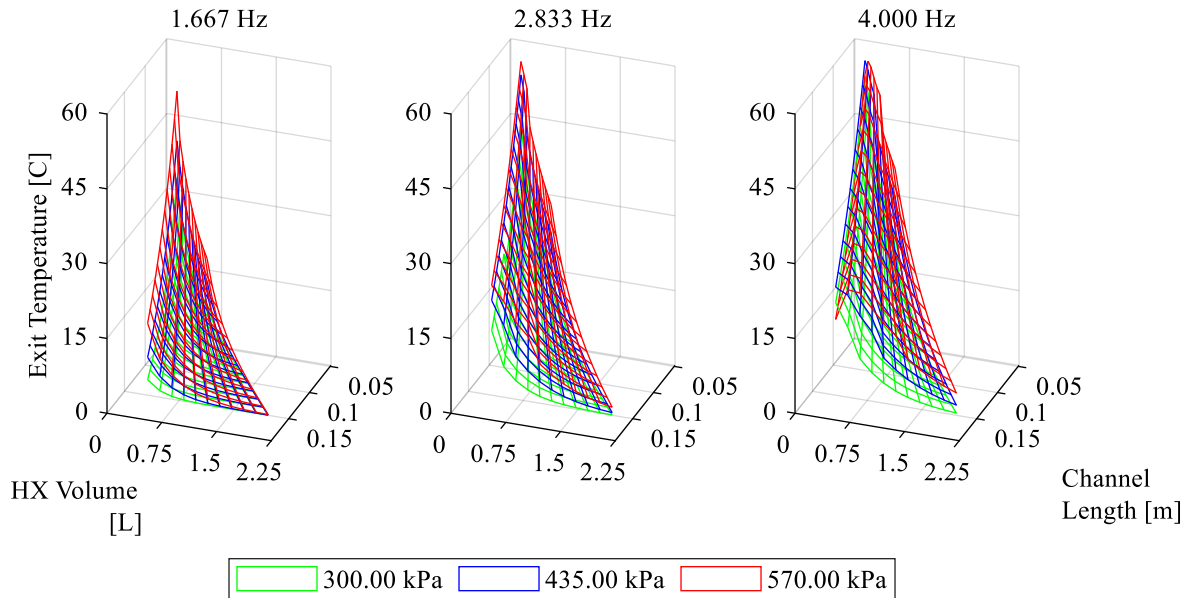


Figure D.1: Plot of exit gas temperature against heat exchanger volume for various channel lengths considered at varying engine pressure and speeds for cooling.

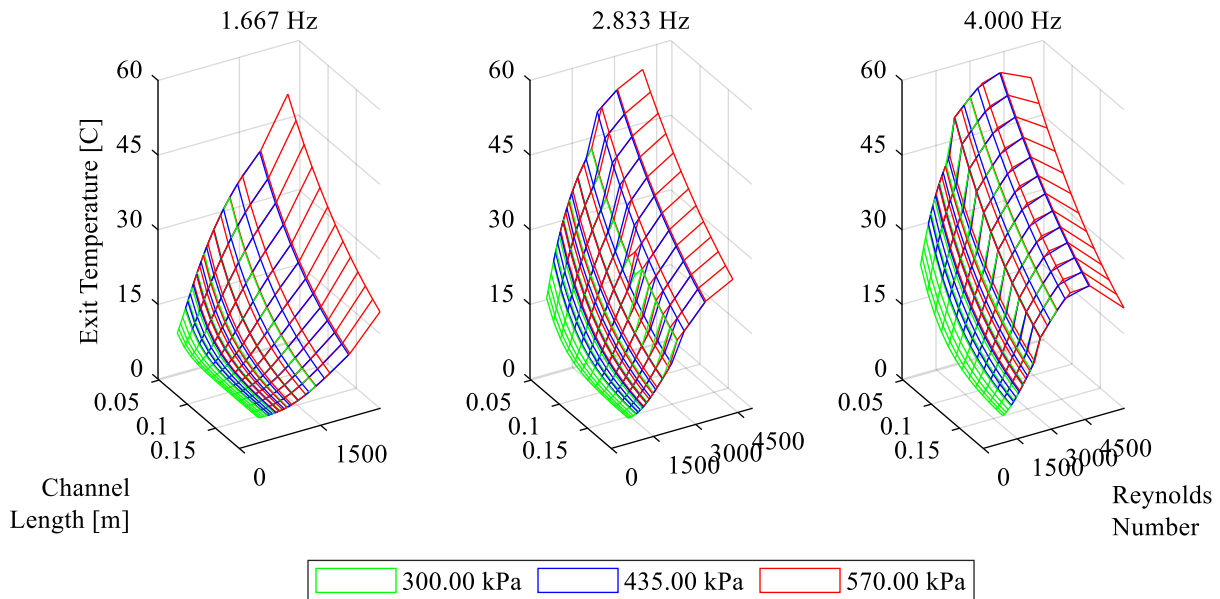


Figure D.2: Plot of exit gas temperature against Reynolds number for various channel lengths considered at varying engine pressures and speeds for cooling.

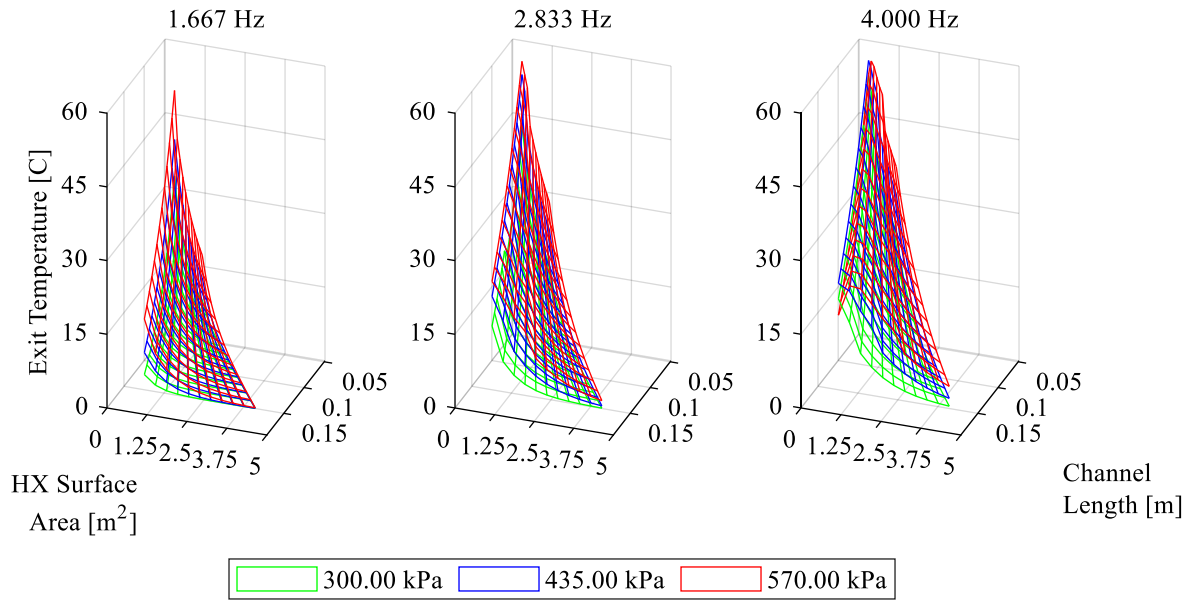


Figure D.3: Plot of exit gas temperature against heat exchanger surface area for various channel lengths considered at varying engine pressures and speeds for cooling.

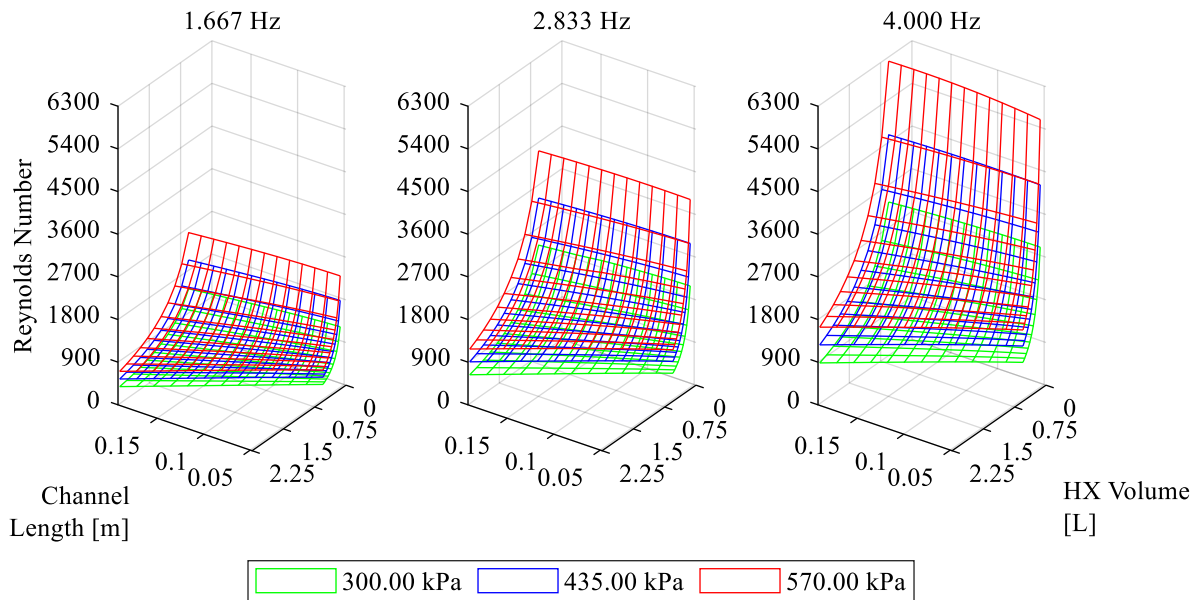


Figure D.4: Plot of Reynolds number against heat exchanger volume for various channel lengths considered at varying engine pressures and speeds for cooling.

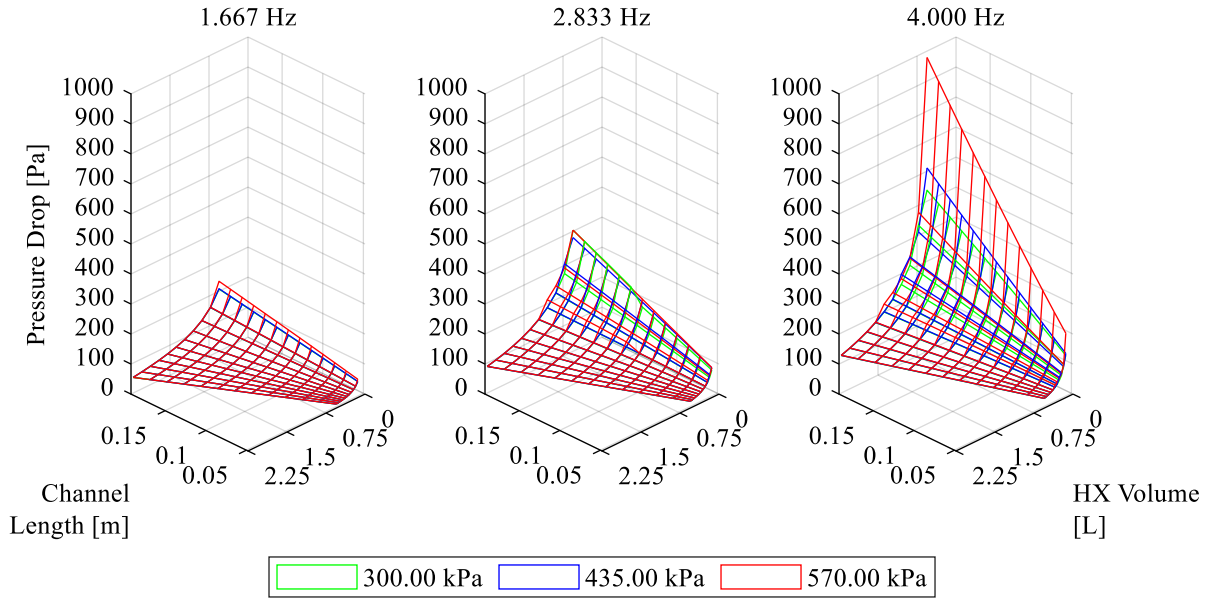


Figure D.5: Plot of pressure drop against heat exchanger volume for various channel lengths considered at varying engine pressures and speeds for cooling.

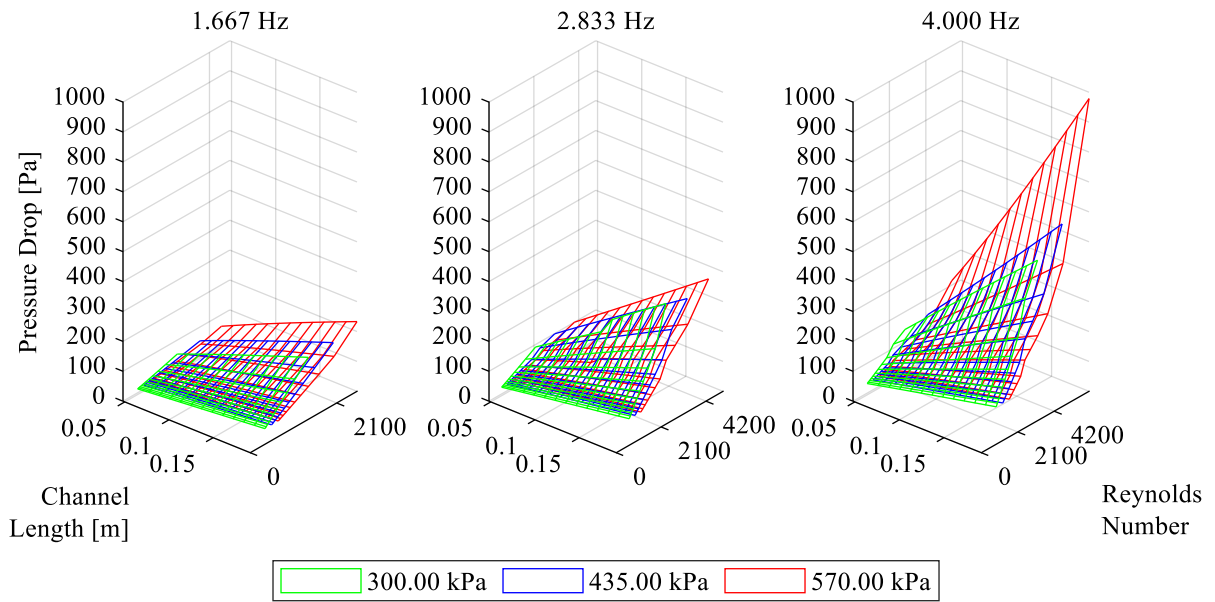


Figure D.6: Plot of pressure drop against Reynolds number for various channel lengths considered at varying engine pressures and speeds for cooling.



## Appendix E Schmidt model derivation for Gamma type Stirling Engines

The following derivation of the Schmidt model for gamma type Stirling engines begins from the isothermal model presented in Section 3.2.1. The ideal gas law relation shown in equation (3.22) relates the instantaneous pressure in the engine to the volumes and temperatures of the engine spaces, following the temperature profile shown in Figure 3.18. This is shown below with the mean effective regenerator temperature shown in full. Note that the compression and expansion space clearance volumes are assigned to the temperatures of the compression and expansion spaces respectively.

$$p = mR \left( \frac{V_c}{T_c} + \frac{V_{clc}}{T_c} + \frac{V_k}{T_c} + \frac{V_r \ln\left(\frac{T_h}{T_c}\right)}{(T_h - T_c)} + \frac{V_h}{T_h} + \frac{V_{cle}}{T_h} + \frac{V_e}{T_h} \right)^{-1} \quad (E.1)$$

The compression space and expansion space volume variation with respect to crank angle are defined in terms of the displacer piston swept volume and power piston swept volume for gamma-type engines, as presented in equations (3.25) and (3.26), reproduced here as:

$$V_e = \frac{V_{disp}}{2} (1 + \cos(\theta + \alpha)) \quad (E.2)$$

$$V_c = \frac{V_{disp}}{2} (1 - \cos(\theta + \alpha)) + \frac{V_{power}}{2} (1 + \cos(\theta)) \quad (E.3)$$

Equations (E.2) and (E.3) are substituted into equation (E.1), and after simplification the following relation is obtained:

$$p = mR \left( B + \frac{V_{disp}}{2T_h T_c} (T_c - T_h) \cos(\theta + \alpha) + \frac{V_{power}}{2T_c} \cos(\theta) \right)^{-1} \quad (E.4)$$

where  $B$  is as defined in equation (3.40), reproduced here as:

$$B = \frac{V_{disp}}{2T_c} + \frac{V_{power}}{2T_c} + \frac{V_{clc}}{T_c} + \frac{V_k}{T_c} + \frac{V_r \ln\left(\frac{T_h}{T_c}\right)}{T_h - T_c} + \frac{V_h}{T_h} + \frac{V_{cle}}{T_h} + \frac{V_{disp}}{2T_h} \quad (E.5)$$

To further simplify equation (E.4) trigonometric substitution using the cosine addition formula can be employed. The simplified equation is:

$$p = mR \left( B + \left( \frac{V_{disp}}{2T_h T_c} (T_c - T_h) \cos(\alpha) + \frac{V_{power}}{2T_c} \right) \cos(\theta) - \left( \frac{V_{disp}}{2T_h T_c} (T_c - T_h) \sin(\alpha) \right) \sin(\theta) \right)^{-1} \quad (E.6)$$

To simplify the equation so that there is only one varying sinusoidal term, the following trigonometric substitution can be used. Note the addition formula for cosine, multiplied by a constant  $C$ :

$$C \cos(x + y) = C \cos x \cos y - C \sin x \sin y \quad (E.7)$$

If one of the angles,  $y$ , is constant, the equation can be rearranged into the following form:

$$C \cos(x + y) = a \cos x - b \sin x \quad (E.8)$$

where  $a$  and  $b$  are:

$$a = C \cos y \quad (E.9)$$

$$b = C \sin y \quad (E.10)$$

The right-hand side of equation (E.8) is similar to the following expression from equation (E.6), where  $x$  is  $\theta$ :

$$\left( \frac{V_{disp}}{2T_h T_c} (T_c - T_h) \cos(\alpha) + \frac{V_{power}}{2T_c} \right) \cos(\theta) - \left( \frac{V_{disp}}{2T_h T_c} (T_c - T_h) \sin(\alpha) \right) \sin(\theta) \quad (E.11)$$

By comparison, the values of constants  $a$  and  $b$  are found as:

$$a = \frac{V_{disp}}{2T_h T_c} (T_c - T_h) \cos(\alpha) + \frac{V_{power}}{2T_c} \quad (E.12)$$

$$b = \frac{V_{disp}}{2T_h T_c} (T_c - T_h) \sin(\alpha) \quad (E.13)$$

The value of constants  $C$  and  $y$  can found from manipulation of equations (E.9) and (E.10). By squaring both equations and adding them, the value of  $C$  can be found as:

$$C = \sqrt{a^2 + b^2} \quad (E.14)$$

By dividing equation (E.10) by (E.9), the value of  $y$  can be found as shown below.

$$y = \arctan\left(\frac{b}{a}\right) \quad (\text{E.15})$$

By substituting in the values of  $a$  and  $b$  to equations (E.14) and (E.15), the values of  $C$  and  $y$  are found to be as shown in equations (3.41) and (3.42), reproduced here:

$$C = \sqrt{\left(\frac{V_{disp}(T_c - T_h)}{2T_h T_c} \cos(\alpha) + \frac{V_{power}}{2T_c}\right)^2 + \left(\frac{V_{disp}(T_c - T_h)}{2T_h T_c} \sin(\alpha)\right)^2} \quad (\text{E.16})$$

$$y = \arctan\left(\frac{\frac{V_{disp}(T_c - T_h)}{2T_h T_c} \sin(\alpha)}{\frac{V_{disp}(T_c - T_h)}{2T_h T_c} \cos(\alpha) + \frac{V_{power}}{2T_c}}\right) \quad (\text{E.17})$$

Using the substitution presented in equation (E.8) and knowing the values of the constants, the instantaneous pressure can be found as shown in equation (3.39) and reproduced here as:

$$p = \frac{mR}{B + C \cos(\theta + y)} \quad (\text{E.18})$$

To determine the total mass of air in the engine, the mean cycle pressure can be found from the average function value as shown below, with the final expression being the same as in equation (3.43):

$$p_{mean} = \frac{1}{2\pi} \int_0^{2\pi} \frac{mR}{B + C \cos(\varphi)} d\varphi = \frac{mR}{B \sqrt{1 - \left(\frac{C}{B}\right)^2}} \quad (\text{E.19})$$

where:

$$\varphi = \theta + y \quad (\text{E.20})$$

To determine the total work per cycle, the sum of the work done by the expansion space and the compression space is taken. As noted in section 3.2.1, the sum of the derivatives of the expansion space and compression space volume with respect to crank angle is equivalent to the derivative of the total engine volume with respect to crank angle. With this simplification, one integral for work will be evaluated as:

$$W = \int_0^{2\pi} p \frac{dV_T}{d\theta} d\theta \quad (\text{E.21})$$

Substituting in the expressions for compression space and expansion space volume variation from equations (E.2) and (E.3) into equation (3.46), the derivative of total volume variation with respect to crank angle can be found as:

$$\begin{aligned} \frac{dV_T}{d\theta} &= \frac{d}{d\theta} \left( \frac{V_{disp}}{2} (1 + \cos(\theta + \alpha)) \right) \\ &\quad + \frac{d}{d\theta} \left( \frac{V_{disp}}{2} (1 - \cos(\theta + \alpha)) + \frac{V_{power}}{2} (1 + \cos(\theta)) \right) \quad (E.22) \\ &= \frac{d}{d\theta} \left( \frac{V_{power}}{2} \cos(\theta) \right) = -\frac{V_{power}}{2} \sin(\theta) \end{aligned}$$

This can then be substituted into equation (E.21) and simplified to give the closed-form expression for indicated work as shown in equation (3.47), reproduced here:

$$W = -\frac{mRV_{power}}{2B} \int_0^{2\pi} \frac{\sin(\theta)}{1 + \frac{C}{B} \cos(\theta + y)} d\theta \quad (E.23)$$

This expression is integrated using a Fourier series expansion using the method described in Urieli and Berchowitz [20]. The Fourier series expansion will be applied to the equation for pressure shown below, expressed in terms of the substitution  $\varphi$  given in equation (E.20). This expansion is valid for piecewise regular functions which satisfy the Dirichlet conditions [85].

The function for pressure given below:

$$p(\varphi) = \frac{mR}{B \left( 1 + \frac{C}{B} \cos(\varphi) \right)} \quad (E.24)$$

satisfies these conditions for  $\frac{C}{A}$  less than 1.

The Fourier series expansion for the above equation is given as follows [85]:

$$p(\varphi) = \frac{a_0}{2} + \sum_{n=1}^{\infty} (a_n \cos(n\varphi) + b_n \sin(n\varphi)) \quad (\text{E.25})$$

where:

$$a_n = \frac{1}{\pi} \int_0^{2\pi} p(\varphi) \cos(n\varphi) d\varphi \quad n = 0, 1, 2, \dots \quad (\text{E.26})$$

$$b_n = \frac{1}{\pi} \int_0^{2\pi} p(\varphi) \sin(n\varphi) d\varphi \quad n = 1, 2, \dots \quad (\text{E.27})$$

The pressure function in terms of  $\varphi$  is an even function, which can be shown by plotting any instance of the function that satisfies the condition that  $\frac{c}{A}$  be less than 1. It follows then that the integral for the constants  $b_n$  are all equal to zero, as the integral of the resulting odd function can be shown to be zero over the interval 0 to  $2\pi$  using a simple substitution.

Thus, the integral for indicated work can be expressed using the Fourier series expansion as:

$$W = -\frac{V_{power}}{2} \int_0^{2\pi} \sin(\theta) \left( \frac{a_0}{2} + \sum_{n=1}^{\infty} a_n \cos(n\varphi) \right) d\theta \quad (\text{E.28})$$

The above expression can be expanded and expressed solely in terms of the integration variable  $\theta$ :

$$\begin{aligned} W = & -\frac{V_{power}}{2} \frac{a_0}{2} \int_0^{2\pi} \sin(\theta) d\theta - \frac{V_{power}}{2} a_1 \int_0^{2\pi} \cos(\theta + y) \sin(\theta) d\theta \\ & - \frac{V_{power}}{2} \sum_{n=2}^{\infty} a_n \int_0^{2\pi} \cos(n(\theta + y)) \sin(\theta) d\theta \end{aligned} \quad (\text{E.29})$$

The value of the first term can be easily seen to be zero. The value of the third term can also be shown to be zero using the product to sum formula for  $\sin(x) \cos(y)$  and integrating, noting from the cosine addition formula that  $\cos(n(\theta + y)) = \cos(y)$  for any  $\theta$  equal to a multiple of  $2\pi$  including zero.

The resulting expression for indicated work is then:

$$W = -\frac{V_{power}}{2} a_1 \int_0^{2\pi} \cos(\theta + y) \sin(\theta) d\theta \quad (E.30)$$

This can then be integrated, again using the product to sum formula and integrating term by term to give the following:

$$W = \frac{V_{power}}{2} a_1 \pi \sin(y) \quad (E.31)$$

The value of the constant  $a_1$  can be found by integration of the following expression:

$$a_1 = \frac{mR}{A\pi} \int_0^{2\pi} \frac{\cos(\varphi)}{1 + \frac{C}{B} \cos(\varphi)} d\varphi \quad (E.32)$$

Using a table of integrals [86] and integrating in two steps and evaluating then simplifying, the value of the constant is found to be:

$$a_1 = \frac{2mR}{C} \left( 1 - \frac{1}{\sqrt{1 - \left(\frac{C}{B}\right)^2}} \right) \quad (E.33)$$

Finally, the expression for indicated work over a cycle can be found after simplification to be as follows:

$$W = \frac{V_{power} \pi m R}{C} \left( 1 - \frac{1}{\sqrt{1 - \left(\frac{C}{B}\right)^2}} \right) \sin(y) \quad (E.34)$$

This expression can then be expressed in terms of the mean cycle pressure as shown in equation (3.48).

# Appendix F Sensitivity Results from Schmidt Model Evaluation

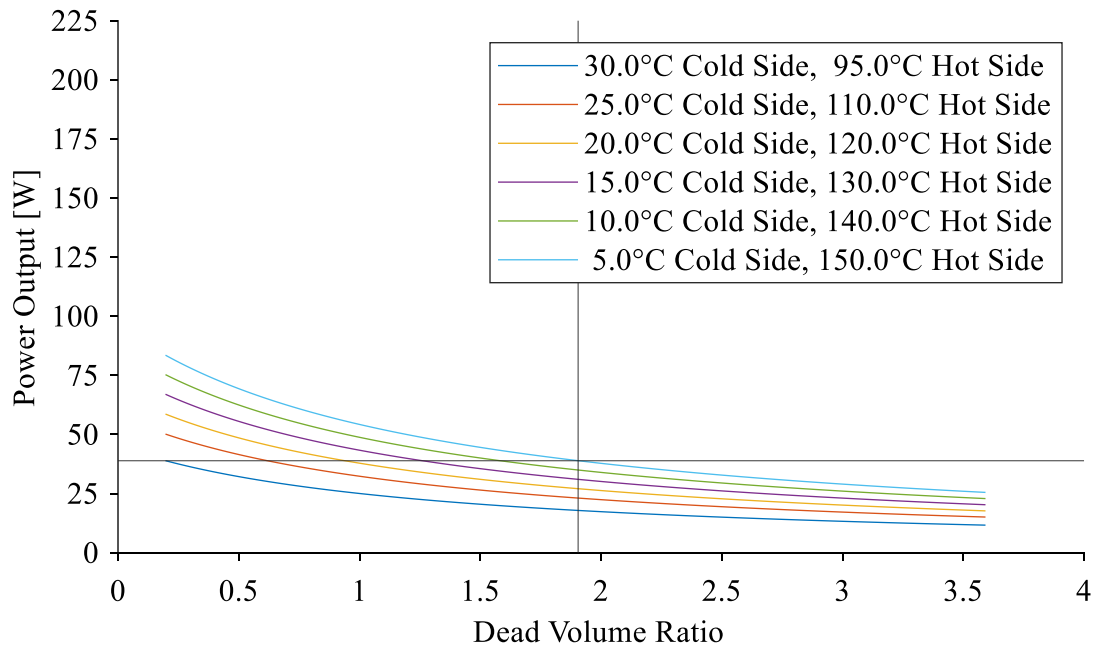


Figure F.1: Plot of power output calculated by Senft's derivation for Gamma engine Schmidt model against DV ratio for various hot and cold side temperatures at an engine pressure of 300 kPa and engine speed of 2.833 Hz.

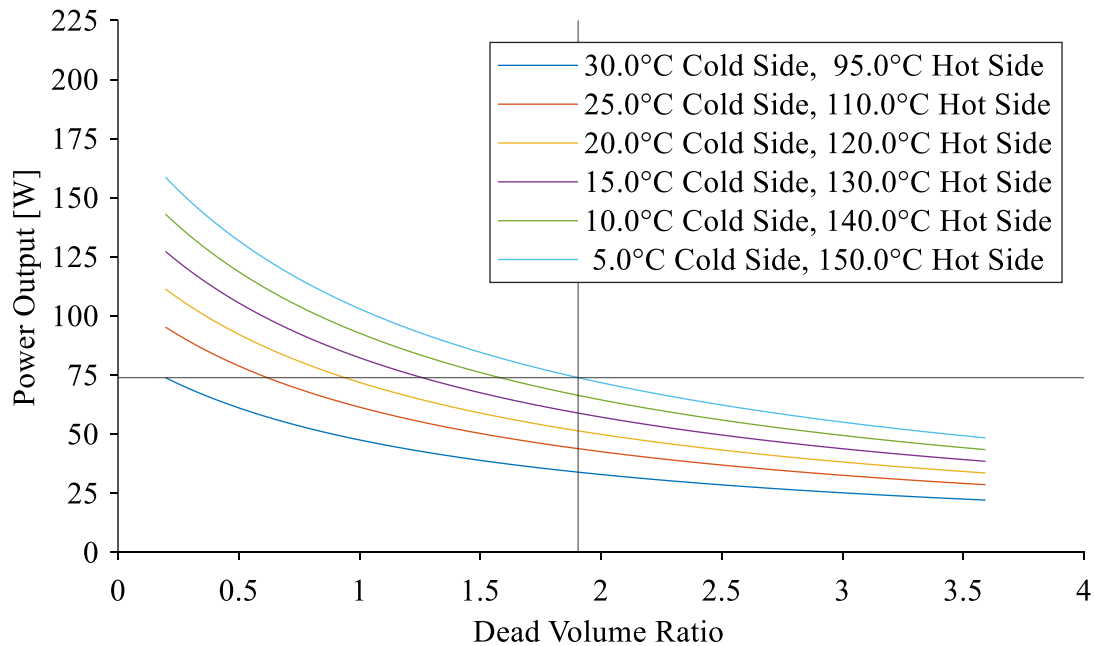


Figure F.2: Plot of power output calculated by Senft's derivation for Gamma engine Schmidt model against DV ratio for various hot and cold side temperatures at an engine pressure of 570 kPa and engine speed of 2.833 Hz.

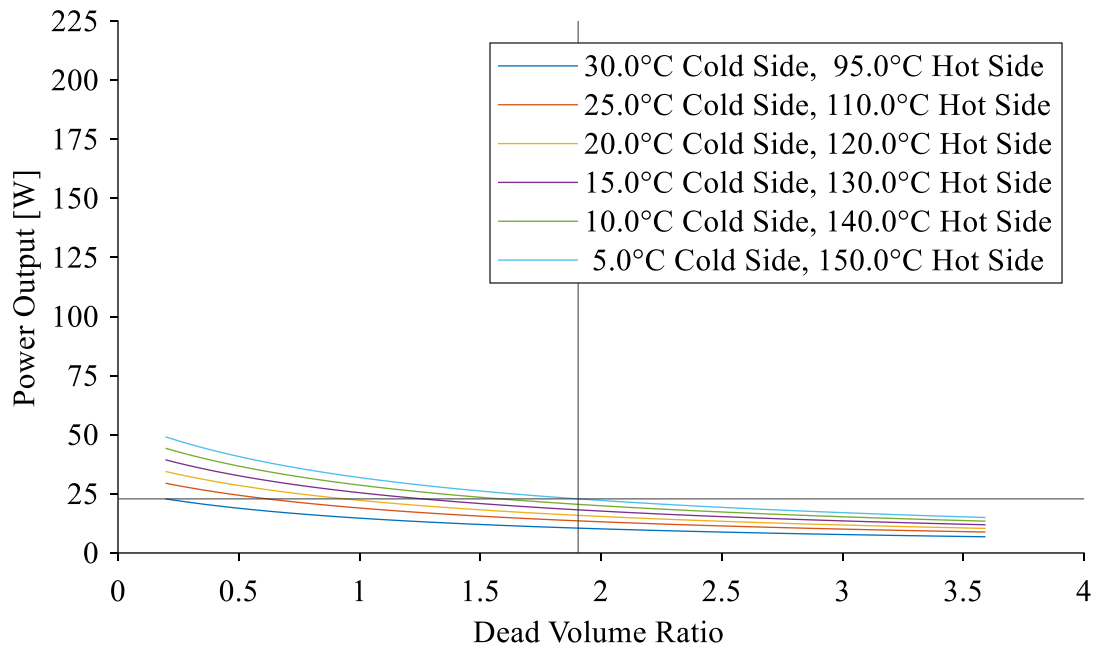


Figure F.3: Plot of power output calculated by Senft's derivation for Gamma engine Schmidt model against DV ratio for various hot and cold side temperatures at an engine pressure of 300 kPa and engine speed of 1.667 Hz.

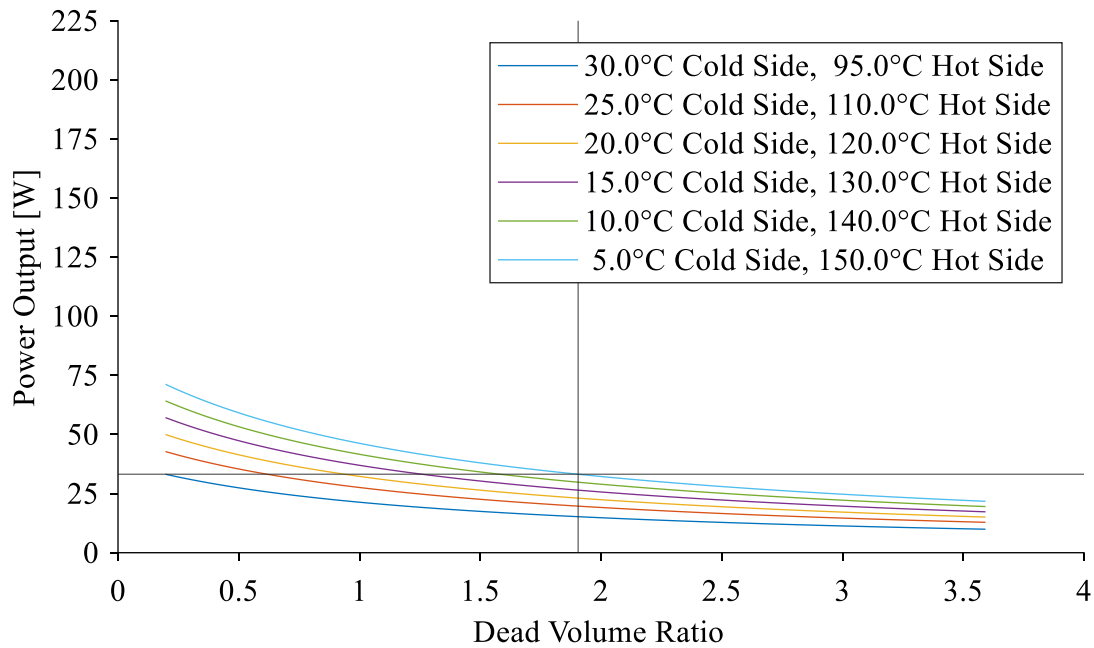


Figure F.4: Plot of power output calculated by Senft's derivation for Gamma engine Schmidt model against DV ratio for various hot and cold side temperatures at an engine pressure of 435 kPa and engine speed of 1.667 Hz.



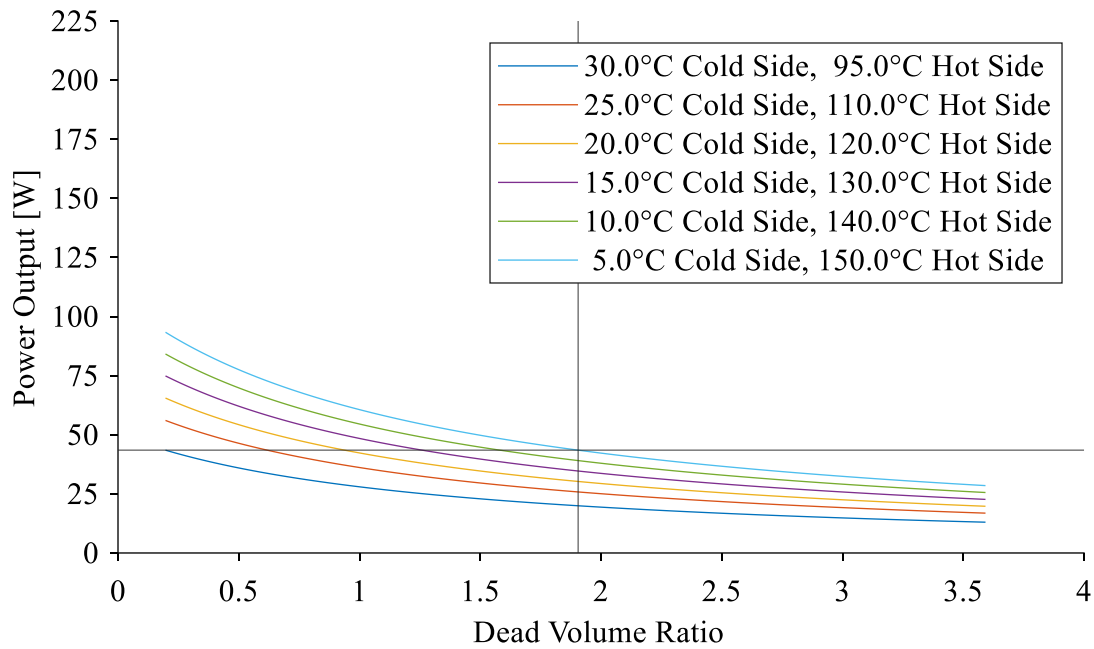


Figure F.5: Plot of power output calculated by Senft's derivation for Gamma engine Schmidt model against DV ratio for various hot and cold side temperatures at an engine pressure of 570 kPa and engine speed of 1.667 Hz.

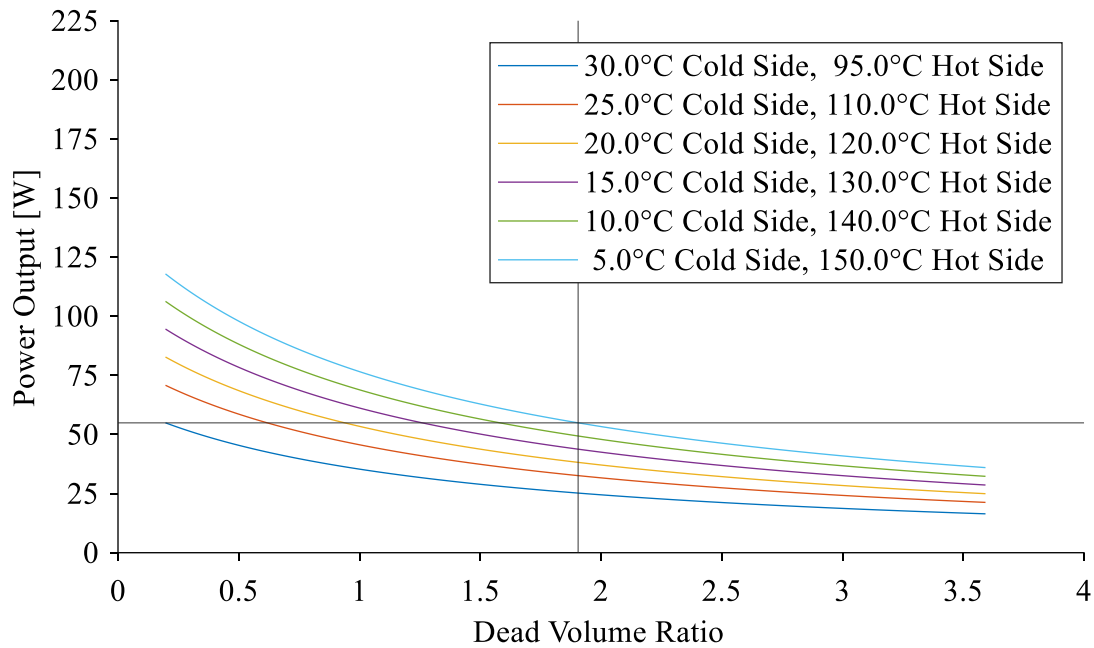


Figure F.6: Plot of power output calculated by Senft's derivation for Gamma engine Schmidt model against DV ratio for various hot and cold side temperatures at an engine pressure of 300 kPa and engine speed of 4.000 Hz.

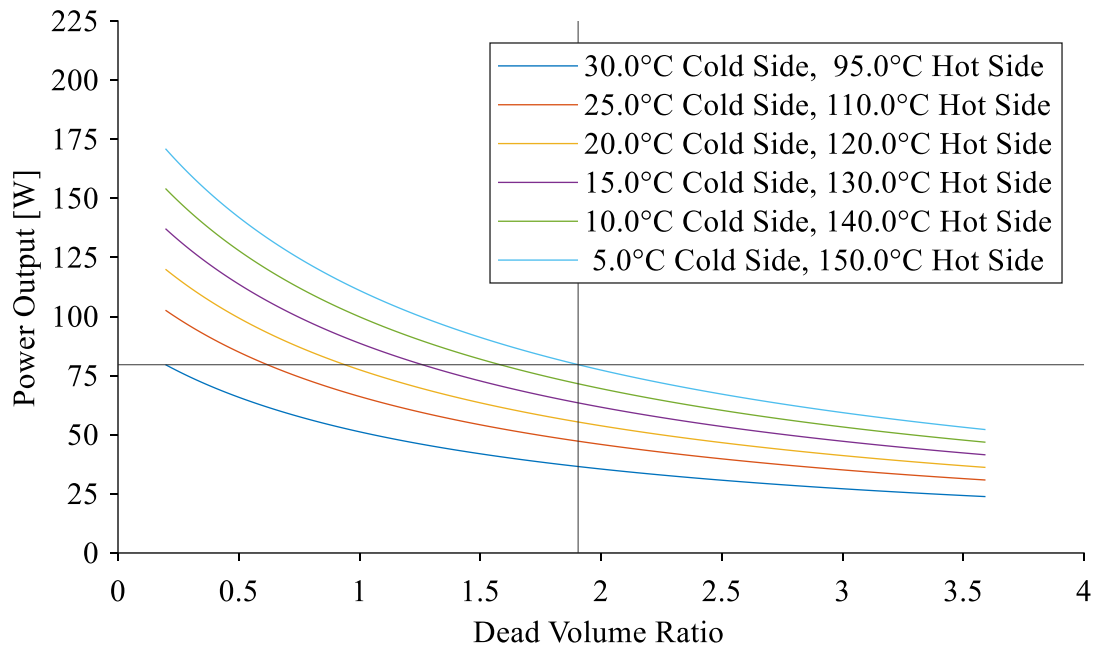


Figure F.7: Plot of power output calculated by Senft's derivation for Gamma engine Schmidt model against DV ratio for various hot and cold side temperatures at an engine pressure of 435 kPa and engine speed of 4.000 Hz.

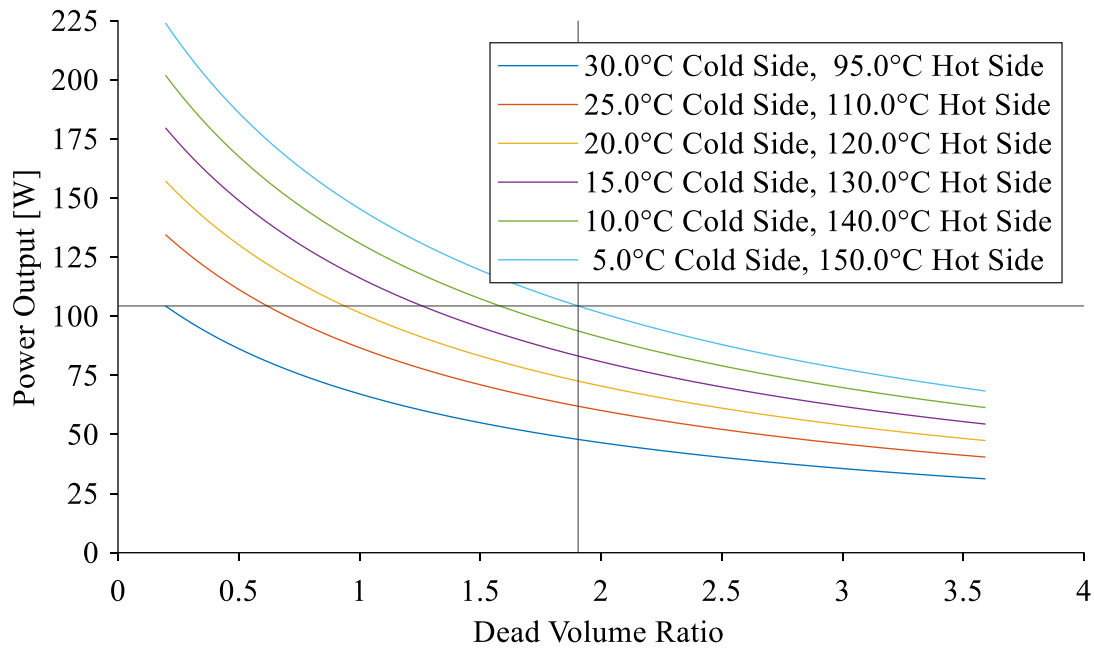


Figure F.8: Plot of power output calculated by Senft's derivation for Gamma engine Schmidt model against DV ratio for various hot and cold side temperatures at an engine pressure of 570 kPa and engine speed of 4.000 Hz.

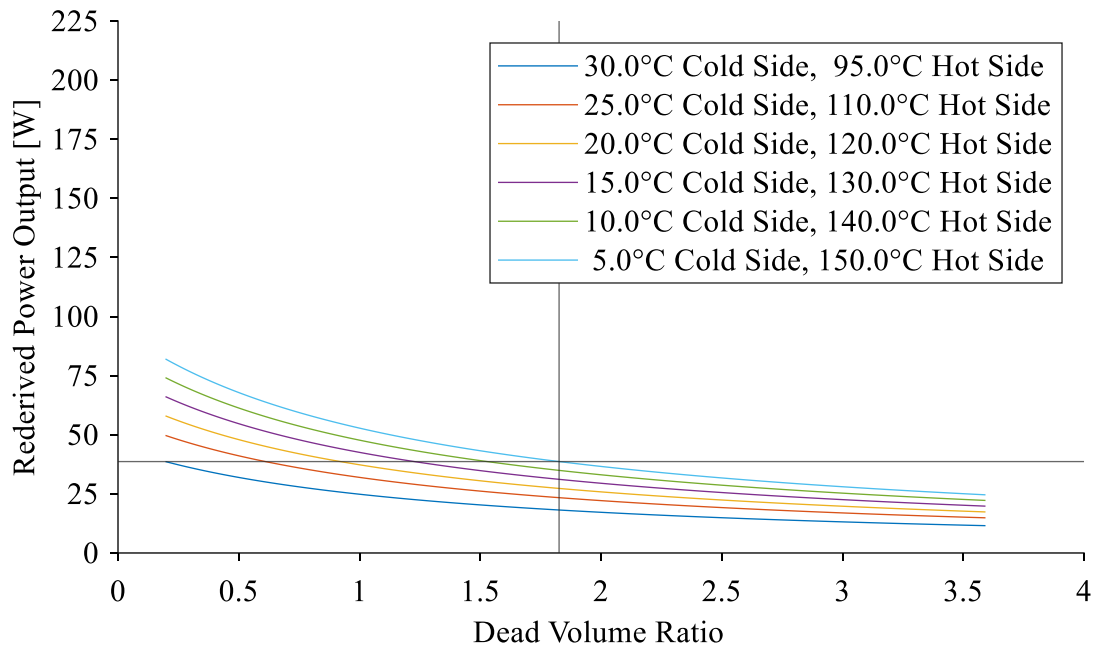


Figure F.9: Plot of power output calculated from isothermal derivation of Schmidt model for Gamma engines against DV ratio for various hot and cold side temperatures at an engine pressure of 300 kPa and engine speed of 2.833 Hz.

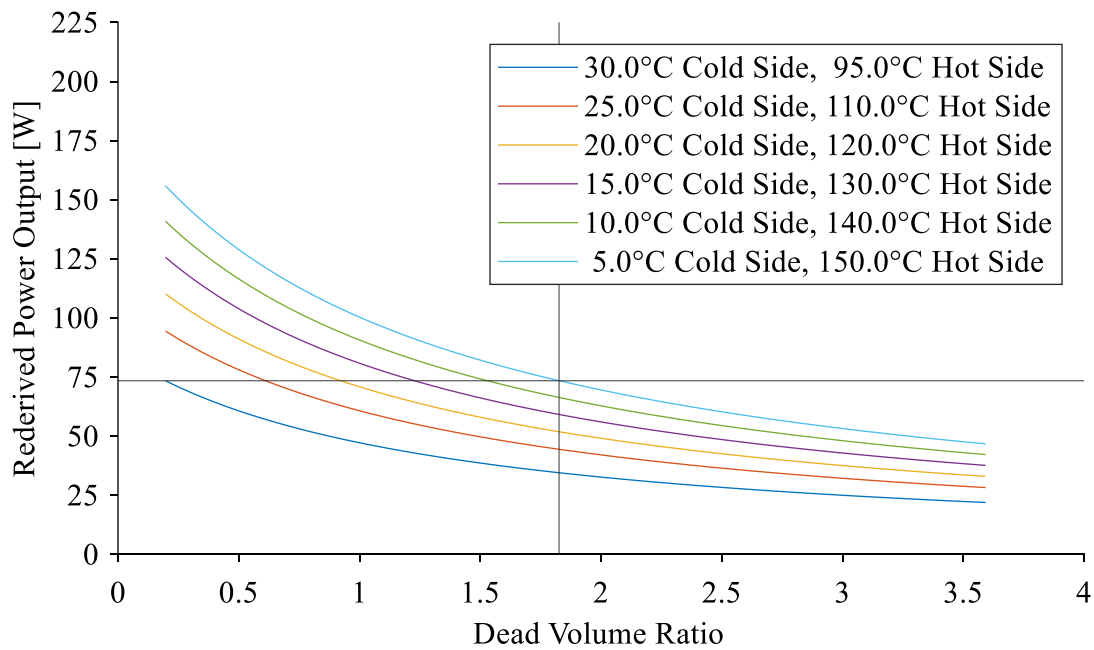


Figure F.10: Plot of power output calculated from isothermal derivation of Schmidt model for Gamma engines model against DV ratio for various hot and cold side temperatures at an engine pressure of 570 kPa and engine speed of 2.833 Hz.

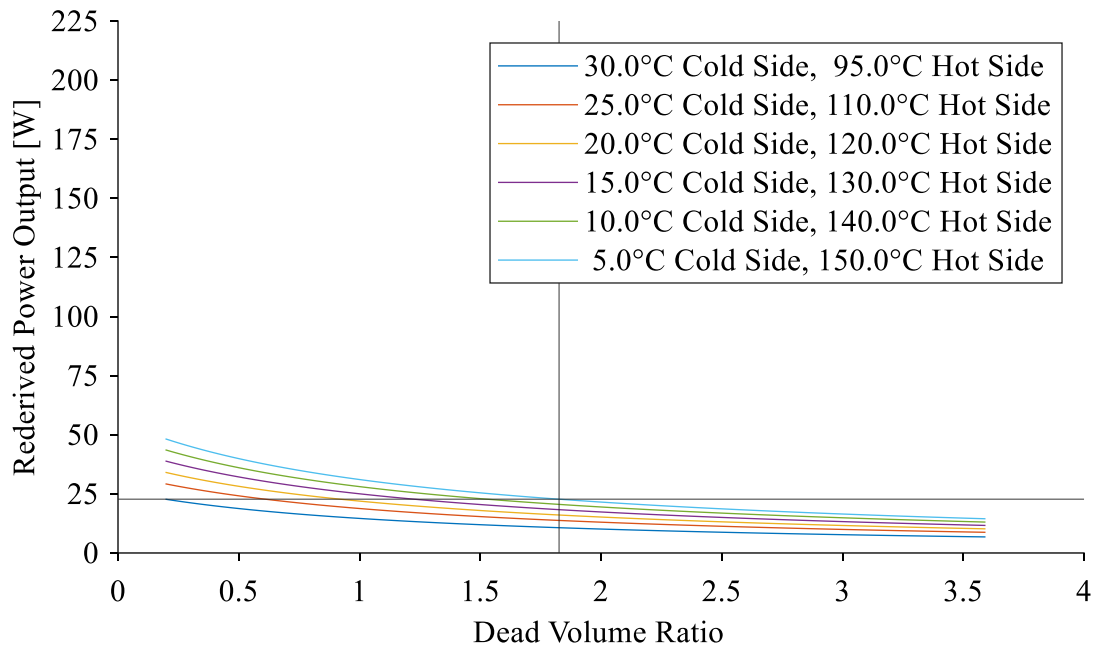


Figure F.11: Plot of power output calculated from isothermal derivation of Schmidt model for Gamma engines against DV ratio for various hot and cold side temperatures at an engine pressure of 300 kPa and engine speed of 1.667 Hz.

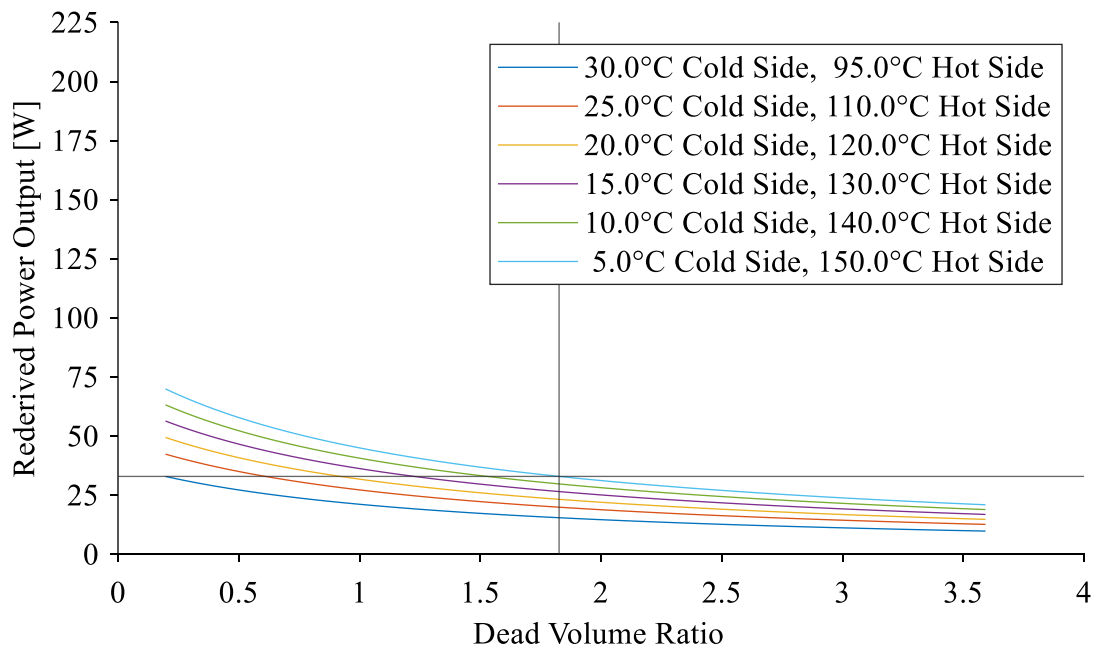


Figure F.12: Plot of power output calculated from isothermal derivation of Schmidt model for Gamma engines against DV ratio for various hot and cold side temperatures at an engine pressure of 435 kPa and engine speed of 1.667 Hz.

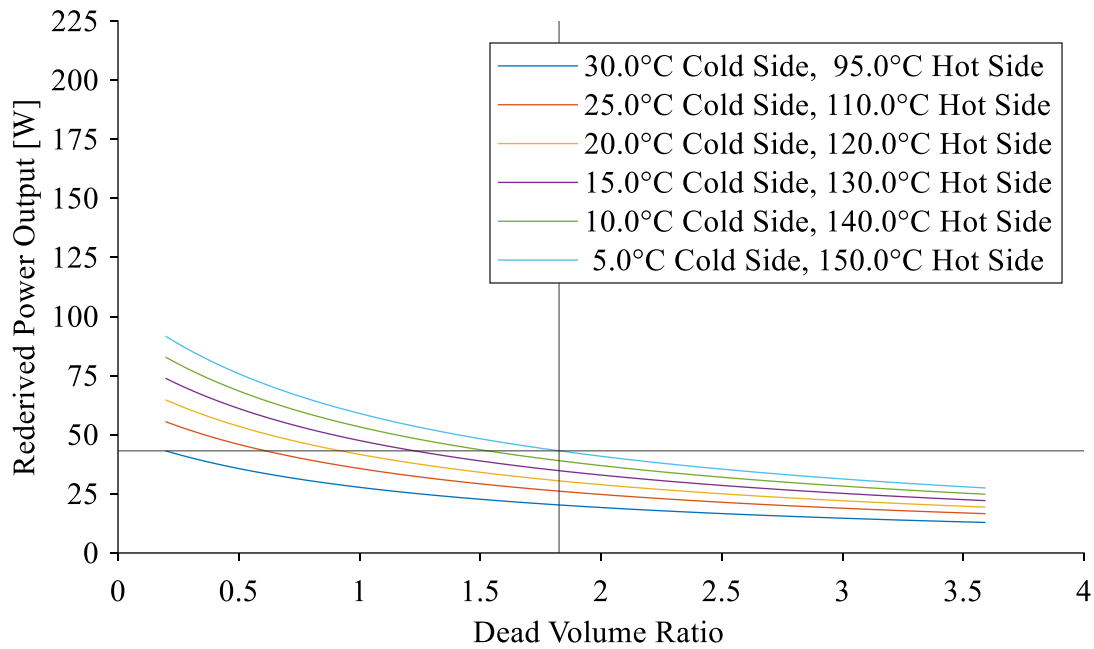


Figure F.13: Plot of power output calculated from isothermal derivation of Schmidt model for Gamma engines model against DV ratio for various hot and cold side temperatures at an engine pressure of 570 kPa and engine speed of 1.667 Hz.

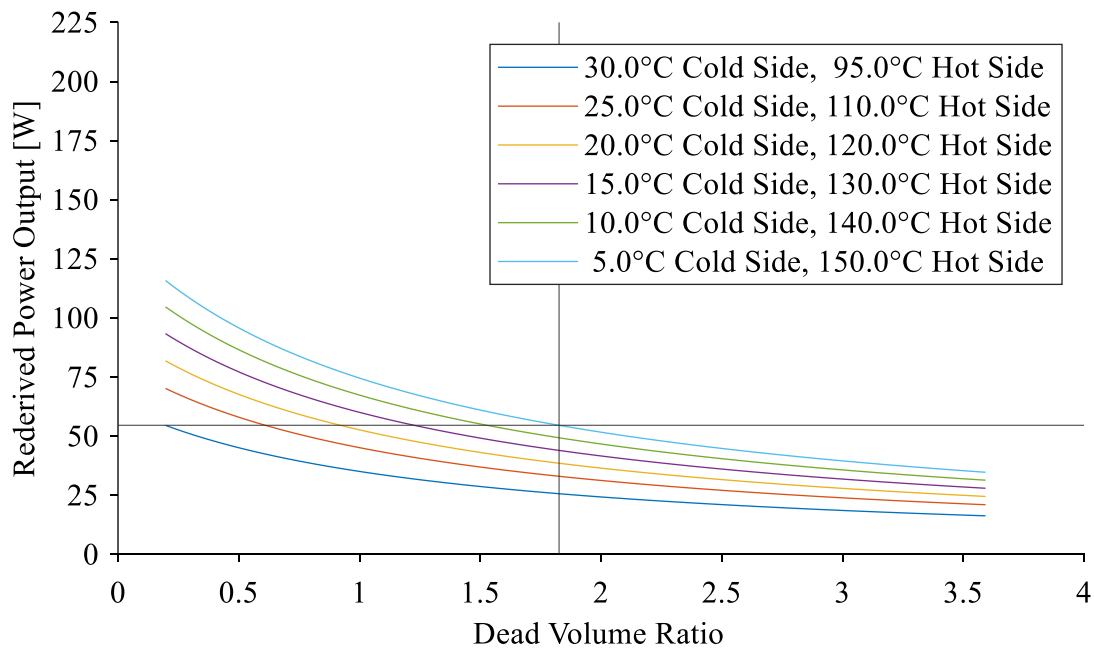


Figure F.14: Plot of power output calculated from isothermal derivation of Schmidt model for Gamma engines model against DV ratio for various hot and cold side temperatures at an engine pressure of 300 kPa and engine speed of 4.000 Hz.

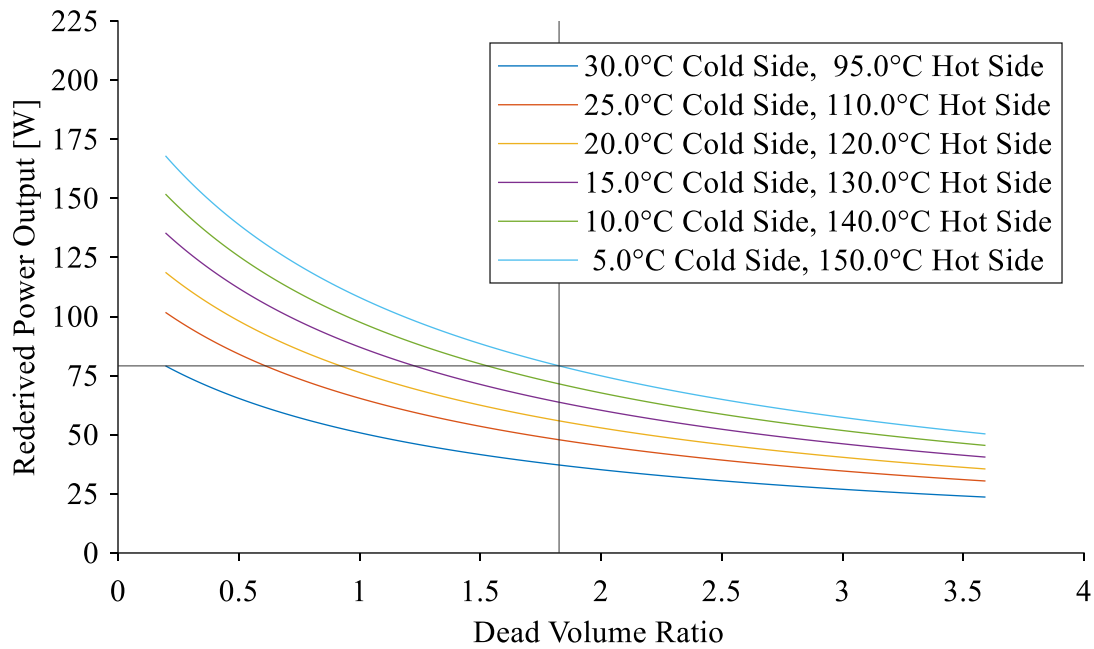


Figure F.15: Plot of power output calculated from isothermal derivation of Schmidt model for Gamma engines against DV ratio for various hot and cold side temperatures at an engine pressure of 435 kPa and engine speed of 4.000 Hz.

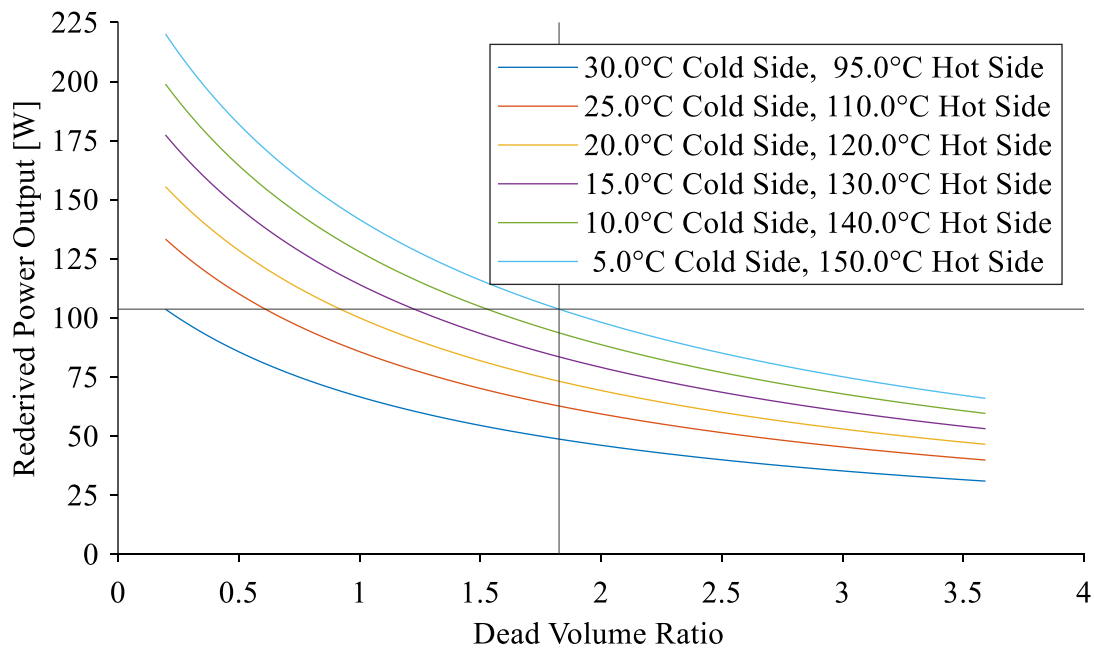


Figure F.16: Plot of power output calculated from isothermal derivation of Schmidt model for Gamma engines against DV ratio for various hot and cold side temperatures at an engine pressure of 570 kPa and engine speed of 4.000 Hz.

# Appendix G Summary of Sage Model Inputs

## G.1 Sage Inputs from Sage Listing File

Sage version 11 Listing Inputs and Recasts

### Contents

- stirling machine
  - 1 ..... pressure source
  - 2 ..... expansion space
    - 2.1 ..... cylinder-space gas
    - 2.2 ..... thick surface
  - 3 ..... compression space
    - 3.1 ..... cylinder-space gas
    - 3.2 ..... thick surface
  - 4 ..... regenerator
    - 4.1 ..... random fiber matrix
      - 4.1.1 ..... matrix gas
      - 4.1.2 ..... rigorous surface
    - 4.2 ..... distributed conductor
  - 5 ..... hot HX
    - 5.1 ..... duct gas
    - 5.2 ..... conductive surface
    - 5.4 ..... distributed conductor
    - 5.5 ..... line temperature drop
  - 6 ..... cold HX
    - 6.1 ..... duct gas
    - 6.2 ..... conductive surface
    - 6.4 ..... distributed conductor
    - 6.5 ..... line temperature drop
  - 7 ..... connecting pipe
    - 7.1 ..... cylinder-space gas
    - 7.2 ..... thick surface
  - 8 ..... power cylinder
    - 8.1 ..... cylinder-space gas
    - 8.2 ..... thick surface
  - 9 ..... displacer piston and cylinder
    - 9.1 ..... cylinder liner
    - 9.2 ..... piston shell
    - 9.3 ..... simple-crank piston
      - 9.3.1 ..... neg-facing area
      - 9.3.2 ..... pos-facing area
  - 10 ..... power piston and cylinder
    - 10.1 ..... cylinder liner
    - 10.2 ..... piston shell
    - 10.3 ..... simple-crank piston
      - 10.3.1 ..... neg-facing area

stirling machine

Inputs		
<b>NTnode</b>	<b>number time nodes</b>	<b>13 or VARIABLE</b>
<b>per Chapter 6</b>		

Lnorm	length scale (m)	1.000E-02
FreqNorm	frequency scale (Hz)	6.000E+01
Pnorm	pressure scale (Pa)	1.000E+06
Tnorm	temperature scale (K)	3.000E+02
Qnorm	heat flow scale (W)	1.000E+02
Vnorm	voltage scale (V)	1.000E+01
Inorm	current scale (A)	1.000E+00
<b>Freq</b>	<b>frequency (Hz)</b>	<b>VARIABLE per</b>
<b>Chapter 4, 6, 7</b>		
Gas	working gas	Ideal Air
DispD	displacer cylinder diameter (m)	2.000E-01
PowerD	power piston diameter (m)	8.573E-02
DispStroke	displacer stroke length (m)	7.500E-02
<b>CR</b>	<b>compression ratio (NonDim)</b>	<b>1.100E+00 ONLY</b>
<b>for Section 7.5</b>		
<b>PowerStroke</b>	<b>pp stroke (m)</b>	<b>7.500E-02 for</b>
<b>all EXCEPT</b>		
<b>PowerStroke = (CR-1)*(HXV+RegV+DispV+4.62E-6+1.660E-04)/(Pi*sqr(PowerD/2)) for Section 7.5</b>		
<b>NumSlots</b>	<b>number of hx openings (NonDim)</b>	<b>VARIABLE per</b>
<b>Chapter 7</b>		
<b>HXLen</b>	<b>hx length (m)</b>	<b>VARIABLE per</b>
<b>Chapter 7</b>		
SlotWidth	width of hx channels (m)	1.000E-03
SlotHeight	height of hx channels (m)	2.000E-02
FinThick	fin thickness (m)	1.460E-03
1 pressure source		
Inputs		
<b>Pcharge</b>	<b>charge pressure (Pa)</b>	<b>VARIABLE per</b>
<b>Chapter 4, 6, 7</b>		
2 expansion space		
Inputs		
<b>NCell</b>	<b>number spatial cells</b>	<b>5 or VARIABLE</b>
<b>per Chapter 6</b>		
Length	mean-flow length (m)	4.083E-02
Twall	wall thickness (m)	1.000E-03
Tinit	initial temperature (NonDim, K)	unit spline...
	(0.000E+00, 3.000E+02)	
	(1.000E+00, 3.000E+02)	
Recasts		
<b>Volume = (Pi/4*sqr(DispD)*(DispStroke/2))+204.98E-6/2 for all EXCEPT</b>		
<b>Volume = (Pi/4*sqr(DispD)*(DispStroke/2))+204.98E-6/2+NumSlots*(SlotWidth+FinThick)*SlotHeight*(0.01215 OR 0.0254) for Section 7.4</b>		
Swet = Pi*DispD*DispStroke/2		
2.1 cylinder-space gas		
Inputs		
<b>Fmult</b>	<b>flow friction multiplier</b>	<b>1.000E+00 for</b>
<b>all EXCEPT 5.000E-01 for Section 6.3.2</b>		
Hmult	heat transfer multiplier	1.000E+00
Kmult	axial conduction multiplier interior	1.000E+00



KmultBnd	axial conduction multiplier endpoints	0.000E+00
UpwindFrac	upwind weight for density interpolation	1.000E-02
Outputs		
<b>DispV</b>	<b>displacer cylinder volume</b>	<b>Vmean*2 for</b>
<b>Section 7.5</b>		
2.2 thick surface		
Inputs		
Kmult	axial conduction multiplier	1.000E+00
D	transverse conduction distance (m)	1.000E-02
Solid	solid material	Alum6061
3 compression space		
Inputs		
<b>NCell</b>	<b>number spatial cells</b>	<b>5 or VARIABLE</b>
<b>per Chapter 6</b>		
Length	mean-flow length (m)	4.083E-02
Twall	wall thickness (m)	1.000E-03
Tinit	initial temperature (NonDim, K)	unit spline...
	(0.000E+00, 3.000E+02)	
	(1.000E+00, 3.000E+02)	
Recasts		
<b>Volume = (Pi/4*sqr(DispD)*(DispStroke/2))+204.98E-6/2 for all EXCEPT</b>		
<b>Volume = (Pi/4*sqr(DispD)*(DispStroke/2))+204.98E-</b>		
<b>6/2+NumSlots*(SlotWidth+FinThick)*SlotHeight*(0.01215 OR 0.0254) for Section</b>		
<b>7.4</b>		
Swet = Pi*DispD*DispStroke/2		
3.1 cylinder-space gas		
Inputs		
<b>Fmult</b>	<b>flow friction multiplier</b>	<b>1.000E+00 for</b>
<b>all EXCEPT 5.000E-01 for Section 6.3.2</b>		
Hmult	heat transfer multiplier	1.000E+00
Kmult	axial conduction multiplier interior	1.000E+00
KmultBnd	axial conduction multiplier endpoints	0.000E+00
UpwindFrac	upwind weight for density interpolation	1.000E-02
3.2 thick surface		
Inputs		
Kmult	axial conduction multiplier	1.000E+00
D	transverse conduction distance (m)	1.000E-02
Solid	solid material	Alum6061
4 regenerator		
Inputs		
<b>NCell</b>	<b>number spatial cells</b>	<b>7 or VARIABLE</b>
<b>per Chapter 6</b>		
Length	canister length (m)	2.540E-02
Din	inner-wall ID (m)	2.070E-01
Solid	canister material	PEI
Tinit	initial temperature (NonDim, K)	unit spline...
	(0.000E+00, 3.000E+02)	

	(1.000E+00, 3.000E+02)	
Dout	outer-wall OD (m)	2.470E-01
Win	inner-wall thickness (m)	1.000E-03
Wout	outer-wall thickness (m)	1.000E-03

#### 4.1 random fiber matrix

Inputs		
Porosity	porosity (void/total)	9.600E-01
Dfiber	fiber diameter (m)	1.000E-04

##### 4.1.1 matrix gas

Inputs		
<b>Fmult</b>	<b>flow friction multiplier</b>	<b>1.000E+00 for</b>
<b>all EXCEPT 5.000E-01</b>	<b>for Section 6.3.2</b>	
Hmult	heat transfer multiplier	1.000E+00
Kmult	axial conduction multiplier interior	1.000E+00
KmultBnd	axial conduction multiplier endpoints	0.000E+00
UpwindFrac	upwind weight for density interpolation	1.000E-02
Outputs		
<b>RegV</b>	<b>regenerator volume</b>	<b>Vmean for</b>
<b>Section 7.5</b>		

##### 4.1.2 rigorous surface

Inputs		
Kmult	axial conduction multiplier	1.000E+00
D	transverse conduction distance (m)	1.000E-02
Solid	solid material	Polyester

#### 4.2 distributed conductor

Inputs		
D	solid y-thickness (m)	1.000E-02

#### 5 hot HX

Inputs		
<b>NCell</b>	<b>number spatial cells</b>	<b>7 or VARIABLE</b>
<b>per Chapter 6</b>		
Roughness	mean wall roughness / Dhyd (NonDim)	1.000E-03
<b>Tinit</b>	<b>initial temperature (NonDim, K)</b>	<b>unit spline...</b>
	(0.000E+00, VARIABLE per Chapter 4, 6, 7)	
	(1.000E+00, VARIABLE per Chapter 4, 6, 7)	

Recasts  
 Length = HXLen  
 Wchan = SlotWidth  
 Hchan = SlotHeight  
 Nchan = NumSlots  
 Tfin = FinThick

##### 5.1 duct gas

Inputs		
<b>Fmult</b>	<b>flow friction multiplier</b>	<b>1.000E+00 for</b>
<b>all EXCEPT 5.000E-01</b>	<b>for Section 6.3.2</b>	

Hmult	heat transfer multiplier	1.000E+00
Kmult	axial conduction multiplier interior	1.000E+00
KmultBnd	axial conduction multiplier endpoints	0.000E+00
UpwindFrac	upwind weight for density interpolation	1.000E-02
Klocal	local-loss coefficient	1.500E+00
TbInNeg	incoming relative turbulence neg bnd	1.000E+00
TbInPos	incoming relative turbulence pos bnd	1.000E+00

Outputs

<b>HXV</b>	<b>HX volume</b>	<b>Vmean*2 for</b>
------------	------------------	--------------------

**Section 7.5**

5.2 conductive surface

Inputs		
D	fin conduction length (m)	2.000E-02
Solid	material	Alum6061

5.4 distributed conductor

Inputs		
D	solid y-thickness (m)	3.500E-03
Solid	material	Alum6061

Recasts

W = (0.1235+0.1235+0.0035)/2\*2\*Pi [solid z-thickness (m)]

5.5 line temperature drop

Recasts

**DeltaT = unit spline...**  
(0.000E+00, -QyPos\*(0.067 OR 0.04925 for Section 6.2))  
(1.000E+00, -QyPos\*(0.067 OR 0.04925 for Section 6.2))

6 cold HX

Inputs		
<b>NCell</b>	<b>number spatial cells</b>	<b>7 or VARIABLE</b>

**per Chapter 6**

Roughness	mean wall roughness / Dhyd (NonDim)	1.000E-03
<b>Tinit</b>	<b>initial temperature (NonDim, K)</b>	<b>unit spline...</b>
	(0.000E+00, VARIABLE per Chapter 4, 6, 7)	
	(1.000E+00, VARIABLE per Chapter 4, 6, 7)	

Recasts

Length = HXLen  
Wchan = SlotWidth  
Hchan = SlotHeight  
Nchan = NumSlots  
Tfin = FinThick

6.1 duct gas

Inputs		
<b>Fmult</b>	<b>flow friction multiplier</b>	<b>1.000E+00 for</b>

**all EXCEPT 5.000E-01 for Section 6.3.2**

Hmult	heat transfer multiplier	1.000E+00
Kmult	axial conduction multiplier interior	1.000E+00
KmultBnd	axial conduction multiplier endpoints	0.000E+00
UpwindFrac	upwind weight for density interpolation	1.000E-02

Klocal	local-loss coefficient	1.500E+00
TbInNeg	incoming relative turbulence neg bnd	1.000E+00
TbInPos	incoming relative turbulence pos bnd	1.000E+00

6.2 conductive surface

Inputs		
D	fin conduction length (m)	2.000E-02
Solid	material	Alum6061

6.4 distributed conductor

Inputs		
D	solid y-thickness (m)	3.500E-03
Solid	material	Alum6061
Recasts		
W = (0.1235+0.1235+0.0035)/2*2*Pi		

6.5 line temperature drop

Recasts

**DeltaT = unit spline...**  
**(0.000E+00, -QyPos\*(0.024 OR 0.02228 for Section 6.2))**  
**(1.000E+00, -QyPos\*(0.024 OR 0.02228 for Section 6.2))**

7 connecting pipe

Inputs		
<b>NCell</b>	<b>number spatial cells</b>	<b>5 or VARIABLE</b>
<b>per Chapter 6</b>		
Length	mean-flow length (m)	3.276E-01
Twall	wall thickness (m)	1.000E-03
Tinit	initial temperature (NonDim, K)	unit spline...
	(0.000E+00, 3.000E+02)	
	(1.000E+00, 3.000E+02)	
Volume	mean volume (m3)	1.660E-04
Recasts		
Swet = Pi*0.0254*Length/2		

7.1 cylinder-space gas

Inputs		
<b>Fmult</b>	<b>flow friction multiplier</b>	<b>1.000E+00 for</b>
<b>all EXCEPT 5.000E-01 for Section 6.3.2</b>		
Hmult	heat transfer multiplier	1.000E+00
Kmult	axial conduction multiplier interior	1.000E+00
KmultBnd	axial conduction multiplier endpoints	0.000E+00
UpwindFrac	upwind weight for density interpolation	1.000E-02

7.2 thick surface

Inputs		
Kmult	axial conduction multiplier	1.000E+00
D	transverse conduction distance (m)	1.000E-02
Solid	solid material	Alum6061

8 power cylinder

Inputs  
**NCell**                    **number spatial cells**                    **5 or VARIABLE**  
**per Chapter 6**  
Length                    mean-flow length (m)                    3.830E-02  
Twall                    wall thickness (m)                    1.000E-03  
Tinit                    initial temperature (NonDim, K)                    unit spline...  
                  (0.000E+00, 3.000E+02)  
                  (1.000E+00, 3.000E+02)  
Recasts  
Volume = (Pi/4\*sqr(PowerD)\*(PowerStroke/2))+4.62E-6  
Swet = Pi\*PowerD\*PowerStroke/2

### 8.1 cylinder-space gas

Inputs  
**Fmult**                    **flow friction multiplier**                    **1.000E+00 for**  
**all EXCEPT 5.000E-01 for Section 6.3.2**  
Hmult                    heat transfer multiplier                    1.000E+00  
Kmult                    axial conduction multiplier interior                    1.000E+00  
KmultBnd                    axial conduction multiplier endpoints                    0.000E+00  
UpwindFrac                    upwind weight for density interpolation                    1.000E-02

### 8.2 thick surface

Inputs  
Kmult                    axial conduction multiplier                    1.000E+00  
D                    transverse conduction distance (m)                    1.000E-02  
Solid                    solid material                    SS304

### 9 displacer piston and cylinder

Inputs  
**NCell**                    **number spatial cells**                    **5 or VARIABLE**  
**per Chapter 6**  
Length                    shell and liner length (m)                    1.931E-01  
Tinit                    initial temperature (NonDim, K)                    unit spline...  
                  (0.000E+00, 3.000E+02)  
                  (1.000E+00, 3.000E+02)  
Recasts  
Dshell = DispD

### 9.1 cylinder liner

Inputs  
Solid                    canister material                    Alum6061  
Recasts  
Wcan = 0.0035

### 9.2 piston shell

Inputs  
Solid                    canister material                    Polyurethane  
Recasts  
Wcan = DispD/2

### 9.3 simple-crank piston

Inputs		
Mass	reciprocating mass (kg)	1.000E+00
Phase	crank phase (deg)	0.000E+00
Recasts		
Rcrank = DispStroke/2		
Lratio = 0.130/Rcrank		

### 9.3.1 neg-facing area

Recasts	
A	$\text{Pi}/4*\text{sqr}(\text{DispD})$

### 9.3.2 pos-facing area

Recasts	
A	$\text{Pi}/4*\text{sqr}(\text{DispD})$

## 10 power piston and cylinder

Inputs		
<b>NCell</b>	<b>number spatial cells</b>	<b>5 or VARIABLE</b>
<b>per Chapter 6</b>		
Length	shell and liner length (m)	1.520E-01
Tinit	initial temperature (NonDim, K)	unit spline...
	(0.000E+00, 3.000E+02)	
	(1.000E+00, 3.000E+02)	
Recasts		
Dshell = PowerD		

### 10.1 cylinder liner

Inputs		
Solid	canister material	SS304
Wcan	wall thickness (m)	1.000E-03

### 10.2 piston shell

Inputs		
Solid	canister material	Alum6061
Wcan	wall thickness (m)	1.000E-03

### 10.3 simple-crank piston

Inputs		
Mass	reciprocating mass (kg)	1.000E+00
Phase	crank phase (deg)	-9.000E+01
Recasts		
Rcrank = PowerStroke/2		
Lratio = 0.146/Rcrank		

#### 10.3.1 neg-facing area

Recasts	
A	$\text{Pi}/4*\text{sqr}(\text{PowerD})$

## G.2 Solid Material Properties

The values of conductivity and specific heat for aluminum 6061 were found from papers by Hossfeld and Roos [87] and Sedighi et al. [88]. Density is a constant in Sage and was determined to be  $2700 \text{ kg/m}^3$  from [89] and Sedighi et al.

*Table G.1 Temperature dependent properties of aluminum 6061 alloy inputted into Sage model.*

<b>Temperature (K)</b>	<b>Conductivity (W/mK)</b>	<b>Specific Heat (J/kgK)</b>
273.15	162	917
310.95	162	945
366.45	177	978
422.05	184	1004
474.15	192	1028

The properties of polyetherimide were taken as constant with respect to temperature. The density was  $1290 \text{ kg/m}^3$ , the thermal conductivity was  $0.22 \text{ W/mK}$ , and the specific heat capacity was taken as  $1666 \text{ J/kgK}$ , from two sources [90], [91].

The properties of polyurethane were taken as constant with respect to temperature. The density of thermal conductivity of the rigid polyurethane foam used as the displacer piston were given in the datasheet at  $288 \text{ kg/m}^3$  and  $0.06 \text{ W/mK}$  respectively [92]. The specific heat capacity was taken to be  $1500 \text{ J/kgK}$  [93].

### G.3 Inputs from Experimental Cases for Sage Validation Cases

Case	Source Temperature	Sink Temperature	Charge Pressure	
	(K)	(K)	Absolute (Pa)	Speed (Hz)
1	4.193E+02	2.844E+02	3.077E+05	3.960E+00
2	4.200E+02	2.843E+02	3.079E+05	3.706E+00
3	4.207E+02	2.842E+02	3.080E+05	3.432E+00
4	4.208E+02	2.840E+02	3.069E+05	3.246E+00
5	4.209E+02	2.839E+02	3.063E+05	3.018E+00
6	4.209E+02	2.838E+02	3.049E+05	2.884E+00
7	4.211E+02	2.835E+02	3.072E+05	2.699E+00
8	4.213E+02	2.833E+02	3.083E+05	2.504E+00
9	4.213E+02	2.832E+02	3.076E+05	2.438E+00
10	4.214E+02	2.831E+02	3.075E+05	2.331E+00
11	4.213E+02	2.831E+02	3.085E+05	2.377E+00
12	4.214E+02	2.831E+02	3.074E+05	2.368E+00
13	4.214E+02	2.830E+02	3.073E+05	2.234E+00
14	4.214E+02	2.829E+02	3.074E+05	2.178E+00
15	4.214E+02	2.829E+02	3.075E+05	2.127E+00
16	4.215E+02	2.828E+02	3.084E+05	2.094E+00
17	4.215E+02	2.827E+02	3.073E+05	2.068E+00
18	4.216E+02	2.826E+02	3.072E+05	1.972E+00
19	4.215E+02	2.826E+02	3.070E+05	1.902E+00
20	4.216E+02	2.825E+02	3.080E+05	1.972E+00
21	4.217E+02	2.824E+02	3.079E+05	1.832E+00
22	4.216E+02	2.825E+02	3.059E+05	1.850E+00
23	4.200E+02	2.851E+02	4.574E+05	2.900E+00
24	4.201E+02	2.851E+02	4.577E+05	2.798E+00
25	4.202E+02	2.850E+02	4.570E+05	2.764E+00
26	4.202E+02	2.850E+02	4.577E+05	2.795E+00
27	4.204E+02	2.847E+02	4.583E+05	2.501E+00



28	4.205E+02	2.846E+02	4.564E+05	2.499E+00
29	4.205E+02	2.846E+02	4.562E+05	2.459E+00
30	4.205E+02	2.846E+02	4.573E+05	2.448E+00
31	4.205E+02	2.845E+02	4.574E+05	2.435E+00
32	4.205E+02	2.845E+02	4.565E+05	2.404E+00
33	4.206E+02	2.845E+02	4.573E+05	2.349E+00
34	4.206E+02	2.844E+02	4.563E+05	2.300E+00
35	4.206E+02	2.844E+02	4.553E+05	2.305E+00
36	4.206E+02	2.843E+02	4.564E+05	2.279E+00
37	4.206E+02	2.842E+02	4.564E+05	2.281E+00
38	4.208E+02	2.842E+02	4.558E+05	2.179E+00
39	4.207E+02	2.842E+02	4.585E+05	2.189E+00
40	4.208E+02	2.841E+02	4.572E+05	2.071E+00
41	4.204E+02	2.860E+02	5.609E+05	2.803E+00
42	4.205E+02	2.859E+02	5.606E+05	2.744E+00
43	4.205E+02	2.858E+02	5.607E+05	2.704E+00
44	4.205E+02	2.858E+02	5.603E+05	2.689E+00
45	4.205E+02	2.858E+02	5.610E+05	2.669E+00
46	4.205E+02	2.858E+02	5.617E+05	2.668E+00
47	4.206E+02	2.858E+02	5.616E+05	2.646E+00
48	4.205E+02	2.858E+02	5.611E+05	2.604E+00
49	4.206E+02	2.857E+02	5.604E+05	2.597E+00
50	4.206E+02	2.857E+02	5.609E+05	2.565E+00
51	4.206E+02	2.857E+02	5.614E+05	2.519E+00
52	4.206E+02	2.857E+02	5.609E+05	2.561E+00
53	4.206E+02	2.857E+02	5.609E+05	2.526E+00
54	4.206E+02	2.857E+02	5.630E+05	2.480E+00
55	4.206E+02	2.856E+02	5.608E+05	2.481E+00
56	4.207E+02	2.856E+02	5.611E+05	2.500E+00
57	4.207E+02	2.856E+02	5.604E+05	2.466E+00
58	4.207E+02	2.855E+02	5.603E+05	2.437E+00

59	4.208E+02	2.854E+02	5.596E+05	2.375E+00
60	4.207E+02	2.854E+02	5.613E+05	2.384E+00
61	4.208E+02	2.855E+02	5.612E+05	2.389E+00
62	4.208E+02	2.854E+02	5.609E+05	2.319E+00
63	4.209E+02	2.853E+02	5.606E+05	2.305E+00
64	4.208E+02	2.853E+02	5.598E+05	2.329E+00
65	4.209E+02	2.851E+02	5.605E+05	2.252E+00
66	4.209E+02	2.852E+02	5.605E+05	2.246E+00
67	4.210E+02	2.851E+02	5.607E+05	2.199E+00
68	4.210E+02	2.850E+02	5.608E+05	2.209E+00
69	4.209E+02	2.851E+02	5.594E+05	2.173E+00
70	4.202E+02	2.868E+02	5.103E+05	3.433E+00
71	4.203E+02	2.868E+02	5.100E+05	3.359E+00
72	4.204E+02	2.866E+02	5.090E+05	3.195E+00
73	4.205E+02	2.865E+02	5.103E+05	3.081E+00
74	4.206E+02	2.863E+02	5.105E+05	2.991E+00
75	4.207E+02	2.862E+02	5.122E+05	2.844E+00
76	4.207E+02	2.860E+02	5.085E+05	2.820E+00
77	4.208E+02	2.860E+02	5.104E+05	2.755E+00
78	4.207E+02	2.859E+02	5.098E+05	2.738E+00
79	4.208E+02	2.857E+02	5.092E+05	2.610E+00
80	4.209E+02	2.857E+02	5.089E+05	2.544E+00
81	4.210E+02	2.855E+02	5.084E+05	2.474E+00
82	4.210E+02	2.854E+02	5.100E+05	2.363E+00
83	4.210E+02	2.854E+02	5.106E+05	2.378E+00
84	4.211E+02	2.853E+02	5.084E+05	2.394E+00
85	4.211E+02	2.852E+02	5.083E+05	2.304E+00
86	4.211E+02	2.852E+02	5.081E+05	2.321E+00
87	4.212E+02	2.852E+02	5.085E+05	2.238E+00
88	4.213E+02	2.850E+02	5.094E+05	2.115E+00
89	4.213E+02	2.851E+02	5.087E+05	2.152E+00

# Appendix H Heat Exchanger Liquids Properties

## H.1 SIL180 Properties

The datasheet provided from the manufacturer for SIL180, shown in Figure H.1, only has a value for specific heat of the fluid at 20 °C, which is far from the set point of 150 °C.

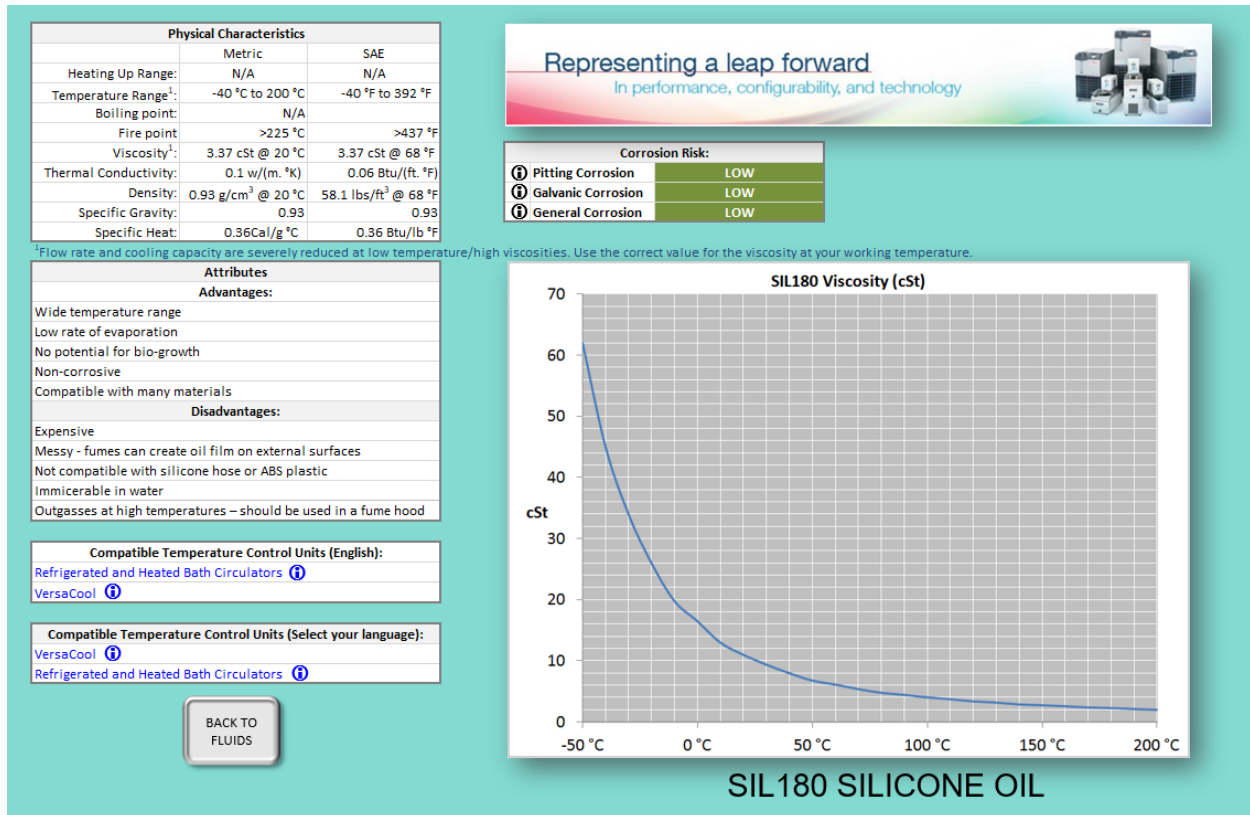


Figure H.1: SIL180 datasheet from manufacturer.

In order to get an estimate of the specific heat of SIL180 at a temperature that is closer to the operating temperature, a similar fluid can be found by comparing the properties that vary with temperature. Lottmann did this by comparing the measured SIL180 density at various temperatures, shown in Table H.1, and the viscosity varying with temperature from the datasheet, to various similar heat transfer fluids [46].

Table H.1 Measured Density of SIL180 at varying temperatures.

Temperature (K)	Density (kg/m <sup>3</sup> )
294.65	932.323
303.25	904.000
322.65	902.000
334.65	894.118
345.45	889.796
353.25	886.598
362.95	874.747
373.25	862.745
385.15	860.417
393.15	855.102
403.15	845.361
414.15	836.735
425.15	828.571
433.15	816.327
443.15	813.861

SYLTHERM 800 from the Dow Chemical Company [94] was found to be similar, and had good agreement in the density and viscosity curves. The specific heat capacity was then estimated at varying temperatures based on the specific heat capacity of SYLTHERM 800. This included an offset from the specific heat capacity curve for SYLTHERM 800, yielding the estimated values of specific heat capacity shown in Table H.2.

Table H.2 Estimated Specific Heat Capacity of SIL180 at varying temperatures.

<b>Temperature (K)</b>	<b>Specific Heat Capacity (J/kgK)</b>
293.15	1511
303.15	1528
313.15	1545
323.15	1562
333.15	1579
343.15	1596
353.15	1613
363.15	1630
373.15	1647
383.15	1664
393.15	1681
403.15	1698
413.15	1715
423.15	1732
433.15	1749
443.15	1766

The thermal conductivity was taken as constant from the manufacturer's datasheet.

## **H.2 Ethylene Glycol Water Mixture Properties**

As the ethylene glycol water mixture was originally mixed at Terrapin and subsequently topped up with water, the mass fraction of ethylene glycol was now unknown. To determine the mass fraction, the density of the ethylene glycol at 5 °C was measured by measuring the weight and volume of a quantity of ethylene glycol. Then, from the known densities of water and ethylene glycol at 5 °C the mass fraction was determined to be approximately 30% ethylene glycol and 70% water. The specific heat capacity, conductivity, density, and viscosity of the ethylene glycol water mixture is then determined from a datasheet [95].

# Appendix I CFD Air Side Temperature Validation

## Cooling Cases

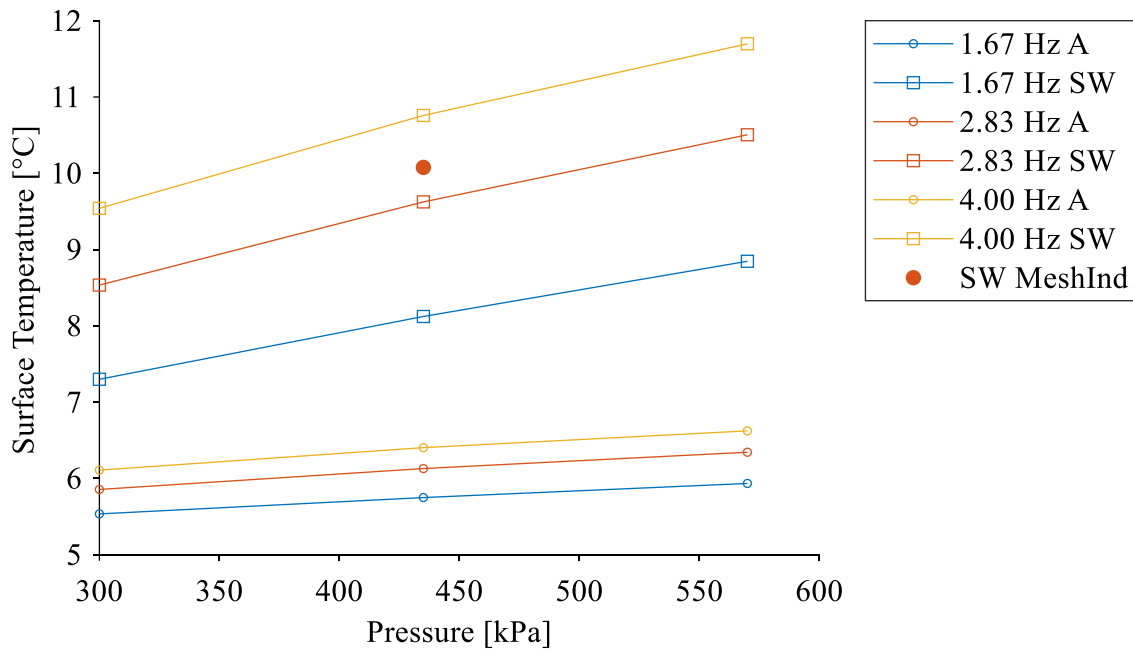


Figure I.1: Plot of solid temperature determined from analytical solution and simulation for varying engine pressure and speed for the cooling case.

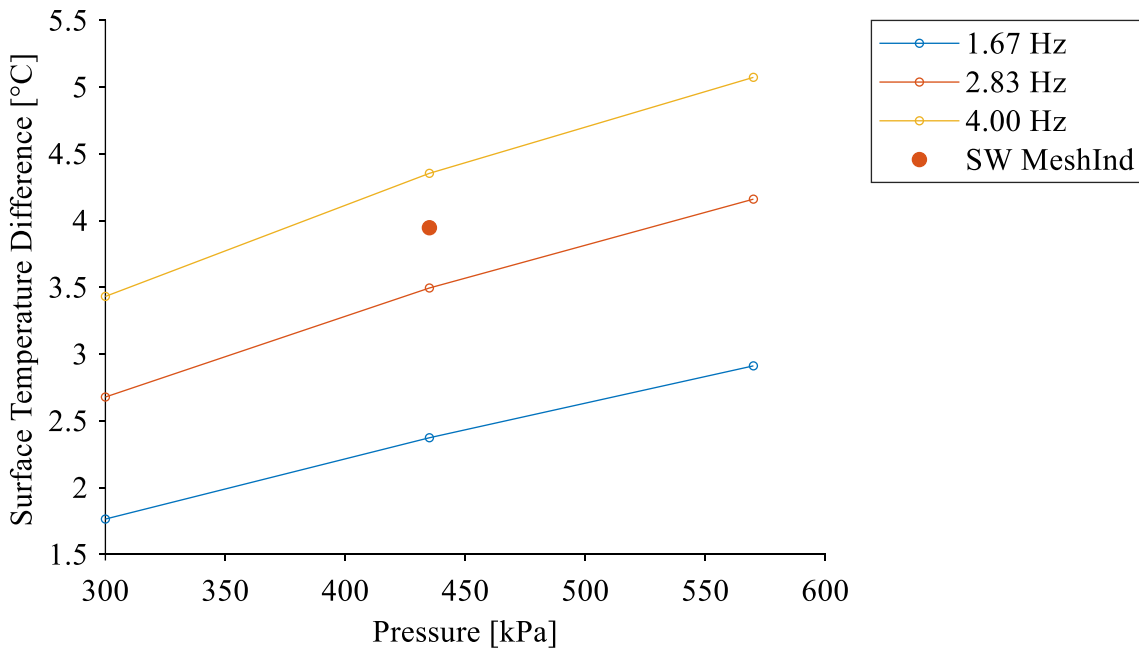


Figure I.2: Plot of absolute value solid temperature difference between analytical solution and simulation for varying engine pressure and speed for the cooling case.

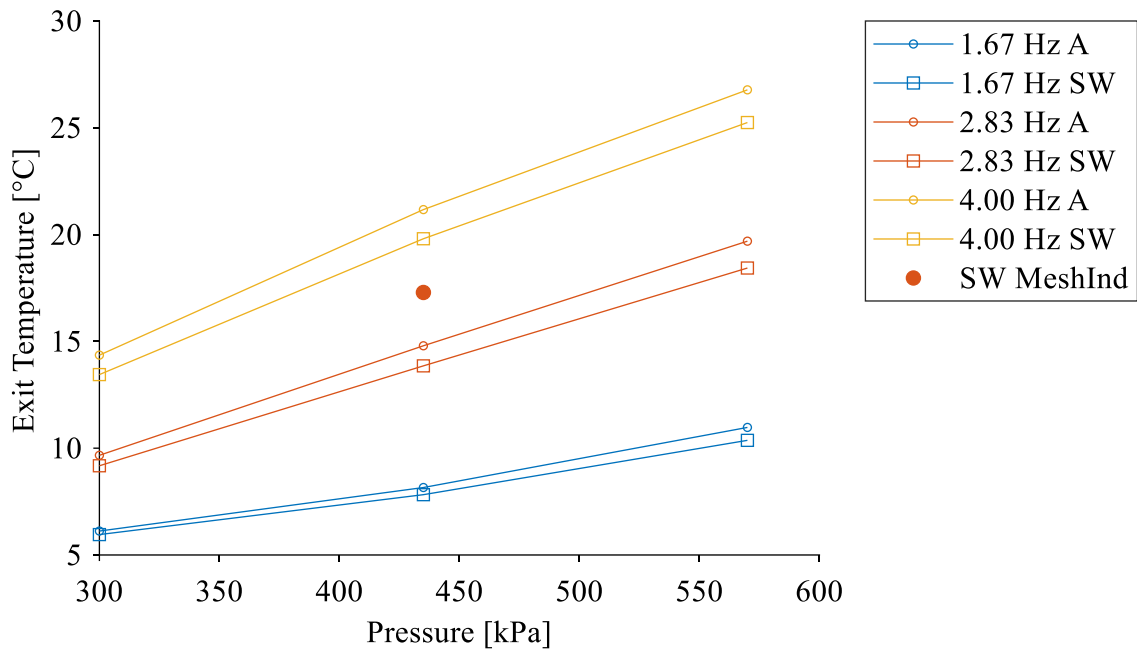


Figure I.3: Plot of exit air temperature determined from analytical solution and simulation for varying engine pressure and speed for the cooling case.

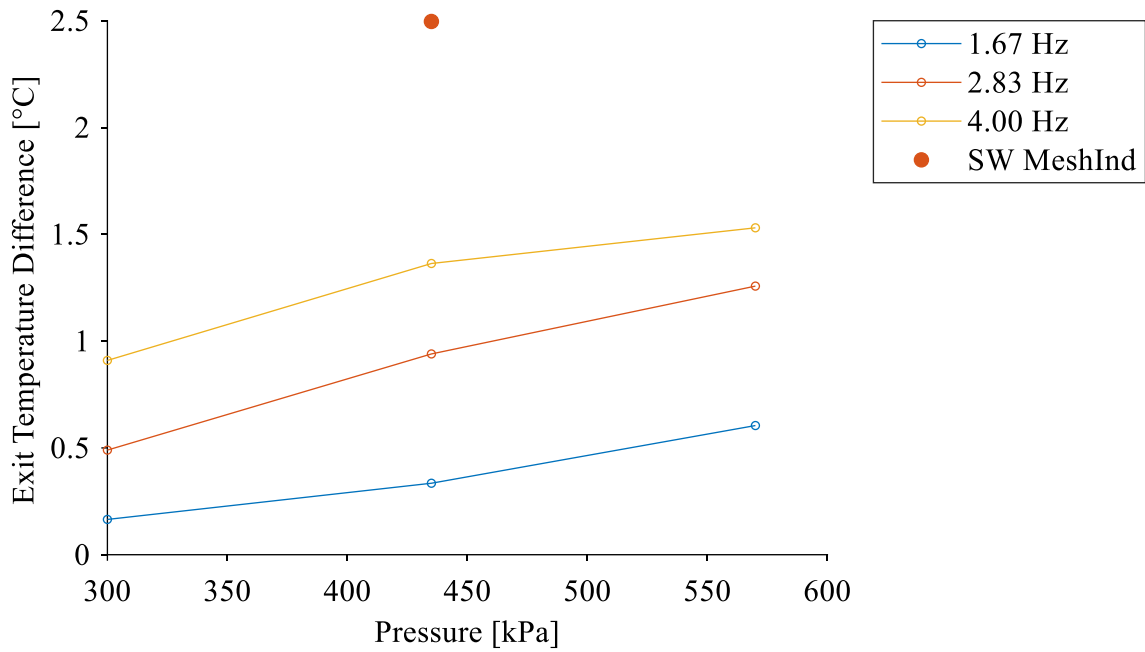


Figure I.4: Plot of absolute value exit temperature difference between analytical solution and simulation for varying engine pressure and speed for the cooling case.



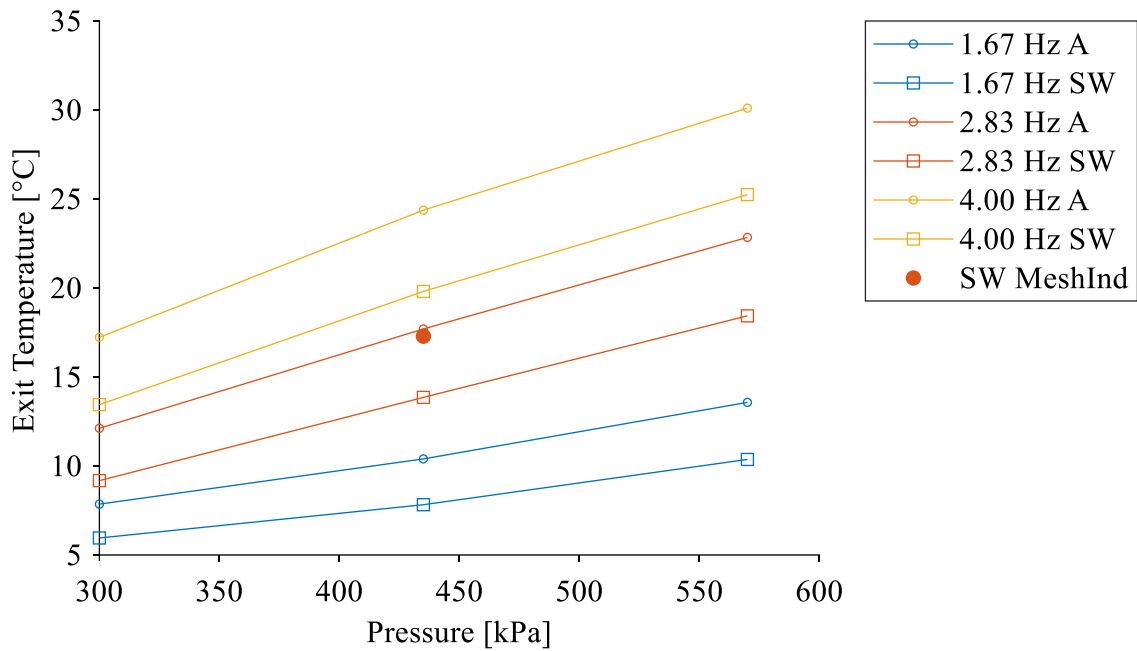


Figure I.5: Plot of exit air temperature determined from analytical solution using simulation solid temperatures and simulation solution for varying engine pressure and speed for the cooling case.

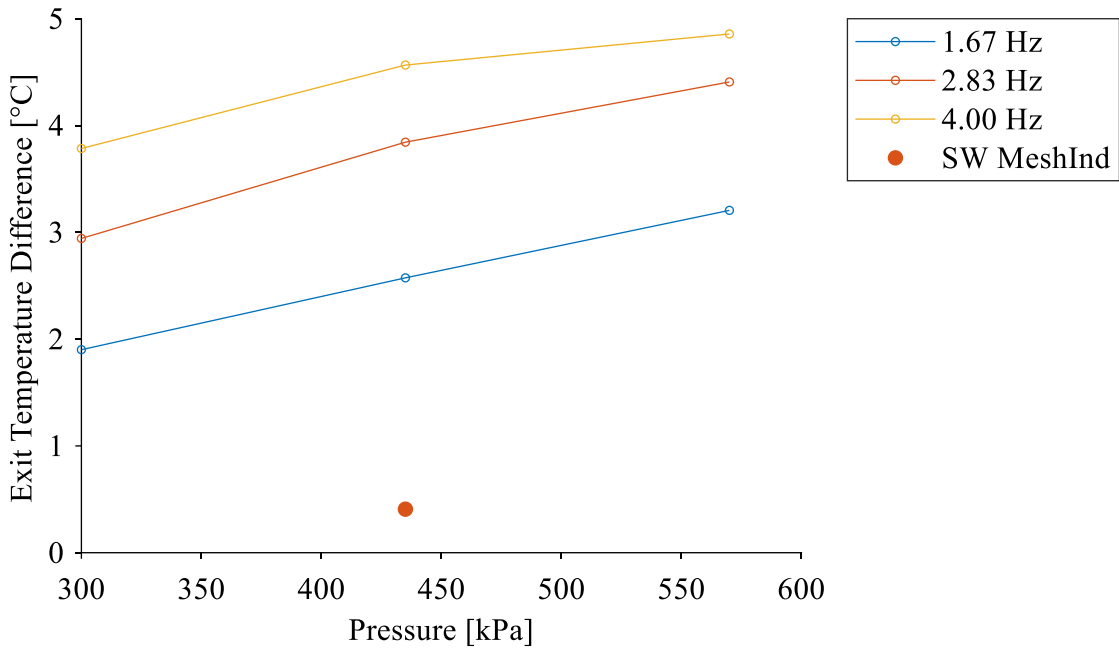


Figure I.6: Plot of absolute value exit air temperature difference between analytical solution using simulation solid temperature and simulation solution for varying engine pressure and speed for the cooling case.